

SCIENTIFIC PROGRAMME

- Fundamental processes
- Production of highly charged ion beams
- Production of high intensity ion beams
- Radioactive Ion Beams and charge breeders
- Controls and diagnostics
- Codes and simulations
- Beam extraction and transport
- Industrial application of new technologies

INTERNATIONAL ADVISORY COMMITTEE

Luigi Celona | Chair, INFN-LNS, Italy
Sandor Biri | ATOMKI, Hungary
Atsushi Kitagawa | NIRS-QST, Japan
Hannu Koivisto | JYFL, Finland
Guillaume Machicoane | NSCL-MSU, USA
Takahide Nakagawa | RIKEN, Japan
Vadim Skalyga | IAP-RAS, Russia
Thomas Thuiller | LPSC, France
Klaus Tinschert | GSI, Germany
Richard C. Vondrasek | ANL, USA
Mi-Sook Won | KBSI, South Korea
Daniel Xie | Lawrence Berkeley Lab, USA
Hong-Wei Zhao | IMP, China

LOCAL ORGANIZING COMMITTEE

Gaetano Agnello | INFN-LNS
Giuseppe Castro | INFN-LNS
Giacomo Cuffone | INFN-LNS
Santo Gammino | INFN-LNS
David Mascali | INFN-LNS
Lorenzo Neri | INFN-LNS
Pietro Piscioffa | University of Catania and INFN-LNS
Gino Sorbello | University of Catania and INFN-LNS
Giuseppe Torrisi | INFN-LNS



XXIII

INTERNATIONAL WORKSHOP ON ECR ION SOURCES

10-14 September 2018

Diocesan Museum, Catania, Italy



<http://ecris18.lsn.infn.it>



M. S. H. D. E. P. L. L.

PETRVS GALLETTI
PESSE FENIOME PACTIBVS RELEGGE
DE VIRE CUM PENSIOIBVS TRIVMS
ET JACOBVS ANSINCTOR
C. G. E. V. A. L. S.

A. G. O. M. E. T. I.

Foreword

The 23rd International Workshop on ECR Ion Sources (ECRIS2018), was held from 10th to 14th September 2018 in Catania, Italy.

The Electron Cyclotron Resonance ion sources (ECRIS) have a wide number of applications both in the accelerator facilities, increasing the beam energy and intensity, and in the industrial applications, making more efficient the industrial processes.

The workshop, organized by the Istituto Nazionale di Fisica Nucleare-Laboratori Nazionali del Sud (INFN-LNS), was aimed to highlight the state of the art in ECR Ion Sources Science&Technology, and to reinforce the common ground and synergies among the different actors in the field.

The workshop was held in the halls of the Catania Diocesan Museum, located in the heart of the old city with several archaeological and cultural attractions situated nearby.

The venue is placed at the foot of the Etna - the highest and most active Volcano of Europe - in a city that is now experiencing its third millenium of history since its establishment in 730 BC.

The International Advisory Committee (13 members from 10 countries) set up a scientific program of 45 talks and 22 posters covering themes relevant to the production of beams.

Along with “traditional” applications of ECRIS such as Radioactive Ion Beams and charge breeders, Production of highly charged ion beams, Controls and diagnostics, Production of high intensity ion beams, Codes and simulations, Beam extraction and transport, several new developments in the field were presented at the workshop. Among those are the efforts in the commissioning of the first 4th generation ECRIS working at 45 GHz at IMP and the progress of the 3rd generation sources at LBNL, IMP, RIKEN and MSU. The results of the commissioning of new sources named HIISI (JYFL), AISHa (INFN-LNS) and PS-ESS (INFN-LNS) have been presented. The status and upgrades of the ECR based ion sources in use on the major facilities worldwide (RIKEN, GANIL, CERN, Texas A&M, KVI, CERN, MedAustron, QST NIRS, KBSI, IMP, JYFL, LBNL, MSU, JINR, IAP-RAS) have been also reported. New ideas have been presented from different groups, in particular ATOMKI, JYFL and INFN-LNS teams presented innovative plasma diagnostic methods based on high resolution spectrometers and spectropolarimeters.

Three round tables have been also inserted in the program on subjects covering a key role in the future evolution of ECR ion sources: “Future magnetic system for ECRIS”, “Future of ECRIS: beyond the scaling laws?”, “Extraction and transport of intense beams” chaired respectively by D. Leitner (LBNL, USA), H. Koivisto (University of Jyväskylä, Finland) and P. Spaedtke (GSI, Germany). A total of 97 participants from 15 countries have been recorded.

For the sixth successive time Panttechnik awarded the Geller prize. The prize has been established 10 years ago for the 18th ECRIS workshop in Chicago (2008), and it rewards an exceptional contribution of young talented researchers (under 41) to the development of ECR sources. This time the committee chaired by Mi Sook Won (KBSI, South Korea) and consisting of Santo Gammino (INFN-LNS, Italy), Takahide Nakagawa (RIKEN, Japan), Daniel Xie (LBNL, USA) and Hog-Wei Zhao (IMP, China) selected Vadim Skalyga (IAP-RAS, Russia) for his outstanding contribution to the field of ECRIS working in gasdynamic regime.

Luigi Celona
ECRIS 2018 Chairman

Workshop Chair

Luigi Celona INFN-LNS, Italy

International Advisory Committee

Sándor Biri	ATOMKI, Hungary
Atsushi Kitagawa	NIRS, Japan
Hannu Koivisto	JYFL, Finland
Guillaume Machicoane	NSCL-MSU, USA
Takahide Nakagawa	RIKEN, Japan
Vadim Skalyga	IAP-RAS, Russia
Thomas Thuiller	LPSC, France
Klaus Tinschert	GSI, Germany
Richard C. Vondrasek	ANL, USA
Mi-Sook Won	KBSI, South Korea
Daniel Xie	Lawrence Berkeley Lab, USA
Hong-Wei Zhao	IMP, China

Local Organizing Committee

Gaetano Agnello	INFN-LNS, Italy
Giuseppe Castro	INFN-LNS, Italy
Giacomo Cuttone	INFN-LNS, Italy
Santo Gammino	INFN-LNS, Italy
David Mascali	INFN-LNS, Italy
Lorenzo Neri	INFN-LNS, Italy
Pietro Pisciotta	Univ. of Catania and INFN-LNS
Gino Sorbello	Univ. of Catania and INFN-LNS
Giuseppe Torrisi	INFN-LNS, Italy

Editorial board

Pietro Pisciotta	Univ. of Catania and INFN-LNS
Volker RW Schaa	GSI Helmholtzzentrum für Schwerionenforschung

Contents

Preface	i
Foreword	iii
Committees	iv
Contents	v
Papers	1
MOA3 – First Ion Beams Extracted from a New JYFL 18 GHz ECRIS: HIISI	1
MOB2 – Impact of Ion Source Stability for a Medical Accelerator	5
MOB3 – Commissioning of the AISHA Ion Source at INFN-LNS	10
MOC1 – Challenges and Prospects of Electron Cyclotron Resonance Charge Breeding	14
MOC2 – Charge-Breeding of Radioactive Ions at the Texas A&M Cyclotron Institute	20
MOC3 – Charge Breeding Time Studies With Short Pulse Beam Injection	24
MOC4 – SPIRAL1: A Versatile User Facility	29
MOC5 – $1 + / N +$ Method: Numerical Simulation Studies and Experimental Measurements on the SPIRAL1 Charge Breeder	34
MOC6 – Redesign of the GANIL GTS ECRIS for $1+/n+$ Studies	39
TUA1 – Development of Riken 28 GHz SC-ECRIS for Production of Intense Metal Ion Beam	44
TUA2 – Present Status and Future Prospect of Heavy Ion Radiotherapy	49
TUA3 – New 28-GHz Superconducting ECR Ion Source for Synthesizing New Super Heavy Elements of $Z > 118$	53
TUA5 – High Power Operation with SECRA-II Ion Source	58
TUB2 – Plasma Heating and Innovative Microwave Launching in ECRIS: Models and Experiments	63
TUB3 – A Possible Optimization of Electron Cyclotron Resonance Ion Sources Plasma Chambers	67
TUP01 – Status of the Carbon Ion Source Commissioning at MedAustron	71
TUP02 – An Irradiation Test Facility at INFN-LNS: Status and Perspectives	75
TUP03 – Production of Various Ion Species by Gas Pulsing Technique for Multi Ion Irradiation at NIRS-HEC Ion Source	79
TUP04 – Commissioning of the Proton-Linac ECR Source for FAIR	82
TUP06 – Progresses in the Installation of the SPES-Charge Breeder Beam Line	85
TUP07 – Addressing Contamination in ECR Charge Breeders	90
TUP09 – Operation of the PHOENIX V3 ECRIS Applying Double Frequency Heating	94
TUP10 – HTS Magnet Technology as Path to Fourth and Fifth Generation ECR Ion Sources	97
TUP11 – The First Measurement of Plasma Density by Means of an Interfero-Polarimetric Setup in a Compact ECR-Plasma Trap	102
TUP12 – Results of the Optical Emission Spectroscopy diagnostics of the ESS proton source	107
TUP13 – Characterization of ECR Plasma by Means of Radial and Axial X-Ray Diagnostics	111
TUP14 – Multi-Diagnostic Setup to Investigate the Two-Close-Frequency Phenomena	115
TUP15 – X-Ray Investigation on the Superconducting Source for Ions (SuSI)	120
TUP19 – Status Report on the AEER-U Ion Source at KVI-CART	125
TUP20 – Homogenous Dense Plasma Fluxes Formation From High Frequency ECR Discharge	128
TUP21 – Study of the Lead Evaporation from the Oven of the GTS-LHC Ion Source	131
TUP22 – Production of Intense Metal Ion Beams at the DC-60 Cyclotron	136
TUP23 – Operation of the GTS-LHC ECR Ion Source in Afterglow With Varying Klystron Frequency	139
TUP25 – Study of the Influence of Magnetic Field Profile on Plasma Parameters in a Simple Mirror Trap	144
TUP26 – A Particle-in-Cell/Monte-Carlo-Collision Code for the Simulation of Stepwise Ionization of Lithium in 2.45 GHz ECR Ion Source	148
TUP27 – Numerical Simulations of Magnetically Confined Plasmas	152
WEA3 – Plasma Instability Studies of the SuSI 18 GHz Source	157
WEA4 – Time Resolved X-Ray Measurements in a Simple Mirror Trap	162
WEA5 – Effect of the Two-Close-Frequency Heating to the Extracted Ion Beam and to the X-Ray Flux Emitted by the ECR Plasma	165
WEB1 – Simulations of ECRIS Performance for Different Working Materials	170
WEB2 – Plasma Modelization and Study for the PHOENIX V3 ECR Ion Source	176
WEB4 – Practical Use of High-Temperature Oven for 28 GHz Superconducting ECR Ion Source at RIKEN	180
THA2 – Point-like Neutron Emission Observation Using a Neutron Generator Based on a Gasdynamic ECR Ion Source	185

THA4 – Development of LECR4 Ion Source for Intense Beam Production and LECR5 for SESRI Project	188
THA5 – Gasdynamic ECR Tandem Ion Source for Negative Hydrogen Ion Production	191
THC1 – Development of 2.45 GHz ECR Ion Source at IMP	195
THC2 – Development of Test Bench of 2.45 GHz ECR Ion Source for RFQ Accelerator	198
THC4 – Development of Compact 2.45 GHz ECR Ion Source for Generation of Singly-Charged Ions	202
FRA1 – High Resolution Spectrometer Development for Use in ECR Ion Source	207
FRA3 – High Resolution Spectropolarimetry: From Astrophysics to ECR Plasmas	209
FRB2 – Impact of the Two Close Frequency Heating on ECRIS Plasmas Stability	214
Appendices	219
List of Authors	219
Institutes List	223
Participants List	227

FIRST ION BEAMS EXTRACTED FROM A NEW JYFL 18 GHz ECRIS: HIISI*

H. Koivisto[†], T. Kalvas, R. Kronholm and O. Tarvainen, Department of Physics, University of Jyväskylä (JYFL), 40500 Jyväskylä, Finland

Abstract

A new 18 GHz ECR ion source HIISI is under commissioning at the Accelerator Laboratory at the University of Jyväskylä (JYFL). The main purpose of HIISI is to produce high-intensity ion beams for nuclear physics programme and high-energy beam cocktails for radiation effects testing of electronic components. The initial commissioning results in (18+14) GHz operation mode using 24 segment sextupole (1.3 T) were performed in autumn 2017. A stronger 36 segment sextupole (1.42 T) was constructed and tested during the spring 2018 demonstrating improved performance of HIISI. As an example, Ar¹²⁺ intensity of 0.57 mA was reached with 19.5 kV extraction voltage and total microwave power of 2.35 kW. In this article we will present the latest development work, ion beam intensities of oxygen, argon and xenon, and future prospects of HIISI.

INTRODUCTION

The K130-cyclotron [1] at JYFL is equipped with an AECR-U type, room temperature (RT) 14 GHz ECR ion source [2] for heavy ion production. The old 14 GHz ECR ion source has worked reliably for more than 60000 plasma-on hours since its construction in 1999. Most of the beams have been produced from natural or enriched gases or by using the MIVOC method [3]. Typical requested energy of the projectile is 5 MeV/u, which requires a q/A -ratio of 0.2. For example, in the case of argon and xenon ion beams charge states of 8+ and 27+ are often needed. Due to the demand for more intensive beams of highly charged ions and also for higher energy for irradiation tests of space electronics the project for a new ECR ion source was initiated in 2013. At the end of 2013 the Academy of Finland funded the JYFL Accelerator Laboratory to design and construct an 18 GHz ECR Heavy Ion Ion Source Injector (HIISI, ref. [4-6]). The objective of HIISI was two-fold: 1) the intensity of medium charge state ion beams, such as Ar⁸⁺ and Xe²⁷⁺ ($E \approx 5$ MeV/u), has to be increased by a factor of 5 and 2) the energy of heavy ion beams ($A > 100$) has to exceed the value of 15 MeV/u. The first requirement is set by the nuclear physics program and the latter one by the irradiation testing program for the space electronic components. The testing program requires 10^6 particles/s/cm² on the irradiation target station. In the case of xenon, which is the heaviest element in 16 MeV/u

cocktail, this corresponds to charge state of 44+, and the extracted ion beam intensity of about 10 nA when the total transport efficiency of accelerator facility is taken into account. In 2013, the presented requirement was beyond any existing RT-ECRIS, which forced us to design and construct a new room temperature 18 GHz ECRIS. In this article the present status of HIISI will be given.

HIISI SPECIFICATIONS

In 2013 only three ECRISs were able to produce the xenon ion beam intensity (Xe⁴⁴⁺/10 nA) required by the irradiation testing program at JYFL. Those ECR ion sources are VENUS [7], SECRAL [8] and SUSI [9]. The experimental data and operation parameters revealed that SUSI is able to produce the Xe⁴⁴⁺ ion beam intensity of about 100 nA in 18 GHz operation mode ($B_{inj} = 2.8$ T/ $B_{ext} = 1.3$ T and $B_{rad} = 1.35$ T) and at the microwave power of about 4 kW. In addition, it has produced 730 μ A of Ar¹²⁺ with total microwave power of 3.8 kW. The aforementioned magnetic field configuration can be obtained by using normal conducting solenoids and permanent magnets. Consequently, it was decided that SUSI magnetic field configuration and plasma chamber dimensions will be used as the design goal of HIISI.

HIISI has two innovative features, which make it special compared to any other RT ECR ion source: 1) its permanent magnet array is vacuum insulated and 2) cylindrical symmetry of the plasma chamber has been broken. Both features have thoroughly been described in ref. [4 – 6]. The vacuum insulation allows the cooling of the permanent magnets, which improves the properties of the permanent magnets. The intrinsic coercivity H_{cJ} and residual magnetic induction B_r for the selected magnet grade (N45SH) increase 0.55 %/°C and 0.12 %/°C, respectively, when the temperature of the permanent magnet decreases. The HIISI design allows cooling of the permanent magnets to -20 °C. This will increase the H_{cJ} and B_r values from 1595 kA/m and 1.35 T (at 20 °C) to about 2100 kA/m and 1.42 T (at -20°C), respectively. According to demagnetization analysis HIISI is safely operated as long as the permanent magnet temperature does not exceed room temperature.

The cooling capacity of the HIISI plasma chamber allows the use of microwave power of up to 4 kW. The cooling geometry of the plasma chamber and the refrigerated PM array have been presented thoroughly in references [4-6]. Further development of the refrigerated permanent magnet array could make the construction of 1.5 T ECR ion source sextupole possible. This would

*The project has received funding from the EU Horizon 2020 research and innovation programme under grant agreement No 654002 and the Academy of Finland under the Finnish Centre of Excellence Programme 2012-17 (Nuclear and Accelerator Based Physics Research at JYFL

[†] hannu.koivisto@phys.jyu.fi

Content from this work may be used under the terms of the CC BY 3.0 licence (© 2018). Any distribution of this work must maintain attribution to the author(s), title of the work, publisher, and DOI.

allow plasma heating at the microwave frequency of 21 GHz.

Two complete sextupoles have been constructed for HIISI: 1.32 T (24-segm.) and 1.42 T (36-segm.) sextupoles. The 24-segment sextupole was constructed for the testing and mastering of the new technology and subsequent transfer of the new experience and know-how for a more advanced and complicated 36-segment configuration. The magnet grade of N45SH was used in both configurations. The HIISI specifications are presented in Table 1.

The layout of the HIISI ion source is presented in Fig. 1. The main design objective, to match the magnetic field configuration of HIISI with that of SUSI, was met with the aid of the afore-mentioned innovative solutions for the permanent magnet array and for the plasma chamber.

The microwave power is injected using 3 separate waveguide lines: 1) WR-62 waveguide for 18 GHz/2 kW klystron, 2) WR-62 waveguide for 14.5 GHz/2 kW klystron and 3) WR-75 waveguide for 8-18 GHz TWTA/250 W. So far, HIISI has been operated in (18 + 14.5) GHz operation mode at the power of up to 2 kW and 0.4 kW, respectively. In accordance of an updated plan the TWTA waveguide line will be dedicated for 2nd 18 GHz/2kW klystron increasing the total capacity at this frequency to 4 kW.

The ions are extracted through an 8 mm plasma electrode aperture and through a 25 mm acceleration gap at the voltage ranging from 10 kV to 20 kV. Downstream from the puller the beam is focused by two accelerating einzel lenses. The beam is further focused and matched

into the double focusing, 90-degree, $r = 550$ mm, bending magnet using a large aperture (144 mm) solenoid magnet.

Table 1: HIISI Specifications

Main frequency	18 GHz/2 kW
Secondary frequency	14.5 GHz/2 kW
TWTA	8-18 GHz/250 W
$B_{inj}/B_{min}/B_{ext}$ (nominal)	2.7/0.43/1.3 T
B_{end} (24/36-segm.)	1.32T/1.42 T
V (inside resonance surface)	0.36 litres/18 GHz
Resonance length (on axis, nom. B field configuration)	130 mm (18 GHz)
Plasma chamber dimensions	d = 100 mm / L = 400 mm
Cooling capacity of plasma chamber	4 kW
HV (presently limited to)	≤ 20 kV/5 mA
Plasma electrode aperture	8 mm in diam.
Power consumption of coils (nom. B fields)	150 kW
Inj./Ext. pressure	$1.7 \times 10^{-7}/2 \times 10^{-8}$ mbar

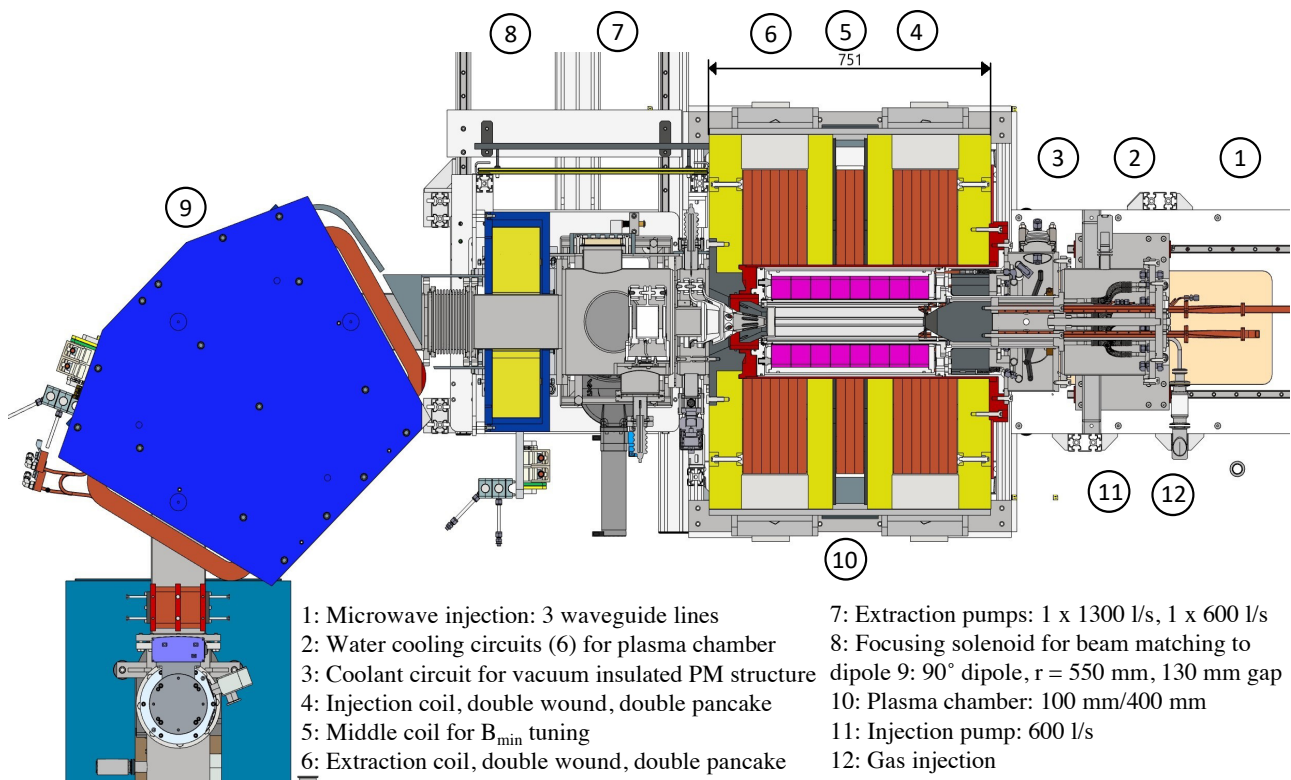


Figure 1: Layout of the HIISI ion source and beam transport line.

HIISI PERFORMANCE

The testing of HIISI was started in September 2017 by producing highly charged ion beams from oxygen and argon plasmas. During the first days the intensity of 0.5 mA was reached for O^{7+} and Ar^{12+} ion beams demonstrating a performance of HIISI. The source was operated with total microwave power up to 2.4 kW (18 GHz + 14.5 GHz). The refrigerated permanent magnet structure was kept at 10°C. It was also found out that the cooling of the vacuum chamber, which provides the vacuum insulation for the permanent magnet sextupole was inadequate: we were able to operate the ion source only about 2 hours, at around the microwave power of 2 kW, before the set value for the temperature interlock was reached. This problem was solved for the 36-segment PM sextupole. The record intensities for oxygen, argon and xenon are presented in Table 2. The results were obtained regardless of relatively high background pressure inside the injection chamber of HIISI (1.7×10^{-7} mbar).

Table 2: Record Intensities for Oxygen, Argon and Xenon.

oxygen		argon		xenon	
q	I [μ A]	q	I [μ A]	q	I [μ A]
6+	1320	11+	680	26+	300
7+	620	12+	570	27+	196
		13+	330	29+	60
		14+	195	30+	46
		16+	54	31+	27

HIISI vs JYFL 14 GHz ECRIS

The 36-segment sextupole (1.42 T) and the modifications for the HIISI injection geometry were completed in spring 2018. This allowed us to start an active testing campaign of HIISI to better define its performance and the subjects for further development. Figure 2 shows the argon charge state distribution when HIISI was tuned for Ar^{12+} ion beam. The figure also shows the record argon ion beam intensities produced by the JYFL 14 GHz ECRIS. The comparison demonstrates that the requirement set by the nuclear physics program has been met.

The HIISI extraction optics has been designed for the total ion beam current and the extraction voltage of up to 5 mA and 20 kV, respectively. The first experiments have demonstrated that the extraction design does not allow to exploit the full potential of HIISI. The argument is supported by three observations: the intensity of Ar^{12+} ion beam increased as a function of 1) the acceleration voltage, 2) the argon feed rate and 3) microwave power. The intensity of Ar^{12+} increased 5-10 μ A per an increment of 0.5 kV. The acceleration voltage was limited to 19.5 kV because at higher values high voltage sparking was observed inside the extraction region. It was also noticed that the Ar^{12+} ion beam intensity increased with the feed rate of argon. After the scanning of the spectrum shown in Fig. 2, the feed rate of argon was increased by a single step of the gas valve. The intensity increased about 20 μ A resulting in an immediate high voltage spark destroying for example a HV power supply. The extraction has to be upgraded before the high intensity ion beam testing is continued.

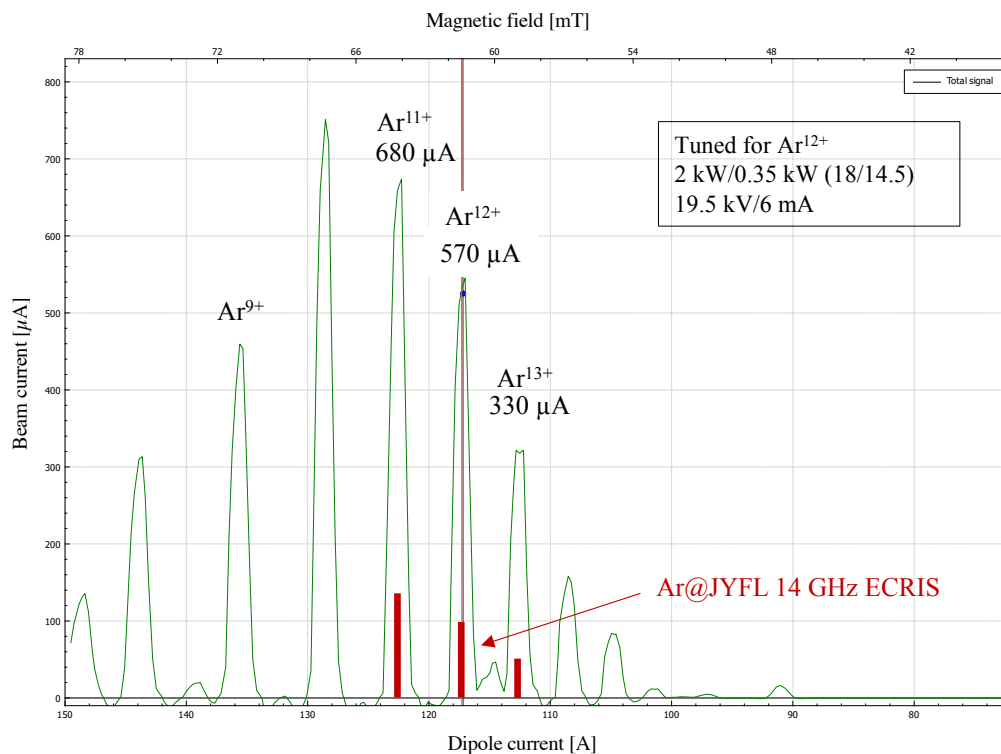


Figure 2: Argon charge state distribution produced by HIISI ion source at JYFL.

Performance vs Space Electronics Irradiation

In order to meet the other requirement of the project (≥ 16 MeV/u) the charge state of at least $44+$ has to be produced in the case of xenon. Due to the extremely challenging nature of the project the ultimate goal set by the irradiation testing program was decided to be pursued via an intermediate step (12.5 MeV/u, Xe^{40+}). The first tests were realized at the end of 2017 using the 24-segment sextupole ($B_{rad} = 1.32$ T). Figure 3 shows the intensity of Xe^{40+} ion beam, measured at the irradiation effect testing station, as a function of the microwave power (18 GHz). As the figure shows the required intensity level of 10^6 counts/s/cm² was easily reached. The figure also shows that the intensity increased vigorously as a function of the microwave power and does not show any sign of saturation below the maximum available microwave power of 2 kW. The test was later realized with the 36-segment sextupole ($B_{rad} = 1.32$ T) resulting in about 3-fold ion beam intensity.

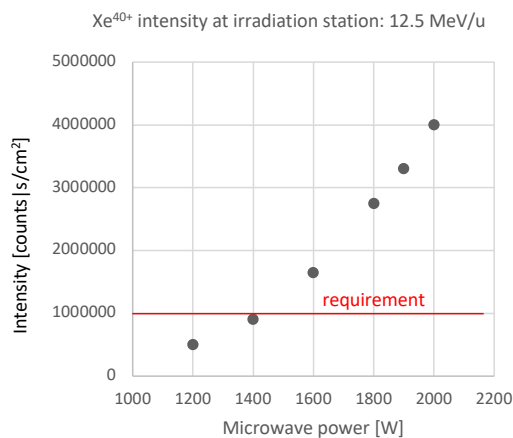


Figure 3: Xe^{40+} particle intensity (12.5 MeV/u) on the irradiation target as a function of the microwave power. The red horizontal line shows the intensity requirement.

CONCLUSION AND FUTURE PROSPECTS

The first experiments have already demonstrated a high performance and potential of HIISI. The experiments also demonstrated that HIISI accepts the microwave power of 2 kW (18 GHz) without any sign of saturation. Consequently, a new 18 GHz/ 2 kW klystron was purchased in order to duplicate the plasma heating power. The experiments have also given valuable information about the most critical factors limiting the beam intensities extracted from HIISI. During the coming months, i.e. during the first half of 2019, two important upgrades will be realised: 1) the microwave power upgrade and 2) the extraction upgrade. The new 18 GHz/ 2 kW klystron has arrived and will be connected to HIISI in the beginning of 2019. The new klystron will be

connected to the waveguide line originally reserved for the TWTA. This allows us to measure the intensity of Xe^{40+} and Xe^{44+} ion beams as a function of the total microwave power up to 4 kW. During the test, the total ion beam current extracted from the ion source will be limited to 5 mA. The design work for the extraction upgrade will be started in the beginning of 2019. The upgraded extraction has to be capable of extracting the total beam intensities of up to 10 mA. In addition, the high voltage capabilities of HIISI will be improved to make the testing and operation at the acceleration voltage of at least 25 kV possible. The HIISI waveguide lines and the injection side will be modified later to maximize the source performance in 3 and 4 -frequency operation modes.

ACKNOWLEDGEMENTS

This work has been supported by the EU HORIZON2020 programme “Infrastructures”, project number: 654002 (ENSAR2) and by the Academy of Finland under the Finnish Centre of Excellence Programme 2012-2017 (Nuclear and Accelerator Based Physics Research at JYFL).

REFERENCES

- [1] E.Liukkonen, *13th. Intern. Conf. on Cyclotrons, Vancouver*,(1992), p. 22.
- [2] H. Koivisto, P. Heikkinen, V. Hänninen, A. Lassila, H. Leinonen, V. Nieminen, J. Pakarinen, K. Ranttila, J. Ärje and E. Liukkonen, *Nucl. Instr. and Meth. in Phys. Res., B*, vol. 174, (2001), p. 379.
- [3] H. Koivisto, J. Ärje and M. Nurmi, *Nucl. Instr. and Meth. in Phys. Res., B*, vol. 94, p.291, (1994), .
- [4] H. Koivisto, O. Tarvainen, T. Kalvas, K. Ranttila, P. Heikkinen, D. Xie, G. Machicoane, T. Thuillier, V. Skalyga, Izotov, *Proceedings of ECRIS-2014 (JACOW), Nizhny Novgorod, Russia*, (2015), p. TUOMMH05, ISBN 978-3-95450-158-8.
- [5] T. Kalvas, O. Tarvainen, H. Koivisto, K. Ranttila, *Proceedings of ECRIS-2014 (JACOW), Nizhny Novgorod, Russia*, (2015), p. WEOMMH04, ISBN 978-3-95450-158-8.
- [6] H. Koivisto, T. Kalvas, O. Tarvainen, J. Komppula, J. Laulainen, R. Kronholm, K. Ranttila, J. Tuunanen, T. Thuillier, D. Xie and G. Machicoane, *Rev. of Sci. Instrum.*, vol. 87(2), (2016), 02A725.
- [7] C. Lyneis, D. Leitner, M. Leitner, C. Taylor, and S. Abbott, *Rev. Sci. Instrum.*, vol. 81, 02A201 (2010).
- [8] H. W. Zhao et al., *Rev. Sci. Instrum.* vol.77, 03A333 (2006).
- [9] C.M. Lyneis, D. Leitner, S.r. Abbot, R.D. Dwinell, M. Leitner, C.S. Silver, and C. Taylor, *Rev. Sci. Instrum.*, vol. 75, pp. 1389 (2004).

IMPACT OF ION SOURCE STABILITY FOR A MEDICAL ACCELERATOR

N. Gambino[†], S. Myalski, L. Adler, F. Ecker, A. De Franco, F. Farinon, G. Guidoboni, C. Kurfürst, M. Pivi, C. Schmitzer, I. Strasik, A. Wastl, EBG MedAustron, Wr. Neustadt, Austria
L. Penescu, Abstract Landscapes, Montpellier, France

Abstract

MedAustron is a synchrotron-based hadron therapy center located in Lower Austria. Accelerated proton beams with energies of 62-252 MeV/u are used to treat patients since 2016. The carbon ion beam is currently under commissioning and will provide treatment in 2019 with energies of 120-400MeV/u. Two of the four irradiation rooms are used for clinical treatment while the preparation of the Gantry beam line is ongoing. Proton beams of up to 800 MeV will be provided for non-clinical research. The Injector features three identical ECRIS from Pantechnik, two of which are used to generate the proton and the carbon beam respectively. The medical environment of the accelerator puts strict requirements on the ion source long-term stability operation. The extracted beam current from the source allow for maximum current fluctuations on the order of $\pm 2.5\%$ on continuous run. In this work we discuss the impact of the ion source performances on the characteristics and stability of the entire accelerator. Further, we discuss the latest progress on carbon commissioning and the future perspectives with particular emphasis on the source requirements.

INTRODUCTION

The MedAustron is a synchrotron-based therapy center for cancer treatment. The design of the accelerator is based on PIMMS and CNAO [1,2]. Currently 26 patients (fractions) per day are treated with proton ion beams since 2016. Medical treatment with carbon ions is planned to start in 2019 [3]. A proton beam up to 800 MeV/u will be provided for non-clinical research.

The Injector shown in Fig. 1 features three identical Superanogan ECRIS from Pantechnik. One is reserved for proton beams production and one for carbon beams production. The third is foreseen as future use for clinical and non-clinical research. The extracted beam from the source at 8 keV/u is transported through the LEBT line to the linear accelerator. The LINAC contains a Radio Frequency Quadrupole (RFQ) module which accelerates the beam to 400 keV/u followed by a Buncher and an IH-Tank cavity where the energy reaches 7 MeV/u and finally by a Debuncher cavity. Through the Mid Energy Beam Transport (MEBT) line the beam is then injected in the synchrotron where it reaches the clinical and non-clinical energies mentioned before. A slow extraction 3rd order resonance method via Betatron Core is used to extract the particles

from the synchrotron. Through the High Energy Beam Line (HEBT) the beam is sent to four available irradiation rooms: IR1 with horizontal beamline for non-clinical research, IR2 with a horizontal and a vertical beamline, IR3 with a horizontal beamline and IR4 with a proton Gantry. The weekly machine uptime during clinical operation between 90% and 97% [4].

THE IONS SOURCE

The identical design and the availability of three independent source lines allows for parallel running of the sources and for source switching in case of emergency. The ion beam in the source is produced through the Electron Cyclotron Resonance (ECR) heating mechanism [5]. The neutral gas is brought into a state of plasma magnetically confined in the vacuum vessel and the ions are extracted from the chamber with a dedicated extraction system. The Superanogan of Pantechnik has been described in detail in [6]. It operates at 14.5 GHz heating frequency and is it entirely equipped with permanent magnets both for the radial magnetic field than for the longitudinal magnetic field with a B_{ECR} of 0.5 T. An axial mirror ratio $B_{\text{max}}/B_{\text{min}}$ about two times higher than the ECR resonance magnetic field is obtained [5].

The plasma has limited contact to the chamber walls and the high charge state ions concentrate in the center of the extracted beam with a triangular intensity distribution. The longitudinal beam profile depends mainly on extraction parameters with respect to the plasma potential. The source body is placed at 24 kV, while a puller electrode is placed at negative potentials of about 2 kV to accelerate the beam towards the focus. The focus electrode on the order of 1.5 kV is fine tuned to adapt the beam size to the focal point of the dipole magnet for a good transmission into the beam line and further matching into the RFQ. The DC Bias tip, introduced from the backside of the vacuum chamber into the plasma, reduces the ion losses towards the injection. The RF tuner position is used to reduce the reflected power. The typical source parameters used for the proton and the carbon source are indicated in table 1:

[†] nadia.gambino@medaustron.at

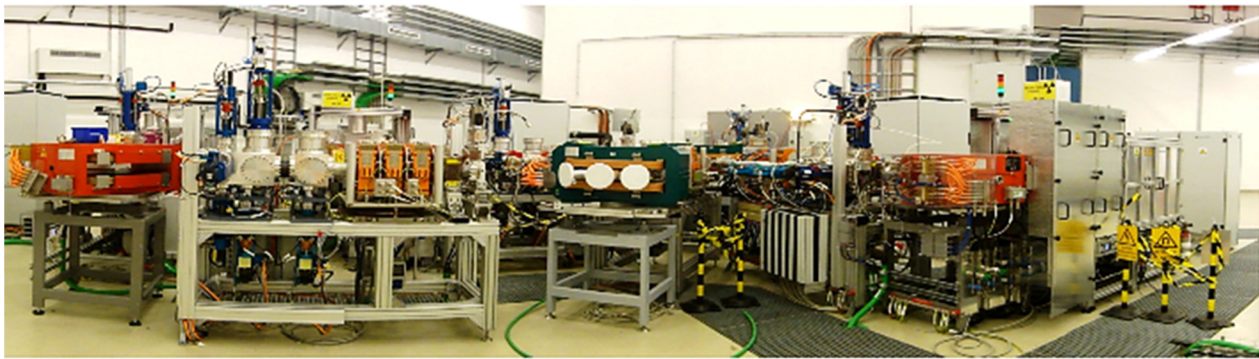


Figure 1: Injector Hall at MedAustron. The source is located within the lead protected cabinet visible on the right side of the figure. The complete layout of the source is shown in [6].

Table 1: Typical Source Parameters for Medical Treatment

Parameter	Proton Source	Carbon Source
RF Frequency (GHz)	14.451	14.464
RF Power (W)	8-10	90-160
Gas Type	H ₂	CO ₂ +He
Extracted Current (µA)	660	95-150

SOURCE PERFORMANCES VERSUS ACCELERATOR STABILITY

The stability of the extracted source current is fundamental for medical treatment. The commissioning of the source occurs according to the main requirements of the entire accelerator (i.e. acceptance window of the RFQ, required intensity into the treatment room etc.). For the acceptance tests, once the stable source settings are found, the extracted current needs to be monitored for more than 24 hours [6]. The extracted current stability needs to be on the order of $\pm 2.5\%$. The source performances are constantly monitored via a current transformer (CTA) located into the LEBT (non-destructive BD device) during the daily beam quality assurance before clinical treatment starts (i.e. the daily QA) (mainly for the proton source) or via destructive devices (Faraday Cups) during beam commissioning (currently mainly for the carbon source). Figure 2 shows the daily recorded current from the proton source with the LEBT-CTA and the current recorded with the current transformer in the MEBT line. One can observe how the current is slowly drifting over months towards higher values for fixed source parameters (within 6 months from 675 uA to 700 uA, i.e. of 4%). Also, it was measured that the source emittance slowly drifted towards bigger values with respect to the reference. In turn, this drift influences the intensity into the room, which slowly decreases over time and leads to longer treatments times. Longer treatment time, i.e. the in-room time is not beneficial for the patient neither for an efficient treatment and this is why to eventually recover the intensity by recommissioning the source.

After the source recommissioning, the MEBT-CTA recovers of about 20% and also the shot to-shot reproducibility improves. It is also interesting to note that while the MEBT-CTA increases, the LE-CTA decreases before and after the recommissioning. During recommissioning it was needed to find a complete new set-point for the source due to a drift of emittance which was increasing towards higher values with respect to the reference. The source recommissioning occurs within a strict release process, which has to be planned in advance. It is not possible to change or adapt the source parameter during clinical treatment without having first a detailed impact of analysis of the change and the by having the approval from the QA department. Once a stable set-point is found it is not possible to adapt any parameter in case of need, but a new release has to be planned.

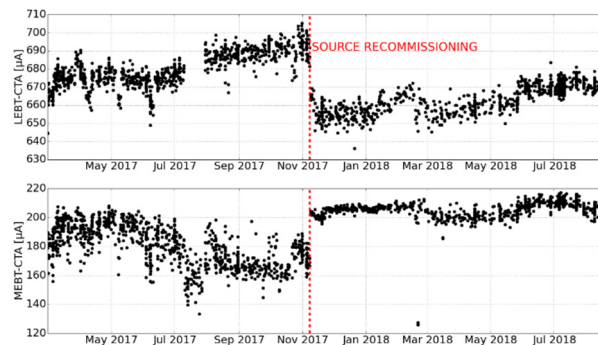


Figure 2: LEBT (top) and MEBT (down) current versus time measured during the daily quality assurance of the beam before medical treatment, i.e. during beam QA. The main source parameters that are tuned are: the RF Frequency and the forward RF power, the extraction voltages such DC Bias and Focus Voltage, the gas amount injected into the plasma chamber, the RF Tuner position and the solenoid current placed at the entrance of the RFQ.

The overview on how the source recommissioning impacts over the whole machine performances is visible in Fig. 3. In this figure, the transmission over the different sections of the accelerator is shown. The LEBT to LINAC transmission is improved of almost 10%, and, overall the transmission is improved in the entire accelerator. The number of

extracted particles increases from about $1.1 \cdot 10^9$ to $2.1 \cdot 10^9$ particles at extraction.

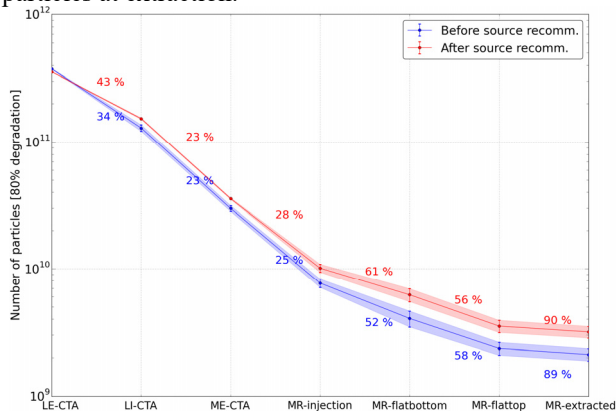


Figure 3: Transmission efficiency in the different sections of the accelerator before and after source recommissioning from LEBT to LINAC, from LINAC to MEBT, from MEBT to synchrotron injection (MR-injection), from injection to capture (MR-Flatbottom), from start to end acceleration (MR-Flattop), from end acceleration to extraction (MR-extracted).

CARBON SOURCE COMMISSIONING PHASE II

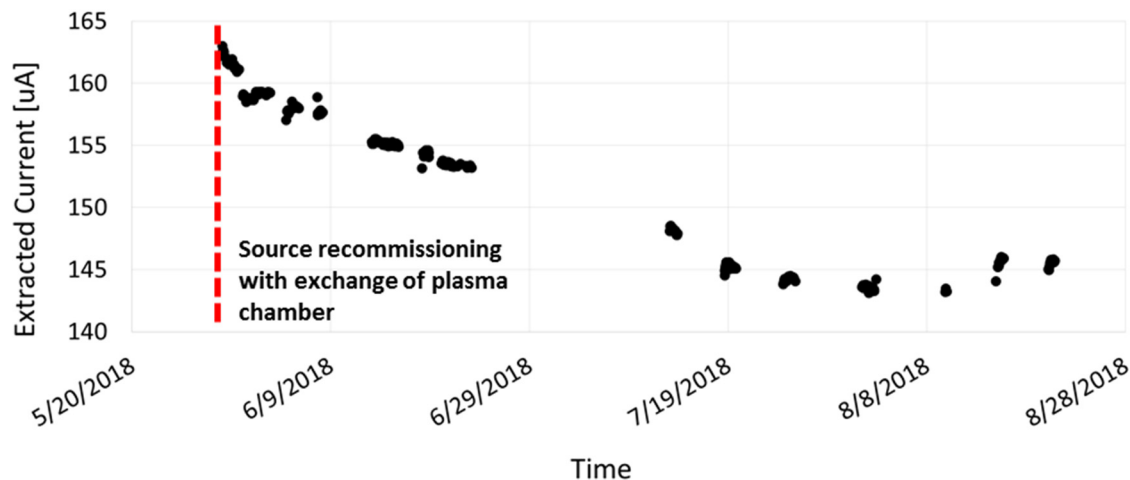


Figure 4: Extracted current vs. time recorded with a Faraday Cup since last plasma chamber exchange. It is not possible to record the current with the Faraday Cup continuously due to ongoing beam commissioning with carbon.

To be able to investigate such scenario we first of all performed a frequency tuning and measured the extracted current versus the resonance frequency below 14.5 GHz. The results are shown in Fig. 5 together with the reflected power measured at 30 W of forward RF Power. Even if different resonance peaks can be found within 14 GHz and 14.50 GHz we defined as “unstable range” the one between 14 to 14.4 GHz. The unstable range is hardly tunable due to high reflected powers when ramping up the RF power even by tuning the other source parameters at the detected resonance points. In the stable range instead, it is possible

First carbon source commissioning occurred at the end of 2017 together with the rest of the injector (LEBT and LINAC) [6]. Source was recommissioned at the end of May 2018 after the plasma chamber was exchanged due to carbon deposition on the chamber wall. Since end of May, the carbon source runs continuously over 24 hrs end will be used for clinical treatment in 2019. Current studies focus on source degradation and long-term maintenance strategies. As it can be seen in Fig.4, after the plasma chamber was exchanged, the source current could not be stabilized immediately and exponentially dropped from 163 uA to 145 uA within about 45 days under the circumstances of not changing or adapting any source parameter. This strategy aims to have a realistic view of the source behavior during the future clinical treatment. Since end of July the source reached a stable point at around 143 uA. This drift of course cannot be accepted once the source will be used for clinical treatment due to the stability requirements. Therefore, the latest studies focused on finding a stable set-point where the extracted current can be decreased or increased according to the intensity requirements into the treating room and to make the RF power as a clinically modifiable parameter. Ideally, this will be done by only adapting the RF forward power without necessarily tuning the other source parameters out of an official release process.

to ramp up the RF power while keeping a low reflected power.

In the stable range it is also possible to keep a low signal to-noise ratio for a large range of powers as shown in Fig.6 where the extracted current versus the RF power is plotted for three different frequencies. As it can be seen from this figure, the best results in terms of low signal to-noise ratio in a large range of RF powers are obtained around 14.46 GHz. Also, the emittance does not change while ramping up the power in the stable range [7].

Content from this work may be used under the terms of the CC BY 3.0 licence (© 2018). Any distribution of this work must maintain attribution to the author(s), title of the work, publisher, and DOI.

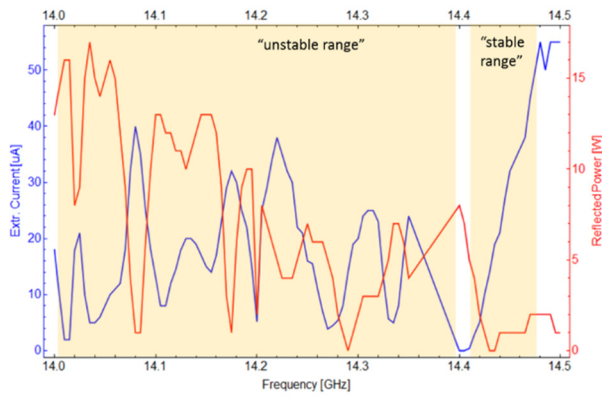


Figure 5: Extracted current and reflected power vs. frequency performed at low RF power (30 W).

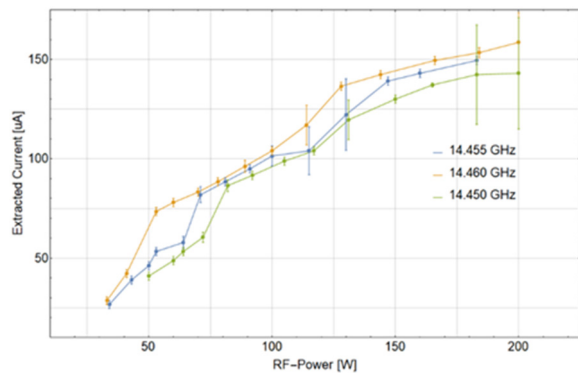


Figure 6: Extracted Current vs. RF Power for three different frequencies.

Once the stable set-point is found, the intensity into the room is measured as a function of the RF power. The highest intensity into the room that was measured so far is of $1.6 \cdot 10^9$ particles with an RF power of 163 W and an extracted current from the carbon source of around $150 \mu\text{A}$ as shown in Fig. 7a. We then reduced the source power due to our target intensity target at flattop (CTS-target) and into the room (DDS-target), i.e. measured through the Dose Delivery System developed from CNAO [8]. With a RF frequency of 14.455 GHz the target is reached with about 98 W. With a RF frequency of 14.464 GHz the target is reached with 89 W as shown in in Fig.7b. In this case we also decreased the DC Bias Voltage of 100 V to reduce its degradation over time and adapted the focus voltage. The limitation of intensity is due to safety reasons related to the maximum intensity allowed into the synchrotron for medical treatment.

It is very important to emphasize that for this stable set-point it is possible to increase or decrease the RF power without affecting the transmission from LEPT to LINAC which is kept at a constant value of around 60% as shown in Fig.8. Thus, the goal of just tuning the RF power according to the needed intensity into the room is reached without necessarily tuning the other source parameters. This is beneficial to compensate for the current decrease shown in Fig.4.

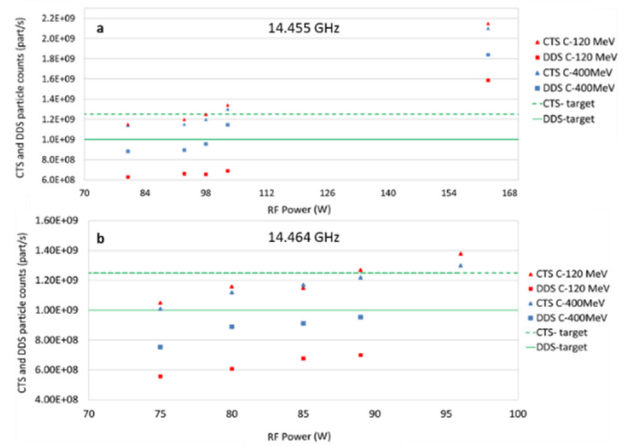


Figure 7: Particle intensity measured into the room with the Dose Delivery System (DDS) and at flattop (CTS) for carbon at 400 MeV and for carbon at 120 MeV with no degradation as a function of source RF Power for 14.455 GHz (a) and 14.464 GHz (b). The current target for the CTS and DDS are also indicated in the figures which corresponds respectively to $1.25 \cdot 10^9$ and $1 \cdot 10^9$ particles maximum.

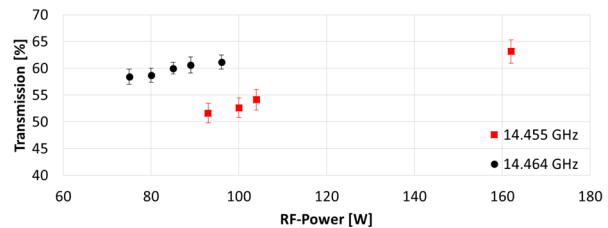


Figure 8: Transmission from LEPT to LINAC versus RF Power for 14.455 GHz and 14.464 GHz.

CONCLUSIONS AND FUTURE PERSPECTIVES

In this work it was shown how the source operation and stability over long term impacts on the performances of a medical accelerator. By retuning the proton source, it is possible to compensate for intensity drifts into the treating room, but to get a full picture of the source behavior, the extracted current trend has to be correlated to the measurements in the different sections of the accelerator. Due to the strict requirements of needed source stability and intensity, which need to be fulfilled on continuous run, a proper maintenance is another key factor for the proper operation of the source. This includes planned slots for re-commissioning which are only possible within official release processes. On the other hand, for the carbon source, it would be beneficial to make the RF power as a clinically modifiable parameter as it is not possible to wait for long stabilization time of several days. Towards this strategy, a stable source set-point was found for which it is possible to have the RF power as unique parameter to tune the intensity into the treating room without affecting the performances of the rest of the machine. Future studies will focus on long term carbon coating effects and needed cleaning scenarios. In

the next future it is also planned to start with the commissioning of the spare third source that could be used as a test stand for plasma physics studies using Langmuir Probes, Optical Spectroscopy or for the production of different ion species such as oxygen and helium.

ACKNOWLEDGEMENTS

The authors would like to acknowledge the entire MedAustron Team for support during the carbon commissioning phase and Mr. Riccardo Monferrato and the ion source team from CNAO, Italy.

REFERENCES

- [1] P. J. Bryant et al., “Developments in the design of proton and ion accelerators for medical use”, *Proc. of EPAC'98*, paper FRX01A (1998).
- [2] U. Amaldi and G. Magrin, eds., “The path to the Italian national centre for ion therapy”, ISBN 978-88-95522-44-9, TERA Foundation (2010).
- [3] C. Schmitzer et al., “Status of Carbon Commissioning of the MedAustron Therapy Accelerator”, in *Proc. 9th Int. Particle Accelerator Conf. (IPAC'18)*, Vancouver, BC, Canada, Apr. 4, pp. 457-459, doi: 10.18429/JACoW-IPAC2018-MOPML027
- [4] C. Kurfürst et al., “Status of the MedAustron Beam Commissioning with Protons and Carbon Ions”, in *Proc. 9th Int. Particle Accelerator Conf. (IPAC'18)*, Vancouver, BC, Canada, Apr. 4, pp. 665-668, doi:10.18429/JACoW-IPAC2018-TU-PAF004
- [5] R. Geller, *Electron Cyclotron Resonance Ion Sources*, IOP Publishing, Bristol and Philadelphia, 1996.
- [6] N. Gambino et al., “Commissioning of the MedAustron Injector for Carbon Ion Treatment Beams”, in *Proc. 17th Int. Conf. on Ion Sources (ICIS'17)*, Geneva, Switzerland, Oct. 4, In press.
- [7] S. Myalski et al., “Status of the carbon ion source commissioning at MedAustron”, in *Proc. ECRIS 2018, 23th Int. Workshop on ECR ion sources (ECRIS18)*, this proceedings.
- [8] S. Giordanengo et al., “The CNAO dose delivery system for modulated scanning ion beam radiotherapy”, in *Med Phys.*; vol. 42(1), pp. 263-75, 2015. doi: 10.1118/1.4903276.

COMMISSIONING OF THE AISHA ION SOURCE AT INFN-LNS

L. Celona[†], G. Castro, F. Chines, S. Gammino, O. Leonardi, D. Mascali, S. Marletta, M. Mazzaglia, A. Miraglia, E. Naselli, L. Neri, S. Passarello, G. Torrisi, INFN-LNS, 95123 Catania, Italy

Abstract

The AISHa ion source has been designed to generate high brightness multiply charged ion beams for hadrontherapy applications, with high reliability, easy operations and fast maintenance. In order to get a compact machine, the radial confinement is provided by a Hallbach-type permanent magnet hexapole structure, while axial confinement is allowed by four high field He-free superconducting magnets, allowing the optimization of the magnetic field gradient at ECR resonance. The present work shows the results of ion source commissioning along with next developments.

INTRODUCTION

The AISHa [1] ion source was funded within the framework of the program of Sicilian Government named PO FESR 2007-2013 and a pool of Sicilian small enterprises was associated with INFN for the realization of this new source. It was designed considering the typical requirements of hospital facilities, in order to provide highly charged ion beams with low ripple, high stability and high reproducibility. The minimization of the mean time between failures is also a key point together with the maintenance operations that should be fast and easy. The features included in the design exploit all the knowledge acquired from INFN-LNS in last decades in the ion source design and realization [2]. The assembly of the source and of the first part of the LEBT has been carried out in the fall of 2016 and it has been completed in the first months of 2017. The main features of the source are listed in Table 1.

THE EXPERIMENTAL SETUP

The analysis of the costs and risks, taking into account the main beams of interest for such kind of application, clearly indicated that the optimal solution is a hybrid magnetic system. It consists of a permanent magnet hexapole and of four superconducting coils to minimize the hot electron component (to keep the superconducting magnets safe) and to optimize the ECR heating by a fine control of the field gradients and of the resonance length. The compact cryostat is equipped with two double-stage cryocoolers that allow reaching the operating conditions in around 40 hours, the magnetic field generated on axis is shown in fig. 1.

Parameter	Value
Axial field	2.7 T–0.4 T–1.6T
Radial field	1.3 T
Operating frequency	17.3-18.5 GHz
Operating power	2 kW (max)
Extraction voltage	40 kV (max)
Chamber dimensions	Ø 92 mm/360 mm
Warm bore diameter	274 mm
Weight	1400 kg

Table 1: AISHa Main Parameters

The RF injection system was designed to operate in both single and double frequency mode in order to exploit at the same time the Frequency Tuning Effect (FTE) and the Two Frequencies Heating (TFH) mechanism.

The 2400 cm³ plasma chamber is placed at high voltage (up to 40 kV). It was designed to operate at a maximum power rate of 2 kW. A 20 mm thick glass and carbon fiber tube, surrounding the hexapole, allows insulating the chamber in order to keep the superconducting magnets and the yoke at ground potential [3]. The microwave amplifier located at ground is insulated from the plasma chamber by a waveguide DC break, designed to permit reliable operation up to 40 kV [4].

The beamline consists of a focusing solenoid placed, downstream the source, a 90° bending dipole for ions selection and two diagnostic boxes. A Faraday Cup, a beam wire scanner and slit allow the beam characterization.

Figure 2 shows a view of the experimental area containing the source together with the low energy beam transfer line for its characterization.

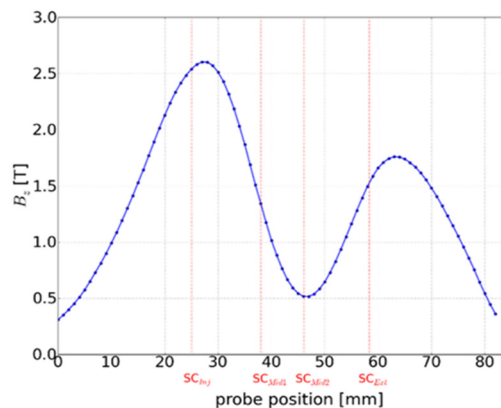


Figure 1: AISHa magnetic field profile

[†] celona@lns.infn.it



Figure 2: The Advanced Ion Source for Hadrontherapy at INFN-LNS in Catania.

COMMISSIONING RESULTS

The beam commissioning has been slowed down from a number of minor obstacles during the phase of functional check of individual ancillary equipment; this was particularly evident when the plasma generator was operated above 1 kW at larger gas load, in order to understand their limits. Some mechanical components demonstrated to generate outgassing, which obliged to open and clean the inner parts twice.

After the refurbishment and minor changes, the base vacuum was always in the 10^{-8} mbar range and the optimization started satisfactorily.

The magnetic trap magnets have been operating routinely at their operational design current without quenching and the measured full axial magnetic field profile confirmed the design specifications [1]. The maximum operational current for the 4 coils is 130A.

Particular attention has been paid to the Quench Detection System of the He-free magnets. The system is fully operative and embedded inside the coil power supplies, but it took some time in order to test different solutions.

The microwave matching was tested with high accuracy by means of a high directivity (40 dB) directional coupler for an accurate measure of the forward and the reflected power. Typical reflected power exceed 2% but after a fast optimization it was 0.1 to 1%.

At the same time, the parameters of the cooling system are interlocked with the klystron to avoid increase of the plasma chamber temperature (permanent magnets are 0.2 mm far from the chamber).

The RF injection system consists of one high power klystron amplifier operating in the 17.3-18.4 GHz frequency range that allows to finely tune the frequency by a Digital Fast Tuner System (DFTS). The operative

microwave frequency will be upgraded to higher frequency in the second phase of commissioning.

The control and safety systems were debugged continuously to provide the highest security and the highest detailed description of all issue events.

During the last six months, to gain experience on the source, it has been decided to begin the operations with Ar and O₂ gases at 20 kV, at the fixed frequency of 17.3 GHz and with 1kW of microwave power. We focused operations on the optimization of gas pressure and magnetic field to better understand the effect of the new approach to microwave-to-plasma coupling and to evaluate the stability of a plasma which is confined by a relatively high magnetic field ("High B mode" [4]) in a quite short plasma chamber.

Figure 3 shows the typical Charge State Distribution (CSD) measured after the 90° analysing magnet in a biased Faraday cup for O and Ar, in the first case He was used as mixing gas while in the second case O was used. The two configurations have different magnetic field profile, microwave power and neutral pressure.

The Oxygen and Argon currents achieved in such conditions are reported in table2.

Table 2: Oxygen and Ar currents @ 1kW power. the optimized values are marked with (*).

Parameter	Value [uA]
O6+ (*)	846
O7+	320
Ar11+	190
Ar12+	140
Ar13+	80
Ar14+	40
Ar16+	2

Content from this work may be used under the terms of the CC BY 3.0 licence (© 2018). Any distribution of this work must maintain attribution to the author(s), title of the work, publisher, and DOI.

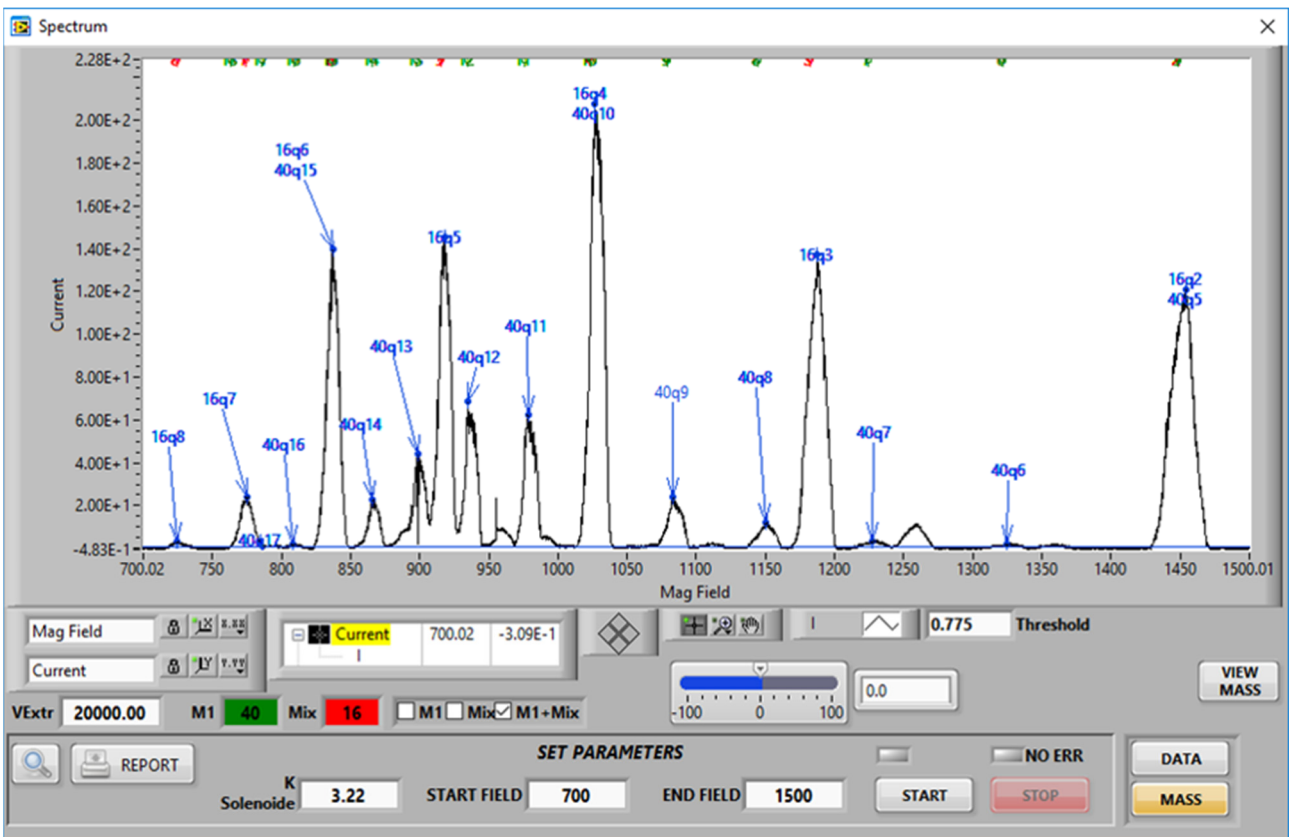
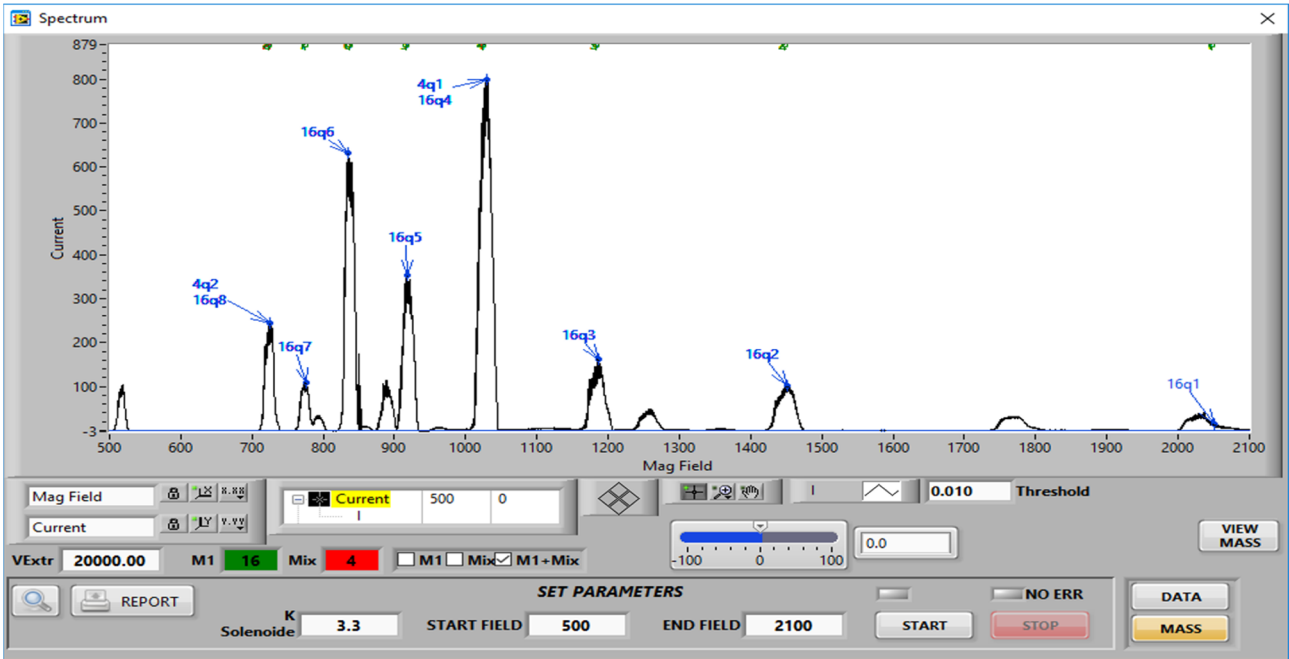


Figure 3: Charge State Distribution (CSD) measured for O and Ar,

CONCLUSION AND NEXT STEPS

The first results obtained in the early commissioning phase of the AISHa source permitted to understand that the

source is well functional even if several steps are needed to optimize its performances for different species.

The first priority is to evaluate systematically the frequency tuning effect together with the possibility to heat the plasma with a second frequency up to 22 GHz.

The bias disk as well as the use of gas mixing will certainly allow to enhance the mean charge state of the extracted beam.

The transverse emittance will be measured by means of an Allison emittance scanner, already installed in the Aisha beam line. Its commissioning is planned before next summer. Systematic studies of the extracted beam and emittance are planned with the aim to optimize the brightness of the beam as a function of the different ion source parameters.

The exceptional flexibility of AISHa trap and RF system is moreover suitable for implementing multi-diagnostics measurements in order to evaluate the impact of the mirror-ratios, of the magnetic field gradients and the interplays with the RF power and frequency on the main plasma parameters such as density and temperature.

The “tool-box” of diagnostics already developed at LNS [5] such as optical spectrometers, X-ray pin-hole cameras [6] and interferopolarimeters [7], will be mechanically adapted to be matched to AISHa setup, thus making this source the first one – among the new generation ECRISs – to be deeply characterized in terms of impact of plasma heating on the plasma properties.

ACKNOWLEDGEMENTS

The authors would like to acknowledge the work carried out by G. Costa and F.M. Noto in the AISHa design phase. The authors also acknowledge the support of the INFN technical staff - G. Calabrese, G. Manno, A. Maugeri, G. Pastore, A. Seminara, S. Vinciguerra - and of the mechanical workshop for the valuable work done in the manufacturing of several items for AISHa. Moreover, the efforts of S. Di Martino and P. Nicotra (Si.A.Tel. srl, Catania, Italy) in providing a reliable control and supervision system are also acknowledged.

REFERENCES

- [1] L. Celona *et al.*, “Design, construction and commissioning of the new superconducting ion source AISHa”, in *Proc. ECRIS/16, Busan, Korea, Aug. 2016*, paper WEPP15
- [2] L. Celona *et al.*, “ECR Ion Source Development at INFN-LNS”, in *Proceedings of ECRIS-2014, Nizhny Novgorod, Russia*
- [3] F. Noto *et al.*, “Structural Mechanics Optimization of the AISHa Ion Source”, *ICCM2015, 14-17th July, Auckland, NZ*
- [4] O. Leonardi, G. Torrisi, G. Sorbello, L. Celona and S. Gammino, (2018). “A compact dc-break for ECR ion source @ 18 GHz”. *Microwave and Optical Technology Letters*. doi: 10.1002/mop.31421.
- [5] T. A. Antaya and S. Gammino, "The superconducting electron cyclotron resonance 6.4 GHz high-B mode and frequency scaling in electron cyclotron resonance ion sources", *Rev. Sci. Instrum.* vol. 65, pp. 1723 (1994)
- [6] G. Castro *et al.*; "Plasma diagnostics update and consequences on the upgrade of existing source", *ICIS 17 proceedings*
- [7] D. Mascali *et al.*; *Review of Scientific Instruments* vol. 87, 02A510 (2016); doi: 10.1063/1.4939201
- [8] G. Torrisi *et al.*; “A new interferometric/polarimetric setup for plasma density measurements in compact microwave-based Ion Sources” *Journal of Instrumentation*, vol. 12, pp. 10, C10003, 2017,

CHALLENGES AND PROSPECTS OF ELECTRON CYCLOTRON RESONANCE CHARGE BREEDERS

T. Thuillier[†], J. Angot, M. Baylac, B.S.B. Bhaskar, J.B. Cully, J. Jacob, T. Lamy, A. Leduc, P. Sole LPSC, Grenoble, France

Abstract

Electron cyclotron resonance charge breeder (ECR CB) is one of the instruments used to boost the radioactive ion beam (RIB) charge state in isotope separator on-line (ISOL) facilities. While the ECR CB can manage intense 1+ RIB without difficulty, the present CB generation co-extracts significant amounts of impurities which can be detrimental to the study of very low intensity N+ RIB in today facilities if no downstream high mass resolution separation is available. This work investigates the improvements achievable with a new generation 18 GHz ECR CB applicable to future facility like EURISOL. The study shows that with a modified ion source geometry, an optimized magnetic confinement, a careful wall metal choice like beryllium, a UHV vacuum technology, the charge breeder performance will improve as follows: 20 % higher capture efficiency, -40% charge breeding time, charge state ion production with mass over charge of 3 up to xenon and over 6 up to uranium, co-extracted contaminant density reduction by a factor 60 to 600. An 18 GHz ECR CB ion source layout is finally proposed for EURISOL.

STATUS OF ECR CHARGE BREEDING

Ion source charge breeders are used in Isotope Separation Online (ISOL) facilities to boost the 1+ radioactive ion beam (RIB) charge state produced by target ion source (TIS) to N+ high charge state. The RIB beam is next filtered by a mass separator and finally injected into a post accelerator. Figure 1 presents the layout of such ISOL installation. Among the numerous key parameters of ISOL facilities, one can cite the:

- reliability and selectivity of the TIS,
- quality of the 1+ RIB purification,
- charge breeding time,
- charge breeding efficiency and
- achievable ion charge state of the charge breeder,
- downstream mass separation of the N+ RIB after the ion source CB.

Two types of charge breeders applicable to ISOL have been developed: the electron beam ion source charge breeder [1] (EBIS CB) and the electron cyclotron resonance ion source charge breeders (ECR CB)[2]. Table 1 presents the majors characteristics of the two ions sources type. Experiments done at CERN and later on both technologies concluded that EBIS CB and ECR CB are complementary[3]. Recently, the ECR CB installed at the CARIBU facility (Argonne National Laboratory, ANL) was stopped and replaced by an EBIS CB[4]. The origin of this decision is as follows. The 1+ RIB signal

intensity of CARIBU was in the range 10^2 - 10^4 /s, lower than expected. The downstream mass resolution after the CB was $M/\Delta M \sim 300$, resulting in a large N+ RIB signal contamination $> 97\%$. The downstream linear accelerator could not purify further the RIB and experiments were eventually not possible.

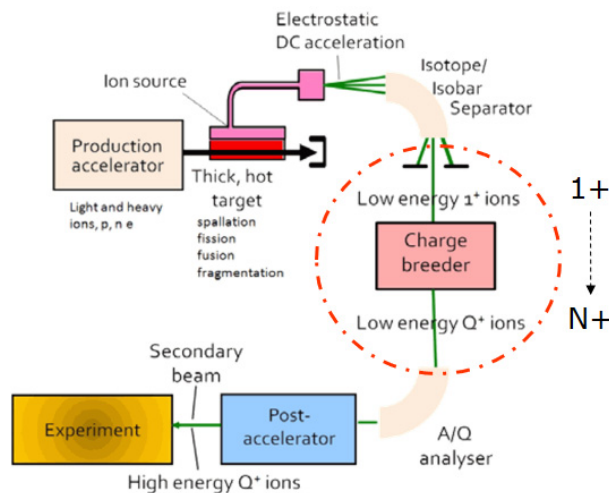


Figure 1: Layout of isotope online (ISOL) accelerator.

Table 1: Today EBIS and 14 GHz ECRIS CB Features.

	EBIS CB	today ECRIS CB
Max. 1+ RIB intensity	$< 10^{10}/s$	$> 10^{14}/s$
CB time to N+ (ms)	10-100	100-300
robustness	medium	High
1+N+ conversion efficiency	25%	5-20%
Operation mode	pulsed	CW or pulsed
RIB total contamination rate extracted	$\sim 10^5/s$	$\sim 10^9$ - $10^{10}/s$
Downstream mass resolution $M/\Delta M$	~ 300	≥ 1000
Upstream requirement	Ion cooling	None
Highest charge state	Bare ions	$A/Q=3 \rightarrow A \sim 60$ $A/Q=7 \rightarrow A \sim 150$

The same situation with low RIB intensity and low downstream mass separation condition also exists at the TRIAC facility (TRIUMF, Canada), but possibilities to purify the beam after the linac with thin strippers save some

[†] thuillier@lpc.in2p3.fr

experiments[5]. There, an EBIS CB will be installed to complement the ECR CB[5]. More recently, SPIRAL1 facility (GANIL) was upgraded with a PHOENIX CB. Thanks to the RIB post-acceleration in the CIME cyclotron, a very high mass separation $M/\Delta M \sim 10000$ is expected [6] granting an efficient cleaning of the N+ RIB signal, making it suitable for final RIB experiments. The SPES facility (LNS), under construction, is also equipped with a medium mass separator $M/\Delta M \sim 1000$ [7]. With a RIB signal intensity of $10^6/s$ and specific background reduction in the ECR CB, a clean N+ RIB signal is also expected.

POSSIBLE ECR CB UPGRADE

Ion Capture

Experimental data, confirmed by calculation and simulation, shows that the 1+ beam capture in existing 14 GHz ECR CB is not optimized: nearly 20% of the incoming ions are ionized on flight to 2+, 3+ and 4+ while crossing the plasma but are not trapped.[8] These ions are directly extracted and are then lost as N+ signals. Figure 2 presents the plasma length required to capture 99% of the 1+ signal as a function of the ECR frequency. One can see that at 14 GHz, a booster with the present measured plasma density [8] would require a 40 cm long plasma to grant a high capture efficiency, while the existing CB plasma is ~ 14 cm (red cross). Because the plasma density is proportional to the ECR frequency to the square ($n_p \sim f_{ECR}^2$), an 18 and 28 GHz ECR CB would need 25 cm and 10 cm plasma length respectively to capture all the 1+ beam.

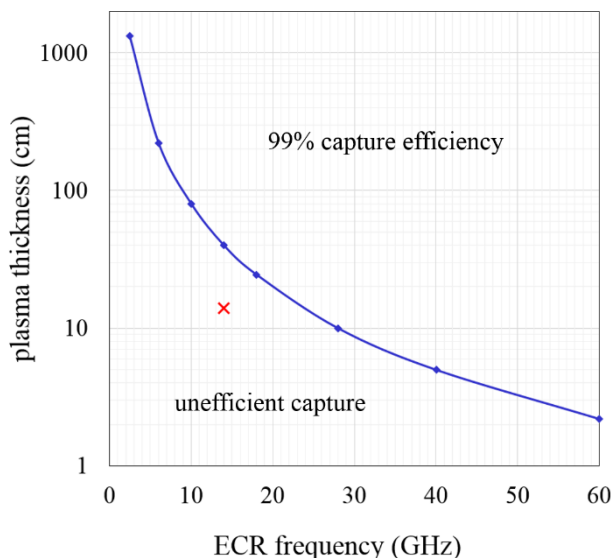


Figure 2: Plasma length required to capture efficiently an incoming 1+ beam as a function of the ECR frequency in an ECR CB (blue line). The existing PHOENIX Booster plasma is located by a red cross.

Charge Breeding Time

Another promising feature of the ECR frequency scaling ($n_p \sim f_{ECR}^2$) is the associated reduction of the charge breeding time τ_{CB} since $\tau_{CB} \propto 1/n_p$. As an illustration, Figure 3

shows how fast the charge breeding time theoretically decreases with the ECR frequency. Table 2 gives an example for the ECR frequency effect on $^{35}K^{10+}$ CB time.

Table 2: Theoretical evolution of the charge breeding time for $^{39}K^{10+}$ as a function of the ECR frequency, using 14 GHz data as a reference. The subsequent effect on material sputtering from the wall is indicated for convenience.

f_{ECR} [GHz]	τ_{CB} [ms]	Relative τ_{CB}	Relative density of contaminants
2.45	262	32	0.03
14	82	1	1
18	33	0.60	1.65
28	21	0.25	4

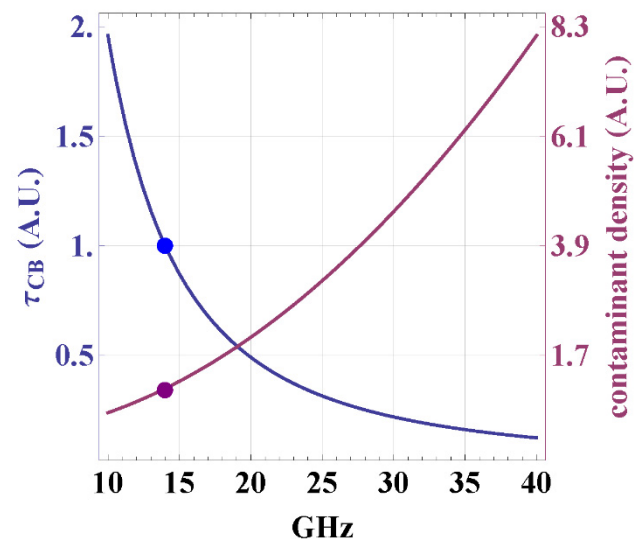


Figure 3: Blue curve, left axis, relative evolution of the charge breeding time as a function of the ECR frequency. The blue point is today 14 GHz ECR CB reference. Purple curve, right axis, concomitant evolution of the contaminant density in the plasma.

On the other hand, when the ECR frequency is increased, the sputtered materials from the walls follow the plasma density, leading to a higher contaminant density in the plasma for a given ECR plasma volume (see Figure 3). Mitigating such an increase of contaminant density would require a high downstream mass resolution $M/\Delta M \sim 10000$ and also other source of background reduction as discussed in the next section.

Background Reduction by Volume Effect

A way to reduce significantly the contaminant density is to increase the plasma chamber dimension. The reason for this effect is as follows. The contaminant flux Φ from the wall is proportional to the plasma chamber cylindrical surface (with radius r and length L):

$$\Phi \propto 2\pi rL + 2\pi r^2 \quad (1)$$

Content from this work may be used under the terms of the CC BY 3.0 licence (© 2018). Any distribution of this work must maintain attribution to the author(s), title of the work, publisher, and DOI.

While the ECR plasma volume V_{ECR} is proportional to the cylinder volume:

$$V_{ECR} \propto \pi r^2 L \quad (2)$$

Leading to a contaminant density C :

$$C \propto \frac{\Phi}{V_{ECR}} \propto \frac{2}{r} + \frac{2}{L} \quad (3)$$

Figure 4 shows how the ECR CB geometry can be optimized to reduce the contaminant density in the plasma. For instance, a plasma chamber with a 10 cm radius and a 80 cm length would divide the contaminant density by a factor of 4 with respect to the existing booster. Such a geometry would compensate the increase of contaminant yield due to a 28 GHz ECR frequency (see table 2).

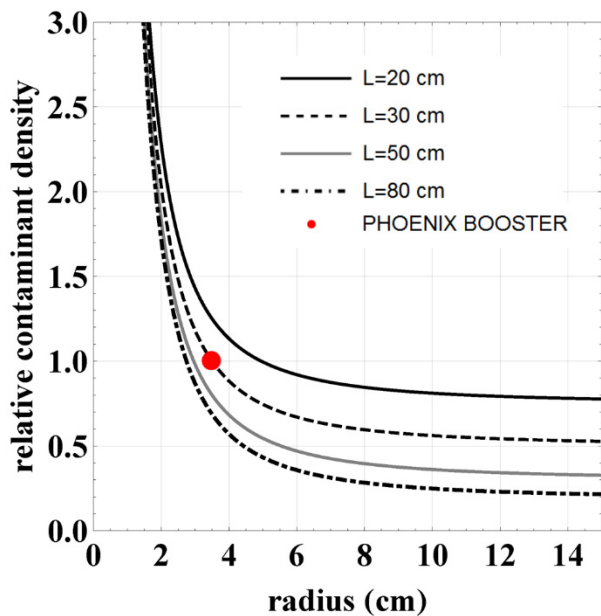


Figure 4: relative contaminant density evolution versus the plasma chamber cylinder radius for various plasma chamber length. The existing PHOENIX ECR CB geometry is indicated with a red dot.

Background Reduction by Wall Material Optimization

A careful ion spectrum analysis of contaminants shows that it is first composed of the chemical species included in the wall metal alloy and second with other elements present as traces in the ore used to build the metal. Further complication comes from the presence of natural isotopes for each

element. Since ECR CB generates multi-ionized ions, the resulting mass over charge ion spectrum includes a very large number of peaks with various intensities. The difficulty for ISOL facility using ECR CB with low downstream mass separation is to find a RIB mass over charge ratio suitable for post-acceleration where the local mass contamination is low. Because high mass elements have more electrons than light ones, the use of material containing heavy masses like stainless steel must be avoided as plasma chamber metal. Several laboratories performed research and development to investigate, reduce or redistribute the contamination sputtered from the plasma chamber wall. LPSC shown that an unstable plasma multiplies by 10 the atom sputtering rate from the walls[9]. KEK converted the material exposed to the plasma to Al [10], while Argonne and TRIUMF laboratories extended the use of this material to ion injection and extraction areas [5,11,12]. Aluminum features interesting advantages for ECR plasma as it is a light metal with a few electrons, it has no stable isotope and the secondary electron emission from the aluminum oxide layer naturally covering the metal surface boosts the electron density. The aluminum deposition at TRIUMF helped reducing background at specific places in the ion spectrum allowing post-acceleration of RIB[5]. ANL will test in a near future conformal coating by atomic layer deposition (ALD) technique [13]. ALD enables to deposit a thick homogeneous Al₂O₃ layer in the ion source. The drawback with layer deposition is that it degrades with time and there is no warranty to keep the contamination level from one layer deposition to another. SPES team has planned to test liners made of monoisotopic materials (Nb,Ta,W) in collaboration with LPSC[14]. Pure aluminum is a soft material with poor mechanical properties and it is unfortunately not possible to machine a whole ECR CB plasma chamber with it. A set of two new materials are proposed in this study to build a plasma chamber: beryllium and AlBeMet©. Beryllium is a very light monoisotopic metal with a melting temperature of 1287°C and high mechanical properties suitable to machine a whole plasma chamber. AlBeMet© is a mixture of aluminium and beryllium which allies the good thermal conductivity of aluminium and the good mechanical properties of beryllium. Figure 4 presents the simulated contaminant spectrum of stainless steel (excluding extra element contamination coming with the stainless steel compounds) and pure beryllium (including all possible trace contaminants). One can see that the beryllium spectrum concentrates the impurities on Be peaks ($A/Q=4.5, 3$ here) and the impurity intensities are a factor 10^2 to 10^5 lower elsewhere.

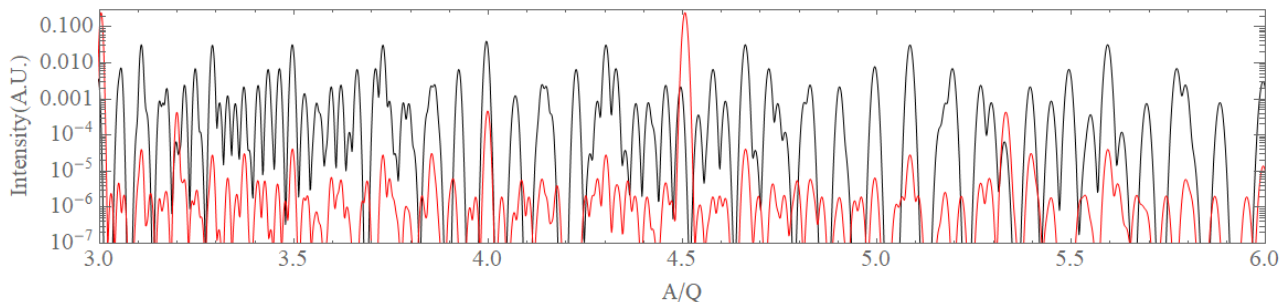


Figure 5: Ion Mass spectrum simulated for stainless steel (black) and pure beryllium (red) plasma chamber.

Gas Background Reduction

Today ECR CB are based on 20 years old technology including plastic o-rings and no bake able assemblies. The base vacuum in the ion source is of the order of 10^{-6} to 10^{-8} hPa at best. The probability of gas ionization being very high in an ECR plasma, a high gas contamination yield comes with the N+ RIB of interest. The contaminants come either from the permeation through o-rings or by the buffer gas injection system used to sustain the ECR plasma. Both source of gas contaminant can be efficiently reduced as follows. A careful new ion source design using ultra high vacuum (UHV) technology and an online system to bake the plasma chamber and the surrounding vacuum chambers up to 300°C would give a base vacuum in the range 10^{-9} to 10^{-10} hPa. A special care must also be taken to the buffer gas injection where a gas purity of 99.999% still brings a large amount of impurities. When limiting buffer gas to H_2 and He, it becomes possible to purify online the injected helped with a 4K cryopump. Completed with a fully bake able gas injection system, the gas contamination from the buffer gas injection will decrease significantly by several order of magnitude at least. Such a clean gas injection system has been successfully implemented on the CARIBU gas catcher at ANL.[15]

High Charge State Improvement

The ECR ion source know how improved a lot since twenty year. Today high efficiency and highly optimized ECR ion sources can produce Xe^{42+} ($A/Q \sim 3$) and U^{42+} ($A/Q \sim 6$) on a daily basis.[16,17]. The key for such improvement are an optimized magnetic confinement [18] and a large plasma chamber radius[16,17,19]. When increasing the plasma chamber radius, the ion confinement time is mechanically increased and it can be argued that the CB time should increase which can be detrimental for an efficient N+RIB post acceleration. But the CB time can also be reduced by adapting the extraction magnetic field intensity which controls the ion extraction. So a flexible ion magnetic confinement produced by hexapole coils and a set of axial solenoids would allow to adapt the ion confinement time and charge state to a specific RIB element.

PROSPECT WITH A NEW GENERATION ECR CHARGE BREEDER FOR EURISOL

The last section demonstrates that there is a clear interest to develop a new generation ECR CB. Table 3 summarizes

the possible set of improvements of ECR CB as a function of the ECR frequency. Depending on the physics needed, a 28 GHz ECR CB can be considered if an important CB time reduction is expected (-75%), the condensable contaminant reduction could reach a factor 20-200 and the gas contaminant a factor 1000 with respect to today ECR CB operated at 14 GHz with a stainless steel plasma chamber. In this case a downstream high mass resolution of ~ 10000 is mandatory, along with a RIB signal $> 10^5$ - 10^6 pps. Another possibility is to choose an 18 GHz upgraded ECR CB which would reduce the CB time by -40% and offer a condensable and gas background reduction in the range ~ 60 -600 and 1000 respectively. The wide know-how on 18 GHz ECRIS would make this latter choice very safe as far as the magnetic field operation safety and ion source performance are concerned.

Table 3: Possible Booster improvements vs ECR frequency. The existing 14 GHz booster being considered as a reference.

f_{ECR} [GHz]	14	18	28
1+/N+ RIB efficiency	+20%	+20%	+20%
Relative τ_{CB}	0%	-40%	-75%
Higher N+ charge state	+20%	+20%	+20%
sputtered contaminant density in plasma	-80%	-67%	-20%
Gas contaminant density	$\div 1000$	$\div 1000$	$\div 1000$
ion spectrum sputtered contamination	$\div 100$	$\div 60$	$\div 25$
	$\div 1000$	$\div 600$	$\div 250$

Figure 6 proposes the layout of a new generation 14-18 GHz ECR CB suitable for a facility like EURISOL. The magnetic field is generated by a set of 8 NbTi superconducting coils. Two large coils are present at each end to pilot the injection and extraction peak field, while 6 smaller coils located in between control the axial magnetic field profile. This results in the possibility to generate very flexible axial magnetic profile, including flat field geometry [20,21], or even two consecutive closed ECR zones. Very long ECR plasma zone can be created up to 500 mm for 14 GHz or 450 mm for 18 GHz. Such a long ECR zone will grant an optimum RIB capture efficiency. Typical axial magnetic field mirrors are displayed in Figure 7. The grey plot indicates a 400 mm long 14 GHz ECR zone, while the black plot shows a 330 mm long 18 GHz ECR zone. The

Content from this work may be used under the terms of the CC BY 3.0 licence (© 2018). Any distribution of this work must maintain attribution to the author(s), title of the work, publisher, and DOI.

radial confinement is done with an NbTi hexapole delivering up to 1.4 T at the plasma chamber wall. The possibility to control independently the radial and axial magnetic

fields will enable to control the ion confinement time and thus find more easily ion source tuning providing short CB time and/or high charge state beams.

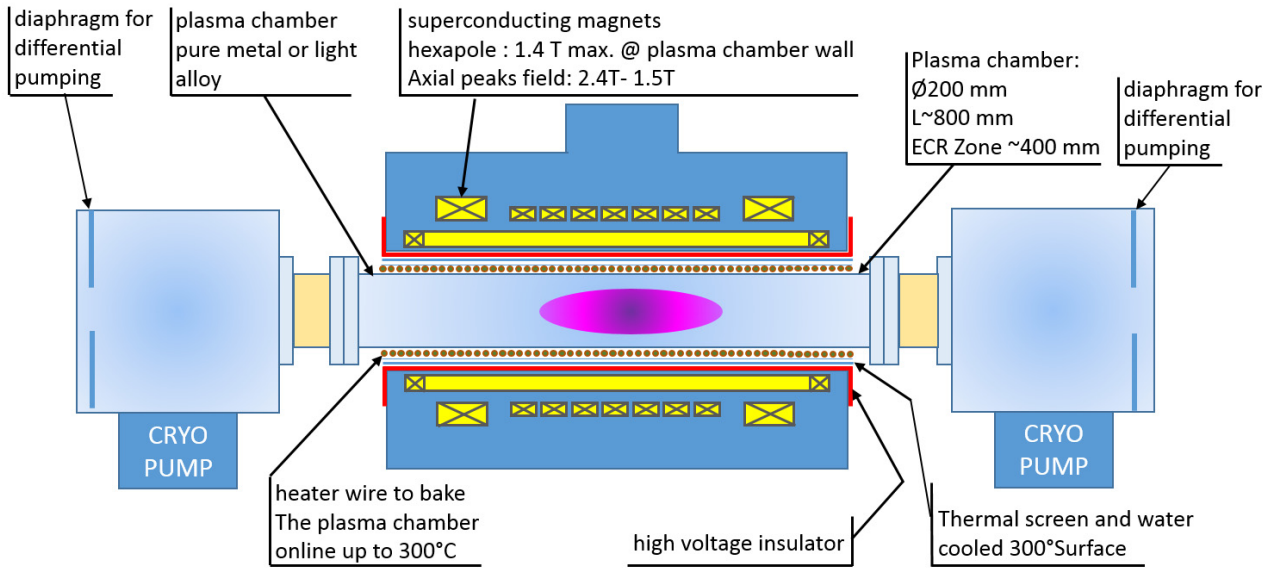


Figure 6: Sketch showing the general features of a new generation ECR CB suitable for EURISOL facility with highly enhanced performances.

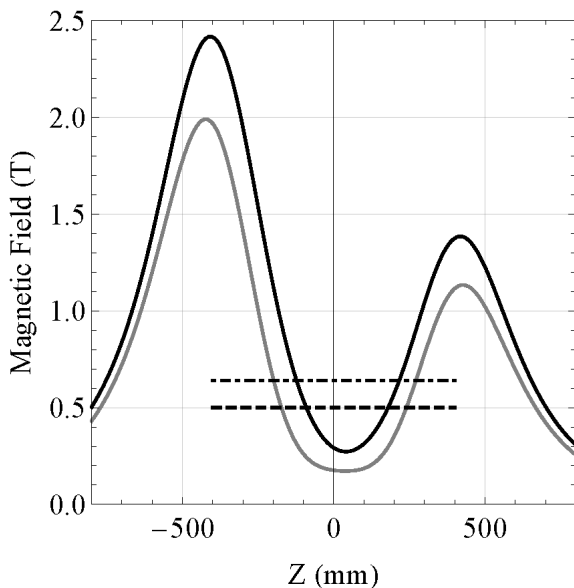


Figure 7: Typical axial magnetic field profile obtainable with the 8 coils proposed for the booster upgrade. Black: 18 GHz profile, Gray: 14 GHz profile. Dashed line: 0.5T (14 GHz resonance). Dotted dashed line: 0.64 T (18 GHz resonance).

The plasma chamber inner bore diameter is 200 mm and its length is 800 mm. The magnet warm bore has a diameter larger than the UHV flanges ones located at each end to ease the assembly/disassembly. The plasma chamber temperature is both controlled by a heating wire and an air cooled tube in order to control the wall temperature from 20°C to 300°C during operation. The heating/cooling

plasma chamber system is surrounded by a radiation shield screen and next a water cooled layer fixing the temperature to ambient. The magnet cryostat is set to ground and separated from the high voltage part by a thick plastic insulator in PEEK or high density polyethylene. The UHV is maintained by a set of cryogenic pumps located on both ion source ends. The surrounding vacuum chambers are fully bake able. Diaphragms are placed around the beam axis to limit any contamination coming from downstream of upstream beam line. The whole parts facing the ECR plasma and composing the vacuum chambers in sight of ion injection and extraction system (not represented in Fig. 7) are made with the same material to minimize the chemical species contamination of the plasma due to sputtering. A candidate for the chosen material is pure beryllium (see former section). Insulators can be done with beryllium oxide or alumina.

REFERENCES

- [1] F. Wenander, "Charge breeding of radioactive ions with EBIS and EBIT", *J. Instrum.*, 5, C10004 (2010)
- [2] R. Geller, C. Tamburella, and J. L. Belmont, "The ISOL-MAFIOS Source", *Rev. Scient. Instrum.*, 67, 1281 (1996).
- [3] P. Delahaye, A. Galatà, J. Angot, J. F. Cam, E. Traykov, G. Ban, L. Celona, J. Choinski, P. Gmaj, P. Jardin, H. Koivisto, V. Kolhinen, T. Lamy, L. Maunoury, G. Patti, T. Thuillier, O. Tarvainen, R. Vondrasek, and F. Wenander, "Optimizing charge breeding techniques for ISOL facilities in Europe: Conclusions from the EMILIE project", *Rev. Sci. Instrum.*, 87, 02B510 (2016).
- [4] S. Kondrashev, A. Barcikowski, C. Dickerson, R. Fischer, P. Ostroumov, R. Vondrasek, A. Pikin, "EBIS charge breeder for CARIBU", *Rev. Sci. Instrum.*, 2014 85(2):02B901. doi: 10.1063/1.4824645.

- [5] F. Ames, M. Marchetto, A. Mjøs, and A. C. Morton, "Charge state breeding experiences and plans at TRIUMF", *Rev. Sci. Instrum.*, 87, 02B501 (2015).
- [6] L. Boy, PhD Thesis, "Problèmes posés par l'accélération d'ions radioactifs dans le projet SPIRAL", Université Pierre et Marie Curie - Paris VI, France, 1997.
- [7] G. de Angelis et al., "The SPES Radioactive Ion Beam facility of INFN", *Journal of Physics*, Conf. Series 580 (2015) 012014.
- [8] O Tarvainen, T Lamy, J Angot, T Thuillier, P Delahaye, L Maunoury, J Choinski, L Standylo, A Galatà, G Patti and H Koivisto, "Injected 1+ ion beam as a diagnostics tool of charge breeder ECR ion source plasmas", *Plasma Sources Sci. Technol.*, 24, 035014.
- [9] O Tarvainen, J Angot, I Izotov, V Skalyga, H Koivisto, T Thuillier, T Kalvas and T Lamy, "Plasma instabilities of a charge breeder ECRIS", *Plasma Sources Sci. Technol.*, 26, 105002 (2017).
- [10] N. Imai et al., "KEKCB electron cyclotron resonance charge breeder at TRIAC", *Rev. Sci. Instrum.*, 79, 02A906 (2008).
- [11] R.Vondrasek, A. Levand, R. Pardo, G. Savard, and R. Scott, "Charge breeding results and future prospects with electron cyclotron resonance ion source and electron beam ion source", *Rev. Sci. Instrum.*, 83, 02A913 (2012).
- [12] R.Vondrasek, J. Clark, A. Levand, T. Palchan, R. Pardo, G. Savard, and R. Scott, "Operational experience with the Argonne National Laboratory Californium Rare Ion Breeder Upgrade facility and electron cyclotron resonance charge breeder", *Rev. Sci. Instrum.*, 85, 02B903 (2014).
- [13] R. Vondrasek, "Addressing Contamination in ECR charge breeders", ECRIS18, JaCoW online proc., these proceedings.
- [14] A. Galata, "Progresses in the installation of the SPES charge breeder beam line", ECRIS18, JaCoW online proc., these proceedings.
- [15] R. Vondrasek, Argonne National Laboratory, private communication.
- [16] H. W. Zhao, L. T. Sun, J. W. Guo, W. H. Zhang, W. Lu, W. Wu, B. M. Wu, G. Sabbi, M. Juchno, A. Hafalia, E. Ravaoli, and D. Z. Xie, "Superconducting ECR ion source: From 24-28 GHz SECRAL to 45 GHz fourth generation ECR", *Rev. Sci. Instrum.*, 89, 052301 (2018).
- [17] D. Leitner, M. L. Galloway, T. J. Loew, C. M. Lynceis, I. Castro Rodriguez, and D. S. Todd, "High intensity production of high and medium charge state uranium and other heavy ion beams with VENUS", *Rev. Sci. Instrum.*, 79, 02C710 (2008).
- [18] D. Hitz, A. Girard, G. Melin, S. Gammino, G. Ciavola, and L. Celona, "Results and interpretation of high frequency experiments at 28 GHz in ECR ion sources, future prospects", *Rev. Sci. Instrum.*, 73, 509 (2002).
- [19] T. Thuillier, L. Maunoury, J. Angot, C. Barué, L. Bonny, J. L. Flambard, J. Jacob, T. Lamy, A. Leduc, F. Lemagnen, C. Peaucelle, and P. Sole, "Effect of the plasma chamber radius on the high charge state production in an ECR ion source", *AIP Conference Proceedings*, 2011, 040020 (2018).
- [20] G. D. Alton, and N.D. Smithe, "Design studies for an advanced ECR ion source", *Rev. Sci. Instrum.*, 65, 775 (1998).
- [21] T. Nakagawa, Y. Higurashi, J. Ohnishi, T. Aihara, M. Tamura, A. Uchiyama, H. Okuno, K. Kusaka, M. Kidera, E. Ikezawa, M. Fujimaki, Y. Sato, Y. Watanabe, M. Komiyama, M. Kase, A. Goto, O. Kamigaito, and Y. Yano, "First results from the new RIKEN superconducting electron cyclotron resonance ion source", *Rev. Sci. Instrum.*, 81, 02A320 (2010).

CHARGE-BREEDING OF RADIOACTIVE IONS AT THE TEXAS A&M CYCLOTRON INSTITUTE

G. Tabacaru, J. Ärje, F. P. Abegglen and D. P. May[†], Texas A&M University, Cyclotron Institute, Texas A&M University, College Station, TX 77845, USA

Abstract

Singly charged, radioactive ions produced by high-energy protons in an ion-guide on-line target-cell have been charge-bred in an electron cyclotron resonance ion source (CB-ECRIS) and subsequently accelerated to high energy by the K500 cyclotron at Texas A&M University. The 1+ ions were accelerated to near the extraction voltage of the ECRIS and then decelerated through the injection-end magnetic mirror field of the ECRIS. The charge-breeding efficiency was only at most 1% into one high charge-state, and as a consequence another method of injection into the ECRIS is being attempted. Direct injection from a 1+ ion source via an rf-only sextupole ion-guide or SPIG has been accomplished with no high-voltage deceleration of ions through the mirror field into the ECRIS. Direct injection of 1+ radioactive ions via a longer (2.5 m) SPIG transporting products from the target-cell to CB-ECRIS is now being implemented.

INTRODUCTION

Reference [1] gives a complete description of the Texas A&M upgrade. As part of the upgrade the K150 cyclotron has been re-commissioned to use as a driver for the production of radioactive ions. The primary method is to first stop radioactive products from beam-target collisions and transport them as low-charge-state ions using the ion-guide on-line technique. This technique was pioneered and continues to be developed at the University of Jyväskylä Cyclotron Laboratory [2]. Using this technique both a light-ion guide (LIG) for reaction products resulting from energetic, light-ion beams (p, d, ³He, or α) and a heavy-ion guide (HIG) for reaction products resulting from energetic, heavy-ion beams are being developed. These ions are then injected into CB-ECRIS for charge-breeding to higher charge states. A low-energy beam of ions of one selected charge-state is then transported to the K500 superconducting cyclotron for acceleration to high energy. Figure 1 illustrates the scheme. Now only the LIG will be considered.

LIGHT ION GUIDE

For LIG an energetic beam of light ions impinges on a thin target to produce radioactive products (via (p,n) for example) that then exit the target to encounter a rapid flow of helium gas. The products are mainly in the ionized state, and in the helium this ionization is reduced to the 1+ charge-state, taking advantage of the unfavorable energetics of neutralization of 1+ heavy ions

colliding with neutral helium. The flow of helium through the target cell ushers the 1+ ions through an orifice into a highly pumped region where the helium can be pumped away. The ions are guided by a small electric field through an aperture in a skimmer electrode after which they can be accelerated to form a low energy (~10kV) beam.

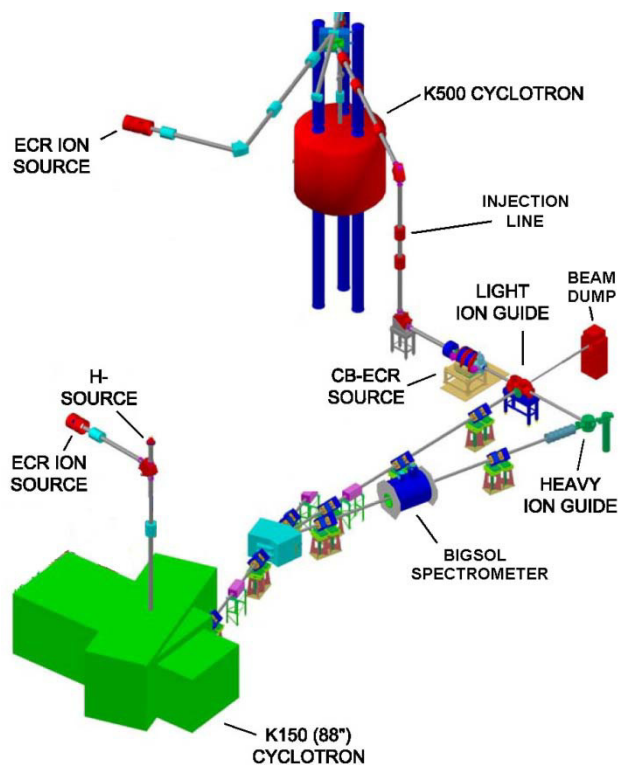


Figure 1: Simplified Layout of the Texas A&M Radioactive Beam Facility.

One disadvantage of this technique is that the ions encounter a significant pressure of helium in the acceleration region which introduces an energy spread in the beam. In order to counter this, a system was introduced where before acceleration the thermalized ions travel along an rf-only sextupole ion guide through a sequence of pumping baffles before being accelerated [3]. References [4] and [5] detail the development of the rf-only ion guide which consists of a parallel array, usually sextupolar, of conducting rods or vanes with low-power,

*Work supported by U. S. Dept. of Energy Grant DE-FG02-93ER40773

[†] may@comp.tamu.edu

high-frequency rf impressed. The rods are alternately phased by 180° so that rf fields of parabolic increasing intensity are set up in the interior of the sextupole. Ions travel through the channel between the rods contained by the rf fields while the helium is pumped away. In reference [3] it is shown that ions accelerated by some initial voltage of several hundred volts are thermalized by collisions with the high pressure of helium before the first pumping baffle and even cooled. As a consequence the ions exit the SPIG into the low pressure region with only a thermal energy spread.

INITIAL SET-UP

Figures 2 and 3 illustrate the LIG-to-CB-ECRIS geometry and the target-cell. Three large Roots blowers are used to handle the large flow of helium gas exiting the target-cell. The SPIG, modelled after reference [3], consists of two sections with two pumping baffles, the first and second sections approximately 8 cm and 40 cm long, respectively, and using 4 mm diameter stainless steel rods arrayed around a 10 mm inner diameter. The exciting frequency is approximately 2 MHz and tuned to minimize reflected power. The target-cell and SPIG are held near the extraction voltage of the CB-ECRIS, and the 1+ beam subsequently accelerated to ground immediately after the SPIG. Table 1 lists four reactions that were focused on.

Reaction	Cross-section [mb] @ E_p [MeV]	Half life
$^{64}\text{Zn}(p,n)^{64}\text{Ga}$	161 @ 14.3	2.6 m
$^{58}\text{Ni}(p,n)^{58}\text{Cu}$	40 @ 14.3	3.2 s
$^{46}\text{Ti}(p,n)^{46}\text{V}$	124 @ 14.3	422 ms
$^{114}\text{Cd}(p,n)^{114}\text{In}$	510 @ 10.3	71.9 s

Table1: Reactions.

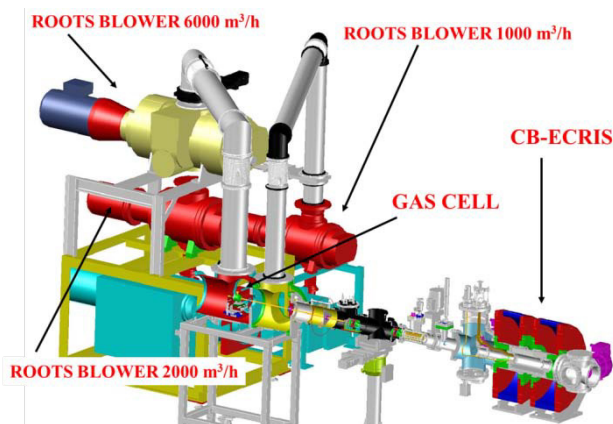


Figure 2: LIG and CB-ECRIS.

The 14 GHz CB-ECRIS [6] is located 2.5 meters from the target-cell. Since it is constructed with a totally surrounding hexapole, it is difficult to achieve a

symmetric geometry on the injection end due to microwave and gas injection. This symmetry is important in the volume where injected beams are encountering the electric field that decelerates the beam into the plasma chamber [7]. Various injection geometries have been tried, including one where the plasma chamber was opened up and extended on the injection end and the microwaves injected into the extension. Charge-breeding was observed for ^{64}Ga , ^{58}Cu , and ^{114}In with the highest efficiency obtained (approximately 1%) for $^{114}\text{In}^{19+}$ ions which were reaccelerated in the K500 cyclotron [8]. The number of radioactive ions injected into CB-ECRIS ranged between approximately 2×10^4 ions/ $\mu\text{Coulomb}$ (^{64}Ga and ^{114}In) to 3×10^3 ions/ $\mu\text{Coulomb}$.

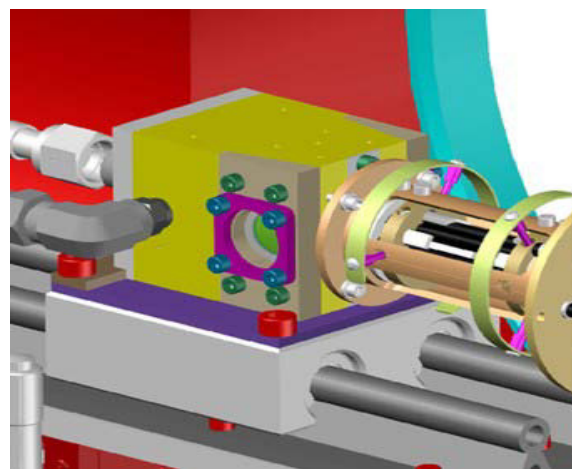


Figure 3: The target-cell and first SPIG section.

DIRECT INJECTION

The short distance (2.5 m) between the target-cell and the CB-ECRIS makes aligning and properly focusing the 1+ beam difficult. Also larger target-cell apertures and higher target-cell pressures cause higher concentrations of helium to migrate into CB-ECRIS. Finally, there is the possibility that a portion of the plasma is back-extracted by the presence of grounded elements in the injection region. With these considerations in mind, in the next phase a method of direct injection of the radioactive ions produced by the ion-guide on-line system is being investigated. With this method the ions travel along an extended SPIG directly into the CB-ECRIS plasma chamber, and these problems can be more easily avoided.

As a first test a 1 meter long SPIG was positioned through the center of a Glaser lens that was similar to the coil on the injection end of the CB-ECRIS and capable of producing a comparable magnetic field. Transport of ions along the SPIG was little affected by the full field of the Glaser as its coil current was increased to its maximum.

Next an aluminosilicate ion gun fabricated by HeatWave Labs, Inc. for the production of singly-charged alkali ions was placed at the entrance of 40 cm long SPIG, and the exit end of the SPIG placed on axis near the maximum axial magnetic field at the injection end of

Content from this work may be used under the terms of the CC BY 3.0 licence (© 2018). Any distribution of this work must maintain attribution to the author(s), title of the work, publisher, and DOI.

the CB-ECRIS (Fig. 4). This arrangement resulted in a good charge-breeding efficiency (Fig. 5), although this was difficult to precisely quantify due to the

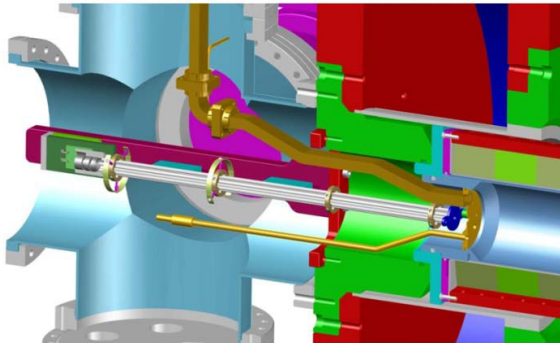


Figure 4: 40 cm SPIG injecting directly into the plasma chamber of CB-ECRIS.

difficulty of measuring the output from the SPIG directly. An estimate of the output was made using a measurement of the current hitting the plasma chamber added to the current measured hitting a faraday cup down-stream of the CB-ECRIS with no high voltage applied to the plasma chamber or SPIG. This measurement indicated an efficiency as high as 10% into one charge-state (8.4 pA of Cs²⁴⁺ out of 70 pA of Cs¹⁺ measured hitting the plasma chamber and 15 pA hitting the down-stream faraday cup). The efficiency peaked at a difference between the source voltage and the CB-ECRIS voltage of 8.5 volts with 5.8 volts FWHM. Charge-breeding of potassium was also attempted with similar results.

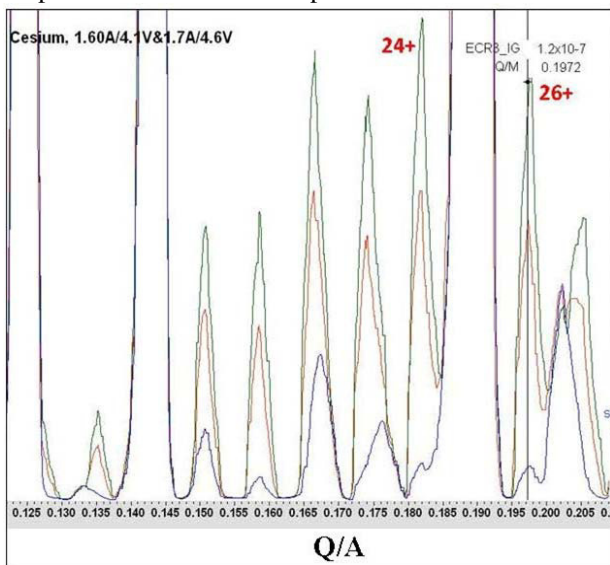


Figure 5: Spectrum of charge-bred Cs. The red and green peaks are Cs charge-states resulting from different 1+ source power levels. The blue is background. 370 enA full scale.

One observation is that the efficiency of charge-breeding continued to improve as the vacuum improved,

although as shown by Fig. 5 there was still the presence of oxygen (from water vapor) and nitrogen (from small leaks). The vacuum never improved at the injection end of CB-ECRIS to below 1×10^{-7} torr, and the introduction of support gas only served to depress the charge-breeding efficiency. The charge-state distribution was quite high even though the microwave power was low (88 watts as measured at the transmitter above the cave shielding). The total extracted current was less than 80 μ A.

Figure 6 illustrates the direct injection scheme and Fig. 7 shows the installed SPIG positioned in the injection end of CB-ECRIS (opposite extraction). The SPIG is made up of vanes instead of rods for more structural stability. In addition to the two pumping baffles from the former scheme, there are two additional baffles with pumping by turbomolecular pumps in between. The entire LIG to CB-ECRIS system will be tested first using a radioactive thorium source placed in the target cell. Later a proton beam will be used to create products for eventual acceleration by the K500 cyclotron.

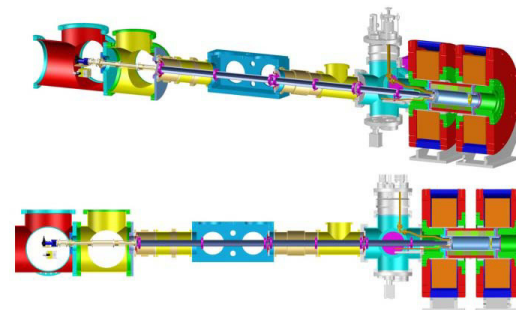


Figure 6: 2.5 meter SPIG joining LIG to CB-ECRIS.



Figure 7: Vaned SPIG and pumping baffle.

FUTURE PROGRESS

The vanned SPIG assembly has been installed, and connections are now being made. It is hoped that injection by an rf-only ion guide will prove an efficient and easily tuned alternative to the accel-decel scheme. If this method proves feasible future progress will focus on a mechanism for moving a section of the SPIG out of line so that a detector station can be positioned in-line in order to accurately measure the output of radioactive products from the LIG. Finally strategies for increasing efficiencies for all species and decreasing breeding times and contamination can be explored.

REFERENCES

- [1] D. P. May, B. T. Roeder, R. E. Tribble, F. P. Abegglen, G. Chubaryan, H. L. Clark, G. J. Kim, G. Tabacaru and J. Ärje, *Proceedings of the 20th International Conference on Cyclotrons and their Applications, Vancouver, Canada (2013)*.
- [2] J. Ärje, J. Äystö H. Hyvönen, P. Taskinen, V. Koponen, J. Honkanen, K. Valli, A. Hautojärvi and K. Vierinen, *Nucl. Instrum Methods, A* vol. 247, pp. 431-4373, (1986)
- [3] P. Karvonen, I. D. Moore, T. Sonoda, T. Kessler, H. Penttila, K. Peräjä, P. Ronkanen and J. Äystö, *Nucl. Instrum Methods*, B266 (2008) 4794-4808.
- [4] H. J. Xu, M. Wada, J. Tanaka, H. Kawakami, I. Katayama, S. Ohtani, *Nucl. Instrum Methods*, vol. A333, pp. 274, (1993) .
- [5] M. Wada, *Nucl. Instrum Methods*, vol. B319, pp. 450-456, (2013).
- [6] W. D. Cornelius, *Proceedings of the 18th International Workshop ECR Ion Sources, Chicago, Illinois*, pp. 167-175, (2008).
- [7] R. Vondrasek, A. Levand, R. Pardo, G. Savard and Scott, *Rev. of Sci. Instrum.*, vol. 02A913, (2012).
- [8] B. T. Roeder, F. P. Abegglen, J. Ärje, G. J. Kim, A. Saastamoinen and G. Tabacaru, *Cyclotron Institute Progress in Research Texas A&M Univ. 2016-2017*, vol. IV-17.

CHARGE BREEDING TIME STUDIES WITH SHORT PULSE BEAM INJECTION

J. Angot[†], T. Thuillier, M. Baylac, T. Lamy, P. Sole, J. Jacob, Université Grenoble Alpes, CNRS, Grenoble INP, LPSC-IN2P3, 38000 Grenoble, France
 O. Tarvainen¹, University of Jyväskylä, Departement of Physics, 40500 Jyväskylä, Finland

Abstract

Investigations on the Charge Breeding (CB) time have been done with the PHOENIX ECR Charge Breeder. The traditional measurement method consists of generating a 1+ ion beam rising front and measuring the time to reach 90% of the final N+ ion beam intensity. In order to study the possible self-consistent effects of the accumulation of injected ions in the plasma and to better understand the 1+N+ process, short Rb⁺ pulses were injected and the time resolved N+ beam responses were measured. The new short pulse CB time method and the experimental results are presented. The effects of several parameters such as the amplitude and the width of the pulse are studied. Calculation methods are proposed for the efficiency and CB time in pulse mode. Compared with the traditional values, the efficiencies are found to be equivalent and CB time shorter by -10% in the case of short pulse injection; showing that the accumulation effect is low in the studied configuration.

The short pulse method was used to study the influence of B_{min} on the plasma behaviour. An increase of B_{min} leads to an increase of the Rb¹⁹⁺ efficiency that is found to be caused by a higher ion confinement time. The results are also used to estimate the 1+N+ efficiencies in the case of Radioactive Ion Beam (RIB) species, showing how the RIB efficiency is reduced as a function of the half-life and charge state.

INTRODUCTION

ECR charge breeders (ECR CB) are used in ISOL facilities to increase the charge state of a Radioactive Ion Beam (RIB) from 1+ to N+. They operate in continuous mode and can accept the injection of high particle flux, more than 10¹³ pps. They are mainly characterized by 3 parameters.

The first one is the Charge Breeding Time τ_{CB} of the charge state of interest N. It is traditionally measured by switching ON the injected beam and measuring the 90 % rise time of the N+ response [1-4]. In order to improve the signal over noise ratio, the time response is averaged over several measurements, the 1+ beam being pulsed ON / OFF at low frequency (about 0.5 Hz) with a duty cycle of 50%. This method is called here Long Pulse Injection (LPI). Figure 1 illustrates the principle of the τ_{CB} measurement with LPI.

The second is the ionization efficiency. It is the ratio between the extracted particle current of charge state N

and the injected particle current. Using the LPI, the N+ particle current is determined taking into account the background level (1+ beam OFF).

The third parameter is the contaminant rate defined as the percentage of contaminants included into the N+ response measurement. It depends on the charge breeder cleanliness, the RIB production yield and the resolution of the downstream spectrometer. In the case of low RIB production yield (10² to 10⁶ pps) and low spectrometer resolution ($\Delta M/M$ of about 1/200), the beam of interest may represent a fraction that can be very small (some %), which has dramatic consequences for the physics experiments [5].

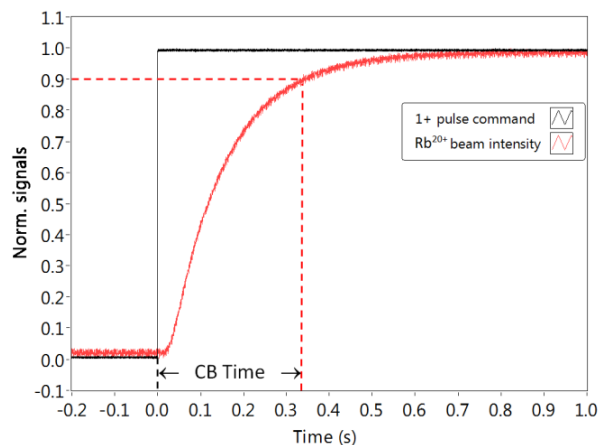


Figure 1: Principle of the traditional τ_{CB} measurement. The dashed lines are the references of the pulse start (black) and 90% level of the Rb²⁰⁺ beam intensity (red).

Motivations for Short Pulse Injection

Previous experiments have shown that the 1+ beam injection can i) modify the CB plasma Charge State Distribution (CSD) [6] and ii) trigger instabilities in a time scale comparable to the CB Time [7].

In addition, the LPI method can appear to be ambiguous because the rise of the N+ response is simultaneously affected by the injection and capture of the 1+ ions and the extraction of the N+ ions. Finally, large discrepancies were reported in the τ_{CB} measurements [8] with only small variations of CB parameters.

For these reasons it was proposed to measure τ_{CB} injecting the 1+ beam with very short pulses [9]. This method is called here the Short Pulse Injection (SPI).

[†] Julien.angot@lpsc.in2p3.fr.

Content from this work may be used under the terms of the CC BY 3.0 licence (© 2018). Any distribution of this work must maintain attribution to the author(s), title of the work, publisher, and DOI.

EXPERIMENTAL SETUP

The SPI was tested with the PHOENIX Charge Breeder on the LPSC 1+N+ test bench. The 1+ ion beam was generated by an ion gun source [10] and the pulse timing system was based on a signal generator to ensure a pre-cise pulse duration and triggering.

The charge breeder wasn't in the configuration offering the best efficiencies [11]. At injection it was equipped with a large diameter decelerating electrode, the HF blocker electrode [12] while the additional soft iron plug that increases the injection axial magnetic field peak was removed [11]. In this configuration, the maximum axial magnetic field was 1.2 T at injection (injection coil current of 1200 A), and 0.9 T at extraction (extraction coil current of 800 A). The charge breeder was equipped with a permanent magnet hexapole generating a 0.8 T radial magnetic field at plasma chamber wall.

Similar to the LPI, the 1+ and N+ beam intensities were measured with 1+ and N+ mass analysed Faraday cups.

RESULTS

N+ Response

The SPI method was tested injecting a Rb⁺ beam into an He plasma. The CB was configured as follows. The microwave power level was 510 W. The injection, minimum and extraction axial magnetic field strengths were simulated to be 1.19 T, 0.44 T and 0.84 T, respectively (injection, median and extraction coils were set to 1185 A, 320 A and 726 A respectively). The pulse duration was reduced until the temporal N+ response becomes constant in shape. Figure 2 shows the Rb¹⁹⁺ time response corresponding to a 2.5 ms SPI together with the integral of this signal i.e. the cumulative distribution function.

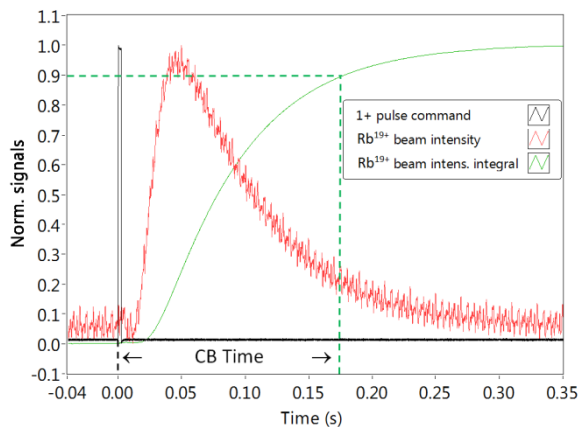


Figure 2: Rb19+ response to a 2.5 ms injected pulse and the corresponding integral function. The dashed lines are the references of the pulse start (black) and 90% level of the Rb19+ integral function (green).

With the SPI method, the efficiency is defined as the ratio between the number of injected particles over the number of extracted particles. It can be calculated by integrating both the 1+ and N+ signals.

The CB Time is defined as the time between the rise front of the 1+ pulse and the necessary time to extract 90% of the N+ ions (Fig. 2).

To compare the values, the Rb¹⁹⁺ efficiency and CB time were measured with both the LPI and SPI methods. The efficiency was found to be the same with both methods at 4.8 %. The CB Time with SPI (178 ms) was found to be shorter than with LPI (191 ms) by -10%, which means that the accumulation effect of the 1+ ions injection into the CB plasma is low in this configuration. Moreover, it can be seen that the N+ pulse is strongly asymmetric, which implies that a large fraction of the ions are produced and extracted at significantly shorter time.

Effect of the 1+ beam intensity

The influence of the 1+ beam intensity on the N+ response was studied in the range of 177 – 644 nA, the other experimental conditions (CB tuning, pulse duration...) being unchanged with respect to the previous measurement. The normalized N+ responses corresponding to several 1+ beam intensities are compared in Fig. 3.

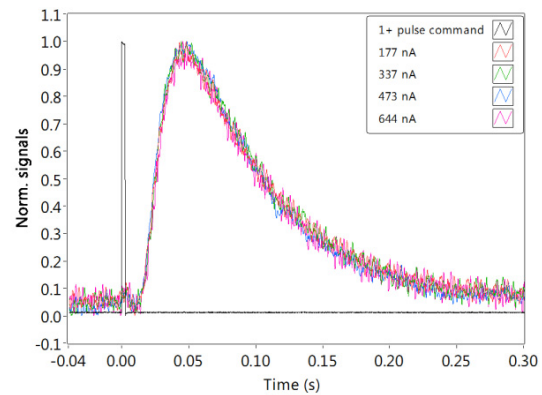


Figure 3: 1+ injection pulse and Rb¹⁹⁺ normalized signal responses to several 1+ beam pulse intensities.

In the studied beam intensity range, the N+ responses are the same, which means that the perturbation caused by the 1+ beam injection on the CB plasma is relatively small.

Influence of the N+ Charge State

Keeping the same configuration and with the same pulse duration, several N+ responses were measured for Rb charge states between 4+ and 19+. The time responses are plotted in Fig 4. These measurements illustrate the step by step ionisation process existing in ECR ion sources plasmas.

Similar results were obtained by several laboratories injecting short pulses of neutrals [13-16]. The goal of these earlier experiments was to study the plasma behaviour and estimate some plasma parameters (ion temperature and density, electron temperature and density...) by using 0 dimension model simulations.

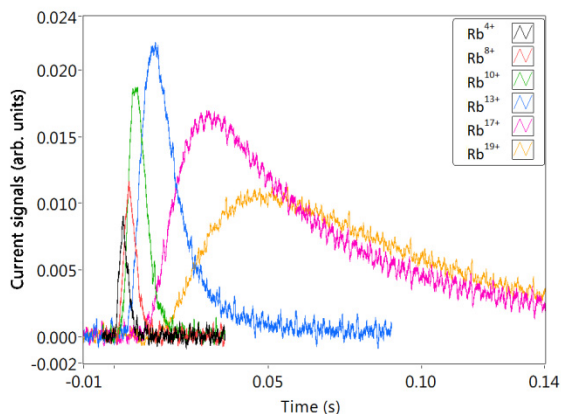


Figure 4: Rb⁴⁺, Rb⁸⁺, Rb¹⁰⁺, Rb¹³⁺, Rb¹⁷⁺ and Rb¹⁹⁺ beam intensity responses to a 2.5 ms injection pulse.

Plasma Behaviour Study Example with B_{min}

Similar to the neutral injection, the SPI can be used to study the CB plasma behavior. As an example, this was done by varying B_{min} . During the experiments, it was noticed that a linear variation of B_{min} in the range 0.432 - 0.444 T induced a linear variation of the Rb¹⁹⁺ efficiency. N⁺ responses were measured for several intermediate B_{min} values, see Fig. 5.

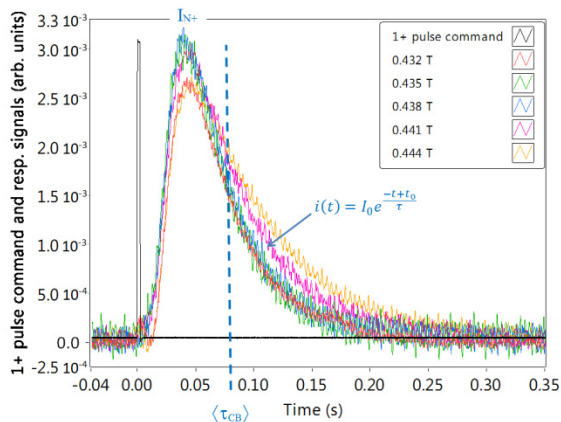


Figure 5: Rb¹⁹⁺ signal responses at several median coil currents.

From the N⁺ response, some parameters can be defined:

- i) I_{N^+} which is the beam intensity peak value
- ii) $\langle \tau_{CB} \rangle$ which is the time average of the N⁺ response and
- iii) τ which is a time constant when fitting the N⁺ response decay with a function of the form $i(t) = I_0 e^{-\frac{t-t_0}{\tau}}$.

Figure 6 shows the relative evolution of these parameters together with the LPI and SPI efficiencies as a function of B_{min} .

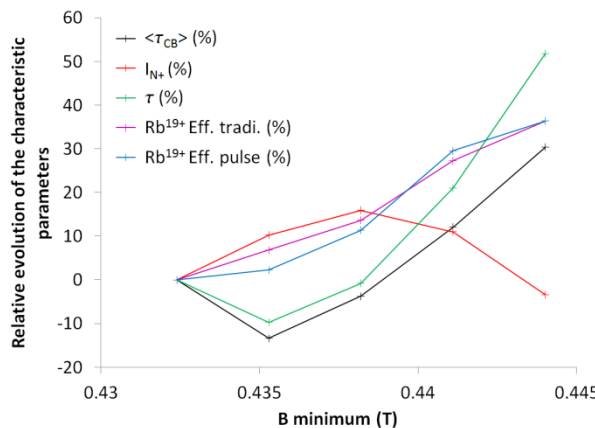


Figure 6: Variation of the time characteristics, maximum current and Rb¹⁹⁺ efficiency as a function of the median axial field.

In the studied range, the LPI and SPI efficiencies are the same. I_{N^+} passes by a maximum value at the middle of the range (+16% at $B_{min} = 0.438$ T) when $\langle \tau_{CB} \rangle$ and τ first experience a decrease of about 10% before substantial increase of respectively 30% and 50%. Since the decay time can be considered to be directly related to the confinement time of the high charge state ions [17], the result implies that at stronger B-minimum the ion confinement is improved.

IMPLICATION ON THE RIB CB EFFICIENCY

Efficiency as a Function of the Half-life

For stable elements, the SPI N⁺ response can be provided during preliminary RIB experiments done with the stable isotope or by earlier CB characterization measurements. If the RIB population decay is considered to be of the form of $N(t) = N_0 e^{-t/\tau_1}$ with $T_{1/2} = \tau_1 * \ln(2)$ and $T_{1/2}$ being the half-life, it becomes possible to estimate the actual RIB efficiency with the stable SPI N⁺ response more accurately than with the LPI method. This was done for Rb isotopes from ⁹³Rb ($T_{1/2}$ 5840 ms) to ⁹⁹Rb ($T_{1/2}$ 50.3 ms), using the ⁸⁵Rb¹⁹⁺ SPI N⁺ response shown above. Figure 7 shows the evolution of the Rb¹⁹⁺ RIB efficiency over Rb¹⁹⁺ stable efficiency ratio as a function of $T_{1/2}$.

Content from this work may be used under the terms of the CC BY 3.0 licence (© 2018). Any distribution of this work must maintain attribution to the author(s), title of the work, publisher, and DOI.

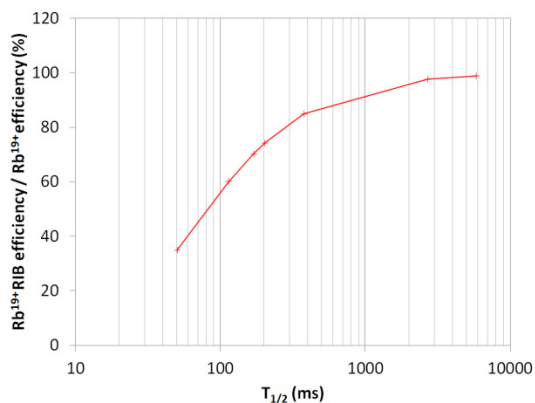


Figure 7: Evolution of the Rb^{19+} RIB efficiency over Rb^{19+} stable efficiency ratio as a function of $T_{1/2}$.

Down to a half-life of about 380ms, corresponding to $^{95}\text{Rb}^{19+}$, the reduction of efficiency is limited to about 15% but at shorter half-lives the CB efficiency starts decreasing rapidly for this charge state. An efficiency reduction of 65% is estimated for $^{99}\text{Rb}^{19+}$ in this case.

Efficiency As a Function of the Charge State

N^+ responses are different depending on the charge state (Fig. 4). The RIB efficiency estimation can be done for each charge state like done in the previous section for Rb^{19+} . Figure 8 shows the estimated efficiency CSD of the radioactive Rb isotopes between ^{93}Rb and ^{99}Rb together with the stable ^{85}Rb one.

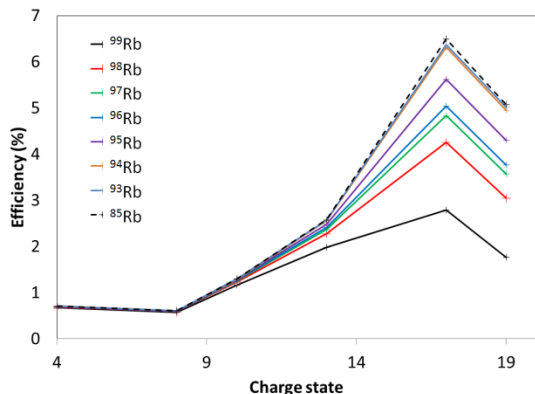


Figure 8: Rb isotope efficiencies as a function of the charge state.

From Fig. 8, it can be seen that the high charge state RIB ions are more affected by decay losses than lower charge state ones leading to a shift of the CSD toward lower charge state. It is clearly visible by plotting the average charge state as a function of $T_{1/2}$, see Fig. 9.

In the presented configuration, the mean charge state shift is of -1.6 when comparing ^{99}Rb with ^{85}Rb .

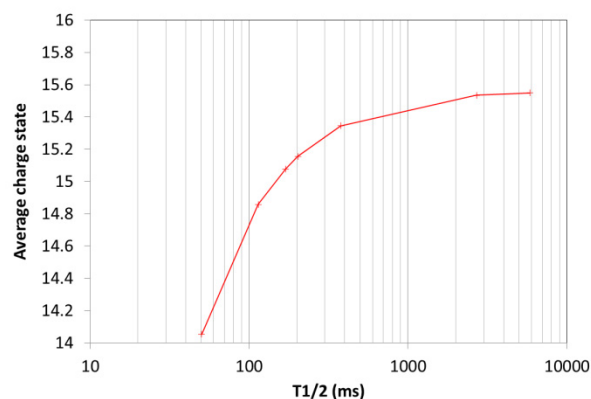


Figure 9: Evolution of the average ion beam charge state as a function of the half-life.

CONCLUSION

Using the SPI method, the temporal distribution of the N^+ beam extracted from the CB was measured. The efficiencies in SPI and LPI were compared and found equivalent. The CB Time with SPI was found shorter than with LPI by -10%.

SPI N^+ responses provide information on the plasma behavior and this method will be of interest to study the influence of the different CB parameters on the efficiency and charge breeding time and more generally on the ECR plasma behavior.

Finally, the N^+ response curves will allow more precise estimation of RIB efficiency as a function of the half-life and charge state which is crucial for ISOL facilities. The method of predicting the RIB efficiencies could be validated by RIB experiments.

REFERENCES

- [1] S. C. Jeong, M. Oyaizu, E. Tojyo, H. Kawakami, H. Ishiyama, H. Miyatake, K. Enomoto, Y. Watanabe, I. Katayama, T. Nomura, M. Matsuda, A. Osa, and S. Ichikawa, "Test results of 18 GHz ECR charge breeder for KEK-JAERI RNB facility", *Rev. Sci. Instrum.* vol. 75, pp.1631, (2004).
- [2] F. Ames, R. Baartman, P. Bricault, K. Jayamanna, M. McDonald, M. Olivo, P. Schmor, D. H. L. Yuan, and Lamy, "Charge state breeding of radioactive ions with an electron cyclotron resonance ion source at TRIUMF", *Rev. Sci. Instrum.* vol. 77, pp. 03B103 (2006).
- [3] L. Maunoury, P. Delahaye, M. Dubois, J. Angot, P. Sole, Bajeat, C. Barton, R. Frigot, A. Jeanne, P. Jardin, O. Kamalou, P. Lecomte, B. Osmond, G. Peschard, T. Lamy, and A. Savalle, "Charge breeder for the SPIRAL1 upgrade: Preliminary results", *Rev. Sci. Instrum.*, vol. 87, pp. 02B508, (2016).
- [4] T. Lamy, J. L. Bouly, J. C. Curdy, R. Geller, A. Lacoste, P. Sole, P. Sortais, T. Thuillier, J. L. Vieux-Rochaz, Jayamanna, M. Olivo, P. Schmor, and D. Yuan, "Charge state breeding applications with the ECR PHOENIX source: From low to high current production", *Rev. Sci. Instrum.* vol. 73, pp.717, (2002).
- [5] R. Vondrasek, J. Clark, A. Levand, T. Palchan, R. Pardo, Savard, and R. Scott, "Operational experience

- with the Argonne National Laboratory Californium Rare Ion Breeder Upgrade facility and electron cyclotron resonance charge breeder", *Rev. Sci. Instrum.* vol. 85, pp. 02B903 (2014).
- [6] O. Tarvainen, T. Lamy, J. Angot, T. Thuillier, P. Delahaye, L. Maunoury, J. Choinski, L. Standylo, A. Galata, G. Patti and H. Koivisto, "Injected 1+ ion beam as a diag-nostics tool of charge breeder ECR ion source plasmas", *Plasma Sources Sci. Technol.*, vol. 24, pp. 035014 (2015).
- [7] O. Tarvainen, J. Angot, I. Izotov, V. Skalyga, H. Koivisto, T. Thuillier, T. Kalvas and T. Lamy, "Plasma instabilities of a charge breeder ECRIS", *Plasma Sources Sci. Technol.* vol. 26, pp. 105002 (2017).
- [8] L. Maunoury, P. Delahaye, M. Dubois, O. Bajeat, C. Barthe-Dejean, R. Frigot, P. Jardin, A. Jeanne, O. Kamalou, P. Lecomte, B. Osmond, G. Peschard, A. Saval-le, J. Angot, T. Lamy, and P. Sole, "SPIRAL1 Charge Breeder: Performances and Status", *Proceedings of ECRIS2016, Busan, South Korea (JACoW, 2016)*, MOFO01.
- [9] O. Tarvainen, J. Angot, I. Izotov, V. Skalyga, H. Koivisto, T. Thuillier, T. Kalvas, V. Toivanen, R. Kronholm and T. Lamy, "The effect of plasma instabilities on the background impurities in charge breeder ECRIS", *Proceedings of ICIS2017, Geneva, Switzerland, T6_Tu_66* (to be published).
- [10] T. Lamy, J. Angot, T. Thuillier, P. Delahaye, L. Maunoury, J. Choinski, L. Standylo, A. Galata, G. Patti, H. Koivisto, O. Tarvainen, "Experimental activities with the LPSC charge breeder in the European context", in *Proceedings of ECRIS 2014, Nizhny Novgorod, Russia (JACoW, 2014)*, WEOBMH01.
- [11] J. Angot, T. Thuillier, O. Tarvainen, M. Baylac, J. Jacob, T. Lamy, M. Migliore and P. Sole, "Recent im-provements of the LPSC Charge Breeder", *Proceedings of ICIS2017, Geneva, Switzerland, T6_Tu_65* (to be published).
- [12] T. Lamy, J. Angot, M. Marie-Jeanne, J. Medard, P. Sortais, T. Thuillier, A. Galata and H. Koivisto, "Fine frequency tuning of the PHOENIX charge breeder used as a probe for ECRIS plasmas", *Proceedings of ECRIS 2010, Grenoble, France (JACoW, 2010)*, WEKOBK03.
- [13] R. C. Pardo, R. Harkewicz, and P. J. Billquist, "Time evolution of charge states in an electron cyclotron reso-nance ion source", *Rev. Sci. Instrum.* vol. 67, pp.1602, (1996).
- [14] V. Mironov, S. Runkel, K. E. Stiebing, O. Hohn, G. Shirkov, H. Schmidt-Böcking, and A. Schempp, "Plasma diagnostics at electron cyclotron resonance ion sources by injection of laser ablated fluxes of metal atoms", *Rev. Sci. Instrum.* vol. 72, pp. 2271, (2001).
- [15] T. Nakagawa, T. Aihara, Y. Higurashi, M. Kidera, M. Kase, Y. Yano, I. Arai, H. Arai, M. Imanaka, S. M. Lee, G. Arzumanyan, and G. Shirkov, "Electron cyclotron resonance ion source developments in RIKEN" (invited), *Rev. Sci. Instrum.* vol. 75, pp. 1394, (2004).
- [16] R. C. Vondrasek, R. H. Scott, R. C. Pardo, and D. Edgell, "Techniques for the measurement of ionization times in ECR ion sources using a fast sputter sample and fast gas valve", *Rev. Sci. Instrum.* vol. 73, pp. 548, (2002).
- [17] D. Neben, G. Machicoane, G. Parsey, A. Pham, J. Stetson and J. Verboncoeur, "An analysis of fast sputtering studies for ion confinement time", *Proceedings of LINAC2016, East Lansing, USA (JACoW, 2016)*, TUPCR032.

Content from this work may be used under the terms of the CC BY 3.0 licence (© 2018). Any distribution of this work must maintain attribution to the author(s), title of the work, publisher, and DOI.

SPIRAL1: A VERSATILE USER FACILITY

L. Maunoury[†], A. Annaluru, O. Bajeat, P. Delahaye, M. Dubois, R. Frigot, S. Hormigos, P. Jardin, O. Kamalou, N. Lechartier, P. Lecomte, B. Osmond, G. Peschard, P. Ujic, B. Retailleau, A. Savalle, J.C. Thomas, V. Toivanen, Grand Accélérateur National d'Ions Lourds, CEA-DRF/CNRS-IN2P3, bd Henri Becquerel, BP 55027, F-14076 Caen cedex 05, France
J. Angot, Laboratoire de Physique Subatomique et de Cosmologie - Université Grenoble Alpes - CNRS/IN2P3 - 53, rue des Martyrs, 38026 Grenoble Cedex, France
E. Traykov, Institut Pluridisciplinaire Hubert Curien, 23 rue du loess, BP 28, F-67037 Strasbourg cedex 02, France

Abstract

SPIRAL1 Upgrade hardware is now almost completed. The FEBIAD 1+ source has been tested for the production of new radioactive isotopes, the SPIRAL1 Charge Breeder (SP1 CB) is in place reproducing nearly the charge breeding efficiencies measured at LPSC laboratory and the infrastructure is operational. The commissioning phase started in the first semester of 2017. It has consisted of a stepwise process to test the upgrade of the SPIRAL1 facility from simple validation (operation of SP1 CB as a stand-alone source) up to the production of the first 1+/N+ Radioactive Ion Beam (RIB) with the $^{37}\text{K}^{9+}$ ion.

This contribution will summarize the different steps completed successfully and especially the measurements performed to validate each of the commissioning stages. These include e.g. ionization efficiency measurements for CB; beam line optics for 1+/N+ and charge breeding tuning. The remaining effort required to ensure the reliability of the complete system for routine RIB operation is also presented. A section will be dedicated to the coupling of SP1 CB to the CIME cyclotron, leading to the delivery of stable beams at unprecedented energies at GANIL.

INTRODUCTION

SPIRAL 1 is in operation since 2001 [1]. Radioactive atoms are produced by fragmentation of heavy ions up to 95MeV/u on a graphite target, and ionized in a multi-charged ECR ion source before post-acceleration in the CIME (Cyclotron d'Ions de Moyenne Energie) cyclotron [2]. This original Target Ion Source System (TISS) [3] was designed to provide mainly gaseous radioactive beams thanks to a cold transfer tube between the target and the ion source, trapping the radioactive condensable elements. The natural extension is to expand the radioactive beam production capability to condensable elements with masses up to 90 a.m.u.; hence, an upgrade of SPIRAL1 has been undertaken. The new configuration is based on the use of the 1+/N+ method developed at LPSC [4]. The aim is to have a larger palette of 1+ TISS devoted to other chemical element families. In this framework, a development of a TISS containing a FEBIAD (Forced Electron Beam Induced Arc Discharge) type ion source [5] is realized and some optimizations are requested to increase the longevity of such a system as well as the global efficiency. Moreover, the

charge breeder has been modified to increase its efficiency based on the conclusions of the Emilie collaboration studies [6]. More adjustments have been achieved during the commissioning phase at GANIL to enhance the production of highly charged ions. It started in June 2017 and ended in July 2018. During this period, numerous tests regarding beam optics, charge breeding efficiencies and coupling with the CIME cyclotron have been investigated to validate the whole system. This paper aims to present the outcomes and demonstrate that the SPIRAL1 facility is far beyond a unique 1+/N+ system.

SPIRAL1 CHARGE BREEDER

Figure 1 displays a scheme of the SP1 CB. It is mainly composed of an electrostatic quadrupole triplet aiming to focus the 1+ incoming beam into the SP1 CB injection part, the SP1 CB itself and an extraction system based on a movable grounded electrode connected to an Einzel lens. The SP1 CB is a version of the PHOENIX charge breeder developed at LPSC laboratory and built by the Pantechnik [http://www.pantechnik.com/] Company. During the commissioning, two main changes and one optimization have been done following the tests of this device done at LPSC in 2015. For the beam injection, an inner part of the injection iron plug, which acts as an RF blocker, was previously made of aluminium; it has been replaced by a soft iron piece having the same design to boost the maximum field at injection from 1.19T to 1.38T.

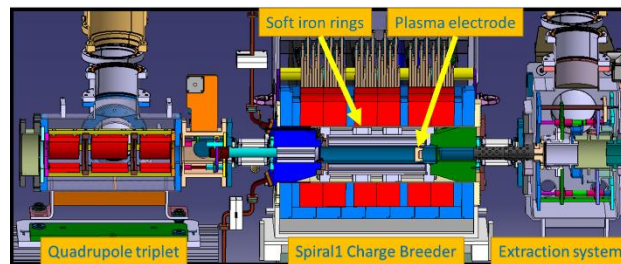


Figure 1: SPIRAL1 Charge Breeder.

At extraction, the plasma electrode has been moved closer to the maximum axial field by 10mm to reduce its interaction with the ECR plasma. The two soft iron rings, existing in the early design of the charge breeder, are placed on each side of the hexapole shaping the minimum

[†] maunoury@ganil.fr

Content from this work may be used under the terms of the CC BY 3.0 licence (© 2018). Any distribution of this work must maintain attribution to the author(s), title of the work, publisher, and DOI.

B axial magnetic profile. An optimization of their location allowed optimizing the charge breeding efficiency. The benefit of these modifications can be seen in the Fig. 2. Two charge state distributions of $^{40}\text{Ar}^{q+}$ extracted at 20kV are displayed: left side (blue) the charge state distribution as measured during the LPSC test in 2015 and right side (orange) as recorded after the adjustments. It is clear that the highly charged ions are enhanced drastically.

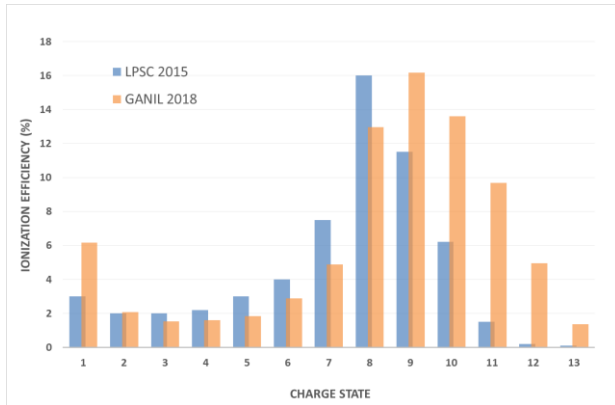


Figure 2: $^{40}\text{Ar}^{q+}$ charge state distributions.

MULTIMODE FACILITY

The upgraded SPIRAL1 facility will not use only the 1+/N+ method but other modes will also be available for providing beams to physicists: shooting through modes and SP1 CB as injector.

Figure 3 shows the four possible ways to use the facility. The two first modes (Fig. 3a and 3b) concern the shooting through modes. The SP1 CB is switched off. In the production cave, either NANOGAN3 TISS or FEBIAD TISS can be used. In the case of the NANOGAN3 TISS, a requirement in the project was to keep the possibility to use this previous system to provide multi-charged RIB's of gaseous elements especially for their post-acceleration by CIME. For the FEBIAD TISS, the monocharged RIB can be either sent towards a tape station to be qualified (intensity and purity) or sent towards the LPCTrap device [7]. In the future, this 1+ beam line will connect SPIRAL1 to the SPIRAL 2 low energy beam facility DESIR (Désintégration, Excitation et Stockage d'Ions radioactifs) [8]. For cleaning up the low energy RIB, a high resolution spectrometer under development at CENBG [9] will be installed before delivering the beam to the new experimental area.

The third mode (Fig. 3c) is the 1+/N+ method. It involves the FEBIAD TISS combined with the SP1 CB, which is switched on. The stable or radioactive beam is then transported to the CIME cyclotron to be post-accelerated and finally delivered to the GANIL experimental areas.

Finally, a new mode (Fig. 3d) is to use the SP1 CB as an injector since it is by itself an ECR ion source capable to provide highly charged ions on its own. In this mode ions are characterised by their M/Q ratio suitable to be accelerated by the CIME cyclotron. Consequently, it opens up a

new way to provide stable beams for users in an energy range from few MeV/u up to around 20MeV/u.

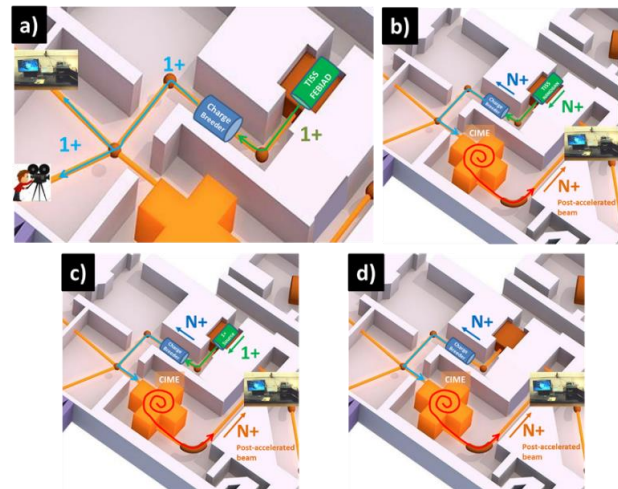


Figure 3: Four modes available at SPIRAL1 facility. a) Shooting through 1+ b) Shooting through N+ c) 1+/N+ d) SP1 CB as injector.

COMMISSIONING PHASE

The commissioning phase started beginning of June 2017. A major part of the commissioning was dedicated to find out the new optic settings as the beam transport line between the TISS and CIME has been largely reshuffled.

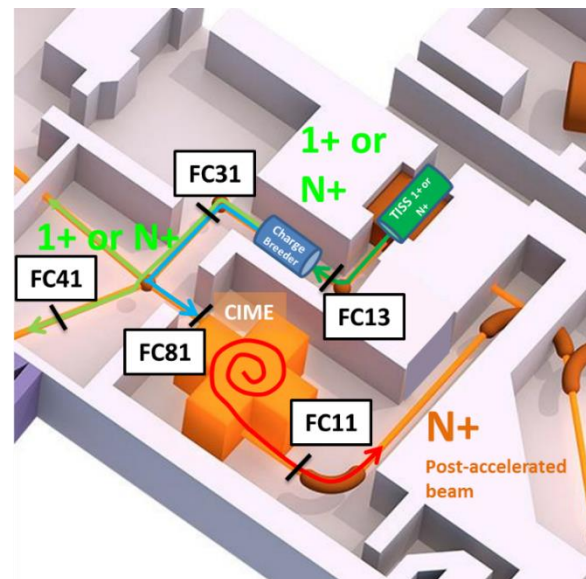


Figure 4: Location of the faraday cups along the SPIRAL1 facility.

A first study was performed regarding the 1+ beam line between the TISS and the entrance of the SP1 CB (switched off). The goal was to transport 1+ beams from the production cave up to the Faraday cup FC31 (downstream the SP1 CB, see Fig. 4, with the highest possible transmission. For this goal, an ion gun has been developed

based on a surface ion source using pellets from the Heat-Wave Labs company [10]. It can deliver stable alkali 1+ beams with an intensity up to several μA over weeks.

Benchmarking the beam characteristics (beam profiles in X and Y at several places and beam currents) using TraceWin code, a set of parameters was found to achieve 79% and 80% transmission for $^{23}\text{Na}^{1+}$ and $^{39}\text{K}^{1+}$. Doing the same work using the NANOGAN3 TISS but for a mul-ticharged ion beam ($^{40}\text{Ar}^{8+}$), the best measured transmis-sion was 62%, lower than those obtained with 1+ ions.

One explanation might come up from the emittance of the beam: In the case of the ion gun (1+ source), the beam emittance is around $30\pi\text{.mm.mrad}$ instead of, at least, $80\pi\text{.mm.mrad}$ for the NANOGAN3 (N+ source). The de-celeration tube at the entrance of the SPI CB complicates the tuning of the beam optics through the charge breeder. It has an inner diameter of 24mm over 80mm length, limiting the size of the beam and the quadrupole triplet produces a strong focusing effect. To overcome this issue, a new de-celeration tube with a larger inner diameter of 48mm will be tested.

To verify the operation of the SPI CB was conform to expectations, some charge breeding efficiencies were rec-ordered, which are presented in Table 1. Even for the K and Ar cases, values are close to the one formerly obtained in 2015 [11]. A larger discrepancy exists for the Na case with a decrease of 47% and 32% for the 7+ and 8 + charge states, respectively. Additional investigation is needed to explain these differences, which are amplified regarding the num-bers obtained recently by the LPSC team [12]: 12.9% charge breeding efficiency for the 8+.

Table 1: Charge Breeding Efficiencies.

Ion	Charge breed- ing efficiency LPSC 2015	Charge breed- ing efficiency GANIL 2018
$^{23}\text{Na}^{7+}$	6%	3.2%
$^{23}\text{Na}^{8+}$	5.3%	3.6%
$^{39}\text{K}^{9+}$	13.0%	11.6%
$^{40}\text{Ar}^{11+}$	12.9%	9.7%
$^{37}\text{K}^{9+}$ ($T_{1/2} = 1.24\text{s}$)		5.3%

For the first time at GANIL, a charge breeding effi-ciency of 5.3% has been recorded for one radioactive ion: $^{37}\text{K}^{9+}$ with a half-life of 1.24s. As compared to the charge breeding efficiency of the stable isotope, it represents around half of the expected value. As the ^{37}K half-life is long regarding the physics processes involved into the charge breeder, it cannot explain this discrepancy. Never-theless, this measurement lasted only four hours, including preparation with stable ^{40}Ar , which was not enough to op-timize properly such efficiency. More TISS to SPI CB cou-pling tests should be done in on-line conditions to improve the overall efficiency.

The parameter, which drives the tuning of the com-plete system, is “efficiency”. As the yield of radioactive at-oms produced in the hot carbon target are limited espe-cially for the very exotic species having short half-life <100ms, it is mandatory to maximize, for each section of the installation, this parameter. Table 2 shows typical num-bers measured and used to predict what will be the radio-active ion beam intensities available on the physicist target. Two modes are compared: the new 1+/N+ mode and the shooting through N+ mode using the previous NANOGAN3 TISS.

It is clear that the new mode 1+/N+ is, globally, less efficient due to the dissociation of the $\text{N}0 \Rightarrow \text{N}+$ ionization scheme into two separated processes: $\text{N}0 \Rightarrow 1+$ followed by $1+ \Rightarrow \text{N}+$. There is a range (0.31% -1.37%) where the 1+/N+ system is equivalent, in terms of efficiency, to the previous system operating at SPIRAL1. In addition, the global acceleration efficiency of CIME is enhanced (35-42%) for the mode using NANOGAN3 TISS regarding previous values recorded before the upgrade of the SPI-RAL1 facility (around 20%). It might be due to the insert of the SPI CB, which, thanks to its plasma electrode aper-ture of 6mm, defines better beam characteristics. Coming back to Table 2, the major bottleneck limiting the total effi-ciency of the complete system is the charge breeding effi-ciency and, to a lesser extent, the ionization efficiency of the FEBIAD source, which is currently around 5-10%. As the R&D program is pursued by a part of our group [13], some new discoveries have been done such as the addition of a heavy buffer gas Xe pulling up the ionization effi-ciency to higher values [12]. Concerning the charge breed-ing efficiency, more work will be undertaken on the injec-tion magnetic field profile as it was the major modification done at the LPSC CB leading to the great values obtained [12].

Table 2: Efficiencies Measured Along the Pathway of the Beam at the SPIRAL1 Facility. See Fig. 4 for the Faraday cups Positions.

Section	1+/N+ mode (FEBIAD)	Shooting through mode N+ (NANOGAN3)
$\epsilon_{\text{N}0 \Rightarrow \text{charged ion}}$	2.5%-50%	5-20%
$\epsilon_{\text{Beam transport} \Rightarrow \text{FC13}}$	>80%	40-70%
$\epsilon_{1+/N+}$	5-15%	-
Beam transport FC13 \Rightarrow FC31	>80%	60-75%
$\epsilon_{\text{Beam transport FC31} \Rightarrow \text{FC81}}$	70-95%	75%
$\epsilon_{\text{Beam acceleration FC81} \Rightarrow \text{FC11}}$	15-30%	35-42%
Total	0.01-1.4%	0.3-3.3%

The new mode “SPI CB as injector” has been investi-gated during this commissioning phase. It should be men-tioned there that the maximum current accepted by the

Content from this work may be used under the terms of the CC BY 3.0 licence (© 2018). Any distribution of this work must maintain attribution to the author(s), title of the work, publisher, and DOI.

CIME cyclotron is around ~80pnA which allows the operation of a wide range of charge states produced by the SP1 CB. Table 3 summarizes the stable beams delivered to physicists for performing physics experiments. The advantages of this operation mode are the following:

- Less cost than using the full GANIL machine
- High versatility especially for delivering beams based on gaseous elements
- Shorter time for tuning the accelerated beam

ONGOING R&D

Obviously, constant R&D is carried on to improve the whole system. It is mainly focused on the two following devices: TISS systems and SP1 CB. Regarding TISS, a R&D has been done to develop a new compact one [14, 15]. In the same hot vacuum vessel, the radioactive atoms are created by fusion-evaporation reactions and ionized through the surface ionisation process. Off-line tests are encouraging and on-line tests are scheduled by spring 2019 at IPNO laboratory to validate the new TISS principle.

Regarding the FEBIAD TISS [13], one of the features for its operation is to have a lifetime of one month including the off line measurements to validate the TISS before installing it inside the production cave. Mostly, R&D targets the protection of insulation against degradation by either the global heat of the system or the carbon vapour coming out from the hot graphite production target.

It is known that the radioactive atoms yields, for specific isotopes, can be enhanced by choosing carefully the material constituting the thick target. Henceforth, R&D related to the development of new targets based on SiC and/or Nb elements are under progress.

Table 3: Stable Beams Produced by the SP1 CB and Accelerated by the CIME Cyclotron.

Element	Charge State	Extraction voltage (kV)	Final energy (MeV)
³⁶ Ar	7	15	3.2
⁸⁴ Kr	11	14.3	2
⁸⁴ Kr	17	21.5	5
⁸⁴ Kr	20	28.8	7
⁸⁴ Kr	23	27.2	15
¹²⁹ Xe	22	13.3	2.5
¹²⁹ Xe	22	26.6	5
¹²⁹ Xe	27	32.7	7
¹²⁹ Xe	29	29.5	13

About the SP1 CB, three topics are investigated. First, the exploration of the ECR plasma properties is needed to get more insights of the physics processes underlying the capture as well as the confinement time processes acting on the global yields of the radioactive ion beams [16]. Secondly, it is of prime importance to improve as much as possible the charge breeding efficiency of light elements

(A<50 a.m.u.). For this purpose, it is foreseen to study the magnetic field at the injection of the SP1 CB in close collaboration with the LPSC team as they obtained [12] values that are the highest for such a device. Finally, a RF amplifier (TWTA type) with a frequency range from 8 GHz up to 18 GHz will be installed close to the SP1 CB. The aims are three- folds: enhancing the highly charged ion creation especially for the new SP1 CB operation mode described above (SP1 CB as injector), improving the charge breeding efficiency [17] and getting a more stable beam during operation.

CONCLUSION

The upgrade of the SPIRAL1 facility is now over. The infrastructure has been modified to fulfil the safety – security requirements as the radiation area is extended by the use of the charge breeder. Ancillaries for the SP1 CB are installed in the adjacent rooms: RF klystron, power supplies for coils, ΔV platform etc.

The FEBIAD TISS has demonstrated its ability to produce monocharged radioactive ion beams with intensity up to 2 10⁶ pps. Ionization efficiency and durability should be improved to match regular operation requirements.

The SP1 CB boosts the monocharged incoming beam with an average charge efficiency beyond 7%. However, this efficiency should be enhanced regarding light elements, which are requested by users. The new optic (setting) has been achieved and well understood for the section upstream the SP1 CB (1+ LEBT) while downstream (N+ LEBT) more investigations are needed using codes like TraceWin to get a better understanding of the parameters found experimentally.

Finally, one can conclude that commissioning phase is over, leaving the way open for the operation phase. A continuous R&D is under progress regarding hot production target materials, new TISSs, SP1 CB and beam optics to improve, at the end, the yields as well as the palette of RIBs available for the users at the SPIRAL1 facility.

ACKNOWLEDGEMENTS

The authors would like to thank all the GANIL technical staff for their support to achieve this upgrade of the SPIRAL1 facility. The authors would like also to give a special thanks to Richard Vondrasek at Argonne National Laboratory for his efficient advices regarding SP1 CB.

REFERENCES

- [1] A.C.C. Villari *et al.*, “The accelerated ISOL technique and the SPIRAL project”, *Nucl. Phys. A*, vol. 693, pp. 465-476 (2001).
- [2] L. Boy, “Problèmes posés par l'accélération d'ions radioactifs dans le projet SPIRAL. Réglage et stabilisation de l'accélérateur.”, Ph.D. thesis, Université de Caen, France, 1997.
- [3] L. Maunoury, “Production de faisceaux d'ions radioactifs multicharges pour SPIRAL: Etudes et réalisation du premier ensemble cible-source”, Ph.D. thesis, Université Paris VI, France, 1998.

- [4] T. Lamy *et al.*, “Charge breeding method results with the Phoenix booster ECR ion source”, in *Proc. 8th Eur. Particle Accelerator Conf. (EPAC’02)*, Paris, France, June 2002.
- [5] P. Chauveau *et al.*, “A new FEBIAD-type ion source for the upgrade of SPIRAL1 at GANIL”, *Nucl. Int. Meth. Phys. Res. B*, vol. 376, pp. 35-38 (2016).
- [6] P. Delahaye *et al.*, “Optimizing charge breeding techniques for ISOL facilities in Europe: Conclusions from the EMILIE project”, *Rev. Sci. Inst.*, vol. 87, pp. 02B510 (2016).
- [7] E. Liénard *et al.*, “Precision measurements with LPSCTrap at GANIL”, *Hyperfine Interactions*, vol. 236, p. 1 (2015)
- [8] <http://pro.ganil-spiral2.eu/spiral2/instrumentation/desir/what-is-desir/>
- [9] T. Kurtukian-Nieto, “SPIRAL2/DESIR high resolution mass separator”, *Nucl. Int. Meth. Phys. Res. B*, vol. 317, p. 284, (2013)
- [10] HeatWave labs, <http://www.cathode.com/>
- [11] L. Maunoury *et al.*, “Charge breeder for the SPIRAL1 upgrade: Preliminary results”, *Rev. Sci. Inst.*, vol. 87, p. 02B508 (2016).
- [12] J. Angot *et al.*, “Recent improvements of the LPSC Charge Breeder”, presented at *ICIS17, Cern, Switzerland, Oct. 2017*, unpublished.
- [13] P. Delahaye *et al.*, “New exotic beams from the SPIRAL 1 upgrade”, presented at *EMIS XVIII, Cern, Switzerland, Sep. 2018*, unpublished.
- [14] P. Jardin *et al.*, “Long-term research and development for the SPIRAL1 facility”, presented at *EMIS XVIII, Cern, Switzerland, Sep. 2018*, unpublished.
- [15] V. Kuchi *et al.*, “High efficiency ISOL system to produce neutron deficient short-lived alkali RIBs on GANIL/SPIRAL 1 facility”, presented at *EMIS XVIII, Cern, Switzerland, Sep. 2018*, unpublished.
- [16] A. Annaluru *et al.*, “ $1+N$ method: Numerical simulations and experimental measurements on SPIRAL1 charge breeder”, presented at *ECRIS’18, Catania, Italy, Sep. 2018*, paper MOC5, this proceedings.
- [17] R. Vondrasek *et al.*, “Performance of the Argonne National Laboratory electron cyclotron resonance charge breeder”, *Rev. Sci. Inst.*, vol. 82, p. 053301 (2011).

“

1+ / N+ METHOD: NUMERICAL SIMULATION STUDIES AND EXPERIMENTAL MEASUREMENTS ON THE SPIRAL1 CHARGE BREEDER

A. Annaluru[†], P. Delahaye, M. Dubois, P. Jardin, O. Kamalou, L. Maunoury, A. Savalle, V. Toivanen and P. Ujic, GANIL, F-14076 Caen, France
E. Traykov, IPHC, F-67200 Strasbourg, France

Abstract

In the framework of the SPIRAL1 facility, the R & D of charge breeding technique is of primary interest for optimizing the yields of radioactive ion beams (RIBs). This technique involves the transformation of mono-charged ion beams into multi-charged ion beams by operating an Electron Cyclotron Resonance (ECR) charge breeder (CB). During the SPIRAL1 commissioning, experimental studies have been performed in order to understand the transport of the beam through the CB with and without ECR plasma. Numerical simulations including ion optics and some ECR plasma features have been developed to evaluate ion losses during the ion transport through the CB with and without a simplified model of the ECR plasma.

INTRODUCTION

The SPIRAL1 facility at GANIL is dedicated to produce and accelerate the stable and radioactive ion beams which are delivered to physicists for nuclear experimental studies. Extending their research on exotic nuclei properties far from stability, an upgrade has been undertaken at SPIRAL1 to extend the range of post-accelerated exotic beams as well as to provide low energy (keV) radioactive beams to the future DESIR (Désintégration, Excitation et Stockage d'Ions Radioactifs) experimental area. Different Target Ion Source System (TISS) based on a forced electron beam induced arc discharge (FEBIAD) type mono-charged ion source [1] has been chosen to provide 1+ beams of condensable elements with high efficiency. The 1+ beams from TISS are mass analyzed and transported to the 14.5 GHz SPIRAL1 ECR charge breeder (CB), which increases the charge state charge of the radioactive ions from 1+ to N+. The extracted high charge state ions are mass analyzed and post accelerated to CIME cyclotron (Cyclotron d'Ions de Moyenne Energie) [2]. Figure. 1 shows the 3D cross-section of the charge breeder placed in the Low Energy Beam Transport (LEBT) between the TISS and the CIME. In the injection side of the CB the beam is focused with an electrostatic quadrupole triplet and the extracted beam is focused with an einzel lens. The charge breeder has gone through several modifications which are reported in [3, 4], and experimental charge breeding results are presented in [5]. During its operation, a few technical changes have been done in the configuration of the charge breeder: the position of two soft iron rings has been modified to optimize the axial magnetic field and the optimiza-

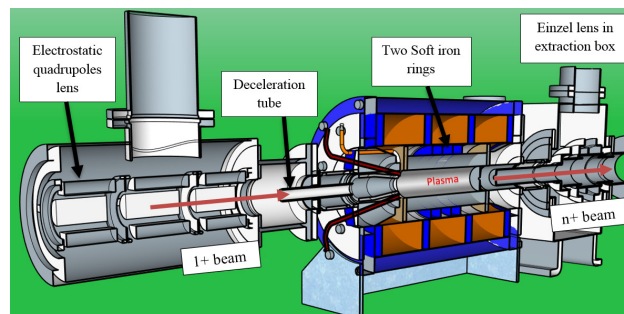


Figure 1: 3D view of ECR charge breeder connected with injection and extraction systems.

tion of the deceleration tube position to study its effect on beam stability and charge breeding efficiency. Experimental studies on LEBT transport and charge breeding efficiencies for $^{23}\text{Na}^+$ and $^{23}\text{Na}^{2+}$ have been carried out to understand the ion losses and 1+ capture processes by ECR plasma. A rough analysis on the experimental studies is described in the following sections by introducing a simplified ECR plasma model utilizing SIMION 3D. The results obtained from the simulations are presented and compared with the experimental ones.

EXPERIMENTAL ACTIVITIES WITH SPIRAL1 ECR CHARGE BREEDER

Modification of Axial Magnetic Field

In ECR ion source based charge breeders, the “Minimum-B” magnetic field structure is created by 2 or 3 independent solenoids (axial field) and hexapole (radial field) magnets enclosed in an iron yoke. In this configuration, the magnetic field is minimum at the center of plasma chamber and increases in all directions. The Minimum-B configuration is essential to form a closed resonance surface in the plasma chamber where ECR condition is fulfilled.

In SPIRAL1 charge breeder, the axial magnetic field (B) can be adjusted with the center coil and two movable soft iron rings (R1 and R2) placed around the hexapole as shown in Fig. 2. Magnetic field calculations were performed with RADIA [6] to study the axial magnetic field profile by adjusting the rings to different positions. Before the modification, the two rings were placed at extraction end of CB. When the rings are pushed to different positions, significant variations were observed in the size of ECR zone in axial direction. Axial magnetic field profiles for different rings position are

[†] arun.annaluru@ganil.fr

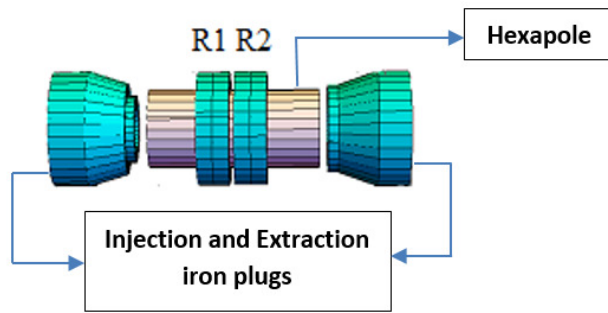


Figure 2: Position of two soft iron rings (R1 and R2) around the hexapole.

shown in Fig. 3. From these B field plots, the soft iron rings

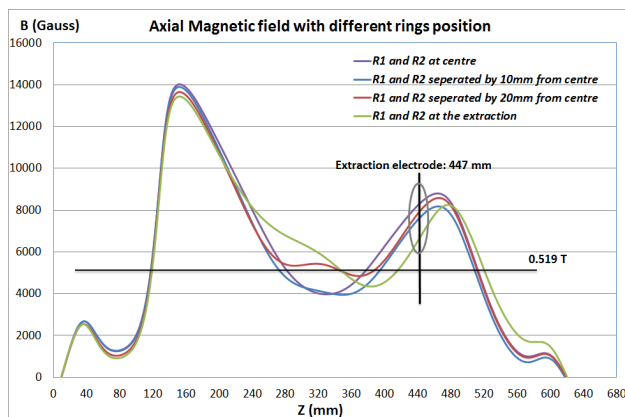


Figure 3: Axial B fields with different positions of the two soft iron rings. a) two rings touched at center (purple) b) rings separated by 10 mm from the center (Blue) c) rings separated by 20 mm from the center (Red) d) two rings at the extraction of CB. Center refers to the center of plasma chamber (320 mm).

Table 1: $^{39}\text{K}^{9+}$ Efficiency Measured at Different Rings Positions. Center Is referred As Center of Plasma Chamber (320 mm)

Rings position	$^{39}\text{K}^{9+}$ efficiency
R1 and R2 at extraction	7.44 %
R1 and R2 touched at center	10.08 %
R1 and R2 separated by 20mm from center	10.88%
R1 and R2 separated by 10mm from center	11.6%

separated by 10 mm from the center of the plasma chamber has been chosen as the best configuration. Because, the size of the ECR zone is larger, compared to the other configurations. Implementing this configuration can increase the ion and electron confinement times in the plasma volume consequently enhance the production of highly charged ions.

To test the theoretical hypothesis, this modification has been executed during the charge breeding of $^{39}\text{K}^{9+}$. During these measurements, Helium was used as buffer gas in CB. Table 1 shows the charge breeding efficiency of $^{39}\text{K}^{9+}$ with different positions of the two iron rings. As a result, with the best configuration charge breeding efficiency of $^{39}\text{K}^{9+}$ has been increased by a factor of 1.5 when compared with initial position of the rings.

Transmission Efficiencies of $^{39}\text{K}^+$ and $^{23}\text{Na}^+$

The thermionic ion gun was used to produce the 1+ ion beams of $^{39}\text{K}^+$ (420 nA) and $^{23}\text{Na}^+$ (550 nA) at 10 kV and 15 kV respectively, with emittance (4σ) of $50\pi\text{.mm.mrad}$ (non-normalized) through the 14.5 GHz SPIRAL1 ECR charge breeder at SPIRAL1. The 1+ and n+ beam lines have been tuned to achieve maximum ion beam current, up to the Faraday cup (FC_{1+}) and likewise to the Faraday cup (FC_{n+}), which is placed after the charge breeder. The starting point for the optics tuning was defined from TraceWin simulation in order to achieve high transmission efficiencies in LEBT. By turning OFF the charge breeder (without plasma and high voltage), the transmission efficiency of 80% and 78% on $^{39}\text{K}^+$ and $^{23}\text{Na}^+$ were recorded at faraday cup (FC_{n+}). The axial B field configuration was: at injection $B_{inj} = 1.41\text{ T}$, at center $B_{min} = 0.42\text{ T}$, at extraction $B_{ext} = 0.5\text{ T}$.

Charge breeding of ^{23}Na

Table 2: Parameters Used in Charge Breeding of Sodium

Parameters	Charge breeding of Na
Magnetic field at injection (B_{inj})	1.41 T
Magnetic field at minimum (B_{min})	0.42 T
Magnetic field at extraction (B_{ext})	0.91 T
RF power (Watt)	540 W

Hereafter, the experiments were performed with helium as buffer gas in ECR charge breeder, which is observed to be the best for optimizing the charge breeding efficiencies of high charge states of K and Na [7]. Please refer to Table 2 for typical values used for charge breeding of Na. The thermionic ion gun was used to produce the $^{23}\text{Na}^+$ beam which was injected into SPIRAL1 charge breeder with an intensity of 550 nA at 20 kV. The emittance (4σ) value for injected $^{23}\text{Na}^+$ is $30\pi\text{.mm.mrad}$ (non-normalized). By proper tuning of ΔV , the charge breeding efficiencies of 0.82%, 3.23%, 3.57% and 1.2% were recorded on Na^{2+} , Na^{7+} , Na^{8+} and Na^{9+} , respectively. ΔV was tuned between 6 V and 8 V. During the measurements, the tuning was observed to be very sensitive with the potential difference (ΔV) between 1+ source and charge breeder. The ΔV value for maximum achieved efficiency is same for high charge states of sodium, which was similar when compared with results obtained for sodium with LPSC PHOENIX charge breeder [8].

Effect of Deceleration Tube Position on Charge Breeding Efficiency

In SPIRAL1 charge breeder, the charge breeding efficiencies for $^{23}\text{Na}^+$ and $^{23}\text{Na}^{8+}$ were recorded at different positions of the deceleration tube. Observing the geometry sub-plot in Fig. 4, the optimum position is found at a distance of 21 mm from the injection plug of CB. The Na^+ beam measured downstream from the charge breeder was stable at the optimum position and became unstable when the tube was moved to the ends. It is also clear that, Na^{8+} plot shows the similar tendency with the position of the deceleration tube when compared with Na^+ . To summarize, this parameter is critical for the beam stability and has shown a clear effect on charge breeding efficiency.

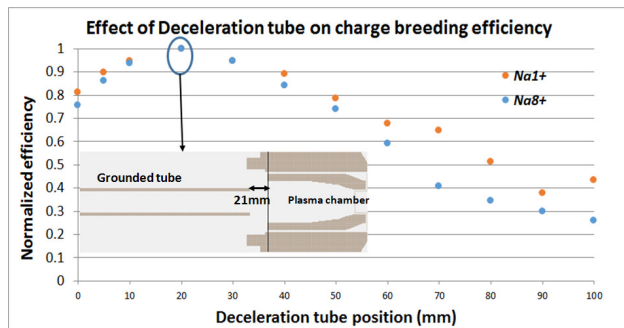


Figure 4: Effect of deceleration tube position on Na^+ and Na^{8+} charge breeding efficiency. At 0 mm, the position of the tube is inside the charge breeder. Measured Na^+ and Na^{8+} curves are normalized to 1 from 8.14% and 3.65%.

Effect of Injected Beam Emittance On Charge Breeding Efficiency

The 20 kV $^{23}\text{Na}^+$ beam was injected into SPIRAL1 charge breeder with an emittance of $30 \pi \cdot \text{mm} \cdot \text{mrad}$ (non-normalized). The ΔV was optimized in order to reach a Charge breeding efficiency of 3.53% on $^{23}\text{Na}^{8+}$. The in-

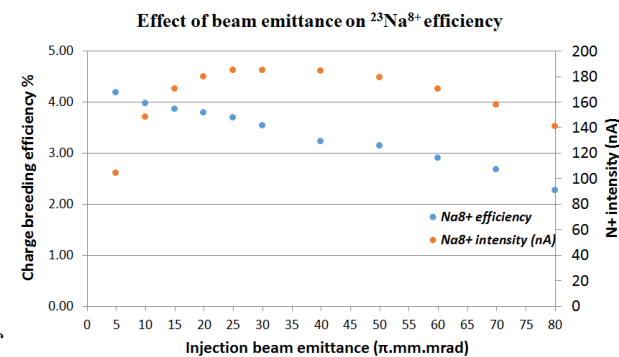


Figure 5: effect of beam emittance on Na^+ and Na^{8+} charge breeding efficiency.

jected beam emittance was then varied from $5 \pi \cdot \text{mm} \cdot \text{mrad}$ to $80 \pi \cdot \text{mm} \cdot \text{mrad}$ by adjusting a set of slits between the 1+ source and the CB. Figure. 5 depicts influence of injection

beam emittance on $^{23}\text{Na}^{8+}$ efficiency and n+ intensity. Observing the intensity plot, a significant drop in beam currents is recorded at low emittance. This drop correlates with the collimating parts of the beam that are actually injected into plasma. Beam currents steadily increases with increase in emittance, which correlates parts of the beam that cannot be injected into the plasma are collimated away by the slits. At higher emittance ($> 60 \pi \cdot \text{mm} \cdot \text{mrad}$), a small drop in beam currents has been observed. It suggests that perhaps increased ion losses in the injection region effecting the injection efficiency. The observed charge breeding efficiency trends steadily decrease with increase in emittance and n+ beam currents.

NUMERICAL SIMULATION STUDIES ON ECR CHARGE BREEDER

Simulation Description

Numerical simulations were performed using SIMION 3D [9] to evaluate the ion losses during the transport of 1+ beam through the charge breeder with and without a simplified model of the ECR plasma. These cases correspond with the situations where the CB is switched off (shooting through mode) and on (charge breeding mode).

The main ingredients of this simulation are; precise geometry of SPIRAL1 charge breeder, ion optics (deceleration tube, electrostatic quadrupole lens, CB extraction einzel lens) and 3D magnetic field of the charge breeder (calculated from RADIA). The electric fields are calculated in SIMION by applying potentials to the geometry electrodes. The geometry is arranged according to the LEBT line in SPIRAL1 as shown in Fig. 6. Additional features are added to the simulations according to our requirements (e. g., plasma potential). For initiating the ions in the simulation, a Matlab code has been developed, which can generate the initial ions using twiss parameters. The energy and mass of 1+ ions can be changed in the code according to our requirements. Furthermore, ion losses in the simulated system are monitored with a dedicated Lua user program.

Ion Transport Through Charge Breeder Without Plasma

In this case, $^{39}\text{K}^+$ and $^{23}\text{Na}^+$ ions at energy of 10 keV and 15 keV are injected into the charge breeder with emittance of $50 \pi \cdot \text{mm} \cdot \text{mrad}$. The emittance used for this case is similar to the experimental once. Figure. 6 shows the simulation of $^{39}\text{K}^+$ ions transported through the CB. In both cases (K^+ and Na^+), It was observed that up to 20% of the initial ions were lost at the extraction aperture.

Ion Transport Through Charge Breeder Plasma

To investigate this process, a simplified plasma model has been introduced in the simulation, which allows to reproduce the trends of experimental ΔV curves. A few regions of fixed potentials are included inside the plasma chamber to approximate the potential distribution in the plasma volume, including the potential dip in the core plasma (see

Content from this work may be used under the terms of the CC BY 3.0 licence (© 2018). Any distribution of this work must maintain attribution to the author(s), title of the work, publisher, and DOI.

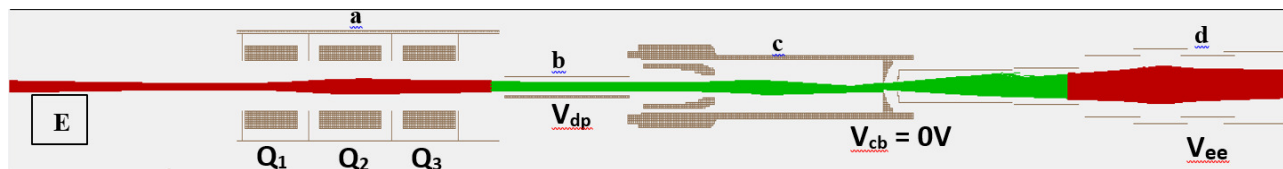


Figure 6: The geometry of electrostatic quadrupole lens (a), deceleration tube (b), ECR charge breeder (c) and extraction einzel lens (d) used in the ion transport simulation. At the point E, 10000 $^{39}\text{K}^+$ ions are initiated with the energy of 10 keV and simulated through ECR charge breeder. The total ions extracted from charge breeder are counted after the extraction system.

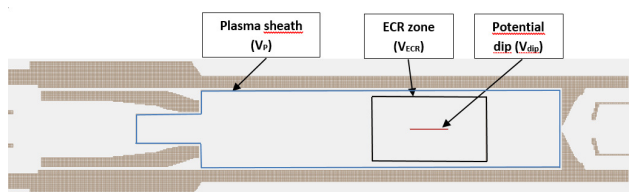


Figure 7: The geometry of ECR charge breeder with the ECR plasma features and ion optics used in the study of 1+ capture processes.

Fig. 7). The plasma potential (V_p) and potential applied at ECR zone (V_{ECR}) are always equal in all cases in order to confine the potential dip inside the resonance zone. The simplified plasma model presented in this paper does not include collisions or other interactions between the ions.

Before initiating the ions in the simulation, the plasma potential (V_p) and potential applied at ECR zone (V_{ECR}) are adjusted to higher value than the potential of charge breeder (V_{cb}) so that the incoming ions are decelerated due to positive plasma potential. The potential dip is always considered as $V_{dip} = V_{ECR} - 1 \text{ V}$. The plasma potential of 10 V has been chosen in order to reproduce the ΔV curves. However, based on experimental optimum ΔV results we know that the plasma potential in reality is lower, most likely below 8 V. But in order to simulate the trends, this discrepancy should not be critical.

Ions are initiated with an emittance of $30 \pi \cdot \text{mm} \cdot \text{mrad}$ at an energy of 20 keV. The ΔV curves in the simulation is defined as the potential difference between the charge breeder and injection energy of 1+ ions. In order to initiate Na^{2+} ion beam in this simulation, a Lua programme has been written to change the charge state of Na^+ to Na^{2+} after entering into ECR zone without disturbing the kinetic energy of ions.

SIMULATION RESULTS AND DISCUSSION

With the transmission simulations (CB off), Transmission efficiencies of 84% and 79% for K^+ and Na^+ were recorded after the extraction system, which are very similar to the experimental results reported in the previous sections. From the observations, 100% transmission has been achieved up to the entrance of CB. The ion losses were observed only at the extraction aperture. Ion losses significantly increase with increase in V_{cb} .

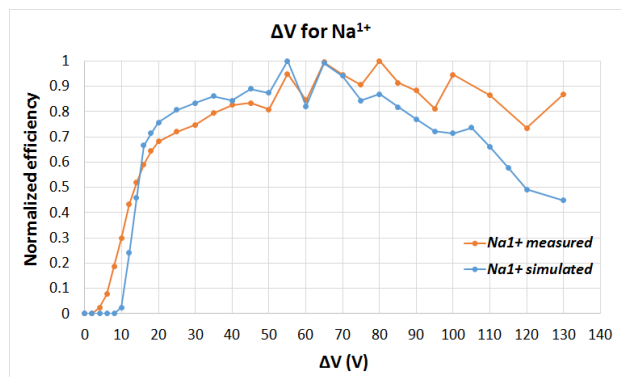


Figure 8: Normalized efficiencies of Na^+ as a function of ΔV . Measured and simulated curves are normalized to 1 from 28% and 24%.

The second part of the numerical simulation concerned the extraction of Na^+ and Na^{2+} through CB plasma volume. From the observations, the recorded simulated curve seems to shift towards higher ΔV when compared with experimental curves. In order to find the best agreement with the experimental curves, the emittance of 1+ beam has been varied to $20 \pi \cdot \text{mm} \cdot \text{mrad}$ by keeping the same twiss parameters. Observing Fig. 8 and Fig. 9, similar trends were recorded for Na^+ and Na^{2+} . At low ΔV , most of the ions are reflected back to the deceleration tube due to positive plasma potential (e.g. 85% of ions with ΔV between 9 - 10 V). When ΔV is at 55 V, the maximum of the Na^+ is obtained, and the ion losses at the entrance of plasma chamber significantly decreased to 15%. Moreover, real discrepancies can be seen after 50V and higher, which was also observed in Na^+ experimental curves. In case of Na^{2+} , the ions are initiated at the core of ECR zone. The observed trends between the simulated and measured data agree, but the simulation seems to significantly over-estimate the efficiency compared to the measured values. This is probably due to the very simplified 1+ \rightarrow 2+ conversion model implemented in the simulations.

The discrepancies observed in the simulations shows that the 1+ (and maybe 2+) beam traversing through the plasma chamber exhibits a periodic focusing/defocusing behavior due to the solenoid field [10], and consequently the phase of this motion at the extraction aperture influences the transmission. Furthermore, as this motion is ion energy dependent, varying ΔV or V_{cb} influences the phase at the extraction aper-

Content from this work may be used under the terms of the CC BY 3.0 licence (© 2018). Any distribution of this work must maintain attribution to the author(s), title of the work, publisher, and DOI.

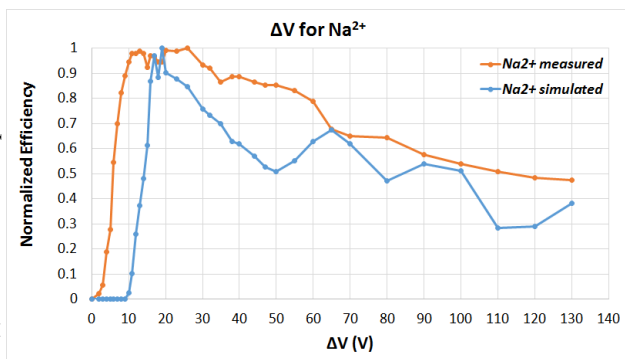


Figure 9: Normalized breeding efficiency of Na^{2+} as a function of ΔV . Measured and simulated curves after are normalized to 1 from 0.9% and 21%.

ture and therefore the transmission. Thus this phenomenon can explain some of the features seen in the simulation results (oscillating transmission). As similar oscillations are present in measured data, it suggests that perhaps similar effects takes place in reality.

SUMMARY AND PERSPECTIVES

Simulations revealed that the ion losses at the extraction aperture are mostly due to the beam oscillations in the charge breeder. The transmission efficiencies obtained from the simulations show good agreement with the experimental results. The ΔV plots for Na^+ and Na^{2+} obtained from a rough analysis performed with the simplified ECR plasma model has shown similar trends when compared with the experimental curves. In future, the simulation model presented in this paper will be improved by distributing the Na^{2+} ions randomly in the core of ECR plasma instead of using a conversion from 1+ to 2+ at a fixed axial position. Simultaneously, the ΔV plots for Na^+ and Na^{2+} will be calculated with a numerical simulation code called MCBC (Monte Carlo Charge Breeding Code) which can model the capture and charge breeding of a beam of ions injected into a plasma [11]. The ΔV plots

obtained from SIMION 3D and MCBC will be compared for further investigation regarding the 1+ capture process by ECR plasma. To complete this analysis, additional experimental data will be gathered from Mg (using He buffer gas) and K (using He and O_2 buffer gas) charge breeding efficiency (also charge breeding time) measurements. This approach can show a possible way to determine the tendency of charge breeding parameters which influences the 1+ ion capture efficiency by the ECR plasma.

REFERENCES

- [1] O. Kamalou *et al.*, in *Proc. of the 13th International Conference on Heavy Ion Accelerator Technology*, pp.20-22 (2015)
- [2] M. Duval *et al.*, in *Proc. of the 14th International Workshop on Magnet Technology, MT-14 Tampere, Finland, June 11-16 (1995)*.
- [3] P. Delahaye *et al.*, *Nuclear Instruments and Methods in Physics Research, A* vol. 693, p. 104 (2012).
- [4] L. Maunoury *et al.*, *Review of Scientific Instruments*, vol. 85, p. 02A504 (2016).
- [5] L. Maunoury *et al.*, in *Proc. of the 22nd International Work-shop on ECR Ion Sources*, Busan, South Korea, 28th August-1st September (2016).
- [6] RADIA magnetic field simulation code, <http://www.esrf.eu/Accelerators/Groups/InsertionDevices/Software/Radia>
- [7] L. Maunoury *et al.*, *Review of Scientific Instruments*, vol. 87, pp. 02B508 (2016).
- [8] T. Lamy *et al.*, in *Proc. of the 18th International Workshop on ECR Ion Sources*, Chicago, Illinois, US, September 15-18, 2008.
- [9] SIMION Ion and Electron Optics Simulator, <http://simion.com>
ScientificInstrumentServices, Inc. (SIS)
- [10] V. Kumar, *American Journal of Physics*, vol. 77, pp. 737 (2009).
- [11] JS. Kim *et al.*, *Review of Scientific Instruments*, vol. 78, pp. 103503, (2007).

REDESIGN OF THE GANIL GTS ECRIS FOR 1+/N+ STUDIES

V. Toivanen[†], P. Jardin, L. Maunoury, C. Michel
Grand Accélérateur National d'Ions Lourds (GANIL), F-14076 Caen Cedex 05, France

Abstract

More than half of the beams produced at GANIL are metallic elements, underlining the importance of their continuing development. Compared to the conventional techniques (oven, sputtering, MIVOC), the 1+/n+ method has demonstrated superior ionization efficiencies, suggesting the potential for improved metal beam production. Dedicated studies are required to assess the feasibility of this approach. The SPIRAL1 Charge Breeder is now in operation at the GANIL radioactive beam facility SPIRAL1. Operation in high radiation area poses challenges for its future development. A separate test stand supporting charge breeder and metal ion beam R&D is thus desirable.

The GTS 14.5 GHz ECRIS has been chosen as a platform for 1+/n+ studies. After the upgrade program of 2017-2018, the GTS provides good performance and versatility, making it well-suited for ion source R&D. A new injection module has been designed for 1+ injection into the GTS plasma to be used in the 1+/n+ studies. It can be easily replaced with the conventional system for normal ion source operation. The design of the new injection system will be presented in detail with ion optical simulations of the 1+ beam injection.

INTRODUCTION

The GTS 14.5 GHz Electron Cyclotron Resonance (ECR) ion source has undergone a substantial upgrade program in 2017 - 2018. As part of this upgrade, the ion source beam extraction system was refurbished, a new center coil was added to improve the magnetic field control and the injection side of the source was redesigned to reach higher injection magnetic fields and to allow double frequency operation in a wide frequency range. These changes are discussed in more detail in Ref. [1]. As presented there, the extraction system and center coil upgrades yielded an improvement of up to a factor of three for the delivered beam currents in 2017. In 2018 the new injection system has been commissioned for operation, which has provided further performance improvements, especially for the high charge state beams. For example, with double frequency operation (14.5 GHz + 11.215 GHz) the GTS has recently produced a 17.5 μA beam of $^{129}\text{Xe}^{30+}$, which is over eight times higher intensity than before the upgrade program.

The motivation for the GTS upgrades has been two-fold. First, the goal was to improve the beam capabilities available for the multidisciplinary low energy beam facility ARIBE (Accélérateurs pour les Recherches Interdisciplinaires avec les Ions de Basse Energie), which is the primary user of the GTS beams. The second goal was to establish a good baseline performance for continued ion source R&D with

the GTS. As these goals have now been achieved, the next phase for the GTS is to utilize it for charge breeding (or 1+/n+ method) research. This will be a second role for the GTS, as it will also continue to serve the ARIBE facility in its conventional ion source configuration.

One potential future application of the 1+/n+ method is enhanced metal ion production. Metal ion beams are currently widely used in the accelerator facilities around the world, and as an example, more than 50 % of the beams delivered at GANIL are metallic elements. This highlights the importance to continue metal ion production development with ECR ion sources. With conventional techniques like sputtering, miniature ovens and MIVOC, the global ionization efficiencies of metal beams is low. Here, the global efficiency is defined as the ratio of the extracted ion flow (all ion species of the element) over the injected neutral flow. Based on the data collected from GANIL operation, published in Ref. [2], the typical measured global efficiencies for sputtering are around 1 %, oven beams around 10 % and MIVOC beams around 20 %. In total, all measured efficiency data is below 30 %. In contrast, experience with charge breeders has shown that with 1+ injection global efficiencies around and in excess of 50 % are achievable (see e.g. Ref. [3]). The higher efficiency would first of all reduce the material consumption, which is not an insignificant consideration for rare and expensive elements and isotopes. Secondly, decrease in injected material would reduce the plasma chamber contamination. Furthermore, decoupling the initial metal ion production and the stepwise multi-ionization allows both of these processes to be optimized independently.

However, dedicated studies are necessary to validate the feasibility of these ideas. One of the main challenges that needs to be assessed is the high intensity operation. Although several measurements performed so far suggest a weak relationship between the 1+ capture and ionization efficiencies and the injected 1+ current, this effect has been mainly studied with low currents up to only a few μA (see e.g. Refs. [4–7]). In order to make 1+/n+ method a realistic alternative for the conventional techniques, it must be demonstrated that the high efficiencies can be retained also with significantly higher current levels. The GTS can provide a suitable test bench for these studies.

The GTS will be used also for studying other aspects of charge breeding. The SPIRAL1 Charge Breeder has been recently installed and commissioned at the GANIL radioactive ion beam facility SPIRAL1 [8]. The role of the machine is to charge breed the singly charged radioactive elements produced by the Target Ion Source Systems (TISS) and deliver the multiply charged ions for post-acceleration and experiments. As an operational machine in a high radiation dose area, the access to the charge breeder will be limited

[†] ville.toivanen@ganil.fr

Content from this work may be used under the terms of the CC BY 3.0 licence (© 2018). Any distribution of this work must maintain attribution to the author(s), title of the work, publisher, and DOI.

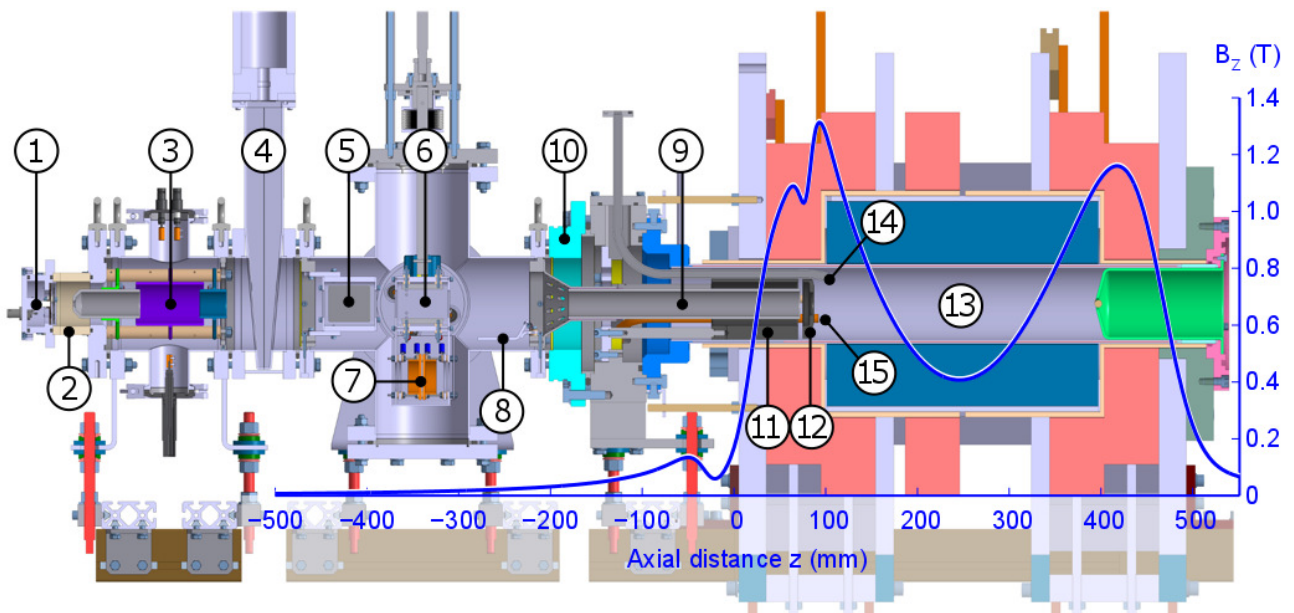


Figure 1: Cross section view of the 1+ beam injection module connected to the GTS. The main parts include (1) a 1+ source, (2) an insulator, (3) a 1+ beam extraction system (a puller electrode and an einzel lens), (4) an isolating valve, (5) horizontal and (6) vertical steerers, (7) two-sided Faraday cup, (8) a beam dump, (9) a grounded guiding tube, (10) a main insulator, (11) an ARMCO cylinder, (12) an ARMCO injection aperture electrode (IAE), (13) the GTS plasma chamber, (14) a WR62 waveguide and (15) a gas injection tube. The second WRD750 wave guide is not visible in this view. The GTS axial magnetic field is also presented.

in the future, which will set restrictions to its development. As such, it will be beneficial to have access to an offline test bench to perform charge breeder specific R&D. The operational experience and mechanical upgrades developed with the test bench can then be transferred to the SPIRAL1 Charge Breeder.

In order to use the GTS for the charge breeding (1+/n+ method) studies, it needs to be modified to allow 1+ beam injection into the ECR plasma. These modifications are presented in the following chapter.

INJECTION MODULE DESIGN

One of the main principles of the GTS modifications is the ability to transition from normal ion source operation to 1+/n+ operation (and vice versa) in a relatively short time. To accommodate this requirement, a new injection side module has been designed which completely replaces the conventional ECRIS injection system hardware when the GTS will be operated with 1+ beam injection. The existing injection system can be pulled out of the ion source on rails and lifted off as a single unit. The dedicated 1+ injection hardware can then be lifted on the rails and connected to the ion source. Including the pumping time, a beam-to-beam time of a few days should be realistic with this approach when the GTS is transitioned between conventional ion source operation and 1+/n+ studies.

The design of the 1+ injection module is presented in Fig. 1. The 1+/n+ studies will start using an existing alkali ion source as the source of singly charged ions. It is based on

thermal ion emission from a heated porous tungsten pellet that is doped with the alkali element of interest. Based on past experience, the source can deliver 1+ ions from nA levels up to around 1 mA, offering a wide current range for experiments. The 1+ source is electrically separated from the rest of the system, and it will be operated at a potential of $V_{1+} = V_{GTS} + \Delta V$, where V_{GTS} is the potential of the GTS plasma chamber and ΔV is an adjustable voltage to allow the ions to overcome the positive plasma potential to enter the GTS plasma volume. The transport section between the 1+ source and the GTS plasma chamber is grounded, so the ion kinetic energy in this region is $e(V_{GTS} + \Delta V)$.

The 1+ source features a Wehnelt electrode to control the beam formation from the heated pellet. Normally the Wehnelt is biased negatively to some hundreds of Volts with respect to the pellet potential. The 1+ source is followed by a beam extraction system consisting of a puller electrode and a positive (decelerating) einzel lens. The pellet source and the extraction system can be separated from the rest of the injection module with a gate valve. This allows manipulation and exchange of the 1+ source without compromising the GTS vacuum.

The design features two independent steerers (horizontal and vertical) which can be used to manipulate the beam as it passes through the injection system. With low steerer voltages the beam alignment with respect to the optical axis can be varied. This can be used to correct beam misalignments or to study the effects of varying the transverse insertion location of the beam into the GTS plasma chamber. The ver-

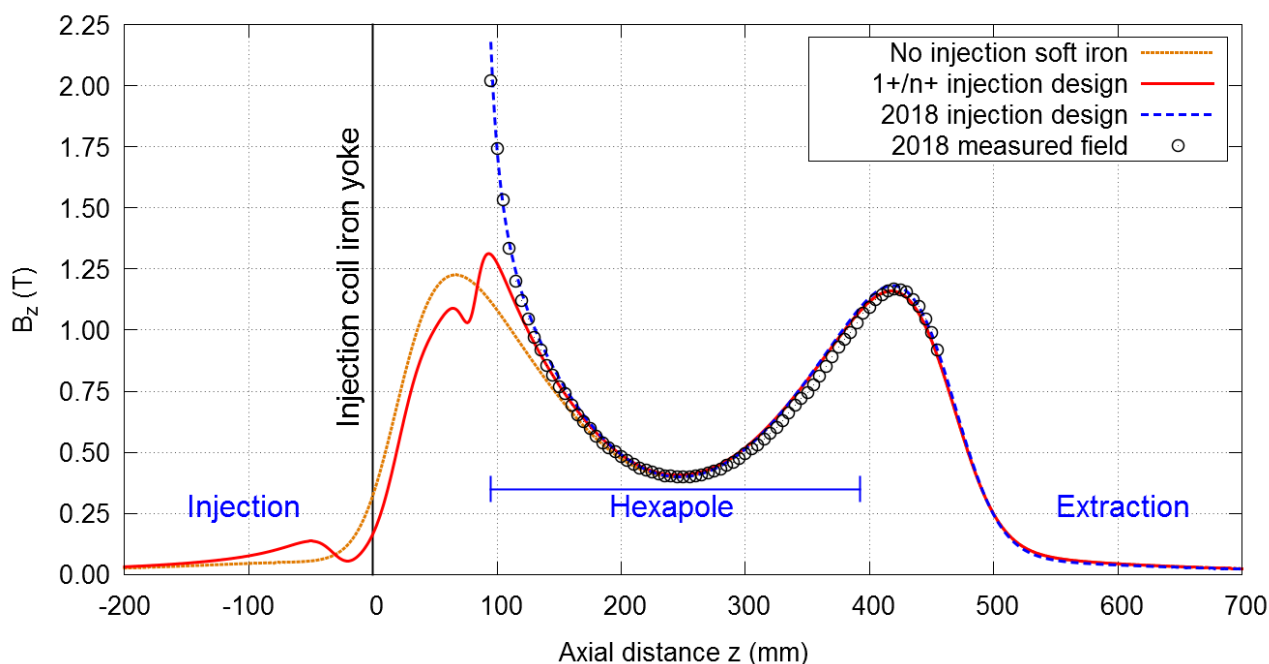


Figure 2: GTS axial field profile with different injection soft iron configurations. The 2018 design corresponds to the new injection system installed in 2018 for conventional ion source operation. In all cases the injection, center and extraction coil currents are 1200 A, 0 A and 1100 A, respectively.

tical steerer is designed to be used also for beam pulsing. In this operation mode the 1+ beam is deviated into a dedicated beam dump. In principle any desired pulse pattern can be created for the of 1+ beam by varying the vertical steerer potential as a function of time. This feature is especially important for the studies involving measurements of charge breeding time.

After the steerers the beam enters a grounded tube that guides the ions inside the GTS high voltage enclosure. The 1+ ions are decelerated into the GTS plasma volume between the end of the grounded tube and a conically shaped injection aperture electrode (see (12) in Fig. 1). The injection aperture electrode can be biased with respect to the plasma chamber potential. In this configuration it can be used in a similar fashion as the biased disc of a conventional ECR ion source. However, as the electrode is situated only around the axis, experimental work is required to determine its effectiveness in 1+/n+ operation.

For beam diagnostics the injection design features a two-sided Faraday cup, which can be moved on an actuator to replace the vertical steerer. The Faraday cup can be used to measure both the 1+ beam current from the 1+ source as well as the beam current of the ions extracted from the GTS plasma chamber towards the injection. In addition, the current collected on the beam dump and on the grounded guiding tube can be measured.

The injection design features two wave guides for microwave injection; a WR62 for nominal 14.5 GHz operation and a double-ridge WRD750 with a wide 8 – 18 GHz range for varied or double frequency operation. Gas injection is

performed through a dedicated gas tube. Due to the Halbach-style hexapole, access through the injection is the only option for microwave and gas insertion. The wave guides and the gas pipe enter the GTS plasma chamber through the edges of the injection aperture electrode with a 120° azimuthal symmetry. This is done to ensure symmetrical cuts on the soft iron pieces to minimize asymmetry in the injection magnetic field. Field asymmetry in this region can lead to unwanted steering of the incoming ions, degrading the injection efficiency [3, 6, 9]. In addition, this solution places the wave guides and the gas pipe between the arms of the star-shaped axial plasma loss pattern.

To allow access for the 1+ beam, the solid soft iron plug that boosts the injection axial magnetic field in conventional ECRIS configuration is not possible in the 1+/n+ operation mode. This unavoidably leads to decreased magnetic field in this region. However, the removal of the injection plug is partly compensated with a new soft iron structure around the space that is required for the beam injection.

The magnetic design calculations were performed with the Radia software [10]. After studying several geometrical options within the boundary conditions set by the GTS structure, a design featuring a hollow ARMCO cylinder located around the grounded tube and a conical ARMCO tip with a smaller 25 mm aperture was chosen (parts (11) and (12) in Fig. 1). The conical piece also fulfills the role of the injection aperture electrode discussed previously. The chosen design provides a 1.32 T axial field maximum, which is located at the injection end of the GTS hexapole magnet. This value is comparable with the injection field of the SPI-

Content from this work may be used under the terms of the CC BY 3.0 licence (© 2018). Any distribution of this work must maintain attribution to the author(s), title of the work, publisher, and DOI.

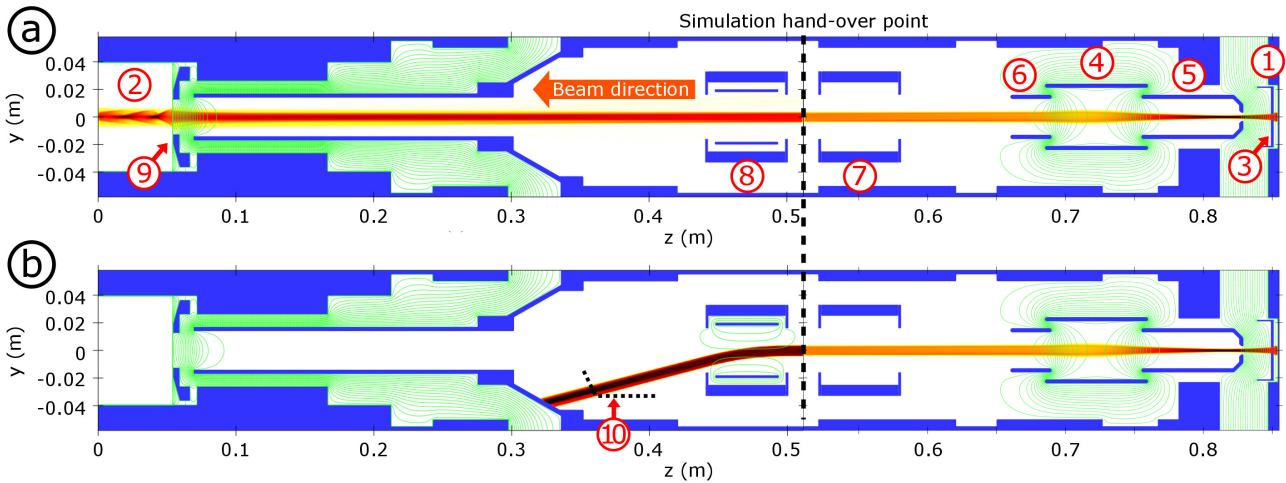


Figure 3: *Case (a)*: Ion optical simulation (trajectory density) for $10\ \mu\text{A}$ of $^{39}\text{K}^+$ ions extracted from the 1+ source (1), transported through the injection module and decelerated into the GTS plasma chamber (2). Plasma potential is 10 V. The 1+ source potential is $V_{1+} = V_{GTS} + \Delta V$, where $V_{GTS} = 15\ \text{kV}$ and $\Delta V = 30\ \text{V}$. The 1+ source Wehnelt electrode (3) is at $V_W = V_{1+} - 600\ \text{V}$ and the einzel electrode (4) at 11 kV. The puller (5) and the last extraction electrode (6) are grounded. Both steerers (7 and 8) are off, i.e. grounded. The injection aperture electrode (IAE) (9) is at GTS chamber potential; $V_{IAE} = V_{GTS} = 15\ \text{kV}$. The 1+ beam transmission from the 1+ source to inside the GTS plasma chamber is 92 %. *Case (b)*: An example of beam deflection with the vertical steerer for pulsed 1+ beam operation. The steerer plates are set to $\pm 3\ \text{keV}$. The location of the beam dump (10) is presented with a dashed line.

RAL1 Charge Breeder and is close to the 1.4 T value of the ECR Charge Breeder at ANL [9], which further increases the confidence to the design. The calculated axial magnetic field is presented in Fig. 2, compared to the current GTS axial field in conventional ion source operation mode. A case without any added soft iron in the injection side of the GTS is also shown. The measured field values with the current injection system are also included, demonstrating the good correlation between the field calculated with the Radia model and the reality. In Fig. 1 the axial field is overlaid with the mechanical design of the injection module and the GTS.

ION OPTICAL SIMULATIONS

The injection module design was developed with the aid of ion optical simulations. The simulations were performed with the code IBSimu [11], utilizing the 3D magnetic field maps calculated for the system with Radia. The simulation model includes the magnetic field present inside the ion source as well as the fringe field that extends into the injection module region. The field map contains both the solenoid and the hexapole field components of the ion source.

A simplified plasma volume is implemented in the simulation model to approximate the influence of the plasma to the 1+ ion trajectories at the entrance to the GTS plasma chamber. The plasma volume is modeled with an analytical electron background which compensates the ion space charge. A constant plasma potential of 10 V is imposed inside the plasma volume and its boundaries are kept constant, as the plasma is assumed not to be significantly influenced by the injected 1+ ions. The axial boundary is set at the

plasma facing surface of the injection aperture electrode. Collisions between injected 1+ ions and plasma particles are not included in the simulation model.

In order to keep the simulation volume at a manageable size and to reduce the system memory requirements, the simulations were performed in two parts. The system is divided in the axial direction with the hand-over point at $z = 0.511\ \text{m}$ in simulation coordinates (see Fig. 3). This location was chosen as it provides a potential free region and thus omitting the geometry on one side of this position does not influence the ion behavior.

The main baseline beam used in the simulations is $^{39}\text{K}^+$, extracted from the 1+ source with voltages around 15 kV. An example of $^{39}\text{K}^+$ injection into the GTS plasma chamber is presented in Fig. 3(a). The extracted beam current is $10\ \mu\text{A}$ and the 4rms-emittance is 20 mm mrad. The relevant potential values are presented in the figure caption. It is observed that the einzel lens provides a small diameter parallel beam through the injection module. 100 % of the 1+ beam is transported through the module and the beam enters the plasma chamber on the optical axis of the system. The beam is decelerated in a controlled manner, though some particle losses are observed here due to ions being reflected back by the plasma potential. This process is mainly dictated by the magnitude of the ion velocity component perpendicular to the plasma sheath with respect to the plasma potential value. In the presented case with $\Delta V = 30\ \text{V}$ the transmission from the 1+ source to the inside of the GTS plasma chamber is about 92 %. However, it is pointed out that these transmission numbers should be taken only as guiding values, as in reality the ion motion in this region is influenced by the

presence of the plasma particles (collisions, thermalisation, diffusion and ions extracted towards injection), which are not included in the current model. Inside the plasma chamber the magnetic field of the GTS has a strong influence on the low energy ions, forcing them into a corkscrew motion.

The effect of varying the bias voltage of the injection aperture electrode ((9) in Fig. 3) was studied with simulations. The bias voltage was varied between 0 V and -500 V with respect to the plasma chamber potential. Based on the simulations the influence of the varied bias on the 1+ beam transmission into the GTS plasma chamber is negligible (< 0.5 %-point). This suggests that the bias can be tuned to optimize plasma processes without compromising the ion injection efficiency.

The vertical steerer is designed to be used for beam pulsing. A simulation demonstrating the redirection of the 1+ beam into the dedicated beam dump is presented in Fig. 3(b).

One of the potential sources of issues with 1+/n+ operation is the ion beam extracted from the GTS plasma chamber towards the injection and the 1+ source. The aperture that allows the injection of 1+ beam into the plasma chamber also unavoidably acts as an extraction channel for the plasma ions. If high amounts of ions are extracted from the plasma through the grounded guiding tube, it could have adverse effects on the operation of the injection module and the 1+ source. In order to study this scenario with simulations, the GTS plasma chamber was populated with oxygen ions and 0.9 mA of ionic current was extracted towards the injection. The oxygen ion population consisted of charge states ranging from 1+ to 8+ following the shape of a typical oxygen charge state distribution produced with the GTS, peaking at the $^{16}\text{O}^{6+}$. Based on the simulations over 90 % of the ions escaping from the plasma chamber are lost inside the grounded tube and only 0.6 % of them reach the 1+ source, amounting to about 5.4 μA in this case. These surviving ions are almost exclusively collected on the Wehnelt electrode, for which this level of additional current will not cause any issues. Similarly, the grounded outer bodies of the steerers will collect a few tens of μA of current, as well as the last grounded electrode of the einzel lens assembly. Based on these results it is not expected that these ions will cause any significant issues for the operation of the 1+ injection module.

CONCLUSIONS

Due to its diverse features, the presented injection module design demonstrates a good potential for 1+/n+ operation

and the related studies. The similarities in the injection magnetic field between the GTS and the SPIRAL1 Charge Breeder and the results of the ion optical simulations give confidence for the design choices. The ion deceleration and insertion into the ECR plasma is a critical part of the system, and the most challenging to model reliably. This is taken into account in the mechanical details of the design to make it easier to vary the system geometry in this location (e.g. the grounded tube dimensions and position, replacement of the injection aperture electrode). This gives flexibility for geometry optimization, as the operational experience with the system increases.

The installation of the injection module and the first measurements with the GTS in 1+/n+ operation mode are expected to take place in 2019. The experiments will start with the existing alkali source to produce the 1+ ions. As the features of this source are well known, it is well suited for the commissioning of the 1+ injection system and its features. The GTS performance can also be benchmarked and compared to the SPIRAL1 Charge Breeder, which has been operated with the same 1+ source. Later the alkali source can be replaced with other 1+ sources to expand the studies to other elements.

REFERENCES

- [1] V. Toivanen *et al.*, in *Proc. of ICIS'17*, Geneva, Switzerland (2017), to be published in the AIP Conference Proceedinds.
- [2] C. Barué *et al.*, in *Proc. of ECRIS'16*, Busan, Korea (2016).
- [3] R. Vondrasek *et al.*, *Rev. Sci. Instrum.*, vol. 82, p. 053301 (2011).
- [4] L. Maunoury *et al.*, *Rev. Sci. Instrum.*, vol. 85, p. 02A504 (2014).
- [5] L. Maunoury *et al.*, in *Proc. of ECRIS'16*, Busan, Korea (2016).
- [6] T. Lamy *et al.*, in *Proc. of ECRIS'14*, Nizhny Novgorod, Russia (2014).
- [7] H. Koivisto *et al.*, *Rev. Sci. Instrum.*, vol. 85, p. 02B917 (2014).
- [8] L. Maunoury *et al.*, in these proceedings.
- [9] R. Vondrasek *et al.*, *Rev. Sci. Instrum.*, vol. 85, p. 02B903 (2014).
- [10] RADIA magnetic field simulation code, <http://www.esrf.eu/Accelerators/Groups/InsertionDevices/Software/Radia>.
- [11] T. Kalvas *et al.*, *Rev. Sci. Instrum.*, vol. 81, p. 02B703 (2010).

DEVELOPMENT OF RIKEN 28 GHz SC-ECRIS FOR PRODUCTION OF INTENSE METAL ION BEAM

Y. Higurashi†, T. Nagatomo, J. Ohnishi, and T. Nakagawa,
Nishina center for accelerator based science, RIKEN, Wako, Saitama 351-0198, Japan

Abstract

To produce intense metal ion beams (e.g., Ti^{13+} , $V^{12+,13+}$, Cr^{13+}) for synthesizing new super heavy elements ($Z=119,120$) at RIKEN, we tried to optimize the performance of RIKEN 28 GHz SC-ECRIS. Based on the “scaling law” and the “high B mode” operation, we systematically measured the beam intensity of various heavy ions as a function of B_{inj} , B_r and B_{ext} with 28 and 18 GHz micro-waves. We observed that B_{ext} is dependent on the charge state of heavy ions as predicted by the “scaling law”. Using these systematics, we obtained $\sim 400 \mu A$ of V^{13+} at the microwave power of 2 kW (28 GHz) and B_{ext} of ~ 1.4 T with 28 GHz. For long term operation, we produced very stable beam of 100-200 μA of V^{13+} ion. Following this, we constructed new 28 GHz SC-ECRIS for new elements synthesis.

INTRODUCTION

At RIKEN, we planned to synthesize new elements, which have atomic number higher than 118, after the experiments for synthesizing the super-heavy element (atomic number of 113).[1] For this purpose, production of intense and stable highly charged metallic ion beams, such as $V^{12+,13+}$ ions, is required. Therefore, we conducted test experiments to produce these beams and studied the optimum structure of the ion source to increase the beam intensity and, especially, the effect of magnetic mirror ratio on plasma confinement, for several years. It is well-known that the “scaling law” [2,3] and the “high B mode” operation [4-6] provide some of the important guidelines to optimize the magnetic mirror ratio of ion sources for production of various charge states of heavy ions. Model calculation based on the Fokker-Planck equation also shows the same tendency as the “scaling law”. [7,8]

As a first step to improve the ion source performance for production of these metallic ion beams, we also conducted a systematic study to optimize the magnetic mirror ratio using the RIKEN 28 GHz SC-ECRIS and the liquid-He-free SC-ECRIS on the bases of these laws. Using the results of the systematic study, we attempted to produce intense metallic ion beams last year.

In addition, to further expand this project, new superconducting RF cavities are now under construction in the downstream of RIKEN heavy-ion linac (RILAC) to increase the beam energy. [9] In this project, we also planned to construct a new 28 GHz SC-ECRIS. Based on the experimental results, we completed the design and the

construction last year. The ion source, the low energy beam transport line and first results for the ion source have been reported in ref. [10]. In this contribution, we present in detail the results of the systematic study and production of highly charged V ion beam.

SYSTEMATIC STUDY

In the test experiments, we used two different types of ion sources, Liquid-He-free SC-ECRIS [11] and RIKEN 28 GHz SC-ECRIS [12]. The main feature of the RIKEN 28 GHz SC-ECRIS is that it has six solenoid coils to produce a flexible mirror magnetic field in the axial direction

and can produce both “classical” and “flat” B_{min} . [13,14]

In the middle of 1980s, the “scaling law” was proposed for describing the effect of the main ion source parameters (microwave power, magnetic field strength, microwave frequency, mass of heavy ions, etc.) on the output beam of highly charged heavy ions. In these papers [2,3], it was reported that the strength of the magnetic mirror affects the optimum charge state, i.e., a higher mirror ratio yields higher charge states of the output ion beam.

It is obvious that the maximum magnetic mirror field at the microwave injection side (B_{inj}), the maximum magnetic mirror field at the beam extraction side (B_{ext}), and the radial magnetic field (B_r) work as parts of the magnetic mirror to confine the plasma. In the middle of 1990s, the “high-B” mode that employs a high magnetic mirror ratio to confine the plasma was proposed to increase the beam intensities of highly charged heavy ions. This principle was adopted by many laboratories in the design of their ECR ion sources. Intense beam of highly charged heavy ions was successfully produced using this method.

In this section, the experimental results (effect of B_{inj} , B_r and B_{ext} on the beam intensity of highly charged heavy ions), which were obtained on the bases of these laws, are presented.

B_{inj} and B_r Effect

Figure 1 a) and b) show the two-dimensional contour plots (B_r vs. B_{ext} and B_{inj} vs. B_{ext}) for the beam intensity of Xe^{22+} produced with RIKEN 28 GHz SC-ECRIS. In these figures, red and blue colors indicate the highest and lowest beam intensity, respectively. In this study, we used the 18 GHz microwave instead of 28 GHz. The minimum strength of the mirror magnetic field (B_{min}) was set to ~ 0.5 T. The extraction voltage and the microwave power were 21 kV and ~ 500 W, respectively. The gas pressure and biased disc condition (negative voltage and position) were slightly changed to maximize the beam intensity at the measurement points.

†higurasi@riken.jp

As shown in the figures, the beam intensity increases with increasing both B_r (or B_{inj}) and B_{ext} and becomes maximum at certain values of these parameters. The values of B_r and B_{ext} to maximize the beam intensity were ~ 1.5 and ~ 1.2 T, respectively (Fig. 1 a)). The corresponding B_{inj} and B_{ext} values were ~ 2.2 and ~ 1.2 T, respectively (Fig. 1 b)). As mentioned in ref. [6] (High B mode operation), $B_{ext} \sim B_r \sim 2.0 B_{ecr}$ and $B_{inj} \sim 4 B_{ecr}$. Therefore, we obtain $B_{inj}/B_{ext} \sim 2.0$ and $B_r/B_{ext} \sim 1.0$, which is almost the same as the results obtained in the test experiments ($B_r/B_{ext} \sim 1.2$ and $B_{inj}/B_{ext} \sim 1.8$).

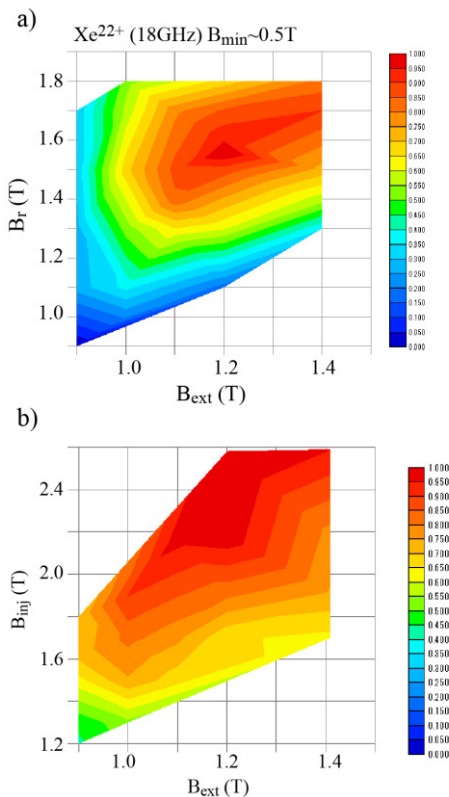


Fig. 1. Two-dimensional contour plot of the beam intensity of Xe^{22+} ion: a) B_r vs. B_{ext} and b) B_{inj} vs. B_{ext} .

To study the relation between B_{ext} and B_{inj} (or B_r) in more detail, we measured and plotted the beam intensities for various charge states of heavy ions as a function of B_{inj}/B_{ext} and B_r/B_{ext} . Figure 2 a) and b) show the normalized beam intensities as a function of B_{inj}/B_{ext} and B_r/B_{ext} with RIKEN 28 GHz ECRIS (18 and 28 GHz microwaves) and Liquid-He-free SC-ECRIS (18 GHz microwave). In Fig. 2, it appears that the beam intensity of various charge state heavy ions produced with our ECR ion sources are saturated at $B_r = 1 - 1.2 B_{ext}$ and $B_{inj} = 1.6 - 2.0 B_{ext}$. The tendency for the results of RIKEN 28 GHz SC-ECRIS looks similar to that for liquid-He free SC-ECRIS. These results are well-reproduced in the ‘‘High B mode’’ operation ($B_{inj}/B_{ext} \sim 2.0$, $B_r/B_{ext} \sim 1.0$).

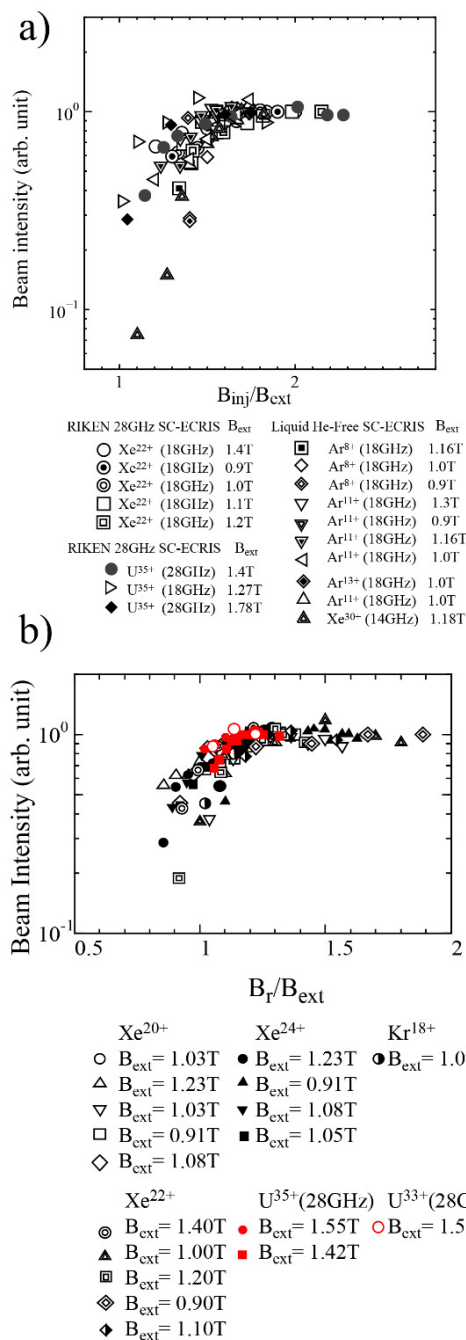


Fig. 2. Beam intensity of highly charged heavy ions as a function of B_{inj}/B_{ext} (a) and B_r/B_{ext} (b).

B_{ext} Effect

To investigate the effect of B_{ext} on the beam intensity, we measured the beam intensity under various combinations of B_r (or B_{inj}) and B_{ext} . Figures 3 a) – c) show the two-dimensional contour plots of the beam intensity (B_r vs. B_{ext}) for highly charged Xe ions. Similar to Fig. 1, the beam intensity increases with increasing B_r and B_{ext} and becomes maximum at certain values of these parameters. As shown in these figures, the beam intensity gradually changed in the highest beam intensity region; therefore, it is difficult

Content from this work may be used under the terms of the CC BY 3.0 licence (© 2018). Any distribution of this work must maintain attribution to the author(s), title of the work, publisher, and DOI.

to determine B_{ext} for maximizing the beam intensity accurately. As a reference, we choose the B_{ext} value, which yields ~95% of the maximum intensity, as the optimum B_{ext} . The optimum B_{ext} for Xe^{27+} is higher than that for Xe^{22+} with 18 GHz microwave. It is also shown that the optimum B_{ext} becomes higher with higher frequency (28 GHz). In this experiment, we choose B_{min} as ~0.5 T for 18 GHz and as ~0.63 T for 28 GHz.

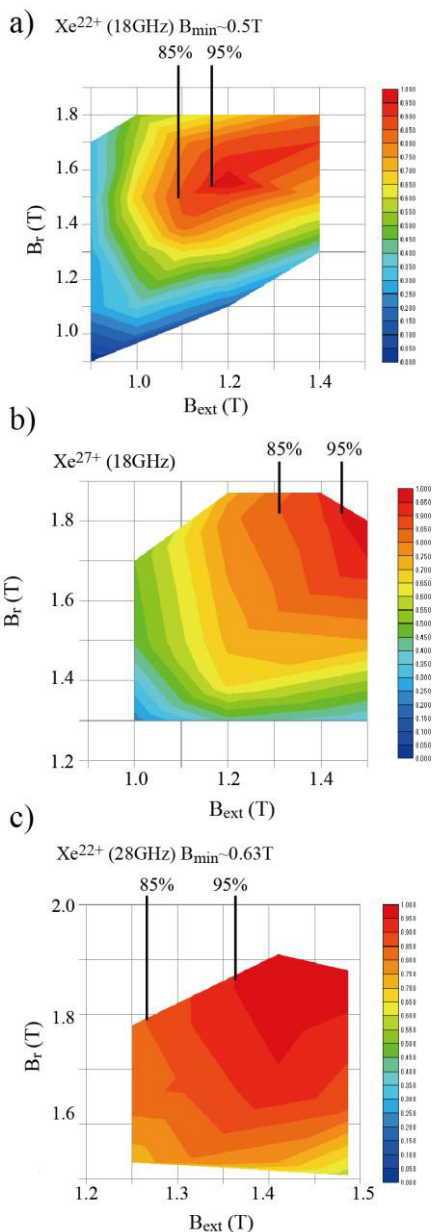


Fig. 3. Two-dimensional contour plot of the beam intensity (B_r vs. B_{ext}): a) Xe^{22+} ion with 18 GHz, b) Xe^{27+} ion with 18 GHz, and c) Xe^{22+} ion with 28 GHz.

Using the same procedures as that for Fig. 3, we measured the optimum B_{ext} for various charge states of Ar and Xe ions with 18 and 28 GHz. Figure 4 shows the optimum B_{ext} for RIKEN 28 GHz SC-ECRIS with 18 GHz microwave as a function of the charge state of Xe ions. The optimum B_{ext} increases from 1.2 to 1.6 T with increasing the

charge state from 22 to 30. We observed the same tendency for the highly charged Ar ions with the liquid-He-free SC-ECRIS. The optimum B_{ext} increases from ~1.1 to ~1.25 T with increasing the charge state from 8 to 13.

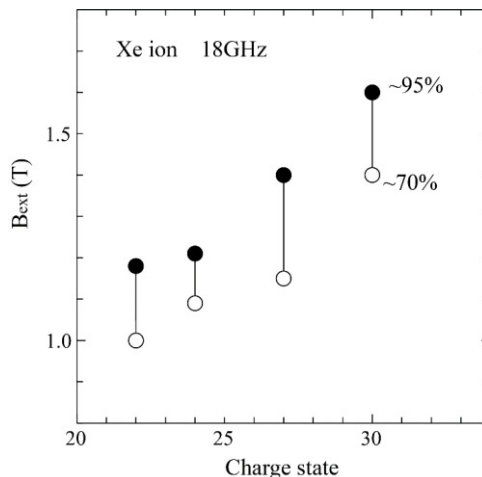


Fig. 4. Optimum B_{ext} for the highly charged Xe ions. Open and closed circles indicate the B_{ext} value, which yields 70 and 95% of the maximum beam intensity, respectively.

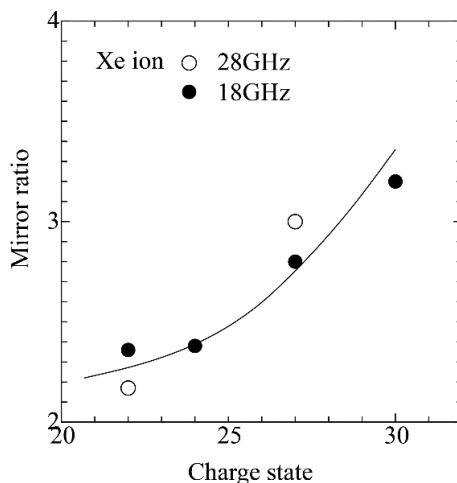


Fig. 5 Optimum mirror ratio ($B_{\text{ext}}/B_{\text{min}}$) for highly charged Xe ions as a function of charge state.

As described in ref. [2, 3], the optimum charge state is dependent on the mirror ratio, when B_{min} is fixed. Therefore, we plotted the experimental results of Xe for 18 and 28 GHz microwave (Fig. 5) and Ar ions (Fig. 6) as a function of the charge state. The mirror ratio increases with increasing the charge state. In Fig. 5, the open and closed circles are the results obtained for 28 and 18 GHz microwave, respectively. The mirror ratio increases from ~2.2 to ~3.2 for both 18 and 28 GHz microwaves with increasing the charge state from 22 to 30. Figure 6 shows the results for Ar ions produced with liquid He-free SC-ECRIS. We also observed that the optimum mirror ratio increases with increasing the charge state. These results can be qualitatively reproduced with the “scaling law” [2, 3].

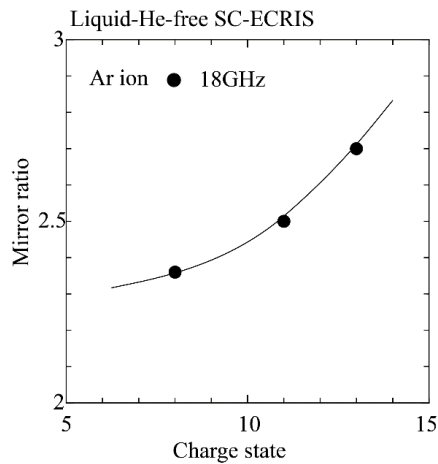


Fig. 6. Optimum mirror ratio (B_{ext}/B_{min}) as a function of charge state of Ar ions.

However, these experimental results were obtained for a low microwave power density (below several 100 W/L). At a higher RF power (~ 1 kW/L), we may observe different tendency.

VANADIUM ION BEAM PRODUCTION

We tried to produce intense beam of highly charged vanadium (V) ions on the bases of the results described in the previous section. For production of the V vapor, we used the high-temperature oven [15]. For long-term operation, we fabricated a new crucible, which has almost two times larger volume than the old one [16]. To obtain sufficient temperature for evaporating the materials, detailed simulation was carefully performed and sufficiently high temperature was obtained to produce the vapor. The detailed results are presented in ref. [15]

As described in refs. [2,3,17], the optimum charge state of the heavy ions is strongly dependent on the electron density (n_e), ion confinement time (τ_i) and electron temperature. For these results described in refs. [2,3,17], it is assumed that V^{13+} ion is in the same region of Xe^{24-27+} ions. As described in ref. [18,19], $n_e \tau_i$ is dependent on the mirror ratio. The magnetic mirror ratio (B_{ext}/B_{min}) for 18 and 28 GHz microwaves is assumed to be 2.2–2.7 from the results described in the previous section and these papers. If we choose $B_{min} \sim 0.6$ T for 28 GHz, the optimum B_{ext} might be 1.3–1.6 T for V^{13+} . Figure 7 shows the beam intensity (upper figure) and X-ray heat load (lower one) as a function of B_{ext} . The extraction voltage was 12.6 kV. Oxygen gas was used to produce plasma. The beam intensity was slightly changed from $B_{ext} \sim 1.6$ to ~ 1.4 T.

Figure 8 shows the typical charge state distribution of highly charged V ion beam at a microwave power of ~ 2 kW (18+28GHz). The ion source was tuned to produce V^{13+} ion beam. Figure 9 shows the beam intensity and X-ray heat load as a function of microwave power for $B_{ext} \sim 1.4$ T. We used the double frequencies (18GHz (several 100 W)+28GHz) injection [20] for obtaining the stable beam. Both the beam intensity and heat load increase with increasing microwave power. At 2 kW, the X-ray heat load was ~ 1.2

W, which is sufficiently low for safe operation of our ion source. The oven power was tuned to maximize the beam intensity at each microwave power. Generally, to maximize the beam intensity, the oven power increased with increasing microwave power. At the microwave power of 2 kW, we need almost 1 kW of the oven heating power. For lower microwave power (~ 1.2 kW), lower oven power was sufficient to maximize the beam intensity; in this case, the consumption rate of the material was ~ 2.4 mg/h, which is sufficiently low to operate the ion source for long term.

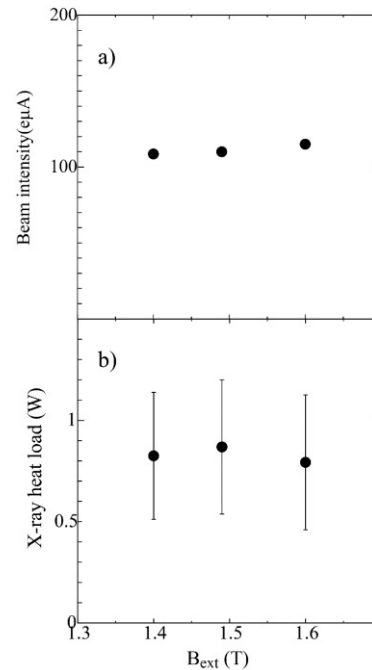


Fig. 7 a) Beam intensity of V^{13+} as a function of B_{ext} . b) X-ray heat load as a function of B_{ext} .

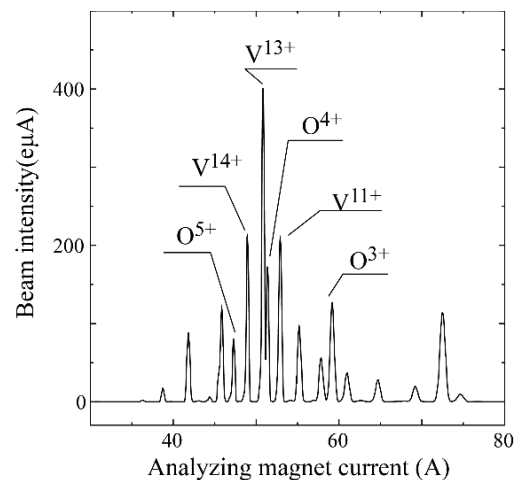


Fig. 8. Charge state distribution of the highly charged V ions.

For long-term operation, we successfully produced an intense beam (100–200 eµA) of V^{13+} . However, we still need to achieve improvement of the high-temperature oven

Content from this work may be used under the terms of the CC BY 3.0 licence (© 2018). Any distribution of this work must maintain attribution to the author(s), title of the work, publisher, and DOI.

performance at higher material consumption for long-term operation, as described in ref. [16].

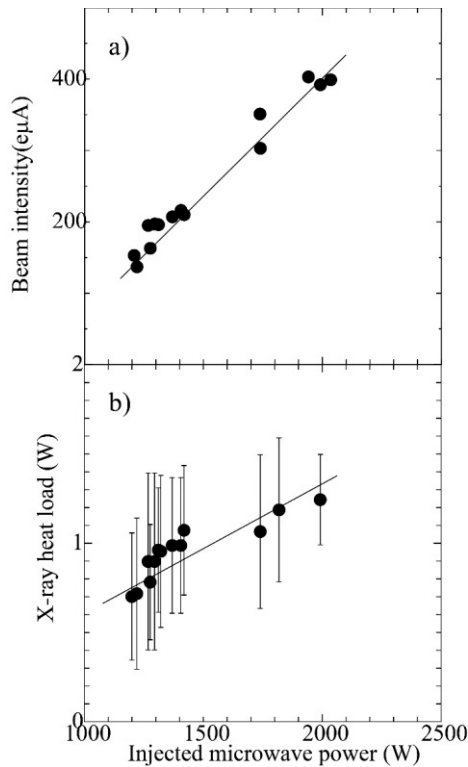


Fig. 9 a) Beam intensity of V^{13+} as a function of microwave power. b) X-ray heat load in the cryostat as a function of microwave power.

CONCLUSION

We systematically studied the effect of the magnetic mirror ratio on the beam intensity of various charge state heavy ions with 18 and 28 GHz microwave. The beam intensity was saturated at $B_{inj}=1.6-2.0B_{ext}$ and $B_i=1-1.2B_{ext}$, which is the same tendency as in the “high B mode” operation. The optimum B_{ext} to maximize the beam intensity is

dependent on the charge state of heavy ion. It can be qualitatively reproduced by the “scaling law”. We produced intense V^{13+} ion beam on the bases of the systematic study. We obtained ~ 400 eµA of V^{13+} ion beam with microwave power of ~ 2 kW and $B_{ext}\sim 1.4$ T. For long-term operation, we produced 100-200 eµA of V^{13+} ion with the new high-temperature oven.

REFERENCES

- [1] K. Morita, *Proceedings of the 14th International Symposium on Nuclei in the Cosmos (NIC2016)*, *JPS Conf. Proc.* vol. 14, p. a010004 (017).
- [2] R. Geller *et al.*, *Proc. 8th Int. Conference on ECR ion sources and their applications*, *NSCL report MSUCP-47* (MSU, Dec. 1987) p.1.
- [3] R. Geller, "Electron Cyclotron Resonance Ion Sources and ECR Plasmas", *Institute of Physics, Bristol*, 1996, and references therein.
- [4] T. Antaya and S. Gammino, *Rev. Sci. Instrum.*, vol. 65, p. 1723, (1994).
- [5] S. Gammino *et al.*, *Rev. Sci. Instrum.*, vol. 67, p. 4109 (1996).
- [6] D. Hitz *et al.*, *Rev. Sci. Instrum.*, vol. 73, p. 509 (2002).
- [7] A. Girard *et al.*, *Phys. Rev.* vol. E62, pp. 1182 (2000).
- [8] A. Girard *et al.*, *Rev. Sci. Instrum.*, vol. 75, 1381 (2004) and references therein.
- [9] O. Kamigaito *et al.*, *Proc. IPAC 2016*, TUPMR022, JACoW.
- [10] T. Nagatomo *et al.*, *in these proceedings*.
- [11] T. Kurita *et al.*, *Nucl. Instr. and Meth. B*, vol. 192, p.429, (2002).
- [12] Y. Higurashi *et al.*, *Rev. Sci. Instrum.*, vol. 85, p.02A953 (2014).
- [13] G. D. Alton and D. N. Smithe, *Rev. Sci. Instrum.* vol. 65, p. 775 (1994).
- [14] Y. Liu *et al.*, *Nucl. Instrum. Methods*, vol. B241, p.965 (2005).
- [15] J. Ohnishi *et al.*, *in these proceedings*.
- [16] J. Ohnishi *et al.*, *Rev. Sci. Instrum.* vol. 87, p.02A709 (2016).
- [17] K. Golovanivsky, *Instrum. Exp. Tech.*, vol. 28, p.989 (1986).
- [18] R. Post, "The course and workshop on Phys. of mirrors", Vienna, Italy, 1987
- [19] N. Itagaki, *et al.*, *J. Plasma Fusion Res. Series*, 4 p. 305(2001)
- [20] Z.Q. Xie, and C.M. Lyneis, *Rev.Sci.Instrum.* vol. 66, p. 4218, (1995)

PRESENT STATUS AND FUTURE PROSPECT OF HEAVY ION RADIOTHERAPY

A. Kitagawa[†], T. Fujita, and M. Muramatsu, National Institute of Radiological Sciences, National Institutes for Quantum and Radiological Science and Technology (QST-NIRS), 4-9-1 Anagawa, Inage, Chiba 263-8555, Japan

Abstract

Heavy Ion Radiotherapy (HI-RT) is one of important applications of an electron cyclotron resonance ion source (ECRIS). At present, ten facilities are under operation and eight are under commissioning or construction. All of them utilize ECRISs for the production of carbon ions, mainly. Heavy ion radiotherapy has been approved to cover by the National Health Insurance in Japan since 2016. In April 2018, fees for treatment in Japan were revised to 1,600,000 Yen for 'prostate tumor' and 2,375,000 Yen for 'bone and soft tissue tumor' and 'head and neck tumor', respectively. The expectation of widespread use has accelerated sharply. There is no failure that disturbs daily treatment due to ECRISs in facilities. The ECRISs have effectively contributed to the stable operation of the present facilities. On the other hand, the cost reduction for a facility has been urged too. Laser ion acceleration has a potential to take over the role of ECRIS in the future. However ECRIS still has a scope of research and development to improve clinical dose distribution for intractable radioresistance tumors at present.

INTRODUCTION

In order to treat a deep-seated tumor with the good localized dose distributions, carbon ion was predicted as one of good candidates for heavy-ion radiotherapy by Robert R. Willson even in 1946[1]. Based on physics, lighter ion species cause larger multiple scattering in the deep side, and heavier ion species give unexpected dose over the end-point due to projectile fragmentation. In addition, the biological dose distribution depends on the depth and thickness of a tumor. In the case of ten and several cm depth and several cm thickness, the linear energy transfer of neon ions is too high than that of carbon ions shown by Lawrence Berkeley Laboratory, University of California in 1980's[2]. Although heavier ions shows other biological advantages like oxygen enhancement ratio, the National Institute of Radiological Sciences (NIRS) chose carbon ions for the clinical trial at the Heavy-Ion Medical Accelerator in Chiba (HIMAC) [3] in 1994. Figure 1 shows biological depth-dose distributions of the Spread-Out Bragg Peak in the case of a depth of 16 cm and a thickness of 6 cm with different ion species. By HIMAC's success, the existing and almost all the planned heavy-ion radiotherapy (HI-RT) facilities require a carbon beam at present.

[†] kitagawa.atsushi@qst.go.jp

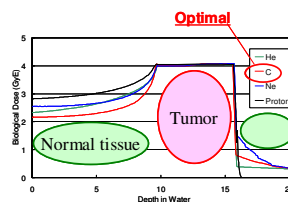


Figure 1: Biological depth-dose distributions of a 6cm Spread-Out Bragg Peak with a depth of 16cm.

The requirement of carbon-beam intensity strongly depends on the facility design, i.e. the volume and shape of the target, the efficiency of the irradiation method, the transmission of the accelerator complex and so on. In order to obtain the biological dose rate of 5 GyE/min. (it's roughly equals to a physical dose of 2 Gy/min.), a few 10^8 particles per second are required at a typical present facility. Long-term stability and reproducibility are important for daily treatment. On the other hand, the short-term stability of the ion sources is not so sensitive. Because the existing facilities consist of a synchrotron and any injector and the fine structure of the beam pulse will almost disappear during the acceleration in the synchrotron. Moreover easy operation and maintenance are also important to reduce the operation cost. An ion source should satisfy these requirements. An electron cyclotron resonance ion source (ECRIS) was expected to realize these requirements. The details and the history of the development of ECRISs have been described in Ref. [4]. As a result, ECRISs have been adopted at all existing carbon-ion radiotherapy (C-RT) facilities.

STATUS OF CARBON-ION RADIOTHERAPY

Clinical results

Clinical data of HIMAC have been accumulated under prescribed clinical protocols since 1994. All the clinical protocols and their results have been reported routinely through an authorities' committee. Since 2016, other Japanese C-RT facilities have gathered their data into a unified clinical database at the National Institute of Radiological Sciences, National Institutes for Quantum and Radiological Science and Technology (QST-NIRS, the former NIRS). At present, the total number of patients in Japan exceeded 20,000. The summaries for various diseases have clearly demonstrated the advantages of C-RT. There are three remarkable advantages of C-RT: lower toxicity, better local control and survival ratio, and shorter treatment period, the so-called Hypo-Fractionation.

Content from this work may be used under the terms of the CC BY 3.0 licence (© 2018). Any distribution of this work must maintain attribution to the author(s), title of the work, publisher, and DOI.

Regarding toxicities, from systematic phase-I/II dose-escalation studies for many kinds of diseases, the safe doses have been determined and irradiation techniques have been improved with the observation of no further severe side effects than have been already observed. The dose fractionations have also been determined as optimal in the same dose-escalation studies. Clinical results are evaluated by two measured clinical statistics, i.e. local control and survival ratios. Good local control ratios have been achieved for some intractable tumors, such as inoperable bone and soft tissue tumors, postoperative pelvic recurrence of rectal cancer, and so on. In these diseases, even if the case is operable, HI-RT gave a large benefit to prevent a great reduction of the organ function due to the resection and to keep the survival ratio comparable to that obtained by the resection. In addition, the benefit of HI-RT over other modalities has been demonstrated in terms of a significant reduction in overall treatment time with acceptable toxicities. Peripheral-type non-small-cell lung cancer has also been very effectively treated by low-LET RT, but usually low-LET RT must divide the dose into 20-30 fractions and a few months are needed for the treatment period. In the case of HI-RT, the number of fractions and treatment period were carefully reduced step by step from 18 fractions over 6 weeks to one single fraction, thus one-day treatment has been realized. The respiratory-gated irradiation method[5,6] for target organs with respiratory movement and multi-port irradiation from 3- or 4-field directions were utilized for all patients to reduce toxicities. For hepatocellular carcinoma, 2 fractions over 2 days have been adopted without severe side effects. Some recent clinical results have been described in Ref. [7-12].

Spread of Treatment

Under the Japanese health insurance system, a new medical technology should verify its effectiveness and safety with adequate evidence during its clinical trial. A goal of the technology is the approval to be covered by the Health Insurance. However, there is an Intermediate phase between the clinical trial and the Health Insurance, the so-called “advanced medicine.” In this phase, an equitable share and medical economy are carefully discussed. A hospital can ask a fee to patients. In 2003, the Japanese Ministry of Health, Labour and Welfare (MHLW) approved carbon ion radiotherapy as the “advanced medicine”. The Japanese government is promoting development of new downsizing technologies under “The 3rd Comprehensive 10-year Strategy for Cancer Control (2004 - 2013)”. NIRS designed a hospital-specified carbon ion radiotherapy facility and developed prototypes of various components. The feature of the design is an exhaustive optimization for treatment by carbon beams. This realized a cost-effective and sure facility’s design. The successful results of developed prototypes also certified manufacturing companies of the minimum business risks. Based on these results, MEXT funded the project of the Gunma University Heavy Ion Medical Center (GHMC) as a demonstration facility.

GHMC has been successfully operated since March 2010[13]. The facility was approved as a commercial medical device by MHLW. At present, ten facilities are in operation and eight are under commissioning or construction worldwide shown in Table 1. Seven of eighteen are located in Japan as the result of the strategy.

Table 1: Carbon-Ion Radiotherapy Facilities Worldwide.

Institute / Hospital (Abbreviation)	Location	Start year
National Institute of Radiological Sciences (HIMAC)	Chiba (Japan)	1994
Hyogo Ion Beam Medical Center (HIBMC)	Tatsuno (Japan)	2002
Institute of Modern Physics (IMP)	Lanzhou (China)	2009
Hidelberg Ion Therapy Center (HIT)	Heidelberg (Germany)	2009
Gunma-University Heavy-Ion Medical Center (GHMC)	Maebashi (Japan)	2010
Centro Nazionale Adroterapia Oncologica (CNAO)	Pavia (Italy)	2012
Kyushu International Heavy-Ion Treatment Center (Saga HIMAT)	Tosu (Japan)	2013
Shanghai Proton and Heavy Ion Center (SPHIC)	Shanghai (China)	2014
Marburg Ion Therapy Center (MIT)	Marburg (Germany)	2015
Kanagawa Cancer Center (i-ROCK)	Yokohama (Japan)	2015
MedAustron	Wiener Neustadt (Austria)	-
Heavy Ion Therapy Facility in Wuwei (HITFiW)	Wuwei (China)	-
Osaka Heavy Ion Therapy Center (Osaka HIMAK)	Osaka (Japan)	-
Heavy Ion Therapy Facility in Lanzhou (HITFiL)	Lanzhou (China)	-
Yamagata University	Yamagata (Japan)	-
Korea Heavy Ion Medical Accelerator (KHIMA)	Busan (Korea)	-
Yonsei University	Seoul (Korea)	-
Taipei Veterans General Hospital	Taipei (Taiwan)	-

The most recent remarkable epoch of C-RT in Japan is that some of diseases have been approved to cover by the National Health Insurance since 2016. In 2016, ‘bone and soft tissue tumor’ has been approved. The Japanese National Health Insurance system is revised every two years. In April 2018, ‘prostate tumor’ and ‘head and neck tumor’

have been added too. The medical expenses in Japan are also revised every two years. The technical fees for C-RT are 1,600,000 Japanese Yen (JPY) for a common cancer, ‘prostate tumor,’ and 2,375,000 JPY for rare cancers, ‘bone and soft tissue tumor’ and ‘head and neck tumor’, respectively. The 70 % of the fee is covered by the government. So that a patient should pay 480,000 JPY and 712,500 JPY, respectively. The fee for an aged patient is reduced less. In addition, the Japanese Government put limitations on a medical expense per month. A patient is also able to receive a support to an excess of the fee. The expectation of widespread use has accelerated sharply. The cost reduction for a facility has been urged. On the other hand, many diseases like ‘lung tumor’, ‘pancreas tumor’ and so on are still in the ‘advanced medicine’ phase. The fee of such diseases is 3,140,000 JPY and patients should pay all of it by themselves. The extension of diseases covered by the National Health Insurance has been urged too.

Contribution From ECRISs

The existed ECRISs have been successfully operated in heavy-ion radiotherapy facilities. GHMC, Saga HIMAT, i-ROCK, Osaka HIMAK, Yamagata, Seoul, and Taipei have been dedicated only for C-RT. These facilities have only one ECRIS due to the reduction of the initial construction cost and the maintenance expense. This means that a failure of the ECRIS causes a fatal trouble for treatment. A copy of a compact magnet ECRIS, Kei2[14], is installed in each facility[15]. Although small leak currents and discharges were observed in some facilities[16], these have been almost improved. There was no failure that disturbed daily treatment due to ECRISs in all facilities in 2017. In addition, the maintenance of the ECRISs become simple year by year. Some facilities put a longer interval for the maintenance than one year. The ECRISs have effectively contributed to the stable operation of the present C-RT facilities.

FUTURE PROSPECT OF HEAVY ION RADIOTHERAPY AND AN ECRIS

Downsizing of A Facility

From the point of view of cost reduction, it seems that a present facility is still too large for a hospital. The size of facility is roughly 3000 m² and its initial construction cost will be ten billion JPY. At present the ECR ion source mainly supplies C⁴⁺ ions. Increasing the charge state can help to reduce the cost of injector. The research and development for the higher charge-state production have been continued. However it is not expected to give a drastic cost reduction.

There is a limitation in the present acceleration principle with electrodes, therefore an innovation to change the existed accelerator structure has been considered. Laser ion acceleration is expected to overcome this limitation. It appears to be closer to realization than it was 10 years ago. QST has started a new ‘Quantum Scalpel project’ to develop the combination of a laser ion injector and a

superconducting synchrotron for HI-RT. Its goal is to realize a facility with a size of 20 x 10 m[17]. It seems ECRISs will not have a place in the future.

Scope of ECRIS Development

On the other hand, laser ion acceleration is not easy technology and is still far from the practical use. A ECRIS should face current issues for the present HI-RT. One example of such issues is the production of multiple ion species. As mentioned in the Introduction section, the reason why NIRS chose carbon ions for treatment was the advantage of carbon ions for the better biological dose distribution shown in Fig. 1. However, this distribution depends on a depth and thickness of a tumor. For example, lighter ions like Li or Be show the better distribution for a deeper and thinner tumor. In addition, the biological effectiveness is varied on the area of the tumor in vivo due to various mechanisms like the oxygen enhancement effect[2]. In order to obtain the maximum effect on a tumor and the minimum effect on normal tissues, various figures of merits for ion species shown in Fig. 2 should be considered. As a conclusion, it’s impossible to obtain the best clinical dose distribution with carbon ion only. Therefore the multiple ion-species irradiation has been planed recently. It is specifically a combination of the carbon irradiation, the irradiation to a radioresistant part located near the central part of tumor with a heavier ion which has a large biological effectiveness, and the irradiation to the environs of a critical organ with a lighter ion which reduce a toxicity[18].

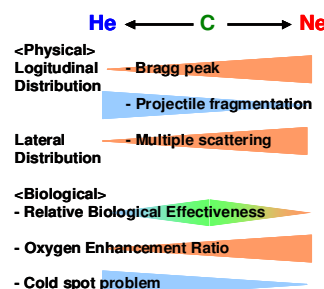


Figure 2: Various figures of merits for ion species.

This irradiation technique should be utilized with the respiratory-gated pencil-beam scanning technique. An injector system for a synchrotron should provide different ion beams sequentially. Although the scheme of the injector system has not been fixed yet, it is expected that one ECRIS produces all necessary ions with different acceleration voltages, instead of a set of multiple ion sources for each ions. This is a new challenge in the ECRIS’s field.

SUMMARY

HI-RT has verified its effectiveness and safety and has reached to the National Health Insurance phase. The treatment fees have decreased to affordable price. The ECRISs have effectively contributed to the stable operation of facilities. ECRIS will be taken over its place by

another technology in the future. However, ECRIS still has a scope of the present research and development to produce various ion species in order to improve clinical dose distribution for intractable radioresistant tumors.

REFERENCES

- [1] Robert R. Wilson, *Radiology*. 47 (5): 487, 1946.
- [2] E.A. Blakely, F.Q.H. Ngo, S.B. Curtis and C.A. Tobias, *Adv. Radiat. Biol.* vol. 11, p. 295 (1984).
- [3] Y. Hirao, *et al.*, *Nucl. Phys. A* vol. 538, p. 541c (1992).
- [4] A. Kitagawa, T. Fujita, M. Muramatsu, S. Biri, and A.G. Drentje, *Rev. Sci. Instrum.* vol. 81, p. 02B909 (2010).
- [5] K. Noda *et al.*, *Nucl. Instrum. Meth. A*, vol. 374, p. 269 (1996).
- [6] S. Minohara, T. Kanai, M. Endo, K. Noda, and M. Kanazawa, *Int. J. Rad. Oncol. Bio. Phys.* vol. 47, p. 1097 (2000).
- [7] D. K. Ebner and T. Kamada, *Front. Oncol.* vol. 6, p. 140, 2016.
- [8] R. Imai *et al.*, *Int. J. of Rad. Onco. Bio. Phys.* vol. 95, p. 322, 2016.
- [9] T. Nomiya *et al.*, *Rad. Onco.* vol. 121. p. 288, 2016.
- [10] M. Koto *et al.*, *Int. J. of Rad. Onco. Bio. Phys.* vol. 100, p. 639, 2018.
- [11] N. Yamamoto *et al.*, *J. Thorac Oncol.* vol. 12(4), p. 673, 2017.
- [12] S. Kawashiro *et al.*, *J. of Rad. Onco. Bio. Phys.* vol. 101, p. 1212, 2018.
- [13] T. Ohno, *et al.*, *Cancers*, vol. 3, p. 4046, 2011.
- [14] M. Muramatsu *et al.*, *Rev. Sci. Instrum.* vol. 76, p. 113304 (2005).
- [15] A. Kitagawa *et al.*, *Proc. of ECRIS2012*, Sydney, 2012, p. 200.
- [16] H. Souda *et al.*, *Rev. Sci. Instrum.*, vol. 85(2), p. 02A934, 2014.
- [17] T. Shirai *et al.*, *Proc. of 14th Annual Meeting of PASJ*, Sapporo, 2017, p. 155 (in Japanese).
- [18] T. Inaniwa *et al.*, *Phys. Med. Biol.*, vol. 62, p. 5180 (2017).

NEW 28-GHz SUPERCONDUCTING ELECTRON CYCLOTRON RESONANCE ION SOURCE FOR SYNTHESIZING SUPER-HEAVY ELEMENTS WITH $Z > 118$

T. Nagatomo[†], Y. Higurashi, J. Ohnishi, A. Uchiyama, K. Kumagai, M. Fujimaki, N. Fukunishi, N. Sakamoto, T. Nakagawa and O. Kamigaito

RIKEN Nishina Center for Accelerator Based Science, Wako, Saitama 351-0198, Japan

Abstract

The RIKEN linear accelerator is being upgraded to provide intense metal ion beams, from Ca and Zn for nuclear structure research to V and Cr for synthesizing new super-heavy elements with $Z > 118$. In 2017, we started to construct a new superconducting electron cyclotron resonance ion source (SC-ECRIS) and a new low-energy beam transport (LEBT). Because of the short development period, we decided to give the new SC-ECRIS the same structure as the RIKEN 28-GHz SC-ECRIS. Although a solenoid and some steering magnets were not ready yet, during summer 2018, an ^{40}Ar beam was successfully extracted as the first beam with the 18-GHz microwave heat source. A pepper-pot emittance meter estimated the horizontal size of the $\text{Ar}^{8+, 9+, 11+}$ beam to be about 70 mm at 1,024 mm downstream from the edge of the analyzing magnet. Furthermore, we successfully obtained the four-dimensional phase-space distribution that is essential for evaluating the validity of the beam optics devices to improve the LEBT. We plan to finish the construction of a 28-GHz gyrotron and the LEBT by the end of 2018.

INTRODUCTION

A project to synthesize new super-heavy elements (SHEs) having an atomic number (Z) larger than 118 was

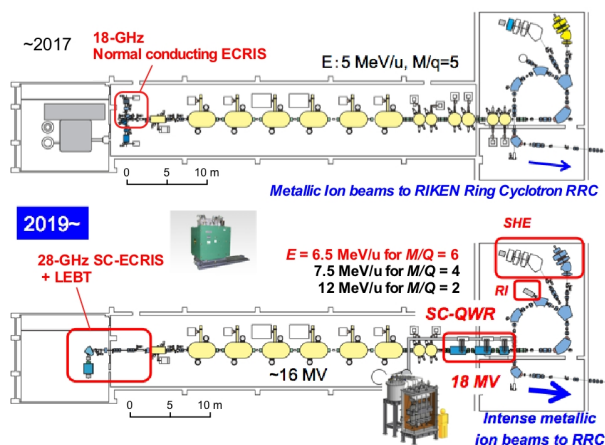


Figure 1: Ongoing upgrade of RILAC since 2017. The normal conducting 18-GHz ECRIS is being replaced with a 28-GHz ECRIS and LEBT. The new SC-QWRs will be installed at the end of drift tubes of the RILAC.

[†] nagatomo@riken.jp

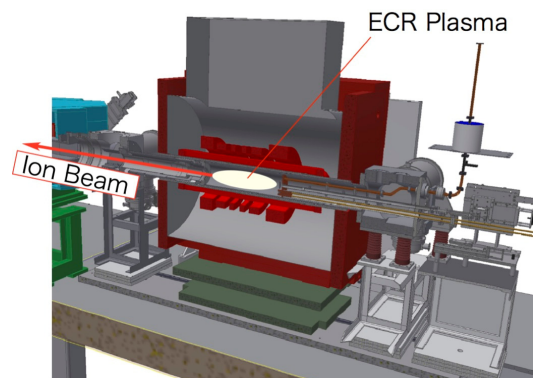


Figure 2: Schematic of the new 28-GHz SC-ECRIS.

started in FY2016. To synthesize SHEs with atomic numbers of $Z = 119$ and 120 , highly intense and highly charged metallic ion beams of V and Cr, respectively, must be provided by the RIKEN linear accelerator (RILAC) [1]. Accordingly, the RILAC upgrade will increase the acceleration energy from 5 MeV/u to more than 6 MeV/u by installing superconducting quarter-wavelength resonators (SC-QWRs), as shown in Fig. 1. However, the RILAC is currently used as a variable-frequency injector for the RIKEN cascaded cyclotron for the Radioactive Isotope Beam Factory [2]. In this operation, the new SC-QWRs will be bypassed because they operate at a fixed frequency. In variable frequency operation, high-intensity Ca and Zn beams will still be required for nuclear structure research, as before. To meet this acceleration scheme without using the SC-QWR booster, the accelerated ions must be given an electric charge higher than that used before. For example, a Ca^{16+} beam is required at currents of $\sim 100 \mu\text{A}$.

Consequently, a wide $n_e\tau_i$ range of $\sim 5 \times 10^8$ to $\sim 5 \times 10^9 \text{ cm}^{-3} \text{ s}$ must be covered, where n_e is the electron density and τ_i is the ion confinement time in the plasma [3] in the ion source. In addition, the development period is limited to about one year. Therefore, we decided to construct the new ion source with the same structure as the RIKEN 28-GHz SC-ECRIS [4,5] and match the new low-energy beam transport (LEBT) to the RILAC radio frequency quadrupole (RFQ).

In this paper, we report the current construction status and describe the first beam extraction, which was performed during the summer of 2018.

Content from this work may be used under the terms of the CC BY 3.0 licence (© 2018). Any distribution of this work must maintain attribution to the author(s), title of the work, publisher, and DOI.

THE NEW SC-ECRIS

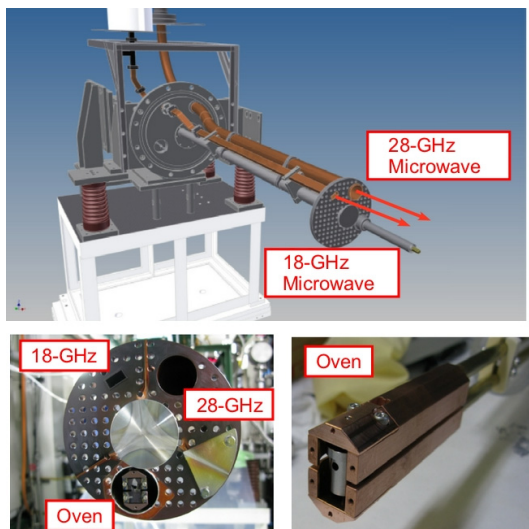


Figure 3: Microwave injection system and high-temperature oven to create metallic ion vapor.

The new ECRIS comprises fully superconducting mirror coils that have the same structure as the RIKEN 28-GHz SC-ECRIS [4]. As shown in Fig. 2, it consists of six solenoidal and hexapole SC magnets that are designed to achieve maximum mirror fields of $B_{inj} \approx 3.8$ T at the microwave injection side and $B_{ext} \approx 2.2$ T at the beam extraction side, a minimum field of $B_{min} < 1.0$ T, and a radial magnetic field at the inside surface of the plasma chamber of $B_r \approx 2.1$ T. The electron plasma confined in the mirror field is heated with 18-GHz and 28-GHz microwaves by the ECR process. Another feature of the ECRIS is that we can use the six solenoidal coils to flexibly change the shape of the ECR surface to create both the “classical” and the “flat” B_{min} structures proposed by Alton et al. [6]. The chamber volume is about 10 L. Schematics of the microwave- and gas-injection systems are shown in Fig. 3. We plan to utilize 18-GHz and 28-GHz microwave heating to generate a high-temperature electron plasma, and these microwaves are generated by a 1.5-kW klystron and a 5-kW gyrotron, respectively. A compact high-temperature (HT) oven, which has a crucible made of thin tungsten and is heated by Joule heating,

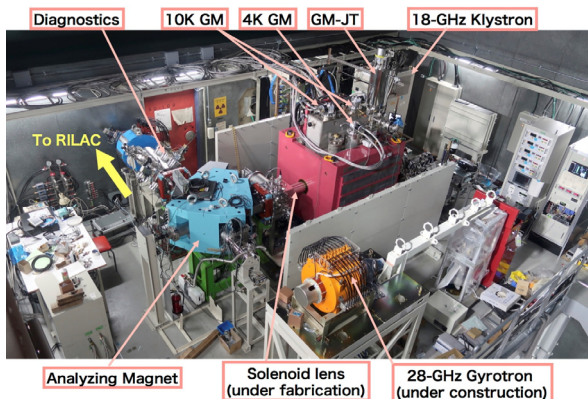


Figure 4: Current construction status of the new 28-GHz ECRIS. The 28-GHz gyrotron and the solenoid lens at the exit of ECRIS is under construction.

was recently developed by Ohnishi et al. [7], and a high-intensity V beam was successfully extracted [3]. We plan to install similar compact HT ovens to create ion vapors of metals such as Ca, Ti, Cr, and Zn in the future.

EXPERIMENTAL SETUP FOR FIRST ARGON BEAM EXTRACTION

The current construction status of the new 28-GHz ECRIS is shown in Fig. 4. Two 10-K GM, one 4-K GM, and one GM-JT cryocoolers were installed in the ECRIS as shown in Fig. 4. The 18-GHz klystron, an analyzing magnet (AM), and a diagnostics chamber were also installed. The pole pieces of the analyzing magnet were specifically shaped to cancel the higher-order magnetic component proposed by Leitner et al. [8]. In the diagnostics chamber, a pepper-pot emittance meter (PEEM) that we previously developed [9] is located 1,024 mm downstream from the edge of the AM. By using the PEEM, four-dimensional phase-space information $\{x, y, x', y', \text{intensity}\}$ can be obtained simultaneously. The Faraday cup is located 420 mm behind the PEEM, and between the PEEM and the Faraday cup a horizontal slit with a 40-mm opening is installed. Two steering magnets were already installed, but their power supplies were not ready for the first extraction. The 28-GHz gyrotron and a solenoid lens that will be placed at the end of the ECRIS are now under construction, and their installation is planned by the end of 2018. Thus, we performed beam extraction with 18-GHz microwave heating with the ^{40}Ar and $^{16}\text{O}_2$ support gas injected into the plasma chamber.

The ^{40}Ar beam was successfully extracted from the new 28-GHz ECRIS on August 9, 2018, as the first beam, and the M/Q spectrum was obtained as shown in Fig. 5. By tuning the ECRIS parameters, we optimized the $^{40}\text{Ar}^{11+}$ beam current with an 18-GHz microwave power of 600 W and an extraction voltage of 15 kV. The maximum $^{40}\text{Ar}^{11+}$ beam current was about $90 \mu\text{A}$, and the drain current in the plasma chamber was about 1.8 mA. The beam current was not as high as expected, and we attributed this to the non-optimized beam transport because of the missing magnets described above.

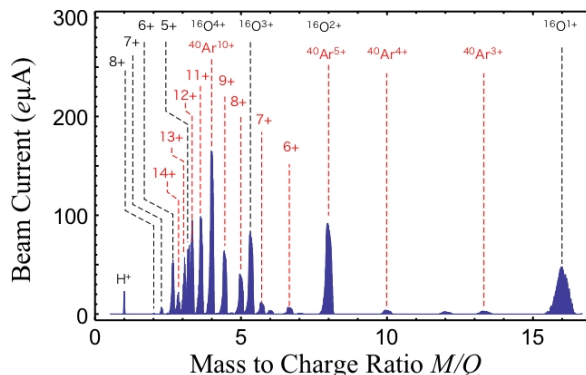


Figure 5: The M/Q spectrum of a ^{40}Ar beam with $^{16}\text{O}_2$ support gas utilizing 18-GHz microwaves with a power of 600 W.

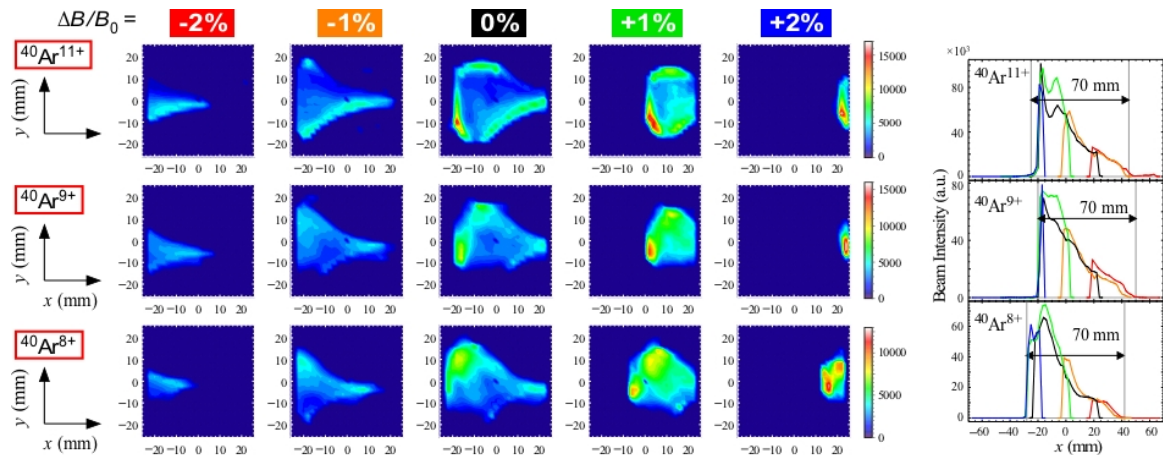


Figure 6: The contour plots on the left show $^{40}\text{Ar}^{11+, 9+, 8+}$ beam profiles obtained using the PPEM with analyzing magnetic field deviations of -2% to $+2\%$. On the right, the beam intensity is projected along the horizontal axis. The color of the projection line indicates the deviation of the magnetic field relative to that for the central trajectory B_0 ; the blue, green, black, orange, and red curves correspond to $\Delta B/B_0 = +2\%$, $+1\%$, 0% , -1% , and -2% , respectively.

We used the PPEM to obtain the $^{40}\text{Ar}^{8+, 9+, 11+}$ beam profiles shown in Fig. 6. From the center column of Fig. 6, the beam size seems to exceed the PPEM scope of an area $5\text{ cm} \times 5\text{ cm}$ square. Thus, we changed the magnetic field of the AM from -2% to $+2\%$ with respect to that of the center trajectory B_0 . By accounting for the position shift corresponding to the magnetic field deviation at the position of the PPEM, the projections of the intensity on the horizontal axis x for each charge state are shown in the right column in Fig. 6. For each charge state, the obtained curves are connected smoothly without any correction, except for the black curves obtained with $B/B_0 = 0\%$. This is reasonable because the black curve shows the signals obtained from the central area of the micro-channel plate (MCP), which was locally damaged by the relatively large number of beam irradiations. The MCP was not new because this measurement was for the pilot

study and we were concerned about damaging the new MCP in the case of a beam handling error. In all cases, the horizontal spreads of the $^{40}\text{Ar}^{8+, 9+, 11+}$ beams were estimated as about 70 mm.

From the PPEM measurement, not only the beam profile but also the emittances were measured. In Fig. 7, the three plots from top to bottom in the left column show the x - y , x - x' , and y - y' projections of the transverse phase-space distribution of the $^{40}\text{Ar}^{11+}$ beam. The top figure shows the hollow triangular beam profile with three intense areas. These are likely to originate from the plasma in the ECRIS or an aberration of the beam optics [10], but further discussion is outside the scope of this report. By selecting each intense area shown in the top row of Fig. 7, the corresponding x - x' and y - y' emittances are shown below each of the profiles. It can be seen that each beamlet occupies specific x - x' and y - y' areas by gating in the x -

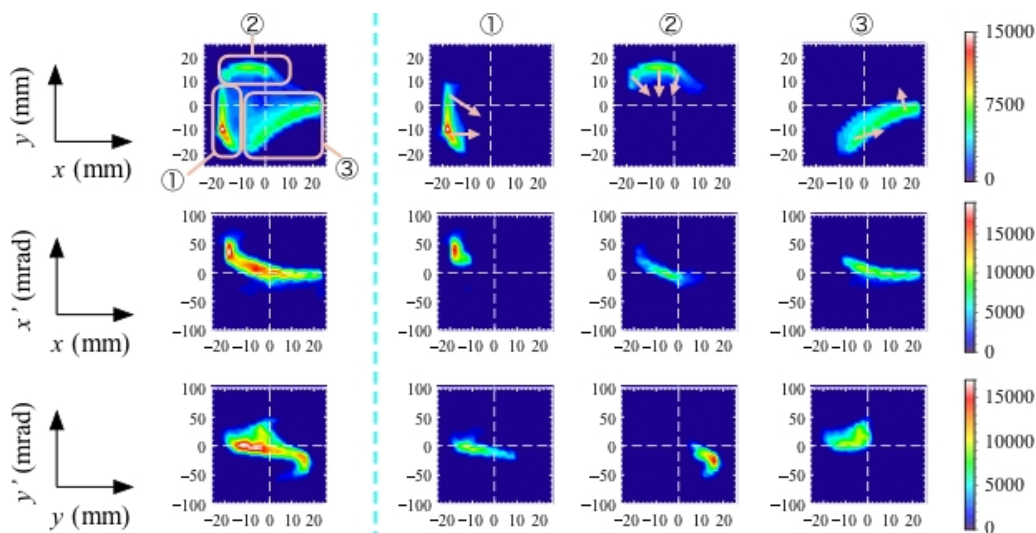


Figure 7: Contour plots showing the projections of the transverse phase-space distribution of the $^{40}\text{Ar}^{11+}$ beam measured by the PPEM. The top, middle, and bottom rows show the x - y , x - x' , and y - y' projections, respectively. In the left column, the x - y projection has a hollow triangular shape with three intense areas. The emittance in each area marked by a red rectangle is illustrated in the three columns on the right. The red arrows show the directions in which the beam components move as the beam progresses along the beam axis.

Content from this work may be used under the terms of the CC BY 3.0 licence (© 2018). Any distribution of this work must maintain attribution to the author(s), title of the work, publisher, and DOI.

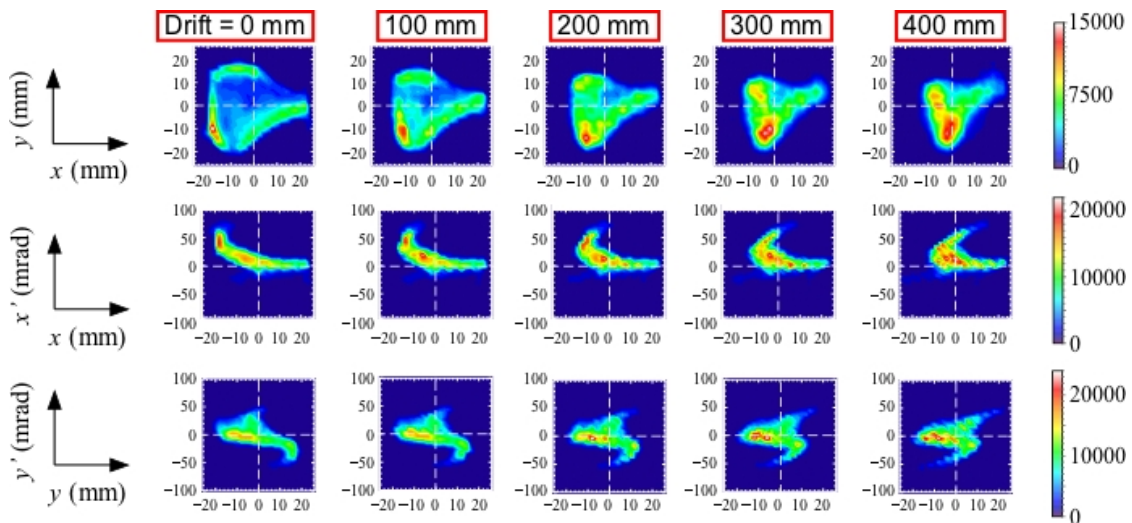


Figure 8: Contour plots showing the simulated evolution of the shape of the $^{40}\text{Ar}^{11+}$ beam (top), the $x-x'$ emittance (middle), and $y-y'$ emittance (bottom) as a function of the drift length from the PPEM. The drift length is provided at the top of each column. The triangular intense beamlets are estimated to converge at a position about 400 mm downstream from the PPEM.

y area only. Taking both the $x-x'$ and $y-y'$ emittances into account, as the beam progresses along the beamline, the beamlets are estimated to move in the directions indicated by the red arrows shown in the top row of Fig. 7. The four-dimensional phase-space distribution was taken into account to simulate the $^{40}\text{Ar}^{11+}$ beam shape evolution with respect to the drift length downstream of the PPEM, as shown in Fig. 8. The movement of the three intense areas of the beam profile is not as simple as those shown in Fig. 7; however, the intense areas are estimated to converge onto an area $30\text{ mm} \times 30\text{ mm}$ square at around 400 mm downstream from the PPEM. As shown in Fig. 8, the transverse phase-space distribution provides essential information for evaluating the validity of the beam optics devices in the immediately downstream LEBT to improve the transport efficiency in the future.

LOW-ENERGY BEAM TRANSPORT

A new LEBT will connect the new ECRIS to the RFQ of the RILAC. The LEBT configuration is as follows: pair solenoid (PSol)–triplet quadrupoles (TQs)–first focal plane (F1)–TQs–second focal plane (F2)–PSol, as

shown in Fig. 9. The PSol consists of two coils with mutually opposing polarities to cancel out the beam rotation induced by the axial magnetic field in the lens. By using a combination of TQs and PSols in the latter half of the LEBT, the horizontal and vertical acceptances at F1 corresponding to those of the RFQ were designed to be an upright ellipse with spatial and momentum axes of 7.4 mm and 19.6 mrad, respectively. The beam transport is optimized to easily fit the acceptance ellipse at F1 using the PSol and TQs in the first half of the LEBT even when the horizontal and vertical focal points are different from each other. The envelopes of the optimized beams with emittances of 145, 200, and 300 $\text{mm} \times \text{mrad}$ are shown at the bottom of Fig. 9. The typical emittance of the beam extracted from the RIKEN 28-GHz ECRIS was measured as $\sim 200\text{ mm} \times \text{mrad}$. From the viewpoint of long-term machine protection from very-high-beam-intensity operation, the beam located outside of the acceptance ellipse needs to be blocked. A set of three horizontal and vertical slits, called triplet slits, will be placed around F1 for this purpose, as shown in Fig. 10. Of course, a spatial slit only provides a vertical limitation in phase space; however,

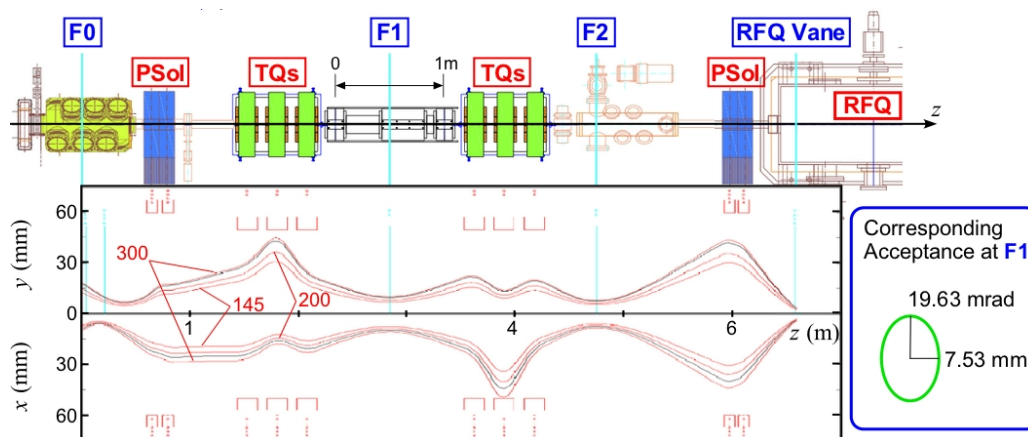


Figure 9: Schematic of the new LEBT (top) and the beam envelopes for which the emittances are assumed as 145, 200, and 300 $\text{mm} \times \text{mrad}$ (bottom). The beam transport is optimized to fit the acceptance at F1, which corresponds to the RFQ acceptance.

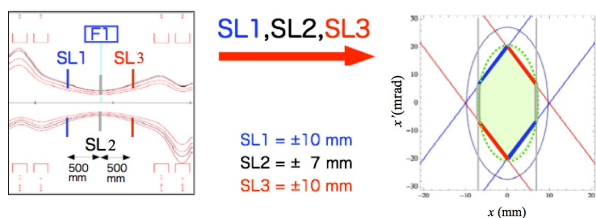


Figure 10: Emittance limitation imposed by triplet slits. The horizontal and vertical slits were located at not only F1 (SL2) but also 500 mm upstream and downstream from F1 (SL1,3). The phase-space limitations by slits SL1, SL2, and SL3 are indicated by blue, grey, and red lines, respectively. By collimation, the beam is confined within the corresponding acceptance at F1 (green dotted ellipse) in Fig. 9.

after a certain drift along the beam axis, the limitation is tilted in proportion to the degrees of x' or y' . Also, by placing a slit at F1, two more slits 500 mm upstream and downstream of F1, with adequate openings, impose a hexagonal limitation, as shown on right side of Fig. 10.

To check the validity of the triplet-slit limitation, we performed 3-D beam tracking with magnetic field mapping by the finite element method. The initial beam was assumed as having a Gaussian distribution in $x-x'$ and $y-y'$ phase space with an emittance of $200 \text{ mm} \times \text{mrad}$. The tilt angles of the emittance ellipses were assumed to be same as those of the envelop calculation in Fig. 9. The results of the tracking simulation with and without the triplet-slit limitation are shown in the top and bottom, respectively, of Fig. 11. From the beam trajectory in Fig. 11, the divergent beam component, which is seen around the RFQ vane region in the no-limitation case, is suppressed by the triplet-slit limitation at F1. Details of the phase space plot show that a small tail still remains, and this is considered to be induced by the aberration of the last PSol because the beam was designed to be widely spread in the lens to fit through the small spatial acceptance of the RFQs, for example, $\pm 3.59 \text{ mm}$.

Fabrication of the beam optics devices, that is, the PSols and TQs, is already complete. The LEBT is now under construction, and we plan to complete it by the end of 2018. After that, we plan to evaluate the validity of the beam optics using an actual beam and PPEM measurements.

SUMMARY AND FUTURE PERSPECTIVES

Construction of the new ECRIS and LEBT for the RILAC was started in 2017 to provide high-intensity beams of ions such as Ca and Zn for nuclear research, and V and Cr for the synthesis of SHEs with $Z > 118$. Because of the very short development period, the new ECRIS has the same structure as the RIKEN 28-GHz SC-ECRIS. With 18-GHz microwave heating, an ^{40}Ar beam was successfully extracted from the new ion source even though several beam optics magnets were incomplete. Using the PPEM, we measured not only the size of ^{40}Ar beams with charge states of 8+, 9+, and 11+, but also the transverse phase space distribution. Especially in the case of the

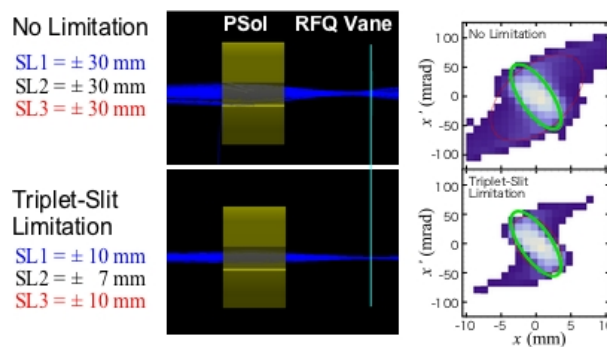


Figure 11: Simulated beam trajectory between the second PSol and the RFQ vane, and the $x-x'$ distribution at the RFQ vane showing the acceptance (green ellipses). Top and bottom panels show the results of simulations with and without the triplet-slit limitation, respectively. The slit limitation at F1 suppresses the divergent component; however, a small tail remains because of the aberration of the PSol.

Ar^{11+} beam, realistic evolution of the beam shape along the beamline was simulated by taking the phase space distribution into account. The LEBT is designed to match the RFQ acceptance and consists of PSol-TQ-TQ-PSol magnets. In addition, the triplet slit located around F1 limits the phase space to block the beam outside the acceptance ellipse. From a 3-D beam tracking analysis, the validity of this limitation was confirmed; however, the beam still has a small tail induced by aberration in the last PSol lens.

Completion of all the remaining components, including the 28-GHz gyrotron, the solenoid at the exit of the ECRIS, and the LEBT, is planned by the end of 2018. After that, we will evaluate the triplet-slit limitation using an actual beam and PPEM measurements. Furthermore, a compact HT oven will be installed, and we will produce metallic beams using highly charged Ca, Ti, and Zn ions, as well as a very intense Cr beam in the future.

REFERENCES

- [1] E. Ikezawa *et al.*, *Proceedings of the 13th International Conference on Heavy Ion Accelerator Technology (HIAT2015)*, Yokohama, Japan, 222 (2015)
- [2] Y. Yano, *Nucl. Instrum. and Meth. B*, vol. 261, p.1009 (2007),
- [3] T. Nakagawa *et al.*, *in these proceedings*.
- [4] T. Nakagawa *et al.*, *Rev. Sci. Instrum.*, vol. 81, p. 02A320 (2010).
- [5] Y. Higurashi *et al.*, *Rev. Sci. Instrum.* vol. 85, p. 02A953 (2014).
- [6] G. D. Alton and D. N. Smithe, *Rev. Sci. Instrum.* vol. 65, p. 775 (1994).
- [7] J. Ohnishi *et al.*, *in these proceedings*.
- [8] M. Leitner *et al.*, *Proceedings of the 15th International work-shop on ECR Ion Source (ECRIS2002)*, Jyväskylä, Finland (2002), unpublished.
- [9] V. Tzoganis *et al.*, *Proceedings of the 13th International Conference on Heavy Ion Accelerator Technology (HIAT2015)*, Yokohama, Japan, vol. 250 (2015),
- [10] Y. Batygin *et al.*, *RIKEN Accelerator Progress Report* vol. 28, p.170 (1995).

HIGH POWER OPERATION WITH SECRAL-II ION SOURCE*

L. Sun[†], W. Lu, J. W. Guo, L. X. Li, Z. Shen, L. B. Li, W. Huang, X. Z. Zhang, H. Y. Ma, Y. Yang, J. B. Li, W. H. Zhang, X. Fang, H. W. Zhao
 Institute of Modern Physics, CAS, Lanzhou, 730000, China

Abstract

SECRAL-II ion source has been successfully developed with the experiences from SECRAL that is another superconducting ECR ion source in operation at IMP. Other than that, SECRAL-II has been intentionally optimized in structure so as to make it optimum for 28 GHz microwave operation. This ion source was available on the test bench in early 2016, and has been used for 28 GHz high microwave power commissioning and tests. With a maximum power 10 kW@28 GHz and 2 kW@18 GHz, very high microwave power density and dense hot plasma could be built in the 5-liter volume plasma chamber. Consequently, very high current density ion beams of high charge states are achievable, which have already exceeded the performance the 24 GHz SECRAL had made couple of years ago. However, there is also the intractable issues stemmed from the hot dense electrons inside the plasma, such as plasma chamber cooling, dynamic heat load to the cryogenic system, and so on. This paper will present the recent results of SECRAL-II operated with high microwave power. The typical consequent issues during the high-power course other than high intensity high charge state ion beam production will be discussed.

INTRODUCTION

Electron Cyclotron Resonance Ion Sources or ECRIS has play an indispensable role in the development of next generation heavy ion accelerators, such as FRIB at MSU, HIAF at IMP, and JLEIC at JLab, and so on [1, 2, 3]. ECRIS is the most efficient ion source in term of the production of dc and long pulse (~ms) highly charged heavy ion beams. After more than 40 years' continuous development by generations of ECRIS sourcerors, the state of the art ECRISs have evolved to 3rd generation, which is represented by superconducting machines, such as VENUS at LBNL, SCECRIS at RIKEN, SECRAL & SECRAL-II at IMP, and so on [4, 5, 6, 7]. High performance superconducting ECRIS provides by far the ultimate conditions for high charge state ion beams production, such as much higher operation microwave frequency, better magnetic field confinement, bigger plasma chamber volume and above all, more flexible conditions for ion source performance optimization. Intense highly charged ion beam production is mainly defined by three key factors, i.e. n_e -plasma density, T_e -electron energy, and τ - exposure time of the ions to a

cloud of plasma electrons. State of the art ECRISs can provide flexible conditions for highly charged ion production with quasi-optimum T_e and τ , however, to get high intensity beams, sufficiently high microwave power, or to some extent the effective power density, is required to achieve high enough plasma density inside the plasma chamber. Therefore, high microwave power operation exploration is very necessary and might be mandatory for next generation heavy ion acceleration routine operation, for instance >0.7 emA U^{35+} for HIAF, >0.5 emA U^{35+} for RIBF, and so on.

SECRAL-II is a fully superconducting ECR ion source recently developed at IMP. Its superconducting magnet structure design inherits the features of SECRAL, except the cryogenic system. Table 1 summarizes the main parameters of SECRAL and SECRAL-II in comparison. The improved cryogenic system of SECRAL-II enables high microwave power operation (up to 10 kW) despite of the high bremsstrahlung radiation to the 4.2 K cold mass and the resultant high dynamic heat load, which allows the exploration of the ion source performance at high microwave power. This paper will report the high-power commissioning results and the typical issues of interests in terms of high power stability and beam quality. Challenges to a high power ECRIS are becoming apparent with increasing power density inside the plasma chamber, which are also discussed.

Table 1: Main Parameters of SECRAL-II

Parameters	SECRAL-II	SECRAL
ω rf (GHz)	18-28	18-24
Axial Field Peaks (T)	3.7 / 2.2	3.7/2.2
Mirror Length (mm)	420	420
No. of Axial SNs	3	3
Br (T)	2.0	1.7/ 1.83
Coldmass Length (mm)	~810	~810
SC-material	NbTi	NbTi
Magnet Cooling	LHe bathing	LHe bathing
Warm bore ID (mm)	142.0	140.0
Chamber ID (mm)	125.0	116.0/120.5
Cooling power@4.2 K (W)	~6	0

HIGH POWER RF SYSTEM

In the high microwave power campaign with SECRAL-II source, several high power microwave generators have been used. 18 GHz CPI DBS-band klystron microwave generator with a maximum microwave power output of 2.4 kW, is used as secondary ECRH (ECR Heating) microwave power source. CPI 28 GHz VGA model CW

*Work supported by MOST (contract No. 2014CB845500), CAS (QYZDB-SSW-JSC025), and NSF (contract No. 11221064)

[†]sunlt@impcas.ac.cn

gyrotron microwave generator with a maximum output power of 10 kW, is adopted as the main ECRH microwave power with regards to SECRAL-II design. A 45 GHz/20 kW gyrotron microwave generator from GyCOM Ltd., is incorporated as an auxiliary ECRH microwave source, and additionally to have a proof of principle test of ECRH with the microwave power system for the 4th generation ECR ion source FECR [8]. As 3 different microwave frequencies are available, flexible choices of ECRH schemes for the exploration of high power operation have been made, for instance 18 + 28 GHz double frequency heating, 28 GHz single frequency heating, 18 + 28 + 45 GHz triple frequency heating and 28 + 45 GHz double frequency heating. As 28 GHz is always the main ECRH frequency with SECRAL-II, the maximum microwave power injected into the ~5 liters plasma chamber is about 12.4 kW (nominal, transmission loss is not counted), which is equivalent to a power density of ~2.4 kW/l. Generally, a >1.0 kW/l power density will be granted as the criteria as high power operation for most of the 18~28 GHz high performance ECRISs. However, very high microwave power density up to 2.4 kW/l is not always effective during the experiments. Typically, the best performance presented in this paper has been obtained with 7~12 kW (respectively ~1.4-2.4 kW/l) for very intense medium charge state heavy ion ($A > 40$) beam production, and 3~8 kW (respectively ~0.6-1.5 kW/l) for very high charge state heavy ion beams production.

high power tests, typically 10 kW (~1.3 kW/l), which are also presented at this workshop [9]. Table 2 lists most of recent results with VENUS@28 GHz, SECRAL@24 GHz, and SECRAL-II@28 GHz. As given in the table, emA order ion beams such as Kr^{18+} (Fig. 1) and so on are achievable now, which is a very important benchmark for next generation heavy ion accelerations composed of either SRF linacs or synchrotrons. Very high charge state ion beams production such as Kr^{3n+} , Xe^{4n+} (Fig. 2) and so on, has pushed the M/Q dc beams extracted with an ECRIS from traditionally >4 to presently <3, which is very attractive to cyclotrons and HCI physics, in terms of machine performance and possible physics investigations.

ION SOURCE PERFORMANCE AT HIGH MICROWAVE POWER

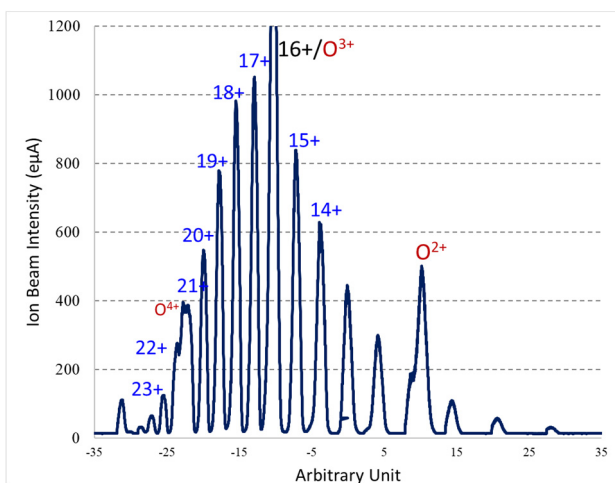


Figure 1: Production of intense Kr^{18+} beam.

At high power ECRH, high density plasma with sufficient energetic electrons are created to strip ions to high charge state. Depending on the source optimization, very intense medium charge state ion beams with the ionization potentials of 0.5~1.0 keV (such as Ar^{14+} , Kr^{18+} ...), and very high charge state ion beams with the ionization potentials of >4.0 keV (such as Kr^{33+} , Xe^{44+} , ...) are produced and extracted. Similar results are also recently obtained with VENUS ion source during several

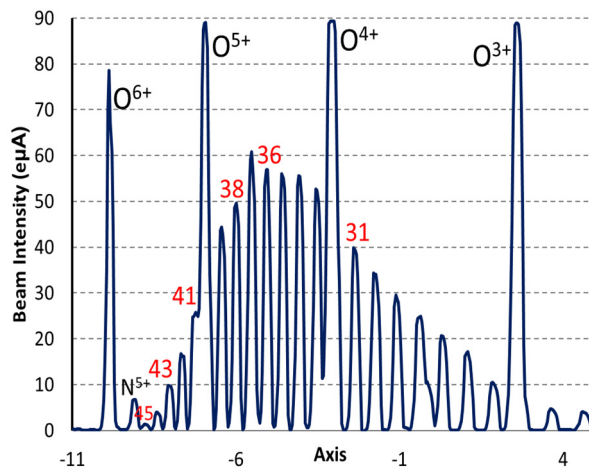


Figure 2: Production of high charge Xe beams.

Table 2: High Intensity and Highly Charged Ion Beams Production With SECRAL-II

Ion	VENUS 2018 10 kW	SECRAL 2016 7~8 kW	SECRAL-II 2018 10 kW
$^{16}O^{6+}$	4750	2300	6700
O^{7+}	1900	810	1750
$^{40}Ar^{12+}$	1060	1420	1190
Ar^{14+}	840	846	1040
Ar^{16+}	525	350	620
Ar^{17+}	120	50	130
Ar^{18+}	4.0	--	14.6
$^{78}Kr^{18+}$	770		1030
Kr^{23+}	420		436
Kr^{28+}	100		146
Kr^{30+}			20
Kr^{31+}	17		7
Kr^{32+}	8.0		0.5
$^{129}Xe^{26+}$		1100	
Xe^{27+}		920	870
Xe^{30+}		360	365
Xe^{34+}	104	120	102
Xe^{38+}	26	22.6	56
Xe^{42+}	6	12	16.7
Xe^{44+}	2	1	3.9
Xe^{45+}	0.88	0.1	1.3

CHALLENGES AT HIGH POWER EXPLORATION

Plasma Over-heating to Plasma Chamber (PCO)



Figure 3: Sectional burnt-out chamber wall.

High charge state ECRIS is characterized by a so-called min-B magnetic field configuration, which can not avoid the problem of localized PCO that is still durable for most of the ECRISs in operation, but at a high power operation condition, it is a problematic issue, especially the 3rd generation ECRISs. Min-B structure magnetic configuration that is a superimposition of an axial mirror field and a radial hexapole field always has 6 very weak $|B|$ points, i.e. 3 at source injection and 3 at source extraction. Plasma flux with energetic particles is much easily lost through those points, which high energy electrons dominates the loss process and energy deposition to the plasma chamber wall. With the increase of ECRH microwave power, more plasma energy or lost energetic electron energy will be deposited on tiny areas and result in a very high localized power density, which is estimated to in the magnitude of $1\sim 10 \text{ MW}\cdot\text{m}^{-2}$ [10]. Such a high power density heat sink to the plasma chamber inner wall can cause immediate boiling of the nearby water inside the cooling channel and isolate the chamber wall from efficient turbulent water cooling. Therefore, only thermal conduction cooling validates for those positions. That's the reason why stainless-steel chamber can only survive much lower microwave power than aluminium chamber. With the increase of ECRH power, temperature at the PCO points will be higher and higher, and eventually the plasma chamber metal will be melted or destroyed by $5\sim 6 \text{ kg}/\text{cm}^2$ pressurized water when the chamber metal yield strength becomes very low. As the radial space of an ECRIS is very valuable, not much space is reserved for a complicated cooling water structure that might be useful for the chamber design. This makes it very challengeable when high power operation is desired. VENUS and SECRAL-II have both reported the problem of chamber burnt-out during high power campaign (Fig. 3). When SECRAL-II was tested with a power density of $2\sim 2.4 \text{ kW}/\text{l}$, 3 aluminium plasma chambers had been destroyed successively. Improved design with better heat conduction effect and more

turbulent cooling water has been made. High power test at the level of $>2 \text{ kW}/\text{l}$ will demonstrate the effectiveness in the near future.

4.2 K Dynamic Heat Load (DHL)

Bremsstrahlung radiation inside ECR plasma has been observed for a long time as researchers tried to do ECRIS plasma investigations, however, dynamic heat load caused by this radiation was only noticed not long time ago during high power ECRH with the 3rd generation ECRIS. Bremsstrahlung radiation X-ray spectrum is quite wide that covers tens of eV to hundreds of keV. Usually, to protect the main high voltage insulator, $1\sim 2 \text{ mm}$ Ta shield will be inserted between plasma chamber and the high voltage insulator. X-rays with the energies below 100 keV are mostly filtered by the Ta shield, however, $1\sim 2 \text{ mm}$ Ta sheet is almost transparent for X-rays with energies higher than 100 keV . With the increase of ECRH power, the quantity of $>100 \text{ keV}$ X-rays that can reach the cold mass, mostly composed of iron and copper, will absorb part of the penetrated rays' energy and cause a certain amount of energy sink into the 4.2 K region, and consequently heat load to the 4.2 K system. It has been observed that the ratio between the heat sink and the ECRH power is dominantly related to the B_{min} field. Figure 4 shows the dependence of the measured DHL vs. the B_{min} values at totally 5 kW microwave ECRH. As SECRAL-II has a maximum DHL tolerance of 6 W , it enables its maximum ECRH power of $\sim 12 \text{ kW}$ for medium charge state ions, and $6\sim 8 \text{ kW}$ for high charge state ion beams, as a consequence of B_{min} optimization. SECRAL-II is obviously qualified for long time operation at the power level of $5\sim 6 \text{ kW}$ with regards to DHL, but degradation of the main insulator under high X-ray flux exposure is still unknown even with Ta foil protection, which is also another potential challenge in high power ECRH operation.

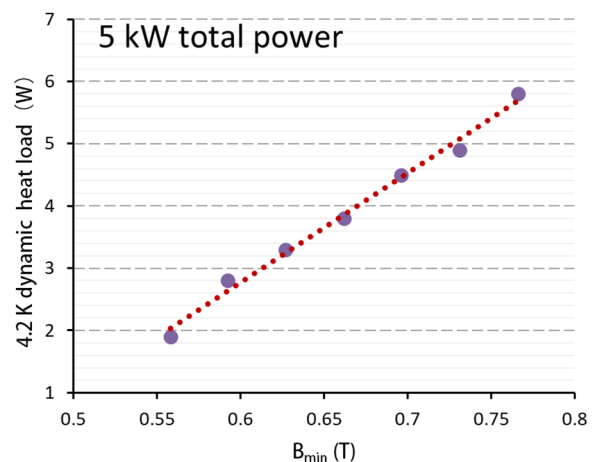


Figure 4: Dynamic heat load vs. B_{min} with SECRAL-II.

Intense Beam Extraction and Beam Quality

Based on traditional understanding of the ion beam behaviour after extraction from magnetized plasma, the emittance is proportional to the ion source field, and therefore the higher the operation frequency, the higher

Content from this work may be used under the terms of the CC BY 3.0 licence (© 2018). Any distribution of this work must maintain attribution to the author(s), title of the work, publisher, and DOI.

the beam emittance [11]. According to the predication, the product is that despite of the obvious beam intensity increment by frequency scaling, ion beam brightness should not have much improvement. And additionally, it has been predicted that with more intense beam extraction at high power ECRH, space charge effect will dominate and degrade the beam quality further more. A triode extraction system has been designed and integrated to SECRAL-II. The highest applicable extraction high voltage was tested up to >30 kV. The extracted mixing beam will be analysed by a high acceptance dipole with double-focusing edges [12]. As the gap is 180 mm, it allows high transmission efficiency of ion beams with big envelope. Second order component of the dipole magnet field has been carefully checked during the magnet design, provided that the beam envelope is not too big (~2/3 of the gap), the influence of sextupole component from the magnet is trivial. Additionally, to have further control of the beam envelope after ion source extraction, a high field solenoid is attached to SECRAL-II magnet. Analysed beams will be monitored by a water cooled faraday cup with the secondary electron suppressor biased to -160 V. A 4-jaw slit system is set upstream of the faraday cup to stop the unwanted beams after beam separation. A set of beam viewer and X/Y allision scanner system is integrated to monitor the beam quality.

Thanks to the 180 mm gap dipole, very high beam transmission efficiency has been observed. For 10 emA total drain current of oxygen beams, a transmission efficiency of ~85% could be made. Even at the total current of 26 emA, ~75% transmission is obtained. Heavy ion beam transmission is always a big challenge. SECRAL-II extraction system can give an estimated transmission efficiency of 85~95% for Xe beams with a total current of no more than 10 emA.

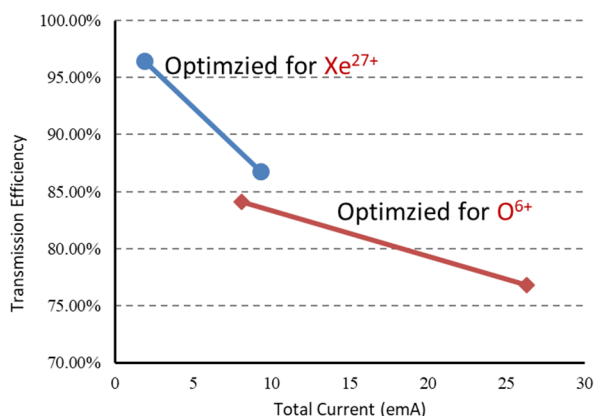


Figure 5: Beam transmission efficiency with SECRAL LEBT at different total beam intensities.

Intense beam extraction and transmission does not indicate obvious degradation of beam quality. With careful handling of the extracted beams, reasonable beam quality could be maintained. Figure 5 gives the evolution total drain current and emittances vs. the extraction ion beams of Ar⁹⁺ and Ar¹²⁺. Obviously, high current beam production is not equivalent to high beam emittances. Medium charge state ion beams, such as Ar⁹⁺ has slightly

worse beam quality with a hollow configuration as indicated in Fig. 6. Ar¹²⁺ beam quality is better as is given in Fig. 7. It is believed that the space charge actually does not dominate intense beam extraction from a high charge state ECR ion source. SPC compensation at the mixing beam line should be sufficiently high to mitigate the resultant effects. However, the spatial distribution of the ions inside the plasma and the source beam emission meniscus has fundamental impact to the beam formation and quality. Further discussion could be also be found in Ref. [12].

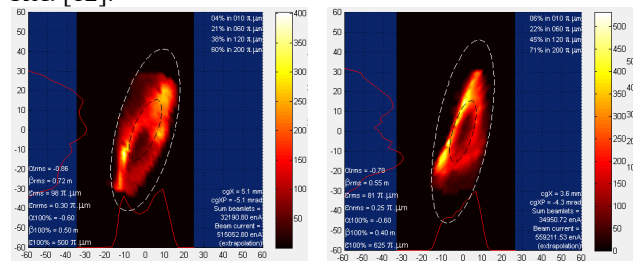


Figure 6: X/Y emittances of ~1.6 emA Ar⁹⁺@20 kV.

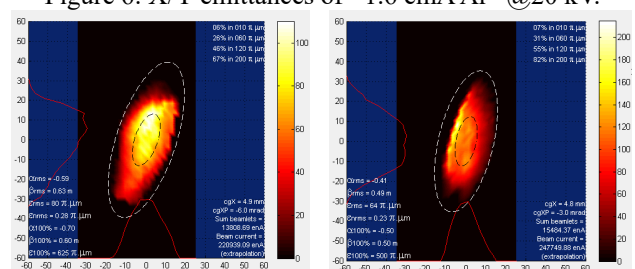


Figure 7: X/Y emittances of ~0.7 emA Ar¹²⁺@20 kV.

CONCLUSION

SECRAL-II ion source has been fully commissioned at high microwave power up to 12.4 kW. Under such an ultimate condition, many promising results have been obtained via effective ECRH, for instance 6.7 emA O⁶⁺, 1.03 emA Kr¹⁸⁺, 14.6 emA Ar¹⁸⁺, 16.7 emA Xe⁴²⁺ and so on. However, these are not the limit of a high performance 3rd generation ECR ion source. Given those critical challengeable problems solved, we may expect better performance:

- Plasma cooling in terms of localized over-heating
- Stable high temperature oven for refractory metal beams
- Dynamic heat load to 4.2 K cryogenic system

REFERENCES

- [1] J. Wei *et al.*, “The FRIB Project-Accelerator Challenges and Progress”, in *Proc. HIAT2012, Chicago, IL, USA*, June 2012, paper MOB01, pp. 8-19.
- [2] Guoqing Xiao, Hushan Xu, Sicheng Wang, “HIAF and CIADS National Research Facilities: Progress and Prospect”, *Nuclear Physics Review*, vol. 34, pp. 275-283, 2017, doi: 10.11804/NuclPhysRev.34.03.275 (in Chinese)

- Content from this work may be used under the terms of the CC BY 3.0 licence (© 2018). Any distribution of this work must maintain attribution to the author(s), title of the work, publisher, and DOI.
- [3] J. Guo, Y. Zhang, “Linac Options for the Ion Injector of MEIC”, in *Proc. HIAT2015*, Yokohama, Japan, Sept. 2015, pp. 212-215.
- [4] J. Benitez *et al.*, “Current Development of the VENUS Ion Source in Research and Operations”, in *Proc. ECRIS’12*, Sydney, Australia, Sept. 2012, paper THX002, pp.153-158.
- [5] Y. Higurashi, J. Ohnishi, H. Haba, M. Kidera, K. Ozeki and T. Nakagawa, “RECENT DEVELOPMENTS OF RIKEN 28 GHz SC-ECRIS”, in *Proc. ECRIS2016*, Busan, Korea, August 2016, paper MOBO04, pp. 10-13.
- [6] H. W. Zhao *et al.*, *Rev. Sci. Instrum.*, vol.81, p. 02A202 (2010).
- [7] L. Sun, W. H. Zhang, X. Fang, *et al.*, “SECRAL II ION SOURCE DEVELOPMENT AND THE FIRST COMMISSIONING AT 28 GHz”, in *Proc. ECRIS2016*, Busan, Korea, August 2016, paper TUAO04, pp. 43-47.
- [8] H. W. Zhao, L. Sun, “Development and status of 45 GHz FECR”, *this proceedings*, MOA1.
- [9] D. Xie, J. Benitez, C. Lyneis, D. Todd, W. Lu, “Exploring the potential of VENUS ion source”, *this proceedings*, MOA2.
- [10] T. Thuillier, J. Angot, J. Y. Benitez, A. Hodgkinson, C. M. Lyneis, D. S. Todd, and D. Z. Xie, *Rev. Sci. Instrum.*, vol. 87, p. 02A736 (2016).
- [11] M.A. Leitner, D.C. Wutte, C.M. Lyneis, “DESIGN OF THE EXTRACTION SYSTEM OF THE SUPERCONDUCTING ECR ION SOURCE VENUS”, in *Proc. of the 2001 Particle Accelerator Conference*, Chicago, IL, USA, June 2001, pp. 67-69.
- [12] Y. Yang, *et al.*, “HIAF front end for transmission and acceleration of 30 μ A $^{238}\text{U}^{35+}$ ”, in *HB2018*, Daejeon, Korea, June, 2018, Talk WEA2WB03.

PLASMA HEATING AND INNOVATIVE MICROWAVE LAUNCHING IN ECRIS: MODELS AND EXPERIMENTS

G. Torrisci*, D. Mascali, G. Castro, L. Celona, G. Mauro, M. Mazzaglia, E. Naselli¹, S. Gammino, INFN-LNS, Catania, Italy, ¹also at University of Catania, DFA, Catania, Italy
A. Galatà, INFN-LNL, Legnaro, Padua, Italy
G. Sorbello², University of Catania, DIIEI, Catania, Italy; ²also at INFN-LNS, Catania, Italy

Abstract

Microwave-to-plasma coupling in ECRIS has been based on the classic scheme of waveguide-to-cylindrical plasma cavity matching. Optimization has been often obtained by empirical adjustments leading to an oversimplified model, obtaining however satisfying performances. In order to overcome the ECR-heating paradigm, on-purpose design of launchers' setup and adequate diagnostics have to be developed. This paper describes three-dimensional numerical simulations and Radio Frequency (RF) measurements of wave propagation in the microwave-heated magnetized plasmas of ion sources. Moreover, driven by an increasing demand of high frequency ECR ion sources, innovative ideas for the geometry for both the plasma chamber and the related RF launching system - in a plasma microwave absorption-oriented scenario - are presented. Finally, the design of optimized launchers enabling "single-pass" power deposition, not affected by cavity walls effects, are described.

INTRODUCTION AND MOTIVATION

In this paper, the electromagnetic wave propagation in microwave-heated plasma confined in a magnetic field, is addressed through numerical simulations and experiments, devoted to understand how the RF wave propagation depends on the electron density profile and external magnetic configuration [1–3]. In particular, we focus on the mechanism of RF propagation into the non-homogeneous magnetized anisotropic lossy plasma of Electron Cyclotron Resonance Ion Sources (ECRIs) [4], ECR-based charge breeder [5] and simple mirror linear plasma trap [6]. A better comprehension of electromagnetic wave propagation and RF power to plasma coupling mechanisms in ion-sources magnetoplasmas is crucial in order to provide a cost-effective upgrade of these machines alternative to the use of higher confinement magnetic fields, higher RF power level and higher pumping wave frequency [7]. Several full-wave numerical simulation codes have been developed [8–12] also exploiting ray-tracing technique [13].

The wave propagation at frequencies in the range 3-40 GHz in ECRIS compact plasma chamber (having magnetic field of the order of few Tesla, electron density in the order of 10^{18} m^{-3}) cannot be predicted by the plane wave model nor addressed by "ray-tracing" often adopted to describe waves in fusion toroidal devices [13–15]. These models, in fact, fail in minimum-B configuration scenarios where the

scale length of plasma nonuniformity, $L_n = |n_e/\nabla n_e|$, and the magnetostatic field nonuniformity, $L_{B_0} = |B_0/\nabla B_0|$, are smaller than the free space, λ_0 , and guided, λ_g , wavelengths.

We used COMSOL Multiphysics [16] software to model a "cold", anisotropic magnetized plasma, described by full-3D non uniform dielectric tensor, enclosed by the metallic cylindrical cavity where the plasma is generated. A proper mesh generation, exploiting FEM-based COMSOL versatility, allowed us to optimally modelize the cavity and microwave waveguide launching structure, with a good computational efficiency and high resolution especially around the resonance regions. The validity of the code was demonstrated by reproducing experimental results obtained with:

- X-ray imaging experiment on ATOMKI ECRIS ion source [4];
- PHOENIX Charge Breeder acceptance test at the Laboratoire de Physique et de Cosmologie [5];
- "Flexible Plasma Trap" (FPT) at INFN-LNS, where the numerical electric field profile has been compared with RF measurements of the wave amplitude inside the FPT plasma chamber [6]

The article is arranged as follows. In the first section wave field solution of the Maxwell's equations taking into account the magnetic field which makes plasma anisotropic, non-uniformity of plasma density, and the metallic plasma chamber is presented. Then, the above listed experimental benchmarks are described. Finally, some perspective is given as short term, mid-term and long term proposals for next generation ECRIS development based on: reshaping plasma chambers with non-conventional features, innovative RF launcher [17] and futuristic all-dielectric mm-waves launching structures.

RF WAVE-PLASMA INTERACTION MODELING

A magnetized plasma in the GHz range frequencies can be modeled as a cold magneto-fluid with collisions where the field-plasma interaction is described by the tensorial constitutive relation $\vec{\epsilon} \cdot \vec{E}$. Typically $\vec{\epsilon}$ is derived assuming a magnetostatic field \vec{B}_0 directed along just one axis. This assumption is valid in most of cases but not in ECRIS where \vec{B}_0 is not strictly axis-symmetric. Considering the actual magneto-static structure of an ECRIS, that is not uniform nor axis-symmetric, $\vec{\epsilon}$ depends in a complex way from the

* giuseppe.torrisci@lns.infn.it

magnetostatic field $\vec{B}_0(x, y, z)$ and the local electron density $n_e(x, y, z)$. Under the “cold plasma” approximation, (i.e. $v_\phi \gg v_{th}$, being v_ϕ the wave’s phase speed and v_{th} the electron thermal speed), the tensor components have been derived as it follows [3]:

$$\vec{\epsilon}_r = \left(\overline{\overline{\epsilon}}' - i\overline{\overline{\epsilon}}'' \right) = \left(\overline{\overline{I}} - \frac{i\overline{\overline{\sigma}}}{\omega\epsilon_0} \right) =$$

$$= \begin{bmatrix} 1 + i\frac{\omega_p^2}{\omega} \frac{a_x}{\Delta} & i\frac{\omega_p^2}{\omega} \frac{c_z + d_{xy}}{\omega} & i\frac{\omega_p^2}{\omega} \frac{-c_y + d_{xz}}{\Delta} \\ i\frac{\omega_p^2}{\omega} \frac{-c_z + d_{xy}}{\Delta} & 1 + \frac{i\omega_p^2}{\omega} \frac{a_y}{\Delta} & i\frac{\omega_p^2}{\omega} \frac{c_x + d_{yz}}{\Delta} \\ i\frac{\omega_p^2}{\omega} \frac{c_y + d_{xz}}{\Delta} & i\frac{\omega_p^2}{\omega} \frac{-c_x + d_{zy}}{\Delta} & 1 + i\frac{\omega_p^2}{\omega} \frac{a_z}{\Delta} \end{bmatrix} \quad (1)$$

where

$$a_m = (-i\omega + \omega_{\text{eff}})^2 + B_{0m}^2 \left(\frac{e}{m_e} \right)^2,$$

$$c_m = B_{0m} \left(\frac{e}{m_e} \right) (-i\omega + \omega_{\text{eff}}),$$

$$d_{mn} = B_{0m} B_{0n} \left(\frac{e}{m_e} \right)^2$$

with $m = x, y, z, n = x, y, z$ and

$$\Delta = (-i\omega + \omega_{\text{eff}})a_x + B_{0z} \left(\frac{e}{m_e} \right) (c_z - d_{xy}) +$$

$$+ B_{0y} \left(\frac{e}{m_e} \right) (c_y + d_{xz}).$$

$\overline{\overline{\epsilon}}'$ is the real part of relative permittivity $\overline{\overline{\epsilon}}_r$, $\overline{\overline{\epsilon}}''$ is the imaginary part, ω the angular frequency of the microwave, $\omega_p = \sqrt{\frac{n_e e^2}{m_e \epsilon_0}}$ the plasma oscillation angular frequency, n_e the electron density, m_e the electron mass, e the electron charge, i the imaginary unit and ω_{eff} the collision frequency; the latter accounts for the collision friction (thus modeling wave damping) and avoids any singularity in the elements of (1). Eliminating the magnetic field between Maxwell’s equations and using the constitutive relations for an anisotropic medium, the wave equation reads as:

$$\nabla \times \nabla \times \vec{E} - \frac{\omega^2}{c^2} \overline{\overline{\epsilon}}_r \cdot \vec{E} = 0 \quad (2)$$

The above wave equation can be solved as a driven problem by a FEM solver that supports a non homogeneous tensorial constitutive relation; in the present work we used COMSOL and an external MATLAB routine allowing the definition of the full 3D dielectric tensor (1). In COMSOL we were able to model the exact shape of the FPT plasma chamber and the waveguide launching structure. The magnetic field and the plasma density were directly imported from experimental measurements. Since in proximity of the resonance surface (individuated by the iso-surface $B_0 = B_{ECR} = \frac{m_e}{e\omega}$ the permittivity varies strongly, the discretization of such a narrow region needed a very fine mesh: to achieve this, we

adopted an adaptive mesh procedure (that was allowed by a specific feature of the solver). An extremely fine mesh has been obtained, thanks to “functional evaluation” based on the electric field gradient.

IMPLEMENTATION AND EXPERIMENTAL BENCHMARKS

Plasma Characterization By Energy Dispersive X-Ray Imaging At the Atomki ECR Ion Source

A Pinhole and CCD based quasi-optical x-ray imaging technique was applied to investigate the plasma of an electron cyclotron resonance ion source (ECRIS). Spectrally integrated and energy resolved images were taken from an axial perspective. We compared the X-ray plasma images recorded by the CCD pinhole camera with the simulated electron density map for two different microwave frequencies. In particular the transversal distribution of the electrons in the energy range 2-30 keV is compared with the filtered X-ray images corresponding to the K-alpha lines of the Argon. The simulations are consistent with the experimental evidence since also the number of warm particles is larger at 12.84 GHz rather than at 12.92 GHz, and the area populated from these particles is broader at 12.84 GHz, [18].

Electromagnetic Analysis of the Plasma Chamber Of PHOENIX ECR-based Charge Breeder At LPSC

During the experiments, by feeding microwaves at 14.324 GHz with a Travelling Wave Tube Amplifier (TWTA), instead of the commonly used Klystron at 14.521 GHz, it was observed an increase of the efficiency of Cs²⁶⁺ and a decrease in its charge breeding time, both of 15%, while the global capture stayed almost constant. This results revealed a huge difference in the electromagnetic behaviour between the two frequencies. The numerical simulations gave us the possibility to evaluate the power absorptions by the plasma. Results show that the 14.324 GHz frequency is three times more efficiently absorbed by the plasma than 14.521 GHz. These results are in very good agreement with the experimentally observed frequency tuning at exactly the simulated frequencies, confirming the model was sufficiently refined to almost reproduce the real-world conditions [19].

Wave Electric Field Profile Measurement Inside FPT Plasma Chamber at INFN-LNS

The section reports about the direct comparison of the numerical results (from our full-wave approach) with the inner-plasma measurements of the electric field amplitude performed by means of a two-pins RF probe. Both simulations and measurements have been done considering the compact plasma trap FPT in a simple mirror configuration. The direct comparison between simulations and measurements demonstrate that the COMSOL simulated RF field profile clearly resembles the experimentally measured ones for three magnetic fields configurations. The RFP influence

is not considered in the FEM simulations, so prediction capability is low. When density increases, the modal behaviour becomes more and more sensitive to the plasma presence within the chamber, whose influence is predicted by the FEM simulations. Therefore, the agreement between FEM predictions and experimental measurements increases [20].

CONCLUSION AND PERSPECTIVES

The excellent agreement between model predictions and experimental data are very promising for the design of future launchers or “exotic” shapes of the plasma chambers in compact machines, such as ECR Ion Sources and other similar devices. We propose hereinafter three different

- Short term (2 years): **Reshaping plasma chambers with non-conventional features for ECRISs.** A novel cavity resonator shape, with a non-uniform cross section matched to the twisting magnetic structure and a new RF launching scheme based on properly matched fundamental mode operating elliptical waveguide and tapered elliptical waveguide is proposed. Preliminary results show that a better geometrical and a dramatically improved RF matching to the new “plasma-shaped” plasma chamber can be obtained.
- Short/mid-term (3 years): **Innovative RF launcher.** A microwave launcher for the FPT, based on a two-waveguide array has been proposed. The experimental characterization is in good agreement with the numerical simulations and it has shown that, setting up a suitable phase difference, it is possible to tilt the angle of maximum radiation up to 40 degree to direct the microwaves towards the peripheral areas of the plasma chamber.
- Long Term (5 years): **futuristic all-dielectric mm-waves launching structures.** The technical challenges at 50 GHz make it attractive to look for new approaches: by taking inspiration from Dielectric accelerator structures we propose the investigation of the emerging electromagnetic concepts about all-dielectric Photonic Crystal (PhC) and Metamaterials structures. They are scalable, potentially low cost, and allow high frequency operation and mature fabrication technologies. Proof-of-concept experiments are taking place at LNS, such as woodpile EBG Waveguide as a DC-break and dielectric Photonic Crystal Waveguide.

REFERENCES

- [1] R. Geller, *Electron Cyclotron Resonance Ion Sources and ECR Plasmas*. Taylor & Francis, 1996.
- [2] L. Celona, S. Gammino, G. Ciavola, F. Maimone, and D. Mascali, “Microwave to plasma coupling in electron cyclotron resonance and microwave ion sources (invited),” *Review of Scientific Instruments*, vol. 81, no. 2, p. 02A333, 2010.
- [3] G. Torrisci, D. Mascali, G. Sorbello, L. Neri, L. Celona, G. Castro, T. Isernia, and S. Gammino, “Full-wave fem simulations of electromagnetic waves in strongly magnetized non-homogeneous plasma,” *Journal of Electromagnetic Waves and Applications*, vol. 28, no. 9, pp. 1085–1099, 2014.
- [4] D. Mascali, G. Castro, S. Biri, R. Racz, J. Palinkas, C. Caliri, L. Celona, L. Neri, F. P. Romano, G. Torrisci, and S. Gammino, “Electron cyclotron resonance ion source plasma characterization by x-ray spectroscopy and x-ray imaging,” *Review of Scientific Instruments*, vol. 87, no. 2, p. 02A510, 2016.
- [5] A. Galata’, D. Mascali, L. Neri, G. Torrisci, and L. Celona, “A three-dimensional numerical modelling of the phoenix-spes charge breeder based on the langevin formalism,” *Review of Scientific Instruments*, vol. 87, no. 2, p. 02B507, 2016.
- [6] S. Gammino, L. Celona, D. Mascali, G. Castro, G. Torrisci, L. Neri, M. Mazzaglia, G. Sorbello, O. Leonardi, L. Allegra, G. Calabrese, F. Chines, G. Gallo, and S. Passerello, “The flexible plasma trap (fpt) for the production of overdense plasmas,” *Journal of Instrumentation*, vol. 12, no. 07, p. P07027, 2017.
- [7] G. Castro, D. Mascali, S. Gammino, G. Torrisci, F. P. Romano, L. Celona, C. Altana, C. Caliri, N. Gambino, D. Lanaia, R. Miracoli, L. Neri, and G. Sorbello, “Overdense plasma generation in a compact ion source,” *Plasma Sources Science and Technology*, vol. 26, no. 5, p. 055019, 2017.
- [8] T. Ropponen, O. Tarvainen, P. Suominen, T. Koponen, T. Kalvas, and H. Koivisto, “Hybrid simulation of electron cyclotron resonance heating,” *Nuclear Instruments and Methods in Physics Research Section A: Accelerators, Spectrometers, Detectors and Associated Equipment*, vol. 587, no. 1, pp. 115 – 124, 2008.
- [9] B. P. Cluggish and J.-S. Kim, “Modeling of wave propagation and absorption in electron cyclotron resonance ion source plasmas,” *Nuclear Instruments and Methods in Physics Research Section A: Accelerators, Spectrometers, Detectors and Associated Equipment*, vol. 664, no. 1, pp. 84 – 97, 2012.
- [10] E. G. Evstatiev, V. A. Svidzinski, J. A. Spencer, and J. S. Kim, “Analytical and numerical modeling of radio frequency electron cyclotron resonance power absorption within the cold plasma picture,” *Review of Scientific Instruments*, vol. 85, no. 2, p. 02A503, 2014.
- [11] V. Mironov, S. Bogomolov, A. Bondarchenko, A. Efremov, and V. Loginov, “Numerical model of electron cyclotron resonance ion source,” *Phys. Rev. ST Accel. Beams*, vol. 18, p. 123401, Dec 2015.
- [12] G. Shirkov and G. Zschornack, “Simulation of ion confinement in an ecr ion source under electron injection,” *Nuclear Instruments and Methods in Physics Research Section B: Beam Interactions with Materials and Atoms*, vol. 95, no. 4, pp. 527 – 532, 1995.
- [13] M. Brambilla and T. Kracken, “Numerical simulation of ion cyclotron heating of hot tokamak plasmas,” *Nuclear Fusion*, vol. 28, no. 10, p. 1813, 1988.
- [14] J. Jacquot, V. Bobkov, L. Colas, S. Heurax, A. Kriivskà, L. Lu, J.-M. Noterdaeme, T. S. Team, and A. U. Team, “Full wave propagation modelling in view to integrated icrh wave coupling/rf sheaths modelling,” *AIP Conference Proceedings*, vol. 1689, no. 1, p. 050008, 2015.

- Content from this work may be used under the terms of the CC BY 3.0 licence (© 2018). Any distribution of this work must maintain attribution to the author(s), title of the work, publisher, and DOI.
- [15] N. Bertelli, O. Maj, E. Poli, R. Harvey, J. C. Wright, P. T. Bonoli, C. K. Phillips, A. P. Smirnov, E. Valeo, and J. R. Wilson, "Paraxial wenzel-kramers-brillouin method applied to the lower hybrid wave propagation," *Physics of Plasmas*, vol. 19, no. 8, p. 082510, 2012.
- [16] COMSOL, "Rf module user's guide, version 5.3,"
- [17] G. Torrasi, G. Sorbello, O. Leonardi, D. Mascali, L. Celona, and S. Gammino, "A new launching scheme for ecr plasma based on two-waveguides-array," *Microwave and Optical Technology Letters*, vol. 58, no. 11, pp. 2629–2634.
- [18] R. Rácz, D. Mascali, S. Biri, C. Caliri, G. Castro, A. Galatà, S. Gammino, L. Neri, J. Pálkás, F. P. Romano, and G. Torrasi, "Electron cyclotron resonance ion source plasma characterization by energy dispersive x-ray imaging," *Plasma Sources Science Technology*, vol. 26, p. 075011, July 2017.
- [19] A. Galatà, G. Patti, L. Celona, D. Mascali, L. Neri, and G. Torrasi, "Electromagnetic analysis of the plasma chamber of an ecr-based charge breeder," *Review of Scientific Instruments*, vol. 87, no. 2, p. 02B505, 2016.
- [20] G. Torrasi, D. Mascali, G. Sorbello, G. Castro, L. Celona, and S. Gammino, "Numerical and experimental characterization of rf waves propagation in ion sources magnetoplasmas," *submitted on IEEE Transactions on Antennas and Propagation*.

A POSSIBLE OPTIMIZATION OF ELECTRON CYCLOTRON RESONANCE ION SOURCES PLASMA CHAMBERS

C. S. Gallo *, A. Galatà, INFN-Laboratori Nazionali di Legnaro, (Padova), Italy
D. Mascali, G. Torrissi, INFN-Laboratori Nazionali del Sud, Catania, Italy

Abstract

In the cylindrical resonant cavities of Electron Cyclotron Resonance Ion Sources (ECRIS), microwave fields are used to generate and sustain the plasma. Normally, resonant modes of a higher order than the fundamental one are excited, due to the high frequency used compared to the dimensions of the plasma chambers: this can lead to small electric fields on the resonant surface, translating in low electrons energy and poor source performances. In this paper, we propose a possible modification of the conventional plasma chambers, resulting from an electromagnetic study carried out on a Caprice-type full permanent magnet ECRIS. Such modification implies the excitation of a “length-independent” resonant mode, having an intense and homogeneous electric field on the plasma chamber axis. This characteristic makes the modification suitable to be applied to numerous ECR sources. The positive effect on the plasma electrons density distribution will be also shown.

INTRODUCTION

Electron Cyclotron Resonance Ion Sources (ECRIS) [1] are nowadays the most effective devices to produce high intensity continuous or pulsed beams of medium-high charge states. In such sources, a plasma is created and sustained through a resonant interaction between microwaves (typically at 14 or 18 GHz) and the electrons motion, and is confined by a particular multi-Tesla magnetic configuration called B-minimum structure, generated by superimposing the field created by two or more coils to the one generated by a hexapole. Considering the particular topology of the magnetic field, the resonant interaction takes place on closed egg-shaped surfaces, called resonance surfaces. The performances of these devices have been evolving during the years following the well known scaling laws [1], the High-B mode concept [2] and the ECRIS standard model [3]: this has involved the necessity to employ higher and higher frequencies and magnetic fields, that often implies the development of expensive and technologically complex devices. At the same time, different “tricks” were discovered and have been applied to boost their performances: in particular, the injection of two close or well separated frequencies [4,5], as well as the fine tuning of a single frequency, known as frequency tuning effect [6]. The main aim of those tricks is to increase the electrons density and energy by optimizing the power absorption by the microwave field. In fact, the beam extracted from an ECRIS consists of those ions that flow from a portion of the resonance surface around the plasma chamber axis toward the extraction aperture, following the magnetic

field lines: consequently, for any given operating frequency and magnetic configuration, it is mandatory to maximize the energy transfer to plasma electrons in that specific part of the resonance surface. For plasma chambers with cylindrical shapes, possible modes that show an intense electric field around the axis and are length-independent are, for example, the $TM_{0,n,0}$ modes: this paper describes a simple but effective modification to the plasma chamber geometry in order to excite the plasma through one of the above mentioned modes, so as to maximize the energy transfer to plasma electrons. The modification has been studied with the electromagnetic solver COMSOL Multiphysics® and validated by simulating the electrons dynamics under the calculated electromagnetic fields, using an ad-hoc code developed in MatLab®.

SIMULATION DOMAIN

The geometry used to validate numerically the modification proposed in this paper is the plasma chamber of the ECRIS called LEGIS (LEGnaro ecrIS) and installed at Istituto Nazionale di Fisica Nucleare-Laboratori Nazionali di Legnaro (INFN-LNL). It is a full permanent magnet source of the Supernanogan type built by the Pantechnik company, whose typical operating frequency is 14.428 GHz. The plasma chamber, made in aluminum, consists in a cylinder with a radius of 22 mm, a length of 128 mm and two holes, one of 24 mm in diameter at the injection side and the other of 7 mm in diameter at the extraction side: Fig. 1 shows the model implemented in COMSOL®, together with the radial microwave input through a rectangular WR62 waveguide located at 10 mm from the injection hole.

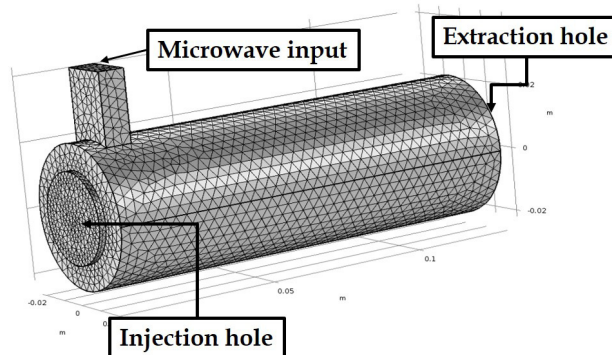


Figure 1: Model of the plasma chamber of the LEGIS source implemented in COMSOL®. Microwaves are injected through a radial rectangular WR62 waveguide. The extraction hole is not visible.

As a first step, the frequencies of the resonant modes $TM_{0,n,0}$ were calculated analytically for the present geom-

* carmelo.gallo@lnl.infn.it

Content from this work may be used under the terms of the CC BY 3.0 licence (© 2018). Any distribution of this work must maintain attribution to the author(s), title of the work, publisher, and DOI.

etry considering $n=1-3$: the values obtained are 5.2 GHz ($TM_{0,1,0}$), 12.0 GHz ($TM_{0,2,0}$) and 18.8 GHz ($TM_{0,3,0}$). Unfortunately, none of those frequencies are compatible with the magnetic structure of the LEGIS source, projected to operate between 14 and 14.5 GHz. In order to make at least one the above mentioned modes suitable for the operation with our source, we considered a reduced plasma chamber radius of 18.3 mm, able to shift the frequency of the $TM_{0,2,0}$ mode at 14.4 GHz. The simulations shown in the following section concern the comparison of two structure: the present geometry of the LEGIS plasma chamber (present chamber) excited at the operating frequency of 14.428 GHz and its possible modification reducing the radius to 18.3 mm (modified chamber), excited with a $TM_{0,2,0}$ mode.

ELECTROMAGNETIC ANALYSIS

The electromagnetic analysis started with the study of the two structures with the Eigenmode solver, that is considering them as ideal cavities, with perfectly conducting boundaries and without any hole, and finding the resonant modes: the maximum element of the mesh size was set to 1.75 mm (about $\lambda_0/6$, where λ_0 is the vacuum wavelength), a good compromise between accuracy of the calculations and computational costs. For the present chamber, the resonant mode closest to the operating frequency is the $TE_{2,1,11}$ at 14.488 GHz, while for the modified chamber we focused on the $TM_{0,2,0}$ mode found at 14.395 GHz. The calculated electric field distribution for the two cases is shown in Fig. 2 it can be clearly seen that the $TM_{0,2,0}$ mode not only has a very intense electric field on the plasma chamber axis, but its maximum value is more than 50% higher compared to the $TE_{2,1,11}$. As a following step, the two holes at injection and extraction were included in the analysis of the two geometries: Fig. 3 shows the results. In both cases we observed a shift in the resonant frequency, in particular of -60 MHz for the present chamber and +37 MHz for the modified geometry, but the $TM_{0,2,0}$ still shows an intense electric field on axis (except for a small decrease close to the injection hole), and its maximum is now twice the one shown by the $TE_{2,1,11}$.

The analysis then moved to the Frequency domain solver, that is the study of the behavior of specific frequencies considering the real geometry and RF excitation port (holes and waveguide input): 14.428 GHz ($TE_{2,1,11}$ mode) and 14.432 GHz ($TM_{0,2,0}$ mode) were chosen for, respectively, the present chamber and the modified chamber. Perfectly conducting boundary was the boundary condition applied to the plasma chamber wall, while for the two holes the perfectly matched layer was chosen, so as to absorb all the outgoing wave energy without any impedance mismatch. The calculations started considering vacuum-filled cavities and 100 W of microwave power, with a mesh size of $\lambda_0/6$: the electric field distributions in logarithmic scale are shown in Fig. 4 for both frequencies. The effectiveness of the modification to the plasma chamber is evident: the $TM_{0,2,0}$ mode shows again a much higher electric field on

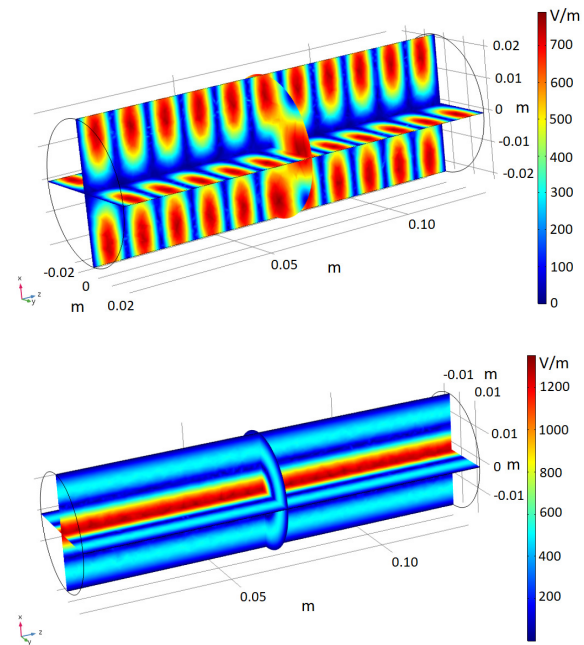


Figure 2: Electric field distribution calculated through the COMSOL® eigenmode solver: the present chamber with the $TE_{2,1,11}$ mode (top), the modified chamber with the $TM_{0,0,2}$ (bottom).

the plasma chamber axis, especially toward the extraction side, and in general a higher electric field compared to the $TE_{2,1,11}$ mode. After the vacuum-filled geometry simulations we included the plasma through the full-3D dielectric tensor, computed by MatLab® for each mesh point given by COMSOL® following the same approach used in [7]:

the plasma was described through the plasmoid/halo scheme [8], considering a dense plasma inside the resonance surface with $n_{\text{plasmoid}}=2.5 \cdot 10^{17} \text{ m}^{-3}$, and a rarified halo outside with $n_{\text{halo}}=n_{\text{plasmoid}}/100$. This time the mesh size used was not uniform, reaching $\lambda_0/10$ around the resonance surface. The results of the calculations for both frequencies are showed in Fig. 5 and summarized in Table 1: the power absorption at the resonance surfaces is evident in both cases but the modified geometry shows a higher electric field in a zone around the axis, especially at the extraction side. Table 1 shows that the modified geometry not only gives a better matching for the microwaves, but also a higher power absorbed by the plasma (around 30% more compared to the present geometry). The difference in the amplitude of the electric field produced in the two analyzed cases is even more evident by looking at Fig. 6, showing the modulus of the electric field on the plasma chamber axis. For the present geometry (top part), the electric field at the resonances is not really different compared to the rest of the plasma chamber, while for the modified geometry (bottom part) two very high peaks are visible in correspondence of the resonances, with an absolute value three times higher compared to the present geometry.

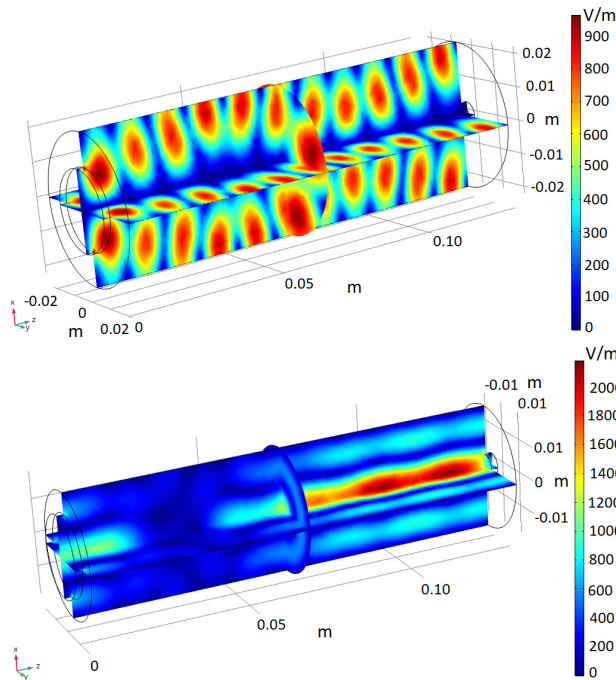


Figure 3: Electric field distribution calculated through the COMSOL[®] eigenmode solver including the injection and extraction holes: the present chamber with the TE_{2,1,11} mode shifted at 14.428 GHz (top); the modified chamber with the TM_{0,2,0} shifted at 14.432 GHz (bottom).

Table 1: Comparison between the two simulated geometries including the plasma.

	Present Geometry	Modified Geometry
Frequency [GHz]	14.428	14.432
Simulated power [W]	100	100
Matched power [W]	69.2	91.7
Plasma absorption [W]	64.5	84.4

ELECTRONS DYNAMICS

The electromagnetic fields calculated for the two geometries were used to simulate the electrons dynamics, using a MatLab[®] code derived directly from the one developed by the INFN ions source group for ions [9]. With such a code we simulated the motion of 100000 electrons, whose starting conditions are located inside the resonance surface, with a time step $T_{step}=10^{-12}$ s and a total simulation time $T_{span}=4\cdot 10^{-5}$ s: the calculations included both electromagnetic and magnetostatic fields, as well as electron-electron collisions and relativistic effects. By using an ad-hoc routine, the code stores particles positions at each time step in a 3D matrix reflecting the domain of the simulation divided in cells of 1 mm³, creating an "occupation" map directly correlated to the electrons spatial density distribution. The projection on the xz plane of the maps for the two geometries is shown in Fig. 7: the present geometry is characterized by low field intensities in the near-axis region, which have been demonstrated to be prone for hollow-plasma generation, i.e.

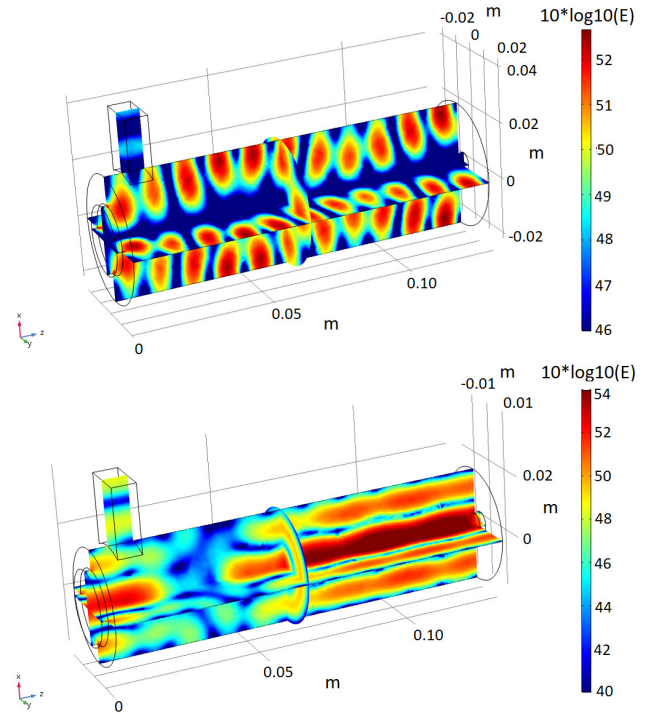


Figure 4: Electric field distribution in logarithmic scale calculated through the COMSOL[®] frequency domain solver: 14.428 GHz for the present chamber (top), 14.395 GHz for the modified chamber (bottom).

the plasma density is low where the electromagnetic field intensity is low as well. The electromagnetic simulations here performed, instead, is promising for a better RF power deposition in the axial region, allowing the formation of a denser and more uniform plasmoid.

CONCLUSIONS AND PERSPECTIVES

The electromagnetic study proposed consists of a cheap and effective modification of the plasma chamber geometry of the ion source LEGIS installed at INFN-LNL, to optimize the electromagnetic coupling to the plasma. The modification was validated by electromagnetic calculation carried out including the plasma through its 3D dielectric tensor, and the electrons dynamics under the resulting electromagnetic field, the magnetostatic field of the magnetic trap and electron-electron collisions. The TM_{0,2,0} mode is able to create an intense electric field on the chamber axis, about three times higher compared to the one created by the TE_{2,1,11} mode, leading to a higher power absorbed in the plasma volume and the formation of a much denser plasma. In principle such modification could be applied to similar geometries of any length. Such calculations will be verified in the next future by comparing the ion output of the LEGIS source before and after the proposed modification.

REFERENCES

- [1] R. Geller, "Electron cyclotron resonance ion sources and ECR" *plasmas*, Bristol : IOP (1996).

Content from this work may be used under the terms of the CC BY 3.0 licence (© 2018). Any distribution of this work must maintain attribution to the author(s), title of the work, publisher, and DOI.

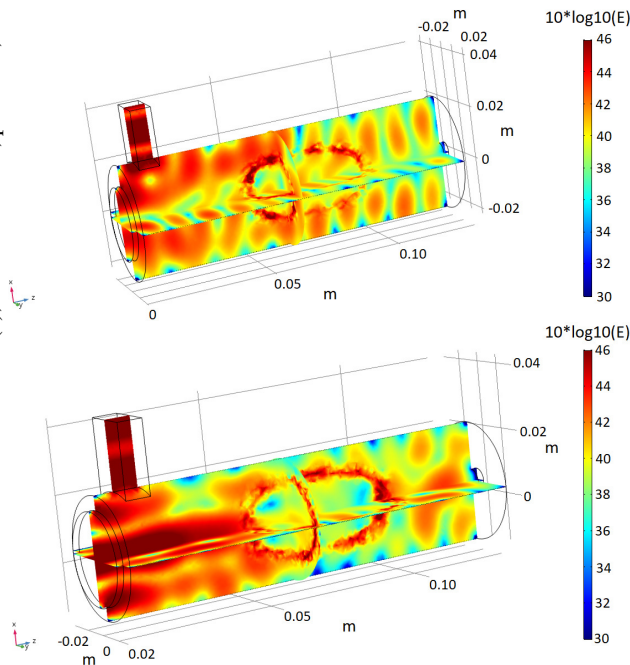


Figure 5: Electric field distribution in logarithmic scale calculated through the COMSOL[®] frequency domain solver and including the plasma: 14.428 GHz for the present chamber (top); 14.395 GHz for the modified chamber (bottom).

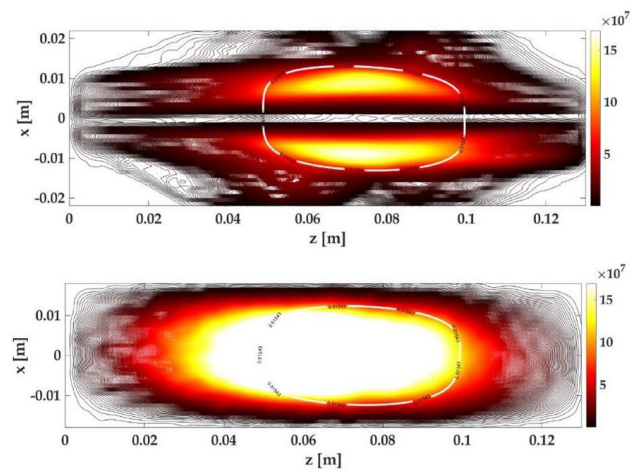


Figure 7: Projection on the xz plane of the occupation maps: present geometry (top) and modified geometry (bottom). The points corresponding to the resonance are indicated by the white dashed lines.

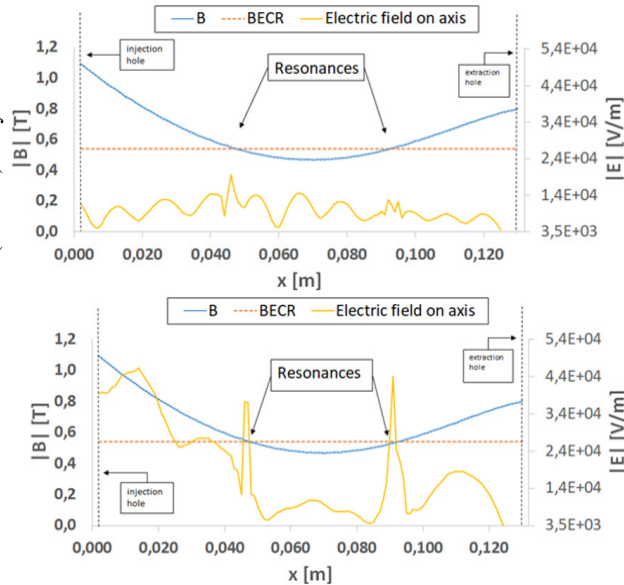


Figure 6: Modulus of the electric field on the plasma chamber axis: present geometry (top), modified geometry (bottom). The points corresponding to the two resonances are indicated by arrows.

- [2] S. Gammino *et al.*, "The role of microwave frequency on the high charge states buildup in ECR io sources", *Plasma Sources Sci. Technol.*, vol. 5, p. 19 (1996).
- [3] T.A. Antaya *et al.*, "The superconducting electron cyclotron resonance 6.4 GHz high-B mode and frequency scaling in electron cyclotron resonance ion sources", *Rev. Sci. Instrum.*, vol. 65, p. 1723, (1994).
- [4] S. Biri *et al.*, "Two-frequency heating technique at the 18 GHz electron cyclotron resonance ion source of the National Institute of Radiological Sciences", *Rev. Sci. Instrum.*, vol. 85, p. 02B507, (2014) .
- [5] Z.Q. Xie, C.M. Lyneis, "Two-frequency plasma heating in a high charge state electron cyclotron resonance ion source", *Rev. Sci. Instrum.*, vol. 66, p. 4218, (1995) .
- [6] L. Celona *et al.*, "Observation of the frequency tuning effect in the 14 GHz CAPRICE ion source", *Rev. Sci. Instrum.*, vol. 79 p. 023305, (2008).
- [7] A. Galatà *et al.*, "Electromagnetic analysis of the plasma chamber of an ECR-based charge breeder", *Rev. Sci. Instrum.*, vol. 87, p. 02B505, (2016).
- [8] A. A. Ivanov and K. Wiesemann, "Ion confinement in elec-tron cyclotron resonance ion sources (ECRIS): importance of nonlinear plasma-wave interaction", *IEEE Trans. Plasma Sci.*, vol. 33, p. 1743, (2005).
- [9] A. Galatà *et al.*, "A three-dimensional numerical modelling of the PHOENIX-SPES charge breeder based on the Langevin formalism", *Rev. Sci. Instrum.*, vol. 87, p. 02B507, (2016).

STATUS OF THE CARBON ION SOURCE COMMISSIONING AT MEDAUSTRON

S. Myalski¹, N. Gambino¹, L. Adler¹, F. Ecker¹, A. De Franco¹, F. Farinon¹, G. Guidoboni¹,
C.Kurfürst¹, L. Penescu², M. Pivi¹, C. Schmitzer¹, I. Strasik¹, A. Wastl¹

¹EBG MedAustron, Wr. Neustadt, Austria, ²Abstract Landscapes, Montpellier, France

Abstract

MedAustron is the synchrotron-based Ion therapy center of Austria. Accelerated proton beams with energies of 62-252 MeV are used to treat patients with cancer since 2016. Carbon ion beam is currently under commissioning and will provide treatment in 2019 with energies of 120-400MeV/u [1]. The Injector features three identical ECRIS from Pan-technik, two of which are used to generate the proton and the carbon beam with an energy of 8 keV/u. The generated beam is sent to a 400keV/u RFQ and a 7MeV/u H-mode Linac. Then follows the injection in a 77 m synchrotron via a middle energy transfer line, where the energies for patient treatment are reached. The beam is sent to four irradiation rooms via a high energy transfer line, two of which are currently used for medical treatment. The medical environment of the accelerator puts strict requirements on the source performances in terms of long term stability and uptime. The extracted carbon intensity needs to be on the order of 150 μ A with maximum current fluctuations of $\pm 2.5\%$ on the continuous run. In this work we discuss the status of carbon commissioning with particular emphasis on the experimental results obtained during the ion source tuning [2].

INTRODUCTION

MedAustron Ion Therapy Center (Fig.1) is a medical facility. This creates an environment significantly different than in research facilities [3]. One source of limitation are law restrictions when using technical devices for patient treatment and procedures that the facility needs to fulfill to be certified for clinical operation. Furthermore sensitive data are processed, therefore certain standards are implemented, which affect not only the clinical part, but the company as a whole. This includes access control, available software, workflow and documentation. The other aspect is related to patients themselves. Each delay or failure directly affects people who wait for their therapy, relying on the help provided to them in a difficult situation created by a medical condition, cancer. Therefore, we continuously work to improve uptime, stability and limit even remote failure risks. This puts significant overhead on all our activities, but also motivates us to look for new ways to improve reliability of the system we use.

Although such work is not directly comparable to scientific investigations, it may provide another point of view on requirements and expectations to the systems used in

non-scientific conditions. Out of three sources we use one exclusively in the medical environment and the second one (carbon source) is just being prepared to include into the medical accelerator by optimizing source performance to required level. The goal of this paper is to present constraints, challenges, the work invested to improve the system and unique opportunities which medical environment provide us.



Figure 1. MedAustron Ion Therapy Center

MEDICAL ENVIRONMENT REQUIREMENTS

Without external limitations the most effective approach to keep beam properties stable would be occasional re-tuning of the source parameters. In our case such approach is not effective because parameters are fixed and cannot be modified without an official release process approved by the QA department.

To allow the device to be used for patient treatment it needs to go through a certification process, which takes into account potential risks for patient, service personnel, other devices as well as natural environment. This process, implemented mostly on large-scale reproducible products, affects how we are able to work with device on the level of complication of Synchrotron. MedAustron Particle Therapy Accelerator (MAPTA) consists of hundreds of devices (ion sources, various magnets, linear accelerator and beam diagnostic devices). Starting from sub-components, through components and functional units it is needed to undergo through multi-step commissioning to make it possible to certify the whole device as a medical machine. This process is required also for parameters, set points and settings. Only when both the machine setup and parameters are 'fixed', the medical verification can commence. During this process various 'failure scenarios', tests and measurements are done. In the end the clinically released set of parameters is allowed to be used for treatment.

This changes the approach to beam stability in the ion source, as even the small change in parameters does include time consuming process of releasing new medical

† szymon.myalski@ifj.edu.pl

Content from this work may be used under the terms of the CC BY 3.0 licence (© 2018). Any distribution of this work must maintain attribution to the author(s), title of the work, publisher, and DOI.

settings. Therefore long term stability, uptime and maintenance planning is of utmost importance.

MAINTENANCE PLANNING

To be able to perform the maintenance two requirements need to be fulfilled:

- Machine cannot be used to treat patients.
- Documentation need to be prepared (such as change impact analysis, change plan, and multiple protocols)

As documentation preparation can take up to a few weeks all activities need to be scheduled well in advance during the so-called service slots. Short service slots occur every 2 weeks, providing 6 hour time for service activities. Long service slots, with 48 available hours are used for bigger tasks and are scheduled every 1.5 months.

Such schedule requires to plan preventive maintenance well in advance to counteract any possible drift or change in the source parameters or failure of the components. In total 29 tasks were defined, grouped into three maintenance types: yearly, half-yearly, quarterly and additional on-demand activities. The tasks range from checks and cleaning to exchanges of o-ring seals and components.

This allow us to identify possible failures early on and plan to exchange affected components. In addition regular exchanges and cleaning keep our source in controlled conditions limiting the need to for recommissioning.

At the moment carbon source is not yet used for medical purposes. Therefore is does not undergo the same processes as proton source. Prolonged use without the major maintenance or exchanges lead to current decrease (see [4]). Carbon deposition on plasma chamber walls changes conductivity of the walls and affects plasma generation. This translates into a lower extracted current of the carbon species we use. Such a situation would not be acceptable in clinical use, therefore we need to identify such factors and introduce measures to prevent such a change. In this particular case, in addition to maintenance plan adaptations, a full source recommissioning was needed.

SOURCE STABILITY

The number of patients MedAustron can treat depends on several factors. Two important ones are beam availability (uptime) and intensity.

On one side maximum beam intensity is limited by legal regulations: taking into account that the safety systems has a certain reaction time, we are not allowed in case of component failure, to exceed a certain maximum dose to the patient. This means that we need to carefully identify and test all failure scenarios by taking preventive actions when needed. This puts a limit on our maximum extracted current.

On the other hand patient treatment is prolonged if the current drops. This can either prolong the time a patient needs to spend in the treatment room, delay treatment time or even require another visit. In addition even short violation of required beam parameters interlocks the machine, leading to a stop of treatment. Therefore, for clinical operation, we can only accept a very stable beam conditions.

As an example of such issue can be presented investigations on the regular current. Initially we were observing 30s current drops on the carbon ion source every 2 hours (Fig.2).

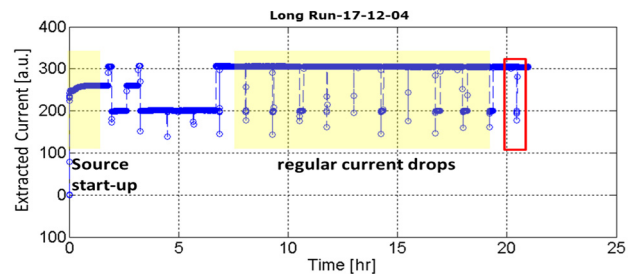


Figure 2. Regular current drops observed in Source 2 [4]. The red rectangle is showing the area presented on the next picture (Fig. 3).

In addition the two step behavior was often triggered by the drops, when beam intensity dropped for some minutes before recovering (Fig. 3). Such beam properties would be not acceptable for clinical operation.

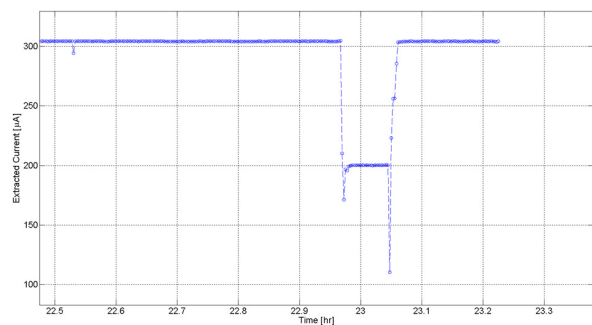


Figure 3. Two step behavior of the current. After the He flow recovers the plasma may stay in a different state leading to a lower source current until it will recover to previous current value.

Investigation of this issue allowed to find correlation to oscillations of support gas flow (He).

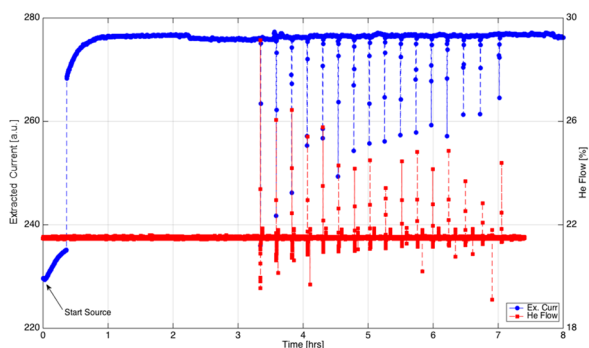


Figure 4. Current drop correlated with support gas flow oscillations

We could finally identify the root-cause of the current oscillations originating from a pressure buildup before the gas flow controller, which was triggering oscillating behavior of flow controller. By upgrading the gas panel system and by adding a pressure relieve valve we could reach a medically acceptable situation for which the beam current is stable for more than 24h (Fig.5).

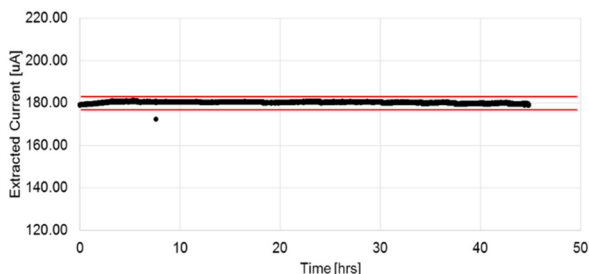


Figure 5. Beam stability after the solving the unstable gas injection.

SOURCE RECOMMISSIONING

Source performance does have an impact on the whole accelerator. We can observe this in the data collected in so-called 'beam QA' which measures beam properties each day, before patient treatment. This provide us an opportunity to observe processes such as radiation damage to detectors, seasonal/temperature performance drifts of some components, aging and effects of the source on the rest of the machine.

At the moment tools for data acquisition and data processing are being actively developed. This should make it possible to record more measurements and understand better when any component of our machine behaves in an unusual way. Due to high statistics, even a sub-millimeter beam deviation or minor decrease in the number of particles is visible. Such events need planned source recommissioning to recover the beam properties to the reference values to increase the stability.

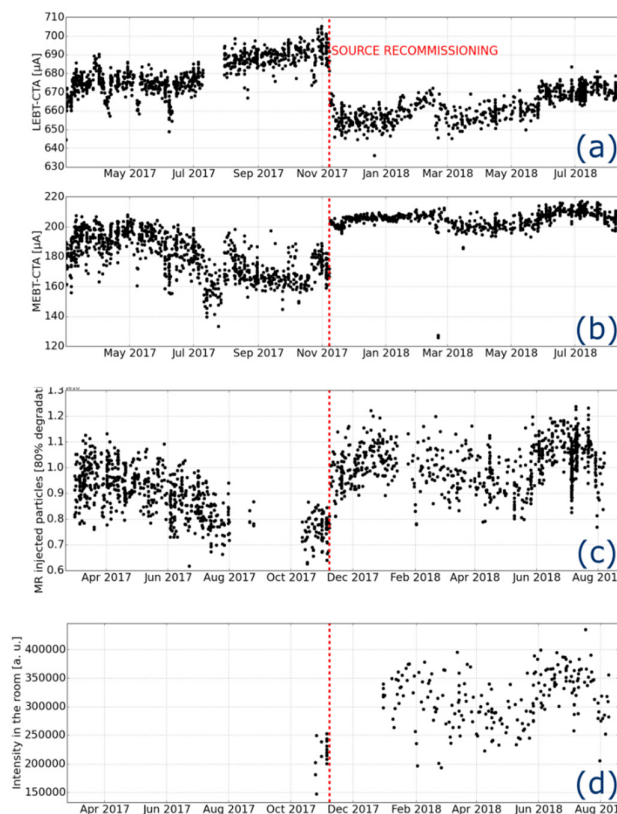


Figure 6. Source recommissioning effect on the machine: (a) Source current in low energy beamline (LEBT-CTA) is lower after the recommissioning. (b) In medium energy beam line (MEBT-CTA) we can observe both higher current and significantly better stability (c) Number of particles injected into the main ring is higher with significant shot-to-shot fluctuation (which is a goal of another investigation) (d) Intensity in the room. Before Nov-2017 it was only measured by medical groups, later it became also part of daily Accelerator Beam QA.

The results of such work are presented on the Fig. 6.

Recommissioning usually includes extensive scan of source parameters (Fig.7,8). In this particular case a set point was needed that produce a constant emittance in a wide range of extracted current and forwarded power. More information can be found in [4]. As one can observe from these figures, the emittance does not change the emittance if the RF power is varied. This makes it possible to have the RF power as a clinically modifiable parameter as discussed in detail in [5]

Content from this work may be used under the terms of the CC BY 3.0 licence (© 2018). Any distribution of this work must maintain attribution to the author(s), title of the work, publisher, and DOI.

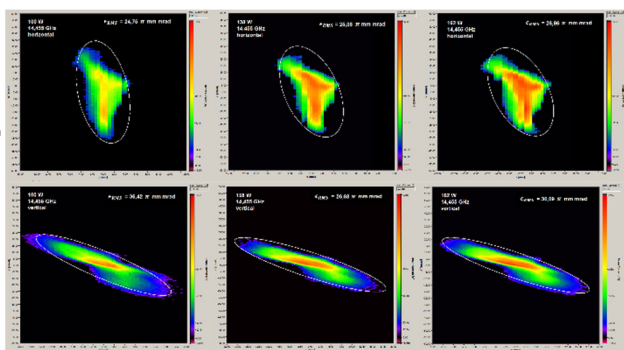


Figure 7. Measured Emittances of the carbon beam produced using a fixed resonance frequency of 14.455GHz for three different forwarded RF power values.

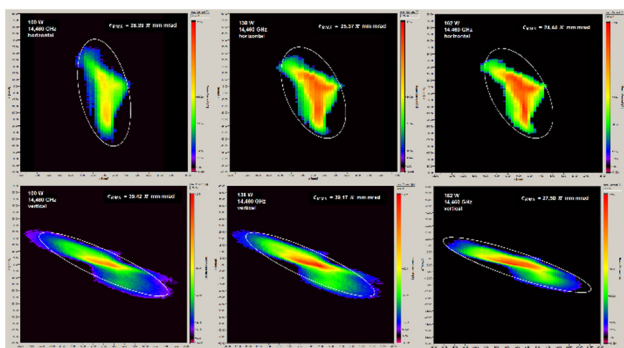


Figure 82 Measured Emittances of the carbon beam produced using a fixed resonance frequency of 14.460GHz for three different forwarded RF power values.

FUTURE PLANS

At the moment our efforts, as Accelerator Physicists in MedAustron, concentrate on the commissioning of the carbon beam for clinical use. This starts with a stable beam current and continues with finding parameters for each device which have an effect on the beam. This work should be finished in 2019, when we will start patient treatment with carbon ions. In that point in time the source 2 settings used for carbon ions, will be “frozen”.

There is one more source waiting to be commissioned in MedAustron: Source 3. It is supposed to be a backup for Source 1 (used for protons) and Source 2 (used for carbon ions). Source 3 should also enable us to test settings, measure source behavior or prepare additional beam species.

In addition, thanks to reproducible conditions we will be able to acquire a collection of data on accelerator performance. Daily measurements are done to verify beam parameters and results are stored. This allow us to analyze long-term trends and seasonal effects. With sufficient amount of data we should be able to better predict machine behavior and preventively act to keep all beam parameters constant. It should also let us do extensive analysis and cross-correlation studies. With improved tools and better measurements this could provide valuable insight on long

term stability, aging effects, reproducibility and maintenance which we want to explore.

ACKNOWLEDGEMENTS

The authors would like to acknowledge the entire MedAustron Team for support during the carbon commissioning phase.

REFERENCES

- [1] C. Schmitzer *et al.*, “Status of Carbon Commissioning of the MedAustron Therapy Accelerator”, in *Proc. 9th Int. Particle Accelerator Conf. (IPAC'18)*, Vancouver, BC, Canada, Apr. 4, pp. 457-459, doi: 10.18429/JACoW-IPAC2018-MOPML027
- [2] N. Gambino *et al.*, “Commissioning of the MedAustron Injector for Carbon Ion Treatment Beams”, in *Proc. 17th Int. Conf. on Ion Sources (ICIS'17)*, Geneva, Switzerland, Oct. 4, In press.
- [3] C. Kurfürst *et al.*, “Status of the MedAustron Beam Commissioning with Protons and Carbon Ions”, in *Proc. 9th Int. Particle Accelerator Conf. (IPAC'18)*, Vancouver, BC, Canada, Apr. 4,, pp. 665-668, doi:10.18429/JACoW-IPAC2018-TU-PAF004
- [4] N. Gambino *et al.*, “Commissioning of the MedAustron Injector for Carbon Ion Treatment Beams”, in *Proc. 17th Int. Conf. on Ion Sources (ICIS'17)*, Geneva, Switzerland, Oct. 4, In press.
- [5] Gambino *et al.*, "Impact of Ion Source stability for a medical accelerator", ECRIS 2018, *23th Int. Workshop on ECR ion sources, this proceedings*

AN IRRADIATION TEST FACILITY AT INFN-LNS: STATUS AND PERSPECTIVES

G.G. Rapisarda^{†1}, V.P. Bonanno¹, R. Catalano¹, G.A.P. Cirrone¹, G. Cosentino¹, G. Cuttone¹, D. Mascali¹, M.S. Musumeci¹, G. Petringa¹, S.M.R. Puglia¹, S. Tudisco¹, D. Rifuggiato¹.

¹INFN-Laboratori Nazionali del Sud, Catania, Italy

Abstract

In the framework of ASIF “ASI Supported Irradiation Facilities” project some beamlines available at Laboratori Nazionali del Sud - Istituto Nazionale di Fisica Nucleare (LNS-INFN) have been dedicated to irradiation tests. These beamlines have been recently upgraded in order to meet the European Space Agency specifications about radiation hardness testing of devices suitable for space applications. The Superconducting Cyclotron K800 installed at LNS can provide protons up to 80 MeV for integrated dose tests and a number of heavy ion beams for Single Event Effect studies. The beamlines are equipped with detectors that allow beam diagnostic in term of spatial uniformity, purity and energy measurements, including on-line monitoring of flux and fluence received by the device under test. Upgrades activities are now ongoing, especially to broaden up the number of available beams, both in terms of ion species and energy, to optimize the switching times from one beam to another. The paper will present an overview of the developed facility, which will take benefit of the ongoing SERSE (the superconducting ECR ion source) revamping: the new gas-box system, plasma chamber and controls system are ready to be installed within autumn 2018.

INTRODUCTION

Among the research activity carried out at at Laboratori Nazionali del Sud of the Istituto Nazionale di Fisica Nucleare (LNS - INFN) based in Catania, a part of the beam time is dedicated to irradiation tests of electronic devices and detectors as well as of cells and biological samples [1].

Irradiation activity takes advantage of a large number of ions that can be accelerated by the 15 MV Tandem Van de Graaff and by the K800 Superconducting Cyclotron (CS). In particular, this last accelerator coupled with the two high performance ECR sources operating at LNS-INFN, that is SERSE and CAESAR, can provide ion beams in a very wide range of mass, from hydrogen to lead, and energy up to 80 MeV/amu.

Two beamlines, Zero-Degree (ZD) and CATANA (Centro di AdroTerapia e Applicazioni Nucleari Avanzate) are equipped for irradiation tests. CATANA beamline is mainly used for hadron therapy purpose with proton beams [2,3], while the ZD beamline can be adapted to perform different kind of irradiation tests using various ion beams provided by the CS, as well as by the Tandem accelerator. Moreover, the ZD beamline is equipped for both in-air and in-vacuum radiation hardness testing.

Recently, in the framework of ASIF “ASI Supported Irradiation Facilities” project, these beamlines and in particular the ZD one have been upgraded in order to meet the European Space Agency (ESA) ESCC No. 25100 specifications about radiation hardness testing of devices suitable for space applications.

THE IRRADIATION FACILITY

Available beams for irradiation at LNS

According to the ASIF project requirements, a list of beams and a number of diagnostic devices have been defined and developed in order to perform irradiation with protons for integrated dose tests and with heavy ion beams for Single Event Effect (SEE) studies.

In particular, for integrated dose tests proton beams are available according to the energies and the flux shown in Table 1. If necessary, energy can be reduced by means of a stack of plastic degraders.

Table 1: Proton Beams: Energies and Flux

Energy <i>MeV/amu</i>	Flux ions cm ⁻² s ⁻¹
10 - 26 from Tandem	up to 10 ⁷
60, 80 from CS*	

SEE tests are performed by using mainly ²⁰Ne, ⁴⁰Ar, ⁸⁴Kr, ¹²⁹Xe beams at 20 MeV/amu, corresponding Linear Energy Transfer (LET) and range in silicon, calculated with SRIM2008, are reported in Table 2. The selected ions provide, at the moment, the best compromise in reducing the time required for beam change (4-8 hours) and in providing a large range of LET values. In in-air irradiation, air is used to reduce beam energy, this provides several LET points up to 60 MeV/(mg/cm²) allowing to measure the cross-section (number of events per unit of fluence) from the threshold to the saturation value.

Table 2: Ions Available For SEE Test.

Ion	Energy <i>MeV/amu</i>	LET ^{SRIM} <i>MeV/(mg/cm²)</i>	Range ^{SRIM} <i>μm</i>
²⁰ Ne	20	1.996	504.54
⁴⁰ Ar	20	6.266	356.49
⁸⁴ Kr	20	21.59	245.12
¹²⁹ Xe	20	44.05	204.46

[†] grapisarda@lns.infn.it

Content from this work may be used under the terms of the CC BY 3.0 licence (© 2018). Any distribution of this work must maintain attribution to the author(s), title of the work, publisher, and DOI.

Beam Diagnostic

Ion beams provided for irradiation test must be analysed in order to verify the beam energy and purity at the device under test (DUT) position, and to measure beam uniformity, flux and fluence.

In details, beam energy and purity are guaranteed by the design of the accelerators and beam transportation devices. Moreover, a two stages ΔE -E detector is available at the DUT position to provide a further check energy and purity. For proton and light ion beams (from $Z=1$ to $Z=8$) accurate energy measurement are accomplished through the measurement of the Bragg-peak in a water phantom. In particular, depth-dose measurements are obtained by using a Markus chamber (Mod 3002) inserted in the water phantom with a spatial resolution of 10 μm .

Regarding spatial uniformity, magnetic elements distributed along the beam line and a set of collimators with different diameters (Fig. 1) provide a beam spot size on DUT from few mm to about 2 cm, according to the user's requests, and uniformity of $\pm 10\%$ over the DUT irradiated area.

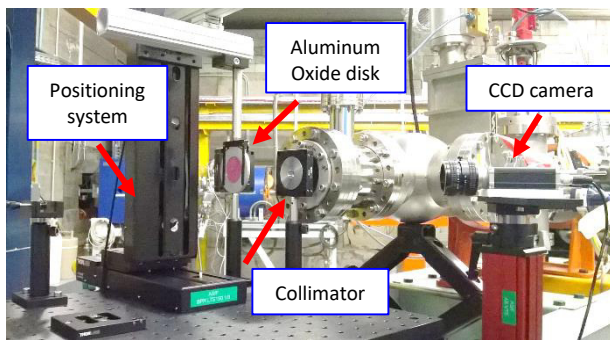


Figure 1: Experimental setup: collimator, aluminium oxide disk and CCD camera for beam profiling and positioning system for DUT placement.

Beam profile is measured acquiring, by means of a CCD camera (Fig. 1), the light emitted by an Aluminum Oxide disk (Fig. 1) when it is hit by the beam. Then, a software allows the on-line analysis of the acquired signal making possible the beam tuning in order to reach the required size and uniformity. In Fig. 2 and Fig. 3 examples of experimental transversal dose profile (with respect to the x and y axes) are shown for the proton and ^{84}Kr beams respectively. Dashed lines indicate the DUT size.

Flux and Fluence measurement are performed on-line by means of a thin plastic scintillator detector EJ-212 Scionix (50,100 μm) (Fig. 4). The thickness is selected such that the scintillator is transparent to the beam. Signal produced by scintillator are sent to a discriminator, converted in TTL standard and sent to a counter. The facility allows to measure fluxes up to 10^6 ions $\text{cm}^{-2} \text{s}^{-1}$. Beam is stopped when the required fluence is reached.

For proton irradiations the fluence can be measured using a Monitor Chamber, designed and built at LNS, allowing to measure up to 10^8 ions $\text{cm}^{-2} \text{s}^{-1}$.

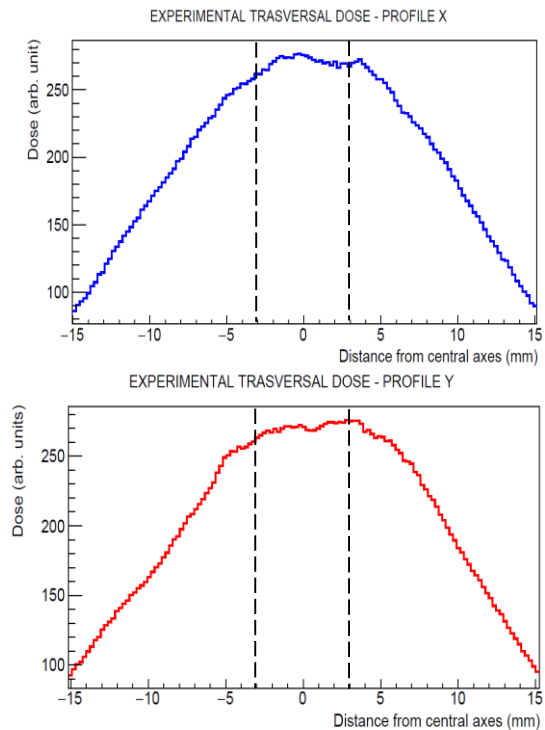


Figure 2: Experimental transversal dose profile for proton beam, with respect to the x (blue) and y (red) axes. Dashed lines delimit the DUT size where uniformity of $\pm 10\%$ is reached.

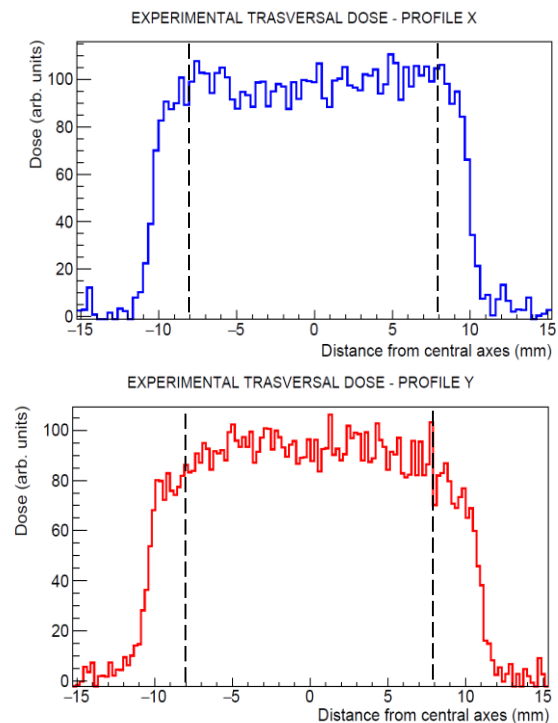


Figure 3: Experimental transversal dose profile for ^{84}Kr beam, with respect to the x (blue) and y (red) axes. Dashed lines delimit the DUT size where uniformity of $\pm 10\%$ is reached.

The output signals from all the beam diagnostic devices can be monitored from the control room during the beam setup as well as during the irradiation runs.

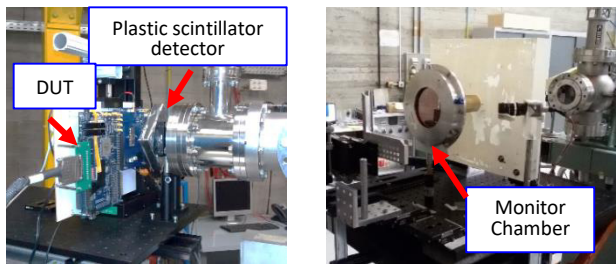


Figure 4: Experimental setup: Plastic scintillator detector and Monitor Chamber used for flux and fluence measurement for heavy ions and protons irradiation respectively. A typical board housing the DUT is also shown in the picture.

DUT Movement

The DUT can be moved along the three axes x-y-z from a remotely controlled positioning system (Fig. 1) made up of two linear motion stages allow up to 150 - 300 mm travel range, with a minimum achievable incremental movement of 0.1 μm and a bidirectional repeatability of 2 μm . Distance along z axis (corresponding to the beam axis) can also be manually changed in a wide range up to about 1.5 m. A laser distance meter allows to check the distance of the DUT from the beam exit window within an accuracy of 1 mm.

A downstream laser and a system of collimators allow the DUT alignment along the beam axis.

All the diagnostic devices are mounted on linear translation stage. In this way, according to the sequence of actions of the standard irradiation procedure, each detector can be moved and placed at the DUT position by a remote control system.

The whole remotely controlled positioning system has been design in order to provide a user-friendly system, guaranteeing high precision and repeatability in the irradiation operation.

PERFORMED IRRADIATION RUNS

From November 2017 to July 2018 five irradiation runs have been carried out at LNS. In particular, two integrated dose test have been performed using 15 MeV protons from Tandem and 60 MeV protons from CS for a total of 2 Beam Time Units (BTU). Energies have been degraded according to the user's request, and the energy values at the DUT position are reported in Table 3. Average proton flux was $10^7 \text{ ions cm}^{-2} \text{ s}^{-1}$. Three runs have been performed for SEE test using ^{40}Ar , ^{84}Kr , ^{129}Xe from CS at 20 MeV/amu, for a total of 8 BTU. Also in this case the ion energies have been re-duced (see Table 3). The average flux required during the runs was from 10^3 to $10^5 \text{ ions cm}^{-2} \text{ s}^{-1}$.

Table 3: Ions employed at LNS for irradiation test (November 2017- July 2018). For proton beams both accelerator machines have been used (*Tandem, **CS).

Ion	Energy on DUT MeV	Beam Time Units (BTU)
H	10*, 30**	2
^{40}Ar	500	8
^{84}Kr	750	
^{129}Xe	612	

At LNS beam time for irradiation test will be available three times per year, 8 BTU per trimester, for totally 24 BTU (192 hours) per year.

PERSPECTIVES AND UPGRADES

In the next future irradiation facility upgrades will be focused especially in the broadening of the beam portfolio and reducing of the switch-over times. In this sense, the irradiation facility will take particular advantage of the upgrade of the SERSE ion source. In particular, a new cryo-cooling system has been already installed, making the super-conductive magnets of the ECR source independent from the Cyclotron cryostat. Moreover, a new plasma chamber and injection system will allow operations at larger extraction voltages and RF power.

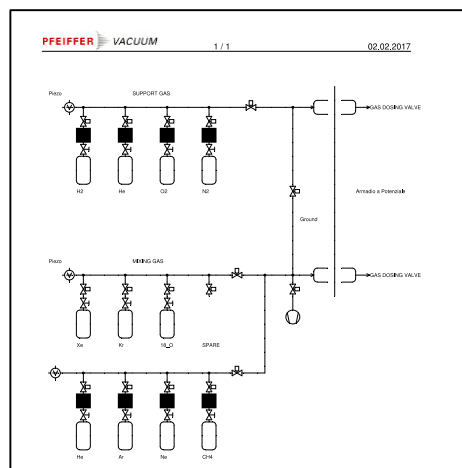


Figure 5: The new designed SERSE gas box.

A new gas box (Fig. 5) has been designed to host “on-board” of the HV platform several gaseous species or “cocktails”. This last upgrade is fundamental for the irradiation facility because will guarantee a faster switch-over of the beam species during irradiation.

In addition, the availability of the SERSE ion source couple with the CESAR one will allow the possibility to provide to the users, during the same irradiation run, both gaseous and metallic ions, with a considerable broadening of the beam availability.

REFERENCES

- [1] A. Ristic-Fira *et al.*, "The late effects of proton irradiation on cell growth, cell cycle arrest and apoptosis in a human melanoma cell line", *J Exp Clin Cancer Res.* 2001 Mar;20(1):135-43.
- [2] G.A.P. Cirrone *et al.*, "Clinical and Research Activities at the CATANA Facility of INFN-LNS: From the Conventional Hadrontherapy to the Laser-Driven Approach", *Front Oncol.* 2017; 7: 223.
- [3] G. Cuttone *et al.* "CATANA protontherapy facility: the state of art of clinical and dosimetric experience", *Eur Phys J Plus* (2011) 126:65. doi:10.1140/epjp/i2011-11065-1

PRODUCTION OF VARIOUS ION SPECIES BY GAS PULSING TECHNIQUE FOR MULTI-ION IRRADIATION AT NIRS-HEC ION SOURCE

M. Muramatsu[†], Y. Iwata, K. Mizushima, T. Inaniwa, A. Kitagawa, QST-NIRS, Chiba, Japan
 K. Takahashi, T. Shiraishi, T. Suzuki, F. Ouchi, T. Sasano, AEC, Chiba, Japan

Abstract

High-energy carbon-ion radiotherapy is being carried out at Heavy Ion Medical Accelerator in Chiba (HIMAC). Over 11000 cancer patients have been treated with carbon beams having energies of between 56-430 MeV/u since 1994. At present, multi-ion irradiation method by various ion species is being studied for optimization of LET and dose distribution. An ion source has to produce the helium, carbon, oxygen and neon at pulse by pulse for this method. Requirement currents for He²⁺, C²⁺, O³⁺ and Ne⁴⁺ are 500, 150, 230 and 300 eμA, respectively. We obtained beam current of 482, 151, and 270 eμA for He²⁺, C²⁺ and O³⁺ with mixed helium and CO₂ gases under the extraction voltage of 27 kV. Beam current of 27 and 15 eμA for C⁵⁺ and O⁷⁺ ions were also obtained in this time. He²⁺ beam include full striped ion such as C⁶⁺, N⁷⁺ and O⁸⁺. We have to increase the purity of He²⁺ beam. The gas feed system was modified for making pulsed gas by using a solenoid valve for switching different gas.

INTRODUCTION

Four ion sources produce various ions for medical use, biological and physical experiment in HIMAC at the National Institute of Radiological Sciences (NIRS). The multi-ion irradiation with dose distribution and Liner Energy Transfer (LET) optimization is being studied at NIRS [1, 2]. Helium, carbon, oxygen and neon ions are considered as ion species for multi-ion irradiation. When we use more than one ion sources, it is possible to switch different ion species easily. However, we considered the switching method with only one ion source. Ionization gases were helium, CO₂ and neon to produce He²⁺, C²⁺, O³⁺ and Ne⁴⁺ ions. These set points of intensity were 500 eμA correspond to He²⁺, 150 eμA to C²⁺, 230 eμA to O³⁺, and 300 eμA to Ne⁴⁺. At first, we tested production of the He²⁺, C²⁺ and O³⁺ with mixing the gases of helium and CO₂ at 18 GHz NIRS-HEC [3]. Next, we measured the switching time of different ion species with gas pulsing technique.

GAS MIXING EXPERIMENT

The CO₂ and helium gases were introduced at the same time to the plasma chamber for production of He²⁺, C²⁺, O³⁺ at this experiment. Dependences of the microwave power and the mirror field were measured under the same parameters. The microwave frequency was 18.0 GHz. The gas flow of helium was 0.075 cc/min. The extraction

voltage was 27.0 kV. The downstream coil current was 500 A. Figure 1 shows microwave power dependence of He²⁺, C²⁺, O³⁺. The gas flow of CO₂ and upstream coil current were 0.016 cc/min and 840 A, respectively. When microwave power was increases, He²⁺ was increased, but O³⁺, C²⁺ was decreases. The microwave power of 800 W was good for production of He²⁺. Figure 2 shows dependence of the upstream coil current. The ion source parameters were same as the microwave power dependence. The respective ions became highest when coil current was 790 A. We obtained the beam current of 482, 151, and 270 eμA for He²⁺, C²⁺ and O³⁺ with microwave power of 800 W and upstream coil current of 790 A. However, the beam current of He²⁺ is not yet reach the requirement value due to the gas mixing effect. If more neon gas is added, it is difficult to reach the requirement value of helium ion.

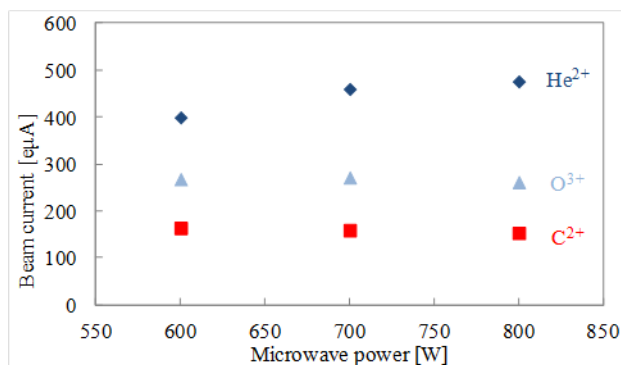


Figure 1: Dependence of microwave power.

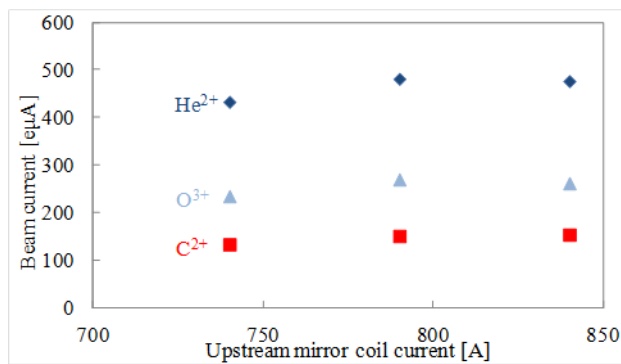


Figure 2: Dependence of upstream mirror magnetic field.

GAS SWITCHING EXPERIMENT

We try to produce He²⁺, C²⁺, O³⁺ and Ne⁴⁺ ions by using helium, CO₂ and neon gases. The high speed solenoid valve (Parker, Series 9) and controller (Parker, Iota One)

[†] muramatsu.masayuki@qst.go.jp

Content from this work may be used under the terms of the CC BY 3.0 licence (© 2018). Any distribution of this work must maintain attribution to the author(s), title of the work, publisher, and DOI.

were used for CO₂ gas line. Figure 3 shows gas piping diagram for NIRS-HEC with gas pulsing technique. The solenoid valve was set in CO₂ line. The helium and neon gases were regulated by a piezo valve (Mass Flow Control valve: MFC).

Figure 4 shows switching time of O³⁺ to He²⁺ comparison between MFC and solenoid valve. We have to wait about 10 minutes for stable beam current of He²⁺ by using MFC. There were residual CO₂ gas in the gas line and vacuum chamber. In the case of solenoid valve, wait time is about 3 minutes. Pulse width was 0.22 msec. The solenoid valve opens 120 msec before the microwave ignition. The influence of residual CO₂ gas is big to the production of He²⁺ ion. The gas pulsing method is effective in a changing ion species.

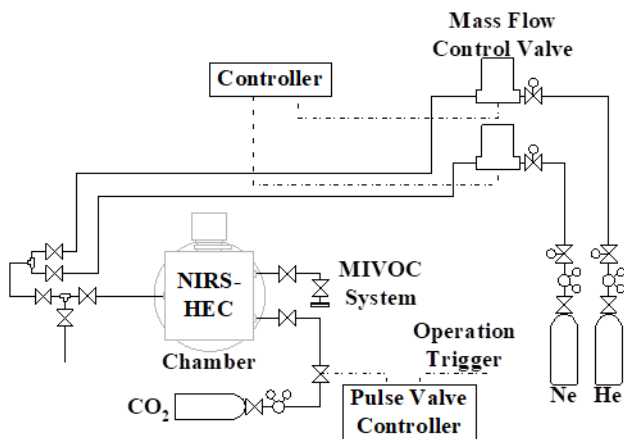


Figure 3: The diagram of gas piping with gas pulsing technique.

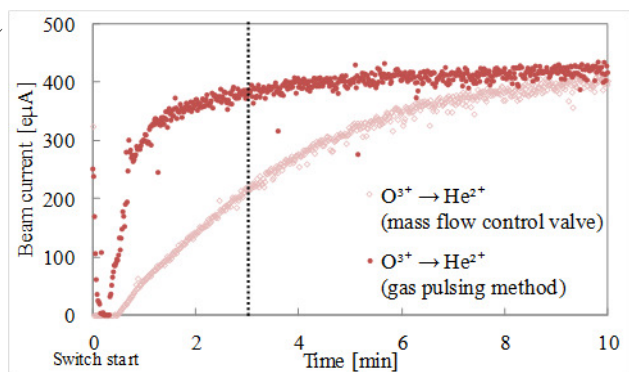


Figure 4: Reproducibility of He²⁺ at the switching of O³⁺ with mass flow control valve and gas pulsing method.

Ion Separation Experiment

Figures 5, 6, 7, 8 shows beam switching time of He²⁺, C²⁺, O³⁺ and Ne⁴⁺. From Fig. 5, switching time for stable the beam current from He²⁺ to other ion species were about 2 or 3 minutes. The helium gas was not affect for production of C²⁺, O³⁺ and Ne⁴⁺ ions. From the Fig. 6 and Fig. 7, switching time of carbon and oxygen was less than 1 minute, because, there was no change the gas. In

the switching time from carbon and oxygen to He²⁺ and Ne⁴⁺ were about 2 or 3 minutes. From Fig. 8, the switching time from Ne⁴⁺ to He²⁺, C²⁺ and O³⁺ ions were 4 or 5 minutes. There was the neon gas affect to production of helium, carbon and oxygen ions.

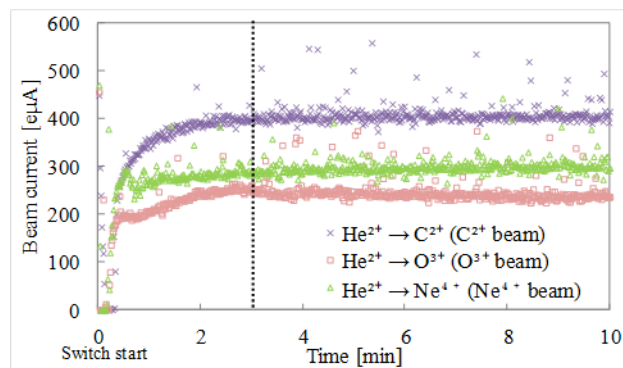


Figure 5: Switching time of C²⁺, O³⁺ and Ne⁴⁺ from He²⁺.

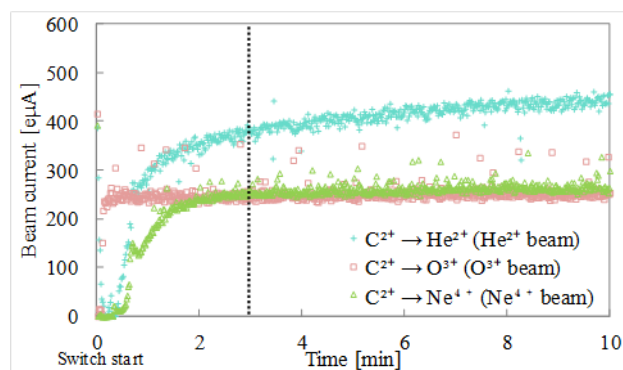


Figure 6: Switching time of He²⁺, O³⁺ and Ne⁴⁺ from C²⁺.

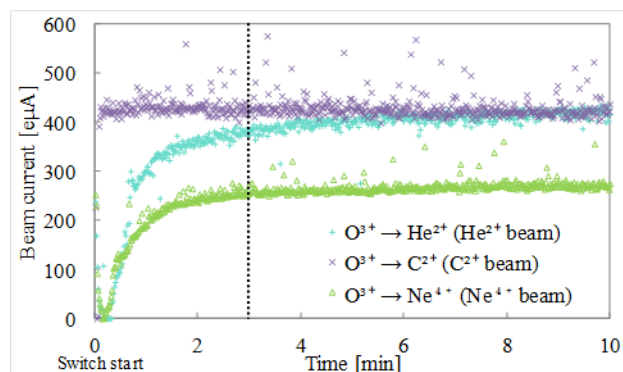


Figure 7: Switching of He²⁺, C²⁺ and Ne⁴⁺ from O³⁺.

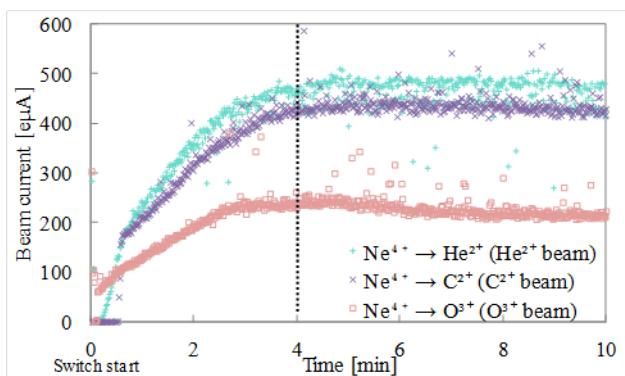


Figure 8: Switching of He^{2+} , C^{2+} and O^{3+} from Ne^{4+} .

Ion Separation Experiment

He^{2+} beam include full striped ion such as C^{6+} , N^{7+} and O^{8+} ($A/Z=2$). We checked impurity of accelerated He^{2+} beam at HIMAC injector. An ion is separated using differences in an energy loss on ion species when an ion

passes a thin foil. Figure 9 shows beam current as a function of magnetic field of bending magnet. Blue line is $A/Z=4$ beam. The energy of accelerated ions was 6 MeV/n. Thickness of Al foil was 5 μm . The NIRS-HEC produced He^+ ion using helium and CO_2 gases. He^+ beam including C^{3+} and O^{4+} is changed to He^{2+} , C^{6+} and O^{8+} by carbon foil after the LINAC. There were two peaks from He^+ beam. Left side peak consists of C^{6+} and O^{8+} ions. Right side peak is He^{2+} ion. Red line is He^{2+} beam with gas pulsing method. There was no C^{6+} and O^{8+} ions. We could optimize the condition for production of He^{2+} ion at NIRS-HEC.

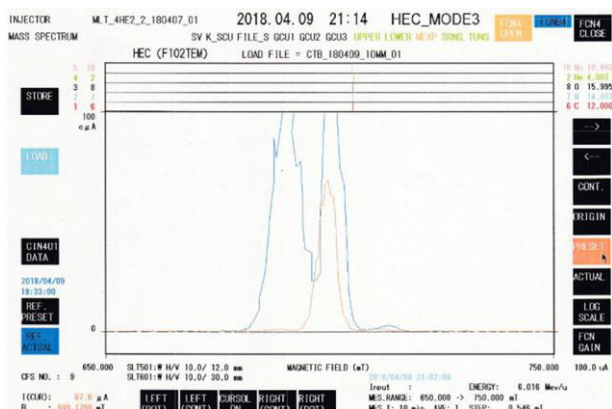


Figure 9: The beam spectrum from He^+ and He^{2+} at after the HIMAC injector.

CONCLUSION FOR THE NEXT STEP

The result of the gas mixing experiment, we obtained beam current of 482, 151, and 270 $\text{e}\mu\text{A}$ for He^{2+} , C^{2+} and O^{3+} with mixed helium and CO_2 gases. The optimal microwave power and upstream coil current were 800 W and 790 A, respectively. From the results of gas pulsing experiment, the switching time from He^{2+} , C^{2+} and O^{3+} to

other ions were 2 or 3 minutes, however, from Ne^{4+} to other were 4 or 5 minutes. We will set the solenoid valve to all of gas line.

REFERENCES

- [1] T. Inaniwa., N. Kanematsu., *Phys. Med. Biol.*, vol. 61 pp. 542–550, (2016).
- [2] T. Inaniwa *et al.*, *Phys. Med. Biol.* vol. 62, p. 5180 (2017).
- [3] A. Kitagawa *et al.*, *Rev. Sci. Instrum.* vol. 69, p. 674 (1998).

Content from this work may be used under the terms of the CC BY 3.0 licence (© 2018). Any distribution of this work must maintain attribution to the author(s), title of the work, publisher, and DOI.

COMMISSIONING OF THE PROTON-LINAC ECR SOURCE FOR FAIR

J. Fils[†], R. Berezov, R. Hollinger, GSI Helmholtzzentrum für Schwerionenforschung GmbH, 64291 Darmstadt, Germany

B. Bolzon, N. Chauvin, O. Delferrière, O. Tuske, Y. Gauthier, Commissariat à l’Energie Atomique et aux Energies Alternatives (CEA), IRFU, 91191 Gif-sur-Yvette, France

Abstract

The Facility for Antiproton and Ion Research (FAIR) presently built in Darmstadt, Germany, will be dedicated to physics of unstable nuclei and antiprotons. The antiproton program at FAIR needs for various experiments the delivery of 7×10^{10} pbar/h beams. Consequently, the acceleration chain composed of a proton-Linac and two synchrotrons, SIS 18 and SIS 100 has to deliver 2×10^{16} protons [1]. To this purpose, a 75 mA/ 68 MeV proton-Linac (p-Linac) is under construction. Its injector is composed of an Electron Cyclotron Resonance (ECR) ion source, a Low Energy Beam Transport (LEBT) line, a 3 MeV Radio-Frequency Quadrupole (RFQ) and a Drift Transport Line (DTL) using Cross-bar H-mode cavities (CH). The CEA/Saclay is in charge, in the framework of a French-German collaboration, of designing, constructing and commissioning the proton-Linac injector composed of both the ECR proton source and the LEBT with dedicated diagnostics [2]. The on-axis species repartition of the proton beam is measured with a Wien Filter (WF), and the 2D-emittance with an Allison Scanner (AS) [3]. The targeted specifications are a proton beam current of 100 mA for an energy of 95 keV at the entrance of the RFQ within an emittance of 0.3π mm.mrad (rms norm). We present in this paper the latest results obtained with the injector in view of commissioning.

PROTON LINAC

At FAIR, the primary proton beam for the antiproton production is delivered by the p-Linac at an energy of 68 MeV and a repetition rate of 4 Hz (Fig. 1). Its main parameters are listed in Table 1.

Table 1: Proton Linac Parameters

Parameter	Value
Beam Energy	68 MeV
Maximum design current	70 mA
Current at SIS18-injection	35 mA
Proton per pulse	$7.9 \cdot 10^{12}$
Beam pulse length	36 μ s
RF-frequency	325.224 MHz
Repetition rate	≤ 4 Hz
Emittance (norm)	≤ 2.1 mm.mrad
Momentum spread (tot., norm)	$\leq \pm 10^{-3}$
Overall length	43 m

[†] j.fils@gsi.de



Figure 1: Schematic of the future p-Linac.

The proton injector being commissioned at CEA/Saclay is composed of the proton source and the LEBT until the entrance of the RFQ (Fig. 2).

PROTON INJECTOR

The proton source, acceleration column and LEBT presently under construction and test at CEA/Saclay has been designed according to the SILHI model and the IPHI deuteron injector.

General Layout

The injector has to deliver a proton-beam at 95 keV with a proton beam intensity of 100 mA at the entrance of the RFQ. All general requirements are listed in Table 2. Its general layout is represented in Fig. 1. Different parts are described more precisely in following sections.

Table 2: Proton Injector Parameters

Parameter	Value
Beam Energy	95 keV
Beam Intensity	100 mA (H^+)
Repetition rate	4 Hz
Energy spread	< 60 eV
Final emittance	$\leq 0.33 \pi$ mm.mrad
Pulse length	$\geq 36 \mu$ s
α Twiss parameter	$0.27 \leq \alpha \leq 0.59$ mm/ π .mrad
β Twiss parameter	$0.037 \leq \beta \leq 0.046$ mm/ π .mrad

Ion Source and Extraction System

Its design was taken from the SILHI high intensity light ion source [4] developed at CEA. The cylindrical plasma chamber, 90 mm wide and 100 mm long, is put on a 100 kV-platform in a Faraday cage. H_2 gas is injected through a capillary. Its flow is tuned by a mass flow controller. To occur, the ECR condition needs the presence of an axial magnetic field produced by two coils, independently power-supplied and tuned in order to reach a constant on-axis magnetic field value of 0.875 T, possibly as close as possible to the ridge output concentrating the 2.45 GHz RF-wave from the magnetron. Electron density is increased thanks to two boron nitride disks inside the plasma chamber.

Content from this work may be used under the terms of the CC BY 3.0 licence (© 2018). Any distribution of this work must maintain attribution to the author(s), title of the work, publisher, and DOI.

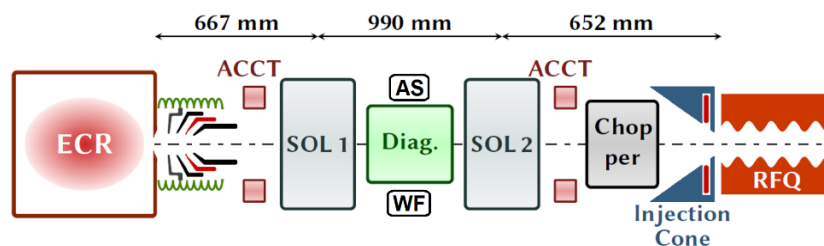


Figure 2: Layout of the proton injector including the ECR proton source, the acceleration column, the solenoids 1 & 2, the diagnostic chamber, two ACCT devices, the chopper chamber and the injection cone before the RFQ line.

The repetition rate is set up to 4 Hz and is operated by the pulsed injection of the RF-signal. The extracted beam is set longer than the desired one at the RFQ entrance: the chopper will cut off rising and falling beam profile parts.

The extraction system is composed of 5 electrodes. Due to the low duty cycle, they are not water-cooled:

- The plasma electrode has a $\varnothing 9$ -mm aperture hole.
- The intermediary or *puller* electrode is tuned downwards relatively to the 95 kV-platform. As we see later, its value influences the beam parameters.
- The 3rd and 5th are put to the earth potential.
- The 4th, called *repeller*, is set to a negative value to hinder electrons to go upstream into the plasma chamber and consequently to ensure a space charged compensation of the beam.

LEBT and RFQ-injection

Imaging and propagation are assured by two solenoids on the model of IFMIF setup, independently tuned up to 450 A [5]. Two magnetic steerers are integrated into both solenoids to realign in both directions the proton beam. The diagnostic chamber is placed between them.

Deviation plates forming a *chopper* will cut the proton beam down to a minimum of 36 μ s with sharp edges. It is coupled to a tungsten cone that intercepts cut proton beam as well as remaining off-axis undesired species. A negatively charged *repeller* plate is located before the RFQ-entrance to block upstream electrons.

All measurements shown in this article were performed with 5 ms-long pulses, which is the upper duration limit of expected proton beams.

Beam Diagnostics

Two Alternating-Current Current Transformers (ACCT) before and behind 1st and 2nd solenoids measure the proton beam time profile and intensity. This last value is compared, only for the commissioning phase, to the current measured with Faraday cup at final beam stop.

On diagnostic chamber are installed:

- a Wien Filter to measure the species fraction
- an Allison Scanner, either vertically or horizontally set up, to measure emittance
- a Secondary Electron emission grid (SEM-grid) will also be installed at GSI.
- also installed at GSI a diamond-shaped slit to reduce the proton beam size.

MEASUREMENTS & RESULTS

As defined in [6], the commissioning at Saclay is divided in 3 different phases. We will present here results for:

- Phase 1: beam intensity, emittance and species proportions from the source directly measured behind the acceleration column with a $\varnothing 9$ -mm aperture.
- Phase 2: same diagnostics are put in the diagnostic chamber directly behind the 1st solenoid.

At the Source Output

H⁺ proportion is represented in Fig. 3. It was measured with WF for different total beam current and different magnetic configuration given by coils intensity. It is given here with couple currents B1 / B2 in A.

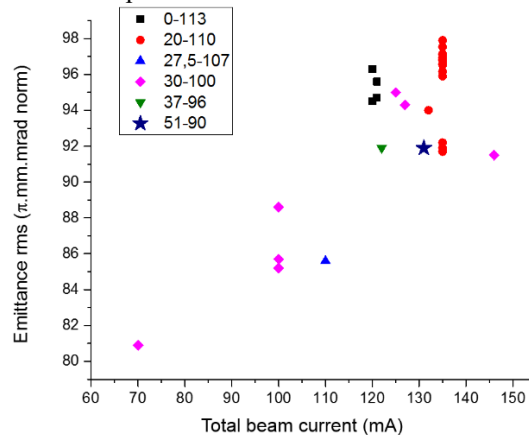


Figure 3: proportion of H⁺ in extracted beam for different coil configurations vs. total beam current

Even if measurement noise is present, yielding $\pm 4\%$ for the (20/110) configuration, a strong trend can be extracted: the higher the total beam current, the higher the proportion of H⁺. A maximum total extracted current of 147 mA was obtained in the (30/100) configuration.

At the RFQ entrance, the normalized *rms* emittance has to be lower than 0.33 π mm.mrad (straight line in Fig. 4). We measured it at source exit for different coil configurations and different total output current by varying the puller voltage. Plots of a series (same magnetic configuration and total beam intensity) are included in a same curve. The dotted line binding plots for the 20/110 case indicates that measured values were data-processed to compensate the acquisition resolution discrepancies with

Content from this work may be used under the terms of the CC BY 3.0 licence (© 2018). Any distribution of this work must maintain attribution to the author(s), title of the work, publisher, and DOI.

the value represented encircled. This last one was measured with the same resolution as the other data bound with solid lines.

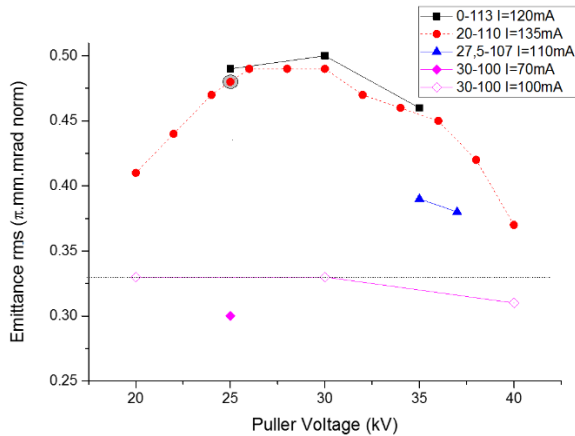


Figure 4: Emittance vs. puller voltage for different coils configurations and total beam current.

Firstly, the higher the total intensity beam is, the higher the emittance, which can be explained by space charge. Secondly, the emittance reaches a maximum around 29 kV of puller voltage. This was already observed on IFMIF [7]. It seems that the puller voltage for these scan values influences the emittance measurement.

Behind 1st Solenoid

Emittance measurements were performed in the diagnostic chamber by varying the current value of 1st solenoid for two different beam total current, 130 mA and 90 mA (Fig. 5). The AS was put horizontally and vertically to check the hypothesis of the beam rotation symmetry.

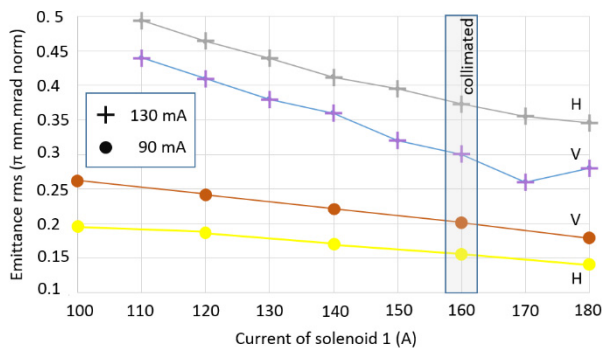


Figure 5: Vertical and Horizontal emittances vs. solenoid current for different total beam current

The tendency to reduce the emittance by increasing the convergence effect of 1st solenoid observed, as well as by reducing the total beam intensity, possibly due to space charge compensation. On the other hand, differences between vertical (V) and horizontal (H) emittances are less easy to interpret: the upper values H or V are not the same according to the total beam current. The ideal would be to dispose of two perpendiculars AS in the diagnostic chamber to compare both without the necessity to open the beam line between horizontal and vertical measurements which modify the measurement conditions.

We analysed the influence of the puller voltage value on the emittance (Fig. 6) in case of a parallel beam. The same tendency occurs as in (Fig. 4): the puller acts as a kind of *condenser* on the beam without changing focusing as shows the inserted emittance figure for 11 kV voltage. Measurement errors should be longer investigated.

Finally, we compared measurement of H⁺ proportion obtained with two methods, one with WF, the other one by analysing the emittance figures with a software developed at CEA [8].

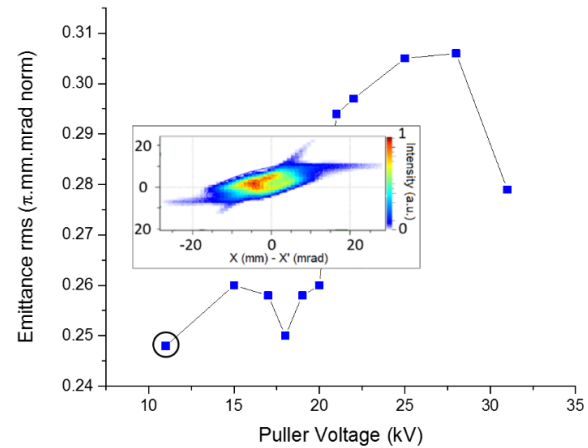


Figure 6: Emittance vs. puller voltage for a total beam current of 90 mA. The insert is the figure for encircled data.

H⁺ proportion is measured for a total beam current of 90 mA. The WF gives 93.5% while the software analysis gives 84.9%. It may be that WF only see the beam centre whereas the software takes into account the whole beam. A same discrepancy was already observed with spectroscopic measurements [6].

Conclusions

First results of emittance value, proton energy and beam current just at the source exit and behind the 1st solenoid show that targeted parameters at the RFQ input are reachable. It has to be confirmed by direct measurements behind the 2nd solenoid in a next step.

REFERENCES

- [1] L. Groening *et al.*, *Proceedings of LINAC2012*, THPB034
- [2] R. Berezov *et al.*, *Rev. Sci. Instrum.* vol. 87, p. 02A705 (2018)
- [3] C. Ullmann *et al.*, *Proceedings of IPAC2014*, TUPRO043
- [4] R. Hollinger *et al.*, *Proceedings of LINAC2006*, TU3001
- [5] N. Chauvin *et al.*, *Proceedings of LINAC2014*, THPP015
- [6] O. Tuske *et al.*, *Rev. Sci. Instrum.* vol. 89, p. 052303 (2018)
- [7] R. Gobin *et al.*, *Rev. Sci. Instrum.* vol. 87, p. 02A726 (2016)
- [8] B. Bolzon *et al.*, *Fusion Engineering and Design* (2018), doi: 10.1016/j.fusengdes.2018.04.128

PROGRESSES IN THE INSTALLATION OF THE SPES-CHARGE BREEDER BEAM LINE

A. Galatà*, C. Roncolato, G. Bisoffi, P. Francescon, L. Bellan, J. Bermudez, D. Bortolato, M. Comunian, A. Conte, M. De Lazzari, F. Gelain, D. Marcato, M. Miglioranza, M.F. Moisisio, E. Munaron, S. Pavinato, D. Pedretti, A. Pisent, M. Rossignoli, M. Roetta, G. Savarese, INFN-Laboratori Nazionali di Legnaro, Legnaro (Padova), Italy,
M. Bellato, INFN-Sez. di Padova, Padova, Italy,
V. Andreev, ITEP, Moscow, Russian Federation

Abstract

Since fall 2017, the ADIGE (Acceleratore Di Ioni a Grande carica Esotici) injector of the SPES (Selective Production of Exotic Species) project entered the installation phase. The injector includes an Electron Cyclotron Resonance (ECR)-based Charge Breeder (SPES-CB) and its complete beam line, as well as a newly designed RFQ, to allow the post-acceleration of the radioactive ions produced in the so-called target-ion source-system. The injector has different peculiarities, deriving from particular needs of SPES: a complete electrostatic beam line equipped with a 1+ source for test purposes, and a unique Medium Resolution Mass Spectrometer (MRMS, $R \sim 1/1000$), mounted downstream the SPES-CB, to clean the radioactive beam from the contaminants induced by the breeding stage. This contribution reports about the status of the installation of the injector, describing the various technical solution adopted, and giving a realistic planning for the commission and following operation of its main parts.

INTRODUCTION

SPES [1] (Selective Production of Exotic Species) is an INFN project with the aim at developing an Isotop Separation On Line (ISOL) Radioactive Ion Beam (RIB) facility as an intermediate step toward EURISOL. The SPES project is under construction at the INFN-Laboratori Nazionali di Legnaro (LNL): the main goal is the production and post-acceleration of exotic beams to perform forefront research in nuclear physics by studying nuclei far from stability. The project is concentrating on the production of neutron-rich radioactive nuclei with a mass range $A=80-160$: they are fission fragments that will be produced by delivering a proton beam on a UC_x target developed at LNL. The proton driver will be a commercial cyclotron [2] with a variable energy (30–70 MeV) and a maximum current of 0.75 mA (upgradeable to 1.5 mA), with the possibility to split the beam on two exit ports. The accelerator was installed in a new dedicated building in 2016 and the factory acceptance tests were successfully carried out in 2017. The radioactive species produced will be extracted as a 1+ beam from dedicated sources [3], cooled in a RFQ-cooler [4] and purified from the isobars contaminants through a High Resolution Mass Spectrometer (HRMS) presently in the design phase.

* alessio.galata@lnl.infn.it

In order to allow post-acceleration with the LNL booster ALPI (up to 10 MeV/A for $A/q = 7$), the project will employ an Electron Cyclotron Resonance (ECR)-based charge breeding technique [5]: the Charge Breeder will be equipped with a complete test bench totally integrated with the SPES beam line. This part of the post-accelerator, together with the newly designed RFQ [6], composes the so-called ADIGE (Acceleratore Di Ioni a Grande carica Esotici) injector [7], whose layout is shown in Fig. 1. Since fall 2017, the injector entered the installation phase: this paper will describe its main components, the various technical solutions adopted, and will report on the status of the installation, giving a realistic planning for the commissioning and following operation of its main parts.

BEAM LINE DESCRIPTION

The ADIGE injector consists of a 1+ beam line producing stable beams for test purposes, and a N+ beam line to deliver the beams extracted from the Charge Breeder to the post-acceleration. Those parts will be described in separated sub-sections.

The 1+ Beam Line

Depending on the particular element to be charge bred, two kind of sources will be employed (alternatively), sharing the same vacuum chamber: a surface ionization source (SIS) or a plasma ionization source (PIS). Those sources are simplified copies of the ones which will be installed in the target-ion source-system of SPES and are described elsewhere [3]: the ionization mechanisms employed will allow the production of beams from most of the elements of the periodic table, except for the refractory metals. The stable 1+ ions produced will be extracted by applying a positive high voltage between 20 keV and 40 keV to the common vessel through a 3 mm hole, and placing a movable electrode at ground potential, in order to optimize the electric field depending on the extracted intensity. The beam will pass through two couples of X-Y electrostatic steerers (± 2 kV max) that will correct possible beam misalignments, and will then be focused by an electrostatic quadrupoles triplet (5 kV max, total length 848 mm) to the first beam instrumentation box, equipped with a faraday cup, two beam profile monitors (one for each transversal plane) and selection slits. Such box is mounted at the object point of the 1+ selection dipole: it is a 90° , 750 mm radius magnet, with entrance

Content from this work may be used under the terms of the CC BY 3.0 licence (© 2018). Any distribution of this work must maintain attribution to the author(s), title of the work, publisher, and DOI.

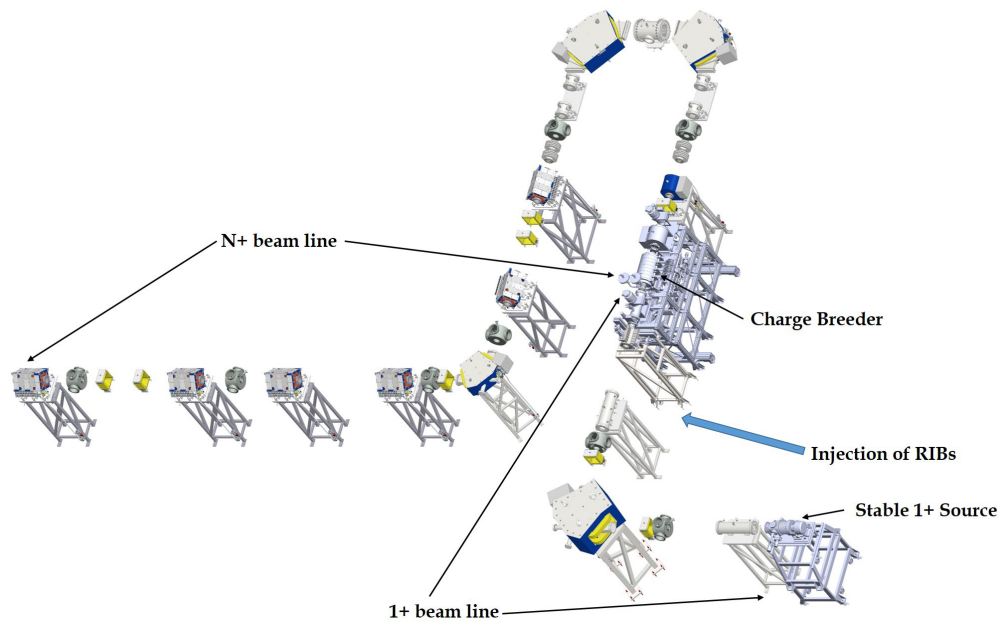


Figure 1: Prospective view of the ADIGE injector with its 1+ beam line (from the 1+ Source to the Charge Breeder) and N+ beam line (from the Charge Breeder on). The position where the 1+ beam line for RIBs will be connected is also shown.

and exit angles of 26.6° and a pole gap of 110 mm. Another beam instrumentation box is placed at the image point of the dipole, and a further electrostatic quadrupoles triplet will focus the beam to the emittance measurement device: it consists of two slit-grid systems, with a spatial resolution of 0.2 mm and minimum and maximum measurable divergence of, respectively, 1.8 and 68 mrad. Finally, the 1+ beam will be injected into the Charge Breeder through a double Einzel Lens (20 kV max). Along the beam line, magnetic steers will give the possibility to correct possible misalignments.

The N+ Beam Line

Charge breeding at SPES will be based on the ECR technique: in particular, the model adopted (SPES-CB) derives directly from the PHOENIX Charge Breeder installed at the Laboratoire de Physique et de Cosmologie [8]. The SPES-CB was delivered to LNL at the end of 2015, after successful acceptance tests carried out between March and April [5]. Highly charged ion beams in the range $4 \leq A/q \leq 7$ will be extracted from this device through a three electrodes extraction system designed at LNL [9], and initially focused by two solenoids (effective length 325 mm, maximum field $B=1.5$ T). It is well known that the breeding stage can introduce contaminants in the extracted beam, coming from two main sources: impurities present in the gas fed into the plasma chamber (normally oxygen), or deriving from the outgassing of the surfaces exposed to vacuum, and the release of particles from the materials constituting the vacuum chamber due to their interaction with the plasma. To face with the first problem, special attention was paid to the surface treatments, in particular of the stainless steel plasma chamber and the iron plug at extraction (ARMCO) [5]. For

the second one, a Medium Resolution Mass Spectrometer (MRMS) was designed with an expected resolving power of $R=\Delta(M/q)/(M/q)=1/1000$ and will be installed downstream the charge breeder: a prospective view is shown in Fig. 2. Its main elements are: four electrostatic quadrupoles (EQ in Fig. 2, 12 kV max), an electrostatic multipole up to 12° pole order (MUL in Fig. 2, 3 kV max), and two bending dipoles (BD in Fig. 2, radius 750 mm, edge angles 33.35° , field homogeneity $\Delta B/B=10^{-4}$); selection slits are foreseen at the object and image points of the spectrometer. To compensate the larger part of the sextupole aberration, the edges of the dipoles were designed with a curvature of 1474 mm and 828 mm at, respectively, the entrance and the exit of the spectrometer: to ensure the desired resolution, it will be mounted on a -150 kV high voltage platform, connected to the beam line through two accelerating columns (ACC in Fig. 2), in order to reach a beam energy of 23 keV/A. An analysis of the expected performances of MRMS was carried out supposing a gaussian shape of all the transported beams, and considering all possible contaminants induced by the breeding stage both from gaseous sources (gas fed, outgassing) and from the surfaces-plasma interaction (AISI 316L for the plasma chamber, AU4G for the extraction electrode), i.e.: C, N, O, Mg, Al, Si, P, S, Ar, Cr, Fe, Mn, Ni, Co, Cu, Zn and Mo; all the isotopes of the considered elements were taken into account. The parameters considered in the analysis are: the dispersion D of the spectrometer ($D=8000$ for the MRMS), the distance d between the peaks of the nominal beam and the contaminants and the slits aperture s ; this last two parameters are expressed in units of σ , the width of the gaussian peaks. Instead of considering two beams with different A/q ratios, we considered the same beam (in our

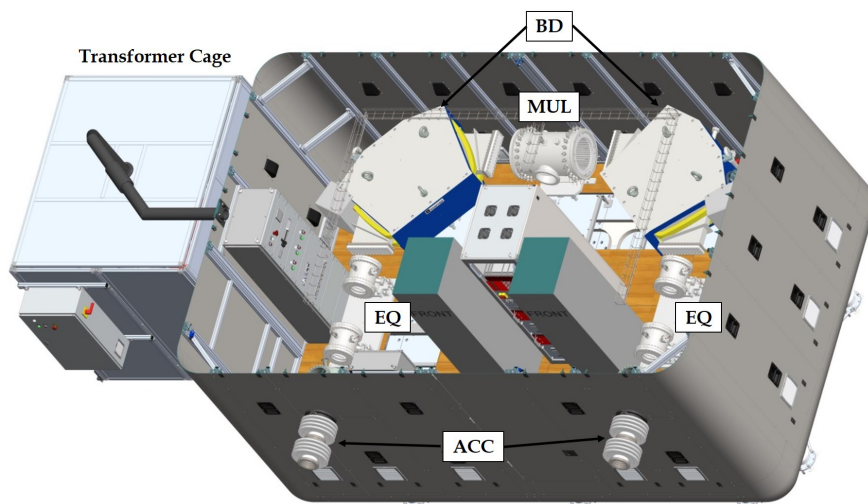


Figure 2: Prospective view of the Medium Resolution Mass Spectrometer installed on its high voltage platform: it consists of four electrostatic quadrupoles (EQ), an electrostatic multipole (MUL) and two bending dipoles (BD). The platform is connected to the rest of the beam line through two accelerating columns (ACC).

case the RIB $^{132}\text{Sn}^{19+}$), one with the nominal momentum p (nominal beam) and the second with a momentum $p+\Delta p$ (non-nominal beam): a separation $\Delta(M/q)/(M/q)=1/1000$ is, in fact, equivalent to a relative difference in momentum $\Delta p/p=1/2000$. Considering this value for $\Delta p/p$ and the value of the dispersion D , the MRMS should be able to separate two peaks at $d=4\sigma$. Clearly, if the two peaks were "delta-Dirac-shaped", the contamination would be 0% for any value of $d\neq 0$, but the gaussian shape changes this scenario, because the tail of the distribution of the non-nominal beam can contaminate the nominal one: this picture is made clearer by looking at Fig. 3, showing two gaussian peaks with the same amplitude, separated by a distance $d=2\sigma$ and with the slits aperture $s=2\sigma$. In this case the spectrometer would keep

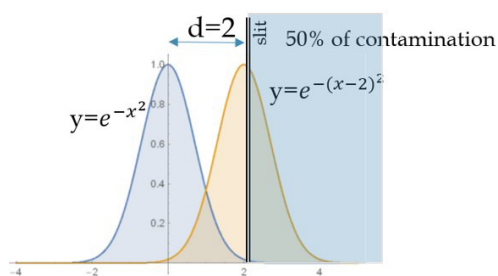


Figure 3: Contamination of the nominal beam (in blue) by the non-nominal one (in yellow) for a separation $d=2\sigma$ and a slits aperture $s=2\sigma$.

the 95% of the nominal beam, but it would be contaminated by the 50% of the non-nominal one. Defining the relative amplitude $A=I_{non-nom}/I_{nom}$ between the non-nominal and the nominal beam, Fig. 4 shows the expected contamination level as a function of the relative amplitude for different values of d , and for a slits aperture $s=d/2$. It has to be observed that, for example, for $d=4$ (the case of the MRMS), even if the evaluation foresees a contamination level of 20% for a

relative amplitude $A=10^2$, the numerical simulations carried out with the TraceWin gave a level of 10% instead; this is due to the fact that the real beam shape is not exactly gaussian. In order to be conservative, the simulations considered beams with an energy spread $\Delta E=15$ eV and a normalized emittance $\epsilon=0.1 \pi$ mm mrad, about twice the one measured during the acceptance tests [5]. It is interesting to see the effect of the

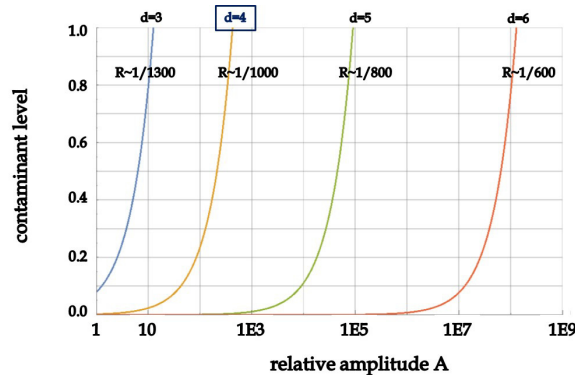


Figure 4: Expected contamination as a function of the relative amplitude $A=I_{non-nom}/I_{nom}$ between the non-nominal and the nominal beam for different values of d and $s=d/2$; the MRMS corresponds to $d=4$.

slits aperture on the contamination for a given value of d : Fig. 5 shows the contamination level as a function of the relative amplitude, for $d=4$ and different slits aperture. It can be seen that, by reducing the slits aperture to $s=1.3$, the contamination level can be kept below 10% even for a relative amplitude $A=10^3$, at the expenses of the 20% of the nominal beam. Further considerations revealed that, increasing the separation to $d=5$ (equivalent to consider a slightly worse resolution $\Delta(M/q)/(M/q)=1/800$), for a slits aperture $s=2$ (95% of the nominal beam kept) a non-nominal beam such that $A=10^3$ would be totally removed, while for $A=10^4$ the

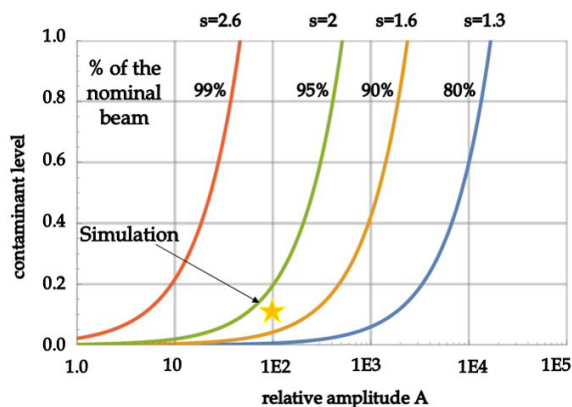


Figure 5: Expected contamination as a function of the relative amplitude $A=I_{non-nom}/I_{nom}$ between the non-nominal and the nominal beam for different values of s and $d=4$. Simulations gave better results compared to the estimation made considering the gaussian shape of the two peaks.

contamination would be 10%. By reducing further s to 1.6 (90% of the nominal beam kept), the contamination would be 0% for $A=10^4$ and only 10% for $A=10^5$. Following those last considerations, and taking into account all the possible contaminants mentioned above, table 1 lists the charge states of typical RIBs expected at SPES that could be accelerated with a very limited contamination.

Table 1: Charge states of typical RIBs expected at SPES that should be free from contamination after passing through the MRMS.

Species	Charge States
^{94}Rb	15+,16+,21+
^{130}Sn	19+,29+
^{132}Sn	19+,21+,23+
^{134}Te	27+,31+
^{133}Cs	20+,22+,23+,26+,28+,30+,31+

Finally, the beam coming out from the MRMS will be focused by magnetic quadrupoles triplets (gradient 1.97 T/m and effective length 237 mm for each quadrupole) and characterized in a beam instrumentation box equipped with an emittance measurement device of the Allison scanner type (not shown in Fig. 1). A further 90° dipole (radius 500 mm, edge angles 26.6°) will bend the beam towards the injection line into the new RFQ (horizontal line in Fig. 1). More or less 30% of the future users at SPES will request beams bunched at 5 MHz instead of the usual 80 MHz of the LNL accelerating structures: to satisfy those requests, two low energy bunchers (LEB) will be installed in the final part of the ADIGE beam line. The bunchers consists of a two harmonic bunching system, known as “double drift method of bunching”, totally equivalent to a triple harmonics system and with a bunching efficiency of at least 60-65%. Two double gap resonant structures will be installed in the beam line and separated by a distance of about 1m: the first buncher

will operate at 5 MHz, while the second one at 10 MHz. The gap voltage is about 1 kV for the two resonators and both will be equipped with movable tuners for a fine tuning of the resonant frequency. To simplify as much as possible the manufacturing of the two resonators, they share most of the components, except for the drift tubes and the spirals: table 2 summarize their technical specifications.

Table 2: Technical specifications of the two harmonic bunching system

	5 MHz	10 MHz
Central tube length [mm]	102	50
Gap length [mm]	2	2
Tube outer radius [mm]	68	68
β_{opt}	0.003515	0.003515
Resonant frequency [Mhz]	5	10
Max surface E-field [Mv/m]	0.296	0.350
Q	900	780

STATUS AND FUTURE PLANS

All optical elements and power supplies of the ADIGE beam line were delivered by the end of 2017 and installed in the III experimental hall of LNL in the first months of 2018 (except for those of the MRMS), together with the 1+ source and the Charge Breeder. Then, the work for the preparation of the electrical and water cooling plants started in March: the main electrical board feeding electricity to the power supplies of the coils and some ancillary systems of the Charge Breeder and to the insulating transformer of the 1+ source was installed and connected. The rest of the power supplies were connected to busways already present in the area, while other electrical boards will be delivered, installed and cabled within Autumn 2018. All the power supplies necessary to operate the 1+ source are referred to its high voltage: a rack containing all those devices is installed on a small high voltage platform designed at LNL and already put in its final position. For safety reasons, this area is shielded by a Faraday cage designed at LNL and constructed by an external company: the access to this area will be managed by a PLE safety level system, designed at LNL and validated by the PILZ company (in charge of the safety system of different parts of SPES); its main components were already mounted. The water cooling system is divided in branches connected to groups of utilities: each branch is equipped with pneumatic valves at the main inlet and manual valves at the inlet and outlet of each utility, together with flow and temperature sensors. Oxygen, conductivity, pH and pressure sensors were installed and will monitor continuously the status of the cooling water. The main cooling circuit of the 3rd experimental hall is a closed circuit with very low conductivity water ($\sim 0.2 \mu\text{S}/\text{cm}$) and a maximum allowed pressure drop of 4-5 bar, and is compliant with almost all the devices installed: the only exceptions are the cooling of the 1+ source (two separated circuits), the plasma cham-

ber of the Charge Breeder and its coils (necessary pressure drop $\Delta p=10$ bar). For those utilities, a special cooling skid was designed in collaboration with the Technical Division of the LNL and already installed. The skid consists of a pump, raising the water pressure to the value necessary for the coils circuit, followed by two branches equipped with manual and pneumatic valves: each branch is then split in two sub-branches, two for the 1+ source, one for the plasma chamber of the Charge Breeder and the other for its coils. In those sub-branches, where the very high pressure is not necessary, pressure regulators will lower it to usable values. All the utilities were connected to the main manifold and first tests of the circuits are expected within September 2018.

All the beam instrumentation boxes and the emittance measurements device of the 1+ beam line are already in their final position: the vacuum system of this part of the line is installed, while the installation of the vacuum tubes is almost completed. Leak tests on the already available parts of the beam line gave positive results. The other beam instrumentation boxes are in the construction phase and should be available by the end of 2018: their installation will start at the beginning of 2019, followed by the installation of the vacuum system of the N+ beam line. The construction of the high voltage platform housing the MRMS has been commissioned to the Pantechnik company: the factory acceptance tests were partially carried out before Summer 2018 and will be completed in the middle of September. The delivery and installation is expected for middle of October, together with all the power supplies necessary to operate the MRMS. The ADIGE control system design is complete and is currently under construction. It is based on the Experimental Physics and Industrial Control System (EPICS) framework, and can be described using a three layer model: the graphical user interface (GUI), the Middle-ware and the Hardware. The GUI is implemented using the Control System Studio (CSS) and connects to the Middle-ware layer using the EPICS Channel Access protocol: it can be based on software infrastructure running on Virtual Machines (EPICS IO controllers) or standard PLCs depending on the device to be controlled. In both cases, this layer represents the intelligent/autonomous part of the system, does not depend from the GUIs and provides all the basic functionalities and automatic procedures. The Hardware is the lowest level, directly connected to the devices to be controlled and used by the Middle-ware layer. For this reason, it can be considered, depending on the device: (i) the device itself if it directly supports an Ethernet-based protocol. This is the case of many high level instrumentation (signal generators, gauge controllers etc); (ii) industrial Standard IO devices (analog/digital), as in the case of simple devices like solenoids, valves, motors, analog references etc. These devices are usually controlled by the middle-ware layer using standard Ethernet protocols or other standard industrial field-buses; (iii) custom hardware, as in those cases where an Industrial Standard peripheral is not available or it is too expensive. At LNL a generic DAQ board has been developed and tested to acquire all the Beam Instrumentation data of the SPES facility: it is based on the Industrial Com

Express standard module, and it can be used with or without μ Processor unit, and so considered part of the Middle-ware or used as a simple IO peripheral depending on the needs.

The planning for the ADIGE injector foresees to start the operation with the 1+ source within the end of 2018: the first tests will be carried out with the SIS and will continue with the PIS. Both kind of sources will be completely characterized in terms of emittance, intensity and beam stability: such experimental activity will continue in 2019 without interfering with the completion of the rest of the ADIGE beam line, due to the absence of Radiation Protection issues and to the proper shielding adopted for the high voltage parts. After the installation of the rest of the beam instrumentation boxes and the vacuum system, the N+ beam line should be available from the middle of 2019: the first tests will be carried out with the Charge Breeder in "source-mode", that is without injecting the 1+ beam. This will allow to continue the characterization of the 1+ sources and, at the same time, to verify the resolving power of the MRMS: to this scope, the Charge Breeder will operate producing a plasma of oxygen mixed with xenon. The relatively high mass of xenon and the high number of stable isotopes will allow the verification of different level of resolution: as an example, the separation of $^{136}\text{Xe}^{25+}$ from $^{131}\text{Xe}^{24+}$ ($R=1/300$), $^{129}\text{Xe}^{19+}$ from $^{136}\text{Xe}^{20+}$ ($R=1/620$), or $^{132}\text{Xe}^{32+}$ from $^{128}\text{Xe}^{31+}$ ($R=1/1000$). The tests will proceed with the injection of the first 1+ beams in the Charge Breeder and will continue in 2020, with the entire beamline up to the injection of the RFQ operational.

REFERENCES

- [1] G. Bisoffi *et al.*, "Progress in the design and construction of SPES at INFN-LNL", *Nucl. Instrum. Meth.*, vol. B376 p. 402, (2016).
- [2] M. Maggiore *et al.*, "SPES: A new cyclotron-based facility for research and application of high intensity beams", *Modern Physics Letter A*, vol. 32, p. 1740010, (2017).
- [3] M. Manzolaro *et al.*, "Ongoing characterization of the forced electron beam induced arc discharge ion source for the selective production of exotic species facility", *Rev. Sci. Instrum.*, vol. 85, p.02B918, (2014).
- [4] M. Maggiore *et al.*, "Plasma-beam traps and radiofrequency quadrupole beam coolers", *Rev. Sci. Instrum.*, vol. 85, p. 02B909, (2014).
- [5] A. Galatà *et al.*, "The new ECR charge breeder for the Selective Production of Exotic Species project at INFN-Laboratori Nazionali di Legnaro", *Rev. Sci. Instrum.*, vol. 87, p. 02B503, (2016).
- [6] A. Pisent *et al.*, "Spes beam dynamics", in *Proceedings of HB2014*, East-Lansing, MI, USA, 2014.
- [7] A. Galatà *et al.*, "ADIGE: the radioactive ion beam injector of the SPES project", *J. Phys.: Conf. Ser.*, vol. 874, p. 012052, (2016).
- [8] T. Lamy *et al.*, "Charge State breeding applications with the ECR PHOENIX source: From low to high current production", *Rev. Sci. Instrum.*, vol. 73, p. 717, (2002).
- [9] A. Galatà *et al.*, "Status of the SPES-charge breeder (SPES-CB) and its beam line at INFN-LNL", *Nucl. Instrum. Meth.*, vol. B376, p. 329, (2016).

ADDRESSING CONTAMINATION IN ECR CHARGE BREEDERS

R.C. Vondrasek[†], Physics Division, Argonne National Laboratory, Lemont, IL, USA 60439

Abstract

The Electron Cyclotron Resonance (ECR) ion source was first utilized for charge breeding in 1995 [1]. Since that time the charge breeding technique has been refined. Single charge state efficiency has improved by a factor of ten, the efficiency discrepancy between solid and gaseous species has narrowed, and low-mass species efficiency has improved. But the limiting characteristic of the ECR charge breeder continues to be a high level of contamination which often obscures the beam of interest [2]. Multiple techniques have been employed to reduce this contamination with varying levels of success, and attempts are currently underway to improve upon the successes achieved to date. This paper will review those past techniques, current attempts, and possible future paths for reducing the contamination level in ECR charge breeders.

INTRODUCTION

Caribu Facility

The CALifornium Rare Isotope Breeder Upgrade (CARIBU) [3] provides radioactive beams to the Argonne Tandem Linac Accelerator System (ATLAS). Fission fragments are produced by a 200 mCi ²⁵²Cf fission source located inside a large-volume helium gas catcher. The fragments are thermalized and rapidly extracted at up to 50 kV forming a low-energy beam of 1+ or 2+ ions. The isotope of interest is selected via a high-resolution (1:20,000) magnetic separator. The beam is then transported to either an in-room experimental area, a remote stopped beam experimental area, or an ion source where the beam is charge bred for subsequent acceleration in the ATLAS linac. Originally, an ECR source charge bred the CARIBU beams, but due to the inability to adequately reduce the stable beam contamination that source was replaced by an EBIS in 2016.

ANL ECR CHARGE BREEDER

The ANL ECR breeder [4] (Fig. 1) is a room temperature source with the plasma excited by two RF frequencies – a 10.44 GHz klystron and an 11-13 GHz traveling wave tube amplifier (TWTA). It has an open hexapole structure providing good pumping to the plasma chamber region and allowing the RF and support gas to be introduced radially. This scheme eliminates the need for cut-outs in the field shaping iron to accept the RF waveguides. The 1+ ions were introduced into the plasma through a grounded high-purity aluminum tube mounted on a linear motion stage with a 30 mm range of travel. The

source is designed to operate at a 50 kV potential although it typically operated at 36 kV.

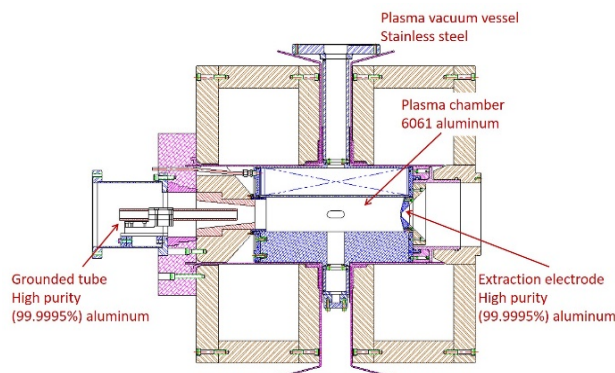


Figure 1: The Argonne National Laboratory ECRCB.

BACKGROUND CONTAMINATION

The background contamination which plagues ECR charge breeders has been well documented [5, 6, 7]. A mass scan of an oxygen plasma in the A/q region in which the ANL ECR breeder operated showed numerous peaks for nitrogen, argon, aluminum, fluorine, and chlorine on the >1 epA scale. Even in A/q regions within the spectrum that showed no background as measured with a picoammeter, a more sensitive examination with a silicon barrier energy detector revealed significant levels of background which dominated the radioactive ion beam of interest, as shown in Fig. 2. In the case of ¹⁴⁶Ba²⁸⁺, the radioactive beam accounted for only 3% of the total rate into the detector. The stable contaminants (Ti, Zn, Zr, Mo, Sn, Xe, Ir, Hg) were all within the LEBT resolution window and could only be eliminated by addressing the contamination at the source. In fact, even with a 1:1000 spectrometer after the charge breeder such as the one employed at SPES [8], only the Zn and Xe would be eliminated from the ¹⁴⁶Ba spectrum.

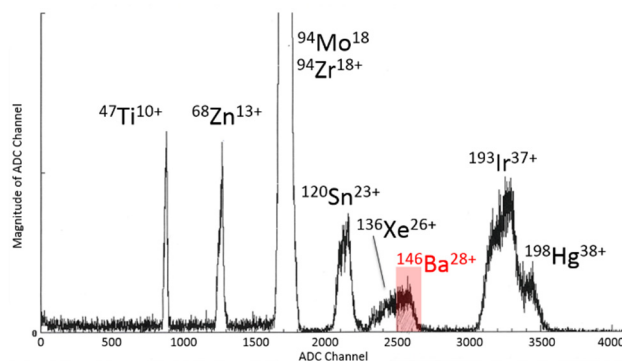


Figure 2: Spectrum is the radioactive beam ¹⁴⁶Ba (highlighted in red) and its contaminants from the ECRCB.

[†] vondrasek@anl.gov

Content from this work may be used under the terms of the CC BY 3.0 licence (© 2018). Any distribution of this work must maintain attribution to the author(s), title of the work, publisher, and DOI.

Sources of Contamination and Reduction Techniques

There were three identified sources of contamination – gases entering the system via leaks or the support gas, loose particulates on the ion source and surrounding vacuum chamber surfaces, and the bulk surfaces exposed to the plasma such as the plasma chamber, the extraction electrode, or the RF waveguides.

Investigation with a residual gas analyzer (RGA) showed that nitrogen and argon contaminants were not constituents of the oxygen support gas but were mainly due to o-ring permeation and to a smaller extent desorption from the plasma chamber and beamline surfaces. The o-rings were integral to the source construction, and their presence resulted in the equivalent of a 10^{-5} Torr- l /sec leak limiting the source to an ultimate pressure of 2×10^{-8} Torr. A method was developed to replace several of the o-rings with indium seals, but the gaseous contaminants were not the dominant problem so this course of action was not pursued.

Wall desorption is normally addressed with a standard thermal bake-out technique, but the presence of the permanent magnet hexapole and the high voltage isolation materials (which are all susceptible to heat damage) precluded this. The vacuum chamber was instead baked out with UV lamps which impart enough energy to desorb the water molecules but do not produce sufficient radiative heat to cause magnet damage. Using this technique, the base pressure was reduced by a factor of two mainly due to decreased water desorption, but there was only a small effect on the overall contaminant load as observed with the silicon barrier detectors.

Particulate contamination was previously addressed by the KEK charge breeding group with sand blasting and high pressure rinsing of the plasma chamber [5]. In the case of the ANL charge breeder, it was not practical to disassemble the ion source so alternative cleaning methods were investigated.

To remove the surface contaminants, CO₂ snow cleaning [9] of the plasma chamber surfaces as well as the injection and extraction hardware was employed. The method is nondestructive, nonabrasive, and residue-free. It is based upon the expansion of either liquid or gaseous carbon dioxide through an orifice leading to the nucleation of small dry ice particles in a high velocity gas carrier stream. The CO₂ pellets remove micron and submicron particulates by momentum transfer and hydrocarbons via a freeze-fracture mechanism. The high-velocity carrier gas propels the contaminants out of the system thus eliminating the need for high pressure rinsing and allowing the entire process to be done in situ.

The last source of contamination was sputtering of the plasma chamber and extraction electrodes, constructed of 6061 aluminum alloy, and the copper RF waveguides. The

6061 alloy has components of magnesium, silicon, titanium, chromium, manganese, iron, copper, and zinc - many of which were observed background contaminants.

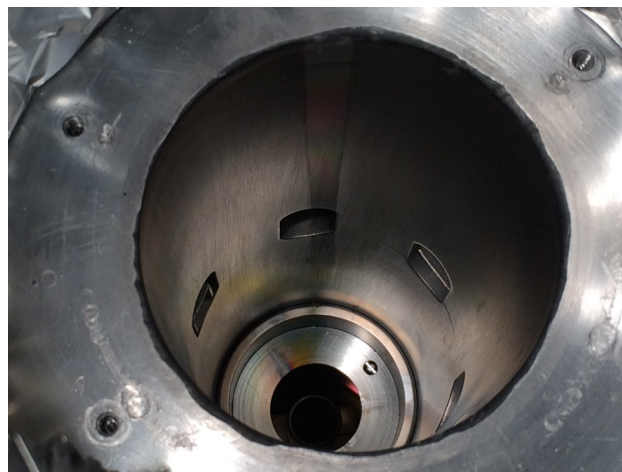


Figure 3: The ANL ECRCB plasma chamber after coating with ultra-high purity aluminum. Note the shadow at the top of the chamber caused by the high current lead which shows the uncoated surface. The aluminum disk at the injection side also still shows the plasma loss lines demonstrating the limitations of the evaporation coating technique.

New versions of the extraction electrode and the grounded tube were constructed from ultra-high purity aluminum (99.9995%), cleaned with the CO₂ system, and installed in a clean environment. It was not practical to construct a new plasma chamber from ultra-high purity aluminum. Instead the chamber was CO₂ cleaned and vacuum coated with ultra-high purity aluminum (99.9995%). A tungsten coil which had been saturated with the aluminum was suspended in the middle of the plasma chamber. The source was evacuated to 10^{-7} Torr and the coil heated resulting in an average surface deposition of 1 micron. While the central portions of the plasma chamber were coated, an injection side disk, the radial ports, and an area shielded by one of the high current leads did not receive an adequate amount of flux, as shown in Fig. 3

Contamination Reduction Results

Before the CO₂ cleaning, a mass scan of the source output was performed with analyzing slits set at ± 0.1 mm recording all peaks with an intensity > 1 epA. After the CO₂ cleaning, the scan was repeated with the same source conditions. Reductions in three major contaminants were observed – a factor of 20 reduction for fluorine, a factor of 4 for chlorine, and a factor of 50 for iron.

After the aluminum coating, the mass scan was repeated with the same source settings. The three main contaminants were further reduced – a factor of 160 reduction for fluorine, a factor of 17 for chlorine, and iron was no longer detectable.

While these three components were reduced at the source, the key metric is what is accelerated in the linac. A 98Zr beam had been produced shortly before aluminum coating the source. After coating, a 98Y beam was produced utilizing the same accelerator tune. Energy spectra were obtained for both beams with the silicon barrier detector. As a result of the coating, several of the stable contaminants observed in the silicon barrier spectrum had either been eliminated (iron, cadmium, cerium) or had come down significantly (titanium). A significant 98Mo peak remained and two new contaminants 181Ta and 186W were introduced, all presumably due to the tungsten heating coil used for the evaporation which had a 10 ppm component of molybdenum and a 20 ppm component of tantalum.

Other Reduction Techniques

While the above techniques demonstrated significant reductions in the level of background, especially that due to surface contamination, there are several improvements which can be made.

The o-rings need to be eliminated from the charge breeder design to establish a truly UHV system. This advancement has been incorporated into the construction of the SPIRAL PHOENIX ECR charge breeder [10]. This will eliminate the contribution from any o-ring permeation.

A method of depositing aluminum onto the chamber surfaces without introducing any new contaminants is required. It is possible that a greater reduction in the Mo, Ta, and W components could have been realized if a different heating element was used. Off-line tests with various carbon-based heating elements indicated pyrolytic graphite is the best candidate due to its high temperature performance, high purity, and low reaction rate with the aluminum.

A previously untested technique of introducing a pure aluminum coating is atomic layer deposition (ALD) [11]. This technique utilizes gaseous chemical compounds which bind to exposed surfaces producing a thin film comprised of successfully deposited monoatomic layers. The ECR chamber could be processed in situ using the compound trimethyl aluminum (TMA) [12].

The source chamber would be evacuated to 10-5 Torr and back-filled with the TMA. The TMA chemisorbs to the water monolayer present on the unbaked vacuum surfaces. Once all reactive sites are occupied, the process self-terminates and the remaining TMA is pumped from the chamber leaving a surface of AlCH₃. The system is then back-filled with a carrier gas containing a small amount of water which reacts with the -CH₃ forming CH₄ and resulting in a hydroxylated Al₂O₃ surface thus enabling the cycle to be repeated. The cycle time can be as short as 30 seconds and results in the deposition of a 1.29 Å layer. Assuming an automated system operating on a 30 second cycle time, a one micron layer of aluminum can be deposited in <3 days. Since the process is conformal, all exposed surfaces are coated regardless of geometry.

FUTURE PLANS

The ALD technique will be tested with a new permanent magnet ECR source [13] being installed at ATLAS (Fig. 4). Since all surfaces of the source will be coated – chamber walls, vacuum chamber, RF waveguides, insulators, o-rings – this should result in an absolutely clean surface exposed to the plasma. Tests will be performed regarding source function before and after coating with a focus on source contamination levels. The longevity of the coating will also be an important metric.

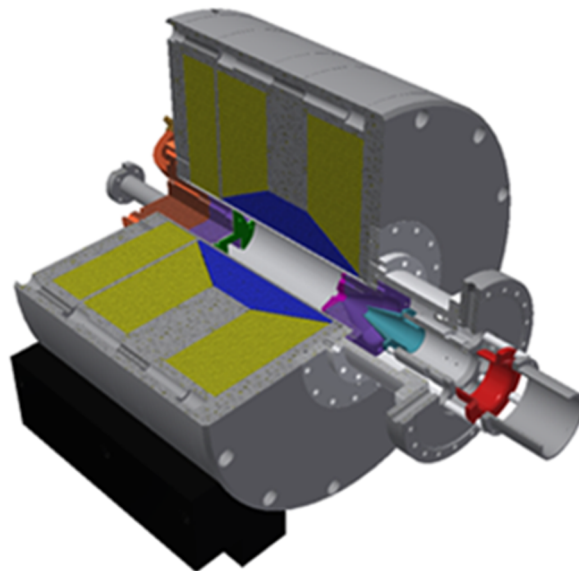


Figure 4: The new all permanent magnet ECR source which is being installed at ATLAS and will be used as test bench for the atomic layer deposition technique.

ACKNOWLEDGMENTS

This work was supported by the U.S. Department of Energy, Office of Nuclear Physics, under Contract No. DE-AC02-06CH11357 and used resources of ANL's ATLAS facility, an Office of Science User Facility.

REFERENCES

- [1] R. Geller, C. Tamburella, and J. L. Belmont, *Review of Scientific Instruments*, vol. 67, p. 1281 (1996)
- [2] R. Vondrasek, J. Clark, A. Levand, T. Palchan, R. Pardo, G. Savard, and R. Scott, *Review of Scientific Instruments*, vol. 85, p. 02B903 (2014)
- [3] R. Pardo, G. Savard, S. Baker, C. Davids, E. F. Moore, R. Vondrasek, G. Zinkann, *NIM-B*, vol. 261, Issues 1-2, p.965, (2007)
- [4] R. C. Vondrasek, R. Scott, J. Carr and R. C. Pardo, *Rev. Sci. Instrum.*, vol. 79, p. 02A901 (2008)
- [5] N. Imai, S. C. Jeong, M. Oyaizu, S. Arai, Y. Fuchi, Hirayama, H. Ishiyama, H. Miyatake, M. H. Tanaka, M. Okada, *et al.*, *Rev. Sci. Instrum.*, vol. 79, p. 02A906, (2008)
- [6] F. Ames, R. Baartman, P. Bricault, K. Jayamanna, *Hyperfine Interactions*, January 2014, vol. 225, Issue 1-3, pp. 63-67 (2013)

- [7] R. Vondrasek, J. Clark, A. Levand, T. Palchan, R. Pardo, G. Savard, R. Scott, *Rev. Sci. Instrum.* 85, 02B903 (2014)
- [8] A. Galata; *IOP Conf. Series: Journal of Physics: Conf. Series* 874 (2017) 012052
- [9] www.co2clean.com
- [10] P. Delahaye, L. Maunoury, R. Vondrasek, *Nucl. Instrum. Meth. A* 693(2012) p. 104-108
- [11] J. Lu, J. W. Elam, and P. C. Stair, *Surface Science Reports*, 71, 410-472, (2016)
- [12] R. Puurunen, *Journal of Applied Physics* 97, 121301 (2005)
- [13] D. Xie, *Review of Scientific Instruments* 73, 531 (2002)

OPERATION OF THE PHOENIX V3 ECRIS APPLYING DOUBLE FREQUENCY HEATING

F. Maimone^{1,†}, T. Thuillier², K. Tinschert¹, J. Jacob², J. Angot², L. Bonny², A. Leduc², P. Sole², R. Lang¹, J. Mäder¹, P.T. Patchakui¹, D. van Rooyen¹

¹ GSI Helmholtzzentrum für Schwerionenforschung, Planckstr. 1, 64291, Darmstadt

² Université Grenoble Alpes, CNRS, Grenoble INP, LPSC-IN2P3, 38000 Grenoble, France

Abstract

PHOENIX V3 is an upgraded version of the V2 ECRIS to be installed at the heavy ion injector at SPIRAL2. The source is under commissioning at LPSC since 2016. One of the main upgrades of the V3 concerns the new microwave injection system including two WR62 waveguide apertures. This new plug having two waveguide ports allows running the ECRIS with the double frequency heating mode by connecting two different high power microwave sources. For the investigation of this plasma feeding method a klystron generator at 18 GHz proving up to 2 kW microwave power was used together with a traveling wave tube amplifier with a 12.75-14.5 GHz bandwidth and 650 W maximum output power. Several experiments were carried out in order to verify the performance with respect to the single frequency operation. Different ion source configurations were investigated and different frequencies and power combinations were analyzed with the aim to maximize the high charge state ion production and to reduce the ion beam instability. The results are reported here.

INTRODUCTION

At LPSC the room temperature PHOENIX V3 ECRIS is under commissioning since 2016. This upgraded version of the PHOENIX V2 ECRIS features a larger plasma chamber, a new hexapole and a reduced vacuum pressure under operation [1]. So far high current of highly charged ions of gaseous and metallic elements has been extracted from this ion source. [2-4].

In order to enhance the high charge state production to fulfil the requirements of SPIRAL2 (i.e. ion beams with intensities of several μA up to ion mass $M\sim 60$) high microwave power and other techniques must be applied.

An operation mode successfully used to enhance the beam current of highly charged ions is the “double frequency heating” which consists of the injection of two electromagnetic waves at different frequencies into the ion source. [5]

For this purpose the PHOENIX V3 is equipped with a new microwave injection system including two separate WR62 waveguide apertures where two different high power microwave sources can be connected. The ion source performance has been tested with double frequency heating and has been compared with the single

frequency operation. Different ion source parameters were investigated and different frequencies and power combinations were analysed with the aim to maximize the high charge state ion production and to reduce the ion beam instabilities. The results are reported here.

EXPERIMENTAL SET-UP

The PHOENIX V3 ECRIS is designed to operate at 18 GHz and a klystron generator proving up to 2 kW microwave power is used for the ion source commissioning.

The double frequency heating has been performed by connecting a Traveling Wave Tube Amplifier (TWTA) with a 12.75-14.5 GHz bandwidth and 650 W maximum output power to the second waveguide port of the injection plug. In order to properly perform the measurements, following components have been used:

- A WR62 high power wideband 20 dB isolator in order to prevent the reflected and cross coupled power to the TWTA;
- Waveguide vacuum windows covering the TWTA's bandwidth and the klystron frequency;
- A specially designed 60 kV DC-Break for the TWTA connection with low insertion loss.

Concerning the DC-Break, full wave simulations were performed at LPSC in order to find the best geometrical configuration and the proper dielectric material to achieve a flat insertion within the bandwidth of the amplifier.

The prototype measurements done with a Network Analyser confirmed that the requirement of a flat insertion loss higher than 0.4 dB in the 12.75-14.5 GHz frequency range is fulfilled.

Two WR62 directional couplers are inserted between the isolator and the ion source. Microwave power probes are connected to each directional coupler to measure the forward and the cross-coupled power from the ECRIS. Once the microwave sources have been connected, safety tests were performed to check the power levels crossing between the two waveguides in order to prevent any damage of the microwave sources.

The measurement campaign was carried out with Argon as main gas and Oxygen as support gas and the main focus was the optimization of the intensity of the extracted Ar^{14+} charge state. A 20 kV extraction voltage and a -2 kV voltage were applied to the ECRIS and to the electron repeller electrode, respectively.

One should note that the second waveguide was used for the first time in the source for this experiment and that the second RF vacuum window was installed 2 days

[†] f.maimone@gsi.de

before starting the experiment. The presented results were achieved within one week and outgassing of the second waveguide was observed during the whole experiment.

The magnetic field configuration was tuned during the measurements, however, already observed during the preliminary investigations, the best performance was measured when the magnetic field is optimized for 18 GHz single frequency operation.

EXPERIMENTAL RESULTS

Preliminary measurements were carried out with the single microwave frequency provided by the 18 GHz klystron in order to study the performances enhancement of PHOENIX V3 when the double frequency heating is applied. The Argon charge state distribution when the ion source settings are tuned to optimize the intensity of Ar¹⁴⁺ is shown in Fig. 1. This spectrum was obtained shortly after venting the source to install the second RF window and the Ar¹⁴⁺ intensity obtained is lower than the usual reference intensity of 120 μ A.

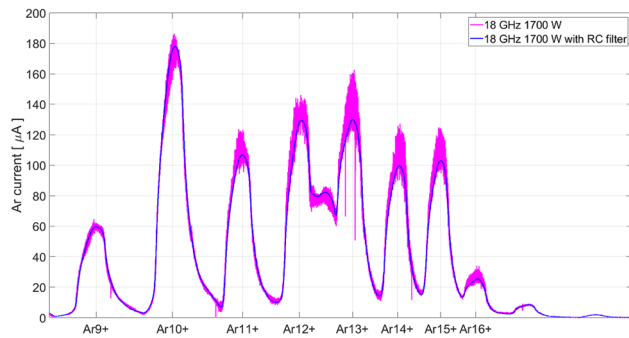


Figure 1: Argon charge state distribution for the single frequency operation.

The maximum current intensities of around 100 μ A of Ar¹⁴⁺ and around 20 μ A of Ar¹⁶⁺ have been achieved with single frequency operation at a maximum power level of 1700 W. Because of the low resolution of the spectrometer dipole the highest measured charge state, i.e. Ar¹⁷⁺, cannot be properly separated from the O⁷⁺. To overcome this drawback, the commissioning of a new bending dipole is ongoing. For this reason the charge states distribution analysis is restricted to the Argon charge states from 9+ to 16+ while the charge states 10+ and 15+ are superimposed to O⁴⁺ and O⁶⁺, respectively.

It was observed that the measured current presented a periodical oscillation, with repetition frequency around 300 Hz, which could be related to plasma instabilities or to electrical noise. The superposition of a second pumping wave reduced such an instability as shown in Fig. 2 where the Ar¹⁴⁺ current evolution, recorded for 5 seconds and 20.000 samples/sec, is plotted. By calculating the standard deviation σ and the mean μ of the measured currents, it is possible to calculate the Probability Density Function:

$$f(x) = \frac{1}{\sqrt{2\pi}\sigma} e^{-\frac{(x-\mu)^2}{2\sigma^2}} \quad (1)$$

This function, calculated for the single frequency operation and for the double frequency heating confirms that this latter technique is useful to reduce the plasma instabilities, as already observed in [6].

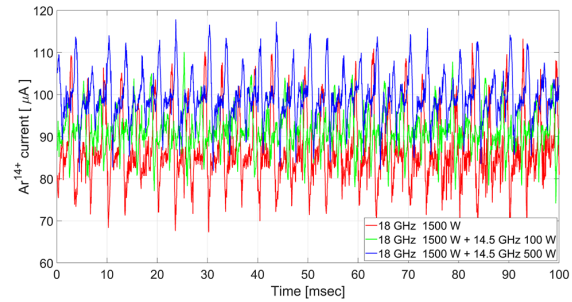


Figure 2: Argon current evolution (20000 samples/sec) for the single frequency operation and for different power combinations of the two frequencies.

In Fig. 3 the normalized Eq. (1) is plotted by using the analysed Ar¹⁴⁺ current data for the single frequency operation and when a second microwave source at 14.5 GHz provides additional power levels. This figure confirms that an additional power of 100 W at a second microwave frequency is enough to reduce the current oscillations and to enhance the extracted current of highly charged ions. This enhancement is also a function of selected frequencies as already measured at GSI [7].

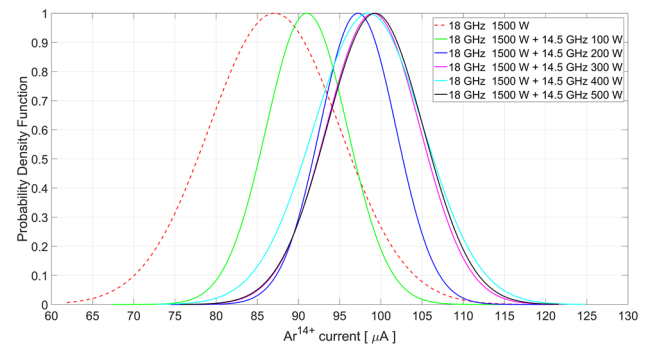


Figure 3: Probability Density Function of the measured Ar¹⁴⁺ current for the single frequency operation and for different power combinations of the two frequencies.

In order to find the second frequency where the Ar¹⁴⁺ current is optimized, a microwave sweeping generator is used to drive the TWTA with frequency ramps between 12.75 and 14.5 GHz in steps of 200 kHz.

Because of the measured oscillating current a RC low-pass filter, with a cut-off frequency < 300 Hz, is used to limit the periodical instability during the frequency sweep. The overall effect of the filter on the analysed current is shown in Fig. 1 (blue vs purple curve). Then the Ar¹⁴⁺ current has been measured while the frequency ramps between 13.8 and 14.5 GHz were performed. The starting frequency was increased since no intensity enhancement was found between 12.75 and 13.8 GHz.

In Fig. 4 is shown the Ar¹⁴⁺ intensity for different power combinations distributed between the 18 GHz generator

Content from this work may be used under the terms of the CC BY 3.0 licence (© 2018). Any distribution of this work must maintain attribution to the author(s), title of the work, publisher, and DOI.

and the frequency tuned TWTA. The highest intensity measured with the single operation at 18 GHz is included in the figure. By comparing the Ar^{14+} currents when a total input power level of 1700 W is sent to the ECRIS at 18 GHz with the case when it is the sum of powers (1400W+300W) delivered from two generators at different frequency (cyan line) it is worth noting a current enhancement, with respect to single frequency operation, independent on the choice of the second frequency.

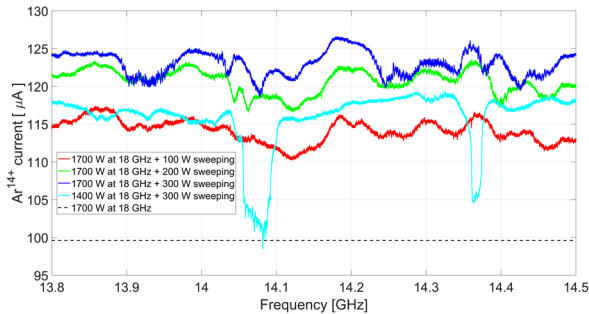


Figure 4: Ar^{14+} intensity comparison between single frequency (dashed line) and double frequency injection.

This enhancement is measured for several higher charge states as shown in the charge states distributions of Fig. 5. The spectra, measured for different frequencies with the highest Ar^{14+} current enhancement, confirm the current gain (up to 15% for Ar^{14+} and up to 34% for Ar^{16+}) obtained with the double frequency system providing the same input power.

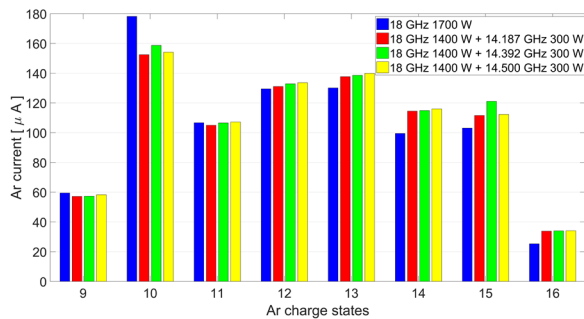


Figure 5: Argon spectra comparison between single frequency injection at 18 GHz and double frequency heating (same input power)

It is also observed that the higher the total forward power and the lesser is the effect of the second frequency on the extracted current. When the maximum power level provided by the klystron, 1700 W, is combined with 100, 200, 300 W coming from the TWTA (see the red, green and blue lines of Fig. 4) the dependence of the extracted current on the second frequency is less than 10 μA . A part of this limitation may be caused by the second waveguide outgassing increasing the neutral pressure in the source and thus reducing the high charge state ion population. Several weeks of operation would be necessary to get rid of the bias outgassing and to investigate further the relation between second RF power and high charge state current improvement. Nevertheless

for the maximum input power configuration, 1700 W at 18 GHz + 300 W at a variable frequency, it is possible to identify the frequencies where the Ar^{14+} current is optimized (the highest peaks of the blue line of Fig. 4): 14.187, 14.366 and 14.5 GHz. The charge states distributions of Argon when 300 W power at these three frequencies is combined with the maximum power of 1700 W at 18 GHz are shown in figure 6. For this configuration up to a 24% Ar^{14+} current gain and up to a 54% Ar^{16+} current gain are obtained with respect to single frequency operation, when the second microwave frequency is set to 14.187 GHz.

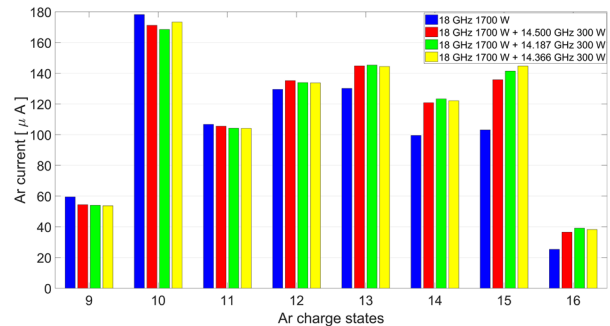


Figure 6: Argon spectra for single frequency injection at 18 GHz and for double frequency heating.

CONCLUSIONS

For the first time the PHOENIX V3 ECRIS has been operated in double frequency mode and an improved stability is measured. The experiment was performed during one week, right after venting the source and installing new second vacuum window and WR62 waveguide, generating transient outgassing. The measurement results were nevertheless quite promising since the maximum extracted Ar^{14+} current is enhanced from $\sim 100 \mu\text{A}$ to $\sim 125 \mu\text{A}$ and the Ar^{16+} current increased from $\sim 25 \mu\text{A}$ to $\sim 39 \mu\text{A}$. A high outgassing effect was experienced for higher power levels of the TWTA, thus limiting the capabilities of the ECRIS to produce still higher intensities in double frequency mode. A longer experiment would be necessary to get rid of outgassing and to check the real gain of double frequency at high TWTA power. This result was achieved with a microwave frequency tuning system which allowed to identify the frequencies where the extracted current of higher charge states was optimized.

REFERENCES

- [1] T. Thuillier *et al*, *Rev. Sci. Instrum.*, vol. 87, p. 02A733, 2016.
- [2] T. Thuillier *et al*, *Proc. of ECRIS2016*, Busan, Korea.
- [3] A. Leduc *et al*, *these proceedings*.
- [4] T. Thuillier *et al*, *Proc. of the ICIS17 conference*, 15-20/10/17, Geneva, Switzerland under press
- [5] Z. Q. Xie and C. M. Lyneis, *Rev. Sci. Instrum.* vol. 66, p. 4218, (1995).
- [6] V. Skalyga *et al*, *Phys Plasmas*, vol. 22, p. 083509, 2015
- [7] F. Maimone *et al*, *Rev. Sci. Instrum.* vol. 82, p. 123302, 2011.

HTS MAGNET TECHNOLOGY AS PATH TO FOURTH AND FIFTH GENERATION ECR ION SOURCES

T. Shen*, D. Leitner, L. Garcia Fajardo, S. Prestemon, G. Sabbi
LBNL, Berkeley, California, USA

Abstract

Novel superconducting magnet systems for ECR ion sources (ECRIS) operating at frequencies above 28 GHz is a core technology to be developed. Current state-of-the-art magnet systems are based on the Nb-Ti technology at 4.2 K and are the new standard injectors for next generation heavy ion beam facilities. However, increasing the frequency beyond 28 GHz will further advance the performance of high charge state ECR ion sources. Nb₃Sn provides an immediate option for reaching higher frequencies, but Nb₃Sn designs would ultimately be limited to about 56 GHz. A versatile longer-term option is the high-temperature superconducting magnet technologies, which can enable operations of high field ECRIS magnets at $T \geq 20$ K. The ultimate operating frequency of HTS magnet systems is not limited to 56 GHz but in principle could even attain 84 GHz, due to the critical field and current density limits that can be achieved at high fields. The paper will first discuss the ECR ion source parameters driving the design of the Next Generation Superconducting ECR magnets, and will then focus on HTS magnet technology and its potential to further increase the performance of ECR ion sources.

ECR ION SOURCE PHYSICS PARAMETERS

ECR Ion Source Confinement

ECR ion sources use magnetic confinement and electron cyclotron resonance heating to produce a plasma consisting of energetic electrons (up to hundreds of keV) and relatively cold ions (a few eV). High charge state ions are primarily produced by sequential impact ionization. Therefore, the ions must remain in the plasma long enough (tens of ms) to reach high charge states and the main parameter determining the performance of an ECR ion source is the product of the plasma density and ion confinement time: ($n_e \cdot \tau_i$). Together with the neutral gas density in the plasma this product determines both the peak of the charge state distribution and the highest charge state that can be produced in the plasma. Following the semi-empirical scaling laws first proposed by Geller [1], the plasma density scales with the square of the frequency $n_e \propto \omega_{rf}^2$. As the frequency increases, the magnetic fields have to be scaled accordingly to fulfill the resonant heating condition for the plasma electrons. As a consequence the plasma confinement time (τ_i) in the trap improves since it is proportional to the average field strength and the axial and radial magnetic mirror ratios B_{inj}/B_{min} , B_{ext}/B_{min} , B_{rad}/B_{min} of the magnetic trap [1].

Following these fundamental principles, the trend for new ECR ion source constructions has been to design for both the highest confinement fields and highest heating frequency resulting in a number of high performance ECR ion sources developed over the last few decades. Compiling results from these high performing devices, guidelines for the design of an optimized magnetic confinement field configurations were established applicable to any heating frequency of an ion source [2]. These established field ratios are listed below with F_{rf} being the chosen operating microwave frequency for the new ECR ion source, with B_{inj} , B_{ext} , B_{min} , the maxima and minimum fields of the magnetic mirror, and B_{rad} the radial field strength on the plasma chamber wall.

- $B_{ECR} = F_{rf}(GHz)/28(GHz) \cdot T$
- $B_{inj}/B_{ECR} = 4$
- $B_{rad}/B_{ECR} = 2$
- $B_{ext} \approx 0.9B_{rad}$

For the minimum B-field of the trap one can find [2, 3]

- $B_{min} \approx 0.4B_{rad}$ and
- $0.4 < B_{min}/B_{ECR} < 0.8$

Another important parameter for establishing the overall plasma confinement is the electron energy distribution in the ECR plasma, which can be characterized by three components: a cold population (20 eV) - important for the overall plasma density and confinement time; a warm population (up to 100 keV) - responsible for the ionization process, and a hot population with a high energy tail reaching up to several hundreds of keV, which is highly confined in the core of the plasma and quasi collisionless. While the hot electron population does not contribute to the ionization process, these hot electrons are nevertheless crucial to establish the electrostatic confinement for the ions in the trap. Therefore, their presence is a necessary condition for the creation of high charge state ions [3]. However, one undesired consequence of this hot electron population is the creation of high energy x-rays that penetrate the plasma chamber and, in the case of a superconducting ECR ion source, add a substantial heat load to the cryostat. It would be desirable to optimize this temperature while minimizing the x-ray production and maintaining a strong electrostatic confinement. Results from recent x-ray studies suggest that this could be possible [4,5].

Key results from experimental studies to understand the role of the hot energy tail ECR plasma are summarized below:

* tshen@lbl.gov

Content from this work may be used under the terms of the CC BY 3.0 licence (© 2018). Any distribution of this work must maintain attribution to the author(s), title of the work, publisher, and DOI.

- The high temperature tail of the electron energy spectrum (with energies above 200 keV) is key to establishing the electrostatic confinement necessary for the creation of high charge state ions.
- The hot electron temperature neither depends on the magnetic field gradient at the ECR zone as previously believed [6] nor on the heating frequency. The temperature mainly depends on the absolute value of the minimum B-field [4, 5].
- For a given minimum B-field higher heating frequencies will result in higher plasma densities (frequency scaling law still applies) [5]
- Lower gradients at the ECR zone improve the microwave heating efficiency [6].
- The plasma density increases linearly with power until a threshold density is reached where non-linear phenomena occur [1]. Therefore, for a given confinement configuration the x-ray heat load depends linearly on the microwave power. The threshold density is proportional to the square of the microwave frequency [4–7].

Tuning Considerations

These results have important consequences for the operation of high field, high frequency superconducting ECR ion sources. Since the electron temperature is nearly independent from the heating frequency, the minimum B-field allows to control the hot electron temperature and therefore the x-ray loading into cryostat at the expense of power efficiency. Consequently, next generation ECR ion sources are typically operated at lower minimum B-fields; high performance superconducting 28 GHz ECR ion sources typically operate with a B_{min}/B_{ECR} between 0.4 to 0.6, while conventional magnet ECR ion sources (6–18 GHz) can operate at a ratio of B_{min}/B_{ECR} between 0.6 and 0.8 to optimize the electrostatic confinement conditions and microwave heating efficiency in the trap. However, as mentioned above, the magnetic field gradient at the ECR zone improves the heating efficiency and allows to reach higher plasma density at a lower power density. Fig. 1 from [6] illustrates this dependence. While the same charge state distribution and currents can be achieved with both field configurations, the higher minimum B-field (shallower magnetic field gradient at the ECR heating zone) requires only 2/3 of the power to reach the same performance (see Fig. 1 from [6]). As demonstrated in [6], the charge state distributions and the warm electron densities are nearly identical in both cases.

Most superconducting ECR ion sources utilize 4 K cryostats using cryocoolers that typically provide less than 10 W of cooling power. This limitation forces the ECR operator to restrict the tuning range to minimum B-fields B_{min} that balance the available cooling power with the x-ray heat load from the plasma. Since the absorption coefficient decreases logarithmically with x-ray energy while the x-ray energy increases linearly with B_{min} , the x-ray heatload increases exponentially with the B_{min} value. On the other

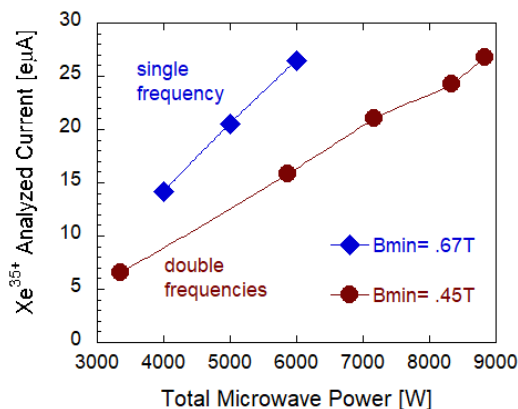


Figure 1: Power dependence of Xe^{e35+} production for a B_{min} of 0.67 T using 28 GHz single frequency heating to a B_{min} of 0.45 T using 18+28 GHz double frequency heating. [6]

hand, for a constant B_{min} field configuration, the x-ray load (plasma density) increases only linearly with power. Consequently, it is often more beneficial to operate at lower B_{min} and compensating the reduced heating efficiency with higher microwave power. This tuning restriction is one of the reasons, why none of the 3rd generation superconducting ECR ion sources have reached their performance limits with microwave power yet.

Status of the field - High Field Superconducting ECR Ion Sources

In the last two decades, Nb-Ti Superconducting ECR ion sources have been established as state of the art injectors for heavy ion facilities. Pioneered by the VENUS ECR ion source [8], which was the first superconducting ECR ion source with a magnetic confinement field optimized for operation at 28 GHz, several ECR ion sources were built for frequencies of 24 GHz to 28 GHz with similar confinement fields using either the same geometry as VENUS (Sextupole magnets are placed inside the solenoids) [9–11], or in case of SECRAL [12], a converted geometry (solenoids are placed inside the sextupole). All of these sources have fulfilled or exceeded their expected performance and continue to improve as more power is coupled efficiently into the plasma [12, 13]. The magnetic field ratios as described in the previous section are utilized for all these source designs. To reach these values inside the plasma chamber, the maximum field on the sextupole conductor reaches 6 to 7 T, which is at the limit of what is feasible to achieve using Nb-Ti technology at 4.2 K. In order to further extend ECR ion source designs to frequencies well above 28 GHz, new superconductor magnet technology will be needed for the 4th and 5th Generation ECR ion sources. Presently, Nb₃Sn conductors, for which the upper critical field limit increases to about 20 T at 4.2 K [14], will most likely lead the way to develop 4th generation ECR ion sources with an operational range of 40 to 50 GHz. An ambitious project is currently underway at the Institute for Modern Physics (IMP) in Lanzhou to build the first Nb₃Sn ECR ion source optimized for operation at 45 GHz [12, 15].

The design was developed as a collaboration between IMP and the Lawrence Berkeley National Laboratory. The cold mass is currently under construction [15]. Thinking beyond this frequency range, the use of high temperature superconducting (HTS) cuprate conductors will need to be developed and applied to ECR ion source technologies. A fully high temperature high field superconducting magnet would offer advantages over the conventional 4 K conductors, in particular in terms of robustness of handling the x-ray load and the ultimate fields that can be reached. Operating at 20 K would allow to explore the ECR source performance without the limit of the cryostat cooling power limits that are present at 4 K or 2 K systems. In the next sections we explore the state of the art high temperature superconducting magnet and its potential to develop ECR ion source structures.

STATUS OF THE FIELD - HTS MAGNETS

The superconductor and magnet communities have long been seeking to broaden the application scope to higher fields at low temperatures (4.2–20 K) or higher temperatures (20–77 K) using HTS conductors. Arduous conductor development efforts over the past three decades have resulted in commercially produced HTS conductors including Bi-2212, Bi-2223, and $REBa_2Cu_3O_x$ (REBCO). They are produced in practical forms of metal/superconductor composite conductors and available in lengths suitable for making magnets. Their upper critical magnetic fields (see Fig. 2) exceed 50 T at 4.2 K which is well above Nb-Ti (≈ 14 T at 1.8 K) and Nb_3Sn (≈ 26 –27 T at 1.8 K), making them potentially useful for making high-field magnets, such as 30 T superconducting solenoids needed for 1.3 GHz NMR spectrometers, 20 T accelerator dipoles for a potential high-energy upgrade of the LHC, and > 28 GHz ECRIS magnets. The whole wire engineering critical current densities of these high performance conductors in comparison with Nb-Ti and Nb_3Sn conductors are plotted in Fig. 2. While Nb-based superconducting materials have reached their peak performance, the engineering critical current density of HTS wires continue to rise [16, 17].

At the front of HTS magnet technology research, significant progress has been made, particularly in small-bore solenoids made of REBCO, enabling the successful realization of a 32 T user solenoid constructed at the National High Magnetic Field Laboratory [18, 19]. However, this record magnetic field was realized in a small bore (40 mm) using only short conductor piece lengths (<100 m). The magnet also has a relatively low total stored energy of 1.3 MJ. Even for this solenoid magnet system, a key challenge is protection against quenches when the winding loses superconductivity locally, creating local hot spots with temperature and thermal-induced stress that may, without suitable protection, lead to degradation. The 32 T HTS magnet is protected with a battery bank that provides an energy input of 130 kJ at 400 V to a set of heaters embedded into HTS coils, a system that is inconvenient to implement for a user magnet. Several other HTS magnets systems, however, have been de-

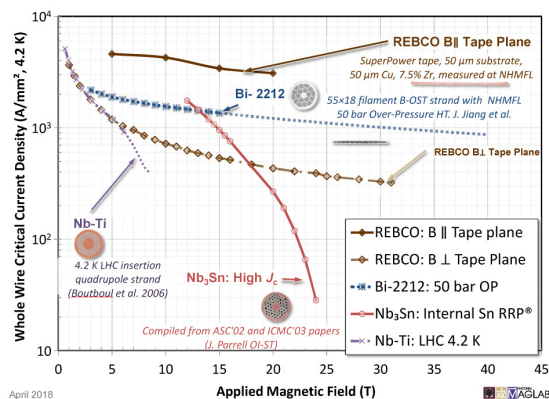


Figure 2: Critical current density (J_c) of different HTS and LTS technologies at 4.2 K [14]

graded during quench [20–22]. Extending this technology to ECR magnets is challenging and will require long and focused industrial conductor R&D. The magnet system for ECRIS is unique and much more complex than the small solenoids currently being built and tested. The sheer size of the magnet system and a combination of coils present unique challenges for HTS conductor and magnet technologies, and it would represent one of the most complex HTS magnet system ever engineered and fabricated. A potential solution to the quench protection problem of REBCO magnets is to build REBCO coils with metallic insulation such as stainless steel or without any insulation between turns ((NI)-REBCO conductors) [18, 24, 25], allowing adjacent turns to share electric current during a quench or allow to bypass a hot spot and flow into the adjacent turns preventing quenches. Both options are of great interest for high field ECR magnet structures. Particularly, the (NI)-REBCO conductors can use REBCO-tapes with only 10 μ m thick Cu or less and therefore has a much improved yield stress of ≈ 1100 MPa.

The disadvantage of this technique is the slow charging and discharging time of these structures in the order of T/hour [18, 26]. Therefore, this technique would only be useful for a quasi static magnet such as the sextupole, where field changes would only be done occasionally. On the other hand the solenoids can be either constructed from REBCO tape insulated with metallic insulation (as proposed in the conceptual magnetic design in the next section) or possibly as a hybrid magnet combining (NI)-REBCO coil insert with a low current density trim coil to enable faster tuning time within a small range.

Using tuning parameters from the last several years of the LBNL VENUS source [27] as an example, the source tuning is typically restricted to a narrow range. The injection solenoid is typically tuned within about $\pm 5\%$, the extraction solenoid is typically tuned within ± 5 – 10% of the sextupole field. The middle field solenoid has the largest tuning range of $\pm 30\%$. However, the fast tuning range (for a particular

Content from this work may be used under the terms of the CC BY 3.0 licence (© 2018). Any distribution of this work must maintain attribution to the author(s), title of the work, publisher, and DOI.

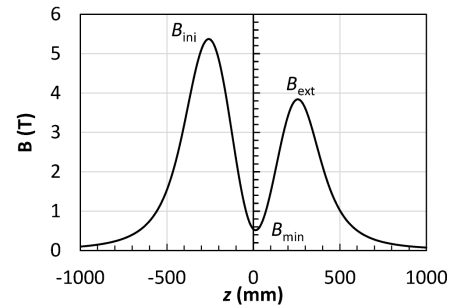
optimization or study) could be restricted to $\pm 5\%$ for a given field configuration.

Extending the conductor properties to the highest conceivable ECR magnet structure one can make a first cut - envelope concept for an ECR ion source working even at 80 GHz. Similarly to Nb-Ti and Nb₃Sn magnets, the coupling between the coils driven by multiple power supplies, protecting against quenches induced through external noise (such as high voltage sparks in operations) is a major issue for these magnet systems. In addition, the shear conductor lengths required for ECR magnets makes this structure very challenging. Before one can think of constructing a structure that pushes all limits of this technology, smaller scale coupled coil prototype HTS magnet system should be pursued to better understand the engineering issues associated with ECR structures. The magnet system case study below describes a 37.5 GHz ECR magnet structure for which we propose using stainless steel insulated coils for the solenoid system and (NI)-REBCO for the sextupole system. While challenging, this design is well within the magnetic margins of the HTS technology and would be a goal that could be realized within the next decade.

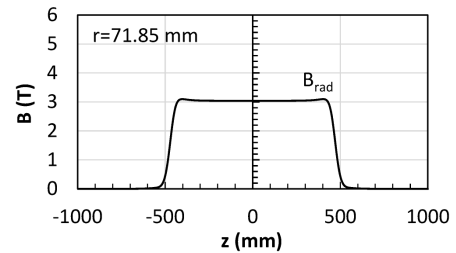
MAGNETIC FIELD PROFILES FOR A 37.5 GHZ ECRIS

Fig 3 presents preliminary field profiles of an HTS (REBCO) magnet that meets performance requirements of a 37.5 GHz ECRIS, whose key parameters are listed in Table 1. The sextupole coils are assembled from six flat race-track coils, a geometry that is favorable for fabricating magnets using REBCO tapes, whereas solenoids are stacked from double-pancake coils, also wound with REBCO tapes. A clear difficulty for building such magnet system is the quench protection. The sextupole coils are designed to be built with the (NI)-REBCO magnet technology; they are compact, working at a high overall coil current density of 800 A/mm² [25]. The metallic-insulation REBCO magnet technology for the three solenoids is selected to provide a ramp rate dI/dt required for tuning the magnetic mirror fields. A concern of the design is the stress management with increasing magnetic fields. A simple BJR hoop stress calculation results in stress values greater than 470 MPa in the injection solenoid which is well within the performance of the conductor specified in the table 1 (30 μ m thick Hastelloy substrate, 3.6 μ m Ag, 15 μ m Cu, and a yielding stress of 800 MPa). As comparison 470 MPa would exceed the yielding strength of the RRP (Restack Rod Process) Nb₃Sn conductor (50% Cu and a yielding stress of 250 MPa). Due to the expected high stress, the overall coil current density of the injector solenoid is reduced to 310 A/mm² in order to provide some engineering margin to the design.

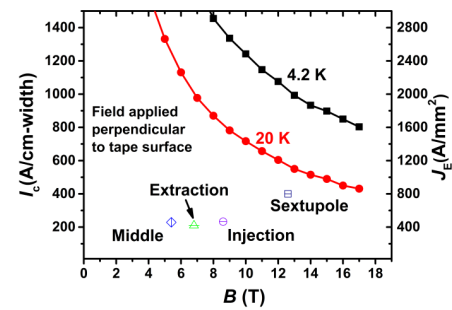
The piece lengths required for each double pancake coil is about 3 km for each sextupole coil (19 110 m total) and 1 km for the solenoids (28 021 m total), respectively (Table 1). Using a market average price of \$60/m (8 mm wide tape) the conductor costs result in \$1.1 million for the six sextupole



(a) Nominal magnetic field density along the main axis of the ECRIS (at $r = 0$ mm).



(b) Sextupole (only) field density (at $r = 71.85$ mm)



(c) Working point of the injection, middle, extraction solenoids, and the sextupole. Critical surface of the REBCO tape at 20K and 4.2K with the field applied perpendicular to the tape's wide surface.

Figure 3: Key magnetic parameters of the 37.5 GHz ECRIS

coils, and \$1.5 million for solenoid coils. At present, the REBCO industry is, though barely, capable of delivering conductors with such lengths with the caveat that there may be non-uniformities in the conductor with occasional I_c drop by 10% or higher [28]. There is a report indicating that such I_c drops along the length of conductor can be tolerated for (NI)-REBCO coils [23].

CONCLUSION

Over the last several decades, ECR ion source performance has been pushed forward by increasing the magnetic field and the operating frequency. With the current state of the art 28 GHz ECRIS, a limit of what is feasible with established superconducting magnet technology has been reached. Nb₃Sn is the logical next choice for higher frequency sources [12] and will dominate the 4th Generation ECR ion sources developed over the next decades. In this

Table 1: Key parameters of the solenoids and sextupole coils for a conceptual 37.5 GHz ECRIS REBCO magnet working at 20 K. The solenoids are based on a partial-insulated REBCO magnet technology. The sextupole coils are based on a (NI)-REBCO magnet technology, and working at a high coil current density of 800 A/mm².

Solenoid Coils	Injection	Middle	Extraction	Sextupole Coils	
Fabrication Method	Stack of Double Pancakes (DP)			2-layer flat racetrack coils DP technology	
Mirror Length (mm)	500			Plasma Chamber Radius	70
B_0 (T)	5.4	0.5-1.0	3.8	Field at Plasma Chamber Wall	3
B_{peak} (T)	8.6	5.4	6.8	Bore Diameter	200
Inner Diameter (mm)	352	352	352	Inner Winding Radius (mm)	15
				Coil Width (mm)	16
Thickness (mm)	32	32	32		36
Length (mm)	194.4	64.8	145.8		1000
Operating Current (A)	186	183	168		320
J_{coil} (A/mm ²)	310	305	280		800
Peak Hoop Stress	469	290	335		
	REBCO Tape				
Thickness (mm)	0.05	0.05	0.05		0.05
Width (mm)	8	8	8		8
Insulation	Stainless steel 25 μ m in thickness			none between turns	
Number of Double Pancakes (DP)	12	4	9		2
Tape Piece Length/DP (m)	1040	1040	1040	per sextupole coil (m)	3185
Total Tape Length (m)	12480	4160	9360	Total (m)	26000

paper we proposed to pursue HTS technology, which might lead the path to the 5th Generation ECR ion sources. While magnetic fields for frequencies up to 80 GHz are in principle within the reach of this technology, we presented the design of a much more modest system operating at 37.5 GHz that will allow to better understand and solve the key technology issues associated with emerging conductor materials.

REFERENCES

- [1] R. Geller, in *Electron cyclotron resonance ion sources and ECR plasmas*, CRC Press, UK, 1996, pp. 394-398.
- [2] D. Hitz *et al.*, *Rev. Sci. Instrum.*, vol.73, p. 509 (2002).
- [3] D. Leitner, *et al.*, *Proc. of Intern. Conf. on Cyclotrons, (CYCLOTRONS'2007)*, Giardini Naxos, Italy, 2008.
- [4] J. Benitez *et al.*, *22nd Intern. Workshop on ECR Ion Sources*, Busan, Korea, (ECRIS'16), MOCO04 (2016).
- [5] D. Neben *et al.*, *23rd Intern. Workshop on ECR Ion Sources*, (ECRIS'18), Catania, Italy, this conference (2018)
- [6] D. Leitner *et al.*, *Rev. Sci. Instrum.*, vol. 79, p. 033302 (2008).
- [7] C. Lyneis *et al.*, *22nd Intern. Workshop on ECR Ion Sources*, Busan, Korea, (ECRIS'16), (2016).
- [8] M. Leitner, *et al.*, *Phys. Scripta* Vol. T 92, 171 (2001).
- [9] G. Machicoane *et al.*, *21st Intern. Workshop on ECR Ion Sources, (ECRIS'14)*, Nizhny Novgorod, Russia, MOOMMH03 (2014).
- [10] G. Machicoane *et al.*, *23rd Intern. Workshop on ECR Ion Sources, (ECRIS'18)*, Catania, Italy, this conference (2018)
- [11] T. Nakagawa *et al.*, *Rev. Sci. Instrum.*, vol. 81, p. 02A320 (2010).
- [12] H.W. Zhao, *et al.*, *Phys. Rev. Accel. Beams*, Vol. 20, p. 094801, 2017.
- [13] D. Xie *et al.*, *22nd Intern. Workshop on ECR Ion Sources*, Busan, Korea, (ECRIS'16), THAO01, (2016).
- [14] P.J. Lee, NHMFL, Florida State University. <http://www.magnet.fsu.edu/magnettechnology/research/asc/images/jcprog-06-112706col.png>
- [15] H.W. Zhao, *et al.*, *23rd Intern. Workshop on ECR Ion Sources*, (ECRIS'18), Catania, Italy, this conference (2018).
- [16] T. Shen, *et al.*, arXiv preprint arXiv:1808.02864 (2018).
- [17] G. Majkic, *et al.*, *Supercond. Sci. Technol.* 31, 10LT01 (2018).
- [18] S. Hahn, *et al.*, *IEEE Trans. Appl. Supercond.*, vol. 21, p. 1592 (2011).
- [19] NHMFL, Press Release, <https://nationalmaglab.org/news-events/news/new-world-record-magnet-fulfills-superconducting-promise> (2017).
- [20] Y. Terao, *et al.*, *IEEE Trans. Appl. Supercond.*, vol. 23, (2013).
- [21] Y. Terao, *et al.*, *IEEE Trans. Appl. Supercond.*, vo. 24, p. 1 (2014).
- [22] K. Kajita, *et al.*, *IEEE Trans. Appl. Supercond.*, vol. 26, p.1 (2016).
- [23] S. Hahn, *Supercond. Sci. Technol.* vol. 21, p. 105017 (2016).
- [24] S. Yoon, *Supercond. Sci. Technol.* vol. 29, p. 04LT04 (2016).
- [25] J.-B. Song, *Supercond. Sci. Technol.* 28, 114001 (2015).
- [26] K. Yanagisawa, *et al.*, *IEEE Trans. Appl. Supercond.*, vol. 26, p.1, (2016)
- [27] D. Todd, private communication, Berkeley (2018)
- [28] A. Sundaram, *et al.*, *Supercond. Sci. Technol.* vol. 29, p. 104007, (2016).

THE FIRST MEASUREMENT OF PLASMA DENSITY BY MEANS OF AN INTERFERO-POLARIMETRIC SETUP IN A COM- PACT ECR-PLASMA TRAP*

E. Naselli^{†1}, D. Mascali, G. Torrasi, G. Castro, L. Celona, S. Gammino, M. Mazzaglia, G. Sorbello²,
Istituto Nazionale di Fisica Nucleare, Laboratori Nazionali del Sud (INFN-LNS), 95123 Catania,
Italy

¹also at Department of Physics and Astronomy, University of Catania, Via Santa Sofia, 64, 95123
Catania, Italy

²also at Department of Electrical, Electronics and Computer Engineering (DIEEI), University of Ca-
tania, viale A. Doria, 6, 95125 Catania, Italy

Abstract

This paper presents the first measurement of plasma density by a K-band microwave polarimetric setup able to measure the magnetoplasma-induced Faraday rotation in a compact size plasma trap. The polarimeter, based on rotating waveguide OMTs (OrthoModeTransducers), has been proven to provide reliable measurements of the plasma density even in the unfavorable conditions $\lambda_p \sim L_p \sim L_c$ (being λ_p , L_p and L_c the probing signal wavelength, the plasma dimension and the plasma chamber length respectively) that complicates the measurements due to multi-patterns caused by reflections of the probing wave on the metallic walls of the plasma chamber. An analysis method has been developed on purpose in order to discriminate the polarization plane rotation due to magnetoplasma Faraday rotation only, excluding the effects of the cavity resonator. The measured density is consistent with the previous plasma density interferometric estimations. The developed method is a powerful tool for probing plasmas in very compact magnetic traps such as Electron Cyclotron Resonance Ion Sources and for in-plasma β -radionuclides' decay studies.

INTRODUCTION

For the development of future ECRIS dedicated and advanced plasma diagnostic tools will be crucial. It is particularly necessary to implement non-intrusive diagnostics for probing electron density and temperatures. Among the others, a special mention is worth by Optical Emission Spectroscopy (OES) [1,2] and X-rays spectroscopy (XRS) [3] which however are both able to measure "partial" densities only, i.e. the ones related to specific energy domains.

Interferometry and microwave polarimetry (i.e., taking profit by magnetoplasma induced Faraday Rotation) are able to probe to whole plasma electron population, regardless of energy contents. These techniques have been fruitfully applied already in large-scale fusion reactors [4] and – regarding the Faraday rotation especially – are a standard in astrophysical plasmas, where used for either magnetic field and/or stellar density measurements [5].

However, the implementation of both the techniques in compact plasma traps, such as ECRIS, is still a challenge: the main constrain consists in the small-size of the plasma chamber and of the plasma itself if compared with the probing wavelength. The following condition holds: $\lambda_p \sim L_p \sim L_c$, being λ_p , L_p and L_c the probing signal wavelength, the plasma dimension and the plasma chamber length respectively. That means, interference effects due to the metallic walls of the plasma chamber cannot be neglected, and in some conditions even prevail. A specific approach has been therefore proposed and implemented, and a new double-purpose tool named VESPRI has been constructed: it is a microwave interfero-polarimeter suitable for total electron density measurements in ECRIS plasmas. At least for the interferometry in compact devices, data are already published elsewhere [6].

Hereby we show the data coming from polarimetric measurements (preliminary dataset are already commented in the paper [7]) that have allowed the first line-integrated measurement of plasma density via Faraday-rotation in ECRISs.

EXPERIMENTAL SETUP

The measurement of the magnetoplasma induced rotation of the polarization plane in the VESPRI setup has been based on broadband waveguide OrthoModeTransducers (OMTs) system (see Fig. 1).

The turnstile junction OMTs enable the TE₁₁ mode from the circular input port of the conical horn antennas to be split equally into the two single-mode rectangular waveguide outputs TE₁₀ modes, thus obtaining a return loss better than 13 dB in the 18÷26.5 GHz band. One of the two OMTs can rotate at $\pm 95^\circ$, with an angular precision of 0.05° , handling up to 100 W of microwave power (but the probing signal was below 100 mW due to the high sensitivity of the power probe). The OMTs were inserted along the plasma leg, upstream and downstream to the emitting/receiving antennas.

*Work has received funding from 5th Nat. Committee of INFN, under the grants VESPRI and PANDORA

[†] naselli@lns.infn.it

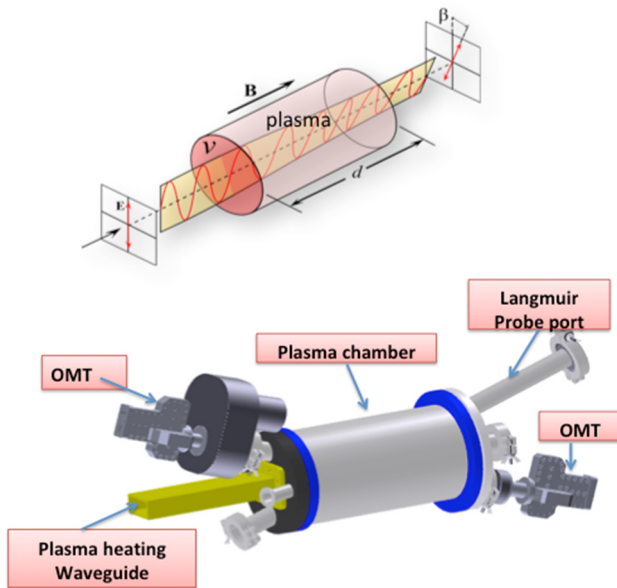


Figure 1: Up – simplified sketch of Faraday rotation induced by the magnetoplasma. Down – Drawing of the Orthomode transducers used as microwave-polarimeters connected to the plasma chamber. A Langmuir probe was simultaneously used to compare density data.

The angle of the rotating OMT is changed (via in-vacuum rotatable joint connection in circular waveguide standard) in order to minimize its received power on the Cross-polar port. In free-space and empty cavity case (i.e., if the cavity effects are negligible), the angle fulfilling cross-polarisation condition corresponds to $\theta = \theta_{\min} = 90^\circ$.

The plasma changes the cross-polarization condition such as $\theta_{\min}^p = \theta_F + \theta_{\min}$, due to the additional depolarization angle θ_F induced by the Faraday effect on the propagating wave.

UNDERLYING THEORY

The derived Faraday's angle can then correlated to magnetoplasma parameters through the well-known relation:

$$\vartheta_F = \frac{\omega}{c} \frac{1}{2} \left(\sqrt{1 - \frac{\omega_p^2}{\omega(\omega - \omega_g)}} - \sqrt{1 - \frac{\omega_p^2}{\omega(\omega + \omega_g)}} \right) = \frac{k'_0 - k''_0}{2} \quad (1)$$

The pulsations appearing in Eq. (1) assume the usual meaning of pumping, gyro and plasma frequencies, while c is the speed of light.

The Faraday angle dependence on such pulsations can be highly simplified in case $\omega \gg \omega_p$ and $\omega \gg \omega_g$, assuming the famous form of the so-called “lambda-squared” law:

$$\vartheta_F = \frac{1}{2c} \left(\frac{\omega_p}{\omega} \right)^2 \omega_g = \frac{e^3 \lambda_p^2 B_0 n_e}{8\pi^2 c^3 m_e^2 \epsilon_0} \quad (2)$$

Equation (2) shows that once known B_0 , i.e. the induction of the externally applied magnetostatic field, is possible to univocally derive the plasma density from a linearized fitting procedure θ_F vs. λ^2 . Actually, for probing microwaves in the range $18 \div 30$ GHz, that is the one of our setup, only the condition $\omega \gg \omega_g$ applies, since the expected densities (order of 10^{12} cm $^{-3}$) violate the second assumption. Hence, Eq. (1) has been developed in series of ω/ω_p , truncating the series at the 4th term:

$$\vartheta_F = \frac{q_e^3}{2cm_e^2\epsilon_0} \int_0^L \left(\frac{nB}{\omega^2} + \frac{q_e^2 n^2 B}{m_e \epsilon_0 2\omega^4} + \frac{q_e^4 n^3 B}{m_e^2 \epsilon_0^2 4\omega^6} + \frac{q_e^6 n^4 B}{2cm_e^3 \epsilon_0^3 6\omega^8} \right) dx \quad (3)$$

The integral stands for the variation of n and B along the line of sight. In general, in ECRIS-like systems, B profile is well-known, while $n(l)$ can be argued depending on the magnetic structure (flat- B field, Simple Mirror, B-minimum) with reasonable precision. Figure 2 shows how big is the difference between the Faraday's law and its approximation, at a density of $3 \cdot 10^{12}$ cm $^{-3}$.

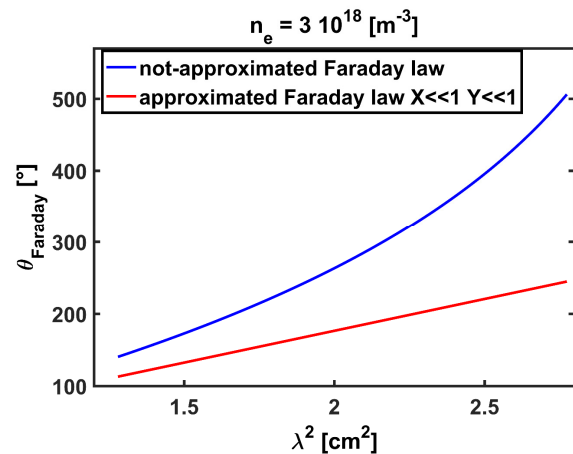


Figure 2: Calculated trends of the expected Faraday angles for approximated and not-approximated Faraday law as a function of λ^2 .

DATA ANALYSIS STRATEGY

Due to the already mentioned cavity-induced effects, which superimpose to the straight signal going from the emitting to the receiving antenna, acquired data vs. frequency (or, equivalently, versus the wavelength) must be accurately depurated by spurious components. In particular, we want that the polarization measurements occur more

Content from this work may be used under the terms of the CC BY 3.0 licence (© 2018). Any distribution of this work must maintain attribution to the author(s), title of the work, publisher, and DOI.

or less as in free-space, where co and cross polarization conditions are well-known, following the Malus' law:

$$P = P_0 \cos^2 \vartheta \quad (4)$$

The frequency scan proceeds from 18 to 26.5 GHz, at steps of 0.6 MHz, thus collecting more than 13000 single frequencies. An analysis routine has been implemented in order to scan the dataset, applying Eq. (4) in terms of statistical agreement to the linearized relation P vs. $\cos^2 \vartheta$.

The filtering consists in eliminating only those frequencies which are dominated by cavity modes and do not fulfil Eq. (4) condition when varying the reciprocal orientation of OMTs. This filtering is practically applied via the statistical correlation parameter R . The higher is the request in terms of R (i.e., for R closer and closer to 1) the lower is the number of frequencies that can be selected. Typically, R parameters > 0.99 were needed in order to obtain datasets with good "signal-over-noise" ratios.

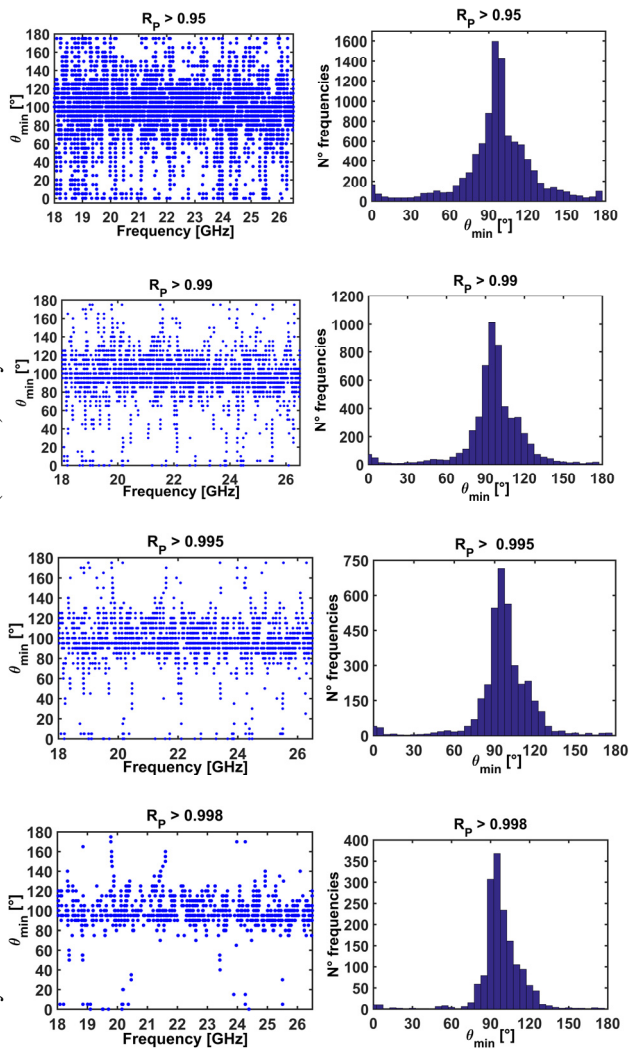


Figure 3: The sequence of plots (scatter and histograms types) represent the selected frequencies dataset at increasing "filtering strength", i.e. for R -parameters closer and closer to 1.

Figure 3 displays a sequence of in-cavity experimentally obtained data sets: the cross-polarization angle (here named θ_{\min}) is measured along the whole frequency scan. Only the frequencies fulfilling Malus law are plotted, at increasing R -correlation parameter. The ideal case corresponding to free-space configuration is when the angle for minimum transmission (i.e., the cross-polar condition) is exactly equal to 90° . Cavity effects, introduce waves scattering then implying a broad distribution of angles for which the cross-polarization condition occurs.

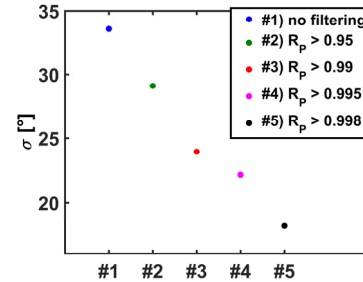


Figure 4: Standard deviation of the histograms in Fig. 3: at increasing R the angular dispersion drops.

The final number of frequencies was a compromise between accuracy of the filtering and statistical consistence of the dataset. From each histogram of Fig. 3 a relative standard deviation can be calculated, as shown in Fig. 4: it somehow relates to the data spread, hence with the accuracy by which the rotation angle can be measured.

EXPERIMENTAL BENCHMARKS IN EMPTY PLASMA CHAMBER

In order to verify that the device is able to distinguish among different polarization angles inside the resonant cavity, we implemented a benchmark setup based on a microwave-wire grid polarizer, according to the sketch of Fig. 5.

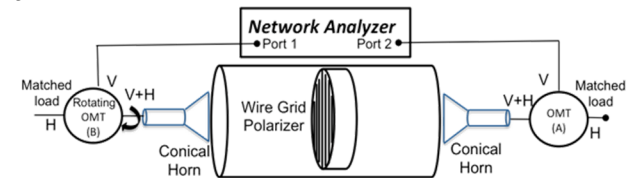


Figure 5: sketch of the experimental setup where a wire-grid microwave polarized has been placed inside the plasma chamber.

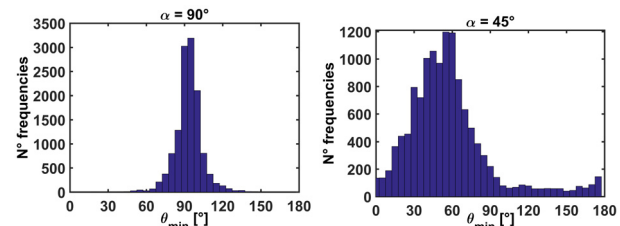


Figure 6: Histograms of minimum-angles in case of polarizer placed inside the plasma chamber, at two different angles. Data show that the device is able to detect a variation of the polarization axis.

The polarizer was placed inside the plasma chamber, around the midplane. The polarizer almost completely fits inside the chamber diameter, and its polarization angle α was rotated at steps of 15° . For sake of brevity, here we present results for 45° and 90° . Figure 6 summarizes the results for these two angles. It is already clear that despite the broad data dispersion due to the in-cavity scattering, anyway the system is able to detect the different polarizer angle. A more quantitative analysis can be carried out.

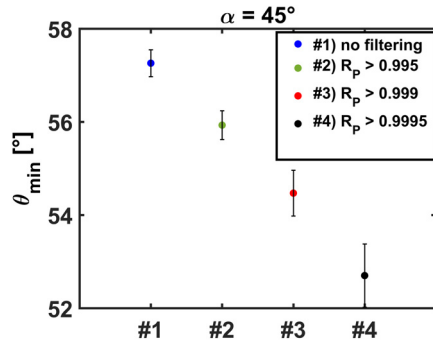


Figure 7: Estimation of θ_{\min} in case of benchmark measurements with the microwave polarizer: data show that at increasing “filtering-strength” in terms of the R parameter, data tend to the expected value.

The results of the quantitative analysis are summarized in Fig. 7. The plot reports the average value of θ_{\min} as coming out from four datasets obtained at different “filtering-strength”, in terms of the correlation R parameter. The standard error is also plotted. It is clear that at increasing R the measured angle becomes closer and closer to the expectation angle $\alpha = 45^\circ$.

These results demonstrate that the developed method is robust in determining any change in the polarization plane of the wave propagating inside a resonant cavity, with a relative error in the order of 10%.

The following step was therefore to measure polarization angle variation induced by the magnetoplasma.

IN-PLASMA MEASUREMENTS

After the benchmark measurements the VESPRI polarimeter has been used for the first time to detect magnetoplasma induced rotation of the probing wave polarization plane. The main results are illustrated in the three plots of Fig. 8.

Each points in Figs. 8a,b,c is the result of an average in θ_{\min} obtained in a given Δf (or, equivalently, $\Delta\lambda$) bin. The bin size is a compromise between the minimal number of points needed for a good best-fit calculation, and the minimal amount of data in a given bin to have a significant estimation of the $\langle\theta_{\min}\rangle$ with its own error-bar. The three plots allow a direct comparison of what happens in three different situations:

- (a) *free space*: the θ_{\min} averages at 90° (standard cross polar configuration), and data have a very low fluctuation around the expectation value; the line corresponds to the attempted correlation to the 4th order truncated Faraday law (Eq. (3)), showing no

- (b) *empty cavity*: the θ_{\min} averages again at 90° (standard cross polar configuration), but now data show wide fluctuations around the expectation value, due to the scattering introduced by the cavity; now the R correlating to Eq. (3) is -0.0094 , again supporting uncorrelated hypothesis for vacuum propagation, despite the presence of the cavity;
- (c) *In-plasma*: in this case, a N plasma has been excited at $1.5 \cdot 10^{-4}$ mbar, using 130 W of microwave power. Now a trend of the θ_{\min} vs. λ^2 is clearly evident. The correlation to the Faraday law is confirmed by the R parameter, being $R=0.88$. Considering the number of points in the best-fit procedure, tables for statistical consistency say this value provides a “very high” probability of dataset correlation to the given mathematical law.

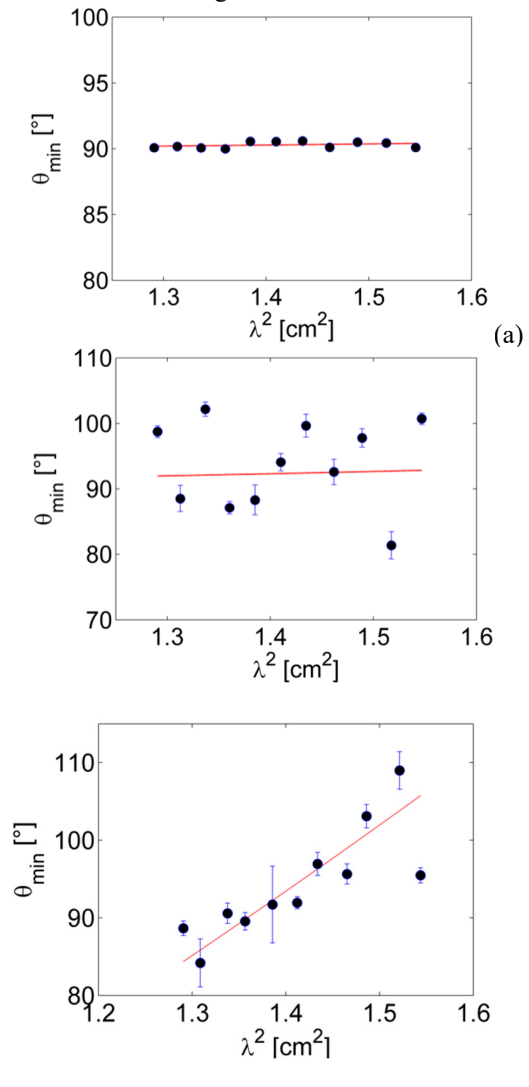


Figure 8: Sequence of plots regarding the θ_{\min} vs. λ^2 when using the 4th term truncated Faraday law (Eq. (3)), in case of: (a) free-space measurements; (b) measurements in an empty plasma chamber; (c) measurements in presence of the magnetoplasma.

Content from this work may be used under the terms of the CC BY 3.0 licence (© 2018). Any distribution of this work must maintain attribution to the author(s), title of the work, publisher, and DOI.

Using Eq. (3) is therefore possible to extrapolate the value of the electron density as a free-parameter of the best fit procedure. The result is displayed in Fig. 9.

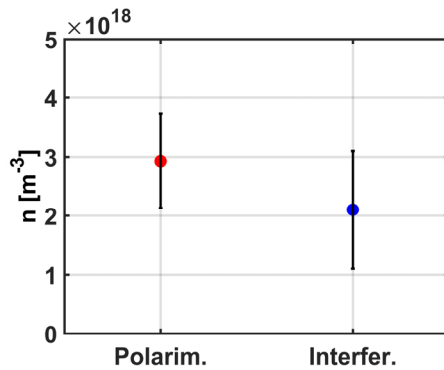


Figure 9: Estimation of the electron density from the best-fit procedure on the dataset of Fig. 8c, according to the equation 3. The result obtained by interferometric measurements [6] is also reported, for comparison.

The polarimetric measurement amounts to $(2.93 \pm 0.8) \cdot 10^{18} \text{ m}^{-3}$, that is in good agreement with interferometric estimations $(2.1 \pm 1.0) \cdot 10^{18} \text{ m}^{-3}$. The special analysis method has also permitted to reduce the relative errors. Langmuir probes measurements in identical physical conditions have been performed and give a density a factor 4 lower: possible explanations have been discussed in details in [6].

CONCLUSIONS

In this paper we have presented the first results concerning the Faraday-rotation measurements in compact plasma traps such as ECR Ion Sources. The developed analysis procedure has permitted to estimate the rotation angle of the probing wave polarization plane, then correlating it to the plasma density value, that can be estimated with a relative error of around 25%. The method opens new perspectives about non-intrusive plasma diagnostics with the goal to improve the tuning of existing machines and the design of the new ones.

REFERENCES

- [1] G. Castro, M. Mazzaglia, D. Nicolosi, D. Mascali, R. Reitano, L. Celona, O. Leonardi, F. Leone, E. Naselli, L. Neri, G. Torrissi, S. Gammino and B. Zaniol, "Application of Optical Emission Spectroscopy to high current proton sources", *this conf. proceeding* (2018)
- [2] Kronholm R, Kalvas T, Koivisto H, Tarvainen O. "Spectroscopic method to study low charge state ion and cold electron population in ECRIS plasma". *Rev Sci Instrum.*, vol 89(4), p. 043506, (2018).
- [3] D. Mascali, L. Celona, F. Maimone, J. Maeder, G. Castro, F.P. Romano, A. Musumarra, C. Altana, C. Caliri, G. Torrissi, L. Neri, S. Gammino, K. Tinschert, K. P. Spaedtke, J. Rossbach, R. Lang and G. Ciavola. "X-ray spectroscopy of warm and hot electron components in the CAPRICE source plasma at EIS testbench at GSI", *Rev. Sci. Instrum.* vol. 85, p. 02A956, (2014)
- [4] E. E. Scime, R. F. Boivin, J. L. Kline, and M. M. Balkey, *Rev. Sci. Instrum.* vol. 72, p. 1672 (2000)
- [5] P.S. Ramkumar and A.A. Deshpande, "Determination of Linear Polarization and Faraday Rotation of Pulsar Signals from Spectral Intensity Modulation", *J. Astrophys. Astr.*, vol. 20, pp. 37-50, (1999)
- [6] D. Mascali, G. Torrissi, O. Leonardi, G. Sorbello, G. Castro, L. G. Celona, R. Miracoli, R. Agnello, and S. Gammino, "The first measurement of plasma density in an ECRIS-like device by means of a frequency-sweep microwave interferometer", *Review of Scientific Instruments*, vol. 87, p. 095109 (2016)
- [7] G. Torrissi, E. Naselli, D. Mascali, G. Castro, L. Celona, G. Sorbello, and S. Gammino, "A new interferometric/polarimetric setup for plasma density measurements in compact microwave-based Ion Sources", *Publishing Ltd and Sissa Medialab Journal of Instrumentation*, vol. 12, (2017)

RESULTS OF THE OPTICAL EMISSION SPECTROSCOPY DIAGNOSTICS OF THE ESS PROTON SOURCE*

G. Castro[†], M. Mazzaglia, D. Mascali, R. Reitano¹, L. Celona, E. Naselli¹, L. Neri, G. Torrisi and S. Gammino,
INFN – Laboratori Nazionali del Sud, Catania, Italy
¹also at Università degli studi di Catania, Catania, Italy

Abstract

The evaluation of the electron density and proton fraction of hydrogen plasmas has a relevant importance for plasma traps used as sources of intense proton, H₂⁺ or H₃⁺ beams. Optical Emission Spectroscopy (OES) enables to evaluate simultaneously and on-line the H/H₂ relative abundances together with plasma and electron temperature. In this work, the experimental results of the OES measurements on the Proton Source of the European Spallation Source plasma has been related to the properties of the ion beam extracted by the source (proton fraction and beam intensity, in particular). Benefit of the diagnostics and the further improvements foreseen in next future will be highlighted.

INTRODUCTION

The Proton Source for the European Spallation Source (PS-ESS) is a Microwave Discharge Ion Source (MDIS) operating at 2.45 GHz microwave frequency for high intensity proton beam generation. PS-ESS has been designed and assembled at INFN-LNS as injector for the European Spallation Source (PS-ESS); it produces pulsed proton beams (14 Hz, 2.84 ms puls) from 40 mA to 90 mA nominal current, at 75 keV energy and 2.25 π mm mrad maximum normalized emittance [1]. The source has been characterized by means of a Faraday Cup, an Emittance Measurement Unit and a Doppler shift measurement unit. The standard beam diagnostics allows the measurement of the beam characteristics (as the extracted current, the species fraction and the RMS emittance). However, the beam properties depend on the characteristics of the plasma which generates it. Good performances of a proton source are obtained only if a homogenous, stable, dense and cold plasma is generated within the proton source. Therefore, the knowledge of the plasma parameters represents a fundamental information for the full comprehension of the source performances, but also an essential information for any further improvement of proton sources and ECRIS.

Among the different plasma diagnostics tools, Optical Emission Spectroscopy (OES) is the only diagnostics which is not affected by the plasma generation and does not affects the plasma itself during measurements. Since OES requires just the light emitted by the plasma, a small quartz window is sufficient for the evaluation of the plasma parameters and of the relative abundances of the neutral species. In this work, the results of the OES characterization

of PS-ESS, performed in the best machine operative conditions, will be described.

EXPERIMENTAL SET-UP

Figure 1 shows a schematic diagram of the PS-ESS OES experimental set-up. It includes the RF power injection system, the three magnetic coils and the OES diagnostics system. PS-ESS is fed by microwaves at 2.45 GHz generated by a Magnetron, while the magnetic field is obtained by means of three solenoids which permit different magnetic configurations, from off-resonance configurations to simple mirror or magnetic beach (see Fig. 2). In this work, OES measurements has been carried out in best PS-ESS experimental performances, obtained in flat magnetic field configuration. The OES diagnostics system consists of a spectrometer ImSpector V8E, coupled to an ACA2040 CMOS camera. The spectrometer resolution is 2 nm and it is sensitive in the spectral range of 380 - 1000 nm. The whole system is connected to the PS-ESS by means of a 1500 μm diameter fiberglass that is, in turn, properly connected to a quartz window, which “looks” towards the centre of the PS-SS plasma chamber.

The whole OES experimental set-up has been properly calibrated and commissioned by using another plasma device, the Flexible Plasma Trap [2]. Preliminary measurements has been already published in reference [3]. The experimental measurements have been carried out at 2.7·10⁻⁵ mbar pressure, measured in low energy beam transport. Simulations performed by Comsol permitted to evaluate the pressure as ~ 3·10⁻³ mbar within the plasma chamber. Microwave power has been increased from 120 to 1200 W.

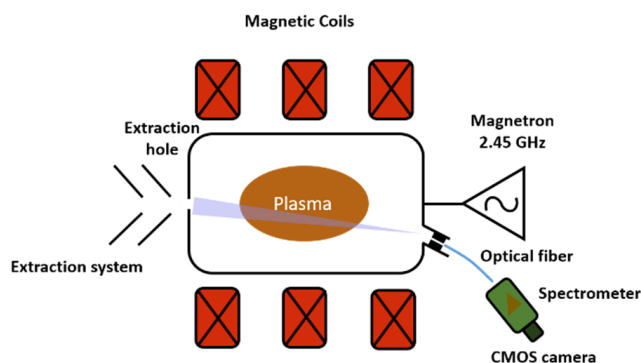


Figure 1: Schematic of the PS-ESS experimental setup at the INFN-LNS.

* Work supported by ESS-Miur and Pandora

[†] Castrog@lns.infn.it

Content from this work may be used under the terms of the CC BY 3.0 licence (© 2018). Any distribution of this work must maintain attribution to the author(s), title of the work, publisher, and DOI.

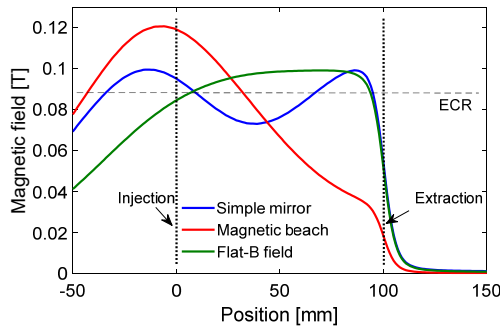


Figure 2: Magnetic field profiles that can be generated by the PS-ESS.

The analysis method is based on the line-ratio method, well-described in references [4-5]. Spectroscopic measurements have been carried out for the Balmer series of atomic hydrogen (H_α to H_γ) as well as for the Fulcher- α transition of the H_2 molecule ($d3\Pi_u \rightarrow a3\Sigma_u^+$). We compared experimental results with theoretical line ratios obtained by applying a collisional radiative (CR) model. In particular, we compared experimental and theoretical H_β/H_γ and H_α/H_β line ratios to simultaneously determine electron density and temperature. Relative abundance between atomic and molecular hydrogen n_H/n_{H_2} ratio can be determined by comparing the $H_\gamma/H_{\text{Fulch}}$ with theoretical data from CR model.

EXPERIMENTAL RESULTS

Figure 3 shows the electron density as a function of the microwave power. Electron density increases with RF power, but it saturates around $1 \cdot 10^{18} \text{ m}^{-3}$ above 800 W. OES density is around 10 times the density cut-off at 2.45 GHz, that is $8.75 \cdot 10^{16} \text{ m}^{-3}$. This implies that probably heating mechanisms other than Electron cyclotron resonance contribute to the plasma heating. The electron temperature is shown in Fig. 4. It lies in the range expected for proton sources and measured by means of other diagnostics ($\approx 10 \text{ eV}$). In particular, electron temperature shows a slightly decreasing trend of electron temperature with microwave power. This trend has been already found in other measurements performed by Langmuir probe [6], and it is probably due to the gradual decrease of the mean free path of electrons during the acceleration process as the density becomes higher and higher.

Finally, Fig. 5 shows the n_H/n_{H_2} ratio as a function of the microwaves' power. n_H/n_{H_2} is around 0.5 at lower power and approaches 2 around 800 W. Unfortunately, it has been not possible to determine the n_H/n_{H_2} ratio above 800 W because the signal to noise ratio of the Fulcher band (necessary for evaluate n_H/n_{H_2}) becomes too low and a huge experimental error arises.

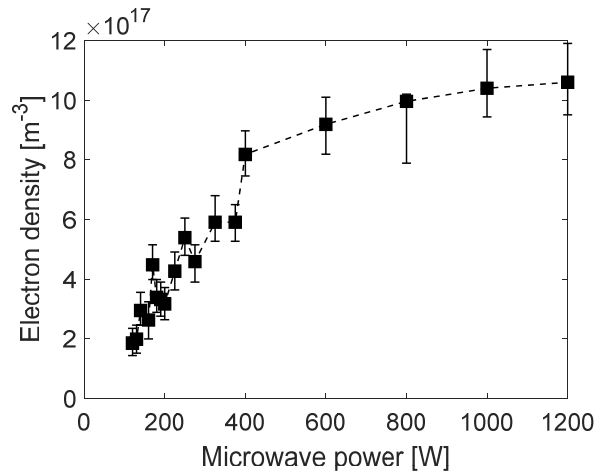


Figure 3: OES electron density as a function of the microwaves' power.

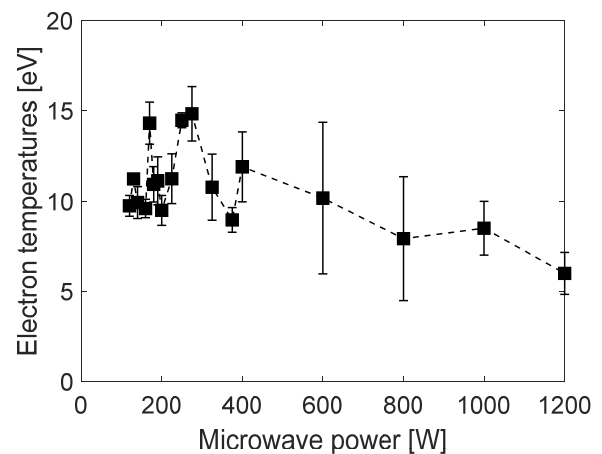


Figure 4: OES electron temperature as a function of the microwaves' power.

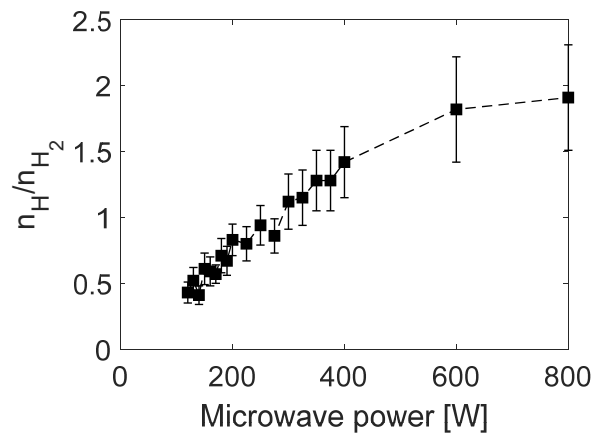


Figure 5: n_H/n_{H_2} ratio as a function of the microwaves' power.

CORRELATION BETWEEN PLASMA AND BEAM PARAMETERS

One of the goal of the current research in plasma physics applied to ECRIS is to relate the plasma parameters to the beam parameters. The commonly used approach is to find a solution of the particle balance equations in a plasma [6-8]. The exact solution of the system of balance equation would enable to foresee the properties of the extracted beam. However, the solution of the balance equations require the knowledge of a huge number of parameters, as the properties of the chamber surface, diffusion coefficients in plasma, motion in the sheath and a lot of other parameters which make balance equations approach very difficult to be practically applied.

An option to reduce the number of balance equations, simplifying the approach, is to use the plasma parameters calculated by OES as input parameters. The simultaneous knowledge of n_H/n_{H^2} and neutral pressure permits to estimate the absolute neutral population within the plasma chamber. Furthermore, electron density and temperature permit to evaluate the reaction rate coefficients of the main reactions occurring in a hydrogen plasma. In this way, balance equations can be reduced to 4 equations in 4 unknowns, namely the H^+ , H_2^+ and H_3^+ density and the ion

confinement time. Once properly solved, the balance equations give information about the density of the different charged particle in the plasma, and therefore they give an evaluation of the properties of the extracted beam. Unfortunately, two free parameters must be taken into account during the study, the ion and neutral temperature, whose values has been fixed on the basis of the available literature. Figure 6 shows the cross sections of the main reaction taken into account to solve the reduced balance equations in a hydrogen plasma. Cross sections lower than 10^{-18} cm^2 have been neglected.

The results show a very strong correlation between the estimation of the reduced balance equations and experimental measurements of the extracted beam performed by means of a Doppler shift measurement unit and of an ACCT.

Figure 7 shows the comparison between the extracted current measured by the ACCT and the extracted current expected after solving the reduced balance equations. As it is evident, estimation and measurements are very close each other, this representing a first benchmark of the used approach. More details about the procedure of analysis together with a general discussion about correlation between plasma and beam parameter will be given in reference [9].

- $\sigma_1: H_2 + e \rightarrow H + H + e$
- $\sigma_2: H_2 + e \rightarrow H_2^+ + 2e$
- $\sigma_3: H_2 + e \rightarrow H^+ + H + 2e$
- $\sigma_4: H_2^+ + e \rightarrow H^+ + H + 2e$
- $\sigma_5: H_2^+ + e \rightarrow H^+ + H^+ + 2e$
- $\sigma_6: H + e \rightarrow H^+ + 2e$
- $\sigma_7: H + e \rightarrow H^{2p} + e$
- $\sigma_8: H + e \rightarrow H^{2s} + e$
- $\sigma_9: H^{2s} + e \rightarrow H^+ + e$
- $\sigma_{10}: H_2^+ + e \rightarrow H + H$
- $\sigma_{11}: H_2^+ + H_2 \rightarrow H_3^+ + H$
- $\sigma_{12}: H_3^+ + e \rightarrow H^+ + 2H$
- $\sigma_{13}: H_3^+ + e \rightarrow 3H$

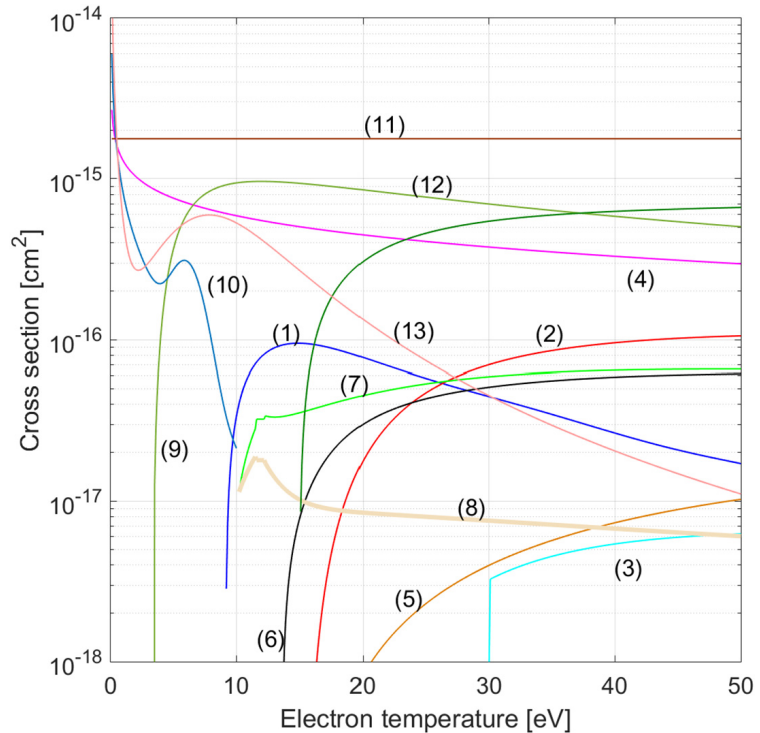


Figure 6: Cross sections of the main reactions occurring in a hydrogen plasma. σ_{11} depends only on ion temperature. σ_1 has been calculated for ion temperature equal to 0.1 eV)

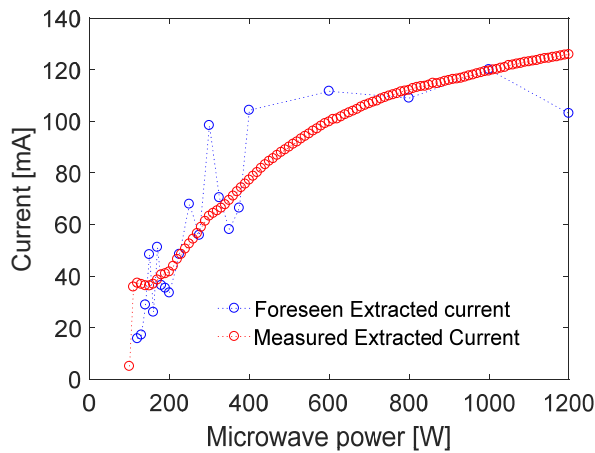


Figure 7: Comparison between extracted current measured by the ACCT and extracted current.

In the next months, the OES diagnostics equipment will be further enhanced after the commissioning of two different instruments for OES. The first one is a 15 μm monochromator detector. Its resolution is enough to characterize molecular rotational temperature and to obtain higher resolution emission lines, needed for extending OES to other plasmas. The second one is SARG, a powerful spectropolarimeter formerly installed at TNG, Telescopio Nazionale Galileo, Canary Islands. SARG allows to reach very high resolution: $R = 160:000$ in the range: 370-900 nm, suitable for ion temperature measurements and/or on-line discrimination of the ionisation states of the ions inside the plasma. First results are expected within the end of this years.

ACKNOWLEDGEMENTS

The support of the 5th National Committee of INFN through the ESS-MIUR experiment is gratefully acknowledged. The contribution of A. Miraglia, F. Chines and of all INFN-LNS mechanic staff is warmly appreciated. The contributions and suggestions of U. Fantz and S. Briefi has been essential for the present work.

REFERENCES

- [1] L. Neri *et al.*, *Journal of Physics*, vol. 874, p. 012037, 2017.
- [2] S. Gammino *et al.*, *Journal of Instrum.*, vol.12, p. P07027, 2017.
- [3] Castro *et al.*, *IOP Conf. Series: Journal of Physics: Conf. Series*, vol. 874 p. 012033 2017
- [4] U. Fantz *et al.*, *Nuclear Fusion*, vol. 46, p. S297, 2006.
- [5] P. Roychowdhury and D. P. Chakravarthy, *Rev. Scie. Instrum.*, vol. 80, p. 123305, 2009.
- [6] H. Zhang, "Ion Sources" (Science Press Beijing and Springer, 1999.
- [7] I. Mendez *et al.*, *J. Phys. Chem. A*, vol. 110, p. 6060, 2006.
- [8] T. Wauters *et al.*, *Plasma Phys. Control. Fusion*, vol. 53, p. 125003, 2011.
- [9] G. Castro *et al.*, "Optical Emission Spectroscopy for Hydrogen plasmas", *paper in preparation*.

CHARACTERIZATION OF ECR PLASMA BY MEANS OF RADIAL AND AXIAL X-RAY DIAGNOSTICS

R. Miracoli[†], ESS Bilbao, Poligono Ugaldeguren III, Pol. A, 7B. 48170 Zamudio, Spain
 G. Castro, L. Celona, S. Gammino, D. Mascali, M. Mazzaglia, E. Naselli¹, G. Torrìsi
 INFN-LNS, Via S. Sofia 62, 95123, Catania, Italy

¹ Università degli studi di Catania, Dipartimento di Fisica e Astronomia,
 Via S. Sofia 64, 95123, Catania, Italy

Abstract

This work presents the X-ray characterization of the plasma generated in a simple mirror axis symmetric trap as a function of the magnetic field profile. A Si-Pin detector has been used to characterize warm electron population in axial and radial directions at two different operating frequencies: 4.1 GHz and 6.8 GHz. Moreover, the hot electrons emitted in axial direction has been measured by means of a HyperPure Germanium (HpGe) detector. Results show that X-ray emission is not homogenous and its homogeneity and temperature depends strongly on the magnetic field profile.

INTRODUCTION

The electron cyclotron resonance ion sources (ECRIS) are mainly used to produce highly charged ions currents for accelerators, nuclear physics research and industrial applications. In recent years many studies have been made in order to understand better the wave-to-plasma interactions that produce plasma instability [1], in particular about the non-linear response of electron heating to pumping wave frequency and anisotropy in plasma density and electron energy distribution function [2,3]. It is observed that B_{min} value (the minimum value in the mid-plane of the plasma chamber), changes the gradient (described here in terms of B_{min}/B_{ECR} ratio) of the magnetic field close to ECR surface. The moderate gradient, obtained for higher B_{min} , increases the ECR heating efficiency and the electron temperature in the plasma. Moreover, it is noted that in a moderate gradient regime the plasmas become unstable and can generate intense emissions of fluxes of bremsstrahlung and microwaves. In this paper we wanted to show the characterization of the Flexible Plasma Trap (FPT) through measurements of x-rays spectra, acquired by HyperPure Germanium (HpGe) and Si-Pin detectors. X-rays were recorded in both the radial and axial directions for different magnetic field profiles and frequency heating.

EXPERIMENTAL SET-UP

FPT is a test bench for plasma diagnostics and development of new sources, operating at INFN-LNS [4]. Three solenoids generate different magnetic profiles

(off-resonance, simple mirror and magnetic beach configuration) and allow to tune the magnetic field value as a function of the frequency. FPT has three different microwave systems, one parallel and two perpendicular respect to the plasma chamber. The axial injection operates from 4 to 7 GHz. The signal is generated by a Rohde & Schwarz generator, amplified by a TWT and sent to the FPT by WRD350 waveguides. The axial microwave line is composed by a directional coupler and an isolator to protect the TWT from the reflected power. The perpendicular microwave launcher can work at 14 GHz and allow operating in double frequency (first and second frequency) mode [5]. The water-cooled copper plasma chamber is 260.1 mm length and its inner diameter is about 82 mm. A stainless-steel vacuum chamber is connected to the plasma chamber to host the vacuum system and the diagnostic tools. Figure 1 shows the schematic drawing of the FPT and the diagnostics.

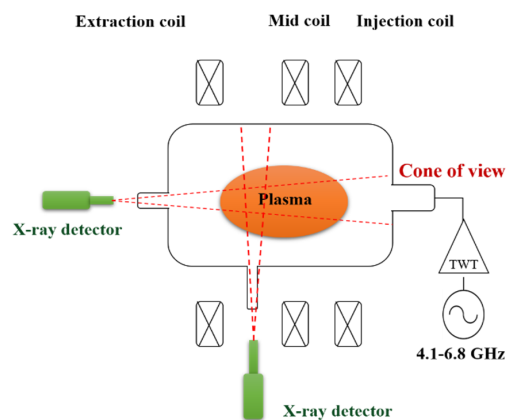


Figure 1: Schematic drawing of the FPT and of x-rays detectors used during the experimental campaign.

High energy X radiation was detected by a HpGe, located on the axial port of the vacuum chamber, the detector was used for monitoring the x-rays generated by the high energy electrons, from inside the plasma or when they hit the vacuum vessel walls. The HpGe consists of a 15 mm thick, 20 cm² crystal protected by a 0.3 mm thick Be window. Its resolution at 122 keV is 0.61 keV. The detector is shielded with lead blocks of 2 cm thickness and $\phi=1$ mm to avoid detecting x-rays scattered from the environmental material. The HpGe detects the radiation

[†] rmiracoli@essbilbao.org

Content from this work may be used under the terms of the CC BY 3.0 licence (© 2018). Any distribution of this work must maintain attribution to the author(s), title of the work, publisher, and DOI.

that pass mostly through the collimator of the vacuum vessel.

In the second part of the investigation two Si-Pin detectors (XR-100CR, AMPTEK) were used, one placed on the axial port of the vacuum chamber and the other on the radial port of the plasma chamber. Their resolution at 5.9 keV are about 200 eV and the Be window has a thickness of 1 mm. Both detectors are used for monitoring the x-rays generated by electrons from a few keV to several tens of keV.

All raw data have been corrected for detector intrinsic efficiencies, which include the correction for the beryllium window, the Kapton foil for vacuum break, and the air attenuation. Once the correction is made it is possible to calculate the spectral temperature, T_e , by fitting a straight line to experimental data in a semilogarithmic plot over a selected range of energy [6]. T_e can be obtained from the inverse of the line slope and is used to determine an estimate for the mean energy of the hot electrons. The x-rays are collimated by a lead cylinder with a hole of $\phi = 1$ mm and 6 cm in length.

EXPERIMENTAL RESULTS

In the first part of the experiment we used the HPGe detector, to investigate how the variation of the magnetic field gradient can affect the rate of axial bremsstrahlung and the electron distribution of energy. For the two-heating frequencies: 4.1 and 6.83 GHz we have fixed the current of the injection and extraction coils and have set the current of the mid coil to shift the B_{min}/B_{ECR} ratio from 0.56 to 1.02. Figure 2 shows some of the magnetic configurations that we used at 6.8 GHz. All data were recorded at a power level of 80 W and typical operating pressures in vacuum chamber are about $8 \cdot 10^{-5}$ mbar.

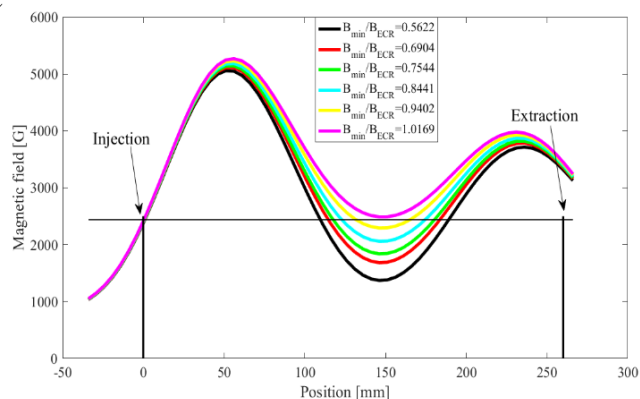


Figure 2: Simple mirror configurations used at 6.8 GHz as heating frequency. The injection and extraction coil currents have been fixed at 440 and 441 A respectively, while the mid coil has been changed from -88 A to 60 A. The change in mid coil current allowed to modify the B_{min}/B_{ECR} ratio along the plasma chamber axis from 0.56 to 1.02. ($B_{ECR} = 2440$ G at 6.8 GHz).

The trend of the rate (counts/s) detected by HPGe, at 6.8 GHz, is shown in Fig. 3, where two regions can be identified: for value B_{min}/B_{ECR} less than ~ 0.8 the x-ray

emitted is negligible while for B_{min}/B_{ECR} higher than ~ 0.8 the rate increases suddenly. At 4.1 GHz, instead, the magnitude of bremsstrahlung changes considerably for $B_{min}/B_{ECR} > 1$. For the first heating frequency value we have calculated the spectral temperature. The energy range where we did the linear fit to semilogarithmic bremsstrahlung spectra was about 50-75 keV for $B_{min}/B_{ECR} > 0.8$, and about 10-16 keV for $B_{min}/B_{ECR} < 0.8$. It was necessary to modify the energy range to calculate the electron temperature because the shape and the intensity of x-ray spectra are completely different in the two regions. In fact, a sharp increase of T_e is illustrated in Fig. 4, where the temperature shifts from 3 to 15 keV.

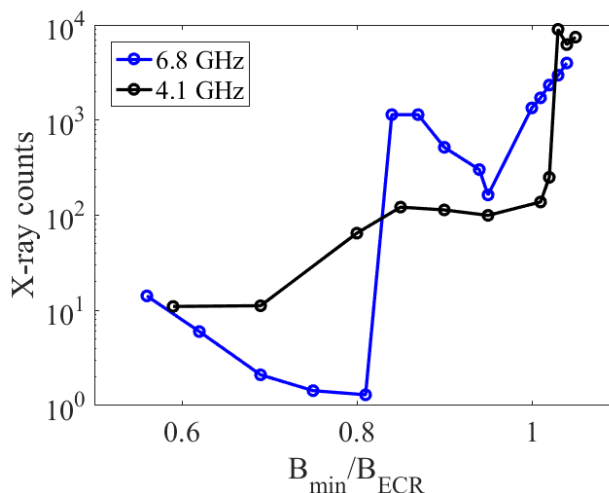


Figure 3: X-ray emission rate versus different simple mirror configurations. For both the frequencies, the pressure and the absorbed power are $8 \cdot 10^{-5}$ mbar and 80 W, respectively.

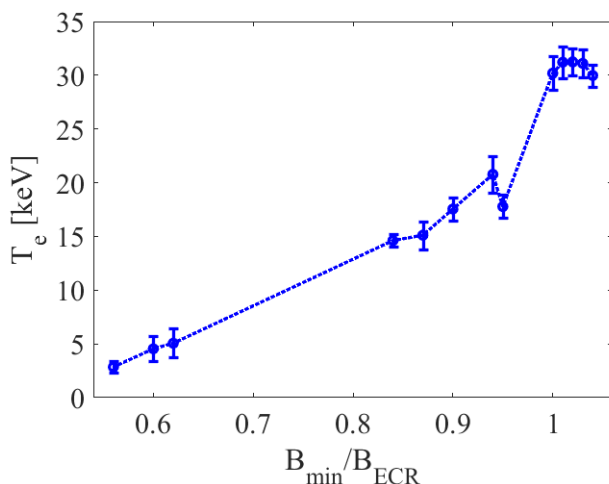


Figure 4: The dependence of T_e versus different simple mirror configurations.

The measurements continued by using the Si-Pin detectors to record radial and axial x-rays spectra, at a power level of 80 W and pressures of about $8 \cdot 10^{-5}$ mbar, as in the first part of the experiment. In Fig. 5 there is a direct comparison between the x-rays spectra measured at both

positions. Here again we wanted to investigate the effects on bremsstrahlung spectra by changing the magnetic field profile. The Bremsstrahlung of the axial x-rays spectrum are much greater than those radial, because the geometric efficiency for the two geometric systems is different. The radial spectrum has only the k_α of Ar (2.96 keV), k_α and k_β of Cu (8.05 keV and 8.9 keV respectively). Instead, in the axial spectrum we can see also k_α of Cr (5.41 keV) and Fe (6.40 keV), due to several scattering coming out from the stainless-steel diagnostic box. The peaks of Ar k_α are less affected from the bremsstrahlung produced outside the plasma chamber and the change in their intensity can be correlated mainly to two different geometric efficiencies (named solid angle and plasma volume).

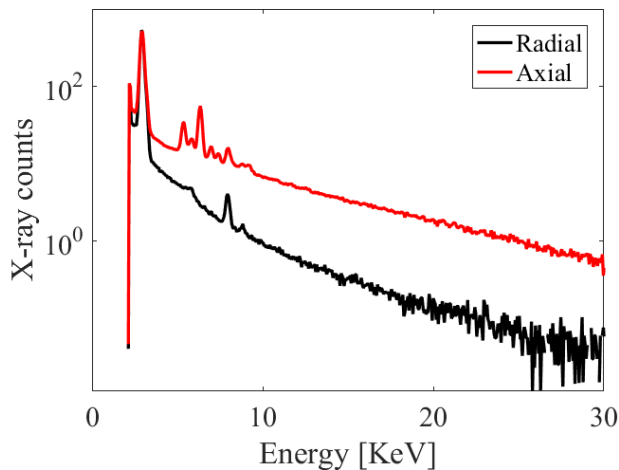


Figure 5: Typical x-rays spectra acquired by Si-Pin from axial and radial ports. Fluorescence lines of Ar and Cu are visible in both spectra. The pressure and the absorbed power are $8 \cdot 10^{-5}$ mbar and 80 W, respectively.

Measurements of Ar k_α intensity and x-rays in both the radial and axial directions, were performed by Kato [7], in an ECR multicharged ions source by changing the microwave power and pressure, but not the magnetic profiles. In Fig. 6 there is the trend of the $k\alpha_{Rad}/k\alpha_{Axl}$, the ratio between the intensity of Ar k_α emitted in radial and axial directions, as a function of B_{min}/B_{ECR} . Axial k_α intensity is about 3-4 times larger than it is in the radial direction and changes slightly from the different magnetic profiles, where each peak has been calculated after having subtracted the bremsstrahlung counts.

Afterwards we used the $k\alpha_{Rad}/k\alpha_{Axl}$ ratio that includes information about the solid angle and plasma volume to normalize the spectra. In Fig. 7, there is the trend of the bremsstrahlung rate detected by Si-Pin. As in the previous measurements shown in Fig. 3, the detectors in both directions reveal few counts for $B_{min}/B_{ECR} < 0.8$ but the rate suddenly increases for $B_{min}/B_{ECR} > 0.8$. In each emission region the axial rate is higher than the radial one. Figure 8 compares the spectral temperature obtained from the axial and radial ports in function of the magnetic profile. The energy range used to do the linear fit was about 10-14 keV for all the spectra. As in the Figs. 3 and 4 two regions can be identified: one with

$B_{min}/B_{ECR} < 0.8$ characterized by few x-ray counts and low temperature (< 5 keV), the other for $B_{min}/B_{ECR} > 0.8$ where plasmas generate strong bremsstrahlung emission and very energetic electrons.

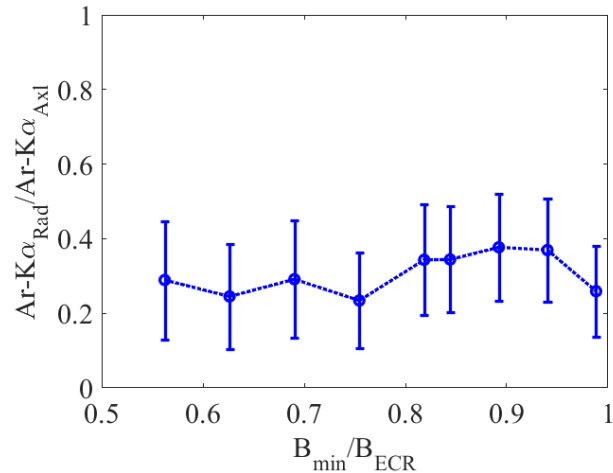


Figure 6: Trend of $k\alpha_{Rad}/k\alpha_{Axl}$ ratio versus different simple mirror configurations.

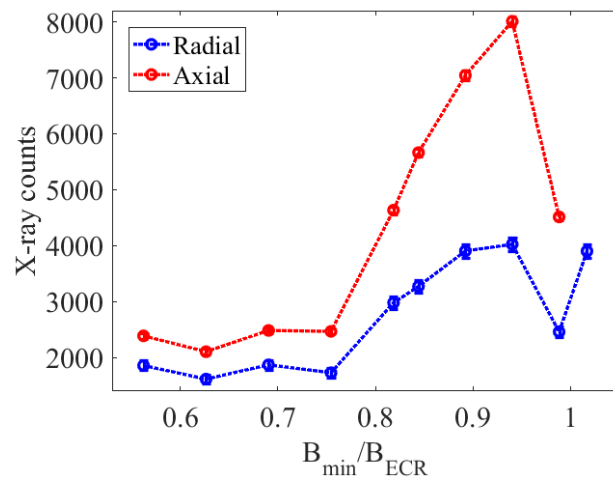


Figure 7: X-ray emission rate acquired from axial and radial ports versus different simple mirror configurations.

It has been observed in previous work [8,9], that the decrease of B_{min} improves the electron confinement, and so the source performance, but when B_{min} is increased ($B_{min}/B_{ECR} > 0.8$) non linear effects take place. The magnetic field gradient becomes lower in a large part of the ECR surface and the electrons gain more energy for a single crossing of the resonance. These hot electrons escape from the magnetic confinement and raise the rate of bremsstrahlung emission.

Moreover, the trends of the temperature measured in both the Si-Pin, make aware that for $B_{min}/B_{ECR} < 0.8$ the electron temperature are almost identical in axial and radial directions, and only in the second region, for $B_{min}/B_{ECR} > 0.8$, the axial T_e increases faster than radial T_e . The trend of the axial T_e obtained with the Si-Pin is similar to the one obtained from HPGe detector, in Fig. 4.

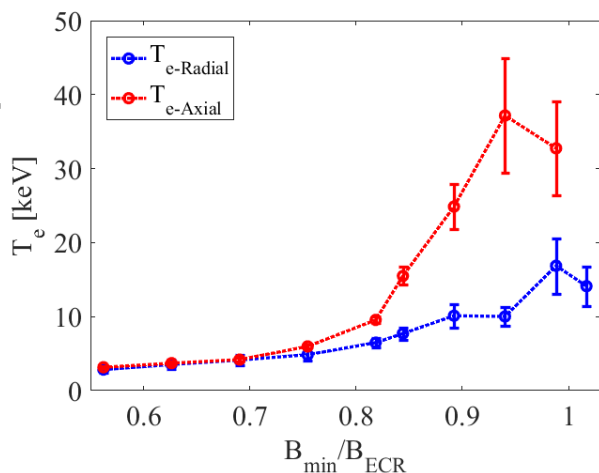


Figure 8: The dependence of T_e versus different simple mirror configurations.

CONCLUSIONS

A study of bremsstrahlung emission was carried out with the FPT at INFN-LNS. The experimental results demonstrate that the x-ray production and electron temperature depend on the magnetic configuration: when B_{min}/B_{ECR} ratio is ≈ 0.8 plasmas start to strong x-ray emission. Furthermore, while for $B_{min}/B_{ECR} < 0.8$ X ray emission show isotropic characteristics, when critical ratio is overcome, radial spectral temperature is lower than axial spectral temperature. The observed critical value of B_{min}/B_{ECR} is compatible with the passage from strong gradient to moderate gradient ECR regime [10]. Moreover, several fingerprints show that above the critical value, cyclotron instability may play an important role as already observed by other authors [2]. A dedicated paper will investigate the cyclotron instability emission revealed above the critical value of B_{min}/B_{ECR} . Further experimental measurements are also planned to characterize better the physic process that lead to the strong plasmas instabilities, with the aim to optimize the design of the future ions sources. FPT represents the better device to investigate the cyclotron instabilities since it allows the installation of different types of diagnostics, not only x-rays detectors, but also optical emission spectrometer [11], pin-hole camera and microwave interferometer [12,13] to characterize different range of the electron distribution function and the density of the whole plasma.

REFERENCES

[1] S. Gammino et al., “Considerations on the role of the magnetic field gradient in ECR ion sources and build-up of hot electron component”, *Plasma Sources Sci. and Technol.*, vol. 18, p. 045016, 2016, <https://doi.org/10.1088/0963-0252/18/4/045016>

[2] O. Tarvainen et al., “Beam current oscillations driven by cyclotron instabilities in a minimum-B electron cyclotron resonance ion source plasma”, *Plasma Sources Sci. and Technol.*, vol. 23, p. 025020, 2014, <https://doi.org/10.1088/0963-0252/23/2/025020>

[3] D. Mascali et al., “Electron cyclotron resonance ion source plasma characterization by X-ray spectroscopy and X-ray imaging”, *Rev. Sci. Instrum.*, vol. 87, p. 02A510, 2016, <https://doi.org/10.1063/1.4939201>

[4] S. Gammino et al., “The Flexible Plasma Trap (FPT) for the production of overdense plasmas”, *JINST*, vol. 12, p. P07027, 2017 <https://doi.org/10.1088/1748-0221/12/07/P07027>

[5] G. Torrisi et al., “A new launching scheme for ECR plasma based on two-waveguides-array”, *Microw. Opt. Technol. Lett.*, vol. 58, p. 2629, 2016, <https://doi.org/10.1002/mop.30117>

[6] D. Mascali et al., “X-ray spectroscopy of warm and hot electron components in the CAPRICE source plasma at EIS testbench at GSI”, *Rev. Sci. Instrum.*, vol. 85, p. 02A956, 2014, <https://doi.org/10.1063/1.4858115>

[7] Y. Kato et al., Pulse height analysis using Si-Pin diode of x-ray irradiated from a 2.45 GHz electron cyclotron resonance multicharged ion source, *Rev. Sci. Instrum.*, vol. 69, p. 1179, 1998, <https://doi.org/10.1063/1.1148659>

[8] J. Y. Benitez et al., Recent Bremsstrahlung Measurements from the Superconducting Electron Cyclotron Resonance Ion Source VENUS, in Proc. 22nd Int. Workshop on ECR Ion Sources (ECRIS’16), Busan, Korea, August 2016, MOCO04, pp. 23-29, <https://doi.org/10.18429/JACoW-ECRIS2016-MOCO04>

[9] J. Noland et al., “Studies of electron heating on a 6.4 GHz ECR ion source through measurement of diamagnetic current and plasma bremsstrahlung”, *Plasma Sources Sci. and Technol.*, vol. 20, p. 035022, 2011, <https://doi.org/10.1088/0963-0252/20/3/035022>

[10] E. Canobbio, “Gyroresonant particle acceleration in a non-uniform magnetostatic field”, *Nucl. Fusion*, vol. 9, p. 27, 1969, <https://doi.org/10.1088/0029-5515/9/1/004>

[11] G. Castro et al., Application of Optical Emission Spectroscopy to High Current Proton Sources, in Proc. 8th Int. Particle Accelerator Conf. (IPAC’17), Copenhagen, Denmark, May 2017, TUPIK020, pp. 1721-1723, <https://doi.org/10.18429/JACoW-IPAC2017-TUPIK020>

[12] D. Mascali et al., “The first measurement of plasma density in an ECRIS-like device by means of a frequency-sweep microwave interferometer”, *Rev. Sci. Instrum.*, vol. 87, p. 095109, 2016, <https://doi.org/10.1063/1.4963710>

[13] Torrisi et al., “Microwave frequency sweep interferometer for plasma density measurements in ECR ion sources: Design and preliminary results”, *Rev. Sci. Instrum.*, vol. 87, p. 02B909, 2016, <https://doi.org/10.1063/1.4933025>

MULTI-DIAGNOSTIC SETUP TO INVESTIGATE THE TWO-CLOSE-FREQUENCY PHENOMENA*

S. Biri[†], J. Pálinkás, Z. Perduk, R. Rácz, Hungarian Academy of Sciences (Atomki), H-4026 Debrecen, Hungary

C. Caliri, G. Castro, L. Celona, S. Gammino, D. Mascali, M. Mazzaglia, E. Naselli, P. Romano, G. Torrisi, Istituto Nazionale di Fisica Nucleare, Laboratori Nazionali del Sud (INFN-LNS), 95123 Catania, Italy

A. Galatà, Istituto Nazionale di Fisica Nucleare, Laboratori Nazionali di Legnaro (INFN-LNL) 35020 Legnaro, Italy

Abstract

While the mechanism is still not fully clear, the beneficial effect (higher intensity of highly charged ions, stable plasma conditions) of the second micro-wave injected to the ECR plasma was observed in many laboratories, both with close and far frequencies. Due to the complexity of the phenomena (e.g. interaction of resonant zones, damped instabilities) complex diagnostic methods are demanded to understand its mechanism better and to fully exploit the potential hidden in it. It is a challenging task since complex diagnostics methods require the arsenal of diagnostic tools to be installed to a relatively small size plasma chamber. Effect of the injected second 13.6-14.6 GHz microwave to the 14.25 GHz basic plasma has been investigated by means of soft and (time-resolved) hard X-ray spectroscopy, by X-ray imaging and space-resolved spectroscopy and by probing the rf signals emitted by the plasma. Concerning the characterization of the X radiation, in order to separate the source and position of different X-ray photons special metallic materials for the main parts of the plasma chamber were chosen. A detailed description and explanation of the full experimental setup and the applied non-invasive diagnostics tools and its roles are presented in this paper.

INTRODUCTION

Electron Cyclotron Resonance (ECR) Ion Sources (ECRIS) are able to produce highly charged plasma in their plasma chamber from which positive ions with very different charge states can be extracted and transported to a target or into an accelerator. In order to deliver more and more intense, higher and higher charged ion beams, first a time-stable, highly ionized plasma has to be generated. By a simplified approach two tasks have to be solved: (1) to inject more and more electromagnetic energy from outside into the plasma on an efficient way and (2) to suppress or decrease those processes (instability, recombination, etc.) which work against the ionization process. The studying the ECR plasma itself for both purposes is thus essential and such investigations have been carried out in many laboratories since the discovery of ion sources of this type.

*Work has received funding from the European Union's Horizon 2020 research and innovation program under grant agreement No 654002 (ENSAR2-MIDAS).

[†] biri@atomki.mta.hu

The ECR groups of two laboratories (Atomki-Debrecen and INFN-LNS Catania) from time to time unify their forces to carry out diagnostics measurements of the ECR plasma for the purposes described above. In an earlier joint experiment [1, 2] a campaign for correlating the plasma density and temperature with the output charge states and the beam intensity for different pumping wave frequencies, different magnetic field profiles was carried out. The results revealed surprisingly very good agreement between warm-electrons density fluctuations, output beam currents and the calculated electromagnetic modal density of the plasma chamber. That experiment was based on the pioneering measurement of this type carried out and published for the first time space-resolved plasma diagnostics measurements by a pinhole X-ray camera [3].

In 2018 a new series of experiment was designed and realized by the collaborating groups. The experiments were carried out in Debrecen, at the Atomki ECRIS Laboratory basing to the Atomki-ECRIS to deliver the necessary plasmas and ion beams.

The main aims were to study these phenomena:

- Exact mechanism of the two-close-frequency heating;
- Role of the 2nd frequency in the suppression of plasma instabilities;
- To obtain volumetric and spatially resolved X-ray emissions from two-frequency plasmas;
- Hard X-ray spectra in unstable regimes;
- Structural changes triggered by instabilities;
- Structural changes when the turbulences are suppressed;

In some of the above goals significant results were obtained, in some others the first promising steps were done. The post-processing of the data is still not finished completely. For the high amount of the material and for the complexity of the results we decided to publish them in three different accompanying papers. The present paper here describes the technical setups of the measurements and shows those technical modifications on the Atomki-ECRIS which were necessary for the investigations. The first part of the results are shown in [4], where an outlook to the history of the two-frequency effect is also presented with references to others' works. The second part of the results, mostly related to the investigation of stable and unstable plasma regimes in single or double frequency operations, is discussed in our third paper [5].

EXPERIMENTAL SETUP

The X-ray diagnostics measurements were carried out in the ECR Laboratory of Atomki, Debrecen. The Atomki-ECRIS is a classical, room-temperature 2nd generation ion source. Its basic operation frequency is 14.25 GHz supplied by a klystron amplifier. A second frequency can be coupled in by the same WR62 waveguide supplied by a TWT amplifier. The axial magnetic field is 1.26 T (injection), 0.39 T (minimum) and 0.95 T (extraction). The hexapole produced magnetic injection at the plasma chamber

wall (R=29 mm) is 1.2 T. The ion source is not connected to accelerator thus it is highly applicable for plasma physics investigations. Further technical and application details are in a summary paper [6].

In order to carry out complex plasma diagnostics we installed and applied a full arsenal of diagnostic tools and methods. Figure 1 shows the simplified drawing of the ECRIS with the applied instruments around it or connected to it. In Table 1 some detailed specifications of the diagnostics tools, are shown.

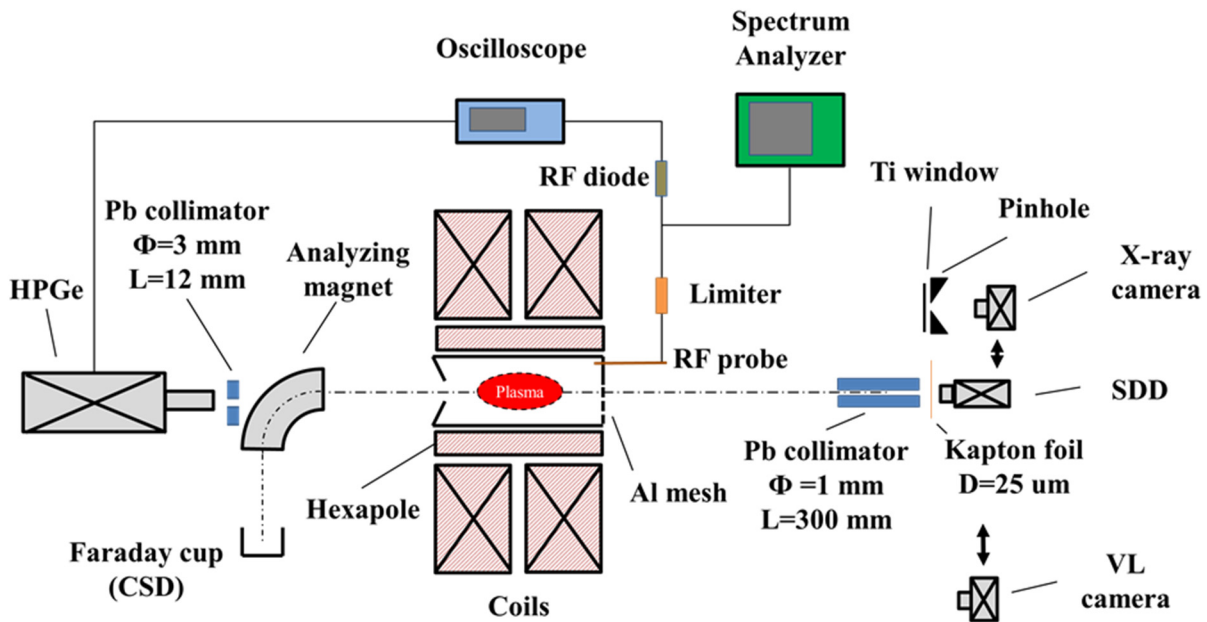


Figure 1: The measuring setup with the ECR plasma in the center.

Table 1. Technical Specifications of the Applied Diagnostics Tools.

Name	Energy range	Type	Resolution	Window	Collimation
Silicon Drift Detector (SDD)	1-30 KeV	XGL-SPCM-8110-CUBE	130 eV	kapton (25 μm, 50 μm) and Be (12.5 μm)	Lead, 300 mm length, 1 mm hole
CCD pinhole camera	1-20 KeV	Andor Ikon	1MP in 13x13 mm	Ti (9.5 μm)	Lead collimation system
Germanium Detector	30-400 KeV	HpGe-D	200 eV	Al	Lead, 12 mm, 3 mm hole
Visible light camera	Several eV	Basler acA2040	4 MP	plexi	-
RF-probe + Spectrum Analyzer	9 kHz – 43 GHz	homemade probe, Anritsu MS2720T SA	from 1 Hz to 10 MHz	-	-

The role of each diagnostics tool is different.

A Silicon Drift Detector (SDD) records x-ray spectra in the 1-30 KeV range. From the spectra electron density and electron temperature can be calculated. A long (300 mm) led collimator with 1 mm hole was used in vacuum conditions to obtain soft X-ray emission only from the plasma region. Cone of view of the detector went through the aperture of the plasma electrode (10 mm) in order to do

not detect X-ray photons coming from the metal parts of the chamber.

Alternatively with the SDD detector, a 1 MP CCD pinhole x-ray camera was mounted to the injection side. The pictures taken by the camera give spectral and structural information on the plasma and on the electron losses. By using 2 mm thick pinhole ($\Phi = 0.4$ mm) and extra led

shieldings, the X-ray picture re-cording was possible in relatively high RF-power operation mode (upto 200 W total incident power). The earlier experiments (see e.g. [7]) were restricted upto several tens of RF-power.

A third alternative at this site is a 4 MP mono-chrome visible light camera. The photos taken from the full plasma or from a selected area contains photons in the eV energy range and thus give information on the low energy component of the electrons energy distribution function (EEDF) exciting visible light transitions of atoms and ions.

The RF probe (mounted into the injection plate of the plasma chamber) together with a Spectrum Analyser (SA) can detect and show the plasma emitted EM waves in the GHz range. In our case the range of interest was 13-15 GHz. If the frequency of the emitted wave differs from the original one(s) it could be a sign of instability in the plasma.

The High Purity Germanium (HPGe) Detector is mounted to the straight axial port of the 90 degree analyzing magnet. Its operation range is 30-400 keV. We used it in two different modes. In time integrated mode the spectral temperature of the plasma can be calculated from the raw data. In time resolved mode we triggered its measurements by the sudden RF signals emitted by the unstable plasma to obtain hard X-ray spectra at different time domains corresponding to unstable and stable plasma regimes. Shaping time of the detector is about 5 us.

During all the measurements a middle-charged argon plasma was kept in the ion source with fixed gas dosing valve and with fixed (maximal) magnetic field. Representatives of the charge state distribution of the extracted ion beam (Ar6+, Ar9+, Ar11+) were continuously monitored which gave information on the ionization efficiency and on CSD shift.

ALTERATIONS ON THE ECRIS FOR THIS MEASUREMENTS

The original plasma chamber of the Atomki-ECRIS is made of stainless steel containing Fe, Cr, Ni, Mo and other components which, of course, appear in the X-ray spectra made the analysis difficult in our earlier experiments. To avoid it, after careful selection, we made or covered the three main parts of the chamber with three different metals. Figure 2 and Table 2 show the details. The new injection plate was made of aluminium allowing the mounting the gas tube, the WR62 waveguide and the RF-probe (Fig.2a, from left to right). The lateral wall was covered with 50 m thick tantalum sheet (Fig. 2b). The Al plasma electrode was covered by a 1 mm thick titanium plate (Fig. 3c, after plasma operation).

From Table 2 is obvious that by using these materials when an argon plasma is present, all the characteristic peaks can be well separated by our soft X-ray detectors between 1.49 and 8.14 keV energies (the expected peaks with increasing order are: 1.49, 1.56, 2.96, 3.19, 4.51, 4.93, 8.14 keV). This solution also makes possible a post-processing energy filtering of the x-ray photos taken by the pinhole camera. If so, the origin of the different X-ray photons and

also the role of the different part of the plasma chamber can be revealed.

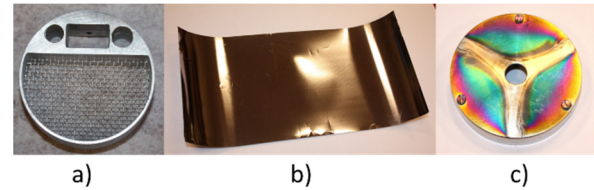


Figure 2: New materials in the plasma chamber. a) Injection plate, aluminum, mesh transparency is 60%. b) Lateral wall is tantalum. c) Plasma electrode covered with titanium.

Table 2: The Most Probable K and L Shell Related Characteristic X-ray Energies From Different Metals.

Part of chamber	Material	K _α (keV)	K _β (keV)	L _α (keV)
Injection plate	Al	1.49	1.56	-
Lateral wall	Ta	57	65	8.14
Plasma electrode	Ti	4.51	4.93	0.45
Plasma	Ar	2.96	3.19	-

During the measurements the ECRIS was operated at maximum coils' power resulting in an axial magnetic field distribution as it is in figure 3. At klystron-mode operation ($f=14.25$ GHz) the ratio of B_{min}/B_{ECR} is 0.76 Tesla which is close to the "critical" 0.75 value for the instability onset, as observed by different authors [8, 9]. When operating the source in two-frequency mode the second frequency can be varied between 13.6-14.6 GHz resulting in a B_{min}/B_{ECR} value between 0.75-0.8. Thus one can study what happens when we approach or pass the critical value both up and down direction without changing the axial magnetic field configuration.

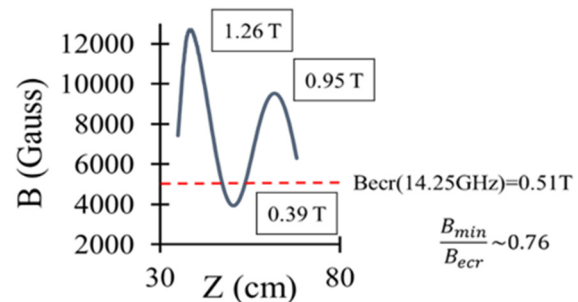


Figure 3: The axial magnetic field distribution of the Atomki-ECRIS at maximum coils fields.

The microwave system was also significantly modified to inject two frequencies and to measure the net incident power with high precision. The plasma chamber size (diameter 58 mm, length 210 mm) of the Atomki-ECRIS is small comparing with most other ECR ion sources and, of

Content from this work may be used under the terms of the CC BY 3.0 licence (© 2018). Any distribution of this work must maintain attribution to the author(s), title of the work, publisher, and DOI.

course, is much smaller than the known experimental fu-sion plasma devices. To use the above mentioned instru-ment arsenal and to install all the measuring tools thus meant a challenge for us and also forced some restrictions and compromises. For the way of studying the two-close-frequency operation mode we decided to use only one waveguide in order not to “occupy” most surface of the in-injection flange. By applying the small size WR62 wave-guide window and two holes for gas injection and for the RF-probe let us to observe more than 60% of the plasma through an aluminium mesh (Fig. 2a). The full micro-wave system is shown in Fig. 4. Both the klystron ampli-fier (14.25 GHz fixed frequency, power max 1000 watt) and the TWTA (13.6-14.6 GHz variable frequency, power

max 500 watt) are fed by sweep oscillators. A special com-biner unifies the two amplified signal and forwards them toward the plasma chamber. At the TWTA branch we in-stalled a phase shifter to explore the effect of the phase shift, if any. A broadband frequency circulator was applied to save the amplifiers from damages caused by reflected powers. A cross-guide was mounted as close to the plasma chamber as possible to the simultaneous measurement of the forwarded and reflected rf-powers. This solution made us possible to fix the net power (which is the difference of the two ones mentioned) at a constant value. Then the waveguide system was connected to the plasma chamber through high voltage and vacuum windows (Fig. 4.).

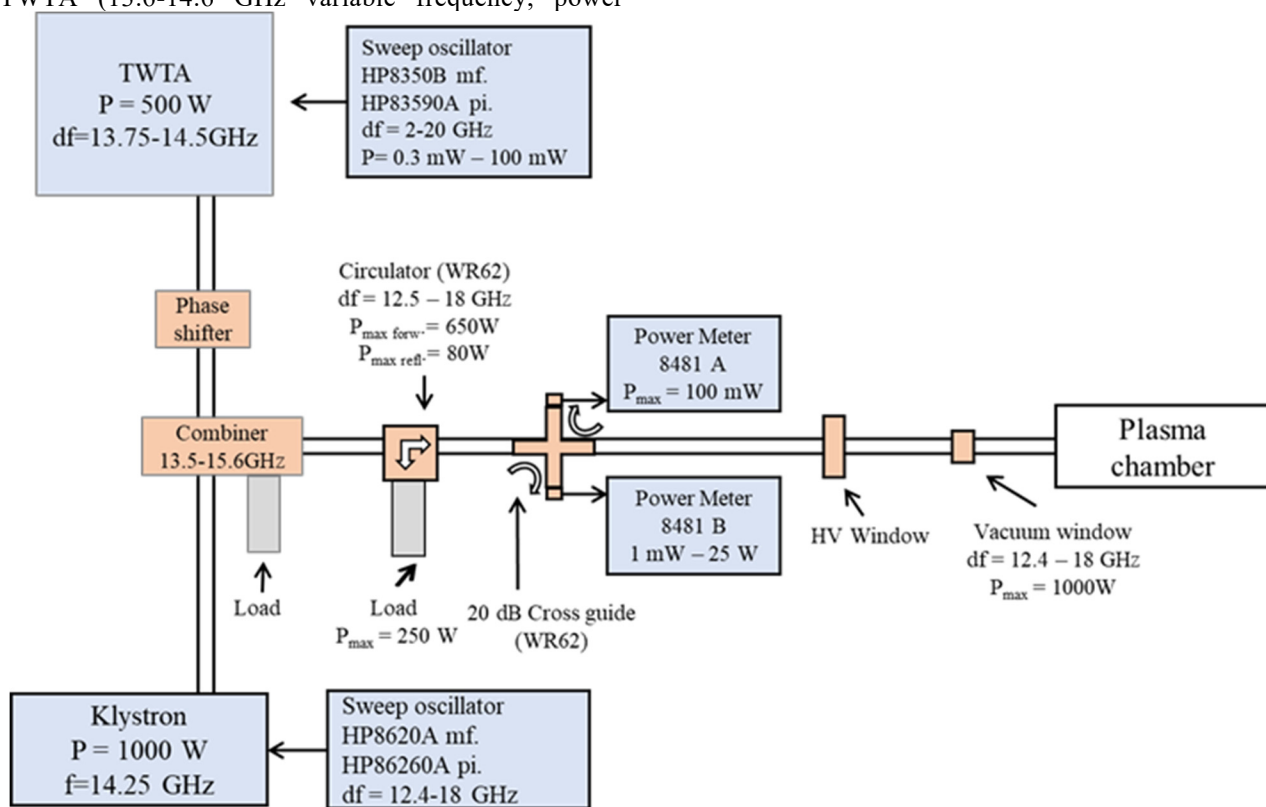


Figure 4: The microwave coupling system to study the two-close-frequency operation mode in ECR ion sources.

TECHNICAL RESULTS

The measurement system described in this paper was assembled and tested in two steps (March and June 2018), first part by part and after that in whole. The ECRIS was always operated with argon plasma with fixed gas flow (optimized for middle-charged argon plasma) but without any mixing gas. The coils currents were at maximum. The applied total micro-wave power was varied between 20 and 200 watt. While 200 W is still a “low-power” operation in the world of highly-charged-ECRISs, in the X-ray measurement history of this kind of plasma it is a big step forward, if we compare with ours earlier settings [3, 2, 7] where we were restricted up to a several tens of watts.

The measuring system operated well, regardless of some smaller technical failures which are unavoidable when working with such complicated setups. By using the silicon drift detector and the long collimator we were able to see only the argon plasma (with tiny titanium peaks from the plasma electrode) in the X-ray spectrum.

The RF-probe together with the Spectrum Analyser recorded signals effectively from the plasma in the GHz region. An example is in Fig. 5 where the source was operated in two-frequency mode. Beside the two main (coupled-in) signals one can see fake peaks as well, caused by the power-limiter (inserted before the SA). The limiter be-ing a nonlinear electrical circuit is operating as frequency mixer and produces such fake peaks. Also there

are signals which are generated in the chamber due to plasma instabilities.

In Fig. 6 we show another example: it is a typical X-ray plasma picture taken by the pinhole camera. Special areas (red quadrants in figure) were selected as ROIs (region of interests) to investigate the count rates in those regions carefully as function of the ion source setting parameters. Areas are corresponding to the plasma region (ROI-2, ROI-3, ROI-4, ROI-8), to the plasma losses on the plasma electrode (ROI-1, ROI-12), to the plasma losses on the lateral wall of plasma chamber (ROI-5, ROI-6, ROI-7), to the whole image (ROI-10), to the background (ROI-9, ROI-11). A comparison with the plasma traces on the extraction electrode (Fig. 2c) is possible and necessary to do.

As mentioned in the Introduction the results of the measurement campaign obtained so far are presented in two other accompanying papers [4, 5].

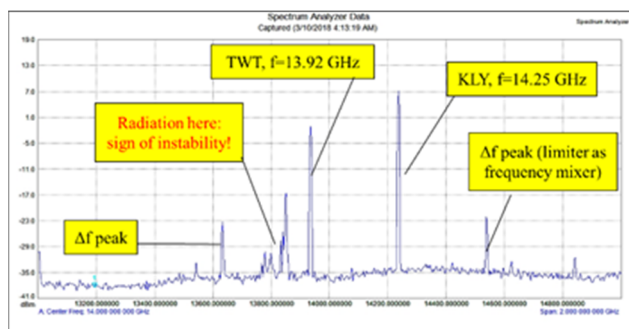


Figure 5: Example of the detected RF-signals emitted by the plasma at coupled 13.92 and 14.25 GHz frequencies.

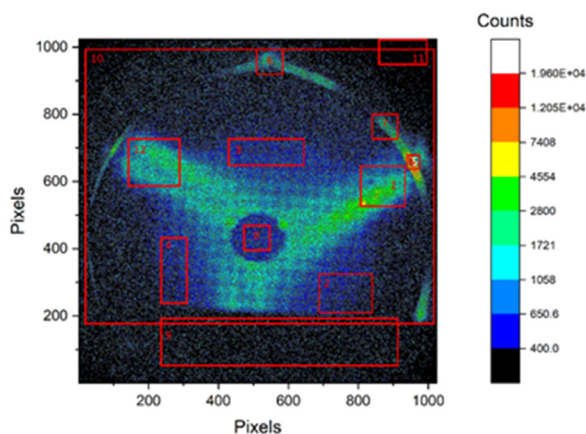


Figure 6: Typical x-ray plasma picture recorded by the pinhole camera. The red quadrants represent the selected ROIs.

REFERENCES

- [1] R. Rácz, et al., “X-ray pinhole camera setups used in the Atomki ECR Laboratory for plasma diagnostics”, *Rev. Sci. Instrum.* vol. 87, p 02A74, 2016 doi: 10.1063/1.4933085
- [2] D. Mascali, et al. “Electron cyclotron resonance ion source plasma characterization by X-ray spectroscopy and X-ray imaging”, *Rev. Sci. Instrum.* vol. 87, p. 02A510, 2016 doi: doi.org/10.1063/1.4939201
- [3] S. Biri, et al., “Imaging of ECR plasmas with a pinhole x-ray camera”, *Rev. Sci. Instrum.* vol. 75, p. 1420, 2002 doi: 10.1063/1.1690476
- [4] R. Rácz, et al., “Effect of the Two-Close-Frequency Heating to the Extracted Ion Beam and to the X-ray Flux Emitted by the ECR Plasma”, presented at the 23rd International Workshop on ECRIS, Catania, Italy, Sept. 2018, paper ID WEA5, this conference
- [5] E. Naselli, et al., “Impact of the two close frequency heating on ECRIS plasmas stability”, presented at the 23rd International Workshop on ECRIS, Catania, Italy, Sept. 2018, paper ID FRB2, this conference
- [6] S. Biri, et. al., “Status and special features of the Atomki ECR ion source”, *Rev. Sci. Instrum.* vol. 83, p. 02A341, 2012 doi: 10.1063/1.3673006
- [7] R. Rácz, et al., “Electron cyclotron resonance ion source plasma characterization by energy dispersive x-ray imaging”, *Plasma Sources Sci. Technol.* vol. 26, p. 075011, 2017 doi: 10.1088/1361-6595/aa758f
- [8] O. Tarvainen, et al., “Beam current oscillations driven by cyclotron instabilities in a minimum-B electron cyclotron resonance ion source plasma” *Plasma Sources Sci. Technol.* vol. 23, p. 025020, 2014 doi: 10.1088/0963-0252/23/2/025020
- [9] S. Gammino, D Mascali, L. Celona, F. Maimone, G. Ciavola, “Considerations on the role of the magnetic field gradient in ECR ion sources and build-up of hot electron component” *Plasma Sources Sci. Technol.* vol. 18, p. 045016, 2009

Content from this work may be used under the terms of the CC BY 3.0 licence (© 2018). Any distribution of this work must maintain attribution to the author(s), title of the work, publisher, and DOI.

X-RAY INVESTIGATION ON THE SUPERCONDUCTING SOURCE FOR IONS (SUSI)*

Derek Neben[†], Jesse Fogleman, Bryan Isherwood, Daniela Leitner¹, Guillaume Machicoane
 Shane Renteria, Jeffry Stetson, Larry Tobos

National Superconducting Cyclotron Laboratory, Michigan State University, East Lansing, MI, USA

¹ Lawrence Berkeley National Laboratory, Berkeley, CA, USA

Abstract

Heavy ion facilities such as the National Superconducting Cyclotron Laboratory (NSCL) often use ECR Ion Sources (ECRIS) for the production of highly charged ions to increase the efficiency of accelerating structures. Axial bremsstrahlung emission was studied on the Superconducting Source for Ions (SuSI) at the NSCL for 18 GHz and 13 GHz operation with oxygen. The hot electron temperatures were estimated from the bremsstrahlung high energy tail and seem to depend only on magnetic minimum in the same way as was found on VENUS [1], even in the case where 18 GHz and 13 GHz frequencies were compared for similarly sized ECR zones. Additionally, the time independent x-ray power increased at a significantly larger rate when operating the source in known regions of instability such as where the magnetic minimum approaches the ECR zone [2]. The results are discussed in the context of electron losses due to magnetic confinement.

INTRODUCTION

We present the bremsstrahlung measurements from a fast sputtering campaign conducted on the Superconducting Source for Ions (SuSI) at the National Superconducting Cyclotron Laboratory (NSCL). The SuSI source is a fully superconducting ECR ion source nominally operating at 18 GHz [3] and 24 GHz [4] microwave frequencies. Following the path set by Geller's scaling laws for ECRIS [5] the plasma density and beam current of ECR ion sources increase with the square of the operating frequency and as proposed more recently [6] with the square of the magnetic field. However, increasing the magnetic field increases the bremsstrahlung emission from the source and stresses the cryostats of 3rd generation fully superconducting ion sources. Dynamic heat loads on the order of several watts [7] have been observed as a result of x-rays produced by bremsstrahlung as electrons escape the ECR plasma, in particular when operating with higher magnetic fields. The x-ray investigation presented herein focused on how x-ray temperature changed with magnetic minimum following measurements previously done by the LBNL group using the VENUS source [1].

Bremsstrahlung results are presented for 18 GHz operation up to 400 W applied microwave power and 13 GHz for a microwave power level of 100 W. Continuous Wave (CW)

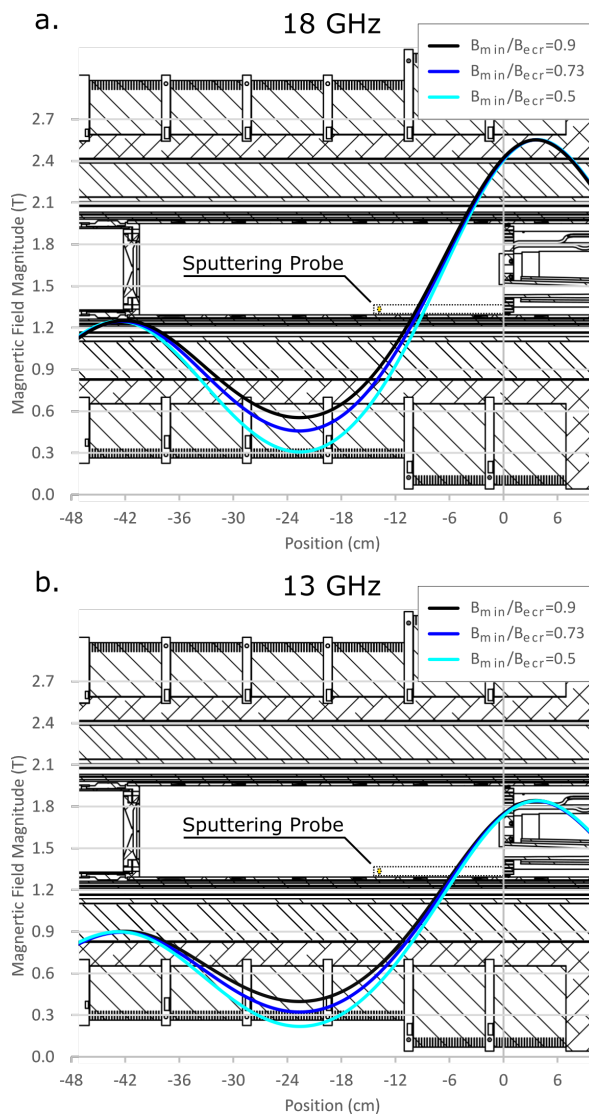


Figure 1: SuSI Magnetic field as simulated using Poisson with the radial sputtering probe developed for SuSI (dotted line). Three field configurations: $B_{min}/B_{ecr}=0.5$, 0.73 , and 0.9 were selected for both 18 GHz and 13 GHz operation. The magnetic fields were scaled with frequency resulting in the same ECR zone size for constant B_{min}/B_{ecr} ratio. The radial sputtering probe was inserted in between the electron flutes on the injection baffle along the plasma chamber wall.

* Work supported by Michigan State University and the National Science Foundation: NSF Award Number PHY-1415462

[†] neben@nsl.msui.edu

Table 1: Characteristics of the Magnetic Field Configurations Used in the Study

Frequency	18 GHz			13 GHz		
	B_{min}/B_{ecr}	0.5	0.73	0.9	0.5	0.73
B_{min} (T)	0.31	0.46	0.55	0.22	0.32	0.40
B_{inj} (T)	2.55	2.55	2.55	1.84	1.84	1.84
B_{ext} (T)	1.25	1.25	1.25	0.90	0.90	0.90
B_{rad} (T)	1.25	1.25	1.25	0.93	0.93	0.93
ECR Length (cm)	16.3	12.8	9.3	16.5	13.0	9.3
B_{ext}/B_{min}	4.03	2.72	2.27	4.09	2.81	2.25

sputtering Charge State Distributions (CSD) are presented comparing 13 GHz and 18 GHz operation for constant microwave power, magnetic minimum (B_{min}), and ECR zone size.

EXPERIMENTAL SET-UP

An off-axis radial sputter probe developed for SuSI was used with a gold sputter sample for these measurements. Gold currents ranging from 100's of nanoamperes to microamperes were used to avoid saturating the plasma with the heavy metal. Microwave power was limited to 400 W to protect the sputter sample and sputtering probe from damage. The probe consists of a conducting inner core and an insulating outer shield, and to provide the sputter sample access to the plasma a small hole was cut at the end of the insulating shield. The outer insulator was cylindrical in cross section with an outer diameter of 11.4 mm and protruded 14.5 cm from the injection baffle. The probe was passed from the injection flange along the plasma chamber wall (see Fig. 1) in between the electron flutes on the injection baffle.

Table 1 summarizes the parameters explored for the study. We used two microwave frequencies and three mirror configurations for each frequency. The fields for the 13 GHz configurations were scaled by the ratio of the frequencies. For constant frequency, the injection and extraction field strengths were fixed varying the magnetic minimum as can be seen in Fig. 1a-b. A field with constant B_{min}/B_{ecr} ratio had a similar ECR zone size.

Typical plasma parameters are summarized in Table 2. Oxygen was used as the mixing gas for each plasma studied, and the leak valve set-point remained constant as the magnetic field was changed within a selection of frequency and microwave power. 13 GHz operation was limited to 100 W, since the narrow bandwidths optimized for the 18 GHz transmission line DC break and the microwave window lead to a high reflected power, while up to 400 W was used for 18 GHz operation. The microwave power for $B_{min}/B_{ecr}=0.9$ (at 18 GHz) had to be limited to 200 W to avoid damaging the probe by the plasma at this field.

Energy resolved x-ray spectra were measured using an axial High Purity Germanium (HPGe) x-ray detector. The HPGe detector was used with an Ortec 671 linear shaper amplifier and Ortec Easy MCA (Multi Channel Analyzer) with pileup rejection to collect the detector signals. This

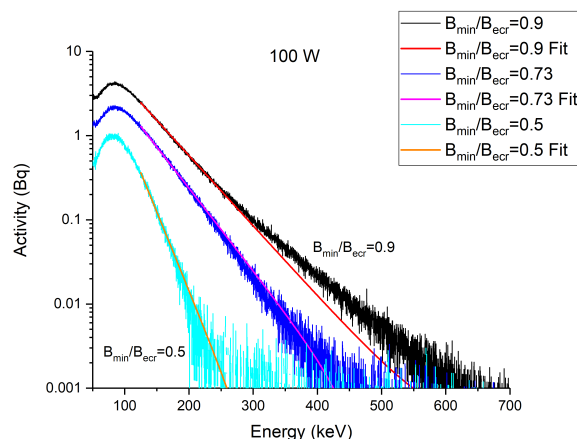


Figure 2: X-ray spectra corrected for detector efficiency and background radiation produced by an oxygen plasma driven at 18 GHz with 100 W microwave power. An exponential decay function was applied to the bremsstrahlung spectra starting at 125 keV through the end of the datafile (1440 keV).

combination of amplifier and MCA with pileup rejection could accept a maximum 20 k counts per second (if uniformly spaced in time), the maximum average count rate observed in the experiment was 2.2 k counts per second and was well within the capabilities of the data acquisition system. The detector was placed at the end of a narrow collimation channel with a tungsten insert similar to the one described in [8]. The collimator allowed an opening angle of about 20 minutes projecting a circle of 13 mm in diameter on the extraction electrode. As the extraction electrode aperture was 8 mm in diameter the observed x-rays were mainly produced by bremsstrahlung from electrons lost from the magnetic trap and striking the extraction electrode. The HPGe detection efficiency was measured off-line using a ^{152}Eu source of known activity. All data were corrected for detector efficiency. The HPGe detector was placed outside the vacuum vessel so the x-rays traveled through 3.3 mm of quartz (vacuum window) and 1.4 m of air gap before reaching the detector. Therefore x-rays of 50 keV or less energy experienced a nonlinear absorption curve with energy and were not considered in the analysis.

Following the deconvolution method prescribed by [9] an exponential function was fitted to the bremsstrahlung spectra extracting an estimate for the hot electron temperature (for a Maxwellian electron energy distribution function). Therefore, any non-Maxwellian features (non-exponentially decaying with energy) such as the peak in x-ray power that typically appears around 80-110 keV as can be seen in Fig. 2 were excluded. Fitting of the x-ray spectra for hot electron temperature began at 125 keV (see Figs. 2 and 3) for all spectra with the exception of 13 GHz operation for $B_{min}/B_{ecr}=0.5$ (the smallest B_{min}) where the fitting region began at 100 keV to accommodate for the overall lower energy bremsstrahlung distribution. The apparent bi-Maxwellian spectra for $B_{min}/B_{ecr}=0.9$ in Fig. 2 had a change

Table 2: Key SuSI Parameters for Two Different Magnetic Field Configurations

Frequency	18 GHz						13 GHz					
	400 W		200 W			100 W			100 W			
B_{min}/B_{ecr}	0.5	0.73	0.5	0.73	0.9	0.5	0.73	0.9	0.5	0.73	0.9	
Drain Current (mA)	1.47	1.71	1.44	1.4	1.33	0.94	1.08	1.08	1.03	1.03	1.03	
Injection Pressure (10^{-8} mbar)	9.1	9.3	13	14	13	8.7	8.9	8.7	6.3	6.1	6.6	
Extraction Pressure (10^{-8} mbar)	1.5	1.6	1.9	1.9	1.8	1.6	1.3	1.6	0.94	0.74	0.92	
O ⁶⁺ Current ($e\mu A$)	59	61	35	64	68	13	30	39	4	17	21	
O ⁴⁺ Current ($e\mu A$)	64	65	81	66	71	32	60	48	42	59	47	
O ²⁺ Current ($e\mu A$)	75	78	83	79	63	60	73	64	73	53	43	

in slope around 300 keV, masking away this feature decreased the temperature by 4% compared to its inclusion. Effects due to bi-Maxwellian features in bremsstrahlung spectra were not accounted for in the dataset as a whole, however isolating the higher temperature component of the spectra at $B_{min}/B_{ecr}=0.9$ in Fig. 2 by fitting from 300 keV resulted in a temperature of 67 keV which is 30% higher than that obtained from fitting at 125 keV.

X-ray power was chosen as a figure of merit of the plasma because it is weighted by the energy and photon counts. X-ray power transported through the collimation channel provides a relative measure related to electron losses because the x-ray production rate on solid targets (extraction electrode) is many orders higher than for gas targets. The total x-ray power emission was calculated by summing the x-ray power for each channel (discretized photon energy bin) of the 13 bit MCA starting at 50 keV through the end of the file at 1440 keV. The x-ray power error was calculated by taking the fractional uncertainty $1/\sqrt{N}$ for a Poisson distribution, with N the number of detections per channel (uncorrected for detector efficiency), and weighing it by the x-ray power in that channel. Each channel x-ray power error was summed in quadrature (assumed independent and random) to generate the total x-ray power error.

RESULTS AND DISCUSSION

The behavior of hot electron temperature with choice of low energy fitting boundary was explored for 18 GHz operation at 100 W, with the intent of estimating the electron temperature error. Figure 3 shows how the hot electron temperature changed with fitting region starting between 80-170 keV terminating at 1440 keV. A data mask that includes the non-exponentially decaying portion of the bremsstrahlung spectra (80-100 keV region) produced an artificially high hot electron temperature from the decrease in slope about the peak in bremsstrahlung power. In the case of $B_{min}/B_{ecr}=0.9$ the temperature increases beyond 120 keV as the higher temperature but lower intensity portion of the hot electron distribution is weighted more strongly. For Figs. 4 and 9 the hot electron temperature error was generated propagating a $\pm 10\%$ deviation in mask energy about 125 keV except for 13 GHz operation at $B_{min}/B_{ecr}=0.5$ when the energy used was 100 keV, in accord with our previous statements. The

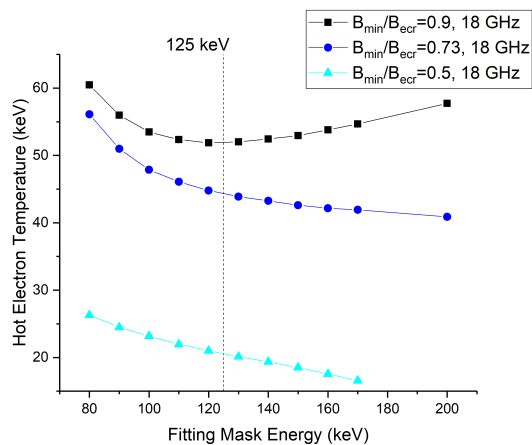


Figure 3: Hot electron temperature from fitting with an exponential decay function for different choices of the starting energy of the fitting function (fitting mask energy). The hot electron temperature changed with fitting range because the plasma generating the bremsstrahlung is not completely Maxwellian. 125 keV was selected as the mask energy to process all spectra (except 13 GHz with $B_{min}/B_{ecr}=0.5$) to minimize the influence of the bremsstrahlung peak around 80-110 keV while maximizing the fitting region.

error bars in this case do not represent a 68% confidence interval but rather the deviation using three fit ranges.

The hot electron temperature (from fitting the bremsstrahlung spectra) increased with magnetic minimum as shown in Fig. 4. The trend and the absolute values of hot electron temperature with increasing B_{min} were consistent (including the rate of change) with the findings in [1], where temperature increased with the absolute value of the magnetic minimum. The two fields: $B_{min}/B_{ecr}=0.5$ at 18 GHz and $B_{min}/B_{ecr}=0.73$ at 13 GHz had approximately the same magnetic minimum ($B_{min}=0.3$ T) and hot electron temperature. For $B_{min}=0.3$ T, the extraction mirror ratio (B_{ext}/B_{min}) was 30% lower at 13 GHz than for 18 GHz (see Table 1). Comparing 100 W cases, the x-ray power for $B_{min}/B_{ecr}=0.73$ at 13 GHz (7.1 ± 0.9 pW) was 30% higher than $B_{min}/B_{ecr}=0.5$ at 18 GHz (5.3 ± 0.7 pW) as seen in Fig. 5 suggesting the difference in x-ray power was the result of the reduced mirror ratio for 13 GHz operation.

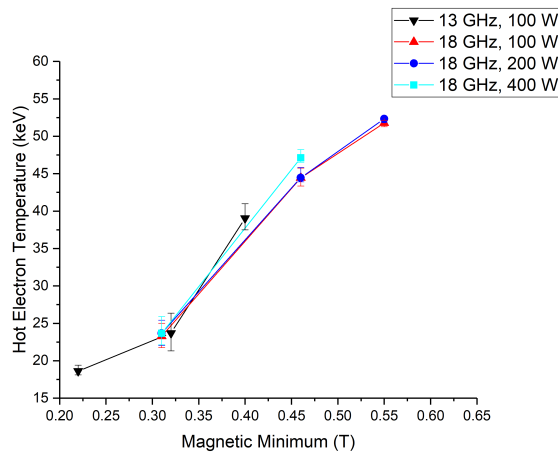


Figure 4: Hot electron temperature from fitting of the axial bremsstrahlung emission. The temperature depended on magnetic minimum independent of frequency and microwave power.

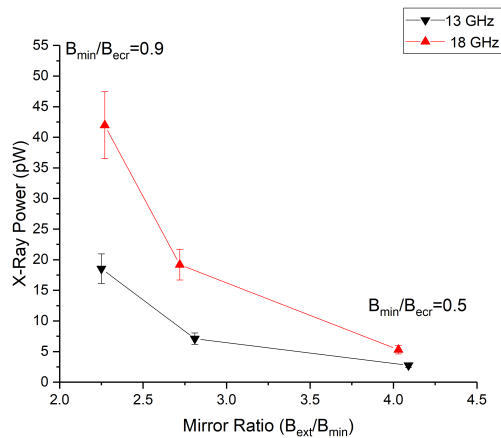


Figure 5: X-ray power with changing mirror ratio (B_{ext}/B_{min}) for 13 GHz and 18 GHz operation with a microwave power level of 100 W.

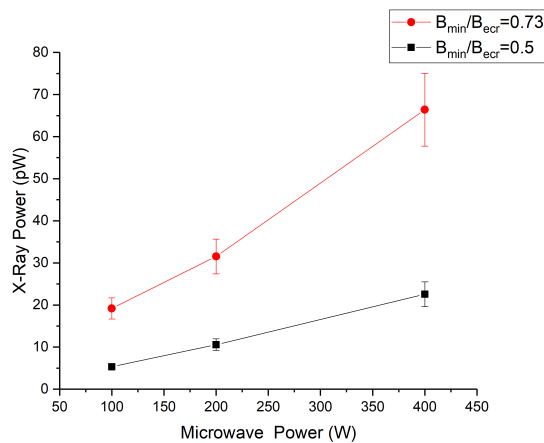


Figure 6: Total integrated x-ray power for all non-attenuated photons (greater than 50 keV) as a function of microwave power at 18 GHz. X-ray power increased linearly with microwave power.

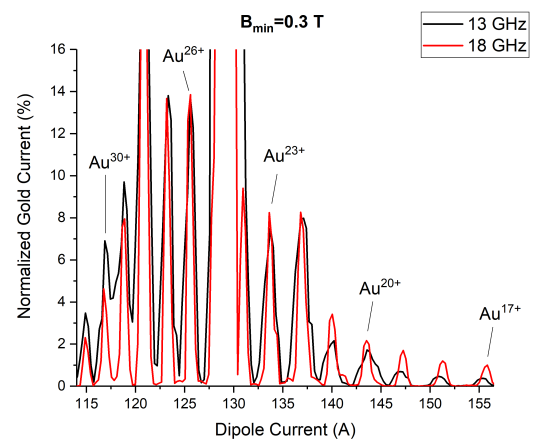


Figure 7: Gold CSD normalized to the sum of all gold currents for $B_{min}=0.3 T$ at 100 W microwave power. The total extracted current for 13 GHz operation was $1.55 e\mu A$ while for 18 GHz operation was $8.80 e\mu A$.

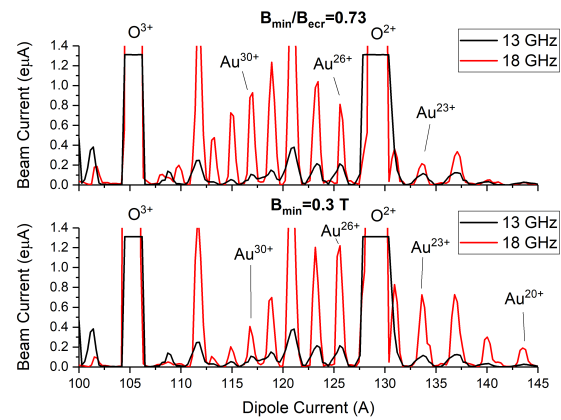


Figure 8: CSD of gold for a sputtering voltage of -500 V and with a microwave power level of 100 W. The gold currents extracted when coupling 13 GHz microwaves to drive the plasma was about an order of magnitude lower than those obtained with 18 GHz microwaves for either constant B_{min} or ECR zone size.

X-ray power increased linearly with microwave power as shown in Fig. 6. A similar relationship was observed as a dynamic heat load on the VENUS cryostat [7]. The hot electron temperature remained static with increasing power as seen in Fig. 4 so the increased power is not from a redistribution of the electrons to higher energies, instead likely the result of increasing plasma density.

Sputtering to produce highly charged ions is sensitive to the local and global plasma density: The sputtering yield (in general) depends on the ion density at the sputter sample while the ionization probability of the neutral sputtered material depends on the electron density along the path of travel through the plasma. The gold CSD's were peaked at the same charge states as seen in Fig. 7 for constant B_{min} , but the lower frequency and mirror ratio produced a slightly larger percentage of high charge states. However, the gold currents when operating at 13 GHz were nearly an order of

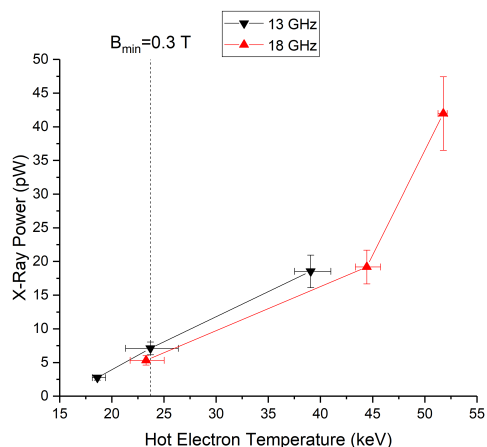


Figure 9: X-ray power as a function of hot electron temperature comparing 13 GHz and 18 GHz frequencies at 100 W microwave power for all six magnetic fields used for the study. For 13 GHz operation, x-ray power increased linearly with electron temperature for each magnetic field configuration while 18 GHz operation generated double the x-ray power for a 17% increase in temperature when changing the magnetic field from $B_{min}/B_{ecr}=0.73$ to $B_{min}/B_{ecr}=0.9$.

magnitude lower than at 18 GHz as shown in Fig. 8 when controlled for microwave power, ECR zone size, and B_{min} suggesting the density was lower for 13 GHz. Higher frequency operation may pay dividends when it comes to metallic beam production even with lower magnetic fields, due to an increased plasma density for the higher frequency. Additionally, for constant mirror ratio, the x-ray power from the 18 GHz plasma was larger than that produced at 13 GHz in Fig. 5 further supporting the established idea that higher microwave frequency generates a denser plasma.

It may be possible that higher 13 GHz power levels could have been used to compensate for the reduced density when compared to 18 GHz operation. In particular, for the case of $B_{min}=0.3$ T an additional 200 W of microwave power (microwave power level of 300 W) would be required to equalize the x-ray power for a mirror ratio of 2.8 in Fig. 5 based on the trend in Fig. 6 obtained at 18 GHz for $B_{min}/B_{ecr}=0.5$. The gold current increased nonlinearly with microwave power at 18 GHz for $B_{min}=0.3$ T for charge states Au^{35+} - Au^{30+} . In particular, Au^{30+} current increased by about a factor of 3 for every factor of 2 increase in microwave power, and if Au^{30+} current increased at a similar rate for 13 GHz operation the gold current at 300 W would have been about $0.6 \mu A$ which is the same order as the measured Au^{30+} current ($0.4 \mu A$) suggesting lower densities obtained with lower microwave frequencies can be compensated for with increased microwave power.

The oxygen support gas currents for 13 GHz and 18 GHz operation for 100 W were often less than a factor of two apart as seen in Table 2. The high charge state performance (O^{6+}) was consistently better for 18 GHz operation than at 13 GHz (except for $B_{min}=0.3$ T where 13 GHz operation slightly outperformed 18 GHz) similar to the behavior reported in [4]

comparing 18 GHz and 24 GHz performance with argon for kilowatts of microwave power.

In all plasmas studied the x-ray power increased as a function of hot electron temperature. For 13 GHz operation the x-ray power increased linearly with hot electron temperature for the three magnetic field configurations. However, for 18 GHz operation x-ray power increased sharply for $B_{min}/B_{ecr}=0.9$ where the x-ray power doubled for only a 17% increase in electron temperature (compared to $B_{min}/B_{ecr}=0.73$) as seen in Fig. 9. For comparison, the x-ray power doubled for a 80% increase in hot electron temperature between $B_{min}/B_{ecr}=0.5$ and $B_{min}/B_{ecr}=0.73$. The increased x-ray power at this field and frequency combination may be the result of cyclotron instabilities, characterized in part by bursts of microwave and x-ray power in ECRIS appearing as the B_{min}/B_{ecr} ratio increases beyond around 0.7 for microwave powers as low as 50 W [2]. Cyclotron instabilities convert hot electron kinetic energy into microwave energy resulting in hot electrons escaping the magnetic bottle [10]. Cyclotron instabilities in the hotter denser 18 GHz plasma for $B_{min}/B_{ecr}=0.9$ ($B_{min}=0.55$ T) likely produced increased hot electron losses resulting in increased x-ray power as measured in our detector. These instabilities may have been present for 13 GHz operation but perhaps due to the lower temperature electrons for $B_{min}/B_{ecr}=0.9$ ($B_{min}=0.4$ T) and the lower plasma density x-ray bursts were too small in amplitude to appear within our measurement sensitivity.

REFERENCES

- [1] J. Benitez, C. Lyneis, L. Phair, D. Todd, D. Xie, "Recent bremsstrahlung measurements from the superconducting electron cyclotron resonance ion source VENUS", in *Proc. ECRIS'16*, Busan, South Korea, 2016, paper MOCO04, pp. 23-29.
- [2] O. Tarvainen *et al.*, *Plas. Sourc. Sci. Technol.*, vol. 23, p. 025020, 2014.
- [3] P. Zavodszky *et al.*, *Rev. Sci. Instrum.*, vol. 77, p. 03A334, 2006.
- [4] G. Machicoane *et al.*, "First results at 24 GHz with the superconducting source for ions (SuSI)", in *Proc. ECRIS'14*, Nizhny Novgorod, Russia, paper MOOMMH03, pp. 1-4.
- [5] R. Geller, "Min-B ECRIS for highly charged ions", *Electron Cyclotron Resonance Ion Sources and ECR Plasmas*, IOP Publishig Ltd., Bristol and Philadelphia, 1996, pp. 394-409.
- [6] C. Lyneis, "Scaling laws in electron cyclotron resonance ion sources", in *Proc. ECRIS'16*, Busan, South Korea, 2016, paper MOCO01, pp. 1-4.
- [7] D. Leitner *et al.*, *Rev. Sci. Instrum.*, vol. 79, p. 033302, 2008.
- [8] T. Ropponen *et al.*, "Bremsstrahlung and ion beam current measurements with SuSI ECR ion source", in *Proc. ECRIS'10*, Grenoble, France, 2010, paper WECAK04, p. 171-174.
- [9] M. Lamoureux and P. Charles, *Radiation Phys. Chem.*, vol. 75, pp. 1220-1231, 2006.
- [10] S. Golubev, and A. Shalashov, *JETP Lett.*, vol. 86, pp. 91-97, 2007.

STATUS REPORT ON THE AECR-U ION SOURCE AT KVI-CART

H. R. Kremers[†], J. P. M. Beijers, S. Brandenburg, B. N. Jones, KVI-CART University of Groningen, The Netherlands.

Abstract

A new hexapole, equipped with a pole tip field of 0.87 T has been installed in the AECR ion source. The new hexapole improves the performance of the source, which includes an observed enhancement in all charge state distributions. For the xenon charge state distribution this resulted in a significant increase of the higher charge states that now allows for the production of an $^{129}\text{Xe}^{33+}$ beam with intensities of 0.5 μA (collimated beam) that can be used for regular operations.

INTRODUCTION

The interest in intense highly-charged heavy-ion beams used by experimentalists and radiation hardness researchers motivates us to further develop our AECR-U ion source [1]. As the production of intense highly-charge heavy-ions ions requires high-magnetic longitudinal and radial confinement fields, a degraded hexapole with pole tip fields of 0.72 T limits us to achieve the high beam-currents for the highest charge-states of heavy ions. The most optimal design strength of the longitudinal and radial magnetic fields with respect to the heating frequency has experimentally been found and described by scaling laws [2]. According to the law $B_{\text{rad}} = 2 \times B_{\text{ecr}}$ our radial field should be close to 1 T ($B_{\text{ecr}} = 0.5\text{T}$). The new hexapole has pole tip fields of 0.87 T; a little lower than the optimal B_{rad} of 1 T. Furthermore, with the installation of the new hexapole, the homogeneity of the magnetic field along the bars improved from 14% to 5% and the maximum value of each bar does now vary within a range of 0.15 Tesla instead of 0.4T. In this paper we describe the exchange of the hexapole including the modification on the plasma chamber. Furthermore, we present beam intensity measurements before and after the replacement of the hexapole and discuss these measurements. Finally, the paper will be close off with the conclusions and a future outlook.

THE HEXAPOLE REPLACEMENT

The conceptual idea behind the design of the hexapole structure is that the design aims for a low background vacuum in the plasma chamber. This is done by incorporating six radial pumping ports in between the magnet bars (Fig.1a.). Unfortunately, it comes with the cost of having no magnetic material at the location of these pumping ports. Therefore, the maximum achievable pole tip fields are lower than for example a Halbach structure [3]. Background pressures are achieved in the order of 2×10^{-8} mbar measured on top of the vacuum chamber. The original design [4] has six pumping slots. But due to a rupture of the aluminium wall between the cooling system and the vacuum chamber of the original chamber, we have changed the six pumping ports of the original design

[†] h.r.kremers@rug.nl

into 6 x 3 smaller pumping slots which, close to the plasma chamber, end in an array of 8 holes with a diameter of 4.8 mm (Fig.1b, 2) which increases the integrity of the support structure.

The Support Structure of the Magnet Bars

The hexapole support structure is made from an 7075 T6 aluminium cylinder in which spaces have been machined by wire cutting in which the six magnetic bars are mounted (Fig.1). The six magnet-bars, made of Nd-Fe-B material, are each build up by two rows of 10 blocks (Fig.1,2), and mounted in a stainless steel AISI 304 can to prevent the magnetic material to oxidize. All blocks are made of MCE N5064 material and have an identical shape with an easy axis of $43 \pm 2\%$ deg (Fig.1f). During operation, the left over spaces around the bars are also used for cooling. The cooling water is directed specifically to the area of the loss-lines (Fig.1c), where the electrons hit the aluminium plasma chamber on the inside. This is done by filling up all the space around the bars with SS sheets and rods (not shown).

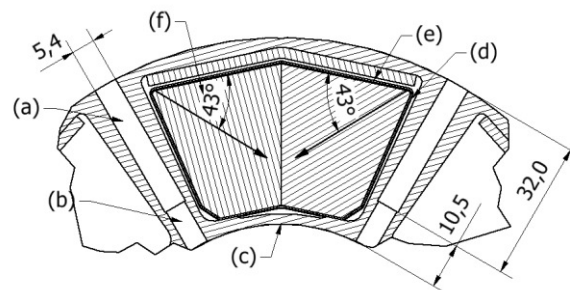


Figure 1: A through cut of a section of the aluminium hexapole container including the canned magnet bar, (a) pumping ports, (b) pumping holes, (c) loss-lines, (d) space filled with SS sheets, (e) can, (f) easy axis.

Pole Tip Field Measurement.

After assembly of the bars in the aluminium container, the hexapole is mounted in a magnetic-field measurement setup. In this setup the hexapole, supported by a v-shaped base, is positioned such that a hall-probe (LPT-141-10s), located at the center line of a hexapole bar, can be moved along the plasma wall. As the actual hall-probe “loop” is located asymmetrically in the head of the hall-probe, a holder is made such that the actual loop inside the probe is symmetrically in front of a pole on a radius of 32.92 mm. The distance between the source axis and the plasma chamber wall is 38.2 mm. To obtain the magnetic field values (Fig.3) at the wall the measured values have been multiplied by $(38.1/32.9)^2$ as the magnetic field quadratically increases as function of the radius. The magnetic field is measured over 300 mm with steps of 1 mm. At every step the longitudinal position and the radial magnet-

ic field are recorded. In the magnetic field measurements one is able to identify the glue space between the blocks as they give a small dip in the magnetic field (<1.5%) as can be seen in figure 3.

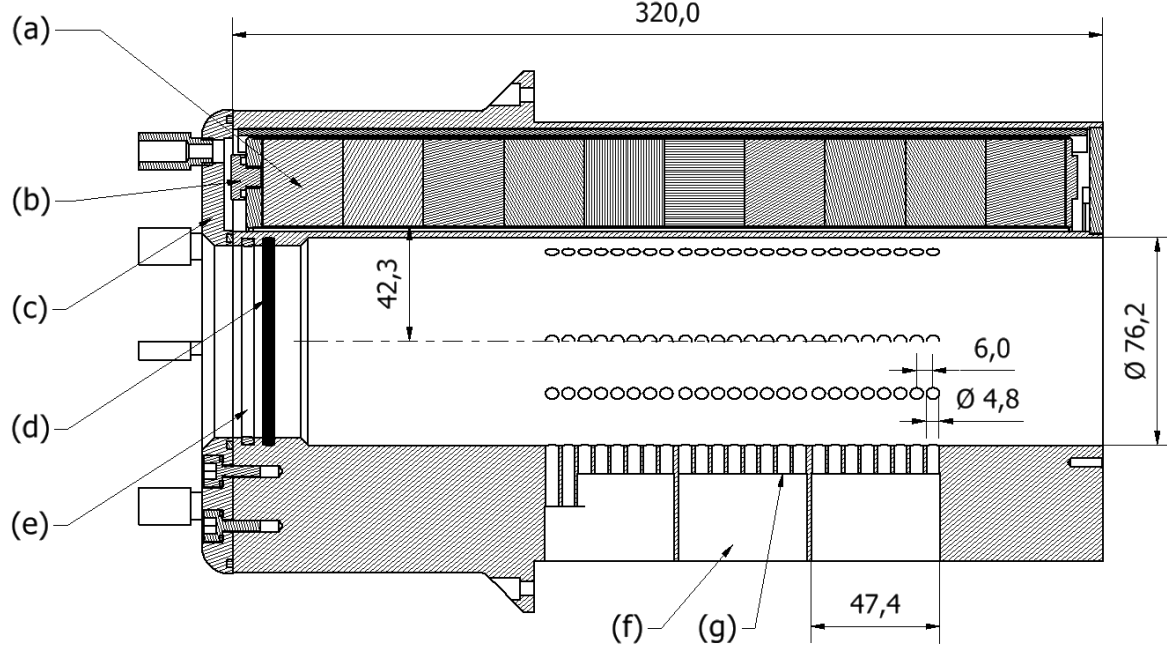


Figure 2: A cut through the hexapole on axis. (a) 10 blocks of magnet bar, (b) closure of the can, (c) lid of the container, (d) RF seal, (e) vacuum seal, (f) pumping ports, (g) pumping holes.

MEASUREMENTS

The measurements of the maximal achieved beam current per charge-state for xe-129, before and after the replacement of the hexapole, are presented in table 1. In both cases, the measurements were carried out with a conditioned ion source. ‘Conditioned’ means that first the ion source runs for 60 hours on oxygen to remove mainly the carbon contaminants in the plasma.

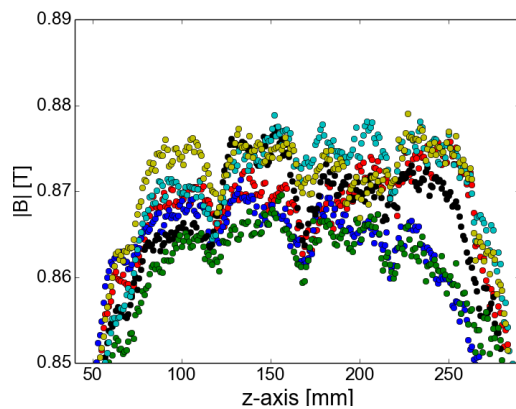


Figure 3: Measured absolute radial magnetic field at radius 38.2 mm of the centre. The different measurements are colour code depending on the pole.

Secondly, another 60 hours is used to reach stable operation to measure the highest beam current per charge-state for the highest charge-states of xenon. The operational pressure in the plasma chamber is $< 10^{-7}$ mbar and

oxygen is used as a mix gas. The optimal bias disk voltage is low in all measurements and ranges from -10V to -60V. Also, double frequency injection was used in all measurements. The frequency of the TWT ranges from 11.5 to 12.3 GHz. The klystron delivered a power of 800 W for the measurement done before the replacement of the hexapole while the optimal power of 500 W was needed after the replacement of the hexapole. The beam currents were measured by a collimated Faraday cup ($\varnothing 6$ mm) in the image plane of the analysing magnet (see table.1).

RESULTS AND DISCUSSION

The maximum beam intensity of the $^{129}\text{Xe}^{33+}$, measured with the new magnet bars, is a factor of 8 higher with respect to the $^{129}\text{Xe}^{33+}$ measured with the old magnets (see Table 1.). Even more, now the $^{129}\text{Xe}^{34}$ and $^{129}\text{Xe}^{35+}$ are detectable and can be used for injected in the AGOR accelerator. The intensity of $^{129}\text{Xe}^{29+}$ stays the same. So, we conclude that the increase of the pole tip fields of the hexapole works very well for high charge states of xenon. Regarding the extracted intensities from the source with respect to the collimated intensities measured at the faraday cup in the image plane of the analysing magnet, one can reason that the extracted intensities are probably a factor of 6 higher as the transmission of the analysing magnet is roughly 50% (for oxygen) and a further attenuation occurs by the collimation at the faraday cup (33%). However, highly-charge heavy-ions tend to be extracted

Content from this work may be used under the terms of the CC BY 3.0 licence (© 2018). Any distribution of this work must maintain attribution to the author(s), title of the work, publisher, and DOI.

close to the axis and therefor the factor of 6 might be an overestimation [5].

Table 1: Measured Xenon Beam Currents

Xenon charge	Beam current	Beam current
	[μ A]	[μ A]
	Old hexapole	New hexapole
29	3.3	3.3
30	1.5	2.7
31	0.68	1.7
32		
33	0.053	0.44
34		0.2
35		0.07

CONCLUSIONS AND FUTURE OUTLOOK

The replacement of the hexapole resulted in an improvement of a factor 2.5 for the $^{129}\text{Xe}^{31+}$ xenon production and a factor of 8 for $^{129}\text{Xe}^{33+}$ production. Even more, higher charge states were detectable as the $^{129}\text{Xe}^{34}$ and $^{129}\text{Xe}^{35+}$ were measured. Due to this improvement KVI-CART is able to provide intense highly-charge heavy-ion beams for experiments and radiation hardness tests for third parties. To increase the intensity even further, an einzel lens will be installed in between the ion source and the analyzing magnet to improve the transmission through the analyzing magnet. Furthermore, to reduce the carbon cleaning-time of the ion source, we plan to demonstrate in the near future that the plasma chamber will be less contaminated with carbon during the production of carbon beams when CO_2 gas is used rather than CH_4 gas.

ACKNOWLEDGMENTS

This project has received funding from the European Union's Horizon 2020 research and innovation program under grant agreement No 654002 and ENSAR FP7 contract No 262010 . Furthermore, it is also financed by the Netherlands Organization for Scientific Research (NWO). Furthermore, the paper is also supported by the University of Groningen. We would like to thank our colleagues of the KVI design, mechanical and IT departments for their contributions and help with the measurements.

REFERENCES

- [1] H.R. Kremers, J.P.M. Beijers, S. Brandenburg and J. Mulder, *High Energy Physics and Nuclear Physics*, vol 31, supp. 1, p. 90, (2007).
- [2] D. Hitz, A. Girard, G. Melin, S. Gammino, G. Ciavola, L. Celona, "Results and interpretation of high frequency experiments at 28 GHz in ECR ion sources, future prospects", *Rev. Sci. Instrum.*, vol. 73 pp. 509–512, (2002).
- [3] K. Halbach, *Nucl. Instrum. Methods*, vol 169, p. 1 1980.
- [4] Z.Q. Xie, C.M. Lyneis, in: *Proceedings of the 13th International Workshop on ECR Ion Sources*, College Station, 26-28 February 1997, p. 16.
- [5] M.A. Leitner, D.C. Wutte and C.M. Lyneis, *Proc. 2001 Particle Accelerator Conf.*, June 18-22, Chicago, IL, 2001, p. 67.

HOMOGENOUS DENSE PLASMA FLUXES FORMATION FROM HIGH FREQUENCY ECR DISCHARGE

S.V. Golubev, R.A. Shaposhnikov[†], I.V. Izotov, R.L. Lapin, S.V. Razin,
A.V. Sidorov, V.A. Skalyga, Institute of Applied Physics Russian Academy of Science, 603950
Nizhny Novgorod, Russian Federation

Abstract

Formation of ion beams with wide apertures and current at level of tens and hundreds Amperes is required in a wide range of studies. Usually plasmas of arc or high-frequency discharges are used for such applications. In this paper the possibility of using of an ECR discharge sustained by powerful millimetre wave gyrotron radiation for these purposes is considered. A high plasma density is required to solve the problem of obtaining high values of ion beam current density. The use of gyrotron as a source of millimetre wave radiation in the ECR discharge makes it possible to obtain plasma with high density and high ionization rate, close to 100%. Earlier at the IAP RAS the possibility of dense plasma fluxes production on the basis of ECR discharge in a magnetic field of one solenoid was demonstrated. In this paper, the characteristics of the outgoing plasma flux (density and homogeneity) were investigated. Estimations of the prospects for using such systems for high-current ion beams formation are presented.

INTRODUCTION

Electron-cyclotron resonance (ECR) ion sources are one of the most widespread types of systems for producing ion beams. Previous experiments in IAP RAS were aimed at creating sources of multiply charged ions with a high plasma density in such magnetic field configurations as open magnetic trap and cusp. It was demonstrated that in such systems the electron concentration can reach values 10^{13} cm^{-3} , electron temperature at the level of 100 eV, and the ion beam current has record values up

to 500 mA [1-3]. System which is based on the ECR discharge in one solenoid magnetic fields has prospects for producing sources of singly charged ions and formation of plasma fluxes with large apertures as an alternative to existing magnetic plasma confinement systems. This paper is concerned with an experimental investigation the transversal plasma fluxes distribution and measurements of plasma parameters obtained in the ECR discharge in a single magnetic coil sustained by a powerful millimeter-wave gyrotron radiation.

EXPERIMENTAL RESULTS

The experiments were carried out at the IAP RAS on facility SMIS 37 (see Fig. 1), partly modified the single coil studies. Gyrotron radiation at the frequency of 37.5 GHz with the power up to 100 kW and pulse duration up to 1.5 ms was used for electron heating and discharge ignition. The microwave radiation is launched through a quasioptical system into the discharge chamber with diameter of 68 mm and 250 mm long placed inside pulsed magnetic coil. Magnetic field in the center of the coil varies from 1 to 4 T. ECR value of magnetic field for the frequency of external electromagnetic radiation 37.5 GHz is 1.34 T.

The operating gas (hydrogen) was inlet into the discharge chamber in pulsed mode along the axis of the magnetic system through a gas-entry system integrated into the electrodynamic system for microwave radiation injection. To control neutral gas inlet the pressure in the gas buffer chamber above the gas valve was varied from 0.25 atm. up

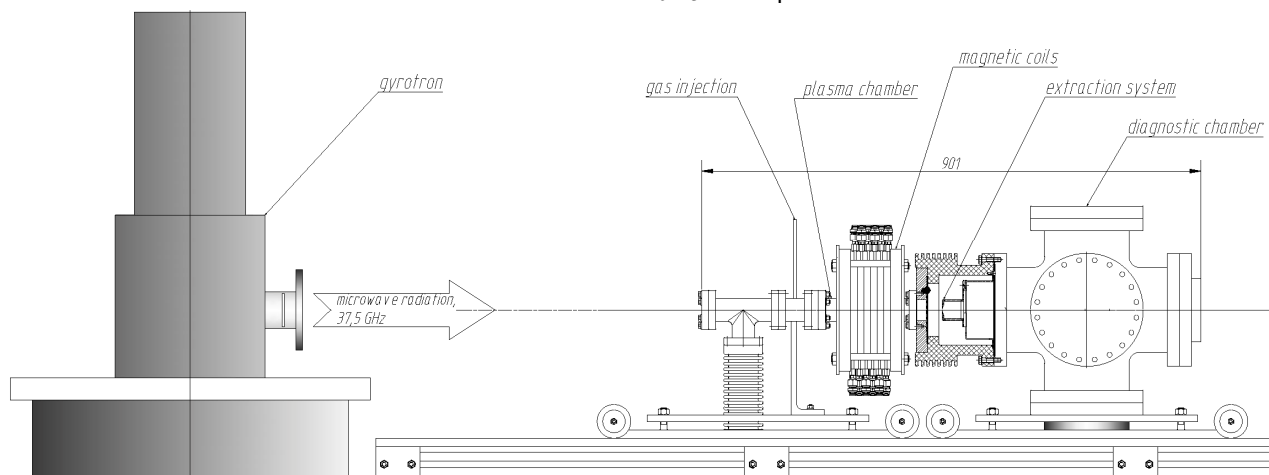


Figure 1: The experimental facility SMIS 37.

[†] shaposhnikov-roma@mail.ru

to 0.92 atm. The first experiments were aimed to determine breakdown conditions in this system. At the first step experiments with a constant neutral gas injection were performed to study the possibility of the discharge ignition and to determine a threshold microwave power for it at various pressures. Breakdown curve plotted according to the experimental data is shown in Fig. 2. Also it was demonstrated that discharge could be realized only if maximum magnetic field in the chamber is above ECR value.

The second part of the experiments was aimed to measurements of transverse profile of the plasma flux outgoing along the axis of magnetic system. During the experiments, the parameters of the system were optimized in such a way as to achieve the most homogeneous plasma flux radial distribution. The measurements were carried out using a Langmuir probe moved both in the radial and in the axial directions. As a result of experiments, the plasma flux profiles were measured at various distances from the center of the magnetic coil.

Example of the radial plasma flux distribution at the distances from the center of the magnetic coil of 31 cm, 21 cm, 12 cm, 10 cm and 8 cm at gyrotron power $Q = 100$ kW and at the value of magnetic field at the center of the probe $B_c = 2.16$ T is shown in Fig. 3. The vertical axis represents the density of the plasma flux, the horizontal axis represents the radial coordinate.

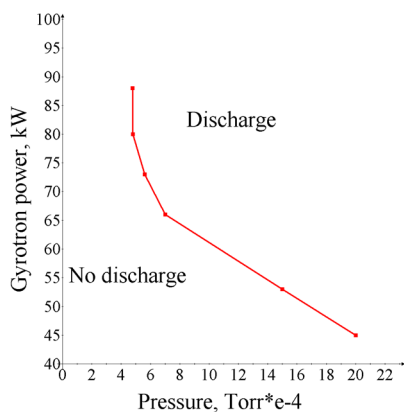


Figure 2: Breakdown threshold curve for hydrogen

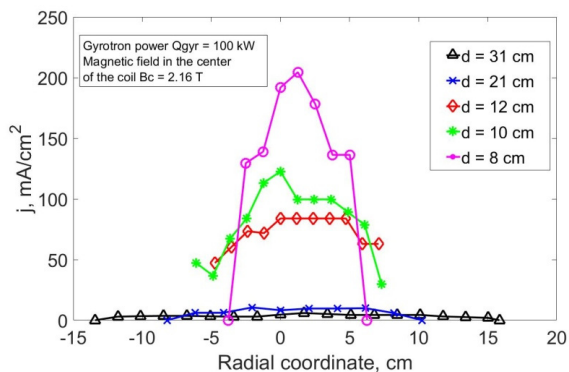


Figure 3: Plasma flux distribution in a cross section, d -distance between the probe and the centre of the coil.

The third part of the experiments was devoted to measuring the plasma parameters obtained as a result of the ECR discharge in the magnetic field of a single solenoid. During

the experiments, the plasma density was measured at a distance of 31 cm from the center of the magnetic coil at different gyrotron powers, result is presented in Fig. 4. It is clearly seen from the dependence that the plasma density in the discharge increases with the microwave power and reach values 10^{10} cm^{-3} . Measurements of the plasma density at various magnetic fields were also done. It is clear from the Fig. 5 that plasma density increases with the growth of the magnetic field.

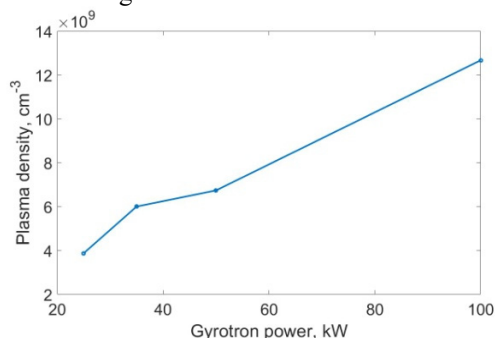


Figure 4: Dependence of plasma density on the gyrotron power, $d = 31$ cm

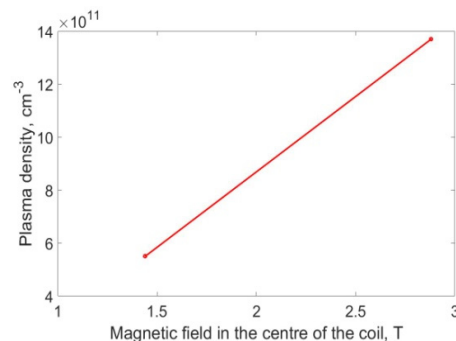


Figure 5: Dependence of plasma density on magnetic field.

The final part of the experiments was concerned with optimization of system parameters on purpose to obtain the maximum electron density in the discharge and to measure the current density of the ion beam. The maximum electron density in the center of the magnetic coil obtained in the experiments was $n_{e,max} = 2 \cdot 10^{13} \text{ cm}^{-3}$, and the electron temperature was in the range $10 - 30 \text{ eV}$. The ion beam current reached 15 mA through a hole with a diameter of 1 mm, which corresponds to the ion current density of $j_{max} \approx 1.5 \text{ A/cm}^2$.

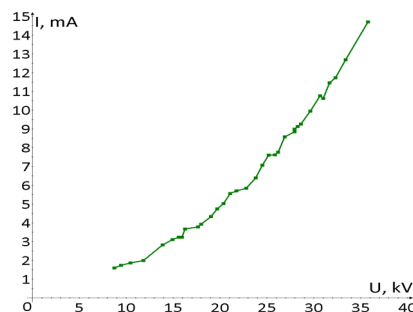


Figure 6: Ion beam current dependence on the extraction voltage.

CONCLUSION

Experimental results obtained during the investigation of ECR discharge in one solenoid magnetic field demonstrated the possibility of producing wide-aperture plasma fluxes with a homogeneous radial distribution at different distances from the magnetic coil. It was also demonstrated that the plasma density increases with gyrotron power and magnetic field. As a result of the experiment parameters optimization plasma density of $n_{\text{max}} = 10^{13} \text{ cm}^{-3}$ and the electron temperature at the level of $T_e \approx 10 - 30 \text{ eV}$ were obtained. Density of ion current extracted through the 1mm hole reached record values $j_{\text{max}} \approx 1.5 \text{ A/cm}^2$. Thus, these experimental results demonstrate that such system has clear prospects for producing of a wide-aperture plasma fluxes with high current density.

ACKNOWLEDGEMENTS

Presented work was supported by the grant of Russian Science Foundation # 16-19-10501

REFERENCES

- [1] S. Golubev, I. Izotov, S. Razin, A. Sidorov, V. Skalyga, A. Vodopyanov, V. Zorin, A. Bokhanov, "High Current ECR Source of Multicharged Ion Beams". *Nuclear Instruments and Methods in Physics Research B*, vol. 256, p. 537 – 542 (2007).
- [2] A. Sidorov, M. Dorf, A. Bokhanov, I. Izotov, S. Razin, Skalyga, V. Zorin, A. Balabaev, P Spädtkke, J. Roßbach, "Multi-aperture ion beam extraction from gas-dynamic electron cyclotron resonance source of multicharged ions". *Review of Scientific Instruments*, vol. 79, p. 02A317 (2008).
- [3] V. Skalyga, I. Izotov, S. Razin, A. Sidorov, S. Golubev, T. Kal-vas, H. Koivisto, and O. Tarvainen, High current proton beams production at Simple Mirror Ion Source 37. *Review of Scientific Instruments*, vol. 85, no. 2, pp. 02A702-1 02A702-3, (2014).

STUDY OF THE LEAD EVAPORATION FROM THE OVEN OF THE GTS-LHC ION SOURCE

T. Kövener^{1 2 *}, D. Küchler¹, V. Toivanen³

¹European Organization for Nuclear Research (CERN), CH-1211 Geneva 23, Switzerland

²University of Hamburg, 20146 Hamburg, Germany

³Grand Accélérateur National d'Ions Lourds (GANIL), F-14076 Caen Cedex 5, France

Abstract

The GTS-LHC ECR ion source at CERN provides heavy ion beams for the chain of accelerators from Linac3 up to the LHC and the SPS fixed target experiments. During the standard operation the oven technique is used to insert lead into the source plasma to produce multiply charged lead ion beams. Many years of experience show that some of the source instabilities can be linked to the oven performance. The evaporation seems not to be constant and when the oven reaches its maximum power, an indication that a refill is required, often half of the original lead sample is still present inside the oven crucible.

A dedicated study of the oven using an offline test stand as well as thermal and gas dynamics simulations intends to help to identify the reasons for these experimental observations. The goal is to find design modifications to stabilize the evaporation rate and to prolong the oven runtime. This contribution presents the latest results of the study.

INTRODUCTION

At CERN a number of experiments, in particular the heavy ion runs at the Large Hadron Collider (LHC) rely on a consistent supply of lead ions delivered by the GTS-LHC ion source [1]. This source uses ovens (schematically depicted and described in Fig. 1 (a)) to produce the lead vapour which is then ionized. The produced ions are then injected into the LHC injector chain starting with Linac3. The oven technique is a widely used method to evaporate substances that are solid at room temperature into the plasma chamber of an ion source. The necessary temperature for such an oven depends on the vapour pressure of the evaporated material. Especially lead has a high gas pressure at relatively low temperatures, which makes the evaporation inside a heated oven a natural choice. During a normal run the oven's power is initially ramped up to a suitable value to initiate the lead evaporation and then it is increased slowly throughout the operation to maintain a sufficient evaporation rate. The adjustment is done manually by the source expert as the evaporation rate differs between individual oven fills. Reaching 20 W, which usually happens after two weeks of operation, indicates the end of the runtime as the oven does not maintain a stable evaporation rate any longer and the oven can not be heated up more without damaging the filament or other oven elements. The general experience though is, that after each

run the oven crucible still contains approximately half of the original lead sample. This is an indication that there might be room to improve the oven runtime when it is understood what causes the drop of the evaporation rate.

To understand the limitation of the oven runtime and the link between input parameters and the evaporation rate, a dedicated offline oven test stand (OTS) is used, that provides several diagnostic tools to study the oven in a source like environment. Figure 1 (b) shows the main parts of the test stand. To monitor the evaporation rate of the oven, an INFICON quartz crystal deposition detector is used [2]. A shutter in front of the sensor that is only opened at predefined times protects the sensor and extends the crystal life time. Visual observations can be made through a vacuum window and K-type thermocouples allow temperature measurements on the outer cover of the oven.

BEHAVIOUR IN OXYGEN ATMOSPHERE

One candidate for a mechanism that limits the runtime of the oven is clogging. It is regularly observed after a two weeks run of the Linac3 ion source that the oven tip is clogged with a formation of material that appears to be lead oxide. As the GTS-LHC ion source uses oxygen as a buffer gas within the plasma chamber it can be assumed that the formation might be due to a chemical reaction between the lead and the oxygen. The oven test stand was used to reproduce and study this behaviour. The clogging was not observed during previous experiments in the OTS, when the oven was operated in vacuum ($< 1.0 \times 10^{-7}$ mbar), or in nitrogen. When oxygen is injected into the vacuum system, the formation of lead oxide is observed at the tip of the oven. A thermo valve controlled by a feedback loop from the vacuum gauge stabilized the total pressure inside the OTS at 1.0×10^{-5} mbar over the duration of the run. The oven was ramped to a sufficient evaporation rate, based on prior experiences on the test stand. During the measurement the oven power was then only adjusted when the signal on the deposition sensor dropped notably. Throughout the experiment the oven tip was photographed to document the formation of the blockage. Figure 2 shows the evaporation rate during the run together with four pictures of the oven tip taken at different times indicated in the plot. Mainly three characteristics could be observed:

- The evaporation rate at a constant power level is decreasing over time. To maintain a relatively constant

* toke.koeverner@cern.ch

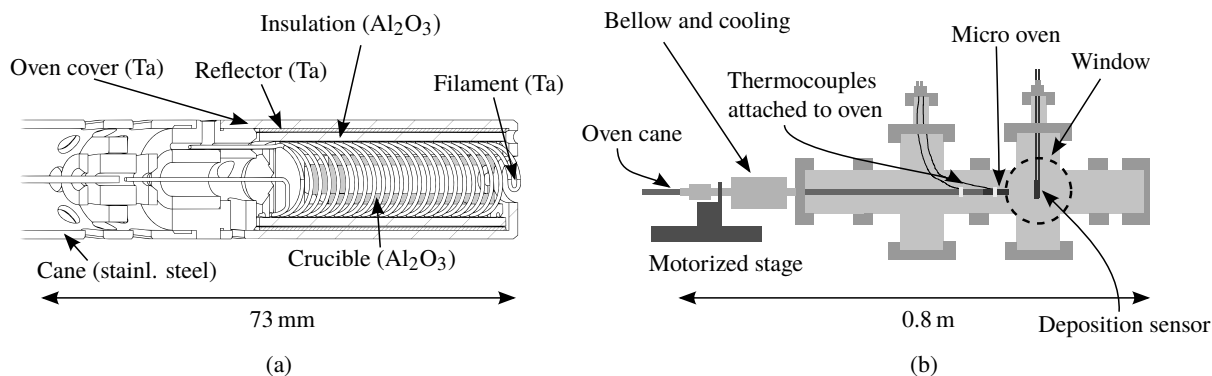


Figure 1: (a) Drawing of the micro oven of the GTS-LHC ion source at Linac3. The alumina crucible containing the lead sample rests inside an alumina structure. A tantalum filament around this structure is heating the crucible. The outer layers serve as thermal insulation. (b) Schematic of the oven test stand. The oven is on the tip of a cane that is used to insert the oven into the chamber. A window next to the oven tip allows visual observation while a deposition sensor measures the evaporation rate. The OTS is evacuated with a turbo-molecular pump and a thermovalve (not depicted) allows a stable atmosphere of a selected gas. A similar graphic is also presented in [3].

output the oven power needs to be increased periodically.

- A blockage at the oven tip was forming that finally blocks the oven completely.
- The measured evaporation rate clearly suggests that its final decrease is due to the complete blockage of the oven tip.

The pictures C and D in Fig. 2 show the transition from a still open to a completely blocked oven. In the time between the pictures the evaporation rate drops to almost zero. Around 14 days after the evaporation started, the blockage closed completely, which compares well with the experience at the operational ion source. Increasing the heating power up to 20 W did not remove the lead oxide formation and could not restore the former evaporation rate. Additionally to the lead oxide blockage that can be seen in the photos of Fig. 2, remaining unoxidised lead could be found inside the oven and behind the blockage. Most likely it was evaporated from the crucible and then deposited on the inner side of the blockage.

It is though noted that the lead oxide formation at the end of the experiment appeared to be bigger than the formations that can usually be observed in the Linac3 ion source. This might be due to a higher oxygen pressure in the experiment than in the real source. However reducing the pressure one order of magnitude already results in no oxide formation at all. Another possible factor, that might influence the formation and thereby the appearance of the oxide blockages in the source is the presence of plasma in front of the oven.

As picture A in Fig. 2 shows, the first decrease in the evaporation rate at a stable power level is not caused by the growing blockage but needs to be explained differently. One possible explanation are regions of differing temperatures within the crucible of the oven. As the vapour pressure and thereby the evaporation rate depends on the temperature, a redistribution of the lead sample for example by consuming material in the evaporation process could lead to decreased

ing evaporation rates. Thermal simulations, presented in [4], predict temperature differences of several tens of degrees Celsius between the end and the tip of the crucible, depending on the total temperature of the oven.

GAS JET GEOMETRY

Observing the build up of the lead oxide at the oven tip gives information about the formation mechanism. Photo A in Fig. 2 shows droplets of lead condensate inside the opening of the oven cover at a time when no oxide is present yet. This hints that the first step in the oxide build up is the condensation of lead vapour at the oven cover. For the condensation to take place the vapour needs to hit those oven parts in significant amounts. Understanding the geometry of the gas flowing out of the crucible can help to understand the reason for the blockage build up and how to mitigate this problem. To find the appropriate way to model the system the gas flow regime needs to be identified, which depends on the present pressures and system dimensions. The Knudsen number K_n is a common coefficient that is used to determine the flow regime. It is the ratio of the mean free path of a gas particle, λ , to the characteristic length of the system, l [5].

$$K_n = \frac{\lambda}{l}. \quad (1)$$

The mean free path can be estimated from the temperature T and present gas pressure p assuming an ideal gas [6].

$$\lambda = \frac{k_B T}{\sqrt{2} \pi \sigma^2 p}. \quad (2)$$

Here k_B is the Boltzmann constant and $\sigma = 360$ pm the diameter of the lead atoms. An assumption for the upper limit of the lead gas pressure at a given temperature inside the crucible can be made using the vapour pressure, p_v , of lead, which can be derived from an empiric formula given in [7]:

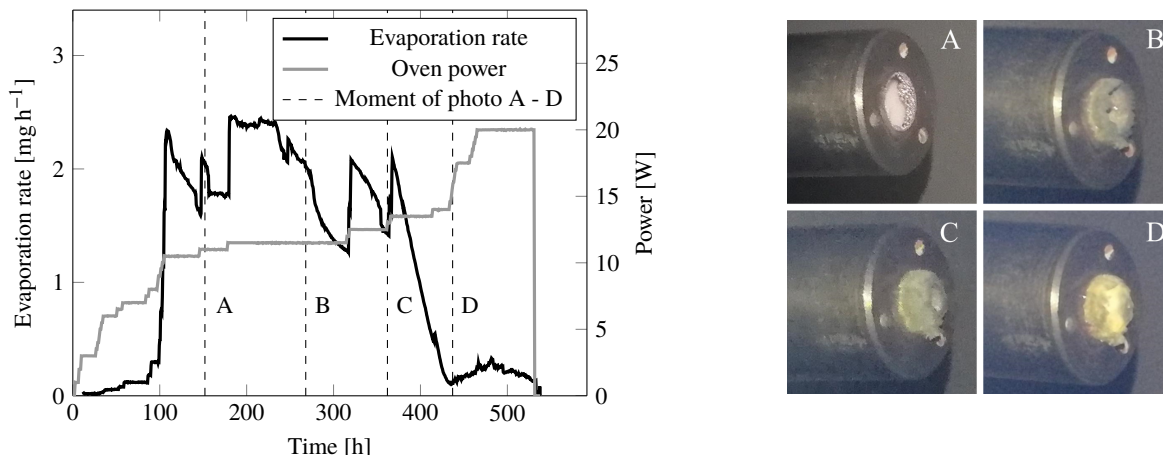


Figure 2: The plot depicts the evaporation rate and the heating power during a heating cycle. The rate was measured every 30 min for 70 s. To convert the deposition signal into an evaporation rate, the total amount of evaporated lead was measured based on the weight of the lead sample at the beginning and the end of the measurement. The dashed lines in the plot indicate the times at which the photos of the oven tip, presented on the right, were taken.

$$\log p_v = 5.006 + A + BT^{-1}, \quad (3)$$

where $A = 5.643$ and $B = -9701$ are coefficients giving the measured vapour pressure of liquid lead in Pa when the temperature T is inserted in K.

The characteristic length in Eq. (1) depends on the geometry of the system. Inside the crucible it is the crucible diameter with $l = 3.4$ mm. Using these estimations the Knudsen number ranges from 96 for $T = 600$ °C to 0.2 for $T = 900$ °C which are realistic temperatures in the crucible, following measurements presented in [4]. It follows that inside the crucible the flow regime is either molecular flow ($K_n > 10$) or Knudsen flow ($10 > K_n > 0.1$), which is a transition regime between free molecular flow and the behaviour of a continuum. In the Knudsen flow the probability of intermolecular interaction is similar to the one of molecule-wall interactions. At the tip of the crucible the pressure drops rapidly due to expansion of the gas, thereby enhancing the mean free path of the gas particles. It can be assumed that due to the low pressures the lead atoms outside of the crucible propagate without significant interaction between them in all relevant distances (1 mm to 300 mm) in front of the oven i.e. in free molecular flow. One consequence of this regime is that a gas jet will not bend around obstacles and no gas will get to regions behind one. In the oven test stand this can e.g. be observed in the form of shadows with no lead deposition on test stand parts that are behind the deposition detector. In the molecular flow regime the particle trajectories only depend on the surrounding geometry and not the amount of other particles present, which makes it possible to simulate the geometry of the gas jet without precisely knowing the actual pressures in the system.

Oven gas jet simulation with Molflow+

The program Molflow+ [8] allows the simulation of gas dynamics in the molecular flow regime with ray tracing

and Monte Carlo calculations. It was used to analyse the particle distribution in the gas jet coming from the oven. The calculated Knudsen numbers show that the validity of the simulation is better outside of the crucible than inside. The simulation is 3 dimensional and contains a model of the oven starting at the inner end of the crucible. Figure 3 shows the geometry and how the particles are tracked through the system. The liquid lead distribution within the crucible during oven operation is not known and not modelled. The simulated particles are simply launched from the inner back wall of the crucible, which resembles a vertical liquid lead surface within the crucible.

One prediction following from the gas jet geometry is the signal reduction of the deposition sensor, when the oven is moved away from the sensor while maintaining a constant evaporation rate. For this the amount of simulated test particles going through a virtual aperture is counted after the simulation ran for a certain amount of time. The position and the diameter of the aperture is chosen to resemble the deposition detector. If the distance to the oven is increased, the amount of test particles traversing the aperture should reduce at the same rate as the signal of the deposition detector does. As shown in Fig. 1 (b) the oven cane is inserted into the test stand through a feedthrough that features a bellow with a motorized stage. This way the oven's distance to the detector can be changed while the oven is operated. Figure 4 shows the result of a measurement where the signal of the deposition sensor was recorded at different distances to the oven and normalized to the maximum signal.

The measurement shows good agreement with the simulation and it can be assumed that the predictions of the jet geometry outside of the oven are close to the real jet. Using the Molflow+ model it can be studied how much of the lead particles exiting the crucible hit the oven parts that showed condensation and later the formation of lead blockages. These are predominantly the front parts of the

Content from this work may be used under the terms of the CC BY 3.0 licence (© 2018). Any distribution of this work must maintain attribution to the author(s), title of the work, publisher, and DOI.

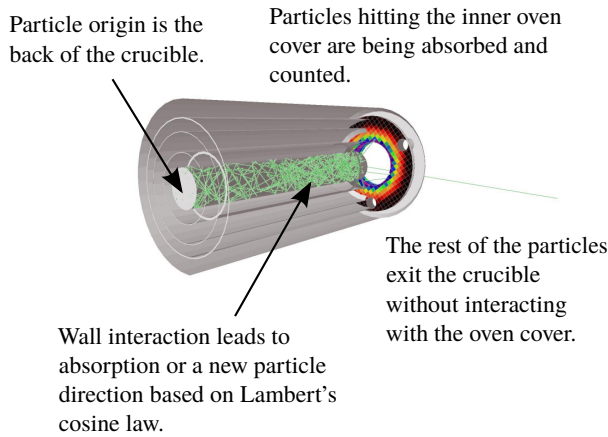


Figure 3: The 3D Molflow+ model to simulate the vapour jet geometry when the molecular flow regime is assumed. Every particle originates from a surface, here the back wall of the crucible inside the oven, starting with a random direction based on Lambert's cosine law. The particle is tracked to the next wall and when its not being absorbed it gets a new direction again based on the cosine law. A detailed description can be found in the Molflow+ documentation [8].

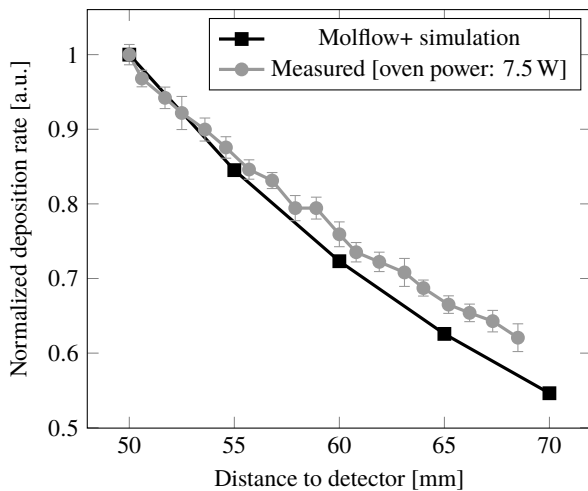


Figure 4: Deposition detector signal at different distances between the oven tip and the detector. Molflow+ predicts a reduction of the signal due to the jet diverging. To compare the deposition rate to the prediction the values are normalized to be one at the distance of 50 mm. The plotted error bars for the measured values show the standard deviation of the detector signal that was averaged over 70 s for each data point.

outer oven cover. Here the simulation predicts that approximately 50 percent of the particles exiting the crucible hit the outer oven cover instead of propagating undisturbed into the plasma chamber (The parts can be seen in Fig. 3). Optimizing the oven geometry by using the model to lower

this percentage might be a way to reduce the effect of oxide blockages on the endurance of the oven. The fraction of gas condensing into lead droplets is however unknown and not described by the simulation.

OUTLOOK

This paper presents experiments and simulations to understand the effect of lead oxide blockages on the oven runtime. The measurement implies that reducing them could help to enhance the oven runtime. Observation at the oven test stand and simulations imply that the formation is caused by the direct lead gas exposure of the outer oven cover. As the gas jet geometry is well described by a Molflow+ model, this model can be used to study geometry changes to enhance the percentage of gas atoms that propagate freely from the crucible into the plasma chamber. Besides the blockages the evaporation rate stability of the oven might also be affected by the temperature profile of the crucible. To study the thermal characteristics of the oven an ANSYS model was developed which is presented in [4] and [3]. The thermal simulations show that the crucible temperature decreases towards its tip. As mentioned this might be a cause of unstable evaporation rates besides the formation of oxide blockages. From the presented studies two goals for the design optimization follow, which can interfere with each other:

- A more homogeneous temperature distribution in the crucible.
- Less lead deposition on the outer oven cover.

To even the temperature distribution within the crucible additional layers of insulation at the oven tip between the crucible and the outer cover are a possible approach. But it needs to be examined whether they could become a new source of blockages. One example for a modification that might have a positive effect in decreasing the lead oxide formation on the outer oven cover is an elongation of the crucible at its front. However this could lead to a less uniform temperature profile in the crucible and thereby less stable evaporation or even blockages within the crucible itself as radiation could transport more heat out of the thermal insulation. The oven test stand allows to test the effects of different design modifications and whether they lead to improvements or not.

REFERENCES

- [1] C. E. Hill *et al.*, "GTS-LHC: A New Source For The LHC Ion Injector Chain," *AIP Conference Proceedings*, vol. 749, no. 1, pp. 127–130, 2005. doi: 10.1063/1.1893381.
- [2] *The official INFICON website*, <http://www.inficon.com>, accessed 2017-10-03.
- [3] T. Kövener, C. Fichera, D. Küchler, and V. A. Toivanen, "Study of the Micro Oven for the Linac3 Heavy Ion Source," *Proc. of the 17th Int. Conf. on Ion Sources, Geneva 2017*, to be published.
- [4] C. Fichera, F. Carra, D. Küchler, and V. Toivanen, "Numerical study of the thermal performance of the CERN Linac3 ion source miniature oven," *Nucl. Instrum Methods Phys Res A*, vol. 901, pp. 21–31, 2018, issn: 0168-9002.

- [5] F. Sharipov, *Rarefied Gas Dynamics: Fundamentals for Research and Practice*. Wiley, 2015, ISBN: 9783527685530.
- [6] J. Jewett and R. Serway, *Physics for Scientists and Engineers with Modern Physics*. Thomson Brooks/Cole, 2008, ISBN: 9780495112402.
- [7] C. B. Alcock, V. P. Itkin, and M. K. Horrigan, "Vapour Pressure Equations for the Metallic Elements: 298–2500K," *Canadian Metallurgical Quarterly*, vol. 23, no. 3, pp. 309–313, 1984. DOI: 10.1179/cmq.1984.23.3.309.
- [8] *The official MOLFLOW+ website*, <https://molflow.web.cern.ch>, accessed 2018-07-31.

PRODUCTION OF INTENSE METAL ION BEAMS AT THE DC-60 CYCLOTRON

V.N. Loginov[†], S.L. Bogomolov, A.E. Bondarchenko, V.E. Mironov,
Joint Institute for Nuclear Research, 141980 Dubna, Moscow Region, Russia
V.V. Alexandrenko, I.A. Ivanov, M.V. Koloberdin, S.G. Kozin, A.E. Kurakhmedov,
D.A. Mustafin, E.K. Sambayev, M.V. Zdorovets,
Astana Branch of Institute of Nuclear Physics, 010000 Astana, Kazakhstan

Abstract

In 2017-2018, research program of the DC-60 cyclotron (Astana Branch of the Institute of Nuclear Physics, Kazakhstan) requests acceleration of intense ion beams of solid elements. Beams of B and Fe ions are produced in ECR ion source by using the volatile compounds, while ions of Li, Mg, P and Ca are produced by evaporation from an oven. Beams of $^{56}\text{Fe}^{10+}$, $^7\text{Li}^{1+}$, $^{24}\text{Mg}^{4+}$, $^{31}\text{P}^{5+}$, $^{40}\text{Ca}^{7+}$, and $^{11}\text{B}^{2+}$ ions were accelerated up to energies of 1.32-1.75 MeV/u.

INTRODUCTION

The DC-60 cyclotron [1] is designed for acceleration of ions from Li to Xe with A/Z in the range from 6 to 12. The accelerator is equipped with the normally-conducting 14-GHz DECRIS-3 ion source [2]. The main parameters of the source are: magnetic fields at the injection and extraction sides of the source are 1.3 and 1.1 T respectively, the hexapole field at the wall is 1.0 T, the source chamber length is 20 cm, and the chamber diameter is 6.4 cm. Microwaves are injected into the source through the coaxial waveguide along the source axis. The extraction voltage of the source is up to 25 kV.

We use three different methods for metal ion production: evaporation of material from container heated by microwaves in the source chamber, evaporation from a filament-heated oven, and injection into the source of volatile compounds that contain the desired atoms.

When producing ions of the solid elements, thin cylindrical tantalum sheet is inserted into the source chamber to facilitate atom recycling from the walls [3]. As a support gas, we always use helium, which was found to be the best choice for production of moderately charged ions requested by the DC-60 cyclotron.

EVAPORATION FROM OVEN

The upper temperature limit for our oven is 900 °C, which defines the range of working materials. The heating power is 25 W, the 0.1-mm diameter nichrome wire is used to heat the tantalum (standard) crucible (SC), with length of 28 mm, inner diameter 2 mm, outer diameter 2.8 mm. The oven is mounted on a movable holder inside the waveguide such that the orifice position can be regulated

in the range (-15÷15) mm in respect to the edge of biased electrode.

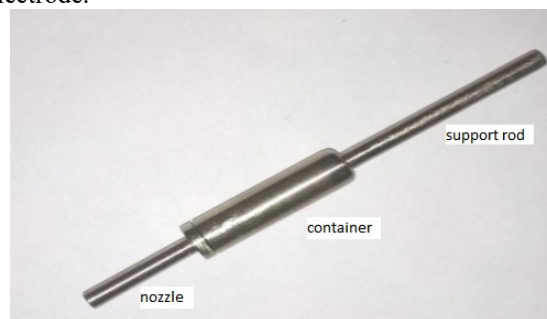


Figure 1: The large volume crucible.

To increase the oven's operational time, we use enlarged crucible (EC) for some materials. This crucible is presented in Fig. 1. The central cylinder contains the working material; inner diameter of the container is 6 mm, outer diameter is 7 mm, the container length is 20 mm. On one side, the container is connected to the solid rod heated by the filament; the rod has the same sizes as the standard crucible. Vapors leave the container through the 10-mm-long nozzle with the inner diameter of 1 mm. Twisted tantalum wire is pressurized inside the nozzle to shield the working material from the plasma and to prevent spilling of the melted material into the source chamber.

The nozzle and container are mainly heated by microwaves with some extra-heating by plasma. The crucible temperature is controlled by moving the holder in and out of the source chamber and by changing the filament current. Heating of the container from backside by filament is optional feature that gives additional control for adjusting the material evaporation rate.

Charge state distributions of the extracted Li ions are shown in Figs. 2 and 3 for enlarged crucible (Fig. 2) and for the standard crucible. Operational temperatures of the crucibles are 200 °C, and metal consumptions are 0.7 and 1.1 mg/h for EC and SC respectively, with the extracted Li^{1+} currents of 200 and 500 μA .

[†] loginov@jinr.ru

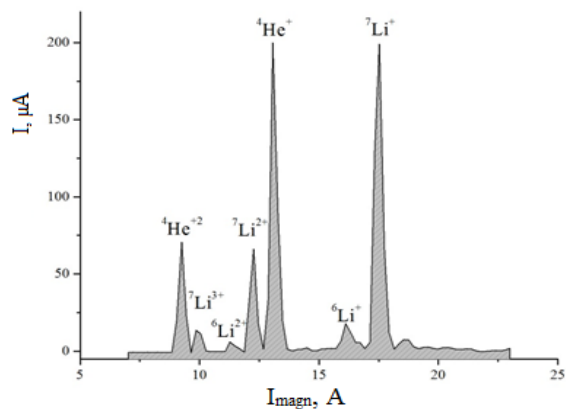


Figure 2: Charge state distribution of the extracted Li ions with the enlarged crucible (EC).

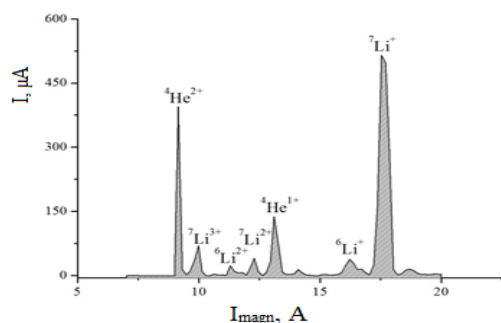


Figure 3: Charge state distribution of the extracted Li ions with the standard crucible (SC).

Current of Mg^{4+} ions (EC) reaches the level of 80 μA at the metal consumption of 2.1 mg/h. The extracted magnesium ion distribution is shown in Fig. 4.

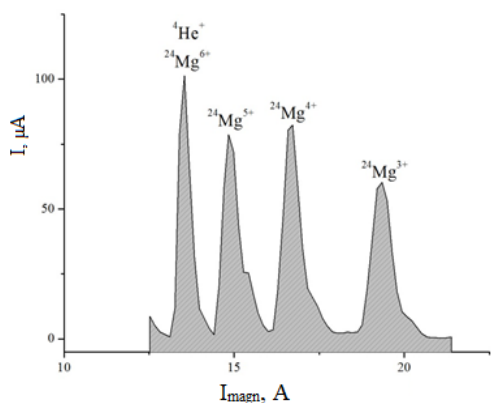


Figure 4: Charge state distribution of the extracted Mg ions (EC).

For calcium ion production, the oven (SC) is heated up to 720 °C. Metal consumption is 0.7 mg/h when tuning the source to extract 140 μA of $^{40}Ca^{5+}$ and 75 μA of $^{40}Ca^{7+}$ ion currents. The current distribution is shown in Fig. 5.

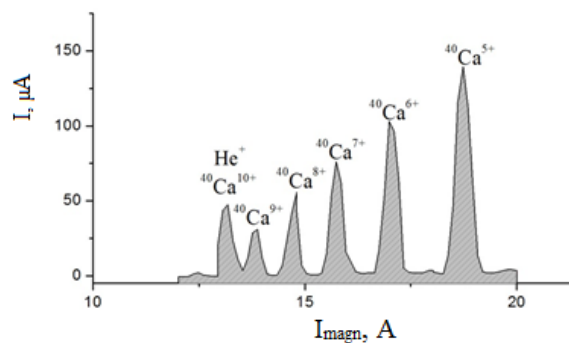


Figure 5: Charge state distribution of the extracted Ca ions (SC).

Oven temperature for production of P ions is 100 °C. Consumption of phosphorus is 1.7 mg/h, and we reach the level of 60 μA for $^{31}P^{5+}$ ion current (Fig. 6). As a working substance we used red phosphorus.

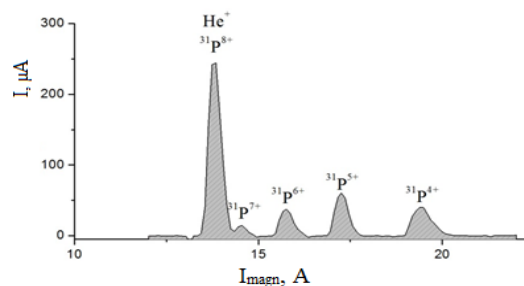


Figure 6: Charge state distribution of the extracted P ions (SC).

MIVOC PRODUCTION OF IONS OF SOLID ELEMENTS

MIVOC (Metal Ions from Volatile Compounds) method is based on use of metal compounds (metallocenes) that have a high vapor pressure at room temperature [4]. Ferrocene $Fe(C_5H_5)_2$ has a vapor pressure of 2.6×10^{-3} Torr at 20 °C, and dicarba-*closo*-dodecaborane compound $C_2B_{10}H_{12}$ has a vapor pressure of about 1-2 Torr. Using these compounds, intense beams of B and Fe ions were obtained for the first time at the DC-60 cyclotron of Astana Branch of INP.

Compound is placed into a glass container connected to the gas transport line at the injection side of the source. No extra heating of the container is needed, and the gas flow into the source is regulated by a needle valve.

Up to 25 μA of $^{56}Fe^{10+}$ ions is extracted in the optimized conditions (Fig. 7) with Fe consumption of 0.8 mg/h.

Content from this work may be used under the terms of the CC BY 3.0 licence (© 2018). Any distribution of this work must maintain attribution to the author(s), title of the work, publisher, and DOI.

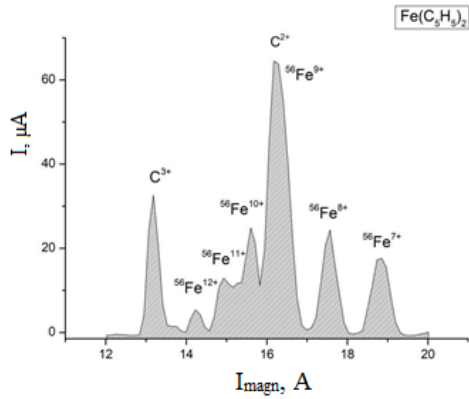


Figure 7: Charge state distribution of the extracted Fe ions.

The maximum current of $^{11}\text{B}^{2+}$ is up to 60 μA . Spectrum of the extracted boron ions is shown in Fig. 8. Consumption of the compound is about of 1.2-1.4 mg/h.

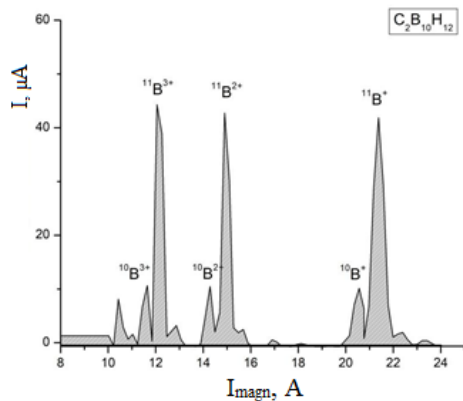


Figure 8: Charge state distribution of the extracted B ions.

The extracted ions of Fe, B, Li, Ca, P, Mg were injected into the DC-60 cyclotron and accelerated up to the energies shown in Table 1. Quality of the beams was good enough to obtain the transmission coefficients from extraction to the target at the level of a few percent.

Table 1: Accelerated Beams

Ion	E, MeV/u	I_{extr} , μA	I_{target} , μA
$^{40}\text{Ca}^{7+}$	1.75	50	1.35
$^{31}\text{P}^{5+}$	1.75	20	0.58
$^{24}\text{Mg}^{4+}$	1.75	46	1.14
$^7\text{Li}^+$	1.32	100	1.5
$^{56}\text{Fe}^{10+}$	1.75	15.6	0.22
$^{11}\text{B}^{2+}$	1.5	24.2	0.7

CONCLUSIONS

Techniques for production of intense beams of solid materials are successfully tested at DC-60 cyclotron. The accelerated beams will be used for experiments in the fields of nuclear physics, solid-state radiation physics, and various applied researches.

ACKNOWLEDGEMENTS

This work was supported by MES RK IRN under grant number AP05133476.

REFERENCES

- [1] B. Gikal, S. Dmitriev, P. Apel, S. Bogomolov, O. Borisov, V. Buzmakov, G. Gulbekyan, I. Ivanenko, O. Ivanov, M. Itkis, N. Kazarinov, I. Kalagin, I. Kolesov, A. Papash, S. Paschenko, A. Tikhomirov, M. Khabarov, *Phys. Part. Nucl. Lett.*, vol. 5, pp. 642-644, 2008.
- [2] A.A. Efremov, S.L. Bogomolov, A.N. Lebedev, V.N. Loginov, N.Y. Yazvitsky, *Proceedings of the 14th International Workshop on ECR Sources, ECRIS99, CERN, Geneva, Switzerland, 3-6 May 1999*, pp. 71 - 74.
- [3] A.A. Efremov, S.L. Bogomolov, V.B. Kutner., A.N. Lebedev, V.N. Loginov, N.Yu. Yazvitsky. "Li and Ca ion beam production". *Proc. of the XV International Conference on Cyclotrons and their Applications. Caen, France, 14 - 19 June, 1998*. pp.145 - 147.
- [4] H. Koivisto, J. Ärje and M. Nurmia, *Nucl. Instr. and Meth. in Phys. Res.*, vol. B94, pp. 291 - 296, 1994.

OPERATION OF THE GTS-LHC ECR ION SOURCE IN AFTERGLOW WITH VARYING KLYSTRON FREQUENCY

D. Kuchler[†], M. O’Neil

CERN, BE Department, CH-1211 Geneva, Switzerland

V. Toivanen

Grand Accélérateur National d’Ions Lourds (GANIL), F-14076 Caen Cedex 05, France

Abstract

The GTS-LHC ECR ion source delivers lead ions for the CERN heavy ion programme at the LHC and the SPS fixed target physics. The source is normally operated with a main microwave frequency of 14.5 GHz in the afterglow mode. As part of the consolidation the microwave generator was replaced with a klystron based generator that allows free variation of the operating frequency in a range of 14.0 – 14.5 GHz.

The aim of this study was to see how the lead charge state Pb^{29+} , which is the main ion species produced for experiments, is influenced by the different frequencies. Variations in performance were observed (beam intensity and beam stability), but no frequencies were found that would provide significant performance improvements compared to normal operation at 14.5 GHz. The results in general suggest that for the GTS-LHC ion source the optimal operating frequency depends on the overall source tuning and the influence of varying the main frequency is comparable to adjusting the other tuning parameters.

INTRODUCTION

The GTS-LHC ECR ion source is based on the original Grenoble Test Source (GTS) and provides since 2005 the CERN heavy ion injector complex with ions [1]. Over the last years the source has delivered lead, argon and xenon ions for the two main clients — the fixed target experiments in the North Area of the Super Proton Synchrotron (SPS) and the experiments at the LHC.

The main 14.5 GHz microwave generator of the source was taken over from the predecessor source (ECR4) and was meanwhile more than 20 years old. As the old generator suffered from increasing failure rate and obsolete components it was decided to replace it within the CERN consolidation project.

Recent experiments with a travelling wave tube amplifier (TWTA) showed that for the lead ion of interest (Pb^{29+}) some increase of the beam intensity can be reached [2]. And as the frequency where this happens is covered by the new microwave generator it became of interest to study the ion beam production varying the frequency from the microwave generator and to see if a similar behaviour as with the TWTA can be reproduced. This would help to get a better understanding of the TWTA experimental results and in the positive case provide more beam for the users.

[†] detlef.kuchler@cern.ch

THE MICROWAVE GENERATOR

The spare generator of the source, which was used in the past for experiments with 18 GHz [3], was delivered by Sairem. To have only one provider for the source microwave generators it was decided to have also the new main generator from Sairem.

The new microwave generator has the following characteristics:

- Klystron based
- frequency range: 14.0 – 14.5 GHz
- number of Klystron channels: 20
- bandwidth of each Klystron channel: 25 MHz
- step size of the synthesizer: 1 kHz
- nominal peak power: 2.2 kW (for a matched load)
- operation mode: cw or pulsed (via external timing)

Table 1: Central Frequencies of the 20 Klystron Channels.

channel number	central frequency/GHz
1	14.0125
2	14.0375
3	14.0625
4	14.0875
5	14.1125
6	14.1375
7	14.1625
8	14.1875
9	14.2125
10	14.2375
11	14.2625
12	14.2875
13	14.3125
14	14.3375
15	14.3625
16	14.3875
17	14.4125
18	14.4375
19	14.4625
20	14.4875

The change of the Klystron channels is motorized and the synthesizer can be programmed via a USB interface from a Windows based computer.

Content from this work may be used under the terms of the CC BY 3.0 licence (© 2018). Any distribution of this work must maintain attribution to the author(s), title of the work, publisher, and DOI.

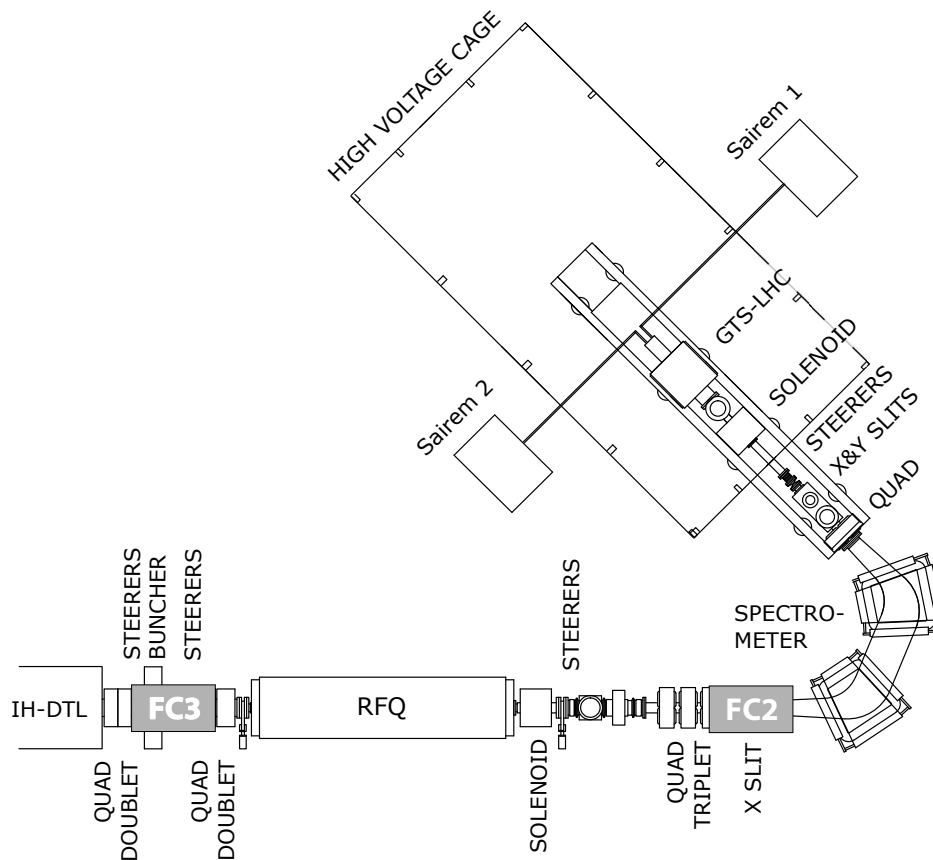


Figure 1: Schematic overview of the low energy part of Linac3. The position of the two Faraday cups (FC2 and FC3) used for the measurements are marked. Sairem 2 is the main microwave generator used for the experiment. Sairem 1 is the spare microwave generator.

The generator communicates via an Ethernet Modbus protocol with an external PLC which is fully integrated in the CERN accelerator controls architecture.

(RFQ) (see Fig. 1). The beam emittance could not be measured.

EXPERIMENTS WITH VARIED FREQUENCY

The experiment was done during the start-up preparation of the source. Before the experiment the source was optimized using a frequency of 14.5 GHz. The source was always tuned on Pb²⁹⁺.

Experiences from the past show that especially for metal ion beams a proper source conditioning may take from several days up to some weeks to reach the full performance (stable and intense beam). Due to the limited time it was not possible to wait for the final optimum conditioning for each frequency step. Data were taken when a temporary stability was reached.

Multiple frequency sweeps were performed with different source settings. The beam intensity was measured in a Faraday cup (FC2) directly after the spectrometer and in a Faraday cup (FC3) after the Radiofrequency Quadrupole

Table 2: Source Settings For Different Frequency Scans.

	a)	b)	c)	d)
microwave power/W	1650	1700	1650	1000
bias disk/V	320	280	300	295
injection sol./A	1270	1270	1270	1270
central sol./A	180	200	150	220
extraction sol./A	1210	1200	1200	1185
gas/a.u.	9.780	9.710	9.740	9.755
extraction voltage/kV	18.89	18.89	18.89	18.89

Before each sweep the source and the Low Energy Beam Transport (LEBT) were optimized. The most relevant ion source parameters for the sweeps are summarized in Table 2 and the resulting ion current behavior as a function of the microwave frequency is presented in Fig. 2. In the sweeps the center frequencies of each channel were used, except for channel 20. For this the center frequency and the highest available frequency (14.5 GHz) were measured. For the cases a) to c) it seems that the starting point was also the

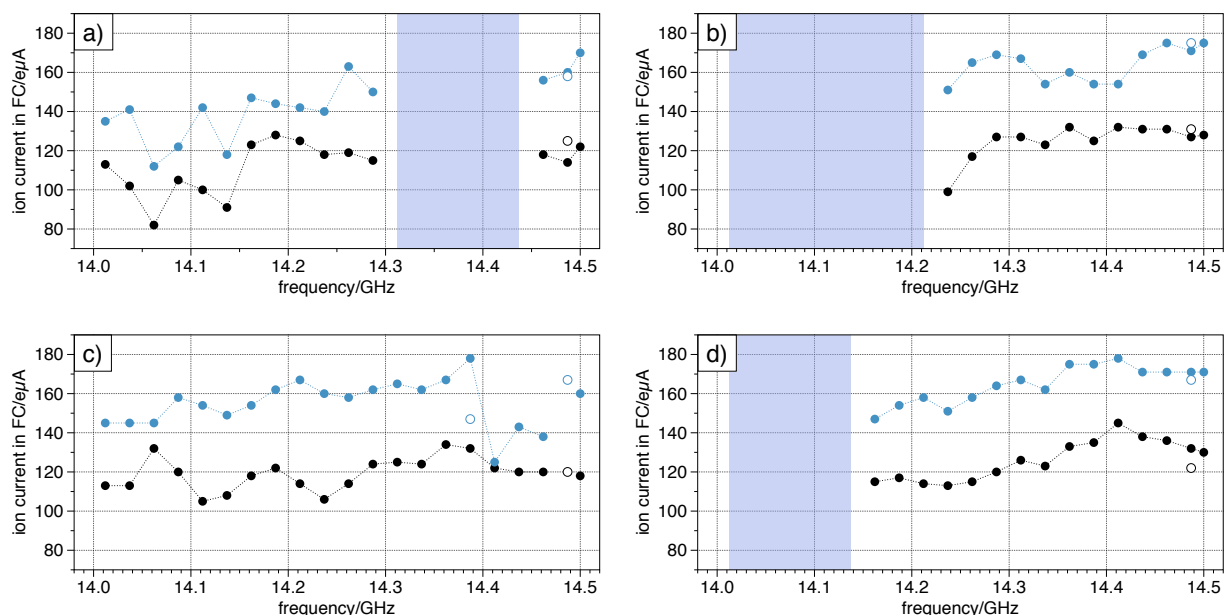


Figure 2: Ion currents in FC2 (blue) and FC3 (black) for different frequency scans. The main source parameters for the different scans can be found in Table 2. Grayed out areas indicate frequency regions with very unstable beam. The open circles indicate repeat measurements after the frequency scan. These measurements can give an impression of the reproducibility.

point with the highest beam intensity in FC2 (sweeps a) and b) were started at channel 20 (14.5 GHz) and sweep c) was started at channel 15 (14.3625 GHz)). For case d) the sweep started at channel 20 (14.5 GHz) and the highest beam current was recorded at channel 17 (14.4125 GHz). All scans went from high to low frequency.

As a general trend one can observe that on average the beam currents seem to increase towards higher frequencies. This could be due to the global frequency scaling effect. On top of the global current increase a fine structure was observed with frequency. But a reproducible, stable pattern independent of the other source parameters could not be identified. Based on the present results one cannot draw a clear conclusion if the fine structure is caused by out-gassing or by improved/degraded ionization conditions due to the varied microwave conditions, or microwave coupling issues.

For some combinations of source setting and frequency it was impossible to stabilize the extracted beam (grayed out regions in Fig. 2). The position and width of these regions vary in dependence of the source settings. No improvement of these beams could be observed over time compared to more out-gassing related instabilities.

Assuming an intensity independent transmission through the RFQ (at least in a certain intensity range) one would expect a constant ratio of the ion beam intensity between FC2 and FC3. But as one can see in Fig. 3 this is not the case. This seems to indicate that the beam emitted from the source occupies a different volume (size and/or shape) in phase space for the different microwave frequencies.¹ It is

¹ As mentioned before it was not possible to measure the emittance directly.

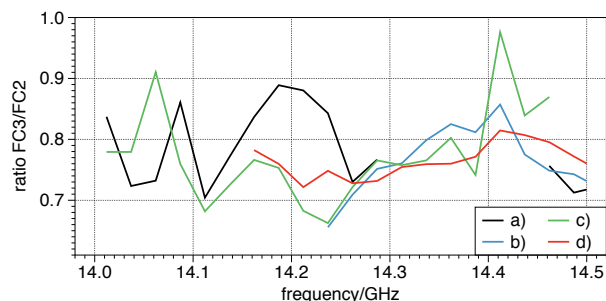


Figure 3: Ratio of the ion beam intensities between FC2 and FC3 given in Fig. 2.

known that the transmission through the LEBT and the RFQ is sensitive concerning changes of the beam energy.

Although the source was well conditioned at 14.5 GHz before the experiment started a significant out-gassing was noticed while changing to some of the lower frequencies. Running the source for a while at these specific frequencies lead to a recovery of the vacuum conditions. The reason for this behaviour could be that with the lower frequencies parts of the plasma chamber gets bombarded with particles which do not see any or only a limited number of particle interactions at the reference frequency of 14.5 GHz.

In general one can say that the tuning of the source influences clearly the response to the different frequencies.

Comparing the charge state distributions of some special cases (see Fig. 4) one can clearly see the enhancement of the beam intensity for lower charge states. The distributions seem to be broadened towards the lower charge states. This

Content from this work may be used under the terms of the CC BY 3.0 licence (© 2018). Any distribution of this work must maintain attribution to the author(s), title of the work, publisher, and DOI.

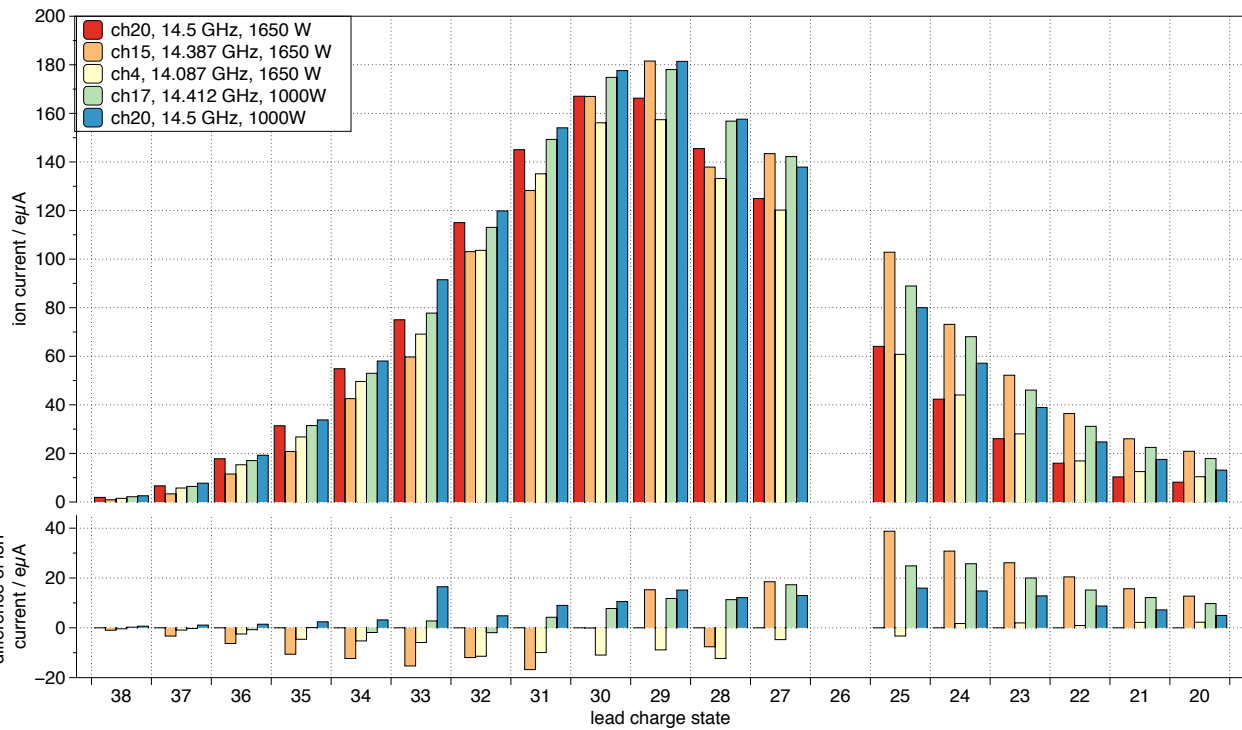


Figure 4: Charge state distributions for different source settings. The lower part shows the difference of the ion current in respect to the nominal setting (ch20). For the relation between channel number and frequency see Table 1.

is also reflected in a tendency of higher total drain current from the source (see Fig. 5).

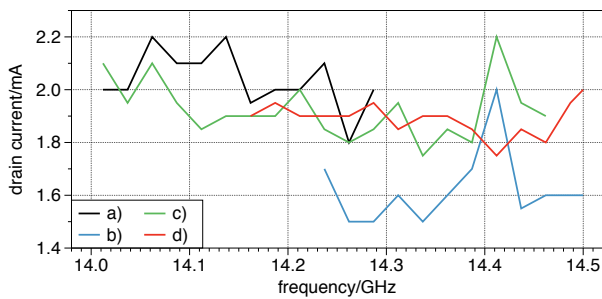


Figure 5: Drain current of the source high voltage power supply for the scans shown in Fig. 2.

Looking at Pb^{29+} one can see some gain for medium frequencies (channel 15 and 17) and also for the reference frequency at lower power. Especially the last case points towards the issue of insufficient conditioning for all the different settings as normally at this low power the beam intensity is also much lower compared to a nominal microwave power of around 1700 W.

If one assumes that the varying frequency alters the exact location of where the plasma particle flux interacts with the chamber wall this shift in performance could be caused by the enhanced recirculation of the lead from the plasma chamber walls and in this case one would expect this to be only a temporary phenomenon.

DISCUSSION AND CONCLUSION

In previous measurements using a TWTA [2] some enhancement of beam intensity around a frequency of 14.2 GHz was observed. A similar behaviour could not be reproduced with the Klystron driven generator. This suggests that the observed effects with the TWTA were caused by the combined influence of the klystron and the TWTA, which were operated in double frequency mode, and the same conditions can not be achieved with only a single microwave source.

Even more the measurements seem to show that there is no clear preferred frequency. The source behaviour found suggests that the frequency becomes a tuning parameter as all the other settings of the source.

This suggests that the observed fine structure in Fig. 2 is not defined by e.g. the plasma chamber geometry or other fixed properties of the source, but is rather the result of dynamic processes taking place in the plasma volume. This result is in line with observations presented in Ref. [4] showing that the frequency structure defined by the chamber disappears in the presence of plasma.

In general it must be stated that the oven settings were not tuned for the different frequencies during the experiments and it was observed that the source condition was clearly altered after performing the frequency sweeps. This makes it difficult to draw strong final conclusions based on these results. Longer runs in the future on selected frequencies will clarify these issues and allow a better assessment of the early findings presented here.

REFERENCES

- [1] C.E. Hill, D. Küchler, C. Mastrostefano, M. O'Neil, R. Scrivens, D. Hitz, L. Guillemet, J. Chartier, J.M. Mathonet, and G. Rey-Giraud, "Experience with the GTS-LHC ion source", 3rd LHC Project Workshop: 15th Chamonix Workshop (2006), pp. 239–241.
- [2] V. Toivanen, G. Bellodi, D. Küchler, F. Wenander, and O. Tarvainen, "Effect of double frequency heating on the lead afterglow beam currents of an electron cyclotron resonance ion source", *Phys. Rev. Accel. Beams*, vol. 20, p. 103402 (2017).
- [3] D. Küchler, M. O'Neil and R. Scrivens, "First experience with the operation of the GTS-LHC ion source at 18GHz", *Proc 18th Int. Workshop on ECR Source*, Chicago (2008).
- [4] V. Toivanen, O. Tarvainen, C. Lyneis, J. Kauppinen, J. Komp-pula, and H. Koivisto, "Electron cyclotron resonance ion source plasma chamber studies using a network analyzer as a loaded cavity probe", *Rev. Sci. Instrum.* vol. 83, p. 02A306 (2012).

STUDY OF THE INFLUENCE OF MAGNETIC FIELD PROFILE ON PLASMA PARAMETERS IN A SIMPLE MIRROR TRAP

M. Mazzaglia^{1,†}, G. Castro¹, D. Mascali¹, R. Miracoli³, S. Briefi², U. Fantz², L. Celona¹, E. Naselli^{1,4}, R. Reitano^{1,4}, G. Torrìsi¹ and S. Gammino¹

¹ INFN – Laboratori Nazionali del Sud, Catania, Italy

² Max-Planck-Institut für Plasmaphysik, Garching, Germany

³ ESS Bilbao, Zamudio, Spain

⁴ Università degli studi di Catania, Catania, Italy

Abstract

This work presents the multiple diagnostics characterization of the plasma in an axis-symmetric simple mirror trap as a function of magnetic field profile (mirror ratios and magnetic field gradient), especially in the quasi-flat B field configuration that is typical of Microwave Discharge Ion Sources, and also of neutral gas pressure and microwave power. The simultaneous use of Optical Emission Spectroscopy, Langmuir Probe and X-ray diagnostics allows the characterization of the whole electron energy distribution function (EEDF), from a few eV to hundreds of keV. Results show non-linear behaviour under small variations of even one source parameter and strong influence on EEDF of the B_{\min}/B_{ECR} ratio. Benefit and next developments will be highlighted.

INTRODUCTION

Plasma diagnostics plays a crucial role for the development of high-performance ion sources for accelerators. A detailed knowledge of the electron energy distribution function (EEDF) is mandatory for any improvement of existing or future devices. For sake of compactness (mechanical constraints limit ECRIS ion source accessibility), historically only a limited number of diagnostics have been applied to ECRIS plasmas. Therefore, in most of the cases, plasma properties were only estimated from semi-empirical considerations. Over the last years, few groups have directly probed ECRIS plasma via diagnostics [1, 2, 3, 4]. Never performed in the past, multi-diagnostics allow to measure simultaneously plasma parameters in different energy domains. At LNS we plan to implement a multi-diagnostics system able to probe the plasma from RF to gamma-ray emission, performing space and time-resolved measurements. In this paper we present data already acquired in multi-diagnostics, at the Flexible Plasma Trap (FPT) test-bench [5], using at the same time Langmuir Probe (LP), optical Emission Spectroscopy (OES) and X-Ray spectroscopy. Despite the results have been obtained on a test-bench, the plasma trap emulates several features of existing ECRIS, and especially we hereby will focus the

simple-mirror and Flat-B field configurations which is common in the field of Microwave Discharge Ion Sources for high current proton beams. The simultaneous use of these different diagnostics allowed to characterize the plasma parameters as a function of the applied external magnetic field, of microwave power and gas pressure.

EXPERIMENTAL SETUP AND DIAGNOSTIC METHODS

Multi-diagnostics measurements have been carried out on the FPT, installed at INFN-LNS and described in [5]. Figure 1 shows a schematic diagram of the FPT, including the RF power injection system, the three magnetic coils, LP, OES and X-rays diagnostics.

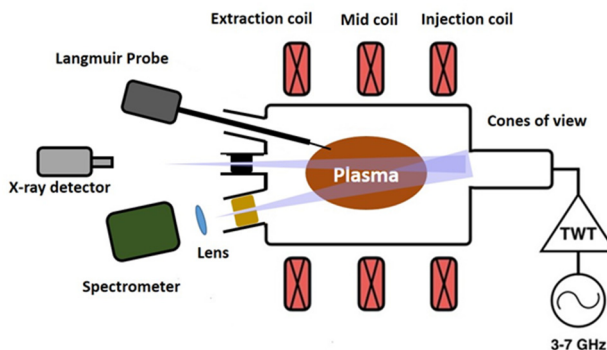


Figure 1: Schematic of the FPT experimental setup at the INFN-LNS.

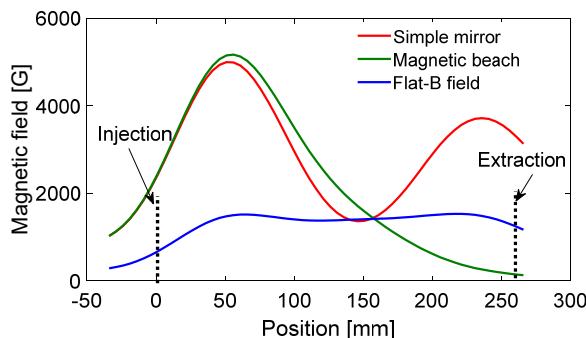


Figure 2: Magnetic field profiles that can be generated by the FPT.

Content from this work may be used under the terms of the CC BY 3.0 licence (© 2018). Any distribution of this work must maintain attribution to the author(s), title of the work, publisher, and DOI.

† maria.mazzaglia@lns.infn.it

The solenoids have been developed in order to allow the generation of different magnetic configurations, from flat-B field to simple mirror or magnetic beach (see Fig. 2).

In this work, we investigated the plasma generated in flat-B field configuration. Microwaves have been generated by a Travelling Wave Tube (TWT) operating in the range 4-7 GHz. Hereinafter, a brief introduction to the diagnostics used during the experimental campaign is given.

LP diagnostics: The Langmuir Probe (LP), although is an invasive diagnostic, represents the easiest way to perform the measurements of density and temperature of low energy plasma electrons (1-100 eV). The probe consists of a tungsten tip with a diameter of 125 μm and a length of 4 mm, inserted in a tungsten core coated with alumina. The plasma parameters have been obtained by the resistivity curve using the theoretical model described in [6]. LP data have been used as cross-checks and benchmarks of OES measurements.

OES diagnostics: OES provide a method to determine plasma parameters in a non-invasive way. However, these diagnostics have the drawback that only line-of-sight-integrated results are obtained. Spectroscopic measurements have been carried out with an intensity-calibrated survey spectrometer ($\Delta\lambda_{\text{FWHM}} \approx 1 \text{ nm}$) for the Balmer series of atomic hydrogen (H_α to H_γ) as well as for the Fulcher- α transition of the H_2 molecule ($d^3\Pi_u \rightarrow a^3\Sigma_u^+$). The measured emissivities have been evaluated with the collisional radiative (CR) models Yacora H and Yacora H_2 [7]. The plasma parameters have been estimated by comparing the line ratio measured during the experimental campaign with the theoretical line ratio estimated by means of a CR model. In particular, we used the H_β/H_γ and H_α/H_β ratios to determine electron density and temperature and $H_\gamma/H_{\text{Fulch}}$ ratio to determine the relative abundance between atomic and molecular hydrogen n_H/n_{H_2} .

X-ray diagnostics: The X-ray volumetric measurement is a powerful method for determining density and temperature of medium-high energy plasma electrons ($> 1 \text{ keV}$). The X-ray flux requires a proper collimation for fixing the solid angle covered by the X-ray detector and an adequate emissivity model for the data evaluation. The plasma emissivity model used is described in references [3, 8]. The X-ray measurements have been carried out with two different detectors: High Purity Germanium (HpGe) for the detection of X-rays in the range 1-100 keV and Silicon Drift Detector (SDD) able to reveal X radiation in the range 1-30 keV.

EXPERIMENTAL RESULTS

The experimental campaign has been carried out in different conditions of neutral pressure, microwave power and magnetic field profile. FPT is a very versatile machine which can operate in Simple Mirror with the possibility to tune the trap at different mirror ratios. That is of particular importance for studying the ECR heating processes as a

function of the magnetic field structure and, in particular, to explore the plasma instabilities triggered by the B-field itself. For this reason, most of the experimental campaign has been devoted to simple-mirror operations, and a wide analysis of the collected data is going to be published elsewhere [9]. For sake of brevity we hereby present a short summary of what obtained in simple-mirror, and a wider analysis of flat-B field configuration. In simple-mirror configuration the microwave frequency has been set at 6.83 GHz. The change in mid coil current allowed to modify the $B_{\text{min}}/B_{\text{ECR}}$ ratio along the chamber axis from 0.56 to 1.04. The measurements have been carried out at two different pressures ($1.5 \cdot 10^{-4}$ and $2 \cdot 10^{-3}$ mbar) and microwave power fixed at 30 and 80 W. While, in flat-B field configuration, the microwave frequency has been set at 4.13 GHz, microwave power at 80, 130 and 160 W and pressure at $1.5 \cdot 10^{-4}$ mbar.

We present data from both the magnetic configurations only from LP data. Electron density and temperature versus the position at $2 \cdot 10^{-3}$ mbar, in simple mirror configuration, are respectively shown in Figs. 3 and 4.

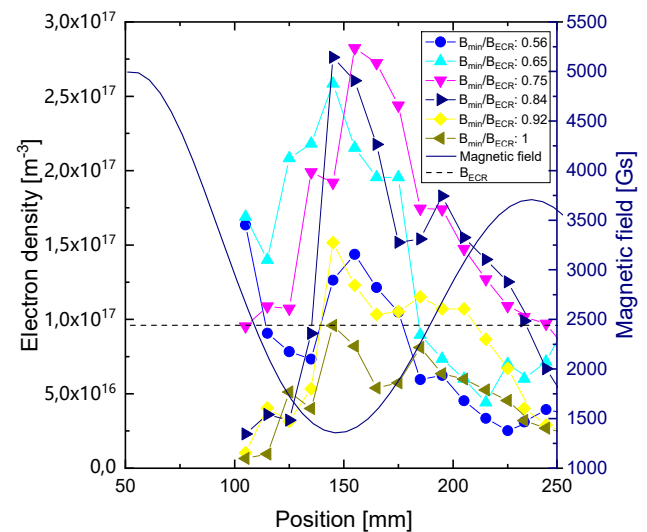


Figure 3: Electron density profiles evaluated by means of LP at 80 W microwave power and $2 \cdot 10^{-3}$ mbar pressure.

Maximum average and peak density is obtained when $0.65 < B_{\text{min}}/B_{\text{ECR}} < 0.84$. The plasma density then drops and at $B_{\text{min}}/B_{\text{ECR}}$ approaching the unity it collapses of a factor five. For smaller ratios the plasma is well peaked around the midplane of the plasma chamber, due to the effective magnetic trapping. Then, the density distribution flattens due the weaker and weaker trapping efficiency.

Concerning the electron temperature (LP is able to probe only the so-called “cold” population), it lies in the range 4-14 eV and it reaches the maximum values around the ECR layers.

Figures 5 and 6 respectively show electron density and temperature versus position at $1.5 \cdot 10^{-4}$ mbar, in flat-B field configuration.

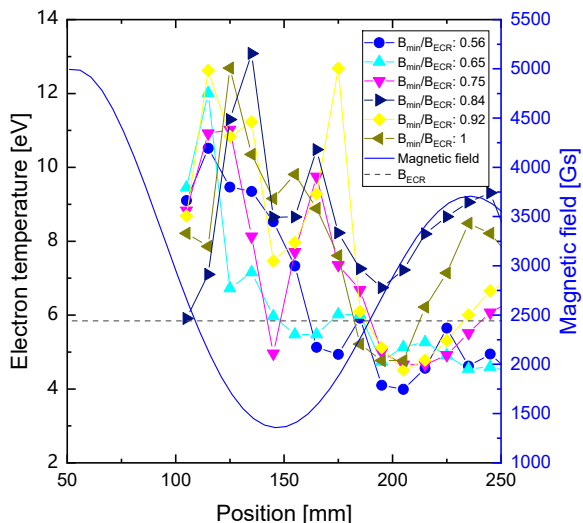


Figure 4: Temperature profiles evaluated by means of LP for 80 W microwave power and $2 \cdot 10^{-3}$ mbar pressure.

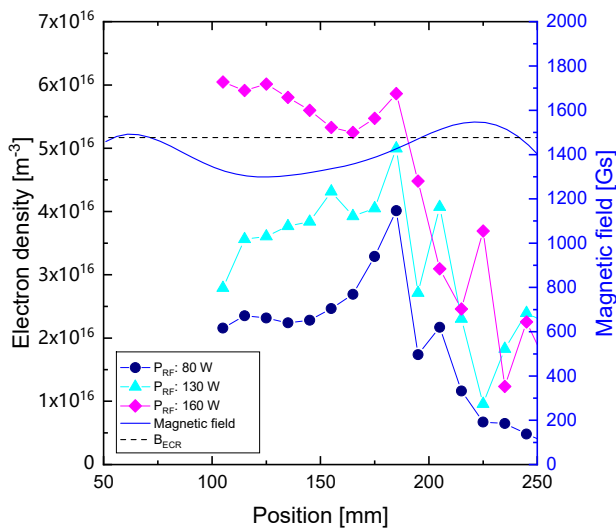


Figure 5: Electron density profiles evaluated by means of LP for three microwave power value (80, 130 and 160 W) and $1.5 \cdot 10^{-4}$ mbar pressure.

It is interesting to compare simple mirror and flat-B configurations. First of all, the absolute value of the plasma density is a factor five lower in flat-B with respect to the simple mirror case. The data comparison shows that the other main difference – as expected – consists in the different distribution of the plasma in the chamber. Simple mirror configuration is acting as a trap for the electrons so that the plasma density is peaked in the central part. However, the comparison with other diagnostics say that the magnetic profile is acting also on the phase space, i.e. on the plasma heating process. X-ray flux dramatically increases when increasing the B_{min} (see data commented in [9, 10]), up to 10^4 cps. A different situation occurs for flat-B field measurements. Only a slight trapping is evident and a much lower X-ray rate was detected (in particular, around

10^2 cps for the lowest pressure regime, i.e. a factor 100 lower than for the simple-mirror configuration) at least in the RF power range we could explore.

In terms of plasma density, LP data in flat-B field configuration were collected for different RF power, showing a clear increase of the plasma density and a broader and broader distribution of the plasma in the chamber (that means a larger number of electrons and ions is generated).

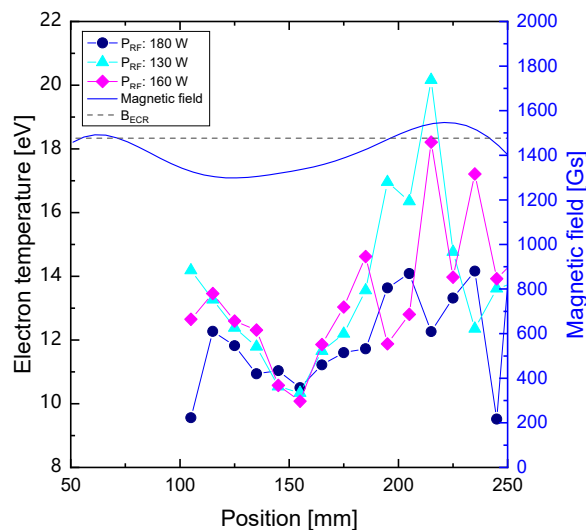


Figure 6: Electron temperature profiles evaluated by means of LP for three microwave power value (80, 130 and 160 W) and $1.5 \cdot 10^{-4}$ mbar pressure.

Concerning the electron temperature, Fig. 6 shows that on average T_e lies in the range 10-20 eV, with some clear peaks (the same for more or less all the RF power levels) occurring close to the ECR layers.

Figure 7 shows the results of the electron density and temperature versus pressure.

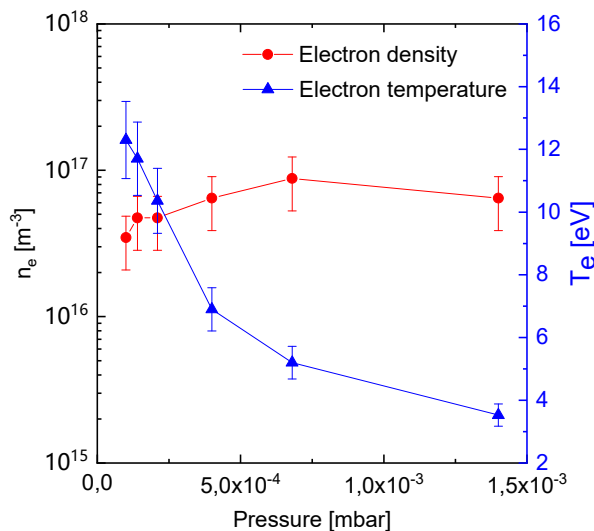


Figure 7: Electron density and temperature obtained from the OES evaluations for varying pressure.

Content from this work may be used under the terms of the CC BY 3.0 licence (© 2018). Any distribution of this work must maintain attribution to the author(s), title of the work, publisher, and DOI.

Electron density slightly increases with pressure from $\approx 3 \cdot 10^{16}$ to $\approx 8 \cdot 10^{16} \text{ m}^{-3}$, whereas the electron temperature decreases from about 12 to 4 eV. Finally, Fig. 8 shows the density ratio of atomic to molecular hydrogen versus pressure. $n(\text{H})/n(\text{H}_2)$ ratio decreases as pressure increases, which can be explained arguing that the continuous injection of H_2 molecules is not compensated by molecules breakdown due to the constant microwave power.

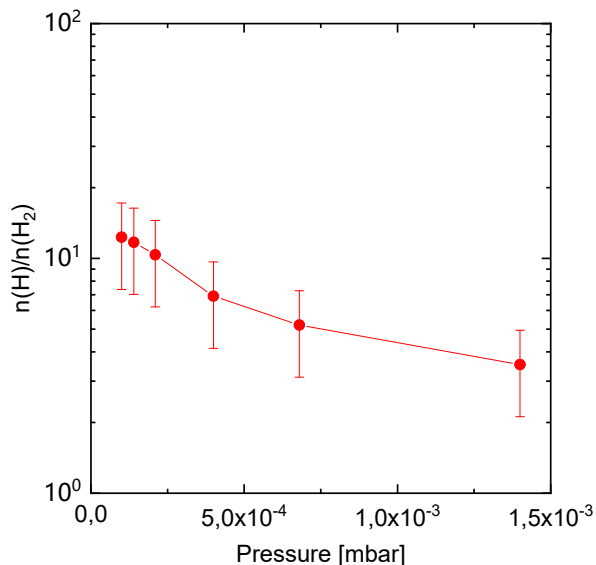


Figure 8: Density ratio of atomic to molecular hydrogen obtained from the OES evaluations for varying pressure.

OES estimations of density and temperature agree very well with the LP data, more than in case of simple-mirror configuration. This may be due to the fact that OES only provide line-of-sight averages of these observables, that in simple mirror configuration are heavily affected by gradients and non-homogeneities of the plasma. In flat-B field, instead, the temperature and density distribution appear to be much smoother.

CONCLUSION AND PERSPECTIVES

The paper reports about an experimental campaign performed with a versatile machine which is able to emulate important features of plasma based ion sources: the axial trapping due to simple-mirror magnetic configuration, or the flat-B field configuration typically used in high intensity proton sources. Data have been collected in multi-diagnostics mode, using simultaneously a Langmuir probe and Optical Emission Spectroscopy, as well as soft-X ray detectors. The plasma density and temperature have been measured in terms of different tunings, and especially in terms of the magnetic field profile. About the point, it is worth mentioning the most significant result was the experimental demonstration of the “scaling rules” impact on the plasma density. In the ECRIS community, in fact, it is well known that the optimal performances are obtained

when $B_{\text{min}}/B_{\text{ECR}}$ is around 0.65 or 0.7. Our measurements are perfectly consistent with this semi-empirical rule, since they show that at those ratios the axial confinement is the most efficient in terms of absolute values of the density and production of X-rays. Smaller ratios mean lower electron temperatures (detrimental for stepwise ionization towards highly charge ions), while larger ratios induce to plasma instabilities, as demonstrated by other authors [11].

In perspective, we plan to further improve the setup including space resolved X-ray spectroscopy and higher resolution optical emission spectroscopy.

Measurements on both simple-mirror and flat-B configuration can drive the design of future ECRIS or MDIS, as well as the better tuning of the existing ones.

ACKNOWLEDGEMENTS

The technical support of Salvo Vinciguerra, Salvo Marletta, Antonino Maugeri, Angelo Seminara, is warmly acknowledged.

The activities presented in this paper have been supported by the PANDORA grant, funded by the 5th Nat. Comm. of INFN, and from the European Spallation Source collaboration.

REFERENCES

- [1] R. Kronholm *et al.*, *Rev. scie. instrum.*, vol. 89, p. 043506, (2018).
- [2] N. K. Bibinov *et al.*, *Plasma Sources Sci. Technol.*, vol. 14 (2005).
- [3] D. Mascali *et al.*, *Rev. scie. instrum.*, vol. 85, p. 02A956, (2014).
- [4] R. Rácz *et al.*, *Plasma Sources Sci. Technol.*, vol. 26, p. 075011, (2017).
- [5] S. Gammino *et al.*, *Rev. Jurnal Instrum.*, vol. 12 (2017).
- [6] G. Castro *et al.*, *Plasma Sources Sci. Technol.*, vol. 26, p. 055019, (2017).
- [7] D. Wunderlich and U. Fantz, *Atoms*, vol. 4 p. 26, (2016).
- [8] D. Mascali *et al.*, *Rev. scie. instrum.* vol. 87, p. 02A510, (2016).
- [9] S. Brieñi *et al.*, submitted to *Plasma Sources Sci. Technol.*
- [10] R. Miracoli *et al.*, *these Proceedings*.
- [11] I. Izotov *et al.*, *Plasma Sources Sci. Technol.* vol. 24, p. 045017, (2015).

A PARTICLE-IN-CELL/MONTE-CARLO-COLLISION CODE FOR THE SIMULATION OF A 2.45 GHz LITHIUM ECR ION SOURCE*

J. F. Zhang[†], S. X. Peng, W. B. Wu, T. H. Ma, T. Zhang, J. M. Wen, Y. X. Jiang, Y. Xu, A. L. Zhang, J. Sun, H. T. Ren, Z. Y. Guo, J. E. Chen

State Key Laboratory of Nuclear Physics and Technology & Institute of Heavy Ion Physics, Peking University, 100871 Beijing, China

Abstract

A 2.45 GHz hybrid ${}^7\text{Li}^{3+}$ ion source has been designed at Peking University (PKU). In order to better understand the physical processes inside the hybrid lithium ion source, a Particle-in-Cell/Monte-Carlo-Collision (PIC/MCC) code is developed recently. In this model, the propagation of the 2.45 GHz microwave is processed using Finite-Difference Time-Domain (FDTD) method, and PIC and MCC method are used to handle the interaction of charged particles with electromagnetic field and collision process between particles, respectively. It can be used to simulate the motion of particles in single spatial dimension and three velocity dimensions, abbreviated as 1D3V. The validity of the PIC method has been confirmed by the simulation of two stream instability in this work. The preliminary simulation results show that the 2.45 GHz microwave energy can be absorbed effectively by electrons in the presence of an external magnetic field of 875 G. And the mirror magnetic field can increase the transverse velocities of electrons.

INTRODUCTION

To fulfil the requirement of the Compact Intense Fast Neutron Facility (CIFNEF) which is proposed by Peking University (PKU) and China Institute of Atomic Energy (CIAE), a 2.45 GHz hybrid ion source for the production of ${}^7\text{Li}^{3+}$ is designed [1]. Its schematic view is plotted in Fig. 1.

This hybrid ${}^7\text{Li}^{3+}$ ion source is composed of a hot surface ionizer and a 2.45 GHz microwave ion source. To get lithium vapour, an oven and a heater are used. In order to avoid the condensation of the lithium vapour, the transport pipeline and the liner are all adiabatic. The red boundary in Fig. 1 will be hot surface. Like other ECR ion source developed at PKU, a three-layer Al_2O_3 window plus a BN disc will be used to introduce the 2.45 GHz microwave into the plasma chamber. A minimum-B magnetic configuration generated by permanent magnets will be used to confine the plasma.

Electron Cyclotron Resonance (ECR) ion sources based on the minimum-B trap are efficient for the production of high charge state ions [2]. One of numerical models which paid more attention on the microwave in the ECR plasma was presented by Muta et al [3].

In Muta's model, a three-dimensional simulation of microwave propagation in an ECR plasma using finite-difference time-domain (FDTD) method has been presented. And the propagation characteristics of the microwave in an inhomogeneous plasma filled in a cylindrical chamber was investigated. In this work, ECR plasma was treated as an anisotropic, dispersive medium. Edgell et al developed a 1D spatially computer model for both electrons and multiple ion species in an ECR plasma [4].

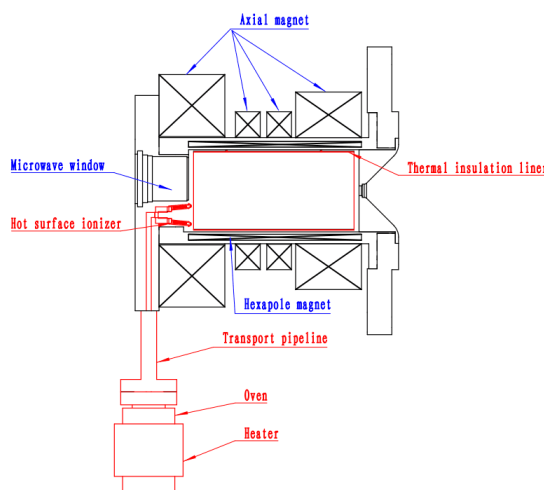


Figure 1: The schematic view of the structure of the ${}^7\text{Li}^{3+}$ ion source.

In that model, ECR heating was treated as a quasi-linear RF-diffusion term including relativistic detuning and RF pitch-angle scattering. Electrostatic models are also used in the simulation of ECR plasma. Dougar et al presented an electrostatic model with the use of an eight-point CIC schemes to simulate the plasma confinement in a minimum-B and a zero-B traps for ion source based on the ECR phenomenon [5]. In 2004, the group of Dougar developed a Particle-in-Cell (PIC) code to simulate the heating and escaping of plasma confined to the 14 GHz minimum-B magnetic trap [6]. The microwaves injected into the chamber were treated as a multimode standing waves regime. Although electromagnetic models are complex, they are close to the real conditions of ECR plasma. Koh et al studied the ECR microwave discharge using a 1D3V electromagnetic Particle-in-Cell Monte Carlo Collision (PIC/MCC) method [7]. In the model, the electric and magnetic fields were calculated

* Work supported by the National Natural Science Foundation of China (Grant No. 11775007 and No. 11575013).

[†] zhangjingfeng@pku.edu.cn

through Maxwell equations. Ardehali et al did the similar work, and the difference was that the propagation of electromagnetic wave in the presence of a constant external magnetic field and a linearly decreasing magnetic field were considered [8].

In the models mentioned above, electrostatic and fluid models are not appropriate to study electromagnetic characteristics of microwave. Electromagnetic particle models are suitable to describe the microscopic features of charged particles and cyclotron resonance motion of electrons. In this paper, a 1D3V PIC/MCC code is developed to simulate the microwave propagation in the plasma. Constant external magnetic fields and a mirror magnetic field are used to study the motions of electrons in the microwave plasma.

MODEL DESCRIPTION

In the 1D3V PIC/MCC code, an electromagnetic wave with frequency of 2.45 GHz feeds into the system along the z axis. The original electrons in the system are heated by absorbing the energy of microwave. When the energy of electrons is above the ionization energy of lithium, the ionization process occurs. The produced plasma is confined by external magnetic field. The ionization process is simulated by MCC, and the motion of particles in the electromagnetic field is simulated by PIC code. The flow chart of the code is shown in Fig. 2.

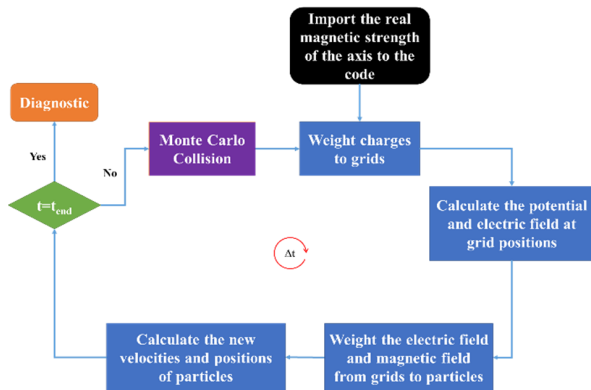


Figure 2: The flow chart of the PIC/MCC code.

The propagation of microwave

In this code, Finite-Difference Time-Domain (FDTD) method is used to simulate the propagation of 2.45 GHz microwave on a spatially discretized mesh. According to Maxwell Eq. (1) and (2), the transformation form (3) to (8) with the assumption that the fields of microwave have no variation in x and y direction can be deduced.

$$\nabla \times \mathbf{E} = -\frac{\partial \mathbf{B}}{\partial t} \quad (1)$$

$$\nabla \times \mathbf{B} = \mu_0 \mathbf{J} + \frac{1}{c^2} \frac{\partial \mathbf{E}}{\partial t} \quad (2)$$

$$\frac{\partial E_y}{\partial z} = \frac{\partial B_x}{\partial t} \quad (3)$$

$$\frac{\partial E_x}{\partial z} = -\frac{\partial B_y}{\partial t} \quad (4)$$

$$\frac{\partial B_z}{\partial t} = 0 \quad (5)$$

$$-\frac{\partial B_y}{\partial z} = \mu_0 J_x + \frac{1}{c^2} \frac{\partial E_x}{\partial t} \quad (6)$$

$$\frac{\partial B_x}{\partial z} = \mu_0 J_y + \frac{1}{c^2} \frac{\partial E_y}{\partial t} \quad (7)$$

$$0 = \mu_0 J_z + \frac{1}{c^2} \frac{\partial E_z}{\partial t} \quad (8)$$

In the equations above, E is electric field, B is magnetic field, J is current density, t is the propagation time of microwave, z is the coordinate of the propagation direction, μ_0 is magnetic conductivity in the vacuum and c is the velocity of light.

A circularly polarized electromagnetic plane wave enters the system at the start point with the assumption that the microwave is absorbed completely at the end of the system.

Particle-in-Cell Part

In this paper, an explicit PIC method is applied to simulate the motion of particles. The length of the system is 103.5 mm which is the real length of the plasma chamber. The system is discretized into 4403 uniform meshes. The charges of particles are distributed in the meshes. And the potential Φ is calculated by Poisson equation as shown in Eq. (9) using multigrid method [9].

$$\nabla^2 \Phi = -\frac{\rho}{\epsilon_0} \quad (9)$$

In the equation above, Φ is the potential, ρ is the charge density and ϵ_0 is the dielectric constant in the vacuum.

The electric field is calculated by Eq. (10) with the method of finite difference.

$$\mathbf{E} = -\nabla \Phi \quad (10)$$

When the process above is finished, weight the electric field and magnetic field from grids to particles. Then calculate the new velocities and positions of particles using relativistic Boris method [10]. When the charged particles collide with the boundaries, they will be absorbed immediately. Constant magnetic fields and mirror field are used in the code.

Monte Carlo Collision Part

The null collision method is used [11] to perform the Monte Carlo Collision in our simulation. As shown in Eq. (11), a maximum collision frequency in space and energy is defined.

$$\nu_{max} = \max_{\mathbf{x}} (n_t(\mathbf{x})) \max_{\epsilon} (\sigma_T(\epsilon)v) \quad (11)$$

In the equation above, n_t is the number density of the particles and σ_t is the cross section of reaction.

Content from this work may be used under the terms of the CC BY 3.0 licence (© 2018). Any distribution of this work must maintain attribution to the author(s), title of the work, publisher, and DOI.

When ν_{max} is got, a total collision probability which is independent of particle energy and position is calculated according to Eq. (12).

$$P_T = 1 - \exp(-\nu_{max}\Delta t) \quad (12)$$

$N_c = P_T N$ particles in the particle list are chosen randomly, and a random number $0 \leq R \leq \nu_{max}$ is selected to determine the type of collision for each particle.

RESULTS AND DISCUSSION

In order to validate the PIC code, the two stream instability process is performed and compared with the results got by Birdsall [12]. Two opposing streams of charged particles with a perturbation in their density are unstable. Two streams of particles with the same mass charge ratio are loaded in the system, and the velocities of the two streams are set as $v_x = 1$ and $v_x = -1$ which are non-dimensional. The perturbation is carried out by adding a small sinusoidal perturbation in the density of the particles of each species. The boundary of the system is periodic. Figure 3 shows the comparison of our simulation results with Birdsall's. It can be seen that the results show good agreement with those from Birdsall, which validates the PIC part of our code.

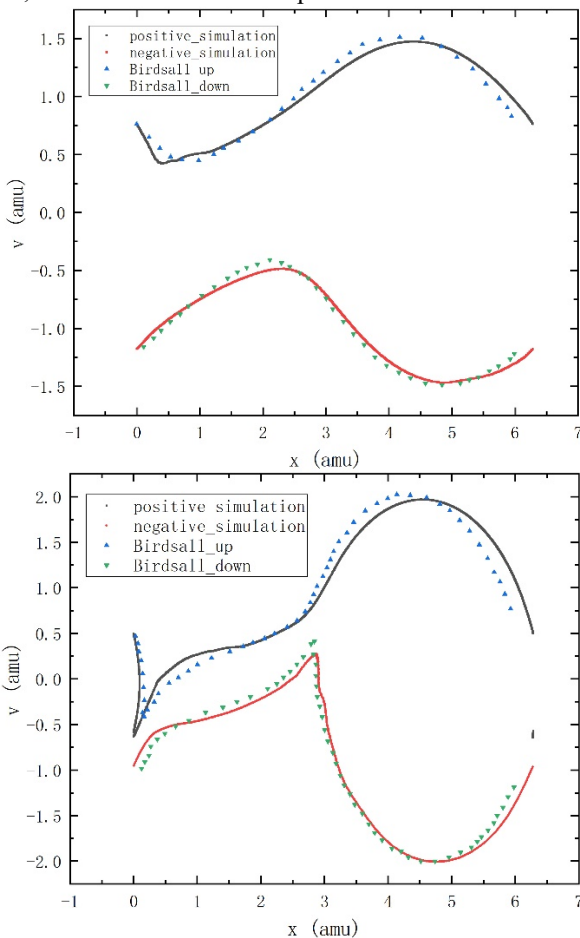


Figure 3: The phase space plots of two stream instability (up figure: $t = 16$, down figure: $t = 18$).

Figure 4 presents the profiles of transverse wave electric field E_y in different magnetic fields. When there are no particles and external magnetic field in the system, the microwave propagates along the axis in a shape of perfect sinusoidal wave. It confirms the validation of the propagation of microwave of the code. When the external magnetic field is 875 G which corresponds to the resonant magnetic field of 2.45 GHz microwave, the profile of E_y shrinks nearly around the zero line. It means that the energy of microwave is strongly absorbed by particles mainly electrons in cyclotron resonance conditions. When the magnetic field is changed to 1875 G, the resonant magnetic field of 5.25 GHz microwave which is much larger than the frequency of the incoming microwave, the profile of E_y damps slightly, which indicates that the microwave can propagate the plasma fluently.

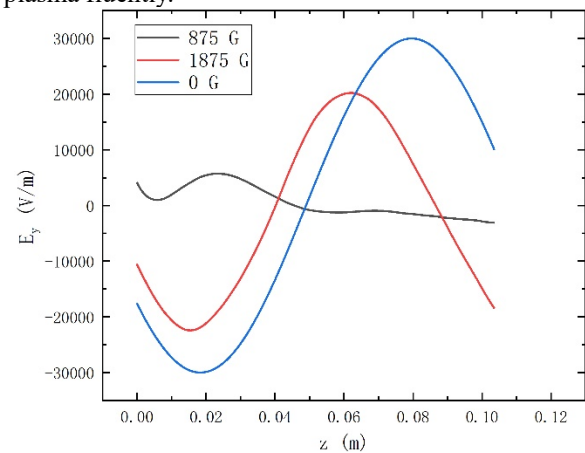


Figure 4: Profiles of transverse wave electric field E_y in different external magnetic fields.

Figure 5 shows the profiles of transverse wave electric field E_y in constant magnetic field and mirror field. The green line represents the strength of mirror field. It is apparent that within the first 40 mm in the axial direction, the strength of mirror field declines and the profile of E_y in mirror field gets close to the zero line faster than the profile of E_y without plasma. After 40 mm, the strength of mirror field arrives at the lowest point and starts to get through the second peak and the profile of E_y in mirror field oscillates around the zero line with smaller amplitude compared with the profile of E_y without plasma. Compared with the profile of E_y in constant 875 G magnetic field, the energy of microwave is absorbed dramatically at the valley of the mirror field.

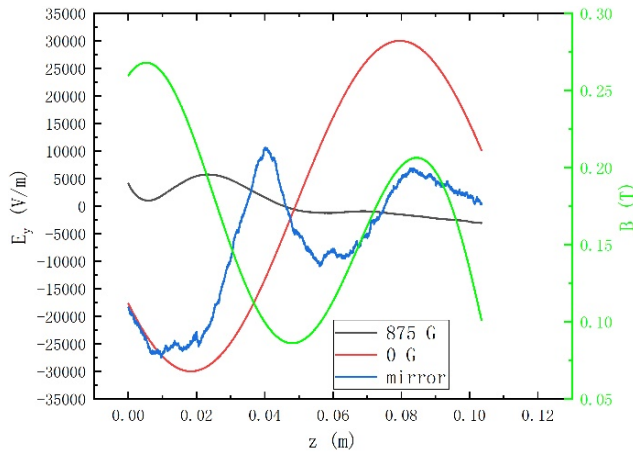


Figure 5: Profiles of transverse wave electric field E_y in constant external magnetic field and mirror field.

Figure 6 displays the v - z phase space distribution of electrons within the mirror field. There is a significant increase of the transverse velocities of electrons at the valley of the mirror field. This phenomenon corresponds to the results of Fig. 5 that the electrons are confined at the valley of the mirror field and absorb the energy of microwave propagating at this area. The axial velocities of electrons do not show any particular change.

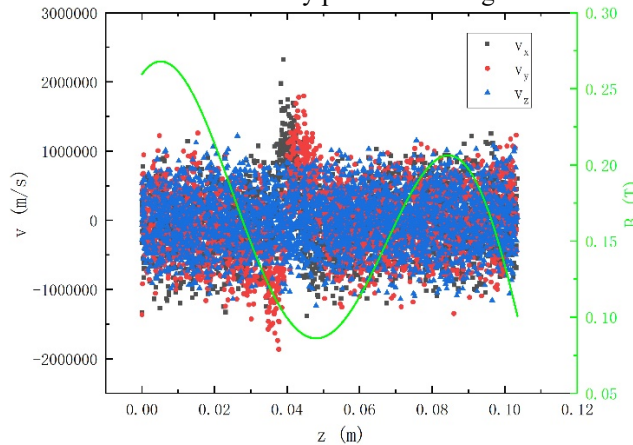


Figure 6: v - z phase space distribution of electrons within the mirror field.

The simulation results indicate that the coupling of the external magnetic field of 875 G and 2.45 GHz microwave can make the microwave lose almost all its energy to the plasma. Electrons trapped in the mirror field absorb the energy of the microwave effectively, gaining their transverse velocities.

SUMMARY AND PROSPECT

A 1D3V PIC/MCC code is developed to simulate the propagation of 2.45 GHz microwave in lithium plasma with constant magnetic field and mirror field and the v - z phase space distribution of electrons within the mirror field is also studied. The simulation results show that the energy of microwave is absorbed significantly when the external magnetic field is 875 G. Electrons trapped in the mirror field can dramatically absorb the energy of

microwave, leading to the increase of the transverse velocities. The motion of electrons in mirror field is meaningful for us to understand the physics of the lithium ion source.

In the future, the behaviour of lithium ions will be considered, including the charge state distribution, the ionization rate, the influence of the density of lithium vapour and so on. All these researches are in progress, and will be reported later.

ACKNOWLEDGEMENTS

This work was supported by the National Natural Science Foundation of China (Grant No. 11775007 and No. 11575013).

REFERENCES

- [1] J. F. Zhang et al., "Preliminary design of a hybrid ion source for ${}^7\text{Li}^{3+}$ generation", presented at ICIS'17, Geneva, Switzerland, Oct 2017, paper T3Mo43, unpublished.
- [2] A. Girard et al. "Modeling of electron-cyclotron-resonance-heated plasmas", *Phys. Rev. E*, vol. 62, p.1182, 2000, [gr1=43144362Sk|vUhyH195144;5](#)
- [3] H. Muta et al. "Three-dimensional simulation of microwave propagation in an electron cyclotron resonance plasma", *Jpn. J. Appl. Phys.*, vol. 36, p.4773, 1997, [gr1=43144462jjap16914776](#)
- [4] D. H. Edgell et al. "Modeling of electron cyclotron resonance ion source plasmas", in *Proc. PAC'01*, Chicago, USA, Jun. 2001, pp. 2135-2137, [gr1=43144392pac1533419;7634](#)
- [5] V. D. Dougar-Jabon et al. "Plasma confinement in an electron cyclotron double cusp trap", *Phys. Scr.*, vol. 62, p.183, 2000, [gr1=431456;2pk|vlcalrhgular1395a3334;6](#)
- [6] V. D. Dougar-Jabon et al. "Properties of plasma in an ECR minimum-B trap via numerical modeling", *Phys. Scr.*, vol. 70, p.38, 2004, [gr1=431456;2pk|vlcalrhgular1373a3336;](#)
- [7] W. H. Koh et al. "Electromagnetic particle simulation of electron cyclotron resonance microwave discharge", *J. Appl. Phys.*, vol. 73, p.4205, 1993, [gr1=4314396241655;55](#)
- [8] M. Ardehali, "Simulation and analysis of electron cyclotron resonance discharges", arXiv preprint physics/9810033, 1998.
- [9] J. H. Ferziger and M. Peric, *Computational methods for fluid dynamics*. Berlin, Germany: Springer, 2012.
- [10] J. P. Boris, "Relativistic plasma simulation-optimization of a hybrid code", in *Proc. 4th Int. Conf. on Numerical Simulation of Plasmas*, 1970, pp.3-67.
- [11] V. Vahedi and M. Surendra, "A Monte Carlo collision model for the particle-in-cell method: applications to argon and oxygen discharges", *Comput. Phys. Commun.*, vol. 87, p.179, 1995, [gr1=431434923343-4955\(94\)33474-w](#)
- [12] C. K. Birdsall and A. B. Langdon, *Plasma physics via computer simulation*, New York, USA: IOP Publishing Ltd, 1991.

NUMERICAL SIMULATIONS OF MAGNETICALLY CONFINED PLASMAS

A. Galatà*, C. S. Gallo, INFN-Laboratori Nazionali di Legnaro, (Padova), Italy
D. Mascali, G. Torrisci, INFN-Laboratori Nazionali del Sud, Catania, Italy

Abstract

Since 2012, the INFN ion source group has been undertaking an intense activity on numerical modelling of magnetically confined plasmas, presently carried out in the framework of the PANDORA project. The aim is the development of a predictive tool for the design of Electron Cyclotron Resonance (ECR) Ion Sources or Traps and ECR-based Charge Breeders, able to determine spatial density and energy distributions for both electrons and ions. The work mainly concerns the study of two aspects: on one hand, the interaction of an ion beam with a magnetized plasma; on the other hand, the microwave-to-plasma coupling, including the 3D plasma electrons dynamics in the confinement magnetic field and intra-particles collisions. This contribution describes the state-of-the-art of the work on both fronts: an overview of the beam-plasma interaction, the latest results about the ECR-plasma density fine structure, as well as electrons spatial temperature distribution will be shown.

INTRODUCTION

For the last years, the INFN ion source group has been focusing its research activity on the PANDORA (Plasmas for Astrophysics, Nuclear Decays Observation and Radiation for Archaeometry) project [1]. Its aim is a feasibility study of a new facility based on a state-of-the-art plasma trap confining extremely energetic plasma, to perform interdisciplinary research in the fields of nuclear astrophysics, astrophysics, plasma physics and applications in material science and archeometry. The plasma will become the environment for measuring, for the first time, nuclear decays rates in stellar-like conditions, in particular for ${}^7\text{Be}$, as a function of the in-plasma ionization state. These studies are of paramount importance for addressing several astrophysical issues in both stellar and primordial nucleosynthesis environment (e.g. determination of solar neutrino flux and ${}^7\text{Li}$ Cosmological Problem). The design of the trap, and in particular its magnetic field, will be based on the "B-minimum" geometry typical of Electron Cyclotron Resonance (ECR) ion sources [2]: in such machines, a dense and hot plasma, made of multicharged ions immersed in a dense cloud of energetic electrons, is confined by multi-Tesla magnetic fields and resonantly heated by some kW of microwave power in the 2.45–28 GHz frequency range. ${}^7\text{Be}$ will be injected inside the trap as a 1+ beam, using the well known ECR-based charge breeding technique [3], while its decay to ${}^7\text{Li}$ through electron capture will be tagged by detecting the 478 keV γ -ray emitted by the transition of ${}^7\text{Li}$ from the excited to the ground state (10% of branching ratio). In this framework,

the efforts are mainly dedicated to two fundamental aspects: on one hand, the development of a complete plasma diagnostic set-up able to detect plasma emission from the visible range to X-ray, in order to obtain spatially resolved ions and electrons density, as well as electrons temperature. Part of this work is presently carried out in collaboration with the Hungarian laboratory ATOMKI [4]. On the other hand, the development of an innovative numerical tool able to describe the interaction of the injected beam with the confined plasma, and also predict the plasma density and temperature fine structure, so as to maximize the injection and subsequent capture of the radioactive ions inside the trap. The paper will describe the state-of-the-art of the work on this last aspect: the results of the simulations of the beam-plasma interaction will be shown first, followed by the progresses made towards a plasma self-consistent description in terms of electrons density and temperature.

THE BEAM-PLASMA INTERACTION

A mentioned before, radioactive species will be injected in the PANDORA trap by employing the charge breeding technique, widely used in Isotope Separation On Line (ISOL) facilities whose aim is the post-acceleration of radioactive ions for nuclear physics experiments. As in the case of the SPES project, under construction at INFN-LNL [5], the charge breeding within PANDORA will be ECR-based: with this technique, the radioactive species produced in the so-called target-ion source-system are extracted as a 1+ beam from dedicated sources, transported along electrostatic beam lines, decelerated to very low energies (in the eV range), and then injected into the Charge Breeder. Once inside the plasma, radioactive 1+ ions suffer a huge number of small angle elastic ion-ion collisions (the so-called Spitzer collisions [6]) that eventually lead to thermalization with plasma ions, and are then extracted as a highly charged ion beam after charge multiplication through step-by-step ionizations by energetic electrons. The INFN ion source group developed an innovative fully 3D numerical approach in a MatLab environment, able to reproduce the beam-plasma interaction and its subsequent ionization [7]. The code implements a formalism based on the Langevin equation [8] to describe the Spitzer collisions, while ionizations are calculated by using the Lotz formula [9] and included with a MonteCarlo approach. The validity of the code was demonstrated by reproducing two experimental results obtained with the PHOENIX Charge Breeder at the Laboratoire de Physique et de Cosmologie, by injecting sodium [10] and rubidium ions [7]. It also revealed to be very useful in understanding the influence of the injected beam parameters on the capture process, in particular the

* alessio.galata@lnl.infn.it

beam emittance and energy spread [11]. The plasma was implemented following the plasmoid/halo scheme [12]: the numerical analysis carried out regarded the effect of different plasma parameters on the capture process, in particular the plasma density and ion temperature (electrons are involved only in the ionization process). An example is given in Fig. 1, showing the percentage of particles losses as a function of the injection energy for different plasma densities and an ion temperature $KT_i=0.5$ eV, by injecting $^{85}\text{Rb}^{1+}$ ions produced by a surface ionization source (see ref. [7]).

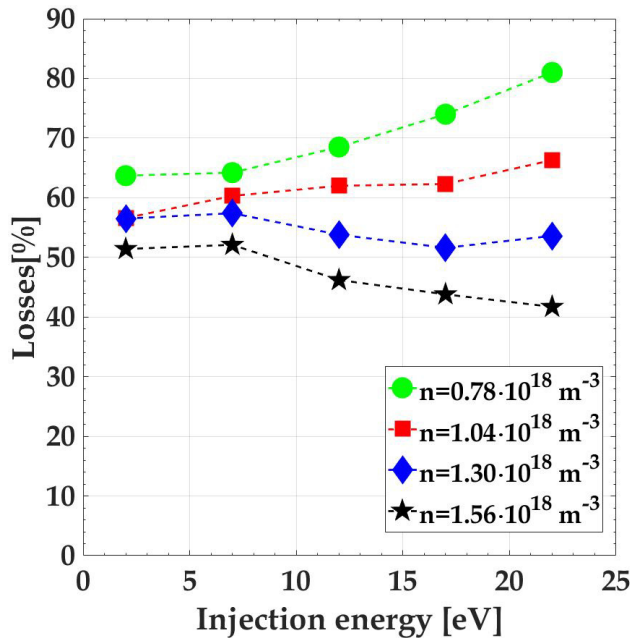


Figure 1: $^{85}\text{Rb}^{1+}$ ions losses as a function of the injection energy for different simulated plasma densities and an ion temperature $KT_i=0.5$ eV.

As expected, ions losses increase by decreasing the plasma density but their trends as a function of the injection energy change going from the highest to the lowest. For the highest one (close to the cut-off for the Charge Breeder's operating frequency of 14.521 GHz), in fact, losses decrease with energy because the friction and diffusion effects prevents injected ions to enter deep inside the plasma for low velocities. On the contrary, for the lowest density the minimum losses appear for the lowest injection energy and then increase steadily: in this case, it is easier for the injected ions to penetrate the plasma at low velocities, but as soon as the energy increases its slowing down capability becomes more and more ineffective. This effect is even clearer by looking at Fig. 2 that shows the ions losses as a function of the injection energy, respectively, in radial direction (radial losses), back to the injection side (axial losses), towards the extraction end plate (extraction losses) and through the 7 mm diameter extraction hole of the Charge Breeder (extracted), for the highest (bottom) and the lowest (top) density.

Following the interpretation above argued, for the highest density and the lowest energy most of the ions are lost from

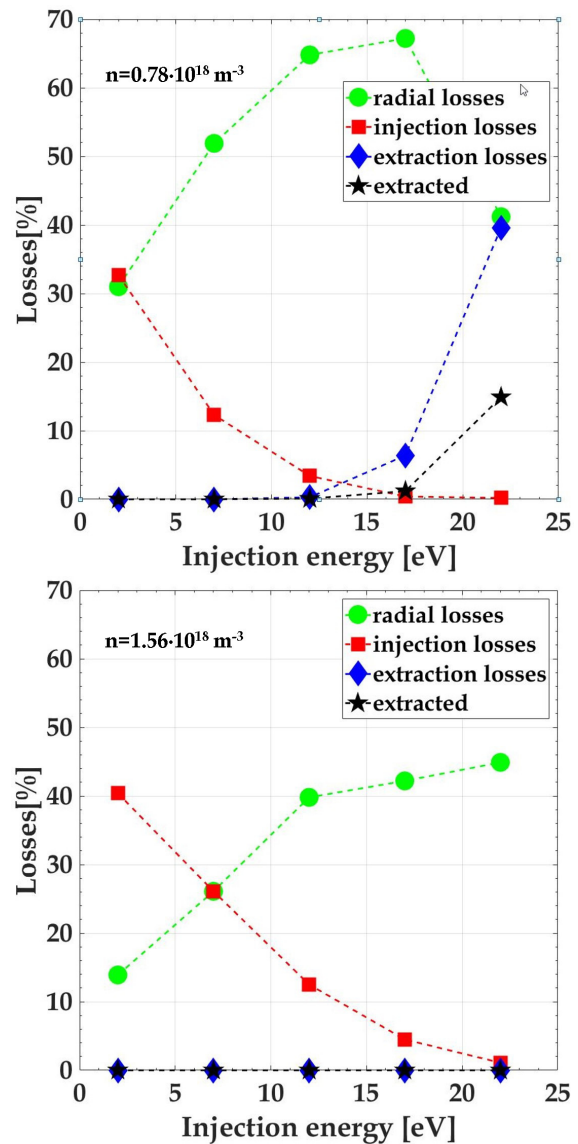


Figure 2: $^{85}\text{Rb}^{1+}$ ions losses in different directions as a function of the injection energy for $KT_i=0.5$ eV, $n=1.56\cdot 10^{18}$ m^{-3} (bottom) and $n=0.78\cdot 10^{18}$ m^{-3} (top). The directions considered are radial (green), back to the injection side (red), towards the extraction end plate (blue) and the one passing through the 7 mm diameter extraction hole of the Charge Breeder (extracted).

the injection side, while radial losses are limited and extraction losses negligible. When the energy increases, losses become mostly radial (increasing steadily) but even at the highest energy extraction losses are not observed. On the contrary, for the lowest density and energy, losses are shared between radial and axial direction: by increasing the energy, injection losses decrease faster than the previous case, while radial losses increase up to a maximum and then decrease due to the simultaneous increase of extraction losses. Some ions come out through the extraction hole, as very often observed experimentally.

The numerical investigation led to the definition of a complete set of beam and plasma parameters able to reproduce experimental results with $^{85}\text{Rb}^{1+}$ ions, as described in ref. [7]: in particular, for the former an injection energy of 7 eV and an energy spread of 2 eV (typical of surface ionization sources); for the latter a plasmoid density $n=1.95 \cdot 10^{17} \text{ m}^{-3}$ and an ion temperature $KT_i=0.3 \text{ eV}$. This last parameter revealed to be very critical for an optimum capture of the injected ions. Very interesting information come from the ballistic of the process: Fig. 3 plots the injected particles trajectories at different time steps. As soon as particles approach the plasmoid, we can observe a spatial spread of the injected particles due to the fact that the energy spread is comparable to the injection energy, while once particles cross the resonance surface most of them remain trapped inside the plasmoid and very few are able to escape it. To detect the X-ray coming out from the plasma of the PANDORA trap with a precise spatial resolution, directly linked to the electrons energetic content, it is important to know the electrons loss paths along the magnetic field lines, because the strong bremsstrahlung emission due to their interaction with the plasma chamber walls could contaminate the measurement. Ambipolar diffusion forces ions and electrons to escape the trap following the same paths, so this information can be obtained also by following ions trajectories. Thanks to a specific routine included in the developed numerical code, it is able to store the positions of ions losses on the plasma chamber walls: Fig. 4 shows such positions in the case of ^{85}Rb ions. The two three-folded "stars" impressed to the plasma by the hexapolar field are clearly visible on the injection and extraction sides, as well as the six stripes in off-poles positions. By pointing the detectors in the zone between two adjacent stripes the influence of the bremsstrahlung emission should be limited or eventually avoided.

ELECTRONS DYNAMICS

The results showed in the previous section were obtained by implementing a realistic, but simplified, plasma-target model. The plasmoid/halo scheme used, in fact, distinguishes between a dense core inside the resonance surface and a rarefied halo outside, but in both zones the ions/electrons density and electrons temperature (at least the warm component, responsible for the ionizing collisions) are supposed to be uniform. In reality this is not the case, and in view of an efficient spatially resolved diagnostics within PANDORA the knowledge of the plasma fine structure is mandatory. Strong efforts have been making to obtain a self-consistent ECR-plasma description, by joining precise electromagnetic calculations, carried out with COMSOL multiphysics, with the electrons dynamics calculated with MatLab. In fact, on one hand in magnetized plasmas excited by microwaves (as is the case of ECR sources and traps) the electromagnetic field set-up inside the plasma chamber determines, through a resonant interaction, the energetic content of electrons and then the plasma density. On the other hand, the plasma is an anisotropic and dispersive medium

characterized by a 3D dielectric tensor, that must be taken into account for the calculation of the electromagnetic field in a kind of self-consistent loop. The approach is being followed consists of different steps: the first starts with the calculation of the electromagnetic field of the empty plasma chamber. Then, this field is used to calculate the dynamics of electrons generated uniformly inside the plasma chamber, by using a MatLab code derived directly from the one developed for ions, including relativistic effects. The code follows the evolution of N electrons until they escape the domain of simulation: at this stage particles dynamics is determined only by electromagnetic and magnetostatic fields. By using an ad-hoc routine, the code stores particles positions at each time step in a 3D matrix reflecting the domain of the simulation divided in cells of 1 mm^3 , creating an "occupation" map. This map is then scaled as it would be equivalent to a uniform density of $2 \cdot 10^{17} \text{ m}^{-3}$, obtaining a density map; this calculation concludes the first step. The density map is used to calculate the value of the plasma dielectric constant in each cell: the second step starts with new electromagnetic calculations, this time including a plasma (through its dielectric constant) distributed like the density map, following the approach used in [13]. Electrons dynamics is calculated again with the magnetostatic and the new electromagnetic field, creating this time not only an occupation (and so a density) map but also an energy map, obtained storing at each time step the energy of the electrons in another 3D matrix. By dividing the energy map to the occupation map, the spatial distribution of the average energy is obtained: by supposing it belongs to electrons with a Maxwell-Boltzmann distribution, a spatial temperature map can be derived by multiplying the average energy for the factor $(3/8)\pi$. With the temperature and density matrices, electrons dynamics is calculated again including this time the presence of the plasma, that is including the electron-electron collisions. Finally, the step is concluded with a new density map that can be used to calculate again the 3D dielectric tensor and then the electromagnetic field: this second step is repeated until the results show self-consistency, that is until the results from consecutive steps show negligible differences in the density and temperature matrices.

The work on this kind of approach is presently ongoing, but the preliminary results are already remarkable: Fig. 5 show the projection on the xy plane (left) and the radial profile along the x axis in the midplane (right) of the density map obtained after the second step, that is including the plasma in the electrons dynamics only one time. The electromagnetic power simulated is 100 W, while the geometry and the confining magnetic field are the same as in ref. [7]. It can be clearly observed that, even if electrons starts uniformly distributed inside the plasma chamber in the first step, at the end of the second one not only the plasmoid/halo structure is automatically formed, but also the fine structure of the plasmoid is clearly visible, a result never obtained with any previous numerical simulation. The plasma concentrates in a region around the axis, with a peak density around $3 \cdot 10^{17} \text{ m}^{-3}$, and its density drops of about one order of magnitude

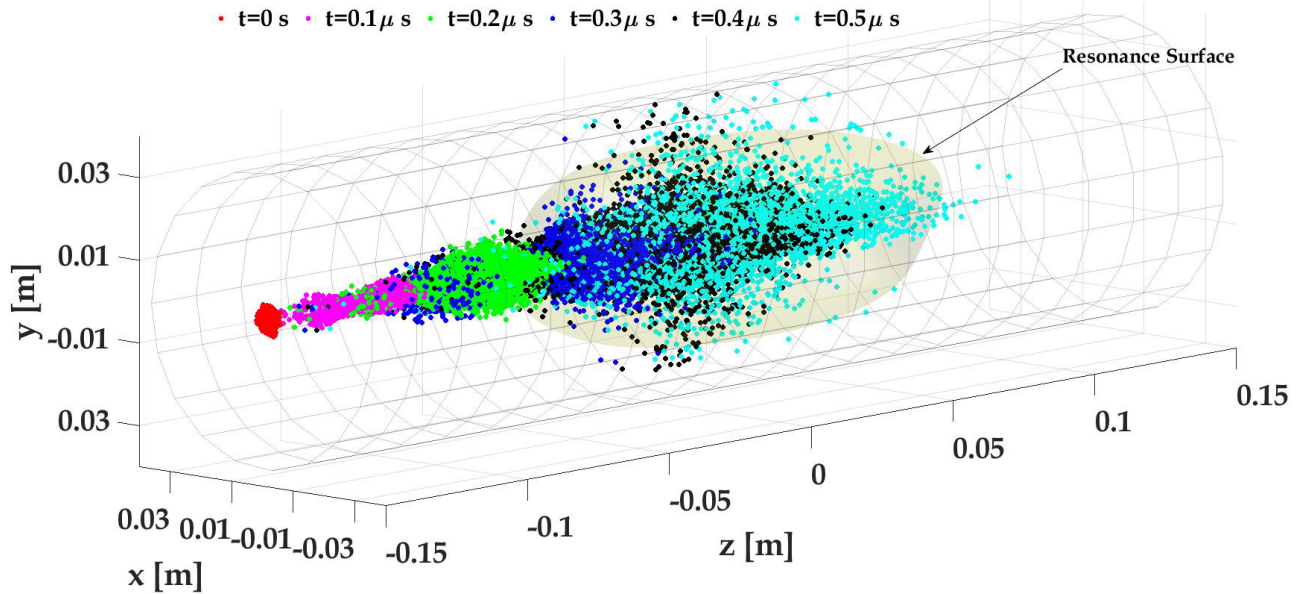


Figure 3: Plot of the injected particles trajectories at different time steps for an injection energy of 7 eV: $t=0 \mu\text{s}$ (red), $t=0.1 \mu\text{s}$ (magenta), $t=0.2 \mu\text{s}$ (green), $t=0.3 \mu\text{s}$ (blue), $t=0.4 \mu\text{s}$ (black), $t=0.5 \mu\text{s}$ (cyan). The cylinder represents the Charge Breeder plasma chamber, while the egg-shaped surface indicates the resonance surface containing the plasmoid.

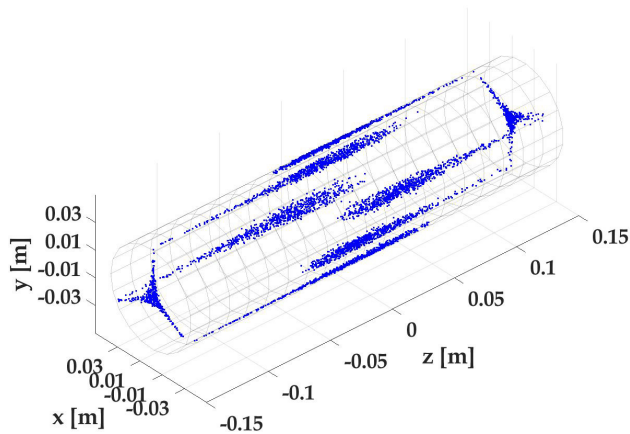


Figure 4: Location of $^{85}\text{Rb}^{1+}$ losses on the plasma chamber walls; the cylinder represents the Charge Breeder plasma chamber.

within the plasmoid, as shown by the radial profile. The results gave also for the first time a picture of the electron temperature distribution: Fig. 6 shows on the top the xz projection of the temperature map. The electrons temperature is not uniform inside the plasmoid but "hot-spots" in the keV appear in different zones: plotting the isosurface of those hot-spots in the bottom part Fig. 6 it is clear that those zone are localized all around the resonance surface, where electrons gain energy interacting with the electromagnetic field. These last results are unprecedented and make the developed numerical code a unique tool for the description of magnetically confined plasma typical of ECR ion sources and traps.

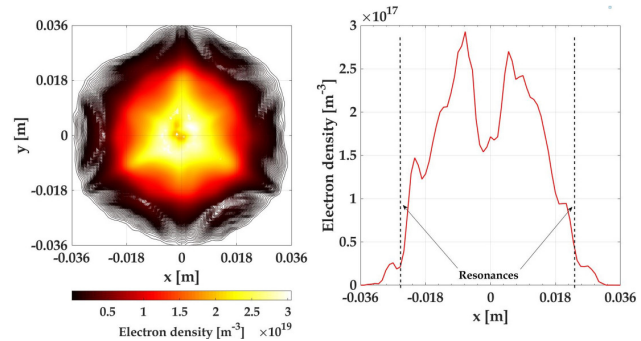


Figure 5: Density plots obtained after two steps of the self-consistent loop: projection on the xy plane (left) and radial profile along the x axis in the midplane (right).

CONCLUSIONS AND PERSPECTIVES

The results shown in this paper confirm the validity of the numerical code developed by the INFN ion source group in describing the beam-plasma interaction: Figs. 1–4, together with those shown in ref. [7,10,11], demonstrate its capability in simulating properly the slowing down and capture of the injected ions for light and heavy species, identifying the beam and plasma parameters playing a key role in the process. The preliminary results of the electrons dynamics show for the first time ever that the ECR plasma automatically assume a plasmoid/halo structure, with a peculiar distribution of density and temperature in the plasmoid. In the next future the efforts will be concentrated in obtaining a self-consistent description of electrons behaviour inside the plasma and the spatially resolved ions charge state distribution, with the aim at developing a complete predictive

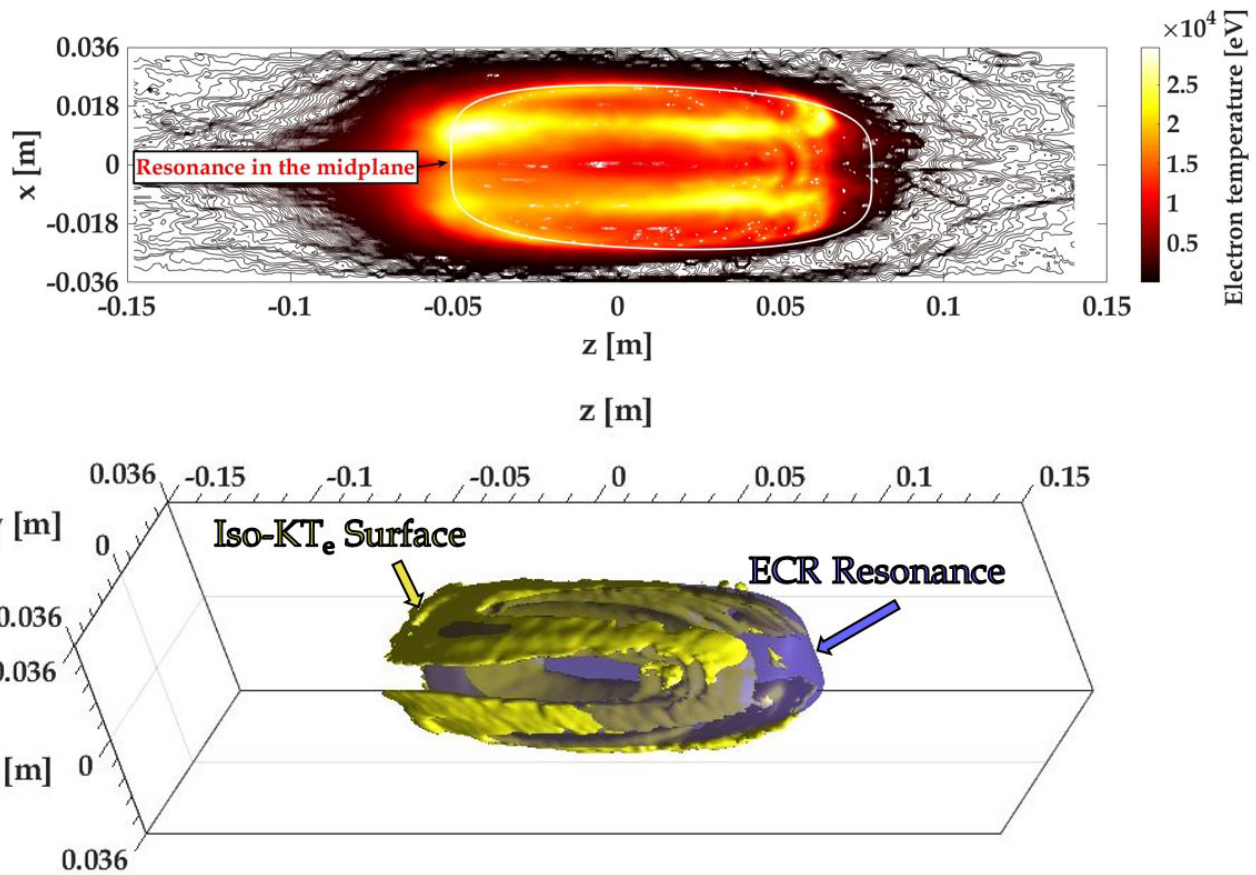


Figure 6: Electrons temperature spatial distribution: projection on the xz plane (up) and isosurface (down). The isosurface shows the points where the temperature has the highest values; the resonance surface is visible in blue.

numerical tool for the design of new ECR ion sources and traps and ECR-based Charge Breeders, in particular in the framework of the PANDORA project.

REFERENCES

- [1] D. Mascali *et al.*, "PANDORA, a new facility for interdisciplinary in plasma physics", *Eur. Phys. J. A*, vol. 53 p. 145, (2017).
- [2] R. Geller, *Electron cyclotron resonance ion sources and ECR plasmas*, Bristol: IOP (1996).
- [3] N. Chauvin *et al.*, "The $1^+ \rightarrow n^+$ charge breeding method for the production of radioactive and stable continuous /pulsed multi-charged ion beams", in *Proceedings of the 14th International Workshop on ECR Ion Sources*, CERN, Geneva, Switzerland, 3–6 May 1999.
- [4] R. Racz *et al.*, *Electron cyclotron resonance ion source plasma characterization by energy dispersive X-ray imaging*, *Plasma Sources Sci. Technol.* **26** (2017) 075011.
- [5] A. Galatà *et al.*, "ADIGE: the radioactive ion beam injector of the SPES project", *J. Phys.: Conf. Ser.*, vol. 874, p. 012052, (2017).
- [6] L. Spitzer Jr, "Physics of Fully Ionized Gases", *Dover Publications, Inc., Mineola, New York* (2006).
- [7] A. Galatà *et al.*, "A three-dimensional numerical modelling of the PHOENIX-SPES charge breeder based on the Langevin formalism", *Rev. Sci. Instrum.*, vol. 87, p. 02B507, (2016).
- [8] W. M. Manheimer *et al.*, "Langevin Representation of Coulomb Collisions in PIC Simulations", *J. Comput. Phys.* vol. 138, p.563, (1997).
- [9] W. Lotz, "An empirical formula for the electron-impact ionization cross-section", *Z. Phys.*, vol. 206, p. 205, (1967).
- [10] O. Tarvainen *et al.*, "Diagnostics of a charge breeder electron cyclotron resonance ion source helium plasma with the injection of $^{23}\text{Na}^{1+}$ ions", *Phys. Rev. Accel. Beams*, vol. 19, p. 053402, (2016).
- [11] A. Galatà *et al.*, "Influence of the injected beam parameters on the capture efficiency of an electron cyclotron resonance based charge breeder", *Phys. Rev. Accel. Beams*, vol. 20, p. 063401, (2017).
- [12] A. A. Ivanov and K. Wiesemann, "Ion confinement in electron cyclotron resonance ion sources (ECRIS): importance of nonlinear plasma-wave interaction", *IEEE Trans. Plasma Sci.*, vol. 33, p. 1743, (2005).
- [13] A. Galatà *et al.*, "Electromagnetic analysis of the plasma chamber of an ECR-based charge breeder", *Rev. Sci. Instrum.*, vol. 87, p. 02B505, (2016).

PLASMA INSTABILITY STUDIES OF THE SUSI 18 GHz SOURCE

Bryan Isherwood[†], Eduard Pozdeyev, Guillaume Machicoane, Jeffrey Stetson, and Derek Neben
National Superconduction Cyclotron Laboratory, East Lansing, MI, USA
Facility for Rare Isotope Beams, East Lansing, MI, USA

Abstract

Instabilities in magnetized plasmas, such as the cyclotron instabilities identified at JYFL [1], can cause fast variations of the extracted Electron Cyclotron Resonance Ion Source (ECRIS) beam current. In order to understand the effect of the radial component and longitudinal gradient of the magnetic field on plasma stability a series of measurements has taken place using the Superconducting Source for Ions (SuSI) at the National Superconducting Cyclotron Laboratory (NSCL). We present here the results from investigations into the instability characteristics of the beam current from SuSI at 18 GHz by varying longitudinal and radial magnetic field profiles, injected microwave power, and bias disk voltage. Our investigation shows multiple regions of beam current variation within the magnetic field vs. power parameter space with multiple distinct modes of variance.

INTRODUCTION

The Facility for Rare Isotope Beams (FRIB) and the National Superconducting Cyclotron Laboratory (NSCL) require intense, high charge state beams for normal facility operations. As a result, any limitation of the transmitted beam current can diminish the total operational capacity of the facilities. The limitation of the extracted beam current from ion sources operated at high magnetic field strengths is one such diminishing factor. Investigations into the limitations of Electron Cyclotron Resonance Ion Source (ECRIS) performance at the high-performance limit for high charge state extraction have made great strides in the last several years. In particular the studies out of Jyväskylä [1,2] and Nizhny Novgorod [3,4] have revealed that kinetic plasma microinstabilities, in the form of cyclotron instabilities, are a driving factor of these limitations.

These instabilities occur in local regions of the ECR plasma where the magnetic field induced temperature anisotropy heavily favors the transverse component of the hot ($T > 10$ keV) electron population, $T_{\perp} \gg T_{\parallel}$ [1]. Those electrons can escape into the magnetic loss cone by depositing the energy stored in their gyro-motion into the background plasma in the form of microwave radiation [3,5]. The plasma, in response to suddenly losing part of its electron population, ejects part of its ion population until quasi-neutrality can be regained. At this point the heating process returns to its desired role of creating more ions until the degree of anisotropy requires the instability to be triggered. These

events create the beam current oscillations that are observed in the extracted beam.

As reported in [2], a threshold has been measured for these instabilities to occur relative to the magnetic minimum and injected microwave power within the plasma chamber. This threshold measurement does not include two key features of the magnetic field structure: the radial field and the field's gradient at the resonance surface. An electromagnet hexapole coil is required in order to probe the former and the latter must be probed by an ECR with more than two longitudinal coils. Insight to the latter issue has been given by Benitez with her measurement of the spectral temperature in VENUS [6]. It was found that the spectral temperature of the plasma is independent of the axial gradient at resonance, while having a strong dependence on the minimum of the field structure. However, this measurement is incapable of distinguishing the degree of anisotropy of the electron population in the system. This limitation is due to its reliance upon a bremsstrahlung spectrum that carries no information on the anisotropy; leaving open an avenue for exploration into the field structures influence upon the ECR plasma characteristics.

We report here measurements into the effect of the hexapole and magnetic field structure upon the state of stability of the ECR plasma. Sweeping the injected microwave power across multiple magnetic field distributions revealed stability characteristics dependent on the field distribution rather than only the minimum value. Two potentially new instabilities were found and are named here as "fast" and "slow", for their repetition frequencies with respect to the previously mentioned cyclotron instabilities. An increasing hexapole was found to decrease the probability of finding a stable operating point in three of four experimental cases. X-ray measurements were also made in order to confirm that the hot electron population is the population predominately affected by the instabilities.

APPARATUS AND PROCEDURE

All measurements were taken using SuSI at the NSCL. The four superconducting solenoid coils and superconducting hexapole create its longitudinal and radial magnetic fields respectively [7]. The four solenoids coils allow us to create different magnetic field distributions with the same B_{min} but with different magnetic mirror ratios at injection and extraction; isolating the effect of the magnetic field distribution from its local minimum. Four sets of fields were used to explore the stability characteristics of the ECR plasma. Each set was designed to have a magnetic mirror ratio that was either larger or smaller than the standard operating field scaling laws [8], for both the injection and extraction sides of the

* Work supported by the National Science Foundation under NSF Grant 1632761

[†] Isherwoo@nsl.msu.edu

Content from this work may be used under the terms of the CC BY 3.0 licence (© 2018). Any distribution of this work must maintain attribution to the author(s), title of the work, publisher, and DOI.

Table 1: Multiple Experimental Ranges Of the Confining Field Were Used. Each Range's Injection And Extraction Mirror Ratio Were Set To Be Higher Or Lower Than the Standard Operating Field. Calculations Were Performed Using Poisson.

	Standard	Range 1	Range 2	Range 3	Range 4
B_{min}/B_{ecr}	0.71	0.70	0.70	0.70	0.70
B_{inj}/B_{ecr}	3.96	4.08	3.70	3.42	4.10
B_{ext}/B_{ecr}	1.94	2.02	1.77	1.94	1.60

ECR plasma chamber. Table 1 shows an example calculation comparing the characteristics of each of the fields, with a $B_{min}/B_{ecr} = 0.7$, to that of the standard operational field, $B_{min}/B_{ecr} = 0.71$. Each of the longitudinal field ranges were measured with each of the radial field settings used, $B_{r,wall} = 1.1$ T, 1.2 T, and 1.322 T, with SuSI's standard operational field setting being $B_{r,wall} = 1.22$. During the measurement the microwave power was swept from 50 W to 550 W in 100 W steps for each magnetic field setting. The extracted beam current, reflected microwave power, and bias disk current were measured during this time to determine if the plasma was unstable. Any operating point that showed periodic beam current oscillations and bursts of microwave radiation were classified as unstable. This created a map of the source's stability characteristics for each field and power setting.

The source was held at a fixed bias of 20 kV during these measurements each of the measurements described above. A 90° dipole was used for charge selection followed by a solenoid focusing lattice to guide the selected charge state current into a Faraday cup. Reflected/emitted microwaves from the plasma chamber were measured with an HP 8473C Low Barrier Schottky Diode connected to a bi-directional waveguide coupler along the path of the injection waveguide. Measuring fluctuations in the bias disk current required connecting an analog-to-fiber converter in parallel with the bias disk power supply. A fiber-to-analog receiver converted the optical signal to a measurable electrical signal. All three electrical signal were measured and recorded in coincidence using a Tektronix MDO3054 oscilloscope. Bremsstrahlung measurements were taken on axis using a High Purity Germanium Detector (HPGe).

An Argon plasma heated with a Klystron driven at 18 GHz was used for all measurements. During the field mapping process the neutral gas pressure was held at 130 nTorr at the injection side of the plasma. The bias disk was held at a constant -17 V as it was found that higher voltages created noise in the measured current that made it difficult to disentangle an unstable operating point from one with a lot of electrical noise.

RESULTS

The measurement revealed an unexpected result: three different kinds of beam current oscillations. Along with the previously reported cyclotron instabilities we also found what have been named "fast" and "slow" instabilities; with the names being a reference to their repetition frequency, f_{rep} , relative to the cyclotron instabilities ($f_{rep,slow} <$

$f_{rep,cyclotron} < f_{rep,fast}$). Figure 1 shows an example each of these instabilities for the 2+ and 8+ charge states of Argon.

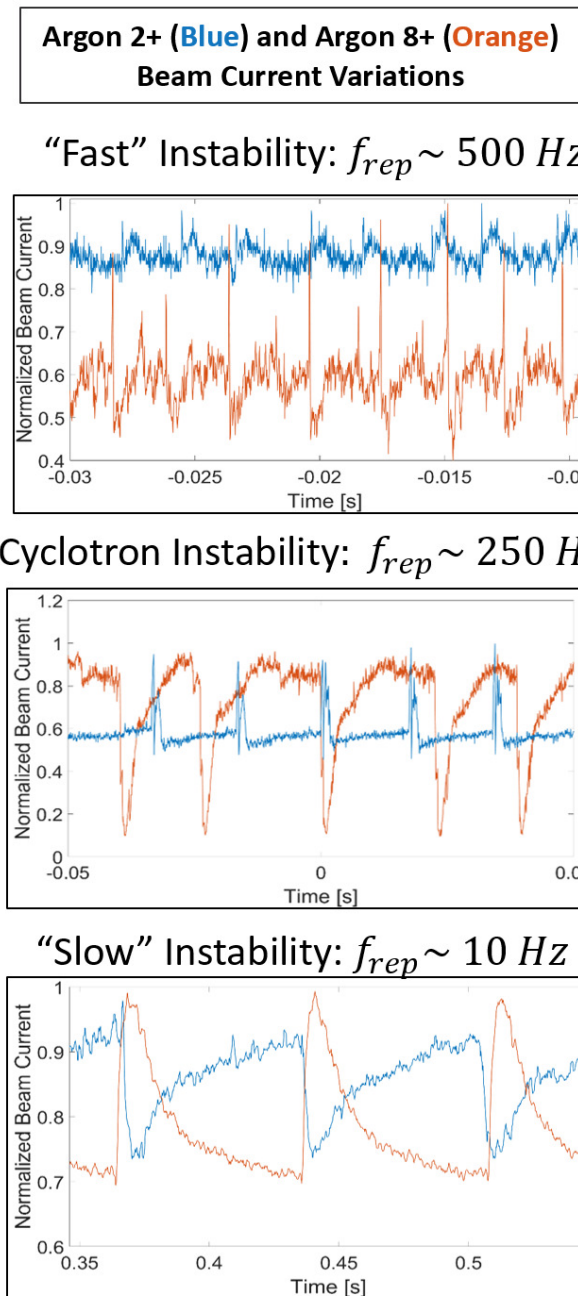


Figure 1: Plots of the manifestations of the instabilities in the extracted beam current.

The "fast" instabilities tend to have spike in beam current lasting about $5\mu\text{s}$ followed by a sudden drop in the beam current leading to a slower recovery period lasting $\sim 100\mu\text{s}$. The cyclotron instabilities demonstrated the characteristics expected from the previous studies, [1,2]. The instability begins with a fast drop in the current lasting $\sim 10\mu\text{s}$ followed by a recovery period on the order of milliseconds to tens of milliseconds. The final instability, the "slow" instability, has the opposite current features of the other two instabilities. For the 8+ charge state we see that there is a first a drop in the beam current on the order of $10\mu\text{s}$ followed by a slow rise and recovery period lasting on the order of 20 ms. As a result, the "slow" instability increases the average beam current extracted from the ion source for a short time. Further investigation shows that each of these instabilities can manifest in each of the extracted charge states. It is easy to see that both the "fast" and cyclotron type instabilities gain current on average for low charge states and lose current on average for high charge states, acting consistently with the features described in [1]. The "slow" instabilities act in the opposite manner; with low charge states losing current on average and high charge states gaining current.

Plots of the microwave signals in coincidence with the oscillating beam current for each of the instabilities are given in Fig. 2. Both the "fast" and cyclotron instabilities are characterized by a sudden burst of microwave energy that lasts on the order hundreds of microseconds for the "fast" instabilities and $\sim 5\mu\text{s}$ for the cyclotron instabilities. The slow instabilities on the other hand only have a sudden increase in the detected microwave power, emitted from the source chamber, that continues to increase slowly and appearing to follow the extracted beam current.

Stability Map

To fully understand how the confining field and the injected microwave power can affect the plasma stability we have created a series of color maps (Fig. 3) displaying whether or not the plasma is unstable and in what way. The first column and the last row (both in green) represent the injected microwave power and B_{min}/B_{ecr} , creating a coordinate grid for each of the field settings used. The maps display the manifestations of the instability, as "fast", cyclotron, or "slow"; displayed as blue, yellow, and red, respectively, in each of the grid coordinates. Each of the maps then represents a single radial field setting, given above each map.

The ECR itself divides the instability region into two sections: with lower power and field settings predominately displaying "fast" instabilities and high field and power settings predominately displaying "slow" instabilities. If there is a stable point to be found, then it would appear between these two regions. While the stability maps presented do show more complexity than the ones presented in [1] and [2] the same general trend with respect to the magnetic field and power does persist. We observe that as the magnetic minimum increases that a stable operating point is more likely to occur for lower injected power, agreeing with the

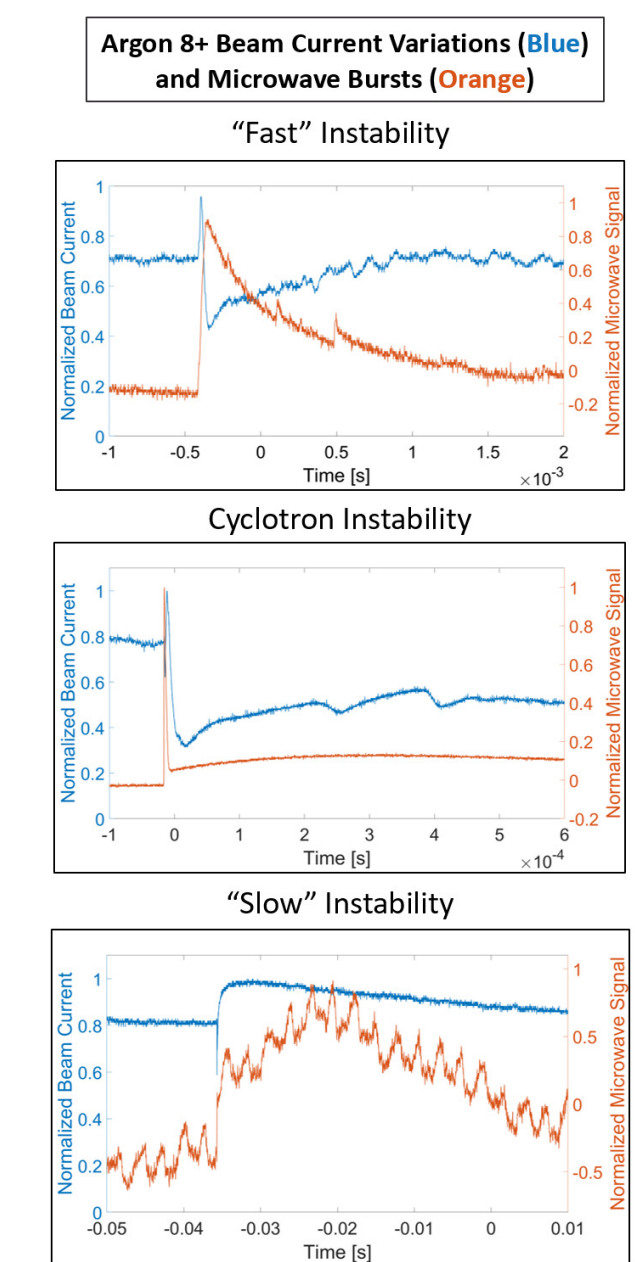


Figure 2: Measurements of each of the instability manifestations for the 8+ charge state in coincidence with their corresponding reflected microwave signal.

results found at JYFL. We find that the hexapole does influence the stability characteristics of the ECRIS plasma, with a general trend of decreasing the probability of finding a stable operating point as the hexapole field increases. As the hexapole field increases the stable region slowly starts to disappear as the two unstable regimes converge towards one another. This trend exists for three of the four experimental ranges used in our measurements, with the exception being the fourth experimental range where the trend reverses. It is also interesting to note that the cyclotron type instabilities are not well represented across the charts, with the "fast"

Content from this work may be used under the terms of the CC BY 3.0 licence (© 2018). Any distribution of this work must maintain attribution to the author(s), title of the work, publisher, and DOI.

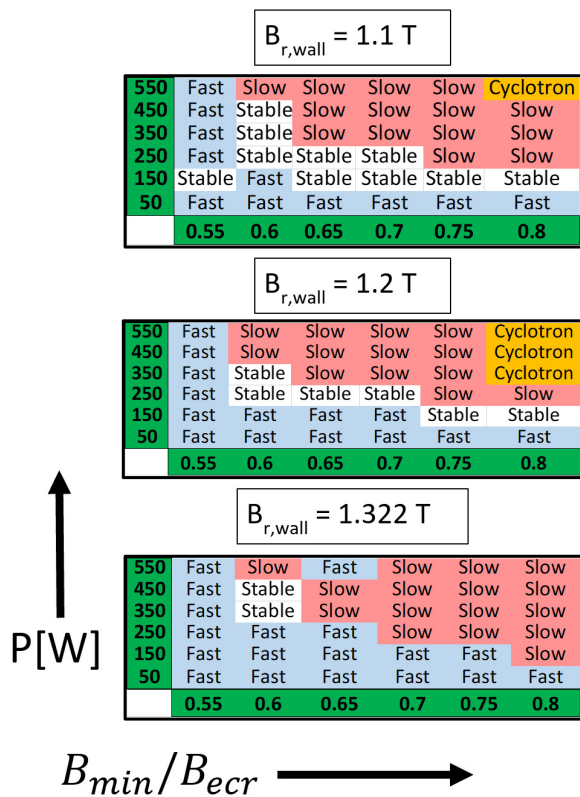


Figure 3: The instability field maps for experimental range 3 at every hexapole field used. The green row and column show B_{min}/B_{ecr} and the injected microwave power, respectively. The blue, orange, and red cells represent the "fast", cyclotron, and "slow" instabilities respectively.

and "slow" type instabilities being the most commonly observed. Once again, the exception to this rule was the fourth experimental range.

Changing the axial field distribution was also found to change the stability characteristics of the plasma. Figure 4 gives an example of the stability map for two of these field distributions for a constant hexapole field strength. It can be seen that lowering the injection and extraction field maximum away from the classical scaling laws makes the plasma more unstable. It is also important to note that the extracted current peaks at a $B_{min}/B_{ecr} = 0.8$ around the distribution prescribed by the scaling laws. This peak occurs at a $B_{min}/B_{ecr} = 0.65$ in the distribution that deviates from those laws. From this we observe that the stability characteristics of the plasma are not entirely dependent on the B_{min}/B_{ecr} value.

Bremsstrahlung Measurements Across the Stability Threshold

Measurements of the bremsstrahlung spectra were taken for both stable and unstable operating conditions. All measurements were taken using experimental range 1, $B_{inj}/B_{ecr} \geq 4$ and $B_{ext}/B_{ecr} \geq 2$. Figure 5 compares the x-ray spectra for two operating points on either side of

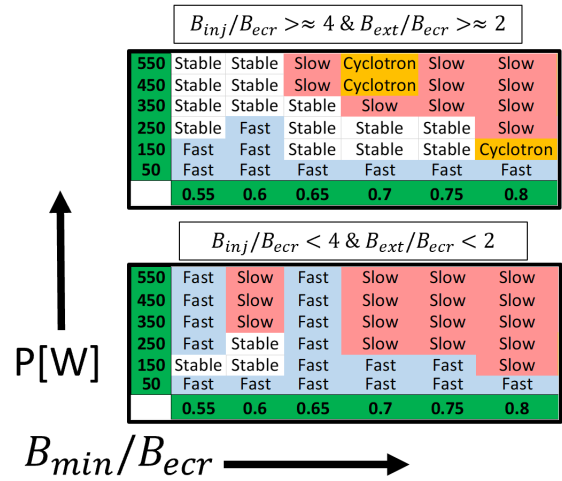


Figure 4: The instability maps for experimental ranges 1 (top) and 2 (bottom). The hexapole field for both maps is 1.1 T at the plasma chamber wall.

an instability threshold. Changing the longitudinal magnetic field profile from $B_{min}/B_{ecr} = 0.567$ to 0.577 induced a "slow" type instability. The injected microwave power and radial field at the wall were fixed at 400 W and 1.1 T, respectively, during these measurements. It is clear from the plot that the spectra do not change from one side of the threshold to the other. This may result from the low duty cycle of the x-ray bursts from the source cavity. It is reasonable to assume that the spectra will look very similar as minor changes to the system will not greatly affect the diffusion of electrons unaffected by the instability out of the plasma. It is necessary to time resolve these measurements for comparisons around the instability threshold. Figure 6 compares the results of the bremsstrahlung spectra for three different magnetic field operating points with fixed injected microwave power and radial field strength at the wall. The first two spectra behave as described in [6] with the final spectra, $B_{min}/B_{ecr} = 0.8$, exhibiting a lowered energy peak over the 75 – 100 keV range but an increased count rate within the 200 – 400 keV portion of the high energy tail. Figure 7 shows four spectra

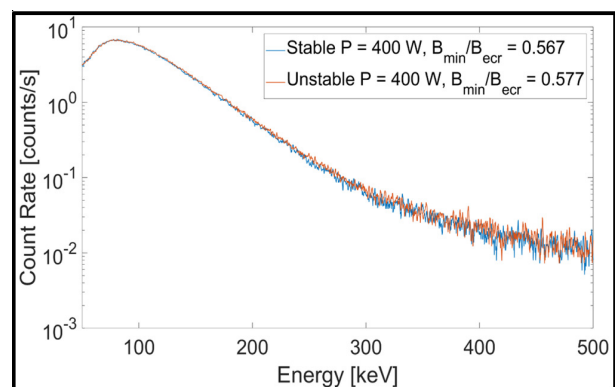


Figure 5: This figure compares the bremsstrahlung spectra on either side of the instability threshold.

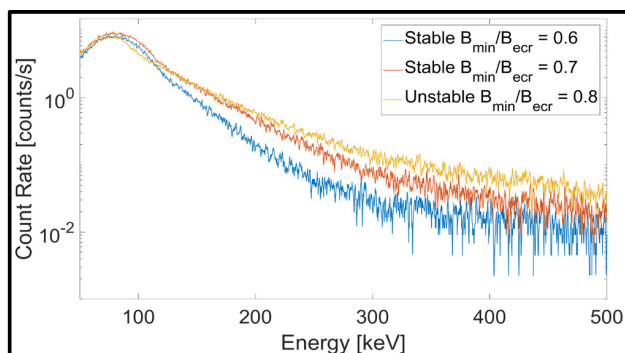


Figure 6: Bremsstrahlung spectra for a constant injected microwave power of 250 W and hexapole field strength at the wall of 1.1 T.

demonstrating the effect of keeping a constant B_{min}/B_{ecr} ratio while varying the injected power and radial field at the wall. The stable operating point with 250 W injected microwave power and a 1.1 T magnetic field at the wall acts as a good point for comparison. We can see that increasing the radial field at the wall by 0.1 T, changing the plasma into the “fast” instability regime, will give a similar effect on the spectra as simply increasing the microwave power by 200 W. Increasing both the injected microwaved power and the radial field at the wall makes the plasma undergo a “slow” type instability and causes a drastic change in the measured spectra. Rather than observing an increase in the count rate equal to the sum of the increase presented by the changing the radial and injected power individually, we find that the 75 keV peak has a lower count rate with a bulging of the 110 - 300 keV portion of the high energy tail.

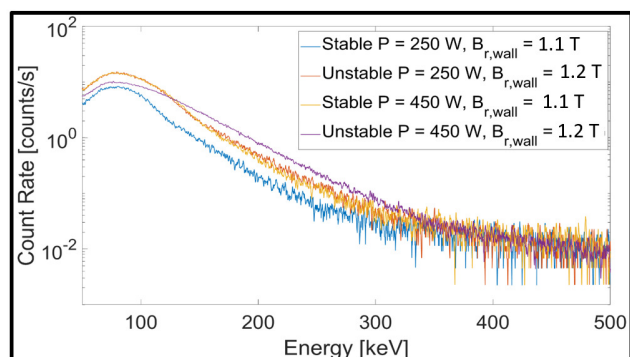


Figure 7: Bremsstrahlung spectra for a constant $B_{min}/B_{ecr} = 0.8$.

CONCLUSIONS

Our recent measurements have provided us insight into how the magnetic field distribution of the ECR ion source confining field affects the stability characteristics of the plasma. We found that the variations of the extracted beam currents, induced by plasma instabilities, can manifest in

three different ways named here as “fast”, cyclotron, or “slow”. Parametric stability maps were accumulated that found that an increasing hexapole field strength made the plasma less stable. It was also found that changing the field distribution away from the scaling laws also makes the plasma more unstable. Bremsstrahlung measurements far from the stability threshold show that higher energy electrons are more likely to escape into the loss cone while the plasma is unstable. Future measurements of the energy spectra around the threshold need to be time resolved in order to determine the shift in the energy content of the distribution of lost electrons.

Future work will include determining the nature of each of the two new instability manifestations. From this we hope to conclude whether or not the different manifestations are caused by different mechanisms. Efforts into creating a time resolved measurement system for the bremsstrahlung spectra are also being planned.

ACKNOWLEDGMENTS

This research was made possible by the NSCL/FRIB Ion Source group staff Jesse Fogleman and Larry Tobos. We also thank the NSCL/FRIB facilities and operational managers including Andreas Stolz, Yoshishige Yamazaki, Thomas Russo, Kent Holland, and Steven Lidia. We also give special thanks to Ollie Tarvainen for providing guidance and advice during the development of our experimental apparatuses.

REFERENCES

- [1] O. Tarvainen *et al.*, “Limitations of the ECRIS performance by kinetic plasma instabilities”, *Rev. Sci. Instrum.*, vol. 87 (2016).
- [2] O. Tarvainen *et al.*, “Beam current oscillations driven by cy-clotron instabilities in a minimum-B electron cyclotron reso-nance ion source plasma”, *Plasma Sources Sci. Technol.*, vol. 23 (2014).
- [3] I. Izotov *et al.*, “Microwave emission related to cyclotron in-stabilities in a minimum-B electron cyclotron resonance ion source plasma”, *Plasma Sources Sci. Technol.*, vol. 24 (2015).
- [4] M Viktorov *et al.*, “Laboratory study of kinetic instabilities in a nonequilibrium mirror-confined plasma”, *Europhys. Lett.*, vol. 109 65002.
- [5] O. Tarvainen *et al.*, “Periodic beam current oscillations driven by Electron Cyclotron Instabilities in ECRIS Plasmas”, in *Proc. ECRIS'14*, paper MOOBMH01 (2014).
- [6] J. Benitez *et al.*, “Recent Bremsstrahlung Measurements from the Superconducting Electron Cyclotron Resonance Ion Source Venus”, in *Proc. ECRIS '16*, paper MOCO04.
- [7] P. Zavodszky *et al.*, “DESIGN, CONSTRUCTION AND COM-MISSIONING OF THE SUSI ECR”, *Proceed. PAC07*, paper FRXAB03.
- [8] C. M. Lyneis, “SCALING LAWS IN ELECTRON CY-CLOTTRON RESONANCE ION SOURCES”, in *Proc. ECRIS '16*, paper MOAO01.

TIME RESOLVED X-RAY MEASUREMENTS IN A SIMPLE MIRROR TRAP

S. Tudisco[†], C. Altana, G. Castro, G. Lanzalone, G. Litrico, A. Muoio, L. Celona, S. Gammino, D. Mascali, M. Mazzaglia, G. Torrisi INFN-LNS, 95123 Catania, Italy
E. Naselli, INFN-LNS, 95123 Catania, Italy
Università degli Studi di Catania, 95123 Catania, Italy
R. Miracoli, ESS Bilbao, 48170 Zamudio, Spain

Abstract

The time-resolved characterization of the X-ray emission represents an innovative technique to investigate the heating mechanism of the warm/hot electron component in ECRIS devices. In this paper, the technique will be described and the results of an experimental campaign of measurements in order to characterize the X-rays emission of an axis-symmetric simple mirror trap will be showed.

INTRODUCTION

The Electron Cyclotron Resonance Ion Sources (ECRIS) are used to produce charged ion beams at high intensity characterized by high stability and high reliability for accelerators and others applications both in nuclear physics and industrial area. Over the years, many studies have been conducted to understand the scaling of plasma parameters as function of tuning parameters, such as pumping wave power and frequency and magnetic field profiles. In particular, it was observed that the $B_{\text{mir}}/B_{\text{ECR}}$ ratio, namely the gradient of the magnetic field, is one of the parameters that mainly generate instability and anisotropy in plasmas: a non-linear increase of X-ray fluxes has been observed.

In this work, we want to investigate the X-ray emission from the Flexible Plasma Trap (FTP) by means of a Hyper-Pure Germanium (HpGe) in time-resolved configuration.

EXPERIMENTAL SETUP

The FTP, designed, developed and installed at INFN-LNS, allows the plasma characterization. The chamber is a cylindrical water-cooled copper vessel with an inner diameter of about 82 mm and a length of 260 mm. The plasma chamber is connected with a stainless-steel made "pre-chamber" in order to host the vacuum system and the diagnostics tools.

The external magnetic field used for ECR heating and plasma confinement is generated by means of three solenoids which allow tuning the magnetic field in function of the frequency. In particular, a simple magnetic mirror, a constant B field along the axis of the cylindrical discharge vessel and a magnetic beach configuration can be generated by tuning the current flowing in the coils. In this work we focused on the investigation of the simple mirror, with varying $B_{\text{mir}}/B_{\text{ECR}}$ ratio. Moreover, FTP has three different

microwaves system, one parallel and two perpendicular respect to the plasma chamber. Microwaves of axial injection are generated by a Travelling Wave Tube (TWT) operating in a range from 4 to 7 GHz. The perpendicular microwave launcher can work at 14 GHz and allow operating in double frequency (first and second frequency) mode [1]. Further information about the FPT can be found in reference [2].

The HpGe detector, located on the axial port of the vacuum chamber, as shown in Fig. 1, was used in order to investigate the X-ray emission from high energy electrons of the plasma or of those that hit the chamber walls.

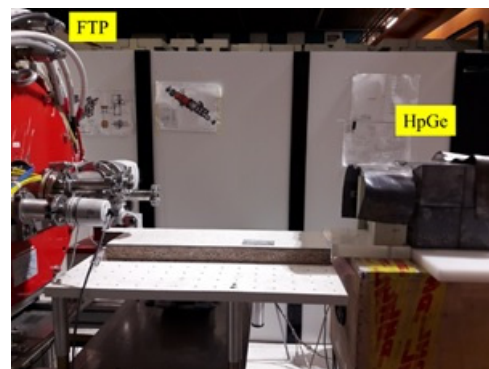


Figure 1: Experimental setup.

The HpGe consists of a 15 mm thick, 20 cm² detector that sits behind a 0.3 mm thick Be window. Its resolution at 122 keV is 0.61 keV. The detector is shielded with lead blocks of 2 cm thickness and $\phi = 1$ mm to avoid detecting x-rays scattered from the environmental material. The HpGe detects the radiation that pass mostly through the collimator of the vacuum vessel.

The detector was connected, at the same time, at the acquisition system MultiChannel Analyzer (MCA) and at the oscilloscope. In order to allow the time resolved X-ray spectroscopy, by means of an external trigger, the plasma was "switched on" for a duration of 40 ms and then it was "switched off". In Fig. 2 is shown a typical signal obtained from oscilloscope.

[†] tudisco@lns.infn.it

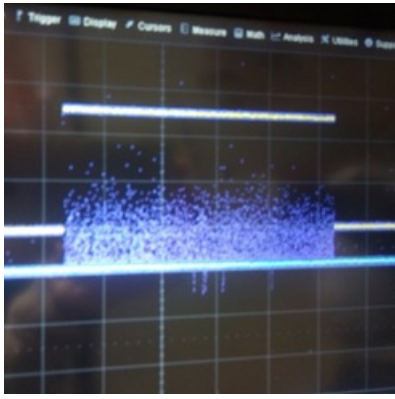


Figure 2: Typical spectrogram of X-ray emission in 40 ms from oscilloscope.

The time-resolved configuration has allowed to obtain preliminary information about the spectral X-ray emission as function of a time interval and to investigate the behaviour of X-ray flux with the increasing of time.

RESULTS

The data were recorded at a power level of 80 W and at operating pressure in vacuum chamber of about 8×10^{-5} mbar. Moreover, the X-ray emission was investigated at two different heating frequencies, 4.1 and 6.83 GHz and varying the B_{min}/B_{ECR} ratio from 0.56 to 1.02, namely setting the current of the injection and extraction coils and changing the current of the mid coils.

In standard configuration, it was observed that, at 6.8 GHz, for value B_{min}/B_{ECR} less than 0.83 the X-ray emitted is negligible and for B_{min}/B_{ECR} higher than 0.83 the rate increase suddenly; while, at 4.1 GHz, the rate of X-ray flux changes considerably for $B_{min}/B_{ECR} > 1$, as shown in Figs. 2 and 3.

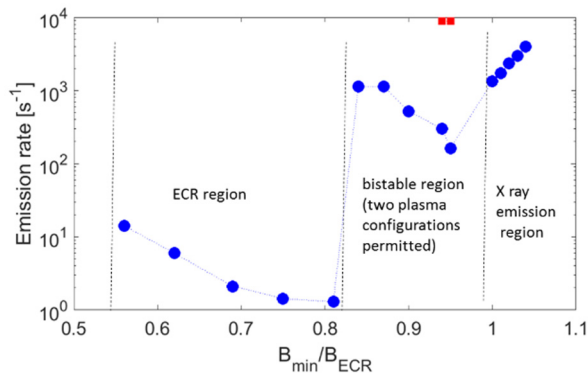


Figure 3: X-ray emission rate versus different simple mirror configurations at 6.83 GHz.

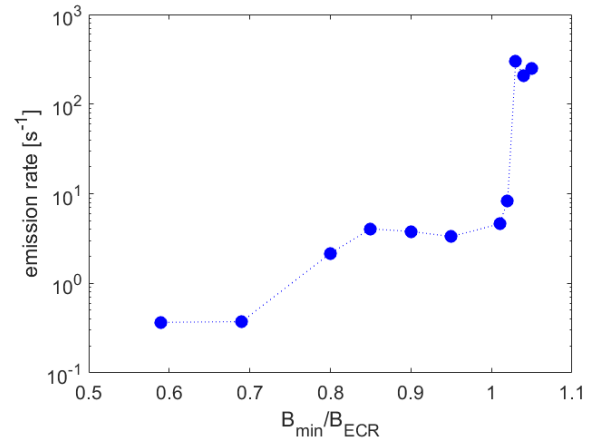


Figure 4: X-ray emission rate versus different simple mirror configurations at 4.1 GHz.

X-ray emission rate was also estimated in time-resolved configuration. In Figs. 5-7 are shown these rates in different plasma configuration: it is possible to observe that in the X-ray region emission ($B_{min}/B_{ECR}=1.01$) the flux increase with time.

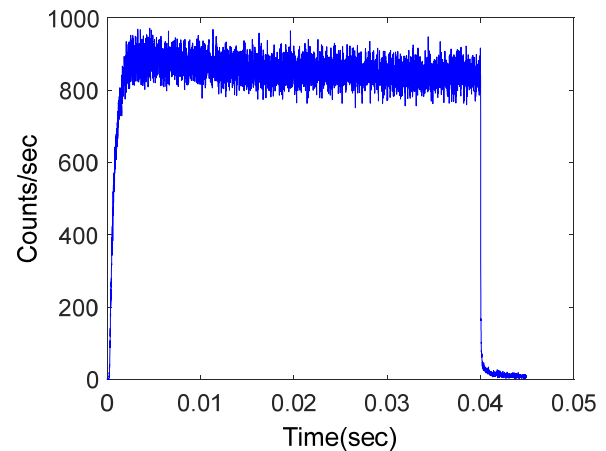


Figure 5: X-ray emission rate as function of time at 6.83 GHz and $B_{min}/B_{ECR}=0.95$.

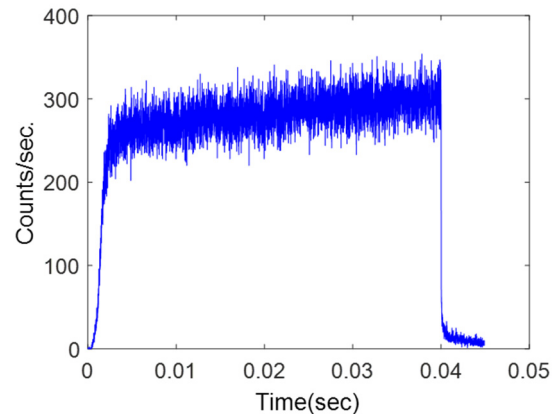


Figure 6: X-ray emission rate as function of time at 6.83 GHz and $B_{min}/B_{ECR}=1.01$.

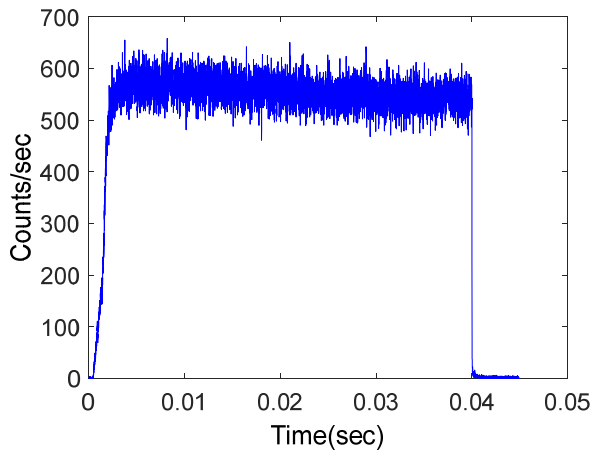


Figure 7: X-ray emission rate as function of time at 4.1 GHz and $B_{min}/B_{ECR}=1.04$.

REFERENCES

- [1] G. Torrisi *et al.*, "A new launching scheme for ECR plasma based on two-waveguides-array", *Microw. Opt. Technol. Lett.*, vol. 58, p. 2629, (2016), doi: 10.1002/mop.30117
- [2] Gammino S *et al.*, *Journal of Instrum.* vol. 12 p. P07027, (2016)

EFFECT OF THE TWO-CLOSE-FREQUENCY HEATING TO THE EXTRACTED ION BEAM AND TO THE X-RAY FLUX EMITTED BY THE ECR PLASMA

R. Rácz[†], S. Biri, Z. Perduk, J. Pálinkás, Institute for Nuclear Research, Hungarian Academy of Sciences (Atomki), [H-4026] Debrecen, Hungary

D. Mascali, M. Mazzaglia, E. Naselli, G. Torrioni, G. Castro, L. Celona, S. Gammino, Istituto Nazionale di Fisica Nucleare, Laboratori Nazionali del Sud (INFN-LNS), [95123] Catania, Italy

A. Galatà, Istituto Nazionale di Fisica Nucleare, Laboratori Nazionali di Legnaro (INFN-LNL) [35020] Legnaro, Italy

Abstract

Multiple frequency heating has been used since the '90 in ECR ion sources as heating schemes able to improve current intensities especially for highly charged ions. More recently “Two Close Frequency Heating”, where the frequency gap is comparable with the scale-length of the resonance, has been proposed, expected also to be sensitive to the relative waves' phase relationship. At ATOMKI – Debrecen a dedicated experiment has been carried out for exploring the effects of the combined frequencies and their relative phase-difference in an argon plasma. The second frequency was finely tuned between 13.6-14.6 GHz with respect to the first one (fixed 14.25 GHz). An optimal frequency gap (in terms of $\text{Ar}^{11+}/\text{Ar}^{6+}$ beam currents ratios) has been experimentally found, in agreement with the theory; the optimal power balance (total RF power was 200 W) between the two frequencies has been determined empirically. A weak but clear effect of the relative phase shift has been observed. Each configuration has been characterized by a multi-diagnostics set-up: HPGe and SDD detectors were used for the X-rays, a RF probe was introduced inside the plasma chamber to detect the radio-emission from the plasma.

INTRODUCTION

Demand from the users of ion beams are continuously motivating the development of ion sources to produce as high current of highly charged ions as possible. Electron Cyclotron Resonance (ECR) Ion Sources (ECRIS) seem to be the best candidates to fulfil the strict requirements in terms of beam intensity, emittance, ion choice, stability, etc [1]. To obtain intense highly charged ion current the ions should be extracted from dense and energetic ECR plasma, having anisotropic distribution of the electrons in the velocity space.

General approach of the way for the improvement is pointed by the scaling laws [2]. Accordingly, higher plasma density is needed to produce higher charge state ions, which requires higher microwave heating power. However in order to still remain below the critical density (to avoid the cut-off of the microwaves), which is scaling with the

frequency square the heating frequency and the corresponding magnetic field should be increased, as well.

Milestones in this way are symbolized by different generations of ECRISs. However, the steps between two generations are money- and time-consuming, requiring many investments from cryogenic and radiofrequency engineering sides. Therefore, at a given generation level (where the magnetic field and frequency configuration is determined) tricks were worked out to significantly improve the beam parameters without drastically changing the ECRIS configuration. They are widely applied in the ECRIS committee e.g. gas mixing [3], biased disc [4], fine frequency tuning [5], and two frequency heating [6].

Since the first half of the '90 multiple frequency heating has been tested and used as a technic which provides remarkable improvement of the ion source performance by improving the stability of the plasma and by shifting the ion charge state distribution toward the higher charge ones [7]. The first experiments providing promising results were performed applying two far frequencies (e.g. 10 GHz + 14 GHz, 14 GHz + 18 GHz) obtaining two well separated ECR heating zones (Two Far Frequency Heating (TFFH)). The effects were explained by the increase of the ECR heating volumes [8]. However, in 2008 Gammino et al. [9] pointed out a possible “extra” interplay between the two resonant zones having the two frequencies close to each other (Two Close Frequency Heating (TCFH)). Particularly, some kind of “electron surfing” is expected; the electrons that leave the first resonant zone may further accelerated by the second one (two close frequency is needed because the phase randomization of the electrons should not be occurred). The idea was confirmed by numerical simulations showing remarkable variation in electron energy as function of the relative phase difference between the two close frequencies.

Independently of the magnitude of the relative frequency difference (TCFH or TFFH) the importance of the fine tuning at least one of the two microwave frequencies was stated, since strong fluctuation of highly charged ions were obtained by slight tuning of the relative frequency difference [10, 11]. In case of TCFH mode the optimal effect was obtained when the distance between the two resonant layers were close to the Larmor radius of the warm electrons [10].

It was highlighted that the plasma stability and therefore the ion beam stability can be improved by adding an extra

[†] rracz@atomki.mta.hu

frequency [12, 13]. Higher net microwave power can be injected to the plasma chamber still maintaining stable plasma conditions at TFH mode therefore, higher current of highly charged ions are reachable.

It was also shown that the instabilities limiting the performance of the ion source is occurred at certain conditions [14] only i.e. at suitably high microwave power and at B_{\min}/B_{ecr} ratios higher than 0.75. As a characteristics of the instabilities, events are followed by sudden radio and X-ray emission from the plasma [15, 16]. These kinetic instabilities are caused by the strongly anisotropic distribution of the electrons in the velocity space and are triggered when the transverse velocity of the electrons respect to the magnetic field starts to dominate over the longitudinal one.

One can roughly summarize that the goal is to verify if two frequency heating can help the ionization efficiency of ECR plasma and can suppress the ion beam oscillation caused by the kinetic instabilities in two far and two close frequency operations, as well. However the mechanism and the dynamics of the processes caused by the second frequency are still not known, furthermore many aspects of the TFH have never been tested experimentally: the power balance between the two frequencies and the relative phase difference between them at TCFH mode.

Therefore we designed and arranged a multi diagnostic setup to investigate the behaviour of a 14.25 GHz plasma when an additional finely tuned frequency close to the first one is added. Beside the ion beam properties (current of multiple charged ions), the setup provides information on the warm and hot electron components of the plasma by measuring the hard and soft X-ray rates by the help of High Purity Germanium (HPGe) Detector and Silicon Drift Detector (SDD), as well. Furthermore the plasma generated microwave signals are able to be monitored through a radiofrequency (RF) probe placed inside the plasma chamber and connected to a spectrum analyser operating in GHz ranges. Parameters of the radiofrequency spectra can be used as an indication of stable and unstable plasma conditions.

As a unique feature, two dimensional information on the plasma structure and electron losses are obtained by X-ray pinhole camera. Effect of the relative frequency phase difference and power balance between the two TCF were explored by these diagnostics tools. This experimental campaign with this arsenal of diagnostics tools provides many important information (a complex image) on the nature of the stable, unstable and two frequency heated ECR plasmas. In this paper we are reporting the part of the obtained results which strictly corresponds to the ion source performance (ion beam, volumetric X-ray emission) while the results more deeply corresponds to the ECR plasma dynamics will be published in other papers [17].

EXPERIMENTAL

The dedicated experiment was carried out at the Atomki ECRIS, in Debrecen. This ion source [18] is a 14 GHz, second generation ECRIS. B-minimum trap consists of two room temperature coils and of a NdFeB permanent magnet hexapole. The radial magnetic field measured at the plasma

chamber wall is about 1.2 Tesla while the axial magnetic peak fields at the axes of the plasma chamber are 1.26 T at the injection side and 0.95 T at the extraction side, and the minimum value (B_{\min}) is 0.39 T. Detailed experimental setup of the whole, complex measurement system together with numerous technical figures and tables for a better understanding, are presented in a separated accompanying paper [19]. Only the main features of the measuring system are summarized in the following paragraphs.

The first 14.25 GHz signal was amplified by a klystron while the second tuneable one (13.6 GHz - 14.6 GHz) was provided by a TWTA. Due to the compactness of the plasma chamber and to the high number of diagnostic tools to be equipped to the ion source it was reasonable launching the heating microwaves through only one waveguide by mixing the two RF signals before the plasma chamber by power combiner. Before the power combiner a phase shifter was inserted into the TWT waveguide line. Both the forwarded and the reflected powers were measured at the closest possible point to the plasma chamber. Argon plasma was generated keeping in most cases the net power ($P_{\text{net}} = P_{\text{forwarded}} - P_{\text{reflected}}$) at fixed 200 Watts. The maximum power was limited by the X-ray imaging system to obtain photos with appropriate signal noise ratios. Gas flow was optimized for middle charged argon ion production.

Two detectors were applied at the injection side, alternatively. SDD was placed at the plasma chamber axis beyond 50 μm thick kapton foil for vacuum break, and collimated by a 30 cm long lead cylinder with a 1 mm drilled hole. The CCD X-ray camera made by 1024 x 1024 pixels operational in the range 500 eV – 20 keV was coupled to a lead pin-hole and placed along the axis, facing the chamber from the injection flange. Titanium windows with 9.5 μm thickness were used to screen the CCD from the visible and UV light coming out from the plasma. In addition, HPGe detector was placed also on the axis, but at the other (extraction) side of the source beyond the 90-degree analysing magnet, closed to a quartz window. The HPGe was collimated by lead blocks through 3 mm hole in diameter.

RF probe was introduced inside the plasma chamber and connected to an Anritsu Spectrum Analyser in order to detect the radio-emission from the plasma. The sudden radio-emission occurred at the beginning of the unstable plasma regime was used to trigger the signals measured by the HPGe detector, as well. Such an arrangement was allowed to record the temporal spectral composition of the emitted X-ray. So, hard X-ray spectra are able to be recorded close to and at unstable plasma conditions.

Placement of the detectors opened the possibility to extract ion beam from the plasma simultaneously with the usage of the diagnostics tools to take note some representatives of the charge state distribution (Ar^{6+} , Ar^{9+} , Ar^{11+}) at different working points.

Plasma chamber of the ion source was changed by applying dedicated materials for different part of the chamber. Tantalum liner was inserted as lateral wall of the plasma chamber, while the plasma electrode was made of Titanium. Injection plate was adapted to the X-ray imaging: the area of the Al made circle shape injection plate was

divided into two regions in the ratio 2:1. The smaller area was used for microwave and gas injection, while the larger part was closed by Al mesh to form closed resonant cavity and to provide transparency for imaging at same time (see the details in [19]).

RESULTS

Response of the ion source to the settings parameters was systematically studied. Presentation of the results in terms of rates of X-ray detectors, and ion beam representatives will follow this structure: (1) effect of the single frequency sweep, (2) effect of the microwave power at selected single frequency, (3) effect of the power balance between two close frequencies (4) effect of the frequency scan at a selected power balance at TCFH mode (5) effect of the phase shift at TCFH mode.

(1) Single Frequency Scan

Figure 1. (a) shows the trend of the representatives of multiply charged ion currents extracted from the ion source as function of the TWT frequency at single frequency heating mode.

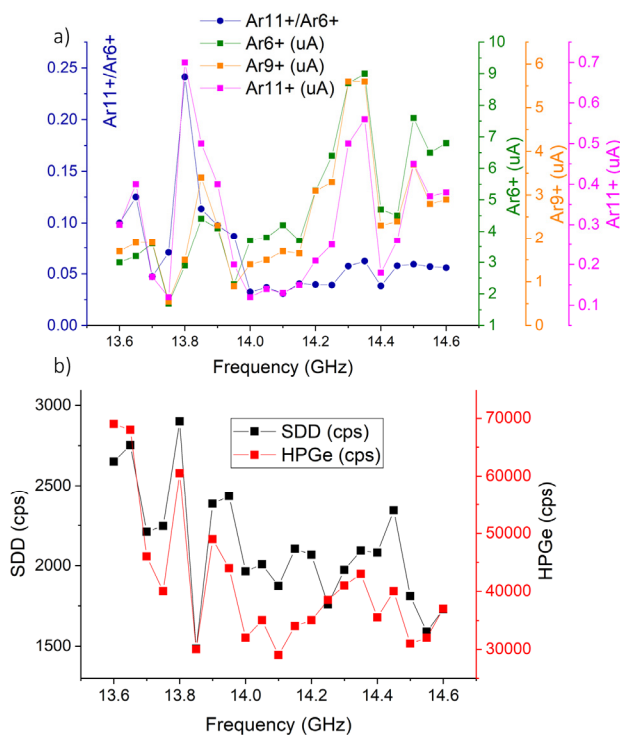


Figure 1: Effect of the single frequency scan to the extracted ion beam and to the plasma emitted X-ray

The net microwave power was always 200W, while the frequency was changed between 13.6 GHz and 14.6 GHz with 50 MHz steps. This fine frequency tuning firmed the nonlinear response of the currents which obtained by many times by many groups. Ar¹¹⁺/Ar⁶⁺ ratios (Fig.1.(a)) has maximum at 13.8 GHz and it has a general rising trend with some fluctuation from the higher frequencies toward

the lower ones. This trend is also visible on the plots showing the rates of soft and hard X-ray fluxes (Fig.1. (b)).

(2) Power Dependence At Single Frequency

Power dependence were measured at 13.8 GHz being the most promising frequency in terms of Ar¹¹⁺ current and Ar¹¹⁺/Ar⁶⁺ ratios. At microwave power lower than 100 W the measured currents corresponding to different charge states are increasing monotonically (Fig. 2. (a)). Above 100 W nonlinear effect appeared in all the three plots cases. Ar⁶⁺ and Ar⁹⁺ currents are decreasing dramatically, while the Ar¹¹⁺ current and the Ar¹¹⁺/Ar⁶⁺ ratio start to increase exponentially. There is a quite significant nonlinear jump in the emitted X-rays above 100 W, as well (Fig. 2. (b)).

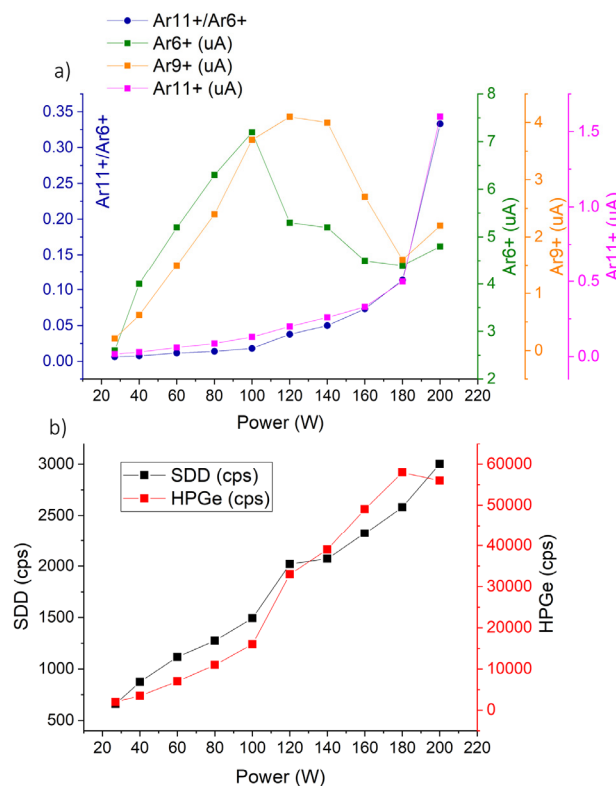


Figure 2: Power dependence of the extracted ion beam and of the plasma emitted X-ray

(3) Power Balance At 13.8 GHz And 14.25 GHz

Power balance between the two injected frequencies was investigated at the fixed 14.25 GHz klystron and 13.8 GHz TWT frequencies. Sum of the two power components was kept always at 200 W net power. Figure 3 shows the tendencies as function of the applied TWT power. While the Ar⁶⁺ and Ar⁹⁺ currents are decreasing with the amplitude of the TWT power Ar¹¹⁺ and Ar¹¹⁺/Ar⁶⁺ are behaves inversely (Fig. 3. (a)). The more dominant of the TWT the higher the emitted hard and soft X-ray fluxes were obtained (Fig. 3. (b)). Instability of the plasma in terms of the plasma emitted RF signals was varying significantly with the power ratios and it was quite low at the 120 W klystron and 80 W TWT power balance case.

Content from this work may be used under the terms of the CC BY 3.0 licence (© 2018). Any distribution of this work must maintain attribution to the author(s), title of the work, publisher, and DOI.

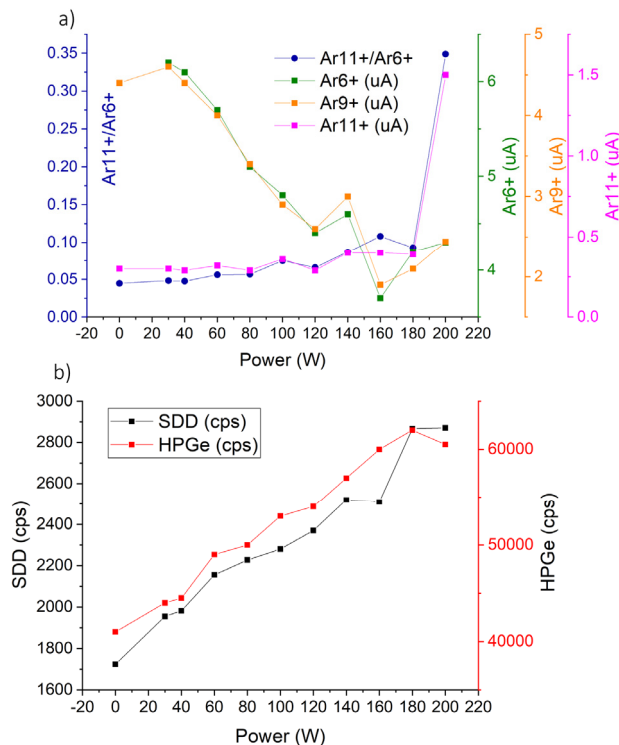


Figure 3: Effect of the power balance between 13.8 GHz and 14.25 GHz to the extracted ion beam and to the plasma emitted X-ray

(4) Frequency Scan At TCFH Mode

Because stable plasma conditions were found around 120 W klystron and 80 W TWT powers, TCFH was investigated at this power balance, keeping the net power always at 200 W, while changing the TWT frequency between 13.6 GHz and 14.6 GHz with 50 MHz steps.

Currents corresponding to different charge states (Fig. 4. (a)) shows rather different trends than the case of single frequency scan (having minimums and maximums at different frequencies), while the obtained Ar¹¹⁺/Ar⁶⁺ ratio behaves very similarly. The two “side peaks” (especially in the 11+ production) located almost symmetrically respect to the main frequency consistent with earlier observations and with TCFH expectations. Both components of the X-ray fluxes (fig. 4. (b)) are decreasing toward the higher frequencies as obtained in single frequency scan case but the overall rate was decreased by about 15 % respect to the single frequency operation mode.

(5) Phase Shift At TCFH Mode

As mentioned in the experimental section our setup provides opportunity to check the effect of the relative phase difference between the two heating microwave. Phase of the klystron related signal was not changed while the TWT signal was phase-tuned finely. The effect was checked at several frequency combinations, at several power balance cases. Significant effect was obtained at 13.8 GHz TWT frequency at a power balance sustaining unstable plasma condition in terms of the plasma emitted

RF signals ($P_{KLY} = 170$ W, $P_{TWT} = 30$ W). About 10 % variation were found in the currents of Ar¹¹⁺, Ar⁹⁺ and ratio of Ar¹¹⁺/Ar⁹⁺ (see Fig. 5).

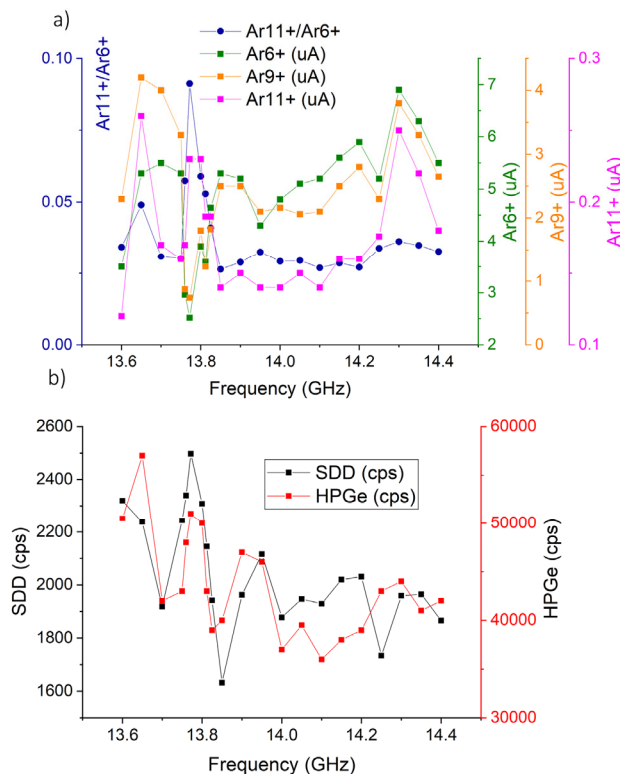


Figure 4: Effect of the frequency scan at TCFH mode to the extracted ion beam and to the plasma emitted X-ray

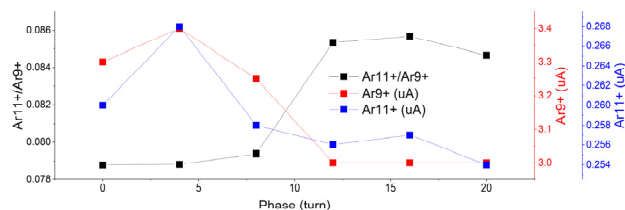


Figure 5: Effect of the relative phase difference at TCFH mode. 20 turns correspond to π phase shift.

DISCUSSION AND OUTLOOK

At single frequency scan the nonlinear behaviour of the emitted X-rays and ion beam intensities as function of the frequency was obtained in accordance with earlier experiments. It can be explained by the ECR heating depends on the excited modes in the plasma chamber, as it was shown in [20]. Due to the applied magnetic field configuration and to the selected frequency range the B_{min}/B_{ecr} ratio was varied from 0.75 – 0.8 (increasing toward the lower frequencies). Tarvainen et al. have shown that kinetic plasma instabilities are triggered always around this configuration [14]. They have controlled the B_{min}/B_{ecr} ratio by tuning the coils current. In this experimental campaign we implemented a different way for the tuning without changing the plasma confinement drastically. The rising trend of the hard X-ray flux toward the lower frequencies can be explained by stronger and more frequent instabilities causing

more energetic warm electrons to be lost on the plasma chamber wall and producing Bremsstrahlung radiation. Stronger evidence is expected by analysing the X-ray photos showing the spatial distribution of plasma losses.

Curves corresponding to the power dependence shows nonlinear behaviour (jump in X-ray emission and CSD shift) above 100 W at 13.8 GHz. It could be the sign of the unstable regime appeared above a threshold level. Power balance between the two frequencies affected not only the X-ray flux but also the CSD of the ion beam and the stability of the plasma. Such an aspect of the TFH has never been highlighted.

We could find optimal frequency gap (to produce intense ion beam) between the two frequencies at TCFH mode at both side of the fixed frequency.

As it was predicted by Gammino et al. [9] by controlling the relative phase difference between the TCF the ion source performance was clearly affected. Effect of the phase shift was rather weak (about 10 %). However, the fact of the effect itself is promising. Therefore more detailed investigation of this phenomena is proposed to find probably more suitable plasma conditions having stronger impact on the ion beam parameters.

At each working points presented in this paper radio-emission spectra was recorded. Results are reported in [17]. Furthermore, spectrally integrated [21] X-ray images were also taken at every configuration. After this main characterisation of the source limited number of working points (being interesting some point of view) were selected for further time-consuming investigations. Spectrally resolved (photon counted) images [21] and temporally resolved hard X-ray spectra were acquired in those conditions and will be presented in separated papers.

ACKNOWLEDGEMENTS

This project has received funding from the European Union's Horizon 2020 research and innovation program under grant agreement No 654002 (ENSAR2-MIDAS). The collaboration also acknowledges the support of the INFN 5th Nat. Comm. Under the Grant Pandora.

REFERENCES

- [1] D. Leitner and C. Lyneis, "ECR Ion Sources", in *The Physics and Technology of Ion Sources*, I. G. Brown, Ed. Weinheim, Germany: Wiley, 2004, pp. 203-233
- [2] R. Geller, *Electron Cyclotron Resonance Ion Sources and ECR Plasmas*, Bristol, UK: J W Arrowsmith Ltd, 1996
- [3] A. G. Drentje, "Techniques and mechanisms applied in electron cyclotron resonance sources for highly charged ions", *Rev. Sci. Instrum.*, vol. 74, p. 2631, April 2003, doi:10.1063/1.1569408
- [4] G. Melin, et al., "Recent Developments and Future Projects on ECR Ion Sources at Grenoble", in *Proc. 10th International Workshop on ECRIS*, Knoxville, Tennessee, USA, Nov. 1990, pp. 1-15
- [5] L. Celona, S. Gammino, G. Ciavola, F. Maimone and D. Mascali, "Microwave to plasma coupling in electron cyclotron resonance and microwave ion sources", *Rev. Sci. Instrum.*, vol. 81, p. 02A333, Feb. 2010, doi: 10.1063/1.3265366

- [6] Z. Q. Xie and C. M. Lyneis, "Improvements on the LBL AECR Source," in *Proc. 12th International Workshop on ECRIS*, Tokyo, Japan, April 1995, pp. 24-28
- [7] S. Gammino, et. al., "18 GHz upgrading of the superconducting electron cyclotron resonance ion source SERSE," *Rev. Sci. Instrum.*, vol. 70, no. 9, p. 3577, Sep. 1999, doi: 10.1063/1.1149962
- [8] R. C. Vondrasek, et. al., ECRIS operation with multiple frequencies, *Rev. Sci. Instrum.*, vol. 77, p. 03A337, March 2006 doi: 10.1063/1.2164895
- [9] S. Gammino, et al., "Numerical Simulations of the ECR Heating With Waves of Different Frequency in Electron Cyclotron Resonance Ion Sources", *IEEE Transaction on Plasma Science*, vol. 36, no. 4, p. 1552, Aug. 2008 doi: 10.1109/TPS.2008.927288
- [10] S. Biri, et al., "Two Frequency heating technique at the 18 GHz NIRS-HEC ECR ion source", *Rev. Sci. Instrum.* vol. 85, p. 02A931, Dec. 2013, doi: 10.1063/1.4829735
- [11] A. Kitagawa, et al., "Practical Comparison of Two-Frequency heating Phenomena in Different ECR Ion Sources", in *Proc. 22nd International Workshop on ECRIS*, Busan, Korea, August 2016, pp. 55-58
- [12] A. Kitagawa, et al., "Two-Frequency Heating Technique for Stable ECR Plasma", in *Proc. 20th International Workshop on ECRIS*, Sydney, Australia, Sep. 2012, pp. 10-12
- [13] V. Skalyga, et al., "Suppression of cyclotron instability in Electron Cyclotron Resonance ion sources by two-frequency heating" *Physics of Plasmas*, vol. 22, p. 083509, Aug. 2015 doi: doi.org/10.1063/1.4928428
- [14] O. Tarvainen, et al., "Beam current oscillations driven by cyclotron instabilities in a minimum-B electron cyclotron resonance ion source plasma" *Plasma Sources Sci. Technol.* vol. 23, p. 025020, April 2014 doi: 10.1088/0963-0252/23/2/025020
- [15] I. Izotov, et al., "Microwave emission related to cyclotron instabilities in a minimum-B electron cyclotron resonance ion source plasma" *Plasma Sources Sci. Technol.* vol. 24, p. 045017, July 2015 doi: 10.1088/0963-0252/24/4/045017
- [16] O. Tarvainen, et al., "An Experimental Study of ECRIS Plasma Stability and Oscillation of Beam Current" in *Proc. 20th International Workshop on ECRIS*, Sydney, Australia, Sep. 2012, pp. 5-9
- [17] E. Naselli, et al., "Impact of the two close frequency heating on ECRIS plasmas stability", presented at the 23rd International Workshop on ECRIS, Catania, Italy, Sept. 2018, paper FRB2, this conference
- [18] S. Biri, et al., "Status and special features of the Atomki ECR ion source", *Rev. Sci. Instrum.* vol. 83, p. 02A341, Feb. 2012 doi: doi.org/10.1063/1.3673006
- [19] S. Biri, et al., "Multi diagnostic setup at the Atomki-ECRIS to investigate the two-close-frequency heating phenomena", presented at the 23rd International Workshop on ECRIS, Catania, Italy, Sept. 2018, paper TUP14, this conference
- [20] D. Mascali, et al., "Electron Cyclotron Resonance Ion Source plasma characterization by means of X-ray spectroscopy and X-ray imaging" *Rev. Sci. Instrum.* vol. 87, p. 02A510, Jan. 2016 doi: 10.1063/1.4939201
- [21] R. Rác, et al., "Electron cyclotron resonance ion source plasma characterization by energy dispersive x-ray imaging", *Plasma Sources Sci. Technol.* vol. 26, p. 075011, July 2017 doi: 10.1088/1361-6595/aa758f

SIMULATIONS OF ECRIS PERFORMANCE FOR DIFFERENT WORKING MATERIALS

V. Mironov*, S. Bogomolov, A. Bondarchenko, A. Efremov, K. Kuzmenkov, V. Loginov, Joint Institute for Nuclear Research, Flerov Laboratory of Nuclear Reactions, Dubna, Moscow Reg. 141980, Russia

Abstract

Free parameters of Numerical Advanced Model of ECRIS (NAM-ECRIS) are selected such as to reproduce the experimental charge-state-distribution of the extracted argon ions for the DECRIS-PM source tuned to produce the maximized Ar^{8+} currents. Using these fixed parameters, we calculate the extracted currents for Kr, Xe and Bi ions in mix with oxygen, for Ca in mix with helium, and for pure O and He plasmas. Comparison is made with the experimental data, good correspondence is observed.

INTRODUCTION

We had already applied our numerical model of ECRIS for studying several important aspects of the source operation [1, 2, 3]. Better understanding is obtained of the source reactions to changes in injected microwave power, gas flow and magnetic field profiles, of the gas-mixing, isotope anomaly, afterglow and others effects. As the next step, we calculate the extracted ion currents for variety of working elements injected into the DECRIS-PM source [4] (all-permanent magnet structure, 14.5 GHz microwave frequency).

The model is still not self-consistent in the sense that some of its parameters should be tuned in order to reproduce the experimentally measured ion currents. These parameters are connected to the unknown value of the microwave electric field at the ECR surface that defines the rate of electron heating and consequently the electron confinement time. As the experimental input we use the charge-state-distribution of argon ions for the source optimized to produce the moderately charged Ar^{8+} ions; at that, injected microwave power is close to maximum value available for the DECRIS-PM source, and the gas flow is relatively high. Selected set of the input parameters is then used for other injected gases and we check whether it is possible to reach a good correspondence with experiments.

BASIC FEATURES OF THE MODEL

The NAM-ECRIS model includes two separate modules that calculate electron (e) and ion (i) dynamics in the source. Ions are supposed to behave differently inside the relativistically broadened ECR zone and outside it: there is no electric field in the zone, ions are retarded by potential dip $\Delta\phi$ when crossing the resonance surface, and the

presheath electric field accelerates ions if they are leaving the potential trap. To characterize the plasma, we calculate two parameters in NAM-ECRIS(i). The ion life time (τ_i) is defined as the ratio between the sum of ion electric charges inside the ECR zone and total electric current of ions toward the source chamber walls and into the extraction aperture. The total ion current is equal to the electron current because of charge neutrality of the plasma. After multiplying the current by mean energy of the lost electrons, we obtain the total power of microwaves coupled to the electron component of the plasma (P_c), neglecting small contributions from other power loss channels.

The averaged electron-ion scattering factor is defined as $\langle n_s \rangle = \sum_i \langle n_i \rangle Q_i^2$, where averaging of ion densities n_i with charge state Q_i is performed over the ECR volume. Spatially resolved array of the electron-ion scattering factors $n_s(x,y,z)$ is prepared by the ion module to be imported into the electron module NAM-ECRIS(e). Also, there are fixed the spatial coordinates of ionization events and ionization potential of the related parent particle (atom, molecule or ion).

The electron module traces movement of a large number of computational electrons in magnetic field of the source. Electrons are injected into the computational domain with initial energies that correspond to the ionization potential of the parent particle and with randomly oriented velocity vector. While bouncing along the source magnetic field lines, electrons experience kicks in the perpendicular direction whenever they cross the ECR surface; the kick's magnitude depends on the local magnetic field gradient, on the electron velocity and on the microwave electric field at the resonance, which is the free parameter in our model [2]. Among other factors, the microwave fields depend on the injected microwave power and on the wave absorption and reflection by the plasma. Our basic assumption is that for the fixed magnetic field profile, the microwave electric fields are the same in the plasmas with the same levels of the injected and of the coupled microwave powers.

Electrons are elastically scattered in electron-ion collisions as defined by the imported map of scattering factors. The scattering rate depends on the electron velocity as v_e^{-3} , and the probability for electrons to be scattered into the loss-cone is decreasing fast while electrons are heated. We define the electron life time τ_e in the similar manner as for ions. The global life time is inversely proportional to the averaged scattering factor and increases with increasing the velocity kick's magnitude. From the

* vemironov@jinr.ru

requirement of charge-neutrality, the electron and the ion life times should be the same.

Basing on these considerations, we define that two plasmas are in the same external conditions if they have the same factors $\tau_i \times \langle n_s \rangle$ and the same fluxes of electrons to the walls. The first requirement assumes that the microwave electric fields at the ECR surface are the same, and the second requirement means that we compare the plasmas with the equal coupled microwave powers. To reach the conditions, we regulate the potential dip value to change the ion life time and scattering factors, and gas flow into the source to change the coupled power.

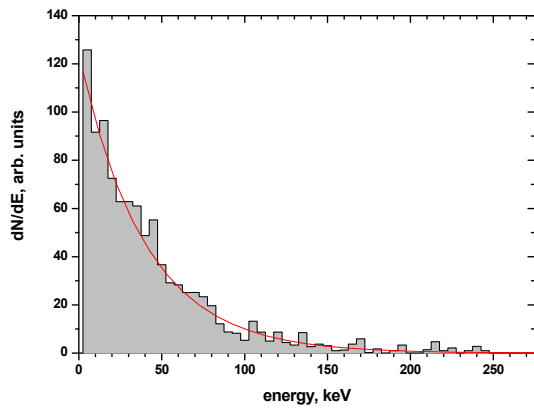


Figure 1: Energy distribution for electrons in the plasma (grey shaded curve) and exponential decay curve with the constant of 40 keV (red).

The calculated energy distribution for electrons in the plasma is shown in Fig. 1. The distribution is obtained for the microwave electric field amplitude of 150 V/cm and for the input ion densities of the argon plasma discussed in the next section. Mean energy of the confined electrons is close to 60 keV, the energy distribution can be approximated by the exponential decay curve with the index of 40 keV. Lost electrons have different energy distribution, with most of the lost electrons having energies below 1 keV.

Most of electrons are confined inside the volume that corresponds to the resonance magnetic field of ~ 0.52 T close to the value for the non-relativistic electrons. Energy distribution of the confined electrons weakly depends on the values of scattering factors and of the microwave electric field for the investigated range of these factors.

We use the energy distribution of Fig. 1 to calculate rates of ionization and of ion heating. Ionization cross-sections are taken from the Burgess-Chidichimo fit (BC) [5]; the requested shifts in the electron binding energies are calculated following Carlson et al. [6]. The ionization rates of [5] are close to the predictions of Lotz [7]. Relativistic correction factor for the rates is calculated according to [8].

Double ionization is found to be important for the ionization balance, the rates are taken either from compilation of Hahn et al. [9] or from the fit of Shevelko and Tawara [10]. Gas heating due to incomplete energy accommodation in collisions of ions with walls is computed either using coefficients of Goodman [11] or setting the thermal accommodation coefficient to 5% for metal elements. Energy of the recycling atoms depends on the charge state of the parent ion and on the plasma potential, which results in larger gas energies for the heavy elements.

RESULTS

Argon

Simulation of the argon plasma in DECRIS-PM is a basis for all other calculations. As an input, we use the experimental charge-state-distribution of the extracted ion currents. It is measured with injected microwave power of 500 W, and with argon flow selected such as to maximize the Ar^{8+} current. No mixing gas was used there. The measured currents are shown in Fig. 2 as open squares.

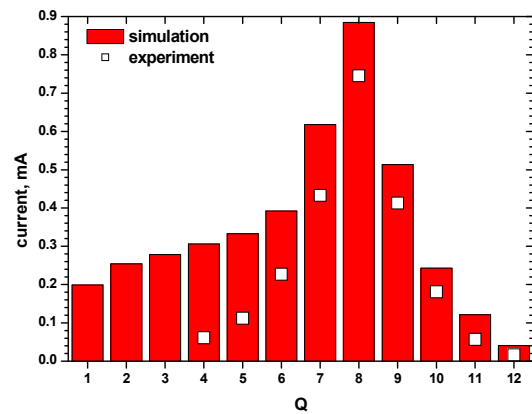


Figure 2: Calculated charge state distribution of the extracted argon ion currents (red columns) and the experimentally measured currents (open squares).

The simulated current charge state distribution (CSD) is shown as the red columns. Gas flow is adjusted to be 1.0 particle-mA, the potential dip value is 0.08 V. The ion temperatures are close to 0.4 eV for all charge states of argon ions, temperature of the neutral argon in the source chamber is 0.1 eV. The ion life time is calculated to be 0.3 ms, with the averaged scattering factor $\langle n_s \rangle$ of $1 \times 10^{13} \text{ cm}^{-3}$ and the mean electron density of $1.2 \times 10^{12} \text{ cm}^{-3}$. For mean energy of the lost electron of 5 keV [3] and total current of electrons toward the walls of 45 mA, the coupled power is 225 W, $\sim 45\%$ of the injected microwave power. The experimental values are reproduced well around the CSD's maximum; deviations are observed for the low charged ions, probably due to underestimation of

Content from this work may be used under the terms of the CC BY 3.0 licence (© 2018). Any distribution of this work must maintain attribution to the author(s), title of the work, publisher, and DOI.

the measured currents caused by losses of these ions in the beam line.

For argon, plasma profile close to the extraction electrode is slightly hollow [1]: relatively slow argon atoms are mostly ionized at the plasma periphery, thus broadening the plasma. Also, the local minimum of magnetic radial profile of the DECRIS-PM source is shifted from the source axis by ~ 5 mm at the middle of the source chamber, which facilitates the plasma localization there.

Calcium and Helium

Simulations of calcium production need in some assumptions concerning sticking of atoms to the walls of the source chamber. We found that the sticking coefficient should be set small to reach the reasonable values of metal ion extraction efficiency. Experimentally, it is measured for our sources that more than 50% of the injected calcium is extracted as ions. The source is equipped with a hot screen that covers both radial and extraction walls; temperature of the screen is around $500\text{ }^{\circ}\text{C}$ in operational conditions. The hot walls increase the recycling probability for calcium atoms.

We use He as the mixing gas for Ca according to the experimental procedure to produce the calcium ions.

The simulated spectra of calcium ion currents are shown in Fig. 3 for clean ^{40}Ca plasma and for mixing Ca with He in proportion Ca(0.25)+He(0.75) and Ca(0.1)+He(0.9), with fractions of the total number of computational particles given in brackets. Experimentally measured currents are shown as open squares (Ca^{11+} optimization); data for Ca^{10+} are missed because of an overlap with the doubly-charged helium.

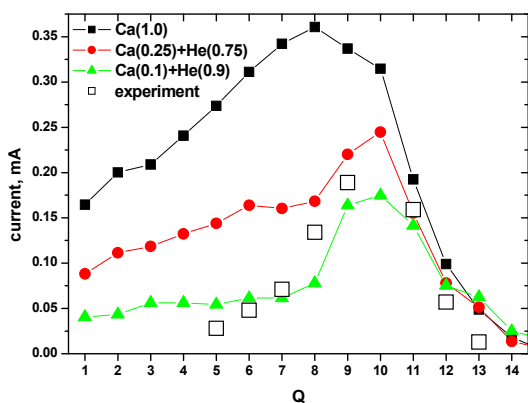


Figure 3: Experimentally measured (open squares) and calculated charge state distributions of the extracted calcium ions for clean Ca (black), Ca(0.25)+He(0.75) (red) and Ca(0.1)+He(0.9) (green) plasmas.

Calcium flow into the source (flux through the extraction aperture) is calculated to be 1.2 mg/h for the clean Ca, 0.7 mg/h for Ca(0.25) and 0.38 mg/h for Ca(0.1) plasmas. Extracted ions constitute 90% of all injected

calcium atoms. The potential dip values for clean and mixed plasmas are 0.09, 0.07 and 0.09 V respectively, with the globally defined (Ca+He) ion life times of 0.35 ms, same for all mixes. Species-resolved ion life times (Ca/He) are 0.35/-, 0.5/0.1 and 0.8/0.1 ms respectively, with increasing life time for the calcium ions after adding more helium. Ion temperatures for the clean Ca plasma are 0.45 eV vs. 0.3 eV for the mixed plasmas, showing ion cooling in the mix due to reduced rate of the charge-change collisions followed by the kinetic energy release [1]. Shift of CSD to the higher charge states is seen with more helium. Efficiency of extracting the high charged ions increases with increasing the mix ratio: Ca^{11+} ions constitute 2% of all injected Ca atoms for Ca(1.0), 2.7% for Ca(0.25) and 5.5% for Ca(0.1).

Plasma radial profile for calcium plasma is strongly hollow, also in the mix with helium. The reason is the same as for argon, but due to the higher ionization rates for calcium and lower energies of the recycling atoms the effect is more pronounced.

For the Ca(0.1)+He(0.9) mixed plasma, the calculated helium ion currents are 1.7 mA for He^{1+} and 0.7 mA for He^{2+} at the helium flux into the source of 4.3 p-mA (particle-mA): flux of helium ions into the extraction aperture is only 50% of the total number of the injected helium atoms. For the clean He plasma, the simulated extracted currents are 1.2 mA and 3.0 mA for singly and doubly-charged ions respectively, with increased He^{2+} ion current compared to the mixed plasma. The potential dip value should be set to 0.7 V to reach the default plasma conditions, and the helium ion life time is 1.0 ms compared to 0.1 ms for the mix with Ca. As it is frequently observed for the gas-mixed plasmas, addition of small amounts of heavy elements strongly decreases currents of the lighter high-charged ions.

Krypton and Oxygen

In practice, oxygen is preferred as the gas-mixer for elements heavier than argon. It had been demonstrated earlier [2] that those single charged oxygen ions, which are created after ionization and dissociation of molecular neutral and singly charged oxygen, have rather high energies of a few eV, making them easy to leave the plasma. The result is that the oxygen plasmas have relatively large potential dips built up to retard ions inside the ECR zone in order to equilibrate the ion and electron losses. The O^{1+} ions produced after the dissociation constitute around 25% of the total number of the singly charged oxygen ions in the plasma, the remaining ions are created after ionization of the atomic oxygen with energies close to the wall temperature.

The charge state distribution of the extracted ion currents for pure oxygen plasma is shown in Fig. 4 as the red columns. The potential dip value is 0.26 V and the ion life time is 0.4 ms with ion temperature of 0.6 eV. For DECRIS-PM source we have no experimental values of the clean-oxygen currents, but the simulated currents are consistent with what is expected for the well-performing

14-GHz source, reaching ~ 2 mA of the extracted O^{6+} ions. The green columns in Fig. 4 show the oxygen currents after adding krypton to the plasma. The potential dip for the Kr(0.2)+O(0.8) mixed plasma is 0.065 V, the oxygen ion temperature is 0.5 eV and the oxygen ion life time is 0.16 ms, much smaller than for the clean oxygen plasma; currents of the high charged oxygen ions are decreased correspondingly.

Reaction of the krypton extracted currents to adding oxygen is shown in Fig. 5. For the Kr(1.0) plasma, the distribution is peaked at Kr^{11+} , and the maximum is shifting to the higher charge states in the mix of Kr(0.2)+O(0.8). At that, potential dip value decreases from 0.075 to 0.065 V, while krypton ion temperature decreases from 0.67 to 0.4 eV mostly because of a reduced heating of ions by the recycled particles. The krypton ion life times are increasing in the mix from 0.28 to 0.47 ms and the mean electron density increases from $1.2 \times 10^{12} \text{ cm}^{-3}$ to $1.4 \times 10^{12} \text{ cm}^{-3}$.

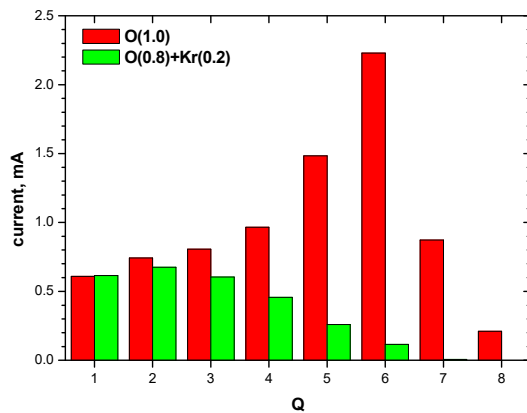


Figure 4: Calculated currents of the extracted oxygen ions for clean oxygen plasma (red) and in mix with krypton (green).

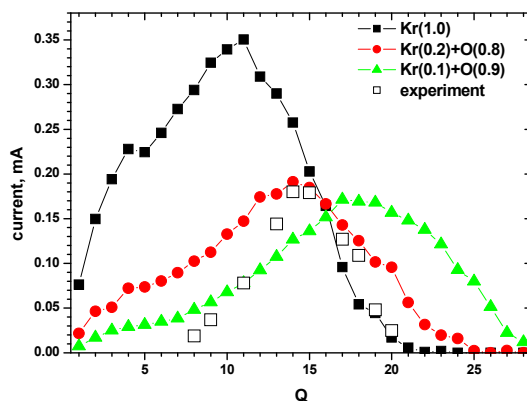


Figure 5: Extracted krypton ion currents for different

mixing ratios with oxygen and the experimental data (open squares).

Experimental data are reproduced when we tune the mix ratio such as to have the krypton ion charge-state distribution peaked at $Q=15+$. Both lowly- and highly-charged ion currents are overestimated. Further increase of oxygen content results in increase of the potential dip value without substantial changes in the ion temperature. For the Kr(0.1)+O(0.9) plasma, the dip is 0.83 V and the CSD's maximum for Kr ions is shifting to $17+$, with decrease of extracted current at the maximum. For the larger mix ratio, both krypton and oxygen ion life times are increasing up to 0.74 ms for Kr and 0.18 ms for oxygen.

Xenon and Bismuth

Simulated charge state distribution of the extracted xenon ion currents is shown as the red columns in Fig. 6. The distribution is compared to the experimental data shown as open squares. The optimized contents in computations are 5% of xenon and 95% of oxygen. The potential dip value is 0.08 V, and the scattering factor is close to the value for argon, $1.25 \times 10^{12} \text{ cm}^{-3}$. The global ion life time that includes both xenon and oxygen ions is 0.28 ms. Flux of xenon atoms into the source (0.1 p-mA) is small in comparison to the oxygen flux of 2.9 p-mA.

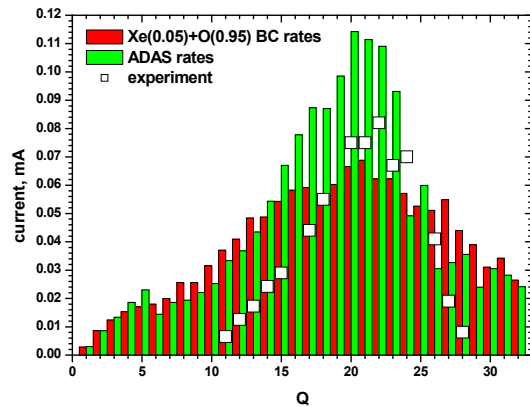


Figure 6: Calculated xenon ion currents (red columns) for the BC ionization rates, for the ADAS ionization rates (green columns) and the experimental values (open squares).

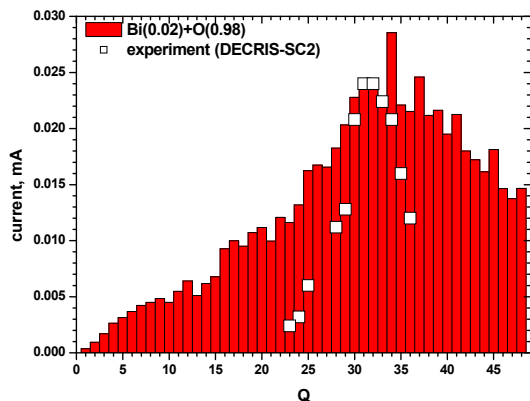


Figure 7: Calculated bismuth ion currents and experimental data for DECRIS-SC2 source (open squares).

As for the krypton plasma, the model overestimates both the low and high charged ion currents, though the currents close to the maximum of the distribution are reproduced well. The Lotz and Burgess-Chidichimo formulas do not include the indirect ionization processes, which results in relative underestimation of the ionization rates for the lowly-charged ions. Also, highly excited metastable ions exist in the ECR plasma, which also affects the total ionization balance [12]. More accurate ionization rates for the highly-charged ions can make the calculations closer to the experiment. To check it, we use OPEN-ADAS rates [13] for xenon. These rates are available for Maxwell-Boltzmann electron energy distribution only and for limited number of heavy elements (Xe and W). We use data for the electron temperature of 50 keV. The simulation results are shown in Fig. 6 as green columns. Correspondence to the experimental points is better compared to the results with the BC rates. Plasma parameters for ADAS ionization rates are close to the BC rate's case.

Distribution for bismuth is calculated with using the BC rates (Fig. 7). No experimental data are available for DECRIS-PM source and we show the unpublished experimental data from the other source (DECRIS-SC2 [14]) for reference. Calculations are done with the mix ratio of Bi(0.02)+O(0.98). Around 25 μA of Bi^{30+} ions are extracted for the potential dip value of 0.073 V and metal consumption of 0.2 mg/h. We assume full recycling of bismuth after collisions with the walls, which makes the given number of the consumption underestimated by factor of two or so. Thermal accommodation coefficient for collisions of bismuth with the walls is set to 0.95 as for calcium. The CSD of the extracted ions is broader than the experimental one, whereas the currents at the CSD's maximum are close to the reference experimental data.

CONCLUSIONS

Extrapolation of the operational conditions of the source tuned to produce the maximized currents of Ar^{8+} ions gives satisfactory results for other working elements. It is possible to reproduce both the absolute values of the extracted ion currents and shapes of the charge state distributions of such gases as helium, oxygen, krypton and xenon. Calculated currents of calcium ions are also close to the measured values.

The gas-mixing effect is clearly seen both in mixes with oxygen and helium, and it is explained by fast losses of the lighter ions followed by increase of the heavy ion life times. Additionally, reduction of the charge-change collision rates in mix with helium improves the ion confinement. There is a need in more accurate ionization rates for heavy species, for elements of up to krypton the Burgess-Chidichimo rates are adequate.

REFERENCES

- [1] V. Mironov, S. Bogomolov, A. Bondarchenko, A. Efremov, and V. Loginov, "Numerical model of electron cyclotron resonance ion source", *Phys. Rev. ST Accel. Beams*, vol. 18, p. 123401, 2015, doi:10.1103/PhysRevSTAB.18.123401
- [2] V. Mironov, S. Bogomolov, A. Bondarchenko, A. Efremov, and V. Loginov, "Numerical simulations of gas mixing effect in electron cyclotron resonance ion sources", *Phys. Rev. Accel. Beams*, vol. 20, p.013402, 2017, doi:10.1103/PhysRevAccelBeams.20.013402
- [3] V. Mironov, S. Bogomolov, A. Bondarchenko, A. Efremov and V. Loginov, "Some aspects of electron dynamics in electron cyclotron resonance ion sources", *Plasma Sources Science and Technology*, vol. 26, p. 075002, 2017, doi:10.1088/1361-6595/aa7296
- [4] G.G. Gulbekian, *et al.*, "Proposed design of axial injection system for the DC-280 cyclotron", *Phys. Part. Nuclei Lett.*, vol. 11, p. 763, 2014
- [5] A. Burgess, M.C. Chidichimo, "Electron impact ionization of complex ions", *Monthly Notices of the Royal Astronomical Society*, vol. 203, pp. 1269–1280, Aug. 1983, doi:10.1093/mnras/203.4.1269
- [6] T.A. Carlson, C.W. Nestor Jr, N. Wasserman, J.D. McDowell, "Calculated ionization potentials for multiply charged ions", *Atomic Data and Nuclear Data Tables*, vol. 2, p. 63, Dec. 1970, doi: 10.1016/S0092-640X(70)80005-5
- [7] W. Lotz, "Electron-impact ionization cross-sections and ionization rate coefficients for atoms and ions from hydrogen to calcium", *Z. Physik*, vol. 216, p. 241, 1968, doi:10.1007/BF01392963
- [8] M. Uddin, A. Haque, K. Karim, *et al.*, "Modified Kolbenedt model for the electron impact K-shell ionization cross-sections of atoms and ions", *Eur. Phys. J. D*, vol. 37, p. 361, (2006), doi:10.1140/epjd/e2005-00305-4
- [9] M. Hahn, A. Müller, and D. W. Savin, "Electron-impact multiple-ionization cross sections for atoms and ions of helium through zinc", *The Astrophysical Journal*, vol. 850, p. 122, Sept. 2017, doi: 10.3847/1538-4357/aa9276
- [10] V.P. Shevelko and H. Tawara, "Semiempirical formula for multiple ionization cross sections of atoms by electron impact", *Phys. Scr.*, vol. 52, p. 649, 1995, doi:10.1088/0031-8949/52/6/007

- [11] Frank O. Goodman, "Thermal accommodation coefficients", *J. Phys. Chem.*, vol. 84, p. 1431, 1980, doi: 10.1021/j100449a002
- [12] A. Borovik Jr., M. F. Gharaibeh, S. Schippers and A. Müller, "Plasma rate coefficients for electron-impact ionization of Xe^{q+} ions ($q = 8, \dots, 17$)", *J. Phys. B: At. Mol. Opt. Phys.*, vol. 48, p. 035203, 2015, doi: 10.1088/0953-4075/48/3/035203
- [13] <http://open.adas.ac.uk/>
- [14] A. Efremov et al., "The preliminary tests of the superconducting electron cyclotron resonance ion source DECRIS-SC2", *Rev. Sci. Instrum.*, vol. 83, p. 02A334, 2012, doi: 10.1063/1.3671746

PLASMA MODELIZATION AND STUDY FOR THE PHOENIX V3 ECR ION SOURCE

A. Leduc*, L. Maunoury, GANIL, 14000 Caen, France
T. Thuillier, Grenoble INP, LPSC-IN2P3, 38000 Grenoble, France

Abstract

In the framework of the Spiral2 project, the PHOENIX V3 Electron Cyclotron Resonance Ion Source (ECRIS) (upgraded version from the previous PHOENIX V2) has been developed to optimize the production of ion beams with charge over mass $Q/A=1/3$. The ion source aims to produce mainly metallic ions. For such beams, the atoms are, for a majority of them, trapped into the plasma wall of the plasma chamber leading to a poor global ionization efficiency. A hybrid particle in cells (PIC) code is under development to study and reproduce the experimental spectrum from ion source PHOENIX V3. The simulation is 3D and focuses on the propagation of the ion. The simulation have several free parameters to adjust the distribution of the ion charge stat at the exit of the ion source. The simulation has already given some encouraging preliminary results.

INTRODUCTION

For plasma modelization, like for the ion thruster, the simulation are done using Particle-In-Cell (PIC) code method. Traditional PIC codes propagate neutral atoms, ions, and electrons in electromagnetic fields. It also includes computation of collisions between particles (neutrals and charged) as well as the resolution of the Poisson equation to, dynamically, take into account the electric field generated by the charged particles. To be confident into the results coming up from the simulation, PIC code must meet specific conditions. The time step of the particles propagation must be less than half of the lowest characteristic time. It is the same for the space discretization, which must be thin enough for the Poisson equation resolution.

In the case of a PIC code applied to an ECR ion source plasma, the characteristic time is the electron rotation period around a magnetic flux line while the Debye length defines the spatial mesh. The ECR ion source plasma contains high-energy electrons; the minimum time step is of the order of picosecond, and the Debye length about micrometer. The aims of the simulation is to reproduce the ionization evolution of charged particles in the ECR ion source for different species and magnetic configuration in order to understand their dynamics of with the final goal to improve the global ionization efficiency. It is necessary to simulate the ion source operation for a duration greater than one milli-second at least in order to reach the equilibrium of the plasma. Propagation of charged particles during a millisecond within these conditions would require too much computing time. It has been decided to approximate some.

* alexandre.leduc@ganil.fr

HYPOTHESIS

To shrink the computing time, it is necessary to reduce the number of mathematical operations done by the simulation does, while meeting the Physics hypothesis.

Electron Simplification

The first assumption is to consider that the electrons, more energetic than the ions, adapt their movements to those of the ions. Hence, it is possible to increase the time step imposed to the simulation by a factor of one thousand but also to reduce the number of particles moving into the simulation.

As the electrons follow the ions, the major electric charged are screened, and the plasma in the ion source is globally neutral. The Poisson equation resolution is no longer needed and neither the ion source mesh with one micrometer side cell. The plasma neutrality and the screening effect of the charged particles involve the nonexistence of plasma sheath and extraction meniscus.

Macroparticles Method

The PHOENIX V3 ion source has a volume of 1.45 liters, and operates with a pressure of 10^{-7} millibar. A rough estimation gives 10^{10} particles. The simulation cannot handle as many particles. The neutral atoms and the ions are injected and propagated, as macroparticle for the simulation. The particle number, and at the same time the macroparticle number, is not constant during the simulation.

It's extremely tough to estimate what value of particles belonging to a macroparticles the system evolves. However, it is important that the macroparticle number present in the simulation doesn't increase too much. For this, it is necessary to establish a maximum for the macroparticle value and modify the particle number per macroparticle during the simulation. The charge exchange involves two macroparticles, whose charges and species may differ. To maintain the global charge and keep an equal charge for the particles in the same macroparticle, all macroparticles must have the same weight. The macroparticles weight variation must hold the charge and the number of particles.

SIMULATION

Propagation in Magnetic Field

The ion source is immersed in a intense magnetic field. The use of the "Leap Frog" method with a magnetic field produces a particles energy divergence. Propagation of charged particles is done with the Boris method [1], and the neutral particles are propagated in a straight line to reduce the computation time. In addition to the magnetic field, some

experimental studies have highlighted the existence of a potential dip inside the plasma, but its position is not well known yet.

The potential dip keeps the ions confined in the plasma center between the axial magnetic field maximums. This trap enhance the multicharged ion production rate. In order to reproduce the experimental spectrum, from the PHOENIX V3 source, the simulation integrates a potential dip model. The potential dip is modelled by a local potential barrier, and located at the level of the ECR resonance.

Collisions

The simulation includes the interaction between the particles and the plasma chamber walls. The interaction with the wall is divided into three steps. First, the particle must go up to the contact of the wall, where it is thermalized [2]. The next action is a test to determine whether the particle sticks on the wall or not. If it doesn't stick, or after that the bond with the wall is broken, the particle is re-emitted. The particle reemission is done according to a hard sphere model [3].

To reproduce the spectrum at the source exit, the simulation must include collisions as electron impact ionization and coulomb collisions. For the collisions application, the plasma chamber is divided into cubic cells, henceforth the collisions are between particles existing in the same cell. The simulation integrates Coulomb collisions through K. Nanbu small-angle collision approximation [4]. This method allows to approximate Coulomb collisions induced by two particles in a plasma during a time step dt .

After Coulomb collisions, the particles are tested depending on the type of collisions: single and double ionizations, radiative recombination, and charge exchange. The cross sections is calculated using the Lotz formula [5] and Bélenger [6] respectively for single and double ionizations, Hahn [7] for radiative recombination, and Gallagher [8] for charge exchange. In order to avoid generating a random number for each possible collision at each time step, the simulation uses the null collision method [9] (Fig. 1).

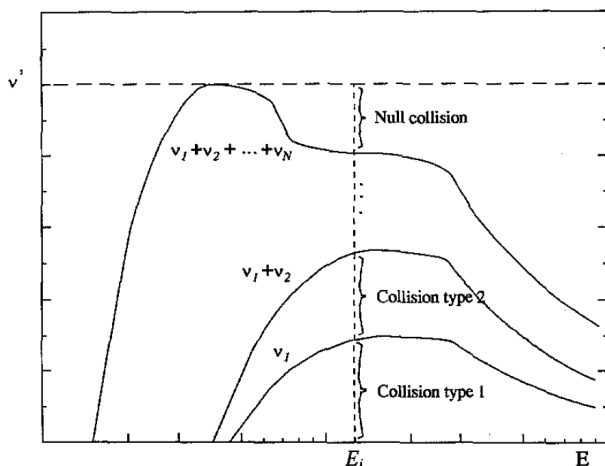


Figure 1: Null Collisions Principle Diagram

Electron Energy Distribution Function

Electrons do not propagate process in the simulation, but they are still needed for the ionization and recombination. Their interaction with atoms and ions is done thanks to the input electron energy distribution and density. The electron density is calculated to neutralize the ion charge density. The electron energy distribution is a combination of electron populations existing in the ion source. Three classes can be defined according to their energies:

- The cold electrons are generated by the ionization collisions or by emission from the wall. They have a low energy of tens electron volts.
- The warm electrons, with energies of the order of one to tens KeV, are derived from cold electrons. Successive interactions with the RF microwave at the ECR zone, they have gained stochastically energy and can actively participate in the ionizations for creating the high charge state ions.
- The hot electrons are very energetic, up to the MeV. This type of electrons have particularly weak ionization or recombination cross sections. The hot electrons participate mainly in the neutralization of the space charge of the ions =.

At first, the simulation is limited to use the of the two first electrons energy distribution components, the cold and warm electrons. They participate mainly to the ionization process, the cold electron act on low charge states while the warm electrons create higher charge states. As discussed in various papers [10–12], the electron energy distribution varies according to the magnetic configuration and the microwave power injected into the ion source.

Using an optimization function, the simulation modifies the electrons energy distribution such the source output spectrum is as close as possible to the experimental one. In addition, to being able to vary the average of the electron energy distribution, it is also possible to modify the energy distribution function that the electrons follow. Three functions of different distributions could be tested:

- A Gaussian distribution function has been chosen for the preliminary tests. However, knowing already that this function is too simple for representing the EEDF, each Gaussian function have two parameters: the center of the Gaussian, which corresponds to the average energy, and the σ that adjusts the energy dispersion.
- The second distribution function is a Maxwellian one. This distribution is more complex to compute but has only one free parameter allowing a faster optimization to fit to the desired spectrum [13].
- The third, and last, is the best to reproduces the electrons energy distribution function observed for ECR ion source. This is a non-Maxwellian function, which requires more time to implement and which request much more computing time [13].

PRELIMINARY RESULTS

The program is code around different function groups :

- A set of functions is used to initialize the simulation (reading of the magnetic field map, ionization energy, physical parameters ...)
- Set of functions is created for the atoms and ions propagation, as well as the particles localization in the ion source
- For the particles interacting at the wall, they can stick to the wall and can be re-evaporated
- The collisions between particles are applied on all the particles in the ion source and not trapped at the surface of the wall
- At the end of the simulation, a set of function are employed to get the particles information: position, impulsion, charge, specie)

The simulation structure, and all the functions involved can be summarized into a chart proposed on Fig. 2.

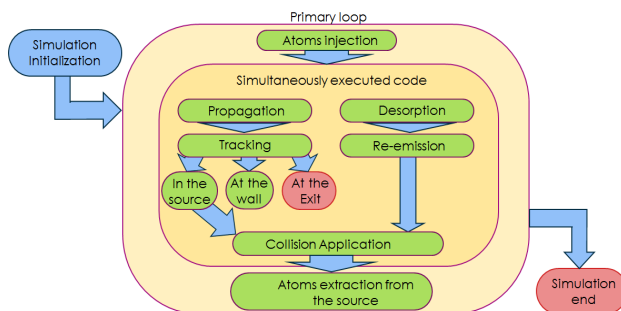


Figure 2: Organization Chart of the Simulation

To find the electron energy distribution function for the cold and the warm electrons which latches the experimental spectrum, an optimization program is used [14]. The optimization code varies the several parameters to reduce a certain value. In our case, the value ($V_{criteria}$ (Eq. (1))) is the gap between the total intensity of the experimental spectrum and the total intensity from the spectrum of the simulation.

$$V_{criteria} = \sqrt{\sum_i \left(I_{exp}(q=i) - \frac{I_{simu}(q=i)}{I_{simu}(q=1)} I_{exp}(q=1) \right)^2} \quad (1)$$

After the preliminary tests, the simulation was able to reproduce an experimental ion spectrum from the ECR Ion Source PHEONIX V3. The first spectrum to recorded is a simple one involving as less as possible ion source parameters. It was produced using only Argon injection, and a very low voltage applied on the bias disc of the source.

To reduce the computing time, the simulation doesn't solve the Poisson equation and considers the plasma sheath

as non-existent. At the walls, the approximation doesn't induce a significant error. However, at the extraction, the sheath is deformed into a meniscus that acts strongly on the ions leaving the ECRIS and traveling through the extraction system. Without the electric field of the meniscus, a lot of ions of the simulation miss the exit of the source and go up to the wall; leading to an extraction not very effective.

To overcome this problem, it was decided to study the ion charge state distribution inside the source between the ECR zone and the Ion source exit [15]. Doing that, it is possible to increase the statistics of the different charge states, and hence to reduce the relative intensities uncertainties of the ion mass spectrum.

For the first spectrum, the minimum value is found for $E_{out} = 220eV$, with E_{out} the cold electron energy, and $E_{in} = 2700eV$, E_{in} the warm electron energy.

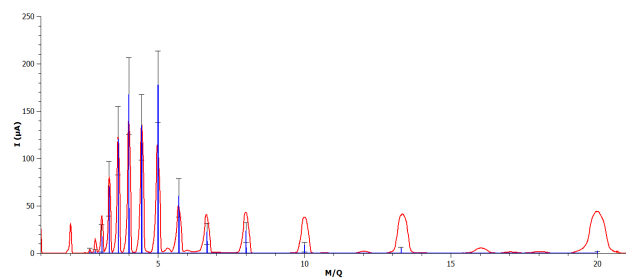


Figure 3: Preliminary Simulation Results

The Fig. 3 shows the experimental spectrum (in blue) and the one from the simulation (in red). There is a difference between the experimental values and the values from the simulation. These differences can be explained in different ways:

- During the experiment, only argon was injected in the ion source. However, the experimental spectrum shows H , H_2 , O and C traces. The presence of different species in the plasma varies the charge states distribution.
- The simulation doesn't reproduce the electric field produced by the bias disk. The experimental spectrum was obtained with a low voltage on the bias disk but not zero. The bias disc has the effect of promote the production of high charge stat. The difference between the experimental voltage (not zero) and the simulated voltage (zero) can explain the spectrum difference.

CONCLUSIONS

The simulation gave some preliminary results, and at the same time proved its effective running. As this first spectrum is encouraging, several improvements were planed :

- The potential dip, and the plasma sheath can be integrated into the simulation through an additional map field. The plasma sheath would have then an effect on charged particles, and the potential dip would be continuous

- The density of electrons can be pre-calculated in a way that electrons follow more the magnetic flux line. The ionizations would occur along the magnetic flux line, and the ions would be confined in the plasma more easily.

In the next months, the PHOENIX V3 ion source will be used to test the production of Ca ion beam with and without liner. Besides various possible improvement, the simulation will also be requested to reproduce the Calcium ion mass spectrum observed experimentally.

REFERENCES

- [1] Higuera, A. V., & Cary, J. R. "Structure-preserving second-order integration of relativistic charged particle trajectories in electromagnetic fields." *Physics of Plasmas*, vol. 24, p. 052104, (2017).
- [2] Goodman, F. O., "Thermal accommodation coefficients." *The Journal of Physical Chemistry*, vol. 84, pp. 1431-1445, (1980).
- [3] Pichard, A., "Développement de faisceaux d'ions radioactifs pour le projet SPIRAL 2". *Diss. Université de Caen*, 2010.
- [4] Nanbu, K., "Theory of cumulative small-angle collisions in plasmas." *Physical Review E*, vol. 55, pp. 4642, (1997).
- [5] Lotz, W., "Electron-impact ionization cross-sections for atoms up to $Z=108$." *Zeitschrift für Physik A Hadrons and nuclei* vol. 232, pp. 101-107, (1970).
- [6] Belenger, C., Defrance, P., Salzborn, E., Shevelko, V. P., Tawara, H., & Uskov, D. B. "Double ionization of neutral atoms, positive and negative ions by electron impact." *Journal of Physics B: Atomic, Molecular and Optical Physics*, vol. 30, pp. 2667, (1997).
- [7] Hahn, Y., "Electron-ion recombination processes-an overview." *Reports on Progress in Physics*, vol. 60, p. 691, (1997).
- [8] Gallagher, J. W., B. H. Bransden, and R. K. Janev. "Evaluated Theoretical Cross Section Data for Charge Exchange of Multiply Charged Ions with Atoms. II. Hydrogen Atom-Partially Stripped Ion Systems." *Journal of physical and chemical refer-ence data*, vol. 12, pp. 873-890, (1983).
- [9] Vahedi, V., and Maheswaran Surendra. "A Monte Carlo collision model for the particle-in-cell method: applications to argon and oxygen discharges." *Computer Physics Communications*, vol. 87, pp. 179-198, (1995).
- [10] Izotov, I., Tarvainen, O., Skalyga, V., Mansfeld, D., Kalvas, T., Koivisto, H., & Kronholm, R., "Measurement of the energy distribution of electrons escaping minimum-B ECR plasmas." *Plasma Sources Science and Technology*, vol. 27, pp. 025012, (2018).
- [11] Ropponen, T., "Electron heating, time evolution of bremsstrahlung and ion beam current in electron cyclotron resonance ion sources." *Research report/Department of Physics, University of Jyväskylä 1/2010* (2010).
- [12] Shirkov, G. D., "A classical model of ion confinement and losses in ECR ion sources." *Plasma Sources Science and Technology*, vol. 2, p. 250, (1993).
- [13] Adrouche, N., "Diagnostic du plasma de la source d'ions ECR SIMPA par spectroscopie X, Collision d'ions néon hydrogénéés avec des agrégats d'argon.", *Diss. Université Pierre et Marie Curie-Paris VI*, 2006.
- [14] J.M. Lagniel, in *Proceedings of the European Particle Accelerator Conference, 2000, Vienna* (<http://accel-conf.web.cern.ch/AccelConf/e00/PAPERS/THP5B05.pdf>), p. 945.
- [15] Edgell, D. H., Kim, J. S., Bogatu, I. N., Pardo, R. C., & Vondrasek, R. C. (2001). "Modeling of electron cyclotron resonance ion source plasmas". In *Particle Accelerator Conference, 2001. IEEE Proceedings*, vol. 3, pp. 2135-2137, (2001)

PRACTICAL USE OF HIGH-TEMPERATURE OVEN FOR 28 GHz SUPERCONDUCTING ECR ION SOURCE AT RIKEN

J. Ohnishi[†], Y. Higurashi, T. Nakagawa, RIKEN Nishina Center, 351-0198 Wako, Japan

Abstract

To accelerate uranium beams at the RI-beam Factory (RIBF) at RIKEN, U^{35+} ions are extracted from a 28 GHz superconducting ECR ion source by using a high-temperature oven. Our high-temperature oven uses a tungsten crucible, joule-heated with a large DC current. The crucible is heated to approximately 2000°C to achieve a UO_2 vapor pressure of 0.1–1 Pa. The high-temperature oven, which is being developed since 2013, was first used to operate the ion source for the RIBF experiments in the autumn of 2016 and was successfully operated for 34 consecutive days. The use of the high-temperature oven enables the extraction of higher intensity and more stable U^{35+} beams compared to the previous sputtering method. However, due to the vapor ejection hole of the crucible getting blocked, the beam time was interrupted in the autumn of 2017. The high-temperature oven was also used to produce high intensity vanadium beams in the 28 GHz ECR ion source. V^{13+} beams with a current of 100 μA or more were supplied to the beam time for experiments on super heavy element synthesis in 2018. This paper describes the crucible design and operation status of the high-temperature oven.

INTRODUCTION

Uranium beams are most frequently used for experiments on unstable nuclei at the RI-beam Factory. U^{35+} ions extracted from a 28 GHz superconducting ECR ion source (SC-ECRIS) [1, 2] are used for the acceleration of uranium beams. The current beam intensity supplied to the accelerators is 100–130 μA at the ion source. Previously, a sputtering method with a metal uranium rod was used in the ion source, but since 2013, we have begun to develop the high-temperature oven (HTO) method [3–5] and have practically used it for the beam time (BT) of RIBF since 2016. The HTO method makes it easier to increase the amount of

vapor supplied to the plasma in an ion source and is more stable than the sputtering method. Therefore, the HTO method enables the increase of the extracted beam current. The HTO is also used to produce vanadium beams in the 28 GHz SC-ECRIS. Several production tests of V^{13+} have been made since Dec. 2016. Vanadium beams were first supplied to the BT in Jan. 2018 and experiments to synthesize the super-heavy element, whose atomic number is higher than 118, were conducted.

HIGH-TEMPERATURE OVEN AND CRUCIBLE DESIGN

Figure 1 shows a schematic of the HTO. Our HTO uses a crucible of pure tungsten in which a high-melting-point material is loaded. The crucible is directly joule-heated with a DC current of 600–700 A to around 2000°C to achieve a vapor pressure of 0.1–1 Pa for uranium oxide. Figure 2 shows two shapes of a crucible (described later). The crucibles are made by machining a tungsten rod, with body and cap fitted but not fixed.

The crucible's shape is designed with ANSYS Multiphysics [6], which can perform electric, thermal, and structural analyses simultaneously. The analyses carried out were reported in Ref. [5]. The ANSYS calculations do not converge when the voltages of the upper and lower copper blocks, given as a boundary conditions, are increased. This is because the electric current density in the upper and lower rods is too high and beyond a cooling limit. Therefore, we needed to optimize the radius of the upper and lower rods and the crucible's body thickness. Figures 2 (a) and 2 (b) show crucible shapes of the previous R345-type and the current R692-type, respectively. Since the R692-type had to be used for a long period of BT, the capacity was designed to be approximately twice as large as that of

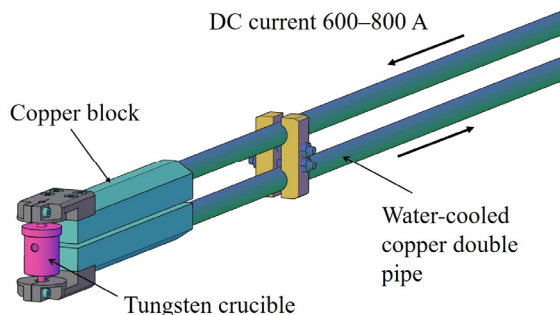
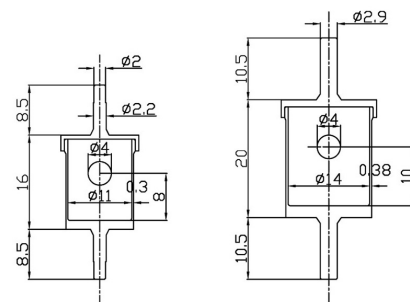


Figure 1: Schematic of the high-temperature oven.



(a) type R435 (previous) (b) type R692 (present)

Figure 2: Schematic of the tungsten crucibles.

[†] ohnishi@riken.jp

Content from this work may be used under the terms of the CC BY 3.0 licence (© 2018). Any distribution of this work must maintain attribution to the author(s), title of the work, publisher, and DOI.

Table 1: Electromagnetic Force

magnetic field (T)	current (A)	rod radii (mm)	electro-magnetic force (N)	share stress (MPa)	bending stress (MPa)
LB435	3.1	507	2.2	42	11
LB692	3.1	679	2.9	72	11

R435-type. Table 1 gives the electric currents, electromagnetic forces and stresses when the two types of crucible are raised to a temperature of approximately 2000°C. Although the electric currents and the forces to which the crucibles are subjected are increased by 33%, it is found that the stresses on the upper and lower rods are almost the same. Figure 3 shows the calculated maximum temperatures of the crucible body as a function of the power of heat generation in the R692-type, and the two curves represent cases with and without a heat shield. The emissivity of the crucible and heat shield are assumed to be 0.35 and 0.15, respectively. In the heat shield case, the maximum obtained temperature was 2065°C with electric current and a power of 687 A and 893 W, respectively. In the R692-type crucible, the maximum limit of the current was around 700 A.

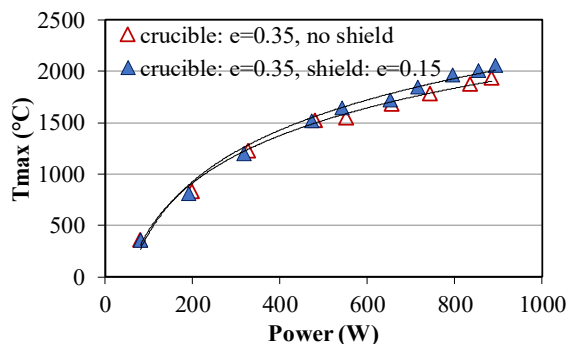


Figure 3: Maximum crucible temperatures as a function of the power of heat generation calculated with ANSYS.

ION SOURCE OPERATION USING HTO

Table 2 lists a summary of the BT, whose beams were supplied from the 28 GHz SC-ECRIS using the HTO. Uranium beams are accelerated to up to 345 MeV/nucleon by one linac and four cyclotrons and are supplied to the experiments at the RIBF. The uranium BT (U-BT) at the RIBF is executed continuously for 1–1.5 months, during which several experiments are conducted. Vanadium beams are accelerated to up to 6 MeV/nucleon by one linac and one cyclotron and used for new super-heavy element synthesis experiments. The latter experiment is also conducted for more than one month. In Table 2, where the operation time is indicated as a sum of two or three numbers a crucible was exchanged during BT.

Uranium Beam Time

Figure 4(a) shows the trend of the beam current of U³⁵⁺, the electric current and the power of heat generation of the

Table 2: Summary Of Beam Time Using HTO

ion	period	beam current (μA)	operation time (d)	material	consumption rate (mg/h)	Aim
U ³⁵⁺	10–11/2016	100–120	34	UO ₂	2.4	RIBF experimen
U ³⁵⁺	5–6/2017	60–120	35	UO ₂	3.2	RIBF experimen
U ³⁵⁺	10–11/2017	80–120	7 + 27 + 10	UO ₂	4.0, 4.2, 12	RIBF experimen
V ¹³⁺	1–2/2018	100–210	20 + 13	metal V	2.2, 4.1	SHE serach
V ¹³⁺	6–7/2018	100–230	23 + 9	metal V	2.0, 3.8	SHE serach

crucible during the U-BT in the autumn of 2016. The beam current of U³⁵⁺ was measured with a Faraday cup positioned down-stream of the analyzing magnet. The beam current can only be measured when the beams are not supplied to the accelerators, and changes according to the width of the slits located upstream. The power of heat generation of the crucible was obtained by subtracting the Joule loss on the support pipes from the total electric power. The uranium beams were supplied to the accelerators from Oct. 10, after a few days of adjustment of the ion source. Looking at Fig. 4 (a), it is clear that the power of heat generation of the crucible was almost constant for one month and that a beam current of 120 μA or more could be maintained.

Figure 4 (b) shows the trend of the U-BT in the autumn of 2017. As can be seen from this figure, we increased the

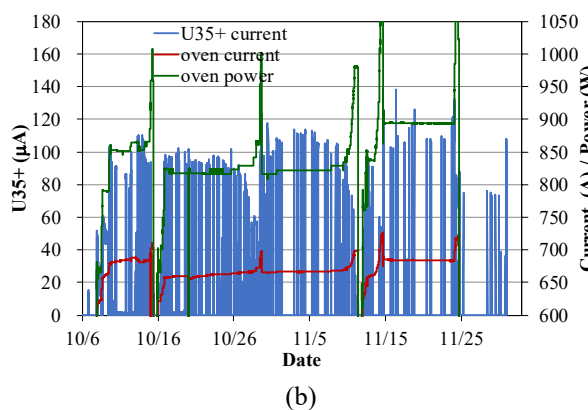
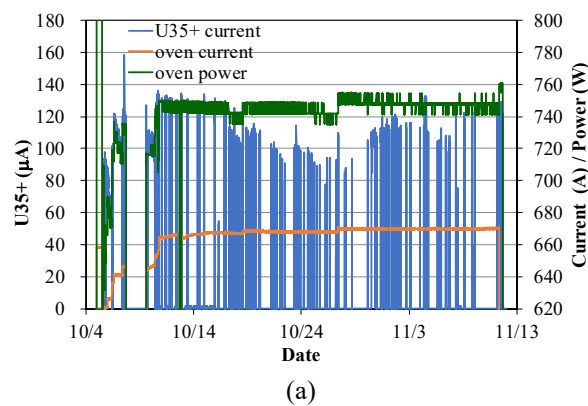


Figure 4: Operational trend of HTO in U-BT of (a) 2016 and (b) 2017.

Content from this work may be used under the terms of the CC BY 3.0 licence (© 2018). Any distribution of this work must maintain attribution to the author(s), title of the work, publisher, and DOI.



Figure 5: Blockage of the vapor-ejection hole of crucibles.

power of the HTO to around 1000 W five times, because the beam intensity decreased. This is because the vapor-ejection hole of the crucible was blocked. The blockage was resolved by raising the temperature of the crucible on Oct. 29 and Nov. 14. However, we had to open the ion source to exchange the crucible on Oct. 15 and Nov. 11. Moreover, we had to stop using the HTO and go back to the sputtering method after Nov. 24. Figures 5 (a) and (b) show photographs of the crucibles whose vapor-ejection holes were blocked. Figure 5 (a) is a photograph taken on Oct. 15, which shows that only the vapor-ejection hole itself was blocked within a short time, while Fig. 5 (b) is a picture taken on Nov. 11 after operation for 27 days. In the case of Fig. 5 (b), it can be assumed that UO_2 deposited on the edge of the heat shield (molybdenum), reached the vapor-ejection hole of the crucible. We later found that the heat shield shown in Fig. 5 (a), whose opening was made larger to reduce the deposition of UO_2 , causes the ejection hole of the crucible to get blocked more easily. Moreover, we made a production test of U^{35+} using the HTO without a heat shield. In this test, it was found that U^{35+} beam currents higher than 100 μA could be obtained by increasing the oven power to 970 W, even without a heat shield. However, after 10 days of operation, the blockage of the ejection hole occurred again.

Vanadium Beam Time

The HTO was also used to produce high intensity vanadium (V^{13+}) beams in the 28 GHz SC-ECRIS. As shown in Fig. 6, we placed a yttria crucible into tungsten crucible

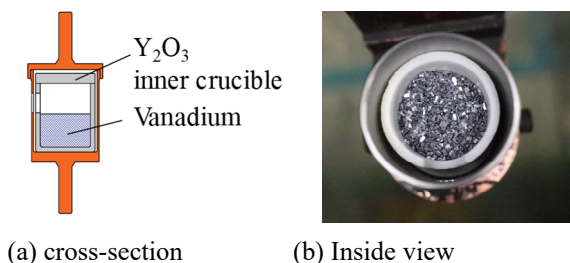


Figure 6: Crucibles for metal vanadium.

(R692-type) and filled it with metal vanadium (vapor pressure: 1 Pa at 1827°C). The fillable amount was approximately 2.0 g. Figure 7 shows the operational trend of the HTO in the second BT, conducted in June–July 2018. A heat shield was not used because the vapor pressure of vanadium is higher than that of UO_2 . In the first half, V^{13+} was supplied at 90–120 μA . After changing the crucible on Jul. 13, the beam current was gradually increased as requested by experimenters. Figure 8 shows the relationship between vapor pressures inside the crucible, estimated from the oven power using the calculation results shown in Fig. 3, and V^{13+} beam currents during Jul. 11–20. It is found that the V^{13+} beam currents within 200 μA are proportional to the amount of vapor.

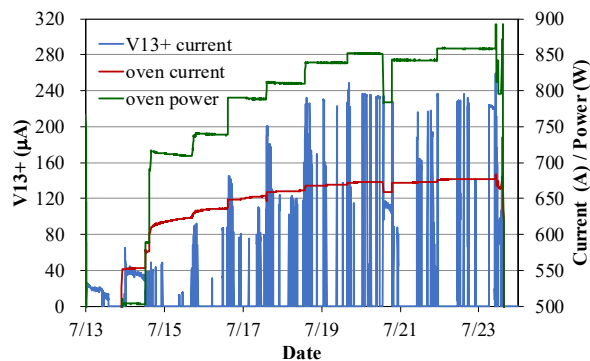


Figure 7: Operational trend of HTO in the second V-BT in 2018.

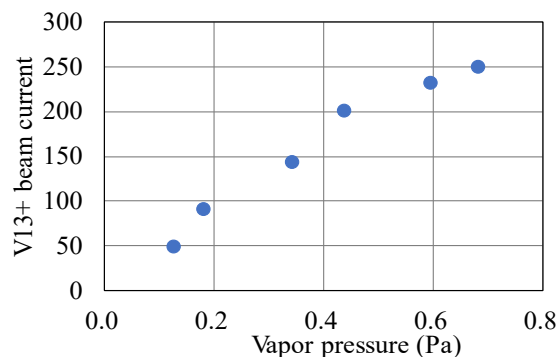


Figure 8: Relationship of vapor pressures in the crucible and beam current obtained in the V-BT during 7/11–20.

Figure 9 shows the temporal change of production efficiencies of U^{35+} and V^{13+} . The production efficiencies are obtained by dividing the number of particles, equivalent to the beam current, of U^{35+} and V^{13+} by those of the UO_2 and V vapor from the HTO, respectively. The data of V^{13+} in Sep. 2017 and U^{35+} in May 2018 are the data obtained in the production tests for approximately two weeks, and effects on the blockage of the ejection hole were removed in these efficiencies. Although the production efficiencies of

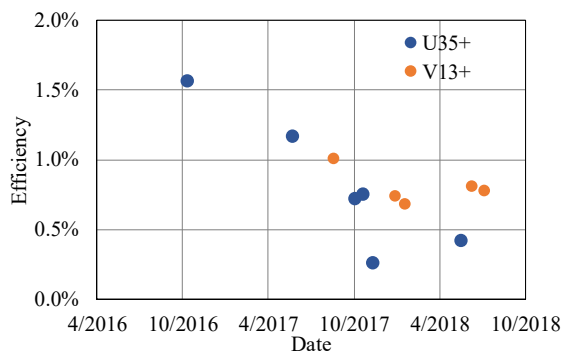


Figure 9: Production efficiencies of U^{35+} and V^{13+} .

V^{13+} do not change significantly, those of U^{35+} clearly decrease with time. Since the production tests of V^{13+} were conducted between Dec. 2016 and Mar. 2017, it is conceivable that the operation for V^{13+} production in the same ion source may be one of the causes of the decrease in the production efficiencies of U^{35+} .

OFF-LINE TEST

Tests of the HTO are performed using the off-line test stand because the 28 GHz SC-ECRIS is occupied by BT for a long time. However, since uranium is a nuclear fuel material and its use is restricted, it cannot be handled by the off-line test stand. Figure 10 shows a schematic of the off-line test stand. The test stand is equipped with a thin film deposition monitor to measure the amount of vapor. The thin film deposition monitor (INFICON) uses a crystal oscillator and is located at approximately 210 mm from the crucible. Figure 11 shows an example of the measured data during a test using vanadium. The left vertical axis dM/dt indicates an increase in the rate of mass per 1 cm^2 (deposition rate) measured by the thin film deposition monitor. The consumption rate of material in the crucible can be obtained by multiplying the measured deposition rate by 835 cm^2 , which was obtained by a calibration. In these data, the consumption rate of vanadium equals to approximately 6 mg/h in an oven power of 800 W . In this measurement example, the oven power has changed in the first 30 minutes. This is presumed to be caused by a decrease in the contact resistance between body and cap of the crucible, and such unstable oven power is sometimes seen at the beginning of

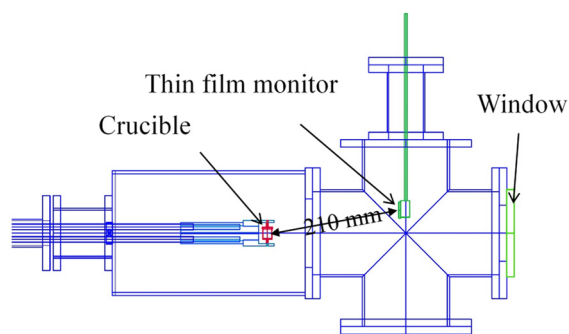


Figure 10: Schematic of the off-line test stand for HTO.

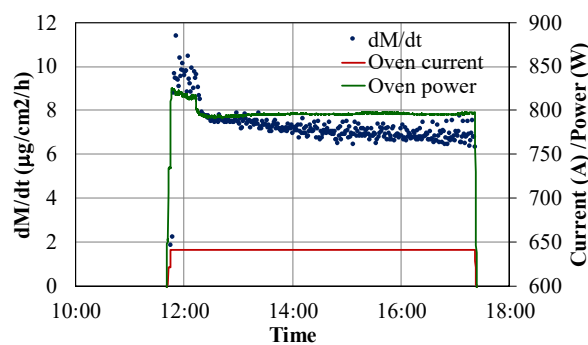


Figure 11: Example of operational trend of HTO in the off-line test stand.

excitation. Although the deposition rate, which is the average value over one minute, is scattered considerably, it is not clear whether this is a measurement problem. Figure 12 shows the deposition rates as a function of the oven power obtained for vanadium and titanium. Titanium was tested by loading metal titanium into a yttria crucible, similarly to vanadium. These results correspond to those where the temperature of metal titanium, in which a vapor pressure reaches 1 Pa , is around 1710°C , 120°C lower than that for vanadium, and show that the amount of vapor of titanium is also sufficient for operation of the ion source.

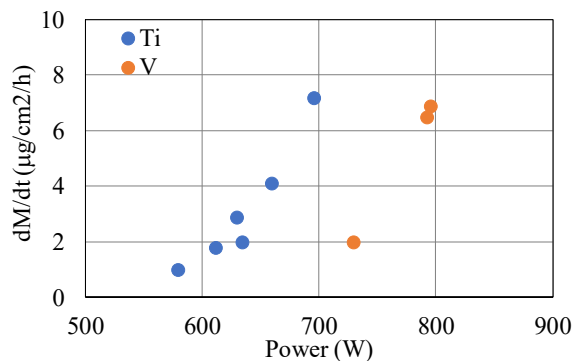


Figure 12: Deposition rate of Ti and V obtained from HTO in off-line test stand.

CONCLUSION

We produced high intensity uranium beams at the 28 GHz SC-ECRIS by using the HTO, and supplied the uranium beams to three BTs at the RIBF since autumn of 2016. In the first BT, we successfully supplied U^{35+} beams with a current of $120\text{ }\mu\text{A}$ or more, for 34 consecutive days. However, in the third BT, we had to interrupt the BT to open the ion source because the vapor-ejection hole of the crucible was blocked. Although the direct cause of the blockage of the ejection hole is not clear, it could be caused by a decrease in time of the production efficiencies of U^{35+} and an increase of the amount of vapor. The HTO could be also used for high-melting-point metals such as vanadium and titanium by placing a yttria crucible in a tungsten one. As

a result, we successfully supplied V^{13+} beams with a current of 100–240 μA to the two BTs for the experiments of super heavy element synthesis.

REFERENCES

- [1] G. D. Alton and D. N. Smithe, “Design studies for an advanced ECR ion source”, *Rev. Sci. Instrum.*, vol. 65, pp. 775 (1994).
- [2] Y. Higurashi, J. Ohnishi, K. Ozeki, M. Kidera, and T. Nakagawa, “Recent development of RIKEN 28 GHz superconducting electron cyclotron resonance ion source”, *Rev. Sci. Instrum.* vol. 85, p. 02A953, (2014).
- [3] T. Loew, S. Abbott, M. Galloway, D. Leitner, and C. M. Lyneis, “Design of a high temperature oven for an ECR ion source for the production of uranium beams”, *Proceedings of PAC07, Albuquerque, New Mexico, USA, 25-29 June 2007*, p.1742.
- [4] J. Ohnishi, Y. Higurashi, M. Kidera, K. Ozeki, and T. Nakagawa, “Development of a high-temperature oven for the 28 GHz ECR ion source”, *Rev. Sci. Instrum.*, vol. 85, p. 02A941, (2014).
- [5] J. Ohnishi, Y. Higurashi, and T. Nakagawa, “Progress in high-temperature oven development for 28 GHz electron cyclotron resonance ion source”, *Rev. Sci. Instrum.*, vol. 87, p. 02A709, (2016).
- [6] <http://www.ansys.com/>

POINT-LIKE NEUTRON EMISSION OBSERVATION USING A NEUTRON GENERATOR BASED ON A GASDYNAMIC ECR ION SOURCE

R.A. Shaposhnikov, S.V. Golubev[†], I.V. Izotov, R.L. Lapin, S.V. Razin,
A.V. Sidorov, V.A. Skalyga, 603950 Nizhny Novgorod, Russian Federation

Abstract

One of the interesting applications of ECR ion sources is their use as a part of neutron generators. The use of high-current gasdynamic sources with plasma heating by high-frequency gyrotron radiation allows to increase neutron yield, and obtain a point-like neutron emission by sharp focusing of a high-quality deuterium ion beam on a target. Such point-like neutron source could perspective for neutron tomography. In the first experiments at the SMIS 37 facility the high-current deuterium ion beam was focused by a simple magnetic coil (magnetic field strength up to 3 T) placed behind two-electrode extraction system on a titanium target saturated with deuterium. It was demonstrated that in such system a weakly descending 60 mA ion beam with the convergence of 50 could be focused in 1 mm spot resulting in 8 A/cm² of current density at the focal plane. Measured neutron yield from the target placed in the focal region under conditions of the beam energy of 80 keV reached a value of 10¹⁰ neutrons per second in 1 ms pulse.

INTRODUCTION

Electron-cyclotron resonance (ECR) ion source is one of the most wide spread types of systems that are designed to produce ion beams of multicharged ions or protons. One of directions of ion sources development is an increase of extracted ion beam current. The problem of the beam current increase is related to the problem of maximum attainable values of plasma density in a discharge. The solution of this problem can be based on the implementation of the gasdynamic plasma confinement regime, which is characterized by a high plasma density and its low lifetime. Previous experiments conducted at the IAP RAS were aimed at investigating the possibility of proton beams formation from the ECR discharge in a simple mirror magnetic trap [1].

The experimentally obtained dependence of the ion beam current extracted through the 10 mm aperture on the extraction voltage demonstrated the possibility of obtaining current values up to 500 mA, which corresponds to a current density about 600 mA/cm².

A pepper-pot method was used in a purpose to measure the ion beam emittance. This method has been described in detail in [2]. The results of measurements showed the possibility of obtaining beams with normalized emittance at

the level of 0.05 pi · mm · mrad. Such a low value of emittance opens the possibility for effective focusing of the ion beam.

IBSimu code [3] was used for ion trajectories simulation in the field of magnetic focusing lens [4]. As a result of numerical simulation, the theoretical possibility of high-current ion beam focusing into a region of the order of 100 μm was demonstrated. The results of numerical calculations demonstrating the possibility of obtaining ion beams with small widths, as well as experimental data on obtaining high-current ion beams, open the possibility of creating a point-like neutron source based on the deuterium-deuterium synthesis reaction, which occurs when a focused beam of deuterium ions hits the deuterium containing target. There is an isotropic neutron emission from the target during the reaction. In this case, the characteristic size of the neutron source is determined by the quality of the ion beam and by the effectiveness of the focusing system.

The main application of the point-like neutron source could be neutron tomography [5].

EXPERIMENTS

Experiments aimed at producing the point-like neutron source were carried out at the SMIS 37 facility (Fig. 1). Gyrotron microwave radiation with a frequency of 37.5 GHz, power up to 100 kW and a pulse duration of 1.5 ms was used for plasma heating and discharge ignition. The plasma was created in a simple mirror magnetic trap operating in a pulsed mode with 0.1 Hz repetition rate. The use of powerful gyrotron radiation allowed to realize a gasdynamic plasma confinement regime with the lifetime $\tau = \frac{R \cdot L}{2 \cdot V_s}$, where R is the mirror ratio, L is the length of the trap and V_s is the ion-sound speed. The operating gas (hydrogen) was inlet into the discharge chamber in pulsed mode along the axis of the magnetic system through a gas-entry system integrated into the electrodynamic system for microwave radiation injection. A two-electrode system consisting of a plasma electrode with a diameter of 10 mm and a puller electrode with a diameter of 22 mm was used in a purpose of ion beam extraction. The distance between electrodes was 15 mm. A magnetic coil which was used as the magnetic lens was placed behind the extraction system. Its magnetic field was regulated independently of the magnetic field of the trap (the magnetic field strength reached 3 T).

[†] gol@appl.sci-nnov.ru

Content from this work may be used under the terms of the CC BY 3.0 licence (© 2018). Any distribution of this work must maintain attribution to the author(s), title of the work, publisher, and DOI.

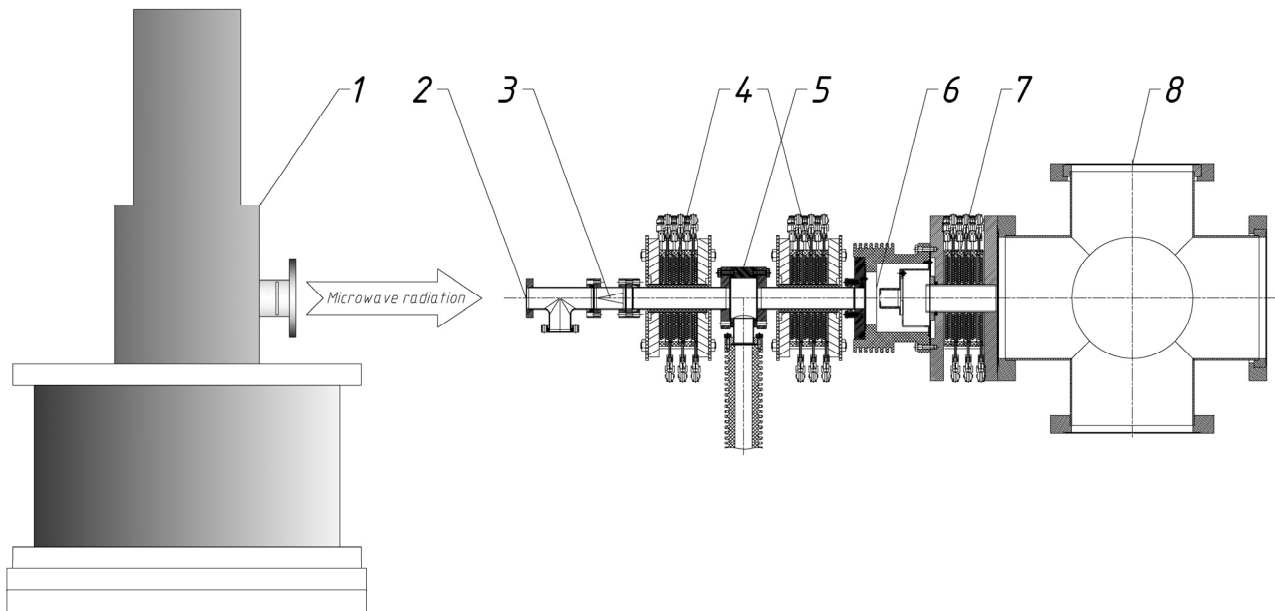


Figure 1: The experimental facility SMIS 37. 1 – gyrotron, 2 - microwave window, 3 - quasi-optical system for microwave radiation coupling into plasma, 4 - pulsed magnetic coils, 5 - discharge vacuum chamber, 6 - extraction system, 7 - focusing lens, 8 - diagnostic chamber.

ION BEAM FOCUSING

The extracted ion beam current in the focal region of the magnetic lens was measured with a Faraday cup. As a result of system parameters optimization the value of an ion beam current at the focus was 50 mA (Fig. 2).

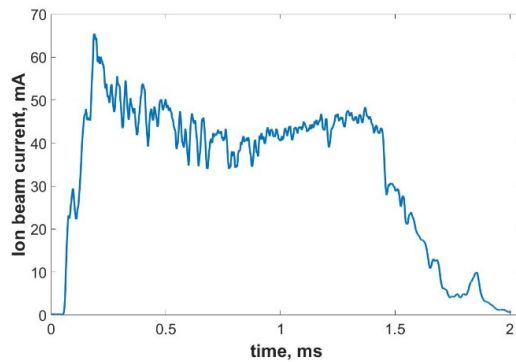


Figure 2: Ion beam current oscillogram at the focus of the lens.

The CsI scintillator located along the axis of the system in the diagnostic chamber after the focusing lens with a diameter of 100 mm was used for the ion beam size diagnostics. Using a special camera "Nanogate" with exposure time of 20 μ s a number of photos of the scintillator luminescence were made to determine the beam dimensions. At optimal system parameters, such as the magnetic field of the trap, the magnetic field of the focusing lens, and the extraction voltage, it was possible to achieve focusing of the ion beam in a spot with 1 mm size.

A typical photo of the scintillator glow and a plot of the radial distribution of scintillator luminescence is shown in

Figs. 3 and 4. The beam size was determined at half of the glow intensity maximum.

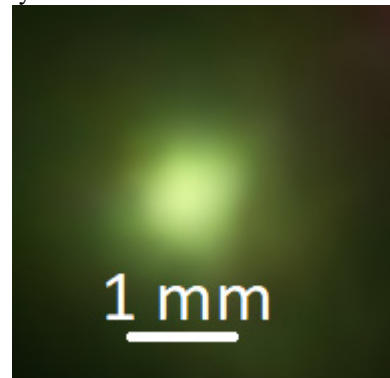


Figure 3: The photo of the scintillator glow at the best focusing parameters.

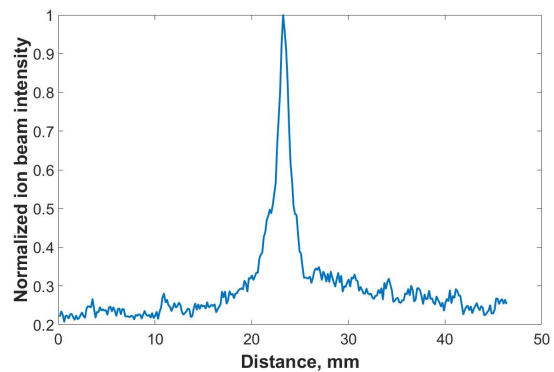


Figure 4: The dependence of normalized ion beam intensity on the radial coordinate.

NEUTRON PRODUCTION

To study the efficiency of neutron generation and to determine the characteristic size of the source, the scintillator was replaced by a titanium-deuterium target, which was irradiated with a focused beam of deuterium ions. Measurements of characteristic neutron flux values were carried out using a calibrated neutron detector. The detector was located at a distance of 1.5 m from the neutron source. These measurements showed that the neutron flux increases with the growth of ion beam current and energy. At the current of 50 mA and energy of 80 keV the neutron flux reaches values of 10^{10} s^{-1} which corresponds to the neutron flux density at the emitting region on the target of $10^{12} \text{ s}^{-1} \text{ cm}^{-2}$. Spatial distributions of the neutron flux were studied using a set of radiochromic films located behind the lead shield near the target (Fig. 5). Such films accumulate defects caused by x-rays and fast particles including neutrons. Figure 6 shows an image of the transverse neutrons flux intensity distribution. The characteristic transverse dimension of the image at a distance of 0.5 cm from the target is about 1 cm, which is due to the isotropic emission of neutrons from the source with dimensions of 1 mm (the size of the deuterium ion beam on the target).

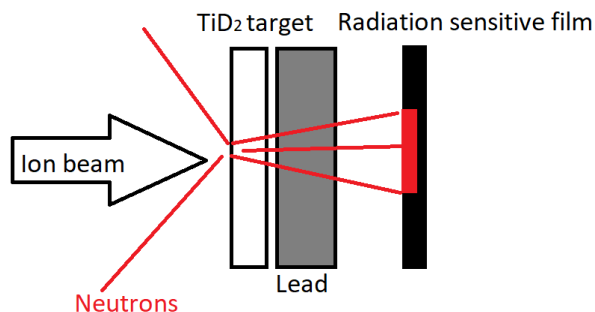


Figure 5: Scheme of the radiochromic film irradiation with the neutron flux.

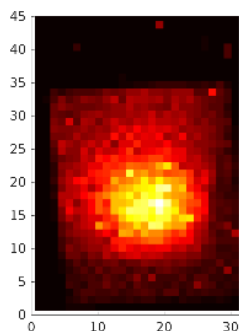


Figure 6: Image of the neutrons flux intensity distribution (dimensions are shown in mm).

CONCLUSION

During the experiments on the focusing of the deuterium ion beam, it was demonstrated the possibility of focusing the extracted beam into a region of 1 mm size. The neutron flux reaches values of 10^{10} s^{-1} what corresponds to the neutron flux density at the emitting region of $10^{12} \text{ s}^{-1} \text{ cm}^{-2}$. Such neutron flux density is perspective for neutron tomography of compact (about 10 cm) objects.

ACKNOWLEDGEMENTS

Presented work was supported by the grant of Russian Science Foundation # 16-19-10501

REFERENCES

- [1] A. Sidorov, M. Dorf, A. Bokhanov, I. Izotov, S. Razin, V. Skalyga, V. Zorin, A. Balabaev, P Spädtke, J. Roßbach, "Multi-aperture ion beam extraction from gas-dynamic electron cyclo-tron resonance source of multicharged ions", *Review of Scientific Instruments*, vol. 79, p. 02A317 (2008)
- [2] A. Septier, *Applied Charge Particle Optics*, Academic Press, New York, 1980, p. 214.
- [3] T. Kalvas, et. al., "IBSIMU: A three-dimensional simulation software for charged particle optics", *Rev. Sci. Instrum.* vol. 81, p. 02B703, (2010).
- [4] S.V. Golubev, V.A. Skalyga, I.V. Izotov, A.V. Sidirov, S. V. Razin, R.A. Shaposhnikov, R.L. Lapin, A.F. Bokhanov, M. Yu. Kazakov, "On the possibility of creating a point-like neutron source", *Radiophysics*, vol. LX,n°10
- [5] Ian S. Anderson, Robert L. McGreevy, Hassina Z. Bilheux, "Neutron Tomography", in *Neutron Imaging and Applications*, Ed. New York, NY, USA: Springer, pp. 81-86, (2009)

DEVELOPMENT OF LECR4 ION SOURCE FOR INTENSE BEAM PRODUCTION AND LECR5 FOR SESRI PROJECT*

C. Qian[†], L. T. Sun, W. Lu, Z. H. Jia, W. Huang, X. Fang, J. W. Guo, H. Wang, Y. Yang, Y. C. Feng, X. X. Li, X. Z. Zhang, Y. J. Yuan, H. W. Zhao, Institute of Modern Physics, CAS, 730000 Lanzhou, China

Abstract

Several intense highly charged heavy ion beams have been produced from Lanzhou ECR ion source No.4 (LECR4) since 2014. Recently an attempt to generate intense light ion beam was tested by High-B mode of LECR4 ion source. We firstly produced 8.72 emA of $^4\text{He}^{2+}$ beam with 1.7 kW of 18 GHz microwave power at 30 kV extraction voltage. According to the experience of LECR4. A new room temperature ECR ion source (named LECR5) has been designed to deliver multiple charge ion beams for the Space Environment Simulation Research Infrastructure (SESRI) at Harbin Institute of Technology. It aims to produce almost all ion beams from H_2^+ to $^{209}\text{Bi}^{32+}$. This article reviews the latest result of LECR4 and preliminary design of LECR5 in detail.

INTRODUCION

ECR Ion Sources are used to produce highly charge state ion beams of intermediate and heavy mass elements. They are widely used to produce ion beams for accelerators, atomic physics research and industrial applications. Some room temperature Electron Cyclotron Resonance ion sources (LECR1, LECR2 and LECR3) have been successively built at IMP [1, 2]. One unique feature of LECR4 is that the solenoid coils are fully immersed in a special me-dium and cooled by evaporative cooling technology when excited [3]. To satisfy the requirement of intense multi-charged ion beam, a research program named Space Envi-ronment Simulation and Research Infrastructure (SESRI). LECR5 was proposed in 2016. The traditional cooling technology that solid quadrate copper wire was used to wind the solenoid pancakes instead of hollow copper wire, which means it is high pressure de-ionized water free.

DEVLOPMENT OF LECR4

LECR4 is used for SSC-Linac injector at Institute of Modern Physics (IMP). The SSC-Linac consists of an ECR ion source, low energy beam transport (LEBT), a 4-rod RFQ, medium energy beam transport (MEBT) and IH-DTL, as shown in Fig. 1. LECR4 was redesigned from DRAGON concept in 2012. Its radial field at plasma cham-ber wall of 76 mm inner diameter is about ~ 1.0 T. LECR4 was built and started commissioning at 18 GHz in 2014. The source has successfully delivered H_2^+ , O^{5+} , C^{4+} , $\text{O}^{4+}\text{C}^{3+}$, Ar^{8+} and Bi^{30+} ion beams for RFQ and DTL com-missioning.

Heavy Ion Beam Production

Based on the original research of LECR4 M/Q selector, an updating selection system for LECR4 has been designed to handle the higher beam intensities. Figure 1 shows the schematic design of the new M/Q selection system. As the actual beam envelope and beam waist cannot be controlled with a single solenoid lens, an additional solenoid is introduced before the dipole magnet. To further study the production of very high charge state heavy ion beams, LECR4 was tested with bismuth by oven, the attempt to produce uranium ion beam by sputtering. Table1 shows some of the latest results from LECR4 and compares beam intensity with other high performance sources for reference [4]. The microwave power is less than 2.3 kW with operation frequency 18 GHz (beam intensity: e μ A).

Table1. Latest Results of LECR4 at 18 GHz in Comparison With Other High Performance ECRIS

	Charge State	GTS	LECR4	
^{16}O	6+	1950	2110	
	7+		560	
	^{40}Ar	8+	1100	1717
		9+	920	1230
		11+	510	620
^{129}Xe	12+	380	430	
	14+	174	185	
	20+	310	430	
	21+	274	320	
	23+		275	
^{209}Bi	25+	244	215	
	27+	168	135	
	28+		170	
	29+		145	
	31+		92	
^{238}U	32+		63	
	31+		35	
	32+		30	

* This work was supported by the NSFC (National Nature Science Foundation of China) research program with Contract No. 11427904

[†] qianc@impcas.ac.cn

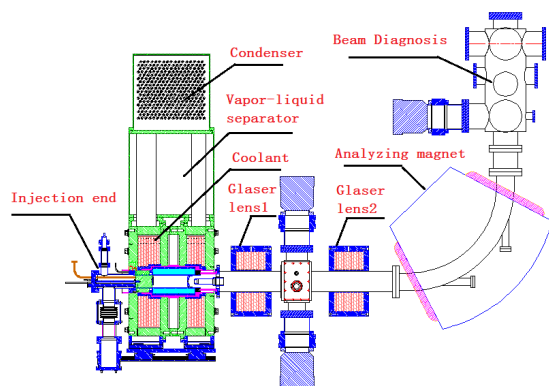


Figure 1. A schematic cross-section view of the LECR4 source body and M/Q selector system

Table 2. Yield Comparison of Various Ion Sources

Ion Source	f (GHz)	Pw (kW)	He ²⁺ (emA)
LECR4	18	1.7	8.74
VENUS	18+28	1.7+1.0	11

High intensity helium ion beam

Multi-charged helium ion is a critical ion in particle physics, material science and medical science. Multi-charged helium ion beam instead of deuterium ion beam for pre-acceleration experiments. With the improvements to the LECR4 lower energy transmission line a new record intensity for the production of helium was achieved. High intensity helium ion beam was tested. Table 2 shows the yield of multi-charged helium ion beam and compares beam intensity with other high performance sources for reference [5]. The extraction high voltage is 30 kV with all total beam is 14.43 emA. The stability monitoring is about 17 hours which the 5 emA multi-charged helium ion beam was produced. As shown in Fig. 2.

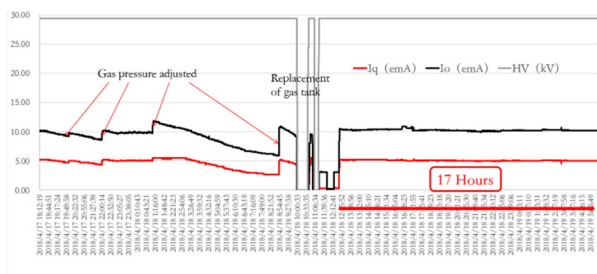


Figure 2. Long period stability monitoring @ 30 kV-5 emA

Double Solenoids To Improve M/Q Resolution

In 2014, The Bismuth ion beams were optimized, the M/Q resolution of LEBT is relatively poor. The beam spots were overlapped for highly charged bismuth ions. Some schemes of improving the M/Q resolution as follows: a) Increasing the deflection angle of the dipole magnet, b) De-creasing the deflection radius of the dipole magnet, c) In-creasing the distance between the dipole magnet and the slit, d) another solenoid to control the beam spot size of the

slit. According to the experiments, the solenoid focusing before the M/Q separation can result in strong degradation of the beam quality and can create a hollow beam structure due to different focal points of different charge states [6]. The hollow beam structure has been observed by several ion source groups. It could possibly be avoided by increasing the space charge compensation and by using electro-static focusing. The beam spot is hollow when optimized the intensity Bismuth ion beams on this ion source. In last, to solve this problem, a Dual-solenoid scheme is proposed, as shown in Fig. 1.

LECR5-SESRI PROJECT

Space Environment Simulation Research Infrastructure (SESRI), which is a scientific project for a major national facility of fundamental research, has recently been launched at Harbin Institute of Technology (HIT). It fills in the blank in national simulation facilities, comprehensive space environment interacting with the material science research platform in the integrated environment of large space. Granted the national funds of 1.8 billion RMB (about 261.4 million USD) to construct 9 sub-system and its supporting infrastructure. Heavy ion accelerator is one of the most important systems. LECR5-SESRI ion source as the injector provides various ion beams from H to Bi. All requirements of ion beams need to be produced by LECR5 is shown in the Table 3. the emittance requirement of hydrogen molecular ion beam is a challenge due to the high-B mode.

Table 3. Requirements of ion beams

Ions	I(euA)	HV (kV)	Beam Emittance (π.mm .mrad)
H ₂ ⁺	250	8	0.8 (norm, 90%)
⁴ He ²⁺	50	8	0.6 (norm, 90%)
⁸⁴ Kr ¹⁸⁺	80	18.667	
²⁰⁹ Bi ³²⁺	50	26.125	

Design of LECR5 Ion Source

The LECR5 has been designed according to the magnetic specification and the experiment of LECR4. To enhance the magnetic field strength, an iron plug is added on the injection side: in such a way, an axial field of 2.6 T at the injection is achievable. The magnetic field value at the extraction of 1.4 T is achievable. As shown in Fig. 3. The radial magnetic field at chamber wall of 1.2 T is achievable. The radial magnetic is composed of 36 segments with traditional Halbach. N50M and N48SH NdFeB permanent magnetic materials are used. The double wall plasma chamber is made of aluminium to enhance the secondary electron emission. The large and long plasma chamber (80

Content from this work may be used under the terms of the CC BY 3.0 licence (© 2018). Any distribution of this work must maintain attribution to the author(s), title of the work, publisher, and DOI.

mm in diameter and 340 mm long) allows a long lifetime for the ions in order to produce high charge states. In such a configuration, the 18 GHz resonance is 132 mm long. As it is a source for tests, one has chosen several frequencies: 14 and 18 GHz. All frequencies could be launched together. The ion source being equipped with a 2 wave guides rf injector. The general picture of the source is presented in Fig. 4. (SN: SoleNoid; AM: Analyzing Magnet; BD: Beam Diagnosis)

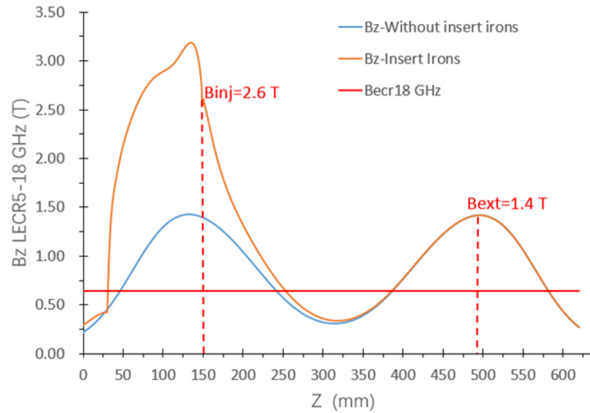


Figure 3. The axial magnetic field configure by simulation

Design of M/Q Selector System

The layout of the beam lines in the ECR vault including the diagnostic beam line for the LECR5-SESRI, which still has to be installed, is shown in Fig. 3. The diagnostic beam line of the LECR5 will have a solenoid directly in the front of the 90° bending magnet. The solenoid focuses the beam into the focal point of the 90° magnet (double focusing action) and behind the magnet a horizontal slit in the second focal point will ensure sufficient mass resolution. The initial focusing distance from ion beam extraction to solenoid inlet is 300 mm. The drift distance from analysis magnet outlet to slit is 900 mm. The diagnostic line is completed with a chamber containing an Aillsion Emittance device for both transversal planes and a Faraday cup.

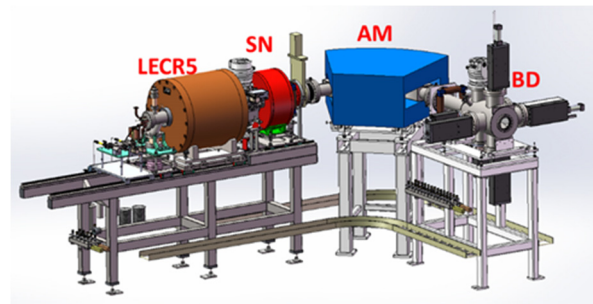


Figure 4. Layout of LECR5 source body and M/Q selector system.

SUMMARY

Double solenoids can control beam toward the ana-lyzing magnet better than single solenoid in more compact Q/A selector system. The 1st or 2st generation ECRIS is the most potential for produce high current high beam qual-ity multi-charged helium ion beam. The performance of LECR4 is still promising when improving the radial mag-netic field and improving the extraction system. Larger plasma chamber and more flexible magnetic field with LECR5.

REFERENCE

- [1] H. W. Zhao, B. W. Wei, Z. W. Liu, Y. F. Wang, and W. J. Zhao, *Rev. Sci. Instrum.* vol. 71, 646 (2000).
- [2] L. T. Sun, H. W. Zhao, Z. M. Zhang, B. Wei, and X. Z. Zhang, *Nucl. Instrum. Methods Phys. Res. B* vol. 235, p. 524 (2005).
- [3] W. Lu, B. Xiong, X. Z. Zhang, L. T. Sun, and Y. C. Feng, *Rev. Sci. Instrum.* vol. 85, p. 02A926 (2014).
- [4] D. Hitz et al, *Rev. Sci. Instrum.* vol. 75, p. 1403 (2004).
- [5] J. . Benitez et al, ECRIS2012, THXO02.
- [6] X. H. Zhang, Y. J. Yuan, X. J. Yin, C. Qian, L. T. Sun, *Nucl. Instrum. Methods Phys. Res. A*, vol. 235, p. 524 (2017).

GASDYNAMIC ECR ION SOURCE FOR NEGATIVE ION PRODUCTION

R. L. Lapin[†], I. V. Izotov, V. A. Skalyga, S. V. Razin, R. A. Shaposhnikov, Institute of Applied Physics of the Russian Academy of Sciences, Nizhny Novgorod, Russia
O. Tarvainen, University of Jyväskylä, Department of Physics, Jyväskylä, Finland

Abstract

H⁻ ion sources are needed in various areas of accelerator technology, such as beam injection into cyclotrons and storage rings and as a part of neutral beam injectors for plasma heating in experimental facilities studying thermonuclear fusion. It was recently demonstrated that gasdynamic ion source based on ECR discharge in a simple mirror trap is very efficient for proton beam production [1]. Here we use the gasdynamic plasma source as the first stage driver of volumetric negative ion production through dissociative electron attachment (DEA) [2]. Experiments were performed with a pulsed 37 GHz / up to 100 kW gyrotron radiation in a dual-trap magnetic system, which consists of two identical simple mirror traps. The first trap was used for the plasma production under ECR condition. Dense hydrogen plasma flux from the first trap flows into the second trap through a perforated plate, which prevented the propagation of microwaves into the second one. The configuration helps to separate plasma volumes with "hot" and "cold" electrons. We present recent experimental results on this topic. A negative ion current density of 80 mA/cm² through 1 mm plasma electrode was demonstrated.

INTRODUCTION

The first attempt to use a gasdynamic ECR discharge for a volumetric negative ion production was performed in 2017 [3]. It was shown that it is possible to achieve total negative ion current of 0.2 mA through 5 mm extraction aperture by optimizing the gas injection scheme, but with high level of impurities caused by residual water. In the present work we demonstrate results of the next stage experiments, in which measures have been taken to reduce the level of impurities.

EXPERIMENTAL SCHEME

We used 37 GHz / up to 100 kW gyrotron radiation for plasma production in a dual-trap simple mirror magnetic system (plug magnetic field ranging from 1 to 2.5 T). In the first trap the plasma was created under ECR condition. Dense hydrogen plasma flux from the first trap was allowed to flow into the second trap through a perforated conducting plate, acting as a microwave reflector preventing electron heating in the second trap. Presumably, that allowed to produce two electron

fractions: "hot" electrons in the first chamber with the energy of about 50 – 100 eV and "cold" electrons in the second chamber, with the energy below 15 eV. The "hot" electrons effectively ionized the gas and excited high vibrational states of hydrogen molecules through excitation to B and C singlet states. These molecules then propagated into the second trap and produced H⁻ ions there as the result of dissociative electron attachment (DEA) with "cold" electrons. Such approach is similar to the one suggested in [4] where 2.45 GHz ECR discharge was used as a plasma cathode producing "hot" electrons. The scheme of the experimental facility is presented in Fig. 1. We used an extraction system consisting of plasma and puller electrodes to form a beam of negative particles and a magnetic filter made of two pairs of rectangular permanent magnets placed after the puller for electron dumping. Both magnet pairs produced a magnetic field transverse to the extracted beam and had the opposite magnetization directions to compensate each other's influence on the ion trajectories. In the first experiment we investigated the influence of the neutral gas injection scheme on the negative ion current. Various gas injection schemes were used: continuous, pulsed and their combination. The pulsed injection was realized with an electromagnetic valve connected to a buffer vessel with pressure of 0.05 - 1 bar.

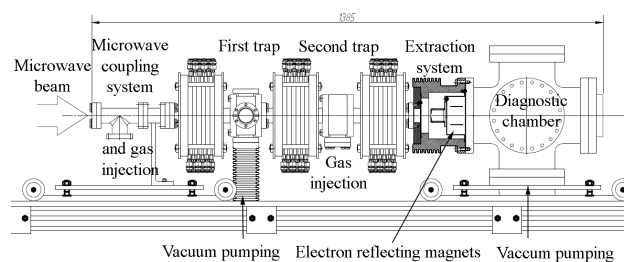


Figure 1: The scheme of the experimental facility.

Various diagnostic tools were used: a magnetostatic analyzer, a Faraday cup and a quadrupole mass spectrometer. The analyzer was used for the measurement of the ion beam spectrum, determination of the impurity level and investigation of the dependence of the H⁻ current on various parameters. The analyzer was used to measure the relative quantity of negative ions, as the significant beam line losses make absolute measurements obscure. Meanwhile, the Faraday cup placed right after the extraction system and electron deflection magnets was used for the measurement of the total current of negative ions. The quadrupole mass spectrometer was used in a diagnostic chamber to determine the composition of the injected gas.

* Work supported by Russian Science Foundation grant #-16-12-10343
[†] lapin@ipfran.ru

RESULTS

The first stage of the experiments was performed with an extraction system consisting of a 5 mm aperture plasma electrode and a 10 mm aperture puller electrode separated by 11 mm. The following scheme of gas injection was used: constant flow of H₂ into the first chamber and pulsed injection into the second chamber. The background pressure in the diagnostic chamber was 10⁻⁶ Torr, gyrotron power up to 80 kW, extraction voltage 12.4 kV. The total current of negative ions measured with the Faraday cup was 0.2 mA and the duration of the pulse was 100 us.

The second stage of experiments was conducted with pulsed gas injection into the second chamber only. In that case the gas diffused into the first chamber, where the hot plasma was generated. The maximum total negative ion current was measured to be 2 mA obtained at 12.4 kV extraction voltage. The dependence of the total negative ion current on the delay between the leading edges of the gas injection and microwave pulse is shown in Fig. 1. The gas injection scheme described above seemed to be the most effective, so it was used hereafter.

The negative ions current ratio was measured with the magnetostatic analyzer and is shown in Table 1.

Table 1. Negative ion current ratio

Ion	OH ⁻	H ⁻	O ⁻	O ₂ ⁻
Relative quantity in analyzer	0.5	1	0.2	2

The dependence of the negative ion current on the magnetic (mirror) field strength is shown in Fig. 2. The most probable way of fragile H⁻ destruction is an interaction with “hot” electrons [2]. Their density increases as the magnetic field increases. The current saturation at B > 2.5 T is supposedly related to this fact.

The measured negative ion spectrum is shown in Fig. 3. H⁻, OH⁻, O⁻, ¹⁹F⁻, O₂⁻, H₂O⁻ and an unknown ion with an atomic mass of 25-27 u were detected. The “mystery ion” could be Al⁻ from the ceramic (Al₂O₃) clamping of the perforated plate placed between the magnetic traps. After the dismantling of the facility it was found out that the PTFE insulation of the grid ground wire was damaged, so that unknown negative ion could also be CN⁻, although C⁻ was not detected.

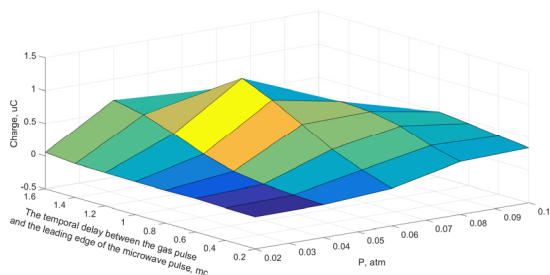


Figure 1: The dependence of the extracted negative ion charge on the temporal delay between the gas pulse and the leading edge of the microwave pulse and gas feed line pressure with 5 mm extraction aperture

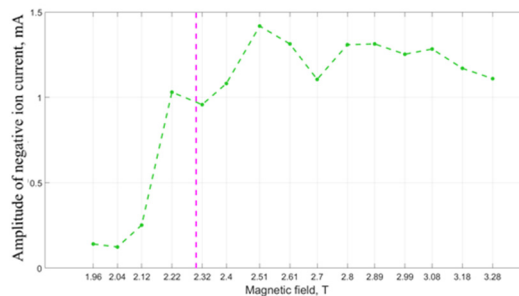


Figure 2: The dependence of extracted on Faraday cup negative ion signal on the strength of the magnetic field with 5 mm extraction aperture. The border of ECR regime is shown with purple line

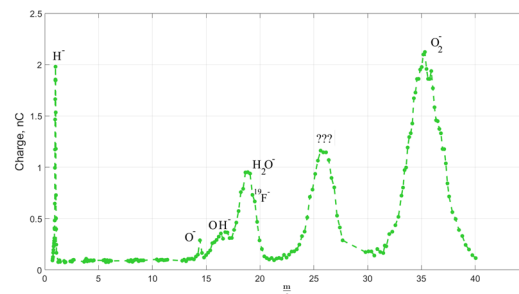


Figure 3: Negative ion spectrum with 5 mm extraction aperture

With the use of the quadrupole mass spectrometer we detected a significant amount of water in the residual gas (see Figs. 4 and 5), which was reduced by means of long-term heating and pumping. The H⁻/O₂⁻ ratio was found to be 2/3 after conditioning of the plasma chambers.

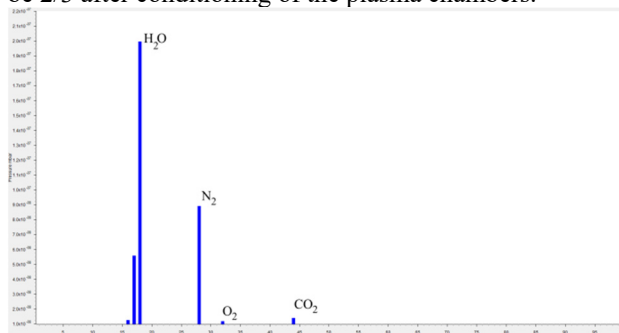


Figure 4: The spectrum of residual gas before final pump out

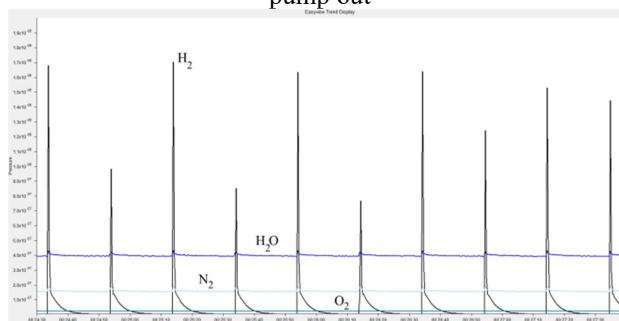


Figure 5: The gas spectrum in the diagnostic chamber during pulsed H₂ injection after the final pump out

Content from this work may be used under the terms of the CC BY 3.0 licence (© 2018). Any distribution of this work must maintain attribution to the author(s), title of the work, publisher, and DOI.

Next stage of the experiments was performed with the plasma aperture of 1 mm and puller aperture of 3 mm spaced 11 mm apart. By tuning the extraction voltage and the gas pressure (both time delay and upstream pressure) a total negative ion current of 0.8 mA was achieved at $U_{\text{extr}} = -20.4$ kV. The dependence of the negative ion current on the extraction voltage for two pressures is shown in Fig. 6. It was shown that after the above-mentioned measures the percentage of impurity ions substantially decreased (see Fig. 7).

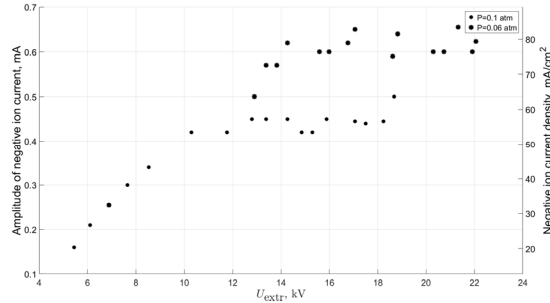


Figure 6: The dependence of the negative ion current and current density on the extraction voltage for several values of pressure in the gas feed line with 1 mm extraction aperture

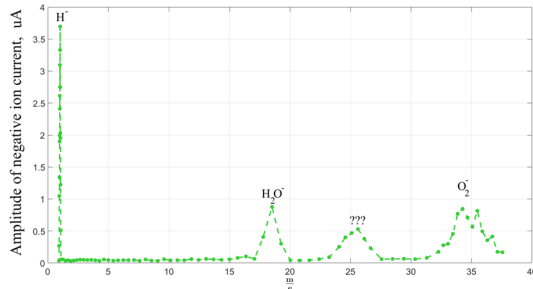


Figure 7: Negative ion spectrum with 1 mm extraction aperture

It is known that the conditions for H_2^+ generation and for the first stage of H^- generation, i.e. populating high vibrational levels through electronic excitation, are similar. As can be seen from Fig. 8, which depicts the spectrum of positive ions extracted from the plasma, there was a presence of such positive ions: the ratio of H^+ / H_2^+ is about 7-8 times, which implies a significant difference between the achieved and optimal conditions for H^- production. We plan to use the ratio as an indicator for future optimization of our experimental conditions.

The next stage of the experiments was performed with 3 mm plasma electrode aperture and 5 mm puller aperture spaced 11 mm apart. A 1.5 mA total current of negative ions was achieved at $U_{\text{extr}} = 24.7$ kV (see Fig. 9). Decreasing the distance between the electrodes by 5 mm provided the maximum total current of negative ions of 1.1 mA - this can be seen in Fig. 10, where the dependence of the current on the voltage for different values of pressure upstream of the valve for this extraction system is depicted.

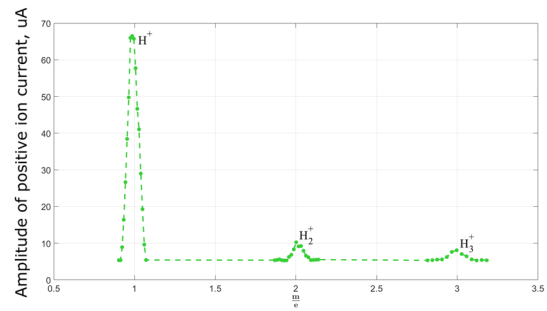


Figure 8: Positive ion spectrum with 1 mm extraction aperture

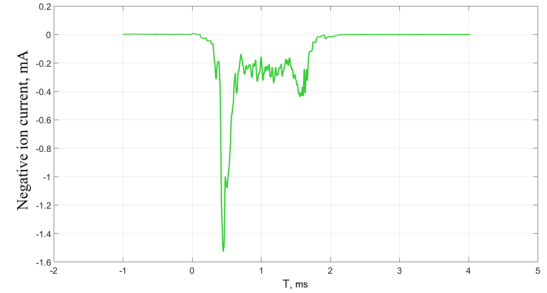


Figure 9: A typical negative ion oscillogram with 3 mm extraction aperture

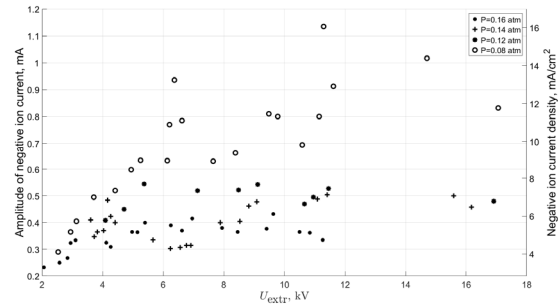


Figure 10: The dependence of the negative ion current and current density on the extraction voltage for several values of pressure in the gas feed line with 3 mm extraction aperture

CONCLUSIONS

We measured dependencies of the negative ion current on various parameters of the two chamber high-frequency gasdynamic ECRIS, leading to the optimization of the extraction system and the gas feed line pressure. A negative ion current density of 80 mA/cm² through 1 mm plasma electrode was demonstrated.

REFERENCES

- [1] Skalyga, V. A., Izotov, I. V., Razin, S.V., Sidorov, A. V., Golubev, S.V., Kalvas, T., Koivisto, H., Tarvainen, O, "High current proton beams production at Simple Mirror Ion Source", *Rev. Sci. Instrum.*, vol. 85, n°. 2. pp. 02A702-1-3, 2014
- [2] Bacal, M., "Physics basis and future trends for negative ion sources" *Nuclear Fusion*, vol. 79, n°2, (2008)

Content from this work may be used under the terms of the CC BY 3.0 licence (© 2018). Any distribution of this work must maintain attribution to the author(s), title of the work, publisher, and DOI.

- [3] Lapin, R. L., Skalyga, V. A., Izotov, I. V., Golubev, S. V., Razin, S. V. and Tarvainen, O. "First experiments on applying the gasdynamic ECR ion source for negative hydrogen ion production" *EPJ Web Conf.* vol. 149. P. 02026-1-2, (2017)
- [4] Keller, R., Luft, P., Regis, M., Wallig, J., Monroy, M., Ratti, A., Syversrud, D., Welton, R., Anderson, D. "A Hybrid Ion-Source Concept for a Proton Driver Front-End" *AIP Conf. Proceedings, American Inst. Of Physics, Melville, NY.* vol.773, p. 104–106, (2005)

DEVELOPMENT OF 2.45 GHz ECR ION SOURCES AT IMP

Q. Wu^{1,2,†}, Y.G. Liu¹, J.L. Liu¹, H.Y. Ma¹, L.T. Sun¹, and H.W. Zhao¹, ¹Institute of Modern Physics (IMP), Chinese Academy of Sciences, Lanzhou 730000, People's Republic of China,
²also at University of Chinese Academy of Sciences, Beijing 100049, People's Republic of China

Abstract

The Ion Source Group at IMP has undertaken series of high intensity ion beam R&D projects. The first project is the development of the intense proton source and low energy beam (LEBT) for China Initiative Accelerator Driven Sub-Critical reactor (CiADS). The specific characteristics of the proton source are long term operation reliability and beam manipulation for the commissioning needs of the SRF accelerator. A low energy beam transport system is used to deliver 35 keV H⁺ beam to the entrance of a 2.1 MeV RFQ. And then the 2.1 MeV proton beam is further accelerated by the superconducting cavities to 25 MeV and eventually goes into a high power beam dumper. The 2nd project is the development of the intense ion source for Jinping underground Nuclear Astrophysics experiments (JUNA). The ion source was requested to provide 10 emA H⁺, 10 emA He⁺ and 2.5 emA He²⁺ beams for the study of (p, γ), (p, α), (α, p) and (α, γ) reactions in the first phase of the JUNA project. The main challenges of ion source for JUNA project are production of intense He²⁺ beam, control of the beam contaminations and wide beam energy range (70~800keV) beam commissioning. Other projects mainly include the development of pulsed intense proton source and LEBT for Compact Pulsed Hadron Source (CPHS) at Tsing Hua university and the commissioning of an intense H₂⁺ ion source. In this paper, the studies of this intense beam injector system, for instance, beam intensities, species and ratio, beam transmission efficiency in LEBT and also the beam matching to the downstream accelerator system will be presented.

INTRODUCTION

The Ion Source Group at IMP has undertaken series of high intensity ion beam R&D projects including development and operation of intense proton source for intense beam accelerators and special experimental platform. A project named China Initiative Accelerator Driven Sub-Critical (CiADS) was launched and begun construction in 2011 by Chinese Academy of Sciences¹⁻³. The CiADS project mainly included superconducting Linac, a spallation target and beam line. The major target of superconducting linac is to demonstrate the key

technologies of 10 mA CW beam of superconducting front-end linac. As a key component of linac, the performance of ion source is very important. a 2.45GHz ECR ion source with the energy of 35 keV was developed to meet the requirements of superconducting linac. Next project named Jinping underground nuclear astrophysics (JUNA) project. Experimental investigations of such tiny reaction rates in laboratories at the earth's surface are hampered by the cosmic-ray back ground into detectors. Jinping Underground Laboratory for Nuclear Astrophysics is being constructed. The project need design of a 10mA, 400kV accelerator. Electron Cyclotron Resonance (ECR) ion source is selected to produce required ion beams such as H⁺, He⁺, He²⁺. The 2.45 GHz ECR ion source has been proved to be able to produce very high beam currents and was successfully used in ADS at the Lanzhou Institute of Modern Physics [1]. Detailed reports on ion source and the elements of beam transport on the platform will be introduced in addition. In this paper, the status of ion source of CiADS project and development of JUNA project were present.

I. RUNNING STATUS OF THE INTENSE PROTON SOURCE FOR ADS LINAC

To produce the requested 10 mA proton beam for China Accelerator Driven Sub-Critical system(C-ADS) [2,3], electron cyclotron resonance (ECR) ion source operating at 2.45 GHz have been developed. As shown in Fig. 1, the cutaway view is the configuration of the proton source and extraction system. The proton source includes a waveguide, all-permanent magnet source body and discharge chamber. A dual-ridge waveguide is connected with the plasma chamber through the microwave window in order to couple microwave power efficiency. The plasma chamber was made of copper, which is 70 mm long and 54 mm in diameter. In order to obtain the small initial emittance, a diameter of 4 mm hole was designed to extraction proton beam. A 3-electrode extraction geometry was designed to extract the 20 mA, 35 keV ion beam. Meanwhile, in order to enhance the operation life of plasma electrode, the Molybdenum electrode with high temperature resistance was fabrication.

† wuq@impcas.ac.cn

Content from this work may be used under the terms of the CC BY 3.0 licence (© 2018). Any distribution of this work must maintain attribution to the author(s), title of the work, publisher, and DOI.

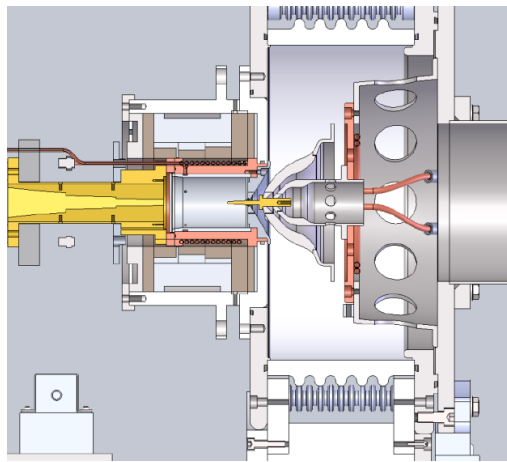


Figure 1: Configuration of the proton source and extraction system.

In order to ensure SRF commissioning and reliability of MPS, an electrostatic-chopper has been installed in the LEBT line that can chop the beam into a pulsed one, and an on-line beam current tuning device was installed in the LEBT to obtain a step value of 0.1mA. In order to obtain the continuously variable beam currents, a set of specially designed on-line tunable circular beam slit has been developed, as shown in Fig. 2. Based on the calculation of proton beam envelope, the maximum diameter of the slit aperture was set to 40 mm. By adjusting the slit opening, the relationship between the aperture and passing beam current could be built. This is very useful tool to control the beam conditions for downstream linac commissioning. And thus it can obviously improve beam commissioning efficiency and reduce the beam loss in the accelerator. The total operation time of the proton source is up to 4000 hours since 2014. Figure 3 shows the operation log with the time of 240 hours. During the machine commissioning with 10 mA pulse beam at 35 keV with a repeat frequency of 1Hz, pulse width of 20 μs for beam emittance measurement and correction of the beam orbit in the MEBT. Many beam trips caused with linac MPS were seen in Fig. 3. During the commissioning period, the Superconducting linac was successfully accelerating the 12.6 mA pulse beam with the energy of 26.1 MeV, a repeat frequency of 1Hz. The 25MeV SRF Linac has been the first superconducting accelerator prototype in the world.

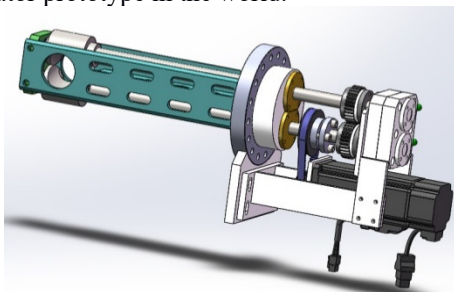


Figure 2: Continuous aperture with servodriven

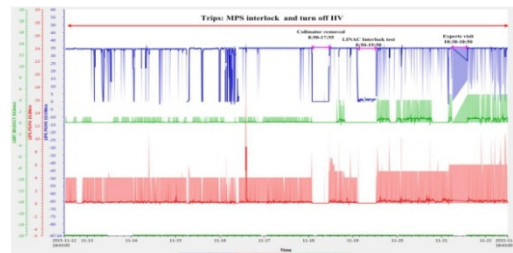


Figure 3: Operation log of the ion source with the time of 240 hours

II. COMMISSIONING RESULTS OF INTENSE BEAM ION SOURCE FOR JUNA PROJECT

The 400 kV high current accelerator is designed to deliver intense low energy proton and alpha beams for JUNA experiments. In 2017, the ion source and LEBT had been successfully developed and connected to the accelerator tube on the ground at Beijing city. Figure 4 shows the front view of the 400 kV accelerator facility. The ECRIS and LEBT system was floated on the 400 kV high voltage platform. In order to research the reliability of the ion source, a 3 hours uninterrupted reliability test has been done with the beam energy of 50 keV and the current intensity of 16.0 mA. The result is shown in Fig. 5, where the red solid line is beam energy, and the blue line represents the total beam current of helium.



Figure 4: Front view of the 400kV high voltage accelerator

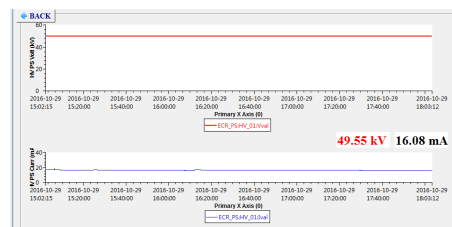


Figure 5: Beam reliability of helium was monitored for 3 hours at the energy of 50 keV

RESULTS

The first stage of the experiments was performed with an extraction system consisting of a 5 mm aperture plasma electrode and a 10 mm aperture puller electrode separated by 11 mm. The following scheme of gas

CONCLUSIONS

We measured dependencies of the negative ion current on various parameters of the two chamber high-frequency gasdynamic ECRIS, leading to the optimization of the extraction system and the gas feed line pressure. A negative ion current density of 80 mA/cm² through 1 mm plasma electrode was demonstrated.

REFERENCES

- [1] Y. He, Z. J. Wang, Y. Liu, X. Chen, H. Jia, Y. Yao, B. Zhang, and H. W. Zhao, "The conceptual design of injector II of ADS in China," in *Proceedings of the IPAC, WEPS053*, 2011.
- [2] Q. Wu, Z. M. Zhang, L. T. Sun *et al. Rev. Sci. Instrum* vol. 85, p. 02A703 (2014).
- [3] Q. Wu, H. Y. Ma, Y. Yang, Z. M. Zhang, L. T. Sun *et al. Rev. Sci. Instrum.* vol. 87, p. 02B903 (2016).

DEVELOPMENT OF A TEST BENCH OF 2.45 GHz ECR ION SOURCE FOR RFQ ACCELERATOR

Sudhirsinh Vala[†], Ratnesh Kumar, Mitul Abhangi, Rajesh Kumar and Mainak Bandyopadhyay,
Ins-titute for Plasma Research, 382428 Gandhinagar, India
also Homibhabha National Institute, 400094 Mumbai, India

Abstract

The optimization of beam quality at the entrance of a RFQ system requires a test bench for the optimization of the ion source and beam parameters. The aim of this test bench is to produce a 5 mA proton/deuterium beam with rms normalized emittances lower than 0.2 pi.mm.mrad for the 5 MeV RFQ. This bench consists of an indigenously developed permanent magnet based 2.45GHz ECR ion source with three electrode ion extraction system and a LEBT to match the beam for the injection into the RFQ. The LEBT system has been designed using TRACEWIN© code. The LEBT parameters have been optimized in order to maximize the beam transmission through the RFQ. The ECR ion source test bench has been setup and operated up to 50 kV. The plasma parameters of the ECR ion source have been measured using optical emission spectroscopy system. The electron temperature and electron density are typically 3.6 eV to 1.3 eV and $1-6 \times 10^{19} \text{ m}^{-3}$ at chamber pressure in the rang of 10^{-4} torr to 10^{-5} torr respectively. Deuterium ion beam of 9.8 mA is extracted from the test bench. This paper presents the design of the test bench, results of latest extracted ion beam and plasma parameters

INTRODUCTION

Institute for Plasma Research is developing a Radio Frequency Quadruple (RFQ) based 5-MeV accelerator facility for fusion material studies. The 5-MeV RFQ accelerator is mainly consist of an ECR ion source, a Low Energy Beam Transport (LEBT) system and a RFQ [1]. The low-energy transport between the ion source and the RFQ, is probably the utmost complex portion of any linear accelerator. LEBT plays an important role to transport the beam from ion source to RFQ as well as in matching the beam properties at the injection plane of the RFQ i.e., twiss parameters α_{Twiss} , β_{Twiss} , γ_{Twiss} and the emittance ϵ . The main objective of the development of this ECR Ion Source (ECRIS) test bench is to produce a 5 mA H⁺/D⁺ pulse/CW ion beam up to 50 keV energy with rms normalized emittance lower than $0.2 \text{ pi}\cdot\text{mm}\cdot\text{mrad}$, as per the requirements of the RFQ accelerator. This paper presents development of the test bench setup, results of ion beam extraction and plasma parameters and the design of the LEBT system.

SETUP OF ECR ION SOURCE TEST BENCH

ECR ion source test bench consists indigenously developed 2.45 GHz ECR ion source followed by three electrode ion extraction system, Einzel lens, vacuum chamber, beam profile monitor, faraday cup and the control system. The photograph of the ECR ion source test bench is shown in Fig.1.

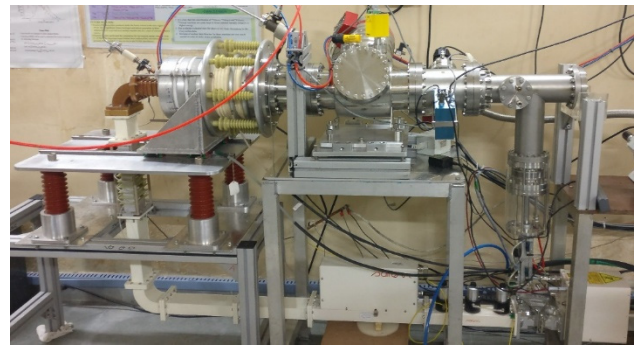


Figure 1: Experimental setup of ECR ion source test bench.

The ECR ion source is floated on a 50 kV high voltage platform. 50 kV HVDC isolation break is present between the ECR ion source and the 2.45 GHz microwave source system. 2.45 GHz microwave is transferred from the microwave source to the plasma chamber of the ECRIS through 3-stub tuner, 50 kV HVDC break, vacuum window, 90 degree bend and a 3-step ridge wave guide. Two 3mm Boron nitride disks are placed at the both end of the circular water cooled plasma chamber. One boron nitride disk at inlet side protects the microwave system from the back streaming electrons from the plasma and also provide the vacuum barrier between the plasma chamber and microwave system. The other disk, near the extraction side, covers the plasma electrode to avoid the high outgassing during plasma discharge [2]. To achieve the resonance magnetic field of 0.0875 T for 2.45 GHz frequency, three axially magnetized permanent NdFeB ring magnets are used. Each ring consists of 24 elementary NdFeB magnet of pre-defined shape and sizes [3-4].

To extract the high quality bright beam from the ECR ion source, a three electrode accel-decel system have been installed. In accel- decel extraction system, first plasma electrode placed at positive 50kV followed by accel electrode at the -2 kV and then decel electrode at ground potential.

[†] sudhir@ipr.res.in

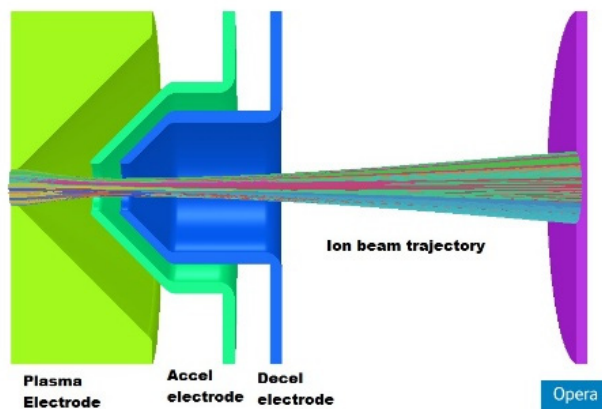


Figure 2: Simulation results of ion beam trajectory of Three Electrode extraction system .

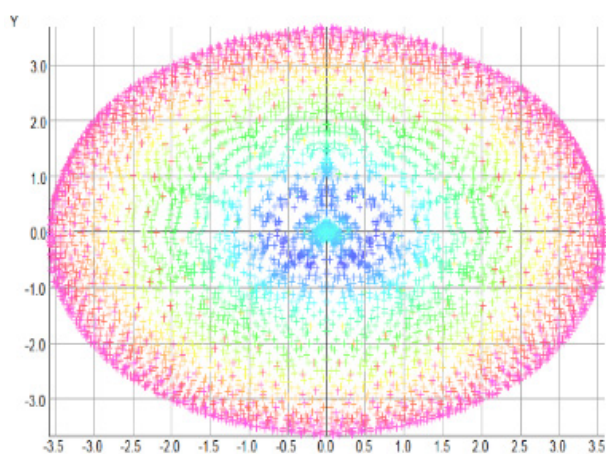


Figure 3: Simulation results of Particle distribution.

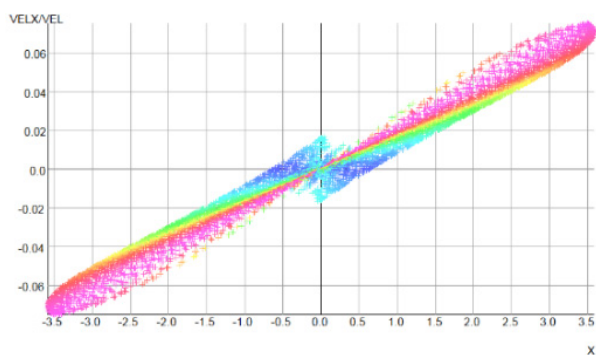


Figure 4: Emittance plot

The extraction aperture of the plasma electrode, accel electrode and decel electrode are 6 mm, 8mm and 8mm respectively. The gap between plasma electrode to accel electrode and accel electrode to decel electrode are 12 mm and 2mm respectively [5-6]. The optimization of electrode size and shape is done with Opera-3D particle trajectory simulation code [7]. The simulated particle trajectory of the extracted deuterium beam and the results of simulated beam profile are shown in Figs. 2 and 3. The calculated normalized emittance of the simulated ion beam is 0.21 pi

mm mrad. The Phase plot of the emittance is shown in Fig. 4. To focus the extracted ion beam into the LEBT, three electrode Einzel system has been installed in the test bench. In the Einzel lens, the outer two electrodes are placed at the ground potential and the middle electrode is supplied up to 20 kV positive high voltage [8]. Each electrode is fabricated using ETP copper having same dimension of 63 mm internal diameter and 53 mm in length. Both outer electrodes are separated by 10mm gap from the middle electrode. Beam focusing simulation have been performed with LORENTZ 3EM code and its ion beam trajectory is shown in Fig. 5 [9]. All the electrodes are placed in the stainless steel vacuum chamber with 35 kV high voltage feed through. The photo graph of the Einzel lens assembly is shown in Fig. 6.

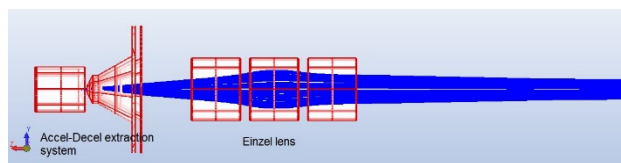


Figure 5: Ion beam trajectory profile using einzel lens.

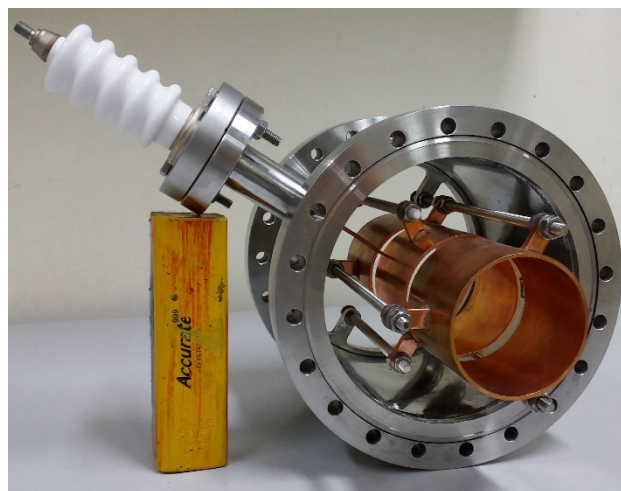


Figure 6: Photographs of Einzel lens assembly.

For the diagnostic of the ion beam parameters, a wire scanner type NEC make beam profile monitor (Model No: BPM-83) and a Pantechnik make faraday cup have been installed in the test bench. One set of turbo molecular pumping system with valves and gauges have been integrated in the test bench to achieve base vacuum of the order of $\sim 10^{-7}$ torr.

Control system of ECR ion source plays an important role in the safe and stable operation of the test bench. The Programmable Logic Control (PLC) based control system is adopted to control the ECRIS. This control system consists of status monitor, status control and device control. The 2.45 GHz microwave source, 50 kV extraction power supply, -3kV accel power supply, 20 kV focusing power supply and mass flow controller have been controlled by 0-10 V analog signal. TMP, Water chiller and hydrogen generator are controlled by digital signal.

RESULTS AND DISCUSSIONS

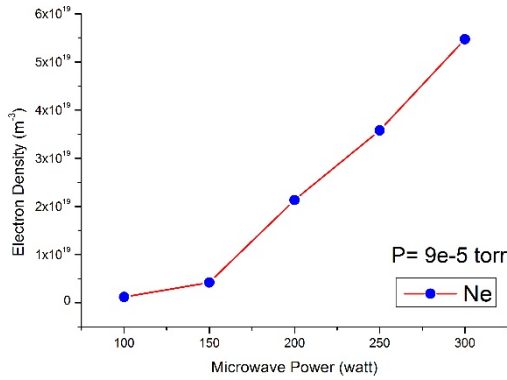


Figure 7: Results of electron density measurement as function of microwave power.

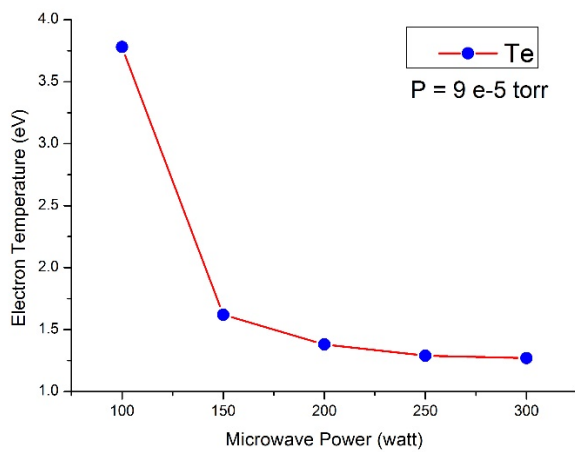


Figure 8: Results of electron temperature measurement as function of microwave power.

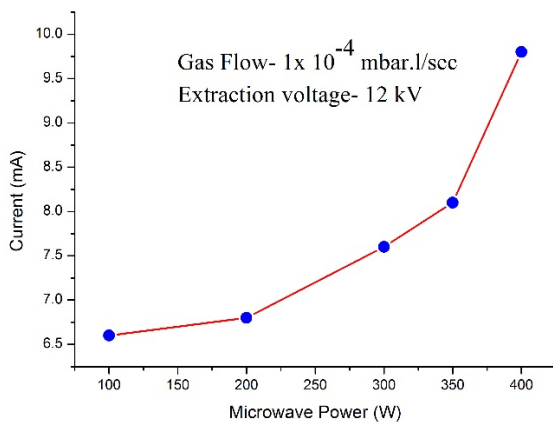


Figure 9: Results of beam current measurement as function of microwave power.

Prior to the fitting of the ion extraction system, the plasma parameters were measured with the optical spectroscopy system [10]. In first set of experiment, the electron density and electron temperature were measured as function of chamber pressure (10^{-4} torr to 10^{-5} torr) and microwave

power (100W-300W). The electron temperature and electron density were typically 3.6 eV to 1.3 eV and $1-6 \times 10^{19} m^{-3}$. Measurements of plasma temperature and density are shown in Figs. 7 and 8. It is found that plasma is over dense.

The ECR ion source has been tuned for extraction of deuterium ion beam. The beam current as a function of microwave power with constant gas flow rate of 1×10^{-4} mbar l/s were measured and the results of it is shown in Fig. 9. Maximum 9.8 mA deuterium beam current was extracted at 400 W microwave power and 14 kV extraction voltage. During experiment it is observed that the focusing of ion beam by einzel lens is not effective for high current ion beam. It is decided to replace the einzel lens by a magnetic lens to achieve a better focusing.

DESIGN OF LEBT

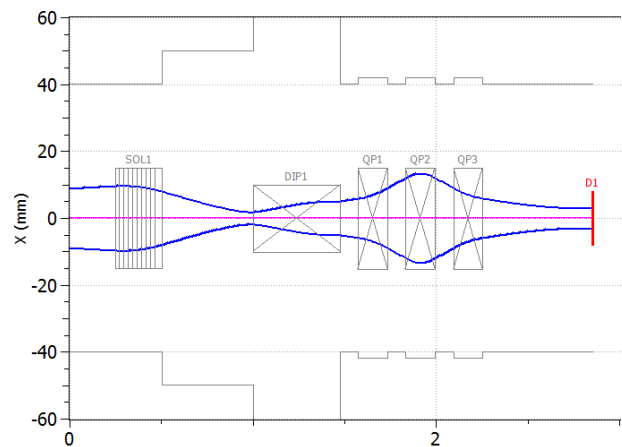


Figure 10: Beam envelop of x-axis for 7 mA ion beam current through LEBT.

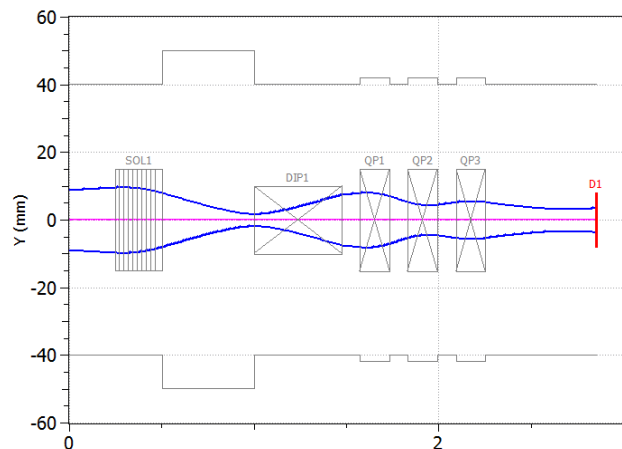


Figure 11: Beam envelop of Y-axis for 7 mA ion beam current through LEBT.

LEBT consists of Magnetic lens (solenoid), Analysing magnet, Quadrupole Magnetic Triplet (QMT) and diagnostics for beam parameters. The conceptual parameters for the beam line components are frozen by analytical calculations. The design of the LEBT has been done using the TRACEWIN code [11]. The LEBT transports the beam

Content from this work may be used under the terms of the CC BY 3.0 licence (© 2018). Any distribution of this work must maintain attribution to the author(s), title of the work, publisher, and DOI.

from the ECR ion source to the entrance of the RFQ. The solenoid focuses the extracted ion beam into the 90 degree analysing magnet, which analyses the ion beam and separates the un-wanted ion species from the ion beam and transports the D^+/H^+ ions. The analysed D^+/H^+ ion beam is again focused into the RFQ by using QMT and then to the beam diagnostics system. The beam diagnostics system includes Beam Profile Monitor (BPM), Emittance scanner and Faraday cup to measure the beam profile, emittance and beam current respectively. The space charge effect has been observed during the simulation and same is optimized during the iteration of the simulation by Space Charge Compensation (SCC). The provision of the SCC is incorporated in the design of LEBT. The optimized beam envelop of x-axis and y-axis for 7 mA ion beam current with 90% SCC are shown in the Figs.10 and 11.

FUTURE PLANS

For the better focusing of the ion beam in to the LEBT, Einzel lens will be replaced with the magnetic lens (Solenoid). Typical length of the solenoid is 255 mm with 0.35 T uniform magnetic field. It is under fabrication and it will be installed soon. To measure the beam emittance at RFQ entrance, dual Allison emittance scanner will be integrated in to the test bench.

SUMMARY

The ECR ion source test bench has been set up and the ECR plasma has been generated using microwave power 100–400 W. The plasma parameters are measured in the ion source using optical spectroscopy method. The measurement of plasma density with different microwave power shows that the plasma is over dense and density of plasma is 500 times than critical density. The extraction system and focusing system have been mounted on ECR ion source test bench and it has been tuned for the beam extraction as function of extraction voltage, microwave power and gas flow rate.

ACKNOWLEDGMENT

The authors wish to acknowledge the assistance and contribution of Mr. Sanket Chauhan for design, fabrication and installation of ECRIS test bench and Ms. Payal Mehta for the measurement of the plasma parameter of the ECR ion source.

REFERENCES

- [1] R. Bahl *et al.*, *Proceedings of IPAC'16*, Busan, Korea
- [2] R. Gobin *et al.*, *Proceeding of ECRIS'12*, Sydney, Australia.
- [3] R. Gobin *et al.*, *Review of Scientific Instruments*, vol. 77, p. 03B502, 2006.
- [4] O. Tuske *et al.*, *Review of Scientific Instruments*, vol. 79, p. 02B710, 2008.
- [5] M. Zhang *et al.*, *Review of Scientific Instruments*, vol. 81, p. 02B715, 2010.
- [6] R. Keller *et al.*, *Review of Scientific Instruments*, vol. 81, p. 02B311, 2010.
- [7] <https://operafea.com>
- [8] Omer Sise *et al.*, *Nuclear Instruments and Methods in Physics Research A*, vol. 554, pp. 114-131, 2005.
- [9] www.integratedsoft.com
- [10] A.T.T. Mostako *et al.*, *IEEE Transactions on Plasma Science*, vol. 44, pp. 7-14, 2016.
- [11] <http://irfu.cea.fr>

Content from this work may be used under the terms of the CC BY 3.0 licence (© 2018). Any distribution of this work must maintain attribution to the author(s), title of the work, publisher, and DOI.

DEVELOPMENT OF COMPACT 2.45 GHz ECR ION SOURCE FOR GENERATION OF SINGLY CHARGED IONS

S. L. Bogomolov[†], A. E. Bondarchenko, A. A. Efremov, Yu. E. Kostyukhov, K. I. Kuzmenkov, V. N. Loginov, D. K. Pugachev, JINR, 141980, Dubna, Russia, R. D. Fatkullin, ITEP, 117218, Moscow, Russia

Abstract

2.45 GHz ECR ion sources are widely used for production of single charged heavy ions and secondary radioactive ion beams. This paper describes the development of a compact ECR ion source based on coaxial quarter wave resonator. The first results of extracted current measurements at different resonator configuration as a function of UHF frequency, power and gas flow are presented. At the extraction voltage about of 10 kV and UHF power about of 100 W more than 500 μA of He^+ ions were produced with the extraction hole of 3 mm in diameter that corresponds to the current density 7.5 mA/cm^2 .

INTRODUCTION

Several ECR ion sources for production of radioactive ion beams operating at 2.45 GHz were developed at the FLNR JINR [1]. Such ion sources are used for production of $^6\text{He}^+$ ions in the DRIBs project [2] and at the MASHA mass-spectrometer [3]. The magnetic system of such sources is composed of NdFeB permanent magnet rings, and it provides the creation of pseudo-closed resonant surfaces (875 Gs). The plasma chamber of such sources is based on a single-mode cylindrical resonator with an internal diameter of 90 mm and a length of 100 mm. The measured gas efficiency of those sources is about 90% for noble gases (Ar, Kr). The transformation time of atoms into ions of this ion source has not been investigated yet, however, according to the results of paper [4], this time decreases with the decrease of the plasma chamber volume.

The volume of plasma chamber can be reduced if the chamber will be based on a coaxial resonator loaded with a capacitor. Pseudo-closed surfaces should be located in the gap of the capacitor to achieve optimum conditions for plasma confinement. In this paper we present the further investigations of the developed ion source [5].

DESIGN OF THE SOURCE

The magnetic system of the source is composed of a radially magnetized ring with an external diameter of 52 mm, an inner diameter of 22 mm and a thickness of 10 mm. The distribution of the magnetic field on the axis of the ring is shown in Fig. 1, the lines of an equal

field are shown in Fig. 2. It can be seen that this magnetic system provides creation of pseudo-closed surfaces with a field level from 875 Gs up to 1750 Gs.

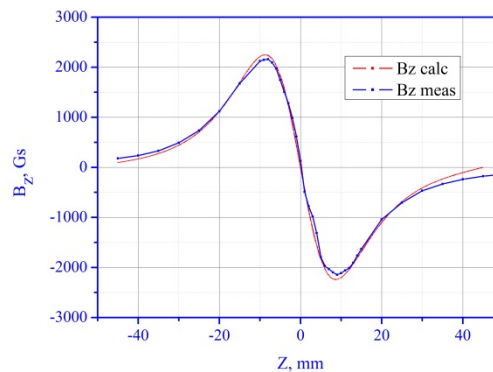


Figure 1: Axial magnetic field distribution of a ring magnet.

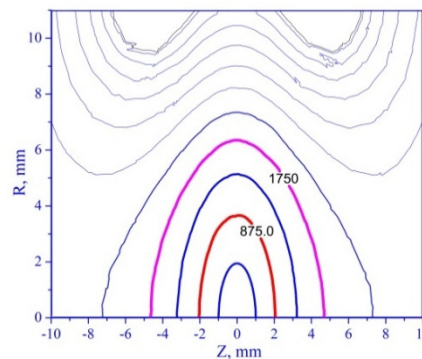


Figure 2: Magnetic field contour plot.

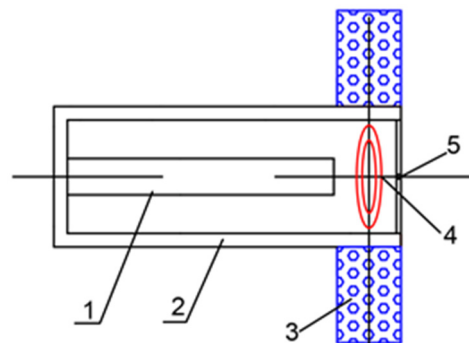


Figure 3: Schematic structure of the ECR ion source based on a coaxial resonator. 1 - central conductor of a coaxial resonator; 2 - resonator casing; 3 - magnetic

[†] sbogomolov@jinr.ru

ring; 4 - closed lines of the magnetic field; 5 - extraction hole.

Schematic structure of the source is shown in Fig. 3, the closed surfaces of the magnetic field are located in the gap between resonator electrodes.

In the source design we decided to use existing N-type connector with KF16 (16 mm internal diameter and 7 mm diameter of central conductor) flange. From the constructional point of view the geometry of resonator with cone transition from internal diameter 25 mm to diameter 16 mm, which fits the internal diameter of the magnet, was chosen. The resonator was designed using CST Studio Suite [6]. The computational model of resonator with cone transition is shown in Fig. 4.

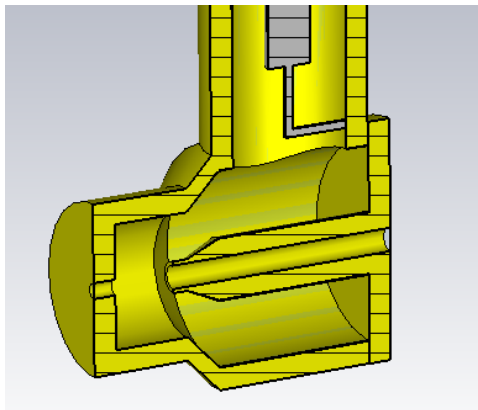


Figure 4: Computational model of coaxial resonator with cone transition.

In a process of calculations the geometrical parameters of resonator were determined for discharge gaps 5, 8 and 10 mm (see Fig. 2). These gaps contain the closed lines of magnetic field 875, 1313 and 1750 Gs correspondingly. The Q factor of resonator was determined about 3500 for all gaps value. Figure 5 shows the calculated electric field in the resonator gap as a function of power for different gap value.

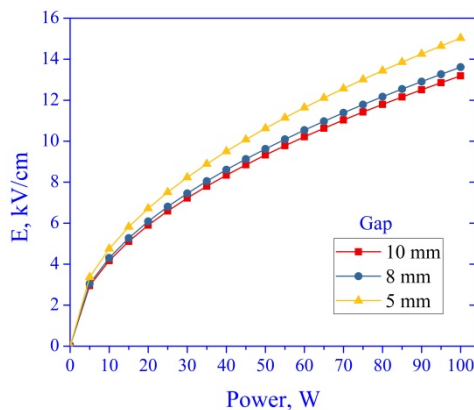


Figure 5: Electric field in the resonator gap as a function of input power.

Based on the modelling results, an ECR ion source was designed and manufactured. Assembly drawing of the source is presented in Fig. 6. The view of the source is presented in Fig. 7.

For changing the resonator gap three sets of the replaceable internal parts of resonator and replaceable plasma electrodes were used, providing the gap sizes of 5, 8 and 10 mm. The diameter of the extraction hole in plasma electrodes is 2 mm.

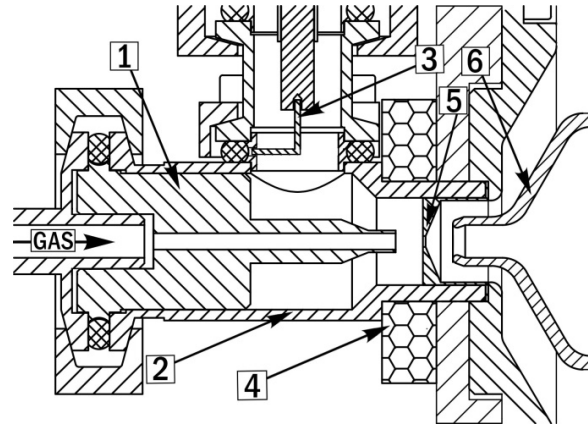


Figure 6: Assembly drawing of ECR ion source: 1 - replaceable internal part of the resonator, 2 - resonator casing, 3 - coupling loop, 4 - permanent magnet ring, 5 - replaceable plasma electrode, 6 - pulling electrode.

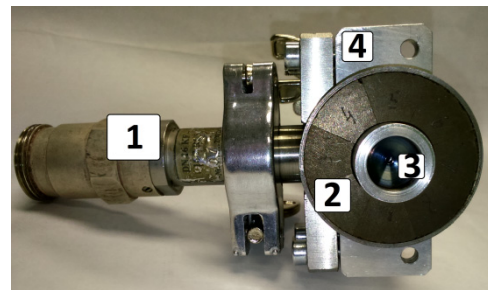


Figure 7: The view of ECR ion source: 1 - coaxial feedthrough, 2 - magnet ring, 3 - plasma electrode, 4 - resonator casing.

EXPERIMENTAL RESULTS

Preliminary Tests

For the preliminary tests the source was mounted on the vacuum volume pumped by the 150 l/s turbopump providing the base vacuum about of $2 \div 4 \times 10^{-6}$ torr. During the source operation the pressure in vacuum chamber was about of 1.2×10^{-5} torr. Solid state UHF generator with the output power up to 100 W in the frequency range of 2.4 ÷ 2.5 GHz was used to feed the source. The UHF power was fed to the coupling loop through a coaxial cable and tuner. Control of the gas flow was performed by the piezoelectric leak valve. A negative potential about of 300 V was applied to the pulling electrode. During tests the current of ions

Content from this work may be used under the terms of the CC BY 3.0 licence (© 2018). Any distribution of this work must maintain attribution to the author(s), title of the work, publisher, and DOI.

incident on the pulling electrode was measured. Argon was used as a working gas. The distance between the plasma electrode and pulling electrode equals to 5 mm in all experiments.

The source was successfully ignited, and Fig. 8 shows the argon plasma view through the gridded plasma electrode. The diameter of the hole covered by grid equals to 12 mm.



Figure 8: Ar plasma view through the gridded plasma electrode at 20W, 2450 MHz.

As a first test we study the minimal ignition power for different resonator gaps as a function of frequency at fixed gas flow (Fig. 9). We consider the discharge is ignited when pulling electrode current of few microamperes is registered. It can be concluded that in a certain frequency range 2450 ÷ 2465 MHz for 10 mm gap, 2430 ÷ 2460 MHz for 8 mm gap and 2425 ÷ 2435 MHz for 5 mm gap, the lowest power (about of 0.5 W) required for ignition is observed. The average required power over the whole frequency range is minimal for 5 mm gap, and maximal for 10 mm.

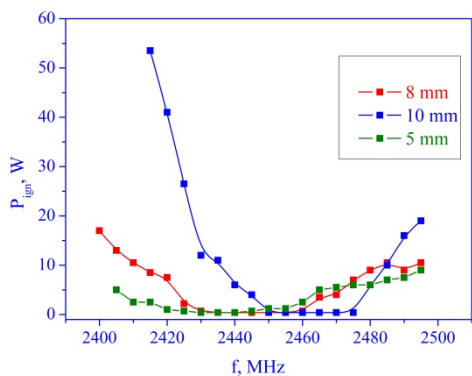


Figure 9: Dependence of the ignition power on the generator frequency for different resonator gaps at fixed gas flow.

The dependence of the ion current on the generator frequency for various resonator gaps at fixed power (20 W) and gas flow is shown in the Fig. 10. For all values of resonator gap the current increases with the frequency of generator. The highest current was produced with resonator gap of 8 mm. All other measurements were performed with this gap value.

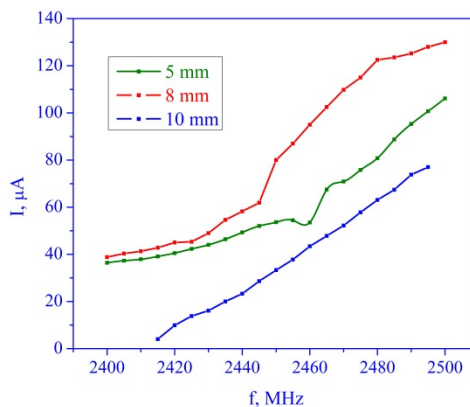


Figure 10: Dependence of the ion current on the generator frequency for different resonator gaps at 20 W.

Figure 11 presents the dependence of the ion current on the generator power at fixed and adjustable gas flow. At fixed gas flow the current shows the saturation with the power more than about 30 W, while with adjustable gas flow the current is increasing linearly with the power level above 30 W.

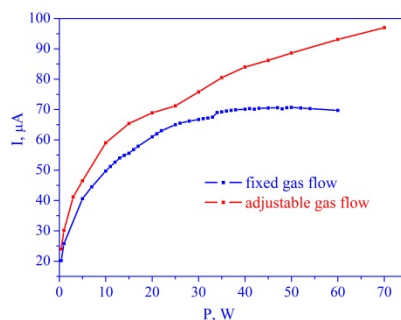


Figure 11: Dependence of the ion current on the generator power at fixed and adjustable gas flow at the frequency 2450 MHz.

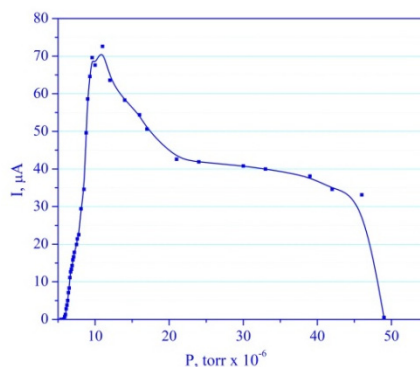


Figure 12: Dependence of the ion current on gas flow.

Figure 12 presents the variation of the ion current with the gas flow (the pressure in the vacuum chamber) at 2450 MHz and 20 W of injected power. By varying the gas flow, one can tune the source for the maximal value of ion current.

Also we checked the influence of the magnet ring centre displacement with respect to resonator gap

centre on the ion current. It was possible to shift the ring towards the plasma electrode to the distance up to 2 mm. The measurements show that the displacement of the magnet ring leads to the decrease of the ion current for the resonator gaps 8 mm and 10 mm.

Experiments At the ECR Test Bench

After preliminary tests the ion source was installed at the ECR test bench which represents a low energy beam transport line with focusing solenoid and 90° analysing magnet. The source can be biased with respect to ground up to 15 kV. All the experiments were performed with He due to insufficient magnetic rigidity of the beam line designed for analysis of multiply charged ions.

At the test bench the influence of the coupling loop length on the value of extracted current was investigated. The geometry of the coupling loop is shown in Fig. 13. The initial length of the loop 8 mm was chosen according to calculations from the point of view minimal VSWR and equivalence of intrinsic and external Q-factor of resonator.

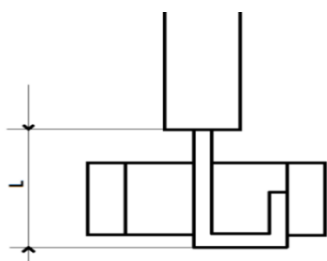


Figure 13: Geometry of the coupling loop.

Three additional loops were manufactured (9, 13 and 15 mm) to establish over coupling mode of communication with the resonator. Over coupling mode is more preferable, since the quality factor of the plasma loaded resonator differs from the intrinsic quality factor of the "empty" resonator, therefore, in the critical coupling mode when the discharge is ignited in the source chamber, the Q factor of the resonator decreases, the VSWR increases and strong reflections arise. Unfortunately, it is nearly impossible to numerically determine the deviation of the intrinsic Q factor from the loaded one using mathematical modelling because of complexity of the processes taking place in the plasma. Therefore, the loops were alternately tested at the source.

The dependence of the He⁺ ion current on the generator frequency was measured for different coupling loop length (Fig. 14). The pressure in the beam line was maintained at the level of ~ 10⁻⁶ torr, extraction voltage U = 8.8 kV, microwave power P = 60 W. For the loop with length of 9 mm the results were very similar to results obtained with the initial loop length. The maximal current (260 μA) was reached for a loop with the length of L = 13 mm,

therefore, optimal matching conditions are observed. All further tests were carried out with this loop.

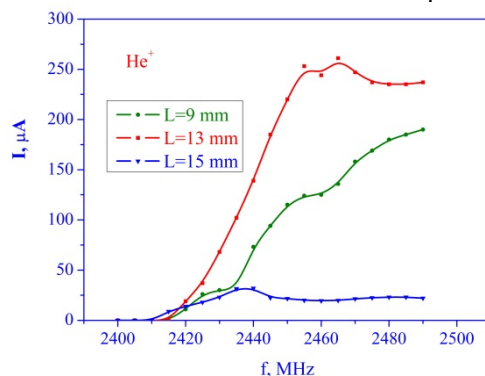


Figure 14: Dependence of the He⁺ ion current on the generator frequency for different coupling loops length.

With the optimized loop we performed the study of influence of injected power, frequency and gas flow on He⁺ ion current. The results were very similar to these one obtained at the preliminary tests. Figure 15 shows the dependence of the He⁺ current on the frequency at different power level. The dependence of the He⁺ ion current is shown at the Fig. 15.

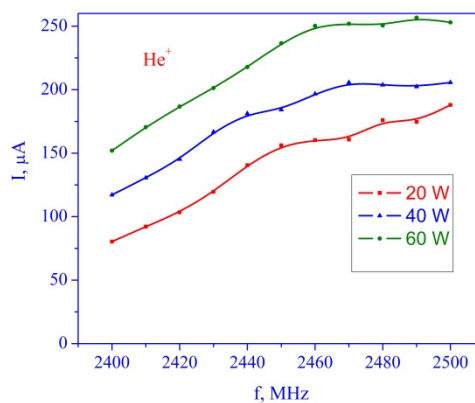


Figure 15: Dependence of the He⁺ ion current on the generator frequency for different power level.

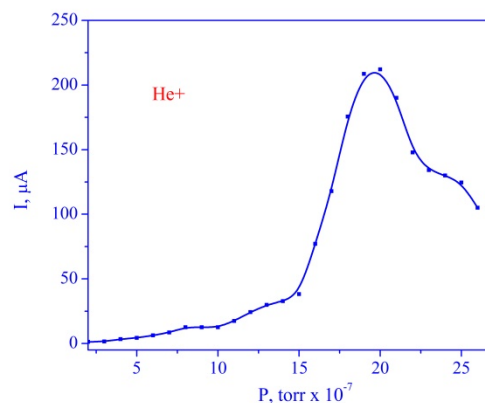


Figure 16: Dependence of the He⁺ ion current on the gas flow at power 20 W, and frequency 2470 MHz.

The dependence of the He^+ ion current on the power at fixed gas flow shows saturation at the power level above 30 W (Fig. 17).

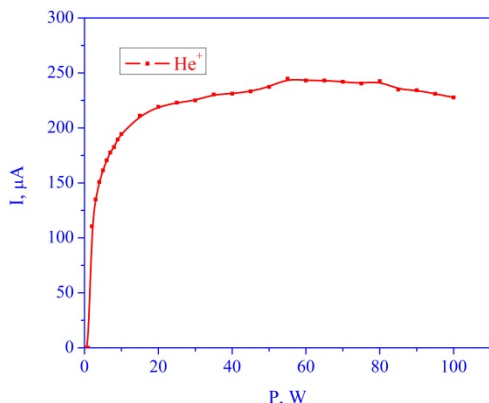


Figure 17: Dependence of the He^+ ion current on the power at frequency 2470 MHz and fixed gas flow.

The dependence of extracted current on the diameter of the extraction hole was investigated. The diameter of extraction hole in the plasma electrode was increased from 2 to 3 mm. Injected power was raised to 100 W. All other parameters were kept by its previous value. By this means, extracted current of He^+ ions increased from 260 μA to 534 μA , that corresponds to the current density $j = 7.5 \text{ mA/cm}^2$.

For the further increase of extracted current we tried to employ well known technique of biased electrode. An insulated aluminium rod 2 mm in diameter was inserted to discharge region axially through the central conductor of resonator (see Fig. 6). Figure 15 presents the He^+ ion current and biased electrode current on bias voltage. He^+ ion current is increased by factor about of 1.4. The saturation of extracted current and biased electrode current with voltage above 30 V is caused by the current limit of power supply. The measurements were performed at 20 W, 2481 MHz and extraction voltage 10 kV.

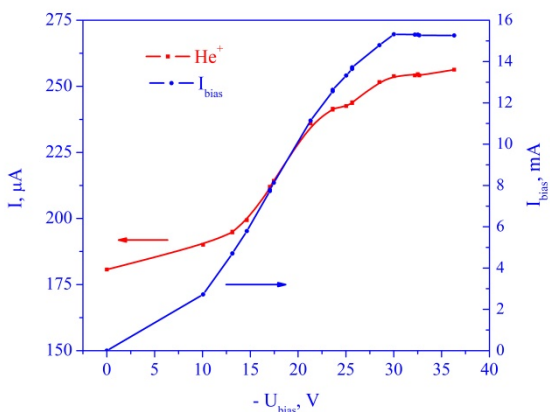


Figure 18: Dependence of He^+ ion current and biased electrode current on bias voltage.

The source was also tested for production of hydrogen ions. The spectrum of hydrogen ions is

shown in Fig. 16. The spectrum contains more than 80% of molecular H_2^+ ions, and about of 3% of protons.

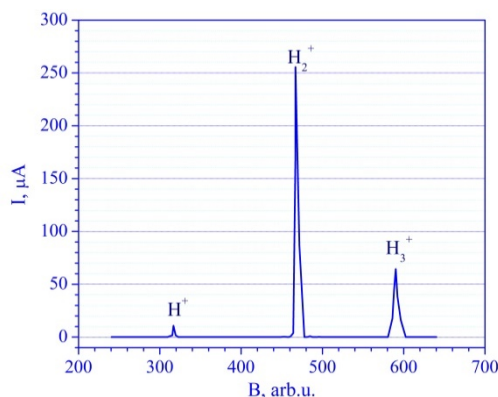


Figure 19: Spectrum of hydrogen ions at 2450 MHz, 60 W and diameter of extraction hole is 2 mm.

CONCLUSION

Compact ECR ion source was designed and tested. The source is suitable for production of low and medium currents of singly charged ions. The current of He^+ ions more than 500 μA is reached with the diameter of extraction hole 3 mm, that corresponds to the current density of 7.5 mA/cm^2 . Promising results are obtained with the use of biased electrode technique. The further study will include the test of the source with heavy ions, such as Kr and Xe, measurements of the gas efficiency and time response of the ion source.

Further investigations required for increasing the proton fraction in the extracted beam.

REFERENCES

- [1] A. Efremov *et al.*, "The 2.45 GHz ECR ion source for the first stage of the DRIBs project," *Nucl. Instr. Meth. Phys. Res. Section B.*, vol. 204, pp. 368–371, 2003.
- [2] G. G. Gulbekian, Yu. Ts. Oganessian, "DRIBs: the Dubna project for radioactive ion beams," in *Proc. of Intern. Conf. on Nuclear Physics "Nuclear Shells — 50 Years". (49th Meeting on Nuclear Spectroscopy and Nuclear Structure). Dubna*, pp. 61-76, 1999.
- [3] Yu. Ts. Oganessian *et al.*, "The project of the mass separator of atomic nuclei produced in heavy ion induced reactions," *Nucl. Instr. Meth. Phys. Res. Section*, vol. 204, pp. 606–613, 2003.
- [4] P. Jardin *et al.*, "Optimization of ECR singly-charged ion sources for the radioactive ion beam production," *Nucl. Instr. Meth. Phys. Res. Section B.*, vol. 204, pp. 377–381, 2003.
- [5] R. Fatkullin, S. Bogomolov, K. Kuzmenkov, and A. Efremov, "Compact 2.45 GHz ECR Ion Source for generation of singly-charged ions," *EPJ Web of Conferences*, vol. 177, p. 08003, 2018. doi:10.1051/epjconf/201817708003
- [6] <https://www.cst.com/>

Content from this work may be used under the terms of the CC BY 3.0 licence (© 2018). Any distribution of this work must maintain attribution to the author(s), title of the work, publisher, and DOI.

HIGH RESOLUTION SPECTROMETER DEVELOPMENT FOR USE IN ECR ION SOURCE*

R. Kronholm[†], T. Kalvas, H. Koivisto and O. Tarvainen
University of Jyväskylä, Jyväskylä, Finland

Abstract

A high resolution spectrometer setup have been developed for optical emission spectroscopy of ECRIS plasmas. The spectrometer has been used in multiple studies with the JYFL 14 GHz ECRIS yielding new information on the low energy electron population and ion temperatures. This is a overview of the development process and recent studies.

INTRODUCTION

Electron cyclotron resonance ion sources (ECRIS) are under constant development, which motivates understanding the plasma properties. Therefore the ECRIS plasma is continuously studied, theoretically, numerically and experimentally. Experimental studies are usually complicated as the measurement setup easily affects the plasma and skew the results.

Spontaneous de-excitation of electronic states of atoms and molecules, present in Electron Cyclotron Resonance Ion Source (ECRIS) plasmas, enables studying them non-invasively through optical emission spectroscopy (OES). A high resolution spectrometer (10 pm FWHM at 632 nm) with phase-sensitive lock-in data acquisition setup has been developed at JYFL specifically for the diagnostics of weak emission lines characteristic to ECRIS plasmas.

PHYSICS BACKGROUND

In ECRIS plasma heating is based on energy transfer from microwaves to electrons via electron cyclotron resonance. This leads to wide electron energy distribution function, starting from cold electrons with a few eV energies up to hot electrons with energies on the order of 100 keV. Collisions between electrons and ions and neutral atoms results to energy transfer from free electrons to electrons bound to potential of the atomic nucleus. If the bound electron receives enough energy, ions are generated or the charge state of the ions is increased. This reaction is called electron impact ionization. In addition to ionization bound electron can be also excited to higher energy state. This reaction is called electron impact excitation. Excited electronic states can decay via radiative transition from higher energy state to lower energy states by emitting electromagnetic radiation. The wavelength of the emitted photon can be expressed as

$$\lambda = hc/(E_J - E_K), \quad (1)$$

* Work supported by European Union's Horizon 2020 research and innovation programme under Grant Agreement No. 654002.

[†] risto.j.kronholm@jyu.fi

where h is Planck constant, c is speed of light, E_J and E_K are energies of the higher and lower energy states, respectively. The intensity of emission is given by

$$I_\lambda = n_J A_{JK}, \quad (2)$$

where n_J is the electron density in energy state J and A_{JK} is the Einstein coefficient for the JK transition.

The wavelength spectrum of emitted light is a fingerprint of an element and therefore optical emission plasma spectroscopy can be used to identify particle species present in the plasma e.g. the impurity content. As the intensity of the emission depends on the ion density and electron energy distribution, the diagnostic can be used to study cold electron energies and relative ion densities [1]. Optical emission lines never have delta function profile ($\Delta\lambda > 0$). In addition to intensity and wavelength of the emission also the broadening of the emission line gives insight on fundamental plasma physics such as ion temperature, pressure, electric and magnetic fields.

MEASUREMENT SETUP

The optical emission spectroscopy setup has been developed mainly for use with the JYFL 14 GHz ECRIS [2]. Nevertheless, the system can easily be adapted to other ECR ion source. The JYFL 14 GHz ECRIS uses a minimum-B magnetic field configuration generated by two solenoid coils and a sextupole permanent magnet array. This magnetic field configuration and microwave plasma heating enables high charge state ion production. The primary heating frequency of the source is 14.1 GHz. The source allows monitoring optical emission both radially (between the magnetic poles) and axially (through an oven port). More information about the source can be found from Ref. [2].

In the case of heavy ion plasma, the number of emission lines in the visible light range is high, which requires a high resolution monochromator to separate individual radiative transitions. High resolution is also beneficial, if the interest is in emission line broadening. The intensity of the optical transition of interest can be very low and, therefore, a high optical throughput and good high signal-to-noise (SNR) is required. The developed OES setup of three main parts: The optical interface between the ion source and the spectrometer, the spectrometer and the data acquisition and control. The spectroscopy setup is described in Ref. [1] in detail.

CONDUCTED EXPERIMENTS

The development process of the high resolution spectrometer setup has been successful. The spectrometer setup is now free of "infant problems" and can be operated on regular

basis. The setup has been used for a number of studies. In Ref. [1] the temperature of the cold electron population was studied by measuring multiple emission lines and using the line-ratio method to analyze the cold electron temperature. The cold electron temperature was measured with the extraction voltage off and on under otherwise identical conditions. The temperature was found to change from 20 ± 10 eV to 40 ± 10 eV, respectively. The rate coefficient of neutral to 1+ ionization was found to decrease to 42 % of the original and 1+ to 2+ ionization to 24 % when the 10 kV high voltage was switched off. Furthermore, it was observed that switching the extraction voltage off reduces the emission intensity of Ar^{9+} ion by almost two orders of magnitude. This highlights the importance of performing plasma diagnostics studies of ECR ion source with the extraction voltage being applied as only then the results are valid in terms of high charge state production.

In Ref. [3] the optical emission spectroscopy was used to study the intensities of the Ar^{9+} and Ar^{13+} optical emission and ion beam current. The relative changes in both the optical emission and the ion beam current were measured in CW and amplitude modulation (AM) operation mode. The results implied that in CW mode the ion currents could be

limited by diffusion transport and electrostatic confinement of these high charge state ions rather than beam formation in extraction region and subsequent transport. Recent studies focusing on emission line broadening have revealed that the ion temperatures in ECRIS plasma can be greater than 10 eV i.e. significantly higher than previously thought. These results will be published shortly [4].

REFERENCES

- [1] R. Kronholm and T. Kalvas and H. Koivisto and O. Tarvainen, *Review of Scientific Instruments* vol. **89**, p. 043506 (2018).
- [2] H. Koivisto and P. Heikkinen and V. Hänninen and A. Lassila and H. Leinonen and V. Nieminen and J. Pakarinen and K. Ranttila and J. Ärje and E. Liukkonen, *Nuclear Instruments and Methods in Physics Research Section B: Beam Interactions with Materials and Atoms* vol.174, pp. 379 - 384 (2001).
- [3] R. Kronholm and M. Sakildien and D. Neben and H. Koivisto T. Kalvas and O. Tarvainen and J. Laulainen and P. Jones, AIP Conference Proceedings, 040014 (2018).
- [4] R. Kronholm et al. to be submitted to *Plasma Sources Science and Technology*.

HIGH RESOLUTION SPECTROPOLARIMETRY: FROM ASTROPHYSICS TO ECR PLASMAS

M. Giarrusso[†], S. Gammino, D. Mascali, M. Mazzaglia, E. Naselli¹, G. Castro, L. Celona,
INFN-Laboratori Nazionali del Sud, I95123 Catania, Italy

¹also at Dip. di Fisica e Astronomia, Università degli Studi di Catania, I95123 Catania, Italy

G. Avila, European Southern Observatory, Munchen, Germany

G. Del Zanna, University of Cambridge, Cambridge, UK

E. Landi, University of Michigan, Ann Arbor, USA

M. Munari, INAF-Osservatorio Astrofisico di Catania, I95123 Catania, Italy

F. Leone², Dip. di Fisica e Astronomia, Università degli Studi di Catania, I95123 Catania, Italy

²also at INAF-Osservatorio Astrofisico di Catania, I95123 Catania, Italy

Abstract

Electron Cyclotron Resonance (ECR) plasmas with high density and high temperature are required by the injectors for the Accelerators and by interdisciplinary studies in Astrophysics and Nuclear Astrophysics. The magnetic traps need a very fine analysis of plasma conditions in terms of density, temperature and ionization state, not allowed by the present diagnostic methods (imaging, low resolution spectroscopy not spatially resolved).

We here describe the results routinely obtained in Astrophysics with high resolution spectroscopy, largely used to analyze astrophysical plasma in the visible range, which allows to determine physical parameters of stars as effective temperature, surface gravity, chemical abundances. In addition, we show that polarimetry is the only technique to derive the morphology of stellar magnetic fields, whose knowledge is necessary for a correct interpretation of spectra from magnetized plasmas. An application of these non-invasive methods to B-min ECR plasma concerning optical emission is discussed in view of a better comprehension of the plasma structure, magnetic confinement properties and heating processes.

INTRODUCTION

Intense beams of multiply charged ions are going to be a critical requirement for experiments in Nuclear Physics, Plasma Physics and Nuclear-Astrophysics. Most of ion sources are plasma-based, where the average charge state ($\langle q \rangle$) and the current intensity (I_q) of the extracted beam depend on the electron density (n_e) and the ion confinement time (τ_q) as $\langle q \rangle \propto n_e \tau_q$ and $I_q \propto \frac{n_e}{\tau_q}$. Among the sources that ensure a good compromise between charge state and current intensity there are the

Electron Cyclotron Resonance Ion Sources (ECRIS, [1]) where the gas injected in a chamber is ionised by microwaves and confined by a Magneto-Hydro-Dynamic (MHD) stable B-min configuration. The ionization efficiency of these systems, producing high density ($n_e \sim 10^{10}$ - 10^{13} cm⁻³) and high temperature ($T_e \sim 0.1$ - 100 keV) plasma, depends on a not yet fully understood large number of parameters, and semi-empirical relations are adopted to optimize the extracted beam. According to the Geller's scaling laws [2] and the so-called "High-B mode" condition for the MHD stability [3], in order to improve the ECRIS performances we have to increase the magnetic field intensity and the microwave frequency. This trend is now limited by the rising costs and feasibility of magnets and RF generators, and a better comprehension of plasma formation and heating is therefore needed, to be performed by means of new diagnostic tools.

Present non-invasive techniques developed for plasma diagnostic range from X-ray to near infrared and are routinely based on imaging and spectroscopy. Anyway these methods are able to characterize plasma electrons, as for the X spectral range (see, e.g., [4,5]).

Not so much information is instead available concerning the ions. In addition, the ion confinement optimization, affected by the still not fully explained gas-mixing effect [6], requires a complete control of cold electrons displacement which is inaccessible by X-ray diagnostics. As to the visible spectral range, low resolution (an arbitrary boundary could be placed at $R = \lambda/\Delta\lambda < 40000$) Optical Emission Spectroscopy (OES) is commonly carried out with the aim to determine electron temperatures and densities as well as to obtain information about atomic and molecular populations by means of the line-ratio method (see e.g. [7]).

* Work supported by 5th Nat. Comm. of INFN under the grants MAPS_3D and PANDORA

[†] marina.giarrusso@lns.infn.it

Content from this work may be used under the terms of the CC BY 3.0 licence (© 2018). Any distribution of this work must maintain attribution to the author(s), title of the work, publisher, and DOI.

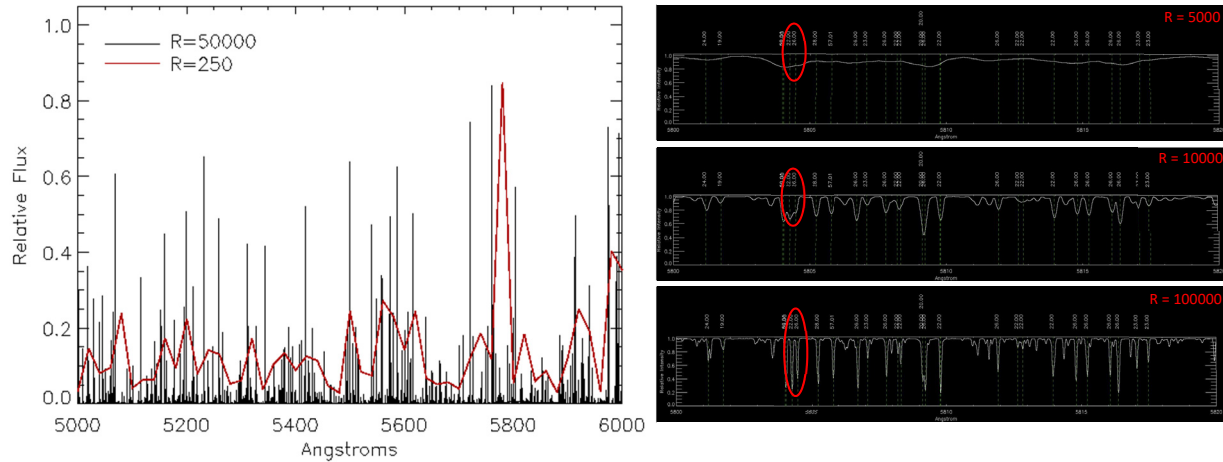


Figure 1: Left panel: small portion of the spectrum from a ThAr hollow cathode lamp as recorded at high ($R = 50000$, black spectrum) and low ($R = 250$, red spectrum) resolution. Spectra have been normalised to their maximum for an easy comparison. Right panel: synthetic solar spectra computed in the same wavelength range with different resolution as indicated on each one.

However, present OES is characterized by the absence of spatial resolution. An example is shown in [8] where the presence of lines from both atomic and molecular transitions in hydrogen spectra testifies the limits in spatially separating hot and cold plasma regions. The spectra were obtained with $R = 250$, which means that it is not possible to identify lines separated less than 2 nm at 500 nm. Low spectral resolution represents a further limit of plasma OES: already in [9] it is discussed the crucial role of spectral resolution for a correct measurement of profiles and wavelength shifts of spectral lines. Therefore, there is a wide room for improvements in ECRIS plasmas diagnostics, particularly in the optical range, for a number of issues; a) measurements of ion temperature; b) determination of in-plasma micro and macro turbulence; c) on-line and non intrusive determination of the inner-plasma charge state distribution; d) investigation of gas mixing dynamics and isotopic effect. All these challenges require $R > 40000$ and, as we will see in the following, the simultaneous implementation of polarimetry. A specific experimental program has been started at INFN in synergy with the Italian Institute for Astrophysics (INAF), under the grant MAPS_3D (MAGnetised Plasma Spectropolarimetry 3D): the projects merges backgrounds, methods and instruments routinely adopted in observational Astrophysics to be implemented in laboratory-plasmas.

STELLAR PLASMA DIAGNOSTIC

We here present the results obtained in Astrophysics by means of high resolution ($R \geq 50000$) spectropolarimetry. This technique, routinely applied to magnetized plasmas in the visible range (e.g. the atmospheres of stars), allows to determine stellar parameters and surface chemical

composition, as well as the magnetic field geometry whose knowledge is necessary for reliable estimations of plasma temperature and density.

High Resolution Spectropolarimetry

We start pointing out the advantage in using high resolution spectroscopy to analyze light from stars. First, for spectral line identification, as clearly shown in Fig. 1: on the left panel a small portion of the spectrum from a ThAr hollow cathode lamp is reported, as recorded by us at $R = 250$ and $R = 50000$ with the Catania Astrophysical Observatory Spectropolarimeter (CAOS@OACT, [10]). It clearly appears that most of the lines are wasted at low resolution because of blending, and so can not be detected. A further example is given on the right panel showing synthetic solar spectra computed in the same wavelength range with different R values. Only through high resolution it is possible to distinguish between near lines of different elements, and then correctly determine stellar metallicity, especially for chemically peculiar stars (see e.g. [11,12,13,14]).

High resolution spectroscopy also allows to detect the presence of isotopes in stellar atmospheres [15] by measuring the isotopic shift of spectral lines. This shift is typically smaller than 0.01 nm, so that $R > 50000$ is required at wavelength 500 nm.

The measurement of velocity fields, that can be estimated only through high resolution spectroscopy on the basis of the Doppler effect, is fundamental to probe stellar plasmas. If a star moves away from us (toward us) with velocity v , its spectrum will be redshifted (blueshifted) of $\Delta\lambda_D = \lambda v/c$ with respect to the synthetic one. In general, the many chaotic or ordered mass flows (e.g. microturbulence, macro-turbulence, oscillations or winds) present in

cosmic objects can be disentangled by analyzing the spectral line profile, if the instrumental spectral resolution is sufficient [16]. As an example the rotational velocity of a star can be measured only if the corresponding line profile is larger than the instrumental profile $\Delta\lambda = \lambda/R$. As a consequence the minimum measurable velocity field is of the order of $v = c \lambda/\Delta\lambda = c/R$, i.e. $v = 1200 \text{ km s}^{-1}$ at $R = 250$ and 3 km s^{-1} at $R = 100000$. Equally is the role of spectral resolution in the determination of the gravity of stars on the basis of the collisional line broadening, that is due to the modification of atomic energy levels due to the interaction between emitters and electrons, ions or neutrals.

If the examined star has a magnetic field, atomic energy levels split in sublevels so that spectral lines also split in a series of Zeeman components. These are called π if $\Delta m = 0$, σ_b (blueshifted with respect the nominal wavelength) if $\Delta m = +1$, and σ_r (redshifted) if $\Delta m = -1$, being m the magnetic quantum number. The average separation in wavelengths among σ_b - and σ_r -components, $\Delta\lambda_\sigma$, is proportional to the modulus of the field, $|\mathbf{B}|$:

$$\Delta\lambda_\sigma = 2 \cdot 4,67 \cdot 10^{-13} \lambda^2 g_{eff} |\mathbf{B}|$$

with λ expressed in \AA , \mathbf{B} in G, and being g_{eff} the effective

Landé factor. Then, in order to measure stellar magnetic field intensity the resolution has to be high enough that $\Delta\lambda \leq \Delta\lambda_\sigma$: the minimum field modulus ($\Delta\lambda = \Delta\lambda_\sigma$) at $\lambda = 500 \text{ nm}$ and for $g_{eff} = 1$ is 85 T with $R = 250$ and 0.21 T with $R = 100000$. With the exception of pulsars and magnetars, the field modulus of magnetic stars ranges from few Gauss [17] up to $\sim 3 \text{ Tesla}$ [18]. Sometimes π - and σ -components are superimposed and appear as a single broadened line rather than a multiplet. In this case high resolution is mandatory for a correct interpretation of the line profile, in order to avoid misunderstanding which could lead to attribute to the star wrong chemical abundances as well as temperature and surface gravity.

Anyway, high resolution spectroscopy is not enough to study magnetic stars. Spectra from magnetized plasma should be not correctly interpreted if we neglect the field geometry: in presence of a magnetic field, emission is not isotropic [19], with the most extreme case of no emission of the Zeeman π -components along the field direction (see Fig. 2). Without information on the field strength and orientation, these weaker spectral lines could be ascribed to a lower density, or assigned to a wrong temperature. In addition, [20] have shown how the magnetic intensification of spectral lines can mimic a larger chemical abundance under the hypothesis of Local Thermodynamic

Content from this work may be used under the terms of the CC BY 3.0 licence (© 2018). Any distribution of this work must maintain attribution to the author(s), title of the work, publisher, and DOI.

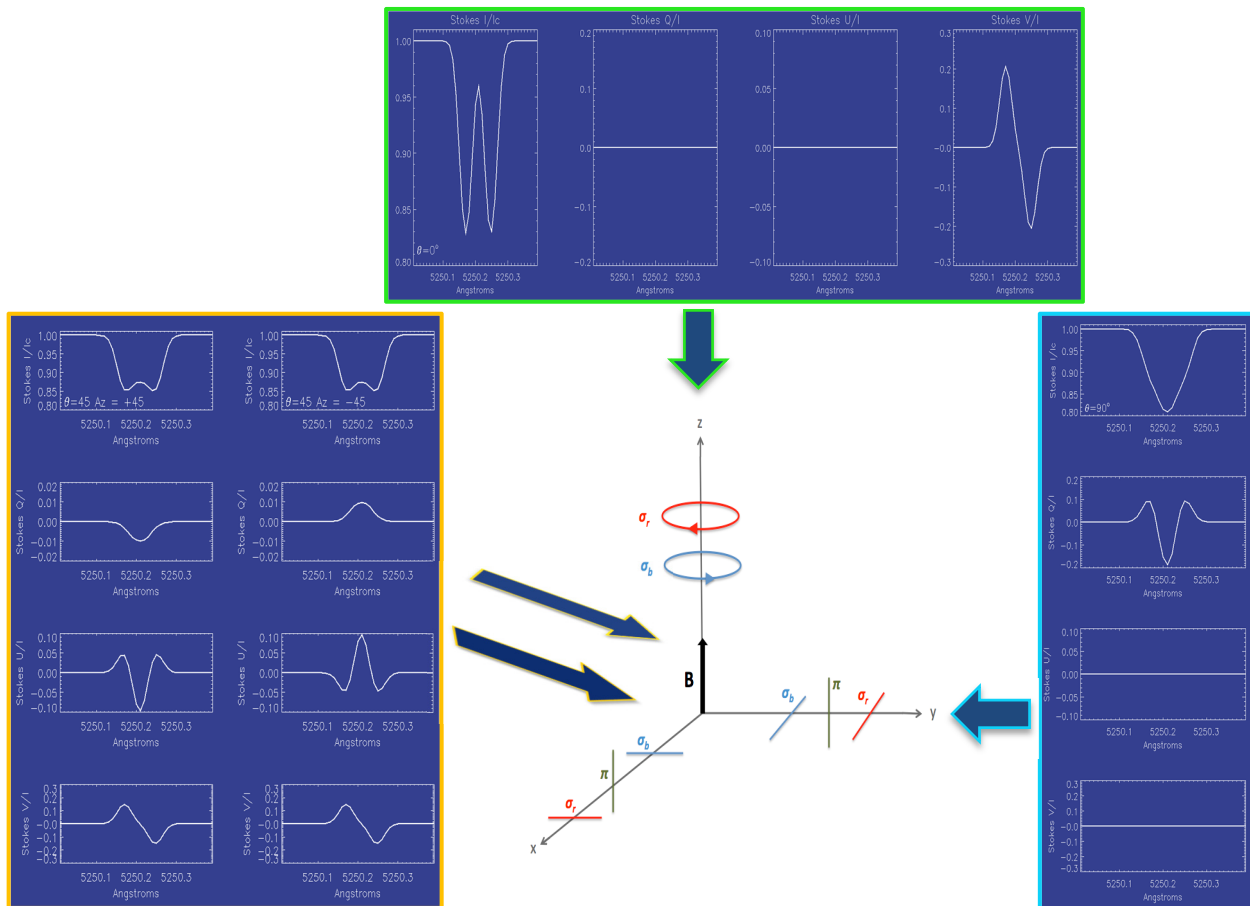


Figure 2: Synthetic Stokes profiles as observed along and transversally to the magnetic field \mathbf{B} (z axis and y axis respectively), and at angle 45° respect to the field direction with Azimuth $+45$ and -45 .

Equilibrium regime.

It is then necessary to simultaneously determine magnetic field modulus and geometry to avoid wrong results. Polarimetry is the only non-invasive technique able to recover the magnetic field configuration. By describing the polarization through Stokes parameters, the magnetic field morphology can be derived from the corresponding profiles observed by means of a polarimeter (Fig. 2). Solar and stellar magnetic fields are commonly reconstructed on the basis of high resolution spectropolarimetry [21] by taking advantage from stellar rotation to determine the 3D geometry. Despite the great potentiality, high resolution spectropolarimetry is a not yet widely adopted technique for in-laboratory plasma diagnostics. One of the few papers on plasma polarization spectroscopy at resolution $R = 44000$ by [22] shows the huge potential of this technique able to disentangle the line-of-sight plasma properties of the TRIAM-IM tokamak.

FROM STARS TO ECR PLASMAS

In view of a better comprehension of the ECR plasma structure, magnetic confinement properties and heating processes, we planned to apply the above discussed methodology of optical diagnostics for astrophysical plasmas to ECR plasmas. As already mentioned, it will be done at Istituto Nazionale di Fisica Nucleare-Laboratori Nazionali del Sud (INFN-LNS) of Catania, within the INFN project MAPS_3D.

High resolution spectroscopy will be carried out with the spectrograph SARG (Spettrografo Alta Risoluzione Galileo, [23]) working in the visible range (from 370 to 1000 nm in a single shot) at resolution $R = 164000$. It was at Telescopio Nazionale Galileo (La Palma, Canary Island) and it is now at LNS after a Memorandum of Understanding between INFN-LNS and INAF-OACT undersigned in August 2017.

The test-bench for plasma analysis will be the Flexible Plasma Trap [24] where the plasma will be created. It is called *Flexible* because of the possibility to change the magnetic field configuration (simple mirror, magnetic beach, quasi-flat) and the direction of microwaves injection with respect to the magnetic field orientation. Plasma emission will be simultaneously recorded from three directions at 90° from each other through three polarimetric units (now under construction) fiber-linked to SARG.

This equipment, together with the development of a new radiative transfer theory, will allow a 3D spectropolarimetric characterization of plasma and magnetic field as generated within the FPT. With the SARG resolution, in fact, it is possible to identify spectral lines separated up to 0.003 nm at $\lambda = 500$ nm, and then also measure isotopic shift. This should be fundamental for the gas-mixing characterization of ECR plasmas, as well as to perform broadening measurements which represent an estimation of plasma turbulence. Finally, the magnetic field inside the FPT is $|\mathbf{B}| \leq 0.3$ T. With $R = 164000$ the minimum field modulus measurable is at least 0.125 T at $\lambda = 500$

nm, thus confirming that an advanced characterization of the so-called magnetoplasma is potentially possible.

First experimental data are expected to be collected within 2019.

REFERENCES

- [1] R. Geller, "Electron cyclotron resonance ion sources and ECR plasmas", *Bristol: Institute of Physics Publishing*, 1996
- [2] R. Geller *et al.*, "The Grenoble ECRIS status 1987 and proposal for ECRIS scaling", in *Proc. 8th Int. Workshop ECR Ion Sources*, East Lansing, NSCL report MSUCP-47, vol. 1, p. 22, 1987
- [3] S. Gammino and G. Ciavola, "The role of microwave frequency on the high charge states buildup in the ECR ion sources", *Plasma Sources Sci. Tech.*, vol. 5, no. 1, pp. 19-27, Feb. 1996, doi:10.1088/0963-0252/5/1/002
- [4] S. Gammino *et al.*, "Considerations on the role of the magnetic field gradient in ECR ion sources and build-up of hot electron component", *Plasma Sources Sci. Tech.*, vol. 18, no. 4, p. 045016, Nov. 2009, doi:10.1088/0963-0252/18/4/045016
- [5] D. Mascali *et al.*, "Electron cyclotron resonance ion source plasma characterization by X-ray spectroscopy and X-ray imaging", *Rev. Sci. Instrum.*, vol. 87, no. 2, p. 02A510, Feb. 2016, doi:10.1063/1.4939201
- [6] A. A. Ivanov and K. Wiesemann, "Ion Confinement in Electron Cyclotron Resonance Ion Sources (ECRIS): Importance of Nonlinear Plasma Wave Interaction", *IEEE Transactions on Plasma Science*, vol. 33, no. 6, pp. 1743-1762, Dec. 2005, doi:10.1109/TPS.2005.860078
- [7] U. Fantz *et al.*, "Spectroscopy—a powerful diagnostic tool in source development", *Nucl. Fusion*, vol. 46, no. 6, pp. S297-S306, June 2006, doi:10.1088/0029-5515/46/6/S10
- [8] D. Mascali *et al.*, "Electromagnetic diagnostics of ECR-Ion Sources plasmas: optical/X-ray imaging and spectroscopy", *Journal of Instrumentation*, vol. 12, no. 12, pp. C12047, Dec. 2017, doi:10.1088/1748-0221/12/12/C12047
- [9] U. Fantz, "Basics of plasma spectroscopy", *Plasma Sources Sci. Tech.*, vol. 15, no. 4, pp. S137-S147, Nov. 2016, doi:10.1088/0963-0252/15/4/S01
- [10] F. Leone *et al.*, "A Method to Calibrate the High-resolution Catania Astrophysical Observatory Spectropolarimeter", *Astron. Jour.*, vol. 151, no. 5, p. 116, May 2016, doi:10.3847/0004-6256/151/5/116
- [11] J. F. González *et al.*, "HD 161701, a chemically peculiar binary with a HgMn primary and an Ap secondary", *Astron. Astrophys.*, vol. 561, p. A63, Jan. 2014, doi:10.1051/0004-6361/201322327
- [12] M. Giarrusso, "The chemical abundances of the Ap star HD94660", in *Proc. 7th European Summer School on Experimental Nuclear Astrophysics Conf.*, Italy, 2014, AIP Conference Proceedings, vol. 1595, pp. 234-237, doi:10.1063/1.4875320
- [13] J. D. Bailey, J. Grunhut and J. D. Landstreet, "A comprehensive analysis of the magnetic standard star HD 94660: Host of a massive compact companion?", *Astron. Astro-*

- phys., vol. 575, p. A115, March 2015,
doi:10.1051/0004-6361/201425316
- [14] G. Catanzaro *et al.*, “CAOS spectroscopy of Am stars Kepler targets”, *Mont. Not. Royal Astron. Soc.*, vol. 451, no. 1, pp. 184-195, July 2015,
doi:10.1093/mnras/stv952
- [15] G. Catanzaro and F. Leone, “Spectroscopic analysis of the SB3 system 74Aqr”, *Mon. Notices Royal Astron. Soc.*, vol. 373, no. 1, p. 330, Nov. 2006,
doi:10.1111/j.1365-2966.2006.11039.x
- [16] D. F. Gray, “The Observation and Analysis of Stellar Photospheres”, *Camb. Astrophys. Ser.*, vol. 20, 1992
- [17] C., Scalia, F. Leone, M. Gangi, M. Giarrusso and M.J. Stift, “The multi-line slope method for measuring the effective magnetic field of cool stars: an application to the solar-like cycle of ϵ Eri”, *Mon. Notices Royal Astron. Soc.*, vol. 472, no. 3, p. 3554, Dec. 2017,
doi:10.1093/mnras/stx2090
- [18] H. W. Babcock, “The 34-KILOGAUSS Magnetic Field of HD 215441”, *Astrophys. Jour.*, vol. 132, p. 521, Nov. 1960, doi:10.1086/146960
- [19] E. Landi Degl’Innocenti and M. Landolfi “Polarization in Spectral Lines”, *Kluwer Academic Publ.*, Dordrecht , 2004, doi:10.1007/978-1-4020-2415-3
- [20] M. J. Stift and F. Leone, “Magnetic intensification of spectral lines”, *Astron. Astrophys.*, vol. 398, p. 411, 2003,
doi:10.1051/0004-6361:20021605
- [21] G. Fleishman, S. Anfinogentov, M. Loukitcheva, I. Mysh'yakov and A. Stupishin, “Casting the Coronal Magnetic Field Reconstruction Tools in 3D Using the MHD Bifrost Mode”, *Astrophys. Jour.*, vol. 839, no. 1, p. 30, 2017, doi:10.3847/1538-4357/aa6840
- [22] T. Shikama *et al.*, “Plasma polarization spectroscopy of atomic and molecular emissions from magnetically confined plasmas”, *Canadian Journal of Physics*, vol. 89, no. 5, p. 495, 2011, doi:10.1139/p10-118
- [23] R. Gratton *et al.*, “SARG: the high resolution spectrograph of TNG”, *Experimental Astron.*, vol. 12, p. 107, 2001, doi:10.1023/A:1016390619881
- [24] S. Gammino *et al.*, “The Flexible Plasma Trap (FPT) for the production of overdense plasmas”, *Journal of Instrumentation*, vol. 12, no. 7, p. P07027, July 2017,
doi:10.1088/1748-0221/12/07/P07027

IMPACT OF THE TWO CLOSE FREQUENCY HEATING ON ECRIS PLASMAS STABILITY

E. Naselli^{†1}, D. Mascali, M. Mazzaglia, G. Torrasi, G. Castro, L. Celona, S. Gammino, F.P. Romano², C. Caliri, Istituto Nazionale di Fisica Nucleare, Laboratori Nazionali del Sud (INFN-LNS), 95123 Catania, Italy

¹also at Department of Physics and Astronomy, University of Catania, Via Santa Sofia, 64, 95123 Catania, Italy

²also at CNR-Istituto per i Beni Archeologici e Monumentali, Catania, Italy

R. Rácz, S. Biri, Z. Perduk, J. Pálinkás, Institute for Nuclear Research, Hungarian Academy of Sciences (Atomki), H-4026 Debrecen, Hungary

A. Galatà, Istituto Nazionale di Fisica Nucleare, Laboratori Nazionali di Legnaro (INFN-LNL) 35020 Legnaro, Italy

Abstract

Several experiments have recently demonstrated that plasma instabilities are powerful limiting factors to the flux of highly charged ion beam extracted from ECRIS. One of the methods for damping the instabilities is to feed the plasma in two frequency heating mode. Since the fundamental physical mechanism is still unclear (diffusion in velocity space? additional confinement?), a deeper experimental investigation is necessary, using multi-diagnostics setups. At ATOMKI-Debrecen the effect on the plasma instabilities of an argon plasma in a “Two Close Frequencies” scheme has been explored. Spectra of radio-emission from the plasma have been collected for different frequency gaps and relative power balances. The measurements show the plasma self-emitted radiation comes out from the internal plasma (i.e. around the lower frequency) but the instability damping can be effective for some specific combinations of frequency-gap and power balance. Radiofrequency spectra have been collected simultaneously produced by the instabilities and detected via a microwave diode connected to a plasma-chamber-immersed multi-pin RF probe.

INTRODUCTION

Electron Cyclotron Resonance Ion Sources (ECRIS) are able to produce beams of highly charged ions with high intensity and stability, which are necessary for accelerators, in applied and nuclear physics research.

In order to produce these beams, continuous improvements of the performances of ECR ion sources are needed. For many years these improvements consisted principally in the use of higher power of RF wave heating, and more intense magnetic field, on the basis of the “scaling laws” [1]. More recently, this approach has become more difficult because of the technological limits.

A deeper knowledge of plasma parameters (electron density, temperature and charge state distribution CSD) is

thus fundamental: characteristics of the extracted beam (in terms of current intensity and production of high charge states) are directly connected with plasma parameters and structure.

Several experiments have in fact demonstrated that plasma instabilities limit the flux of highly charged ions extracted from ECR ion sources, causing beam ripple, as well [2]. The instability threshold depends principally from the strength of the magnetic field in terms of B_{\min}/B_{ECR} and from other parameters as RF pumping power and pressure [3]. Even if many studies have been done, the exact mechanism of turbulent regimes of plasmas is still unknown and a deeper investigation is so necessary.

Plasma kinetic instabilities are characterized by fast RF and X-ray bursts causing performance deterioration of the ECRIS; to overcome this limitation more studies aiming at characterizing in detail this still unknown process and at finding a way for damping the turbulence are required. Some indications say that a key role for damping turbulences may be played by the Two Close Frequency Heating (TCFH).

In this work the experiment that has been done at ATOMKI, Debrecen (Hungary), is presented, where stable and unstable ECR plasmas in a B-min magnetic configuration have been characterized through a multi-diagnostic setup. The characterization has been carried out for the first time in Two Close Frequency Heating (TCFH) mode, through the use of two frequencies with a gap difference of the order of some hundreds of MHz.

It is well known that when the plasma is excited in double (far or close) frequencies, it is possible to observe improvements in the characteristics of the extracted beam. This process is still unknown in detail and here some experimental evidences regarding how the TCFH is able to damp instabilities are presented. Evidences of an increase of the electron confinement inside the “plasmoid region” can be argued from the experimental results.

[†] eugenia.naselli@lns.infn.it

EXPERIMENTAL SETUP

Stable and unstable plasma regimes have been characterized through a multi-diagnostic setup, consisting in a collection of non invasive tools that allows unprecedented investigations of magnetoplasma properties in terms of density, temperature, CSD and inner plasma EM wave emission.

The multi-diagnostic setup includes a multi-X-ray detectors system for X-ray spectroscopy consisting of:

- Silicon Drift Detector (SDD) for plasma density and temperature measurement in soft X-ray domain (Q.E. $\sim 1.0 \div 30$ KeV).
- A High-purity Germanium (HpGe) detector for spectral temperature measurement of hard X-ray domain (Q.E. $\sim 30 \div 400$ KeV), including time resolved spectroscopy.

The other devices of the multi-diagnostic setup are a spectrometer for the plasma-emitted visible light characterization and a two-pins RF probe.

The RF probe, installed inside the plasma chamber in the injection plate, protrudes through one of the gas input holes. It was connected to a Spectrum Analyzer (SA) in order to detect the plasma emitted EM wave in GHz ranges, which typically characterizes the kinetics instabilities. All instabilities were detected via RF spectra.

Alternatively, the RF probe can be connected with a diode and an oscilloscope in order to obtain the total integrated power emitted from the plasma, using this value as trigger signal for instability signature and to perform time resolved X-ray analysis too.

All diagnostic tools can operate simultaneously with the faraday cup in order to measure the charge state distribution. It has been possible to correlate the plasma parameter with the characteristics of the beam extracted on-line.

More details about the general setup, each tool and its own characteristics are well described in [4].

For the microwave coupling for TCFH a Klystron generator (with a fixed frequency of 14.25 GHz) and a TWT amplifier (with a frequency range 13.6 - 14.6 GHz) were used. Through of a power combiner it has been possible to mix the two frequencies to heat and excite the plasma inside the plasma chamber.

EXPERIMENTAL PROCEDURE

The experimental procedure have been done in different configurations.

At the beginning the system was characterized in single frequency heating mode in order to have some reference configurations. Then, the system has been characterized in TCFH mode in order to study the effect of the second frequency on plasma instabilities, and on its structure. The different configurations are here reported:

- 1FH : frequency scan by TWT only
13.6 GHz – 14.6 GHz, $df=50$ MHz @ P=200W
- 1FH : TWT power scan at 13.8 GHz representative frequency, until 200W.

- 2FH : Frequency scan by Klystron 14.25GHz + TWT 13.6GHz – 14.6 GHz, $df=50$ MHz @ P=200W
- 2FH : Power balance @ total net power 200W, TWT 13.8GHz + Klystron 14.25 GHz

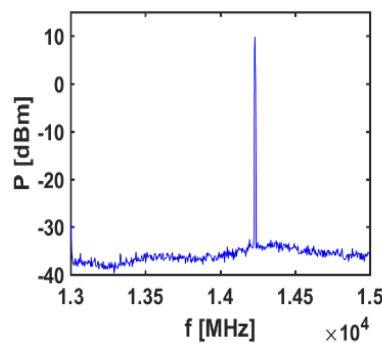
In order to correlate the instability strength of a configuration with other parameters, such as RF power and RF pumping frequency, it is very important to find a quantitative way to define how much a system is unstable. In order to give a quantitative estimation of the strength of the instabilities we introduce the parameter I_s (Instability Strength).

There is a series of issues concerning the quantitative evaluation of the instability strength, and, then, about the eventual correlation of confinement dynamics (plasma vs. losses X-radiation emission) with the I_s parameter itself.

From the point of view of the I_s rigorous definition, some (critical) issues still remain open:

- a) SA measurements are performed without any temporal resolution, whilst instabilities are by definition fast evolving phenomena whose temporal scale lies in the range of $\mu\text{sec.}$ or shorter; hence, any quantitative evaluation of I_s has to cope with integration time of our spectrum analyzer;
- b) due to the still not-perfectly known physical mechanism governing the ECRIS instability dynamics, it is difficult to find rigorous quantitative criteria to evaluate I_s : is more important the total integral of plasma self-generated sub-harmonics or their number? Or their superposition?

In fact, as it is possible to observe in Fig. 1, a stable plasma (Fig. 1-(a)) is characterized by the pumping RF peak only. Whilst unstable configuration can be characterized by a low number of sub-harmonics with a high power in each one (Fig. 1-(b)), or also by a high number of sub-harmonics but at low power (Fig. 1-(c)).



Content from this work may be used under the terms of the CC BY 3.0 licence (© 2018). Any distribution of this work must maintain attribution to the author(s), title of the work, publisher, and DOI.

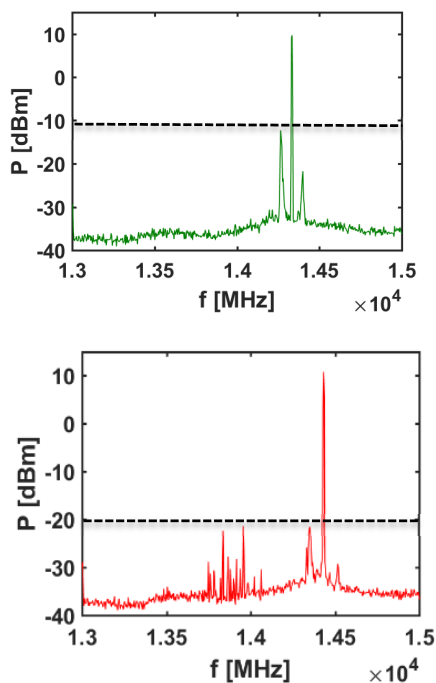


Figure 1: Sequence of SA collected spectra for: (a) stable; (b) unstable but with a small number of sub/up-harmonics at high power; (c) unstable but with a large number of sub-harmonics at low power.

After several attempts, all of them trying to find a significant I_s definition able to quantitatively describe what we got from direct observation, our choice was to define I_s considering both contributions as follows:

$$I_s = \left(\int_{13\text{GHz}}^{15\text{GHz}} P(f)df - P_{mainpeak} \right) \cdot (1 + w(N_{sub} - 1))$$

where $P_{mainpeak}$ is the integral of the power of the main peak of pumping frequency, N_{sub} the number of sub-harmonics and w a weight factor.

With this definition, the I_s parameter has been calculated considering the amplitude (integral of the power) of RF plasma-self emitted signal, once subtracted the main pumping wave contribution; this number has been then multiplied by a factor which takes into account the number of sub-harmonics, N_{sub} with an opportune weight factor w . The weight was calculated in order to give more importance to the total integral of plasma self-generated sub-harmonics than their number.

EXPERIMENTAL RESULTS

In order to validate the I_s consistency we made some plots concerning the I_s behaviour vs RF power, in single and two close heating mode.

The definition of I_s resulted to be consistent with the direct observation of the SA recorded spectrum, increasing steadily with the power, as expected.

Details of correlations with other parameters and time resolved X-ray data are commented in [5].

In this work the attention is focused to instability issues only.

RF Spectra in 1FH - Power Scan @ 13.8 GHz

The plot of I_s vs. RF power is in Fig. 2, and it displays a clear increase of I_s , as expected, but anyway without any evident jump or non-linearity. $I_s > 0$ condition occurs already at 40 W, and this is consistent with the direct observation of SA recorded spectrum.

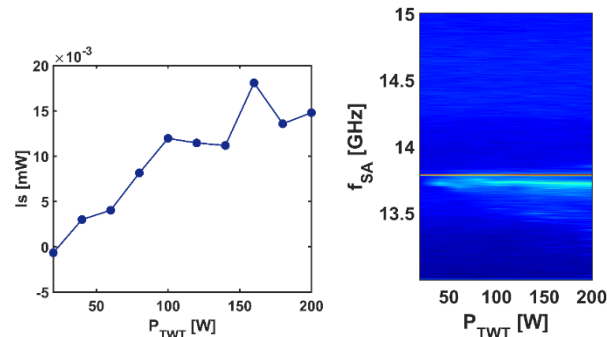


Figure 2: trend of the I_s parameter vs. the TWT power, during the single-frequency power scan. On the right, the spectral evolution of the RF probe detected signal vs. the pumping wave power. Sub-harmonics generation is evident already at around 40W.

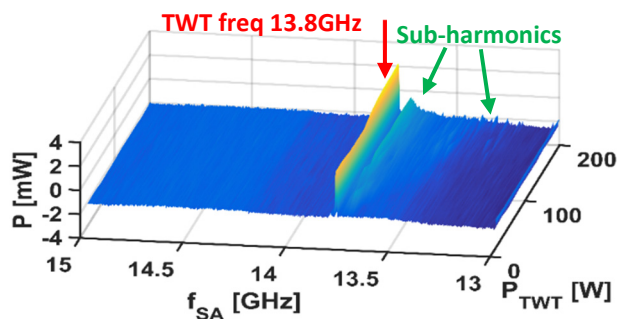


Figure 3: 3D plot of the RF probe detected signal, analysed through the SA. This plot is equivalent to the pseudo-colours plot of Fig. 2-right.

Figure 2-right illustrates the RF probe detected signal via SA analysis, when increasing the pumping wave power: the red line represents the pumping frequency (TWT only @ 13.8 GHz) whilst the green shadows are the sub-harmonics, i.e. the plasma-self generated waves due to the instability onset. It is possible to observe how these additional components become more and more intense and their number increase for higher TWT powers. A “down-shift” of the emitted frequencies is also evident.

Also in Fig. 3 is possible to observe the increase of characteristic sub-harmonic peaks for higher power.

RF Spectra in 1FH - Frequency Scan @ 200W

The trend of I_s vs RF frequency displays a frequency-dependent behaviour (see Fig. 4). To the knowledge of the authors, this is the first time the frequency tuning is

systematically explored for the instability. Is mirrors the strongest instability at the lowest frequency we used, i.e. 13.6 GHz. Even in this case, this is in agreement with the direct experience, both looking to the raw spectrum and to the general conditions of the source (at 13.6 GHz we obtained the largest high-energy X-ray flux, the largest total X-ray dose, etc.).

This is also consistent to the fact that at 13.6 GHz the source is operated well below the B_{\min}/B_{ECR} threshold that is universally considered as the “trigger” for the instability onset. Anyway, the plot shows that the frequency also (and not only the RF power and B_{\min}/B_{ECR} value) affects the instability strength.

Looking to this plot, it is more evident why integral only was not enough for evaluating Is. In fact in the case of 13.6 GHz there are a lot number of sub-harmonics, but with low emitted power.

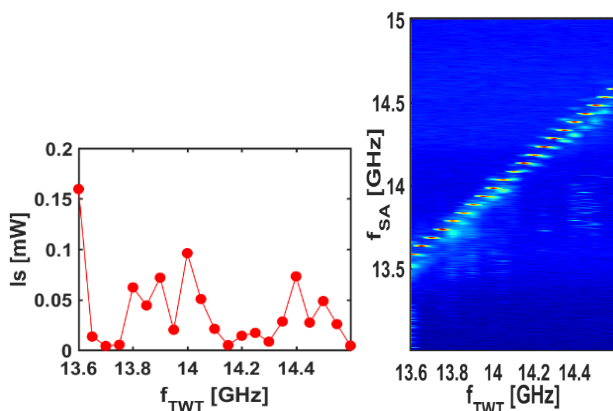


Figure 4: left – trend of I_s parameter during the one-frequency scan; right – spectral structures as detected by the SA at different frequencies, during the single frequency scan.

The “drop” below the pumping-frequency (pump. Freq. lies all along the line $y=x$) gives a qualitative indication about the instability strength which is not only related to the amplitude of the “down-chirp” spot, but also to the frequency spread of the self-generated sub-harmonics; This effect has been included in the above mentioned numerical definition of I_s .

Another very interesting result is that instabilities generate sub-harmonics for all frequencies of TWT, and some up-harmonics appear for higher frequencies only (in particular, above 14.2 GHz).

These plots demonstrate that despite our definition of I_s was difficult, it seems to follow in a reasonable way what happens in the plasma in more or less unstable conditions (depending on the power, magnetic field and frequency).

RF Spectra in 2FH – Frequency Scan @ 200W

The trend of RF spectra vs freq. scan at 2FH plot (Fig. 5) shows first of all that sub-harmonics in double freq. heating

mode and in unstable regimes are always at frequencies lower than the lower of the twos.

In TCFH mode up-harmonics disappear totally. This result, compared with the single frequency case, is very relevant: a possible explanation could be that in TCFH a steeper density profile is generated, since TCFH increases confinement and the plasma is more concentrated in the inner-plasmoid.

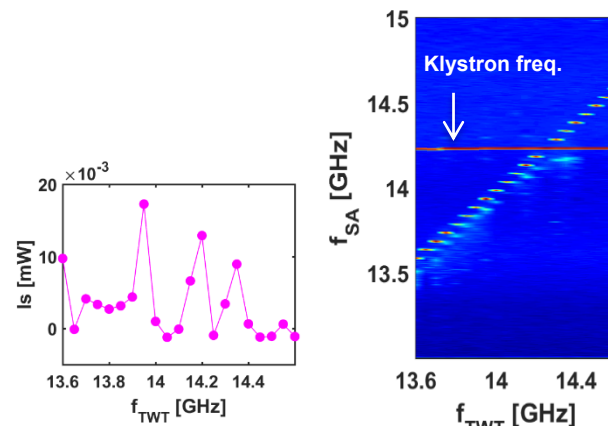


Figure 5: left – trend of I_s parameter during the two-frequency scan; right – spectral structures as detected by the SA at different frequencies, during the double frequency scan (Klystron at fixed frequency, TWT varying from 13.6 to 14.5 GHz).

In Fig. 6 we directly compare the I_s parameter in single frequency and in two close frequencies heating mode: it is possible to observe that the instability strength drops drastically, confirming that the TCFH is able to dump the instabilities.

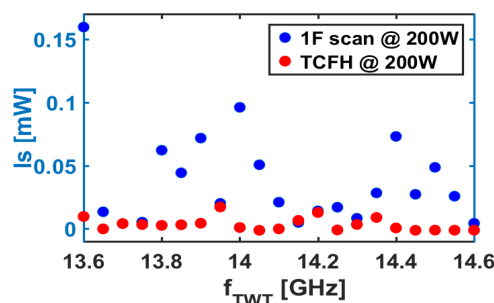


Figure 6: Comparison of the I_s parameter for single and double frequency heating, at fixed power. TCFH damps the instability almost over the entire frequency set.

Figure 7 enters more in details about the relevance of the instability damping at 13.8GHz, 200W, which was a very unstable regime. It is clear that this frequency is highly unstable already at low power levels. Anyway, the addition of the second wave, coming by the Klystron, damps the instability even if the total amount of power reaches 200 W

Content from this work may be used under the terms of the CC BY 3.0 licence (© 2018). Any distribution of this work must maintain attribution to the author(s), title of the work, publisher, and DOI.

(120 W by TWT and 80 W by Klystron). That means the instability can be damped by TCFH.

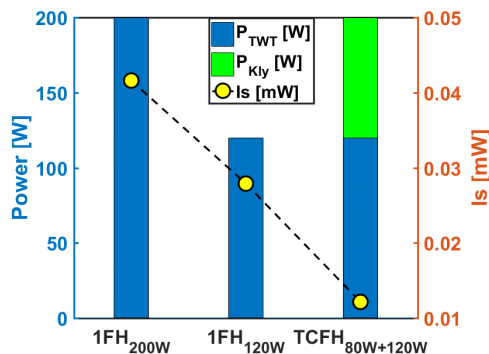


Figure 7: histograms represent the RF power provided in single-frequency or double-frequency mode by the two generators. Yellow dots are the relative I_s factor. The combination of two frequencies is in this case more stable than a single one, even if the power is increased of almost a factor 2.

RF Spectra in 2FH – Power Balance @ 13.8 GHz + 14.25 GHz @ 200W

RF spectra vs power balance plot (Fig. 8) shows that instabilities increase very much for higher power of TWT. This result was somehow expected since the TWT frequency 13.8GHz is much unstable due to the fact that B_{min}/B_{ECR} value is closer to the instability threshold than the Klystron frequency.

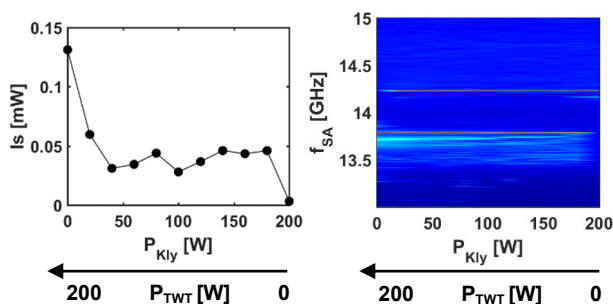


Figure 8: Power Balance scan in case of TCFH: instability strength increases at increasing TWT power, as confirmed by the microwave spectrum depicted on the right.

CONCLUSION AND PERSPECTIVES

The paper reports on an experimental campaign aiming at investigate the impact of TCFH on the plasma stability. At the B_{min}/B_{ECR} values that are typical of the ATOMKI ECRIS, the plasma is prone to kinetic instability development for any frequency we used in the range 13.6-14.5 GHz. The measurements show the TCFH can totally suppress the instabilities if the power balance is suitable. The I_s parameter, that has been evaluated to quantitatively provide the strength of the instability, has been directly correlated to operative parameters (RF power and frequency) in single and double-frequency heating modes, showing a significant drop (one order of magnitude) during TCFH operations, at any second frequency.

REFERENCES

- [1] R. Geller, *Electron Cyclotron Resonance Ion Sources and ECR Plasmas*, Bristol, UK: J W Arrowsmith Ltd, 1996
- [2] S. Gammino, D. Mascali, L. Celona, F. Maimone, G. Ciavola, “Consideration on the role of the magnetic field gradient in ECR ion sources and build-up of hot electron component”, *Plasma Sources Sci. Technol.* vol. 18 (2009), doi:10.1088/0963-0252/18/4/045016
- [3] O. Tarvainen, I. Izotov, D. Mansfeld, V. Skalyga, S. Golubev, Kalvas, H. Koivisto, J. Komppula, R. Kronholm, J. Laulainen and V. Toivanen, “Beam current oscillations driven by cyclotron instabilities in a minimum-B electron cyclotron resonance ion source plasma”, *Plasma Sources Sci. Technol.* vol. 23 (2014), doi:10.1088/0963-0252/23/2/025020
- [4] S. Biri, et al., “Multi diagnostic setup at the Atomki-ECRIS to investigate the two-close-frequency heating phenomena”, presented at the 23rd *International Workshop on ECRIS, Catania, Italy, Sept. 2018, this proceeding*
- [5] R. Racz, et al., “Effect of the Two-Close-Frequency Heating to the extracted ion beam and to the X-ray flux emitted by the ECR plasma”, presented at the 23rd *International Workshop on ECRIS, Catania, Italy, Sept. 2018, this proceeding*

List of Authors

Bold papercodes indicate primary authors; ~~crossed-out~~ papercodes indicate 'no submission'

— A —		Chen, J.E.	TUP26
Abegglen, F.P.	MOC2	Chines, F.	MOB3, THA1, THA3
Abhangi, M.	THC2	Cirrone, G.A.P.	TUP02
Adler, L.	MOB2, TUP01	Comunian, M.	TUP06
Agnello, G.	THA3	Conte, A.	TUP06
Alexandrenko, V.V.	TUP22	Cosentino, L.	TUP02
Altana, C.	WEA4	Cully, J.B.	MOC1
Andreev, V.	TUP06	Cuttone, G.	TUP02
Angot, J.	MOC1, MOB3, MOC4, TUP09		
Annaluru, A.T.	MOC4, MOB5	— D —	
Arbelaez, D.	TUP10	D'Agata, A.	THA3
Arje, J.	MOC2	De Franco, A.	MOB2, TUP01
Avila, G.	FRA3	De Lazzari, M.	TUP06
		Del Zanna, G.	FRA3
— B —		Delahaye, P.	MOC4, MOC5
Bajeat, O.	MOC4	Delferrière, O.	TUP04
Bandyopadhyay, M.	THC2	Dubois, M.	MOC4, MOC5
Barue, C.	WEB2		
Baylac, M.A.	MOC1, MOC3	— E —	
Beijers, J.P.M.	TUP19	Ecker, F.	MOB2, TUP01
Bellan, L.	TUP06	Efremov, A.A.	WEB1, THC4
Bellato, M.A.	TUP06		
Benitez, J.Y.	MOA2, FRA2, FRB1	— F —	
Berezov, R.	TUP04	Fang, X.	TUA5, TUB1, THA4
Bermudez, J.	TUP06	Farinon, F.	MOB2, TUP01
Bhaskar, S.B.B.	MOC1	Fatkullin, R.	THC4
Biri, S.	TUP14, WEA5, FRB2	Feng, Y.C.	TUB1 , THA4
Bisoffi, G.	TUP06	Fils, J.	TUP04
Bogomolov, S.L.	TUP22, WEB1, THC4	Francescon, F.	TUP06
Bokhanov, A.	MOB1	Freeman, S.	MOB4
Bolzon, B.	TUP04	Frigot, R.	MOC4
Bonanno, V.P.	TUP02	Fujimaki, M.	TUA3
Bondarchenko, A.E.	TUP22, WEB1, THC4	Fujita, T.F.	TUA2
Bonny, L.	TUP09	Fukunishi, N.	TUA3
Bortolato, D.	TUP06		
Brandenburg, S.	TUP19	— G —	
		Galatà, A.	TUB2, TUB3, TUP06, TUP14, TUP27, WEA5, FRB2
— C —		Gallo, C.S.	TUB3, TUP27
Calabrese, G.	THA1 , THA3	Gambino, N.	MOB2, TUP01
Caliri, C.	TUP14, FRB2	Gammino, S.	MOB3, TUB2, TUP11, TUP12, TUP13, TUP14, TUP25, WEA4, WEA5, THA1, FRA3, FRB2
Castro, G.	MOB3, TUB2, TUP11, TUP12, TUP13, TUP14, TUP25, WEA4, WEA5, THA1, FRA3, FRB2		
Catalano, R.	TUP02	Garcia Fajardo, L.	TUP10
Celona, L.	MOB3, TUB2, TUP11, TUP12, TUP13, TUP14, TUP25, WEA4, WEA5, THA1, THA3, FRA3, FRB2	Gaubert, G.	MOB4
Chauvin, N.	TUP04	Gauthier, Y.	TUP04
		Gelain, F.	TUP06
		Giarrusso, M.	FRA3

Content from this work may be used under the terms of the CC BY 3.0 licence (© 2018). Any distribution of this work must maintain attribution to the author(s), title of the work, publisher, and DOI.

Glyavin, M.Yu.	M0B1
Golubev, S.	M0B1, TUP20, THA2, THA5
Good, J.	TUB4
Guidoboni, G.	M0B2, TUP01
Guo, J.W.	TUA5, TUB1, WEA2, THA4
Guo, Z.Y.	TUP26

— H —

Hauser, T.	M0B4
Higurashi, Y.	TUA1, TUA3, WEB4
Hollinger, R.	TUP04
Hormigos, S.	MOC4
Huang, W.	TUA5, WEB3, THA4

— I —

Inaniwa, T.	TUP03
Isherwood, B.C.	TUP15, WEA3
Ivanov, I.A.	TUP22
Iwashita, Y.	THC3
Iwata, Y.	TUP03
Izotov, I.	M0B1, TUP20, WEA1, THA2, THA5

— J —

Jacob, J.	MOC1, MOC3, WEB2
Jacob, J.	TUP09
Jardin, P.	MOC4, MOC5, MOC6
Jia, Z.H.	THA4
Jiang, Y.X.	TUP26
Jones, B.N.	TUP19

— K —

Kalvas, T.	MOA3, WEA1, FRA1
Kamalou, O.	MOC4, MOC5
Kamigaito, O.	TUA3
Kazakov, M.Yu.	M0B1
Kearney, K.	M0B4
Kitagawa, A.	TUA2, TUP03
Koeverer, T.	TUP21
Koivisto, H. A.	MOA3, WEA1, FRA1
Koloberdin, M.V.	TUP22
Kostyukhov, Yu.K.	THC4
Kozin, S.G.	TUP22
Kremers, H.R.	TUP19
Kronholm, R.J.	MOA3, WEA1, FRA1
Küchler, D.	TUP21, TUP23
Kumagai, K.	TUA3
Kumar, R.	THC2
Kumar, R.K.	THC2
Kurakhmedov, A.E.	TUP22
Kurfürst, C.	M0B2, TUP01
Kuzmenkov, K.I.	WEB1, THC4

— L —

Lamy, T.	MOC1, MOC3
Landi, E.	FRA3
Lang, R.	TUP09
Lanzalone, G.L.	WEA4
Lapin, R.L.	M0B1, TUP20, THA2, THA5
Lecomte, P.	MOC4
Leduc, A.	WEB2
Leduc, A.	MOC1, TUP09
Leitner, D.	TUP10, TUP15
Lemagnen, F.	WEB2
Leonardi, O.	M0B3, TUP12, THA1, THA3
Leone, F.	FRA3
Li, J.B.	TUA5, WEA2
Li, L. B.	TUA5, TUB1, WEA2
Li, L. X.	TUA5, TUB1
Li, X.X.	THA4
Litrico, G.L.	WEA4
Loginov, V.N.	TUP22, WEB1, THC4
Lu, W.	MOA2, TUA5, TUB1, WEA2, WEB3, THA4
Lyneis, C.M.	MOA2, FRA2, FRB1

— M —

Ma, H.Y.	TUA5
Ma, T.H.	TUP26
Machicoane, G.	TUA4, WEA3, TUP15
Mäder, J.	TUP09
Maimone, F.	TUP09
Manno, G.	THA1, THA3
Mansfeld, D.	WEA1
Marcato, D.	TUP06
Marletta, S.	THA3
Mascali, D.	M0B3, TUB2, TUB3, TUP02, TUP11, TUP12, TUP13, TUP14, TUP25, TUP27, WEA4, WEA5, THA1, FRA3, FRB2
Maugeri, A.	THA3
Maunoury, L.	MOC4, MOC5, MOC6, WEB2
Mauro, G.	TUB2
May, D.P.	MOC2
Mazzaglia, M.	M0B3, TUB2, TUP11, TUP12, TUP13, TUP14, TUP25, WEA4, WEA5, THA1, FRA3, FRB2
McIntyre, C.	M0B4
Michel, C.	MOC6
Miglioranza, M.O.	TUP06
Miracoli, R.	TUP13, TUP25, WEA4
Miraglia, A.	TUP12, THA1, THA3
Mironov, V.	TUP22, WEB1
Mitchell, R.	TUB4

Mizushima, K. TUP03
 Moio, M.F. TUP06
 Morozkin, M.V. MOB1
 Munari, M. FRA3
 Munaron, E. TUP06
 Muoio, A.M. WEA4
 Muramatsu, M. TUA2, TUP03
 Mustafin, D.A. TUP22
 Musumeci, M.S. TUP02
 Myalski, S. MOB2, TUP01

— N —

Nagatomo, T. TUA1, TUA3
 Nakagawa, T. TUA1, TUA3, WEB4
 Naselli, E. TUB2, TUP11, TUP12,
 TUP13, TUP25, WEA4,
 FRA3, FRB2, TUP14,
 WEA5
 Neben, D.E. TUP15, WEA3
 Neri, L. MOB3, TUP12, THA1,
 THA3

— O —

O'Neil, M. TUP23
 Ohnishi, J. TUA1, TUA3, WEB4
 Osmond, O. MOC4
 Ouchi, F. TUP03

— P —

Pálinkás, J. FRB2, TUP14, WEA5
 Papaleo, R. THA3
 Patchakui, P.T. TUP09
 Pavinato, S. TUP06
 Pedretti, D. TUP06
 Penescu, L.C. TUP01, MOB2
 Peng, S.X. TUP26
 Perduk, Z. TUP14, WEA5, FRB2
 Peschard, G. MOC4
 Petringa, G. TUP02
 Pisent, A. TUP06
 Pivi, M.T.F. MOB2, TUP01
 Pozdeyev, G. WEA3
 Prestemon, S. TUP10
 Preveraud, N. MOC3
 Proyavin, M.D. MOB1
 Pugachev, D.K. THC4
 Puglia, S.M.R. TUP02

— Q —

Qian, C. WEB3, THA4

— R —

Rapisarda, G.G. TUP02
 Razin, S. MOB1, TUP20, THA2,

RĄjcz, R. THA5
 Reitano, R. TUP14, WEA5, FRB2
 Ren, H.T. TUP12, TUP25
 Ren, H.T. TUP26
 Retailleau, B. MOC4
 Rifuggiato, D. TUP02
 Roetta, M. TUP06
 Romano, F.P. TUP14, FRB2
 Roncolato, C. R. TUP06
 Rossignoli, M. TUP06

— S —

Sabbi, G.L. TUP10
 Sakamoto, N. TUA3
 Salou, P. MOB4
 Salvatore, S.T. TUP02, WEA4
 Sambayev, Y.K. TUP22
 Sasano, T. TUP03
 Sauce, Y. TUP04
 Savalle, A. MOC4, MOC5
 Schmitzer, C. MOB2, TUP01
 Seminara, A. THA3
 Sevarese, G. TUP06
 Shanks, R.P. MOB4
 Shaposhnikov, R.A. MOB1, TUP20, THA2,
 THA5
 Shen, T. TUP10
 Shen, Z. TUA5, TUB1
 Shiraishi, T. TUP03
 Sidorov, V. THA2
 Siliato, D. THA3
 Skalyga, V. MOB1, TUP20, WEA1,
 THA2, THA5
 Sole, P. MOC1, MOC3, WEB2
 Sole, P. TUP09
 Sorbello, G. TUB2, TUP11
 Stefan, S.B. TUP25
 Stetson, J.W. TUP15, WEA3
 Strašák, I. MOB2, TUP01
 Sun, J. TUP26
 Sun, L.T. MOA1, TUA5, TUB1,
 WEA2, WEB3, THA4,
 THC1
 Sundquist, M. MOB4
 Suzuki, T. TUP03

— T —

Tabacaru, G. MOC2
 Takahashi, K. TUP03
 Takeuchi, Y. THC3
 Tarvainen, O.A. MOA3, MOC3, WEA1,
 THA5, FRA1
 Thomas, J.C. MOC4
 Thuillier, T. MOC1, MOC3, TUP09,
 WEB2
 Tinschert, K. TUP09

Content from this work may be used under the terms of the CC BY 3.0 licence (© 2018). Any distribution of this work must maintain attribution to the author(s), title of the work, publisher, and DOI.

Tobos, L. **TUP15**
 Todd, D.S. **MOA2, FRA2, FRB1**
 Toivanen, V. **MOC4, MOC5, MOC6, TUP21, TUP23**
 Tongu, H. **THC3**
 Torrisi, G. **MOB3, TUB2, TUB3, TUP11, TUP12, TUP13, TUP14, TUP25, TUP27, WEA4, WEA5, THA1, FRB2**
 Traykov, E.K. **MOC4, MOC5**
 Tsvetkov, A.I. **MOB1**
 Tuske, O. **TUP04**

— U —

Uchiyama, A. **TUA3**
 Ujic, P. **MOC4, MOC5**
 Ursel, U.F. **TUP25**

— V —

Vala, S.J. **THC2**
 van Rooyen, D. **TUP09**
 Vondrasek, R.C. **TUP07**

— W —

Wang, H. **THA4**
 Wastl, A. **MOB2, TUP01**
 Wen, J.M. **TUP26**
 Wu, Q. **THC1**
 Wu, W.B. **TUP26**

— X —

Xie, D. **MOA2, FRA2, FRB1**

— Y —

Yang, Y. **TUA5, THA4**

— Z —

Zdorovets, M.V. **TUP22**
 Zhang, J.F. **TUP26**
 Zhang, T. **TUP26**
 Zhang, W.H. **TUA5, TUB1**
 Zhang, X.Z. **TUA5, TUB1, WEA2, WEB3, THA4**
 Zhao, H.W. **MOA1, TUA5, TUB1, WEA2, THA4, THC1**

Institutes List

Abstract Landscapes

Montpellier, France
• [Penescu, L.C.](#)

AEC

Chiba, Japan
• [Ouchi, F.](#)
• [Sasano, T.](#)
• [Shiraishi, T.](#)
• [Suzuki, T.](#)
• [Takahashi, K.](#)

ANL

Argonne, Illinois, USA
• [Vondrasek, R.C.](#)

ATOMKI

Debrecen, Hungary
• [Biri, S.](#)
• [Perduk, Z.](#)
• [Rajcz, R.](#)

Catania University

Catania, Italy
• [Naselli, E.](#)

CEA/DRF/IRFU

Gif-sur-Yvette, France
• [Delferriere, O.](#)

CERN

Geneva, Switzerland
• [Koevener, T.](#)
• [Kuchler, D.](#)
• [O'Neil, M.](#)

Cryogenic Ltd

Acton, London, United Kingdom
• [Good, J.](#)
• [Mitchell, R.](#)

DU

Debrecen, Hungary
• [Palinkas, J.](#)

EBG MedAustron

Wr. Neustadt, Austria
• [Adler, L.](#)
• [De Franco, A.](#)
• [Ecker, F.](#)
• [Farinon, F.](#)

- [Gambino, N.](#)
- [Guidoboni, G.](#)
- [Kurfurst, C.](#)
- [Myalski, S.](#)
- [Penescu, L.C.](#)
- [Pivi, M.T.F.](#)
- [Schmitzer, C.](#)
- [Strasik, I.](#)
- [Wastl, A.](#)

ESO

Garching bei Muenchen, Germany
• [Avila, G.](#)

ESS Bilbao

Zamudio, Spain
• [Miracoli, R.](#)

FRIB

East Lansing, Michigan, USA
• [Machicoane, G.](#)
• [Pozdeyev, G.](#)

GANIL

Caen, France
• [Annaluru, A.T.](#)
• [Bajeat, O.](#)
• [Barue, C.](#)
• [Delahaye, P.](#)
• [Dubois, M.](#)
• [Frigot, R.](#)
• [Hormigos, S.](#)
• [Jardin, P.](#)
• [Kamalou, O.](#)
• [Lecomte, P.](#)
• [Leduc, A.](#)
• [Lemagnen, F.](#)
• [Maunoury, L.](#)
• [Michel, C.](#)
• [Osmond, O.](#)
• [Peschard, G.](#)
• [Retailleau, B.](#)
• [Savalle, A.](#)
• [Thomas, J.C.](#)
• [Toivanen, V.](#)
• [Ujic, P.](#)

GSI

Darmstadt, Germany
• [Berezov, R.](#)
• [Fils, J.](#)
• [Hollinger, R.](#)
• [Lang, R.](#)
• [Mader, J.](#)
• [Maimone, F.](#)

- Patchakui, P.T.
- Tinschert, K.
- van Rooyen, D.

IAP/RAS

Nizhny Novgorod, Russia

- Bokhanov, A.
- Glyavin, M.Yu.
- Golubev, S.
- Izotov, I.
- Kazakov, M.Yu.
- Lapin, R.L.
- Mansfeld, D.
- Morozkin, M.V.
- Proyavin, M.D.
- Razin, S.
- Shaposhnikov, R.A.
- Sidorov, V.
- Skalyga, V.
- Tsvetkov, A.I.

IBAM-CNR

Catania, Italy

- Romano, F.P.

IMP/CAS

Lanzhou, People's Republic of China

- Fang, X.
- Feng, Y.C.
- Guo, J.W.
- Huang, W.
- Jia, Z.H.
- Li, J.B.
- Li, L. B.
- Li, L. X.
- Li, X.X.
- Lu, W.
- Ma, H.Y.
- Qian, C.
- Shen, Z.
- Sun, L.T.
- Wang, H.
- Wu, Q.
- Yang, Y.
- Zhang, W.H.
- Zhang, X.Z.
- Zhao, H.W.

INAF-OACT

Catania, Italy

- Leone, F.
- Munari, M.

INFN- Sez. di Padova

Padova, Italy

- Bellato, M.A.

INFN/LNL

Legnaro (PD), Italy

- Bellan, L.
- Bermudez, J.
- Bisoffi, G.
- Bortolato, D.
- Comunian, M.
- Conte, A.
- De Lazzari, M.
- Francescon, F.
- Galatà, A.
- Gallo, C.S.
- Gelain, F.
- Marcato, D.
- Miglioranza, M.O.
- Mo시오, M.F.
- Munaron, E.
- Pavinato, S.
- Pedretti, D.
- Pisent, A.
- Roetta, M.
- Roncolato, C. R.
- Rossignoli, M.
- Sevese, G.

INFN/LNS

Catania, Italy

- Agnello, G.
- Altana, C.
- Bonanno, V.P.
- Calabrese, G.
- Caliri, C.
- Castro, G.
- Catalano, R.
- Celona, L.
- Chines, F.
- Cirrone, G.A.P.
- Cosentino, L.
- Cuttone, G.
- D'Agata, A.
- Gammino, S.
- Giarrusso, M.
- Lanzalone, G.L.
- Leonardi, O.
- Litrico, G.L.
- Manno, G.
- Marletta, S.
- Mascali, D.
- Maugeri, A.
- Mauro, G.
- Mazzaglia, M.
- Miraglia, A.
- Muoio, A.M.
- Musumeci, M.S.
- Naselli, E.
- Neri, L.
- Papaleo, R.
- Petringa, G.
- Puglia, S.M.R.
- Rapisarda, G.G.
- Reitano, R.

- Rifuggiato, D.
- Romano, F.P.
- Salvatore, S.T.
- Seminara, A.
- Siliato, D.
- Sorbello, G.
- Torrisi, G.

INP NNC RK

Almaty, Kazakhstan

- Alexandrenko, V.V.
- Ivanov, I.A.
- Koloberdin, M.V.
- Kozin, S.G.
- Kurakhmedov, A.E.
- Mustafin, D.A.
- Sambayev, Y.K.
- Zdorovets, M.V.

Institute for Plasma Research

Bhat, Gandhinagar, India

- Abhangi, M.
- Bandyopadhyay, M.
- Kumar, R.K.
- Kumar, R.
- Vala, S.J.

IPHC

Strasbourg Cedex 2, France

- Traykov, E.K.

IRFU, CEA, University Paris-Saclay

Gif-sur-Yvette, France

- Bolzon, B.
- Chauvin, N.
- Gauthier, Y.
- Sauce, Y.
- Tuske, O.

ITEP

Moscow, Russia

- Andreev, V.
- Fatkullin, R.

JINR

Dubna, Moscow Region, Russia

- Bogomolov, S.L.
- Bondarchenko, A.E.
- Efremov, A.A.
- Kostyukhov, Yu.K.
- Kuzmenkov, K.I.
- Loginov, V.N.
- Mironov, V.
- Pugachev, D.K.

JYFL

Jyväskylä, Finland

- Kalvas, T.
- Koivisto, H. A.
- Kronholm, R.J.
- Tarvainen, O.A.

KVI-CART

Groningen, The Netherlands

- Jones, B.N.

KVI

Groningen, The Netherlands

- Beijers, J.P.M.
- Brandenburg, S.
- Kremers, H.R.

Kyoto ICR

Uji, Kyoto, Japan

- Iwashita, Y.
- Takeuchi, Y.
- Tongu, H.

LBNL

Berkeley, California, USA

- Arbelaez, D.
- Benitez, J.Y.
- Garcia Fajardo, L.
- Leitner, D.
- Lyneis, C.M.
- Prestemon, S.
- Sabbi, G.L.
- Shen, T.
- Todd, D.S.
- Xie, D.

LPSC

Grenoble Cedex, France

- Angot, J.
- Baylac, M.A.
- Bhaskar, S.B.B.
- Bonny, L.
- Cully, J.B.
- Jacob, J.
- Lamy, T.
- Leduc, A.
- Preveraud, N.
- Sole, P.
- Thuillier, T.

MPI/IPP

Garching, Germany

- Stefan, S.B.
- Ursel, U.F.

MSU

East Lansing, Michigan, USA
• [Isherwood, B.C.](#)

National Electrostatics Corp.

Madison, Wisconsin, USA
• [Hauser, T.](#)
• [Kearney, K.](#)
• [Sundquist, M.](#)

NIRS

Chiba-shi, Japan
• [Inaniwa, T.](#)
• [Iwata, Y.](#)
• [Mizushima, K.](#)

NSCL

East Lansing, Michigan, USA
• [Leitner, D.](#)
• [Machicoane, G.](#)
• [Neben, D.E.](#)
• [Stetson, J.W.](#)
• [Tobos, L.](#)

PANTECHNIK

Bayeux, France
• [Gaubert, G.](#)
• [Salou, P.](#)

PKU

Beijing, People's Republic of China
• [Chen, J.E.](#)
• [Guo, Z.Y.](#)
• [Jiang, Y.X.](#)
• [Ma, T.H.](#)
• [Peng, S.X.](#)
• [Ren, H.T.](#)
• [Sun, J.](#)
• [Wen, J.M.](#)
• [Wu, W.B.](#)
• [Zhang, J.F.](#)
• [Zhang, T.](#)

QST-NIRS

Chiba, Japan
• [Fujita, T.F.](#)
• [Kitagawa, A.](#)
• [Muramatsu, M.](#)

RIKEN Nishina Center

Wako, Japan
• [Fujimaki, M.](#)
• [Fukunishi, N.](#)
• [Higurashi, Y.](#)
• [Kamigaito, O.](#)
• [Kumagai, K.](#)

- [Nagatomo, T.](#)
- [Nakagawa, T.](#)
- [Ohnishi, J.](#)
- [Sakamoto, N.](#)
- [Uchiyama, A.](#)

Scottish Universities Environmental Research Centre

East Kilbride, United Kingdom
• [Freeman, S.](#)
• [McIntyre, C.](#)
• [Shanks, R.P.](#)

Texas A&M University Cyclotron Institute

College Station, Texas, USA
• [Arje, J.](#)
• [May, D.P.](#)

Texas A&M University, Cyclotron Institute

College Station, Texas, USA
• [Abegglen, F.P.](#)
• [Tabacaru, G.](#)

University Debrecen

Debrecen, Hungary
• [Pálinkás, J.](#)

University of Cambridge

Cambridge, United Kingdom
• [Del Zanna, G.](#)

University of Catania

Catania, Italy
• [Sorbello, G.](#)

University of Michigan

Ann Arbor, Michigan, USA
• [Landi, E.](#)

Università degli Studi di Catania

Catania, Italy
• [Leone, F.](#)
• [Reitano, R.](#)

UNN

Nizhny Novgorod, Russia
• [Skalyga, V.](#)

List of Attendees

<i>NAME</i>	<i>INSTITUTE</i>	<i>COUNTRY</i>
<i>Gambino Nadia</i>	EBG MedAustron, Wr., Neustadt	Austria
<i>Myalski Szymon</i>	EBG MedAustron, Wr. Neustadt	Austria
<i>Guo Junwei</i>	IMP-CAS, Lanzhou	China
<i>Li Jibo</i>	IMP-CAS, Lanzhou	China
<i>Liu Weitao</i>	Western Superconducting Technologies, Xi'an	China
<i>Lu Wang</i>	IMP-CAS, Lanzhou	China
<i>Peng Shixiang</i>	PKU, Beijing	China
<i>Qian Chen</i>	IMP-CAS, Lanzhou	China
<i>Rácz Richard</i>	ATOMKI, Debrecen	China
<i>Sun Liangting</i>	IMP-CAS, Lanzhou	China
<i>Wu Qi</i>	IMP-CAS, Lanzhou	China
<i>Wu Wenbin</i>	PKU, Beijing	China
<i>Zhang Jingfeng</i>	PKU, Beijing	China
<i>Zhao Hongwei</i>	IMP-CAS, Lanzhou	China
<i>Koivisto Hannu</i>	JYFL, Jyväskylä	Finland
<i>Kronholm Risto</i>	JYFL, Jyväskylä	Finland
<i>Kalvas Taneli</i>	JYFL, Jyväskylä	Finland
<i>Annaluru Arun tejaswee</i>	GANIL, Caen	France
<i>Delferrière Olivier</i>	CEA, Saclay	France
<i>Gaubert Gabriel</i>	PANTECHNIK, Bayeux	France
<i>Julien Angot</i>	LPSC, Grenoble	France
<i>Leduc Alexandre</i>	LPSC, Grenoble	France
<i>Maunoury Laurent</i>	GANIL, Caen	France
<i>Salou Pierre</i>	PANTECHNIK, Bayeux	France
<i>Thomas Thuillier</i>	LPSC, Grenoble	France
<i>Toivanen Ville</i>	GANIL, Caen	France
<i>Tuske Olivier</i>	CEA, Saclay	France
<i>Maimone Fabio</i>	GSI, Darmstadt	Germany
<i>Tinschert Klaus</i>	GSI, Darmstadt	Germany
<i>Peter Spaedtke</i>	GSI, Darmstadt	Germany
<i>Biri Sandor</i>	ATOMKI, Debrecen	Hungary
<i>Vala Sudhirsinh</i>	Institute for Plasma Research, Bhat, Gandhinagar	India
<i>Alessio Galatà</i>	INFN-LNL, Legnaro	Italy
<i>Andrea Miraglia</i>	INFN-LNS, Catania	Italy
<i>Antonio Massara</i>	INFN-LNS, Catania	Italy
<i>Concetto Pocorobba</i>	UMAS TECHNOLOGY, Piazza Armerina	Italy

Content from this work may be used under the terms of the CC BY 3.0 licence (© 2018). Any distribution of this work must maintain attribution to the author(s), title of the work, publisher, and DOI.

<i>NAME</i>	<i>INSTITUTE</i>	<i>COUNTRY</i>
<i>Cristian Pocerobba</i>	UMAS TECHNOLOGY, Piazza Armerina	Italy
<i>David Mascali</i>	INFN-LNS, Catania	Italy
<i>Davide Siliato</i>	INFN-LNS, Catania	Italy
<i>Eugenia Naselli</i>	INFN-LNS, Catania	Italy
<i>Francesco Chines</i>	INFN-LNS, Catania	Italy
<i>Franco Leone</i>	INAF, Catania	Italy
<i>Gianni Manno</i>	INFN-LNS, Catania	Italy
<i>Gino Sorbello</i>	Università di Catania, Catania	Italy
<i>Giorgio Mauro</i>	INFN-LNS, Catania	Italy
<i>Giovanni Di Bartolo</i>	CRYOGENIC, Italy	Italy
<i>Giuseppe Calabrese</i>	INFN-LNS, Catania	Italy
<i>Giuseppe Castro</i>	INFN-LNS, Catania	Italy
<i>Giuseppe Gallo</i>	INFN-CT, Catania	Italy
<i>Giuseppe Torrisi</i>	INFN-LNS, Catania	Italy
<i>Lorenzo Neri</i>	INFN-LNS, Catania	Italy
<i>Loreto Di Donato</i>	Università di Catania, Catania	Italy
<i>Luciano Calabretta</i>	INFN-LNS, Catania	Italy
<i>Luigi Celona</i>	INFN-LNS, Catania	Italy
<i>Luigi Cosentino</i>	INFN-LNS, Catania	Italy
<i>Marco Pullia</i>	CNAO, Pavia	Italy
<i>Maria Mazzaglia</i>	INFN-LNS, Catania	Italy
<i>Marina Giarrusso</i>	INFN-LNS, Catania	Italy
<i>Salvatore Marletta</i>	INFN-LNS, Catania	Italy
<i>Maurizio Castro</i>	INFN-LNS, Catania	Italy
<i>Onella Leonardi</i>	INFN-LNS, Catania	Italy
<i>Paolo Nicotra</i>	Si.a.tel, Catania	Italy
<i>Pietro Pisciotta</i>	INFN-LNS, Catania	Italy
<i>Salvo Marleta</i>	INFN-LNS, Catania	Italy
<i>Salvo Tudisco</i>	INFN-LNS, Catania	Italy
<i>Sandra Di Martino</i>	Si.a.tel, Catania	Italy
<i>Santo Gammino</i>	INFN-LNS, Catania	Italy
<i>Vincenza Bonanno</i>	INFN-LNS, Catania	Italy
<i>Riccardo Papaleo</i>	INFN-LNS, Catania	Italy
<i>Iwashita Yoshihisa</i>	Kyoto ICR, Kyoto	Japan
<i>Nagatomo Takashi</i>	RIKEN Nishina Center, Wako	Japan
<i>Bichu Subhash Bhasi</i>	LPSC, Grenoble	Russia
<i>Bhaskar</i>		
<i>Bogomolov Sergey</i>	JINR, Dubna	Russia
<i>Golubev Sergey</i>	IAP-RAS, Nizhny Novgorod	Russia
<i>Izotov Ivan</i>	IAP-RAS, Nizhny Novgorod	Russia

<i>NAME</i>	<i>INSTITUTE</i>	<i>COUNTRY</i>
<i>Lapin Roman</i>	IAP-RAS, Nizhny Novgorod	Russia
<i>Loginov Vladimir N.</i>	JINR, Dubna	Russia
<i>Mironov Vladimir</i>	JINR, Dubna	Russia
<i>Sebastiano Gallo</i>	INFN-LNL, Legnaro	Russia
<i>Shaposhnikov Roman</i>	IAP-RAS, Nizhny Novgorod	Russia
<i>Skalyga Vadim</i>	IAP-RAS, Nizhny Novgorod	Russia
<i>Lee Byoung Seob</i>	KBSI, Busan	South Korea
<i>Won Mi-Sook</i>	KBSI, Busan	South Korea
<i>Aleandro Gaecia Sosa</i>	ESS, Lund	Sweden
<i>Detlef Küchler</i>	CERN, Geneva	Switzerland
<i>Koeverer Toke</i>	CERN, Geneva	Switzerland
<i>Kremers Herman Robert</i>	KVI, Gronigen	The Netherlands
<i>Jeremy Good</i>	CRYOGENIC, London	UK
<i>Roger Mitchell</i>	CRYOGENIC, London	UK
<i>Benitez Janilee</i>	LBL, Berkeley	USA
<i>Bryan Isherwood</i>	MSU, East Lansing	USA
<i>Guillaume Machicoane</i>	FRIB, East Lansing	USA
<i>Leitner Daniela</i>	LBNL, Brekeley	USA
<i>May Donald</i>	TEXAS A&M, College Station	USA
<i>Todd Damon</i>	LBL, Berkeley	USA
<i>Vondrasek Richard</i>	ANL, Argonne	USA
<i>Xie Daniel</i>	LBL, Berkeley	USA